frontiers | Research Topics

Magma-rock and magma-mush interactions as fundamental processes of magmatic differentiation

Edited by
Anastassia Borisova, Wendy A. Bohrson and
Frank John Spera

Published in
Frontiers in Earth Science

ISSN 1664-8714
ISBN 978-2-8325-5299-5
DOI 10.3389/978-2-8325-5299-5

About Frontiers

Frontiers is more than just an open access publisher of scholarly articles: it is a pioneering approach to the world of academia, radically improving the way scholarly research is managed. The grand vision of Frontiers is a world where all people have an equal opportunity to seek, share and generate knowledge. Frontiers provides immediate and permanent online open access to all its publications, but this alone is not enough to realize our grand goals.

Frontiers journal series

The Frontiers journal series is a multi-tier and interdisciplinary set of open-access, online journals, promising a paradigm shift from the current review, selection and dissemination processes in academic publishing. All Frontiers journals are driven by researchers for researchers; therefore, they constitute a service to the scholarly community. At the same time, the *Frontiers journal series* operates on a revolutionary invention, the tiered publishing system, initially addressing specific communities of scholars, and gradually climbing up to broader public understanding, thus serving the interests of the lay society, too.

Dedication to quality

Each Frontiers article is a landmark of the highest quality, thanks to genuinely collaborative interactions between authors and review editors, who include some of the world's best academicians. Research must be certified by peers before entering a stream of knowledge that may eventually reach the public - and shape society; therefore, Frontiers only applies the most rigorous and unbiased reviews. Frontiers revolutionizes research publishing by freely delivering the most outstanding research, evaluated with no bias from both the academic and social point of view. By applying the most advanced information technologies, Frontiers is catapulting scholarly publishing into a new generation.

What are Frontiers Research Topics?

Frontiers Research Topics are very popular trademarks of the *Frontiers journals series*: they are collections of at least ten articles, all centered on a particular subject. With their unique mix of varied contributions from Original Research to Review Articles, Frontiers Research Topics unify the most influential researchers, the latest key findings and historical advances in a hot research area.

Find out more on how to host your own Frontiers Research Topic or contribute to one as an author by contacting the Frontiers editorial office: frontiersin.org/about/contact

Magma-rock and magma-mush interactions as fundamental processes of magmatic differentiation

Topic editors
Anastassia Borisova — Centre National de la Recherche Scientifique (CNRS), France
Wendy A. Bohrson — Colorado School of Mines, United States
Frank John Spera — University of California, Santa Barbara, United States

Citation
Borisova, A., Bohrson, W. A., Spera, F. J., eds. (2024). *Magma-rock and magma-mush interactions as fundamental processes of magmatic differentiation*.
Lausanne: Frontiers Media SA. doi: 10.3389/978-2-8325-5299-5

Table of contents

frontiers
in Earth Science

EDITORIAL
published: 25 March 2021
doi: 10.3389/feart.2021.665588

Editorial: Magma-Rock and Magma-Mush Interactions as Fundamental Processes of Magmatic Differentiation

Anastassia Y. Borisova[1,2]*, *Wendy A. Bohrson*[3] *and Frank J. Spera*[4]

[1]Géosciences Environnement Toulouse, GET/OMP (CNRS, UT3PS, CNES), Toulouse, France, [2]Geological Department, Lomonosov Moscow State University, Moscow, Russia, [3]Department of Geology and Geological Engineering, Colorado School of Mines, Golden, CO, United States, [4]Department of Earth Science and Earth Research Institute, University of California, Santa Barbara, CA, United States

Keywords: magma-rock interaction, magma-mush system, melt-rock interaction, melt-mush reaction, editorial

Editorial on the Research Topic

Magma-Rock and Magma-Mush Interactions as Fundamental Processes of Magmatic Differentiation

Virtually all terrestrial magmas, in all geodynamic settings, interact, sometimes profoundly, with surrounding rocks during their generation, residence at depth, and ascent through the asthenosphere and lithosphere. This results in inevitable interactions (exchanges of heat and matter) described as magma/melt-rock or magma/melt-mush interactions.

The major processes that happen when silicate magma is in contact with surrounding rocks were first defined in the pioneering studies of Bowen (1928) who identified two types of reactions: partial melting of the wall rocks and mineral dissolution in silicate melt. These reactions, which are ubiquitous during magma evolution, are commonly referred to as 'assimilation' (DePaolo, 1981), but may more broadly be called open-system processes. Assimilation, magma mixing, degassing, magma-rock and fluid-rock interactions control magma and fluid composition, metal and volatile contents, and magma physical-chemical properties and mobility. Consequently, the interactions influence volcanic activity, ore deposit formation, growth of the crust, and terrestrial climate. However, the degree, rates, and mechanisms of these reactions are poorly quantified owing to a lack of natural and experimental data and predictive models.

This research volume 'Magma-Rock and Magma-Mush Interactions as Fundamental Processes of Magmatic Differentiation' is devoted to documenting recent achievements in the fields of kinetics and thermodynamics as well as the petrologic and geochemical consequences of magma-rock, melt-rock, and melt-mush interactions. New observations of natural systems and laboratory experimental approaches that address how magma, melt, mush and rock interact are represented by seven articles (Baudouin and Parat; Borisova et al.; Boulanger et al.; Pistone et al.; Sanfilippo et al.; Tassara et al.; Borisova et al.). Examples of these types of interactions include mantle metasomatism (Baudouin and Parat), mineral-melt reaction in the planetary ultramafic protocrust (Borisova et al.) and in the terrestrial mantle (Borisova et al.; Sanfilippo et al.), melt-mush interaction in the crust (Pistone et al.), and thermal and chemical modification of preexisting mushy magma by intrusion of high specific enthalpy (enthalpy per unit mass) magma (Boulanger et al.). The melt-rock interactions also affect the redox state of percolating melts that may become enriched in ore-forming metals (Tassara et al.).

Edited and reviewed by:
Catherine Jeanne Annen,
University of Bristol, United Kingdom

***Correspondence:**
Anastassia Y. Borisova
anastassia.borisova@get.omp.eu

Specialty section:
This article was submitted to
Petrology,
a section of the journal
Frontiers in Earth Science

Received: *08 February 2021*
Accepted: *11 February 2021*
Published: *25 March 2021*

Citation:
Borisova AY, Bohrson WA and Spera FJ (2021) Editorial: Magma-Rock and Magma-Mush Interactions as Fundamental Processes of Magmatic Differentiation.
Front. Earth Sci. 9:665588.
doi: 10.3389/feart.2021.665588

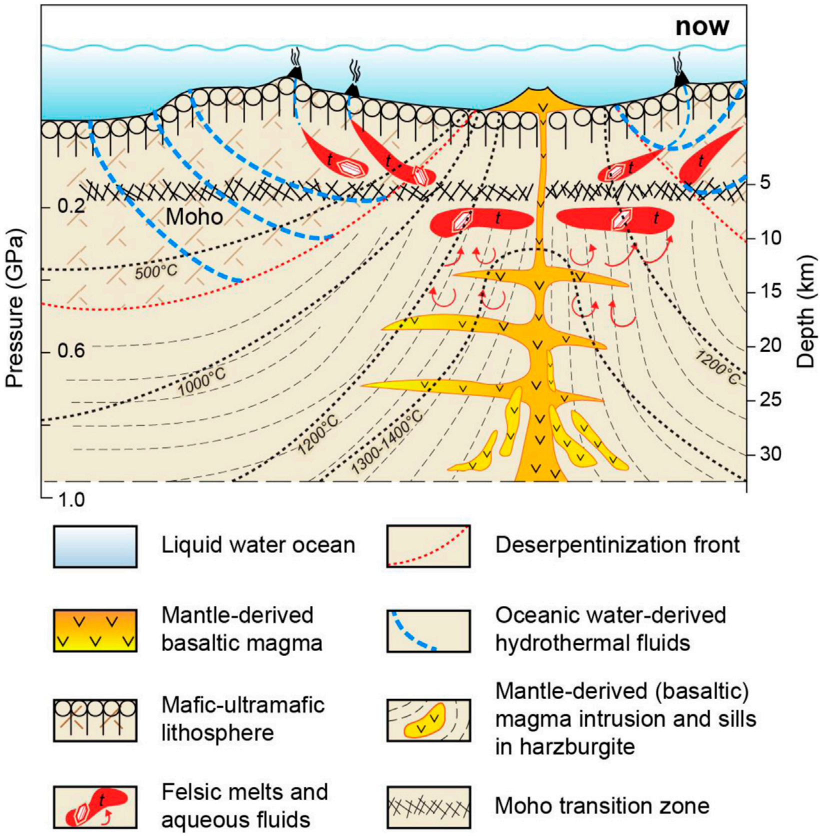

FIGURE 1 | Model of formation of the modern chromitite-dunite zone in the oceanic lithosphere after Borisova et al. Intrusion of mantle-derived magmas into hydrated (serpentinized) mantle initiated the dehydration process and prograde metamorphism. The dehydrated peridotite-basaltic melt interaction produces dunite-chromitite rock sequence associated to the felsic melts and aqueous fluids in the mantle and the mantle-crust transition zone. Borisova et al. demonstrate that similar mechanism of the hydrated peridotite-basaltic melt interaction and partial melting of the peridotite might happen and result in felsic crust formation on early steps of the protocrust evolution during Hadean and Noachian eons on Earth and Mars, respectively.

This spectrum of processes plays a major role in the composition, thickness, and age of the mantle lithosphere and the associated crust.

Experimental Studies of Melt-Rock and Melt-Mush Interactions

The experimental data represented by Borisova et al. suggest that the interaction of serpentinized peridotites (serpentinites) with basaltic liquids can lead to the formation of felsic liquids which may be the prototype of the first continental crust existing on Earth and Mars just after the solidification of their protocrusts and its interaction with seawater (Hadean and Noachian, respectively). The authors demonstrate that this interaction of serpentinized peridotites with basaltic liquids is responsible for the production of felsic crust at depths less than 10 km in geodynamic situations independent of oceanic plate subduction (**Figure 1**). This scenario provides a mechanism for crust generation in accordance with the existing models of pre plate tectonic processes on Earth and Mars.

Borisova et al. have experimentally established the physical-chemical conditions which produce bulk assimilation of serpentinized rocks by basaltic liquids, the formation of magmas generated by melting of serpentinites, and processes which occur along the petrologic Moho between the mantle and the oceanic crust. The generation of depleted MORB melts, high-Mg-Cr cumulates, chromitites, and oceanic boninites and andesites is reliably explained by the efficient reaction of initially anhydrous basaltic melts with serpentinized lithospheric mantle. The work by Borisova et al. challenges the routine interpretation of variations in chemical and isotopic composition of oceanic lavas (e.g., MORB and OIB) solely in terms of deep mantle plume source heterogeneities or/and mechanism of partial melting. Possible shallow-level interactions should not be neglected.

Pistone et al. provided new experimental data applicable to felsic melt and gas mobilization during magma solidification.

These processes may play a major role in magma fractionation at shallow depths (<10 km), where magmas stall rheologically and solidify. These experiments suggest that melt and gas extraction from cooling mushes increases in proximity to their solidus and can operate efficiently through gas filter pressing during cooling. Pistone et al. made estimates of the mechanisms and rates of segregation of gas-rich, crystal-poor magmas to form felsic dykes or eruptible systems feeding volcanoes.

Study of Natural Systems: Subcontinental Lithosphere Mantle (SCLM) Setting

Different physical and chemical parameters (e.g., pressure, oxygen fugacity, composition of magma, rock, or mush) provide fundamental controls on the dynamics and nature of magma-rock-mush interaction. For example, the final rock composition may be influenced, in part, by the degree of equilibrium reached between magma/melt and crystalline phases, and evidence of equilibrium-disequilibrium relationships will likely be preserved in the compositions of minerals rather than in the textures. Energy and mass transfer are also critical controls; for example, rock partial melting and associated contamination of magma are directly related to enthalpy produced during fractional crystallization of a magmatic system and the ability of anatectic melt to be transported into resident magma.

The study by Tassara et al. represents how the process of the melt-peridotite interaction controls the magma oxidation state and therefore the magma metallogenic fertility (Southern Patagonia). These authors demonstrate how changes in the redox state of magmas ascending through the SCLM can favor efficient extraction of Au and related metals from mantle sulfide minerals and melts. This study demonstrates that such interactions would exert a control on the localization of crustal provinces endowed with gold deposits. Thus, knowledge of the redox conditions prevailing in the SCLM as well as the mechanisms of the percolating melt-rock interactions are important for predicting the location and richness of metallogenic provinces (Au etc.).

Baudouin and Parat propose a physical-chemical model of the origin of phlogopite-olivine nephelenites erupted during the early stage rifting (North Tanzanian Divergence). Metasomatism via percolation of deep asthenospheric CO_2-rich alkaline magmas during their ascent produces a range of mantle rock compositions in the thick SCLM. The authors demonstrate that percolation of deep asthenospheric CO_2-rich alkaline magmas might explain phlogopite crystallization and production of such enigmatic lithologies such as glimmerite (consisting almost entirely of phlogopite). The process also affects the rheology of the Tanzanian lithosphere.

Study of Natural Systems: Mid-Oceanic Ridge Setting

Sanfilippo et al. present a natural example of melt channelization and the related melt-rock interaction by reactive porous flow (RPF) of basaltic melt through primitive mafic (olivine gabbro) crystal mush. This example is reported in apparently homogeneous olivine gabbro within a section of the plutonic footwall of the Atlantis Bank core complex on the Southwest Indian Ridge (International ocean discovery program hole U1473A). The cryptic changes toward more evolved compositions are impossible to detect on textural evidence alone. The authors detail that neither crystallization of trapped melt nor diffusion can account for the observed trace element signatures of the minerals. Major- and trace element mineral signatures reveal the occurrence of zoning profiles produced by a process of dissolution-precipitation under decreasing temperature conditions. The melt-rock reaction and reactive porous flow similar to that reported by Sanfillipo et al. may potentially be responsible for a significant proportion of crystal and melt modification in magma reservoirs.

Boulanger et al. reported magma reservoir formation and evolution at a slow-spreading center based on an example of ODP Hole 735B (Atlantis Bank, Southwest Indian Ridge). The authors performed *in situ* micro-analyses of the cumulative phases that document magma emplacement processes and provide evidence for ubiquitous reactive porous flow during differentiation. Boulanger et al. show that the whole section, and related geochemical unit, constitute a single magmatic reservoir, in which the lower unit is formed by stacked primitive sills formed by repeated recharge of primitive melts and melt-present deformation. The melt-rock interactions led to partial assimilation of the crystallizing primitive cumulates, and hybridization with their interstitial melts. The transport of the hybrid melts progressively collected in the overlying mushy part of the reservoir (upper unit) was governed by upward reactive porous flow, and progressive differentiation and accumulation of evolved melts at the top of the reservoir. Boulanger et al. attempted to address timescales for the formation of the reservoir by comparison with preexisting data and models for magma reservoir at slow-spreading ridges. These results provide the first integrated model for magma reservoir formation in the slow-spreading oceanic crust. The model illuminates new perspectives for the comprehension of mush-dominated igneous reservoirs dynamics in the oceanic lithosphere.

AUTHOR CONTRIBUTIONS

All authors listed have made a substantial, direct, and intellectual contribution to the work and approved it for publication.

REFERENCES

Bowen, N. L. (1928). *The evolution of the igneous rocks*. Princeton, NJ: Princeton University Press.

DePaolo, D. J. (1981). Trace element and isotopic effects of combined wallrock assimilation and fractional crystallization. *Earth Planet. Sci. Lett.* 53, 189–202. doi:10.1016/0012-821x(81)90153-9

Conflict of Interest: The authors declare that the research was conducted in the absence of any commercial or financial relationships that could be construed as a potential conflict of interest.

frontiers in Earth Science

ORIGINAL RESEARCH
published: 11 February 2020
doi: 10.3389/feart.2020.00029

Unraveling the Effects of Melt–Mantle Interactions on the Gold Fertility of Magmas

Santiago Tassara[1,2,3]*, Martin Reich[1,2], Brian A. Konecke[4,5], José María González-Jiménez[6], Adam C. Simon[4], Diego Morata[1,2], Fernando Barra[1,2], Adrian Fiege[7], Manuel E. Schilling[8] and Alexandre Corgne[8]

[1] Department of Geology and Andean Geothermal Centre of Excellence (CEGA), FCFM, Universidad de Chile, Santiago, Chile, [2] Millennium Nucleus for Metal Tracing Along Subduction, FCFM, Universidad de Chile, Santiago, Chile, [3] Department of Geology and Geophysics, Yale University, New Haven, CT, United States, [4] Department of Earth and Environmental Sciences, University of Michigan, Ann Arbor, MI, United States, [5] Astromaterials Research and Exploration Science (ARES), NASA Johnson Space Center, Houston, TX, United States, [6] Departamento de Mineralogía y Petrología, Facultad de Ciencias, Universidad de Granada, Granada, Spain, [7] Department of Earth and Planetary Sciences, American Museum of Natural History, New York, NY, United States, [8] Facultad de Ciencias, Instituto de Ciencias de la Tierra, Universidad Austral de Chile, Valdivia, Chile

OPEN ACCESS

Edited by:
Anastassia Borisova,
Centre National de la Recherche
Scientifique (CNRS), France

Reviewed by:
Elena F Bazarkina,
UPR2940 Institut Neel (NEEL), France
Anne-Sophie Bouvier,
Université de Lausanne, Switzerland
Zoltan Zajacz,
Université de Genève, Switzerland

***Correspondence:**
Santiago Tassara
santiago.tassara@yale.edu

Specialty section:
This article was submitted to
Geochemistry,
a section of the journal
Frontiers in Earth Science

Received: 15 October 2019
Accepted: 27 January 2020
Published: 11 February 2020

Citation:
Tassara S, Reich M, Konecke BA,
González-Jiménez JM, Simon AC,
Morata D, Barra F, Fiege A,
Schilling ME and Corgne A (2020)
Unraveling the Effects of Melt–Mantle
Interactions on the Gold Fertility
of Magmas. Front. Earth Sci. 8:29.
doi: 10.3389/feart.2020.00029

The oxidation state of the Earth's mantle and its partial melting products exert a key control on the behavior and distribution of sulfur and chalcophile and siderophile elements between the mantle and crust, underpinning models of ore deposit formation. Whether the oxidized nature of magmas is inherited from the asthenospheric mantle source or acquired during ascent and differentiation is vigorously debated, limiting our understanding of the mechanisms of extraction of sulfur and metals from the mantle. Here, we focused on the redox-sensitive behavior of sulfur in apatite crystallized from quenched alkaline basaltic melts preserved within a peridotite xenolith from the El Deseado Massif auriferous province in southern Patagonia. We took advantage of this unique setting to elucidate the redox evolution of melts during their ascent through the subcontinental lithospheric mantle (SCLM) and grasp the inner workings of the Earth's mantle during gold metallogenesis. Our data reveal that an initially reduced silicate melt (ΔFMQ -2.2 to -1.2) was oxidized to ΔFMQ between 0 and 1.2 during percolation and interaction with the surrounding peridotite wall-rock (ΔFMQ 0 to $+0.8$). This process triggered changes in sulfur speciation and solubility in the silicate melt, boosting the potential of the melt to scavenge ore metals such as gold. We suggest that large redox gradients resulting from the interaction between ascending melts and the surrounding mantle can potentially modify the oxidation state of primitive melts and enhance their metallogenic fertility. Among other factors including an enriched metal source and favorable geodynamic conditions, redox gradients in the mantle may exert a first-order control on the global-scale localization of crustal provinces endowed with gold deposits.

Keywords: melt–mantle interaction, oxidation state, apatite, XANES, gold, ore deposits

INTRODUCTION

The oxidation state of the Earth's mantle is a fundamental parameter on models that attempt to explain the formation of metallogenic provinces on a lithospheric scale (Mungall, 2002; Sillitoe, 2008; Richards, 2015). The oxygen fugacity (fO_2), as well as the contents of sulfur and chalcophile and siderophile elements (i.e., Au, Ag, Cu, Ni, Os, Ir, Ru, Rh, Pt, Pd, Re; *hereafter* "ore metals") of primitive melts associated with the formation of giant ore deposits are frequently attributed to be either inherited directly from their asthenospheric mantle source (Carmichael, 1991; Kelley and Cottrell, 2009), or the result of variable degrees of differentiation at crustal levels (Lee et al., 2002, 2010; Jenner et al., 2010; Tang et al., 2018). In contrast, relatively little attention has been paid to melt–rock interaction processes occurring in the subcontinental lithospheric mantle (SCLM) that might lead to changes in the oxidation state and composition of ascending magmas after partial melting in the asthenosphere and before they reach crustal levels. For example, Chin et al. (2014) and Griffin et al. (2018) explored the effects of the SCLM on the composition of primary asthenosphere-derived melts during their ascent and concluded that metasomatism might be an important process that modifies the composition and fO_2 of ascending melts and fluids. More recently, Tollan and Hermann (2019) also found that arc magmas oxidize during ascent and reaction with surrounding peridotite before reaching crustal levels. Therefore, melt–SCLM interaction processes might have a pivotal impact on the metal fertility of ascending magmas.

Ore metals and sulfur are stored primarily within accessory base metal sulfides and sulfide liquids in the mantle, and their release and transfer into the overriding crust is partially controlled by the fO_2 of the magmatic system (Jugo, 2009; Lorand and Luguet, 2016). This parameter reflects the oxidation state of the system and is commonly expressed as logarithmic units relative to the fayalite–magnetite–quartz mineral buffer (ΔFMQ). Experimental studies have shown that sulfide (S^{2-}) is the dominant sulfur species in silicate melts under reducing conditions ($\Delta\text{FMQ} < 0$) (Jugo et al., 2005a, 2010). In contrast, at $\Delta\text{FMQ} > 2$ the melt is dominated by sulfate (S^{6+}) whereas a sharp transition from sulfide toward the more soluble and oxidized sulfate is observed around $\Delta\text{FMQ} + 1$ (Jugo et al., 2010). Hence, the formation of oxidized magmas can efficiently promote the titration of sulfur and ore metals from the mantle, ultimately increasing the ore metal endowment of the overlying crust (Sillitoe, 2008; Richards, 2015). Furthermore, recent studies have provided evidence that restricted fertile blocks of the SCLM may act as fertile source regions from where ore metals were tapped by partial melting, fluxed melting, or by interaction with ascending melts (Griffin et al., 2013; Groves and Santosh, 2015; Groves et al., 2016; Tassara et al., 2017). However, the impact and extent of silicate melt–SCLM interaction on the composition and oxidation state of ascending melts that ultimately reach the crust to form ore deposits, and the mechanisms of ore metals extraction from the SCLM remain largely unexplored. Therefore, understanding the redox evolution of magmas during their ascent across the SCLM is crucial to unravel the mechanisms of metal enrichment of ascending magmas.

Here, we examine the effects of melt–mantle interaction on the fO_2 and metal fertility by measuring directly the formal oxidation state(s) of sulfur in magmatic apatite contained within quenched silicate glass entrained in a peridotite xenolith from Patagonia, Argentina, which represents a silicate melt that ascended through the SCLM below the El Deseado Massif auriferous province. By combining micro-X-ray absorption near-edge structure (μ-XANES) spectroscopic analysis of sulfur in apatite with petrological and mineralogical data, we show that originally reduced silicate melts that infiltrated a relatively oxidized SCLM interacted with the surrounding peridotite wall-rock, triggering changes in sulfur speciation and solubility. We link this process to the formation of gold-rich magmas during ascent and interaction with the SCLM, providing new insights into how mantle processes may govern the localization of metallogenic provinces in the Earth's crust.

SAMPLE BACKGROUND

This study focuses on a lherzolite xenolith, which represents a portion of the mantle beneath the world-class El Deseado Massif auriferous province (**Figure 1**). The Deseado Massif hosts several Au–Ag epithermal deposits associated with calc-alkaline rhyolites, basaltic andesites, and basalts from the late magmatic stages of the Chon Aike Large Igneous Province (CA-LIP) (Schalamuk et al., 1997). The CA-LIP formed during two major periods between 180 and 155 Ma (Féraud et al., 1999). The early Jurassic event was related to the thermal impact of the Karoo plume head (~180 Ma), whereas the Middle to Late Jurassic events reflects the influence of active subduction on the

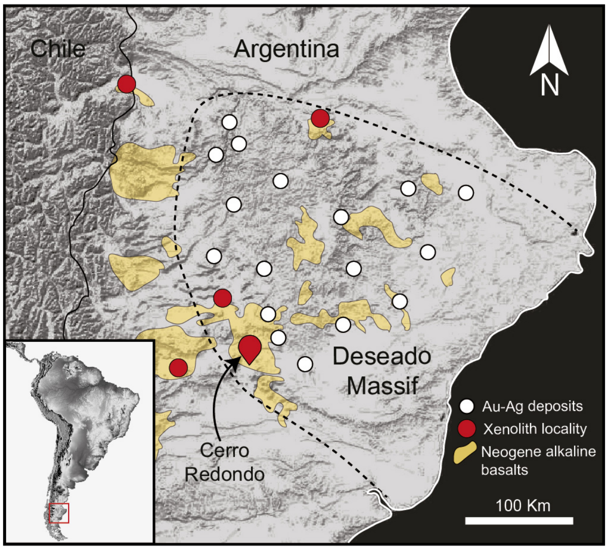

FIGURE 1 | Simplified map of southern Patagonia. The dashed line delimits the Deseado Massif auriferous province. White circles indicate the location of low-sulfidation epithermal gold and silver deposits. Red circles indicate the location of other localities where mantle xenoliths have been reported. Modified after Tassara et al. (2017).

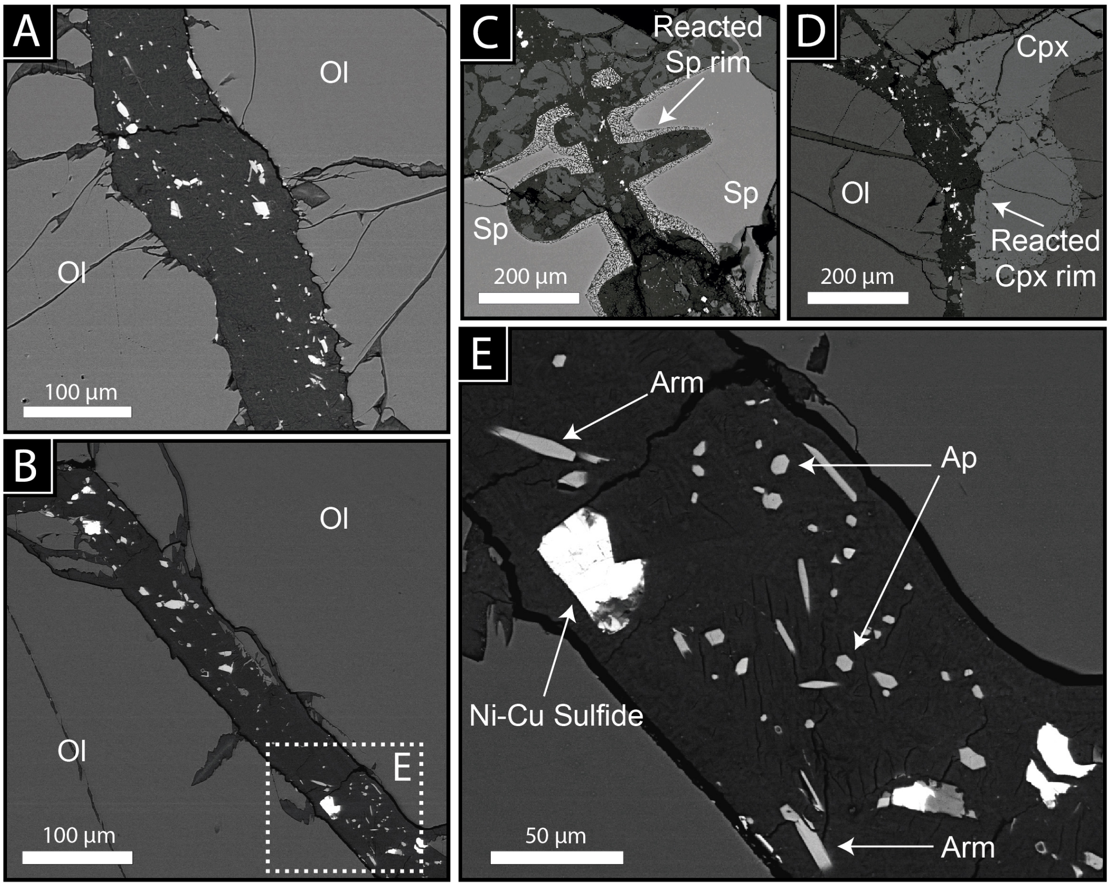

FIGURE 2 | Backscattered electron images of the interstitial glass veinlets in the studied lherzolite. Panels **(A,B)** show a general view of interstitial glass veinlets crosscutting olivine (Ol) grains with their partially crystallized mineral assemblage. Panels **(C,D)** show the reaction rims formed along clinopyroxene (Cpx) **(C)** and spinel (Sp) **(D)** when in contact with the glass veinlets. Panel **(E)** shows a detail of the mineral assemblages present in the interstitial glassy veinlets, including oxidized Ni–Cu sulfides, armalcolite (Arm), and apatite (Ap) with euhedral morphologies.

western margin of Gondwana (∼155 Ma) (Pankhurst et al., 2000). Mantle xenoliths from the SCLM beneath the Deseado Massif were later extruded by extensive Neogene (∼3.5 Ma) back-arc plateau volcanism (Rivalenti et al., 2004).

The studied peridotite is a relatively large (up to 25 cm) protogranular anhydrous lherzolite equilibrated in the spinel facies at temperatures of 1020–1150°C at 13.6 Kb (Tassara et al., 2017). The sample is characterized by the presence of quenched interstitial glass distributed along grain boundaries of the peridotite silicate matrix in the xenolith core forming an interconnected network of veinlets (**Supplementary Figure 1** and **Figure 2**). These veinlets contain a mineral assemblage that includes armalcolite, apatite, ilmenite, K-feldspar, Au-bearing sulfides, and native gold particles embedded within a glassy matrix (Tassara et al., 2017; **Figure 2**). The interstitial silicate glass has strong mineralogical and trace element compositional differences with the host basalt, indicating that the origin of the studied glass veinlets is not related to the infiltration of the host basalt into the xenolith (**Figure 3**). Moreover, the interstitial glass and associated minerals were interpreted as remnants of a Au-bearing, Na-rich silica-undersaturated melt that infiltrated the peridotite. This melt extracted Ni–Cu sulfide liquids from the surrounding peridotite wall-rock and were physically entrained and transported within the silicate melt through the mantle (Bockrath et al., 2004; Ballhaus et al., 2006; Tassara et al., 2018).

ANALYTICAL METHODS

Electron Probe Microanalysis

The chemical composition of apatite, silicates, and oxides was determined by using a CAMECA SX-100 electron microprobe at the University of Michigan in Ann Arbor. An acceleration voltage of 15 keV, a beam current of 10 nA, and a beam size of 2 µm were used for all analyses. Peak counting times of 20 s were used for all elements, except 5 s for F and 60 s for S, as this conditions are the best precautions to prevent electron beam damage of apatite (e.g., halogen migration; Konecke et al., 2019). During the analysis, both SiO_2 and Al_2O_3 concentrations were monitored for contribution of the surrounding glass and mineral phases. Analyses indicating a contribution of the glass were discarded.

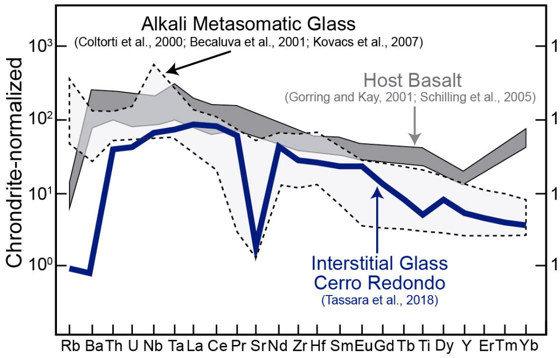

FIGURE 3 | Chondrite-normalized trace element composition of interstitial silicate glasses in the Cerro Redondo peridotite xenolith. The trace element data for the interstitial glass is from Tassara et al. (2018). The dark shade area is the trace element data for the host basalt after from Gorring and Kay (2001) and Schilling et al. (2005). The light gray shaded field is the composition of alkaline metasomatic melts in the upper mantle after Coltorti et al. (2000), Beccaluva et al. (2001), and Kovacs et al. (2007). Figure modified after González-Jiménez et al. (2019).

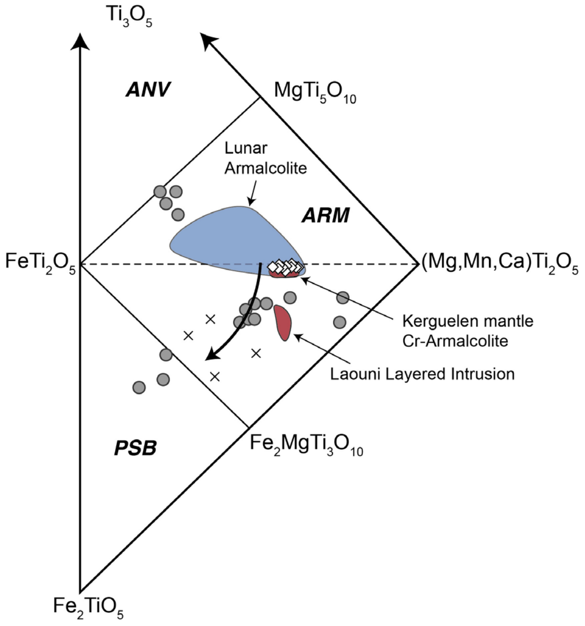

FIGURE 4 | Pseudobrookite group diagram showing armalcolite end members. Modified from Grégoire et al. (2000). Pseudobrookite group diagram composition after Bowles (1988). ANV, anosovite; ARM, armalcolite; PSB, pseudobrookite. Open circles: armalcolite and pseudobrookite from Cancarix, Spain (Contini et al., 1993). Crosses: Armalcolite from Lebombo picrites (Cawthorn and Biggar, 1993). Polygons: Kimberlitic armalcolite from Jagersfontein (Haggerty, 1987). White diamonds: armalcolite from this study. The black arrow represents the compositional evolution of armalcolite at progressively higher fO_2 after Medvedev (1996). End member calculation and classification according to Bowles (1988).

Sulfur X-Ray Absorption Near Edge Structure Spectroscopy

In situ sulfur X-ray Absorption Near Edge Structure Spectroscopy (S-XANES) measurements at the S K-edge were conducted at the GSECARS 13-ID-E beamline, Advanced Photon Source (APS), Argonne National Laboratory, IL. The beamline can cover an energy range of 2.4–28 keV and uses a high-flux beam ($\geq 4.5 \times 10^{10}$ photons/s/100 mA/mm^2) that produces a high spatial resolution micro-focused 2 × 2 μm (μ-XANES) beam by using Kirkpatrick–Baez (KB) focusing mirrors. The energy of the Si (111) channel-cut monochromator was calibrated to the 2481.8 (±0.2) eV white line of the spectrum for clear double-sided adhesive tape. Spectra were collected at ambient temperature and pressure and covered a range of energy from 2450 to 2550 eV, with a step size of 0.1–0.3 eV at the S K-edge (2464–2484 eV) and 1 eV for the pre- and post-edge regions (0.5–3 s scan durations per energy step). Step-scan durations of 1–3 s per energy step were used to achieve higher S X-ray counts required for high-quality spectra, especially in low S-bearing apatite. The analyses were performed directly on rock thick sections and the spectra was collected in fluorescence mode. X-ray fluorescence maps were performed in advance in order to locate the apatite crystals. Previous studies have confirmed that the S oxidation state in apatite remains constant when exposed to the synchrotron beam for over 1 h, demonstrating that beam damage is not an issue (Konecke et al., 2017, 2019).

REDOX STATE DETERMINATION

The fO_2 conditions of the oxide-silicate assemblage in the host peridotite were calculated using the methods described by Wood et al. (1990) for olivine–orthopyroxene–spinel equilibrium and at 13.6 Kb and 1020°C, yielding ΔFMQ values between 0 and +0.8 (**Supplementary Tables 1, 2**), consistent with redox constraints for most SCLM peridotites reported in the literature (Ballhaus, 1993; Richards, 2015).

The oxidation state of the infiltrating silicate melt was determined, on the other hand, by using two independent approaches based on the composition of armalcolite and apatite, respectively. Terrestrial occurrences of armalcolite [$(Fe,Mg)Ti_2O_5$] are exclusively associated with metasomatic melts in the upper mantle and high-Ti primitive lavas (Haggerty, 1987; Bowles, 1988; Contini et al., 1993; Grégoire et al., 2000). Compositional analysis of armalcolite shows that it contains a high concentration of Cr (1.73 and 2.16 wt.%) and is among the most MgO-enriched compositions reported in both lunar and terrestrial occurrences (**Supplementary Table 3**). Stoichiometric calculations indicate that armalcolite has near zero trivalent Fe and Ti concentrations (**Supplementary Table 4**). Similar compositions were reported for Cr-bearing armalcolite found in the Kerguelen island mantle xenoliths (Bowles, 1988; Haggerty, 1991; Grégoire et al., 2000; **Figure 4**). In an attempt to constrain the oxidation state of lunar basalts, Friel et al. (1977) performed experimental studies on the stability of synthetic armalcolite as a function of fO_2 at 1200°C and 0.001 Kb. This experiment and observations in natural samples (Grégoire et al., 2000) demonstrated that Cr-rich and near-zero Fe^{3+}

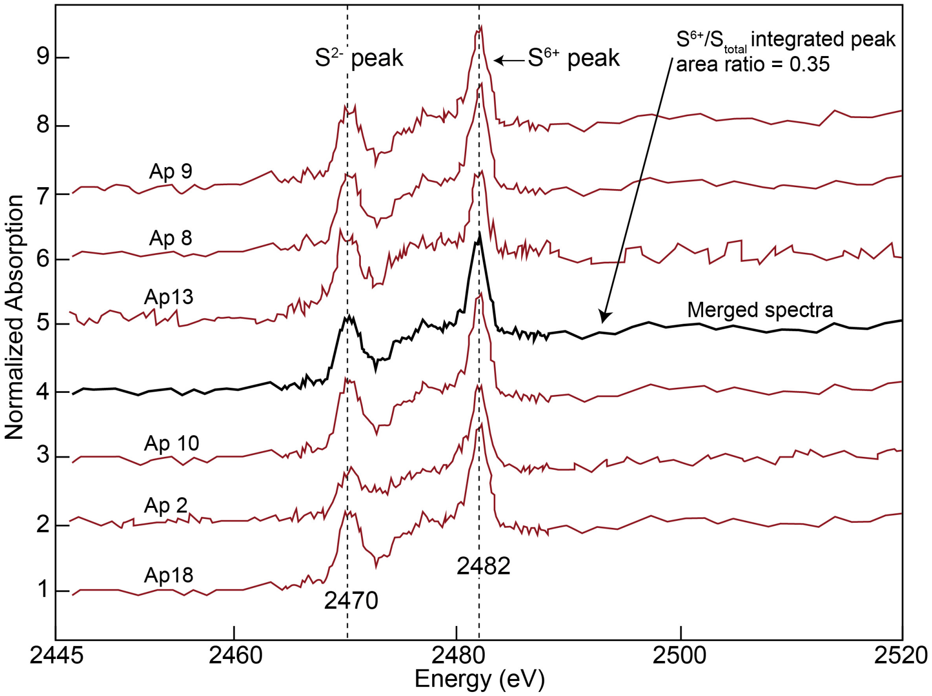

FIGURE 5 | Sulfur μ-XANES spectra of the studied apatite. Averaged μ-XANES spectra showing the oxidation state of sulfur in apatite crystallized from a silicate melt that percolated through the subcontinental lithospheric mantle in southern Patagonia, beneath the Deseado Massif.

variety of armalcolite forms only under reducing conditions (fO_2 between $10^{-12.5}$ and $10^{-13.5}$ Kb), i.e., ΔFMQ ≈ -2.2 to -1.20 (cf. Figure 4 in Friel et al., 1977). In addition, these authors showed that at even lower fO_2 conditions (between $10^{-15.2}$ and $10^{-15.8}$ Kb), armalcolite breaks down to form Mg-rich armalcolite plus ilmenite. Based on experimental data, we constrained the oxidation conditions of the infiltrating silicate melt at the time of armalcolite crystallization in the mantle at ΔFMQ ≈ -2.2 to -1.2, whereas the presence of ilmenite suggests ΔFMQ values closer to -2.2 (Friel et al., 1977). Importantly, it has been documented that whereas armalcolite is stable as a single phase at pressures up to 10 Kb, armalcolite + ilmenite + rutile assemblages form at pressures between 10 and 14 Kb. Thus, the fact that armalcolite + ilmenite is present in the studied veinlet indicates that either the armalcolite suffered slow cooling allowing it to partially transform to ilmenite (Lindsley et al., 1974), or that the crystallization of armalcolite suffered occurred at > 10 Kb, where both phases are stable (Friel et al., 1977). Either case indicates that armalcolite did not simply crystallized at low pressure during rapid cooling of the sample but rather formed at depth and suffered at least some slow cooling before the xenolith was brought to the surface.

Apatite [$Ca_5(PO_4)_3(F,Cl,OH)$] also occurs embedded within the interstitial silicate glass, commonly forming isolated clusters of crystals of up to ~8 μm in size (**Figure 2**). The apatite crystals are euhedral and show typical hexagonal and acicular shapes, indicating that it crystallized from the surrounding melt upon rapid quenching (Piccoli and Candela, 2002), possibly during the xenolith eruption (Tassara et al., 2017). Electron probe microanalysis (EPMA) revealed that apatite corresponds to the F-rich endmember (**Supplementary Table 5**), which suggests a late crystallization from the silicate melt associated with increasing differentiation (Nash, 1984). Sulfur concentrations in the analyzed apatite are between 40 and 170 μg/g with a few grains showing concentrations below detection limits (~30 μg/g) (**Supplementary Table 5**). The sulfur μ-XANES spectra of the studied apatite grains revealed two dominant peaks at ~2469.7 (sulfide) and ~2481.8 eV (sulfate), indicating that both species were incorporated within the apatite structure (**Figure 5**). The sulfite (S^{4+}) peak (~2478 eV) very likely is present in all spectra but cannot be resolved due to the overlap of the broad sulfide peak. To alleviate this, the peak integration of the broad sulfide peak was used to determine the S^{6+}/S_{tot} area ratio calculation, identical to the fitting methods developed and implemented by Konecke et al. (2017, 2019). The integrated S^{6+}/S_{total} peak area ratios were determined following the methodology of Konecke et al. (2017) and range between 0.28 and 0.48 (**Figure 5**). In order to reduce crystal orientation effects on the relative integrated area of the different peaks of the μ-XANES spectra, several apatite spectra were collected, normalized (e.g., baseline removal and intensity normalization), and then merged (Konecke et al., 2017) to obtain an average spectrum representative of the bulk sulfur oxidation state of the studied apatite grains. Also, several apatite grains with different morphologies, including elongated (approximately parallel to the *c*-axis) and euhedral hexagonal apatite (approximately perpendicular to *c*-axis) were analyzed and no significant variation in the S^{6+}/S_{tot} ratios were observed. The averaged integrated S^{6+}/S_{total} peak area can be used to estimate the fO_2 of the infiltrating silicate melt from which apatite crystallized. Experiments performed by Konecke et al. (2017, 2019) showed that apatite formed at $\Delta FMQ = 0$ has a S^{6+}/S_{total} ratio of ~0.14, whereas apatite that crystallized at $\Delta FMQ \approx +1.2$ is characterized by a S^{6+}/S_{total} ratio of ~0.95. This implies that apatite undergoes a pronounced shift from sulfide- to sulfate-dominated species with changing oxidation conditions, similarly to silicate melts (Jugo et al., 2010). The integrated S^{6+}/S_{total} ratio of the individual studied apatite ranges from ~0.28 to ~0.48, and the integrated S^{6+}/S_{total} ratio resulting from merging all spectra is ~0.35 (**Figure 5**). The latter values indicate that the oxidation state of the infiltrating silicate melt at the time of apatite crystallization was $0 < \Delta FMQ < +1.2$. Given that the S^{6+}/S_{total} ratio and log (fO_2) follow a near linear trend within this range (Konecke et al., 2019), we infer that the final oxidation state of the silicate melt at apatite formation was between ΔFMQ +0.3 to +0.4 [±0.5, 2σ], which is within the fO_2 estimated for the peridotite wall-rock. Considering that an increase in pressure shifts the stability field of sulfide toward more oxidizing conditions (Matjuschkin et al., 2016) and inferring that apatite follows a similar trend, we conclude that a ΔFMQ +0.3 to +0.4 represents a minimum fO_2 value for the silicate melt.

DISCUSSION

The interstitial network of glass veinlets in the peridotite xenolith represents a Na-rich silica undersaturated melt that percolated through the SCLM and quenched during the rapid eruption of the xenolith (Tassara et al., 2018). Although the potential re-heating of the xenolith during entrapment in the host basalt could alter the original nature of the entrained veinlets, we observe no signs of perturbation in the integrity of the sample. Sharp contacts between the xenolith and host basalt, as well as the relatively large size of the xenolith indicate that ascent was very fast, precluding the possibility of ascending during sufficient time to transfer significant heat to the internal parts of the xenolith (O'Reilly and Griffin, 2010; and references therein). Based on our data, we

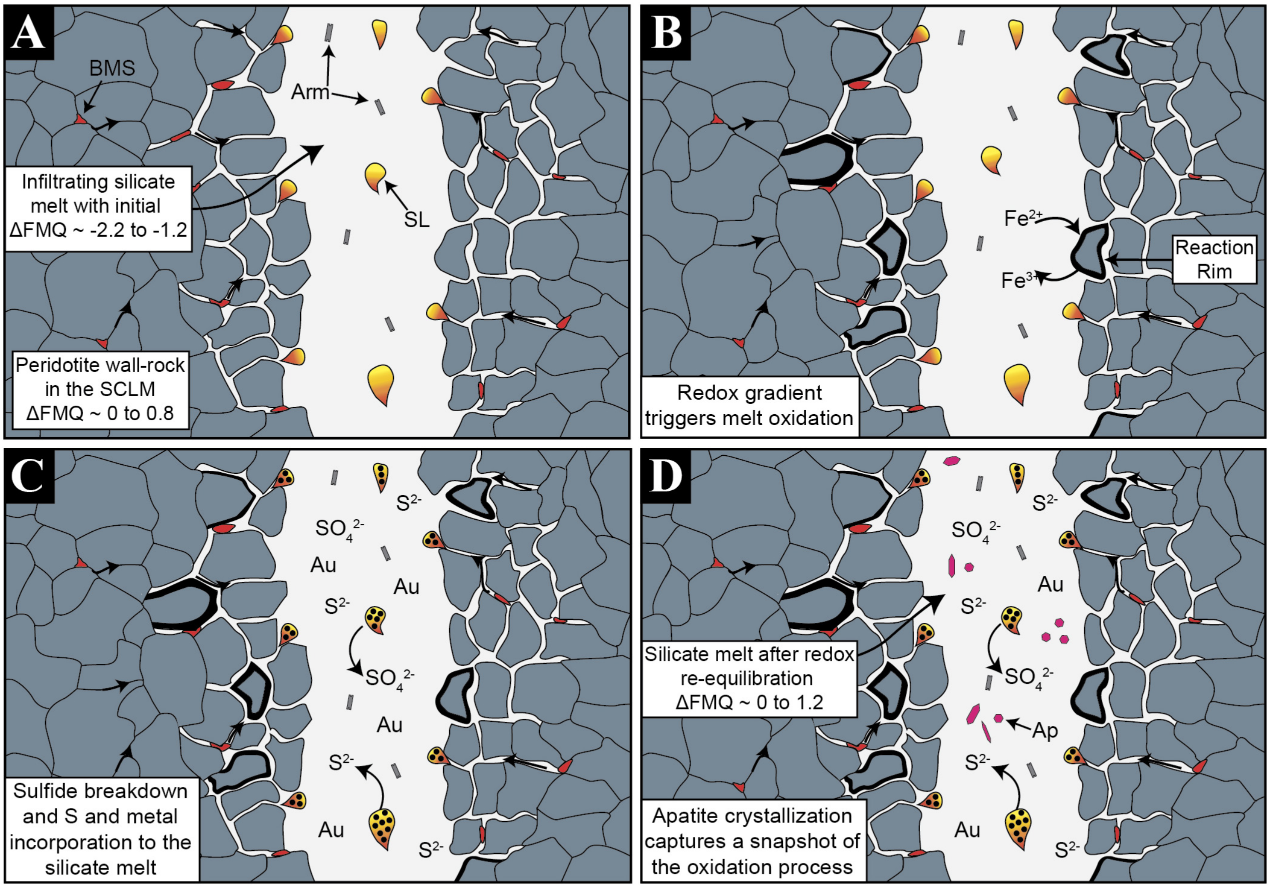

FIGURE 6 | Mechanisms leading to oxidation of percolating melts and ore metals incorporation. **(A)** The reduced silicate melt enters the subcontinental lithospheric mantle, entraining immiscible sulfide liquids. A redox gradient is generated between the reduced melt and the more oxidized peridotite wall-rock. **(B)** The silicate melt starts to re-equilibrate with the surrounding peridotite wall-rock. **(C)** Increasing oxygen fugacity triggers changes in the sulfur solubility promoting metal sulfide breakdown and release of sulfide, sulfate, and Au into the percolating silicate melt. **(D)** Quenching upon rapid ascent induced apatite crystallization, which records a snapshot of the melt-SCLM interaction process.

propose that the mineral assemblage associated with the glassy vein (armalcolite and apatite) records two different oxidation states of the percolating silicate melt, and where armalcolite formed under highly reducing conditions (ΔFMQ −2.2 to −1.2), followed by the crystallization of apatite under more oxidizing conditions (ΔFMQ 0 to +1.2).

Melt Oxidation During Interaction With Surrounding Mantle

The reduced armalcolite-bearing silicate melt (ΔFMQ −2.2 to −1.2) infiltrated a relatively more oxidized peridotite (ΔFMQ 0 to +0.8), producing a large redox gradient, i.e., a ΔfO_2 of near 3 log units between these two components (**Figure 6A**). The final redox conditions after oxidation of the reduced silicate melt and reduction of the relatively oxidized peridotite will depend on the mass balance between the more reduced and more oxidized components (Evans and Tomkins, 2011). Apatite crystallized from the surrounding silicate melt after the melt–peridotite interaction started, containing both sulfide and sulfate as evidenced by our μ-XANES data (**Figure 5**). The presence of sulfate in apatite requires the reaction between two components, i.e., a highly reduced melt with a S^{6+}/S_{total} ~0 and low sulfur content (Jugo et al., 2010) that reacted with a more oxidized and sulfide-bearing peridotite (ΔFMQ 0 to +0.8).

In the SCLM, the oxidation state is governed by minerals that have a high content of Fe^{3+} such as spinel and clinopyroxene (Wood et al., 1990). These two phases are the first minerals to react with the melt when the redox conditions are disturbed, as has been reported during the mixing process between two compositionally distinct magmas (Fiege et al., 2017). Clinopyroxene and spinel from the studied peridotite show reaction rims when in contact with the reduced infiltrating silicate melt (**Figures 2B,C**) indicating that $Fe^{2+} \leftrightarrow Fe^{3+}$ exchange between the peridotite wall-rock and the infiltrating silicate melt could have occurred, explaining the oxidation of the melt (Cooper et al., 1996; **Figure 6B**). Other than Fe, sulfur also has a large oxidation potential (Evans and Tomkins, 2011), and an increase in the oxidation state of the melt after melt–peridotite interaction would promote an increase in the sulfur solubility of the infiltrating silicate melt (Jugo et al., 2005b). Thus, at higher redox and sulfur solubility conditions (Jugo et al., 2005b), the sulfide liquids entrained in the percolating silicate melt will partially oxidize, breaking down and dissolving in the surrounding melt (**Figure 6C**). Decreasing pressure during ascent could potentially boost the breakdown of the sulfide phases, as the solubility of S in the melt will increase (Mavrogenes and O'Neill, 1999). However, if only this had been the mechanism of sulfide breakdown, no sulfate would be observed as the system would remain reduced (Matjuschkin et al., 2016). Therefore, an oxidation mechanism is still needed to account for the sulfate in the system. The apatite crystallized from the melt after the melt–peridotite interaction will incorporate both sulfide and sulfate in varying proportions, according to the S^{6+}/S_{total} ratio of the melt; therefore, apatite will record the oxidation state of the silicate melt during interaction with the surrounding peridotite wall-rock (Konecke et al., 2017; **Figures 5**, **6D**).

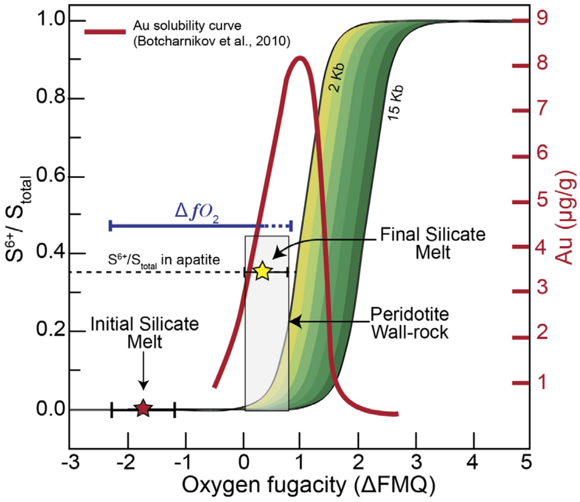

FIGURE 7 | Redox evolution of the silicate melt and the effect of redox gradients on Au solubility. Plot of S^{6+}/S_{total} vs. oxygen fugacity, expressed log units relative to the fayalite–magnetite–quartz mineral buffer (ΔFMQ). The diagram shows the initial and final redox conditions of the originally reduced silicate melt that interacts with the more oxidized peridotite wall-rock (1020°C and 13.6 Kb). The empirical approach for the determined fO_2 conditions of the initial and final silicate melt is from experiments performed at 1200°C and 0.001 to 14 Kb (armalcolite), and 1000°C 3 Kb (apatite). The green shaded area illustrates the changes in S^{6+}/S_{tot} in silicate melts with pressure after Jugo et al. (2010) and Matjuschkin et al. (2016). The red line corresponds to Au solubility in S-bearing basaltic glasses at 1050°C and 2 Kb (Botcharnikov et al., 2011). The redox gradient generated between the melt and the peridotite wall-rock, defined as ΔfO_2, promotes oxidation of the infiltrating melt leading to optimal Au solubility conditions.

Scavenging Sulfur and Ore Metals From the Lithospheric Mantle

The process described above explains the oxidation of silicate melts that ascend through the SCLM with the concomitant destabilization of ore metal-bearing sulfides (or sulfide melts) and incorporation of sulfur. Hence, sulfide breakdown will not only release sulfur but also its contained ore metals (Lorand and Luguet, 2016), such as Au (**Figure 6D**), which under certain circumstances could lead to metal enrichment in the percolating silicate melts. The solubility of Au in sulfur-bearing silicate melts is maximized when sulfur is dissolved as both sulfide and sulfate species (Cooper et al., 1996) and when the sulfide concentration is near the sulfide-saturated threshold (Botcharnikov et al., 2011; Li and Audétat, 2012; Zajacz et al., 2012; Jégo et al., 2016). **Figure 7** shows that the estimated fO_2 of the silicate melt after reacting with the peridotite wall-rock is between ΔFMQ 0 and +1.2. Sulfur μ-XANES in apatite indicates that the S^{6+}/S_{total} ratio is ~0.35 and the presence of sulfide liquids within this silicate melt indicates that the melt was once sulfide saturated. These redox conditions are in good agreement with those that maximize Au solubility of sulfur-bearing basaltic melts, determined experimentally by Botcharnikov et al. (2011) at 1050°C and 2 Kb (**Figure 7**), meaning that the highest Au solubility was achieved during redox re-equilibration within the

SCLM. In addition, the mineral assemblage associated with the studied melt contains native gold particles included within the sulfides as well as embedded within the quenched glass (Tassara et al., 2017). The native gold micro-particles in the sulfides have euhedral and hexagonal forms (Tassara et al., 2017) and likely crystallized from the sulfide liquids during desulfurization, after oxidation of the surrounding silicate melt (Tassara et al., 2018). Continued oxidation and desulfurization would result in the release of these Au micro-particles into the silicate melt. The Au micro-particles embedded within the glass have irregular shapes (Tassara et al., 2017), pointing to partial dissolution in the surrounding melt. This is in good agreement with Au solubility experiments (Botcharnikov et al., 2011; Jégo et al., 2016) and indicates that the studied silicate melt had an enhanced capability for transporting significant amounts of Au (**Figure 7**).

In summary, mantle-derived and metal-rich sulfides entrained within reduced percolating silicate melts (e.g., Bockrath et al., 2004; Ballhaus et al., 2006; Tassara et al., 2018) may release significant amounts of sulfur and Au due to the transient increase in fO_2 caused by melt–peridotite interaction during melt ascent across the SCLM (**Figure 6**), acting as an efficient mechanism for sourcing metals from the deep lithosphere, and resulting in Au enrichment of ascending silicate melts by almost one order of magnitude.

CONCLUDING REMARKS

The role of melt–peridotite interactions is being increasingly recognized in the literature as a key factor controlling the fO_2 of silicate melts percolating through the mantle in various tectonic settings (e.g., Tollan and Hermann, 2019). Our data from the El Deseado Massif auriferous province in southern Patagonia are in agreement with this point of view. Moreover, we suggest that changes in the redox state of ascending magmas during ascent throughout the SCLM can boost the potential for efficient extraction of Au and other metals from selected mantle regions, increasing their ore-fertility. Sillitoe (2008) emphasized that the recurrent generation of major gold deposits and belts in North and South America remains uncertain. Among the factors explaining the occurrence of metallogenic provinces dominated by one or more ore metals, widely contemplated possibilities include heterogeneously distributed metal preconcentration, favorable redox conditions, or other parameters somewhere above the subducted slab, between the mantle wedge and upper crust (Sillitoe, 2008). We argue that the formation of restricted blocks of crust highly endowed with gold deposits requires, in addition to hydrothermal processes in the upper crust, the efficient extraction of Au from refertilized and oxidized domains of SCLM (Rielli et al., 2017). Evidence presented here suggests that redox gradients between ascending magmas and the surrounding mantle can trigger the destabilization of mantle sulfides and sulfide melts, resulting in the release of their Au cargo into the silicate melt fraction. Our model proposes an efficient mechanism for the transfer of Au and associated metals from enriched portions of the SCLM to ascending magmas, helping to improve our understanding of metallogenic processes that operate on a lithospheric scale.

DATA AVAILABILITY STATEMENT

All datasets generated for this study are included in the article/**Supplementary Material**.

AUTHOR CONTRIBUTIONS

All the authors contributed substantially to the manuscript as a team including sampling, data acquisition and interpretation, construction of the model, and writing, and analyzed and discussed the data and revised the manuscript, which was written by ST and MR. Specifically, MR, DM, FB, and JG-J conceived and designed the study. ST and BK carried out the EPMA data acquisition, under the supervision of AS. ST and BK carried out the μ-XANES data acquisition, under the supervision of AF. MS and AC provided the samples. ST and MR were involved in the preparation of figures.

FUNDING

This study was funded by the Iniciativa Científica Milenio through Millennium Nucleus for Metal Tracing along Subduction Grant NC130065. Additional funding for analytical work was provided by the FONDAP project 15090013 "Centro de Excelencia en Geotermia de Los Andes, CEGA." ST acknowledges CONICYT for support through a Ph.D. scholarship #21170857. Grants RTI2018-099157-A-100 and RYC-2015-1796 provided funding for sample preparation and EPMA analyses. This research used resources of the Advanced Photon Source, a U.S. Department of Energy (DOE) Office of Science User Facility operated for the DOE Office of Science by Argonne National Laboratory under Contract No. DE-AC02-06CH11357. The DID-UACh project #S-201505 financed the fieldwork.

ACKNOWLEDGMENTS

We thank Tony Lanzirotti and Matt Newville for assistance with μ-XANES analyses at the GeoSoilEnviroCars (Sector 13), Advanced Photon Source (APS), Argonne National Laboratory.

SUPPLEMENTARY MATERIAL

The Supplementary Material for this article can be found online at: https://www.frontiersin.org/articles/10.3389/feart.2020.00029/full#supplementary-material

REFERENCES

Ballhaus, C. (1993). Redox states of lithospheric and asthenospheric upper mantle. *Contribut. Mineral. Petrol.* 114, 331–348. doi: 10.1007/bf01046536

Ballhaus, C., Bockrath, C., Wohlgemuth-Ueberwasser, C., Laurenz, V., and Berndt, J. (2006). Fractionation of the noble metals by physical processes. *Contribut. Mineral. Petrol.* 152, 667–684. doi: 10.1007/s00410-006-0126-z

Beccaluva, L., Bianchini, G., Coltorti, M., Perkins, W. T., Siena, F., Vaccaro, C., et al. (2001). Multistage evolution of the European lithospheric mantle) new evidence from Sardinian peridotite xenoliths. *Contribut. Mineral. Petrol.* 142, 284–297. doi: 10.1007/s004100100288

Bockrath, C., Ballhaus, C., and Holzheid, A. (2004). Fractionation of the platinum-group elements during mantle melting. *Science* 305, 1951–1953. doi: 10.1126/science.1100160

Botcharnikov, R. E., Linnen, R. L., Wilke, M., Holtz, F., Jugo, P. J., and Berndt, J. (2011). High gold concentrations in sulfide-bearing magma under oxidizing conditions. *Nat. Geosci.* 4, 112–115. doi: 10.1038/ngeo1042

Bowles, J. F. W. (1988). Definition and range of naturally occurring minerals with the pseudobrookite structure. *Am. Mineral.* 73, 1377–1383.

Carmichael, I. S. E. (1991). The redox states of basic and silicic magmas: a reflection of their source regions? *Contribut. Mineral. Petrol.* 106, 129–141. doi: 10.1007/bf00306429

Cawthorn, R. G., and Biggar, G. M. (1993). Crystallization of titaniferous chromite, magnesian ilmenite and armalcolite in tholeiitic suites in the Karoo Igneous Province. *Contribut. Mineral. Petrol.* 114, 221–235. doi: 10.1007/bf00307757

Chin, E. J., Lee, C.-T. A., and Barnes, J. D. (2014). Thickening, refertilization, and the deep lithosphere filter in continental arcs: constraints from major and trace elements and oxygen isotopes. *Earth Planet. Sci. Lett.* 397, 184–200. doi: 10.1016/j.epsl.2014.04.022

Coltorti, M., Becaluva, L., Bonadiman, C., Salvini, L., and Siena, F. (2000). Glasses in mantle xenoliths as geochemical indicators of metasomatic agents. *Earth Planet. Sci. Lett.* 183, 303–320. doi: 10.1016/s0012-821x(00)00274-0

Contini, S., Venturelli, G., and Toscani, L. (1993). Cr-Zr armalcolite-bearing lamproites of Cancarix, SE Spain. *Mineral. Magaz.* 57, 203–216. doi: 10.1180/minmag.1993.057.387.02

Cooper, R. F., Fanselow, J. B., and Poker, D. B. (1996). The mechanism of oxidation of a basaltic glass: chemical diffusion of network modifying cations. *Geochim. Cosmochim. Acta* 60, 3253–3265. doi: 10.1016/0016-7037(96)00160-3

Evans, K. A., and Tomkins, A. G. (2011). The relationship between subduction zone redox budget and arc magma fertility. *Earth Planet. Sci. Lett.* 308, 401–409. doi: 10.1016/j.epsl.2011.06.009

Féraud, G., Alric, V., Fornari, M., Bertrand, H., and Haller, M. (1999). 40Ar/39Ar dating of the Jurassic volcanic province of patagonia: migrating magmatism related to Gondwana break-up and subduction. *Earth Planet. Sci. Lett.* 172, 83–96. doi: 10.1016/s0012-821x(99)00190-9

Fiege, A., Ruprecht, P., and Simon, A. C. (2017). A magma mixing redox trap that moderates mass transfer of sulfur and metals. *Geochem. Perspect. Lett.* 3, 190–199. doi: 10.7185/geochemlet.1722

Friel, J. J., Harker, R. I., and Ulmer, G. C. (1977). Armalcolite stability as a function of pressure and oxygen fugacity. *Geochim. Cosmochim. Acta* 41, 403–410. doi: 10.1016/0016-7037(77)90268-x

González-Jiménez, J. M., Roqué-Rosell, J., Jiménez-Franco, A., Tassara, S., Nieto, F., Gervilla, F., et al. (2019). Magmatic platinum nanoparticles in metasomatic silicate glasses and sulfides from Patagonian mantle xenoliths. *Contribut. Mineral. Petrol.* 174, 47.

Gorring, M. L., and Kay, S. M. (2001). Mantle processes and sources of Neogene slab window magmas from southern Patagonia Argentina. *J. Petrol.* 42, 1067–1094. doi: 10.1093/petrology/42.6.1067

Grégoire, M., Lorand, J.-P., O'Reilly, S. Y., and Cottin, J. Y. (2000). Armalcolite-bearing, Ti-rich metasomatic assemblages in harzburgitic xenoliths from Kerguelen Islands: implications for the oceanic mantle budget of high-field strength elements. *Geochim. Cosmochim. Acta* 64, 673–694. doi: 10.1016/s0016-7037(99)00345-2

Griffin, W. L., Begg, G. C., and O'Reilly, S. Y. (2013). Continental-root control on the genesis of magmatic ore deposits. *Nat. Geosci.* 6, 905–910. doi: 10.1038/nature13532

Griffin, W. L., Huang, J.-X., Thomassot, E., Gain, S. E. M., Toledo, V., and O'Reilly, S. Y. (2018). Super-reducing conditions in ancient and modern volcanic systems: sources and behaviour of carbon-rich fluids in the lithospheric mantle. *Mineral. Petrol.* 112, 1–14.

Groves, D. I., Goldfarb, R. J., and Santosh, M. (2016). The conjunction of factors that lead to formation of giant gold provinces and deposits in non-arc settings. *Geosci. Front.* 7, 303–314. doi: 10.1016/j.gsf.2015.07.001

Groves, D. I., and Santosh, M. (2015). Province-scale commonalities of some world-class gold deposits: implications for mineral exploration. *Geosci. Front.* 6, 389–399. doi: 10.1016/j.gsf.2014.12.007

Haggerty, S. E. (1987). "Metasomatic mineral titanates in upper mantle xenoliths," in *Mantle Xenoliths*, ed. P. H. Nixon, (Hoboken, NJ: John Wiley and Sons), 671–690.

Haggerty, S. E. (1991). "Oxide mineralogy in the upper mantle," in *Oxide minerals: Petrologic and Magnetic Significance*, ed. D. H. Lindsley, (Chantilly, VA: Mineralogical Society of America), 355–416. doi: 10.1515/9781501508684-013

Jégo, S., Nakamura, M., Kimura, J.-I., Iizuka, Y., Chang, Q., and Zellmer, G. F. (2016). Is gold solubility subject to pressure variations in ascending arc magmas? *Geochim. Cosmochim. Acta* 188, 224–243. doi: 10.1016/j.gca.2016.05.034

Jenner, F. E., O'Neill, H., Arculus, R. J., and Mavrogenes, J. A. (2010). The magnetite crisis in the evolution of arc-related magmas and the initial concentration of Au, Ag, and Cu. *J. Petrol.* 51, 2445–2464. doi: 10.1093/petrology/egq063

Jugo, P. J. (2009). Sulfur content at sulfide saturation in oxidized magmas. *Geology* 37, 415–418. doi: 10.1130/g25527a.1

Jugo, P. J., Luth, R. W., and Richards, J. P. (2005a). An experimental study of the sulfur content in basaltic melts saturated with immiscible sulfide or sulfate liquids at 1300 °C and 1.0 GPa. *J. Petrol.* 46, 783–798. doi: 10.1093/petrology/egh097

Jugo, P. J., Wilke, M., and Botcharnikov, R. E. (2005b). Sulfur K-edge XANES analysis of natural and synthetic basaltic glasses: implications for S speciation and S content as a function of oxygen fugacity. *Geochim. Cosmochim. Acta* 74, 5926–5938. doi: 10.1016/j.gca.2010.07.022

Jugo, P. J., Wilke, M., and Botcharnikov, R. E. (2010). Sulfur K-edge XANES analysis of natural and synthetic basaltic glasses: implications for S speciation and S content as a function of oxygen fugacity. *Geochim. Cosmochim. Acta* 74, 5926–5938. doi: 10.1016/j.gca.2010.07.022

Kelley, K., and Cottrell, E. (2009). Water and the oxidation state of subduction zone magmas. *Science* 325, 605–607. doi: 10.1126/science.1174156

Konecke, B. A., Fiege, A., Simon, A. C., Linsler, S., and Holtz, F. (2019). An experimental calibration of a sulfur-in-apatite oxybarometer for mafic systems. *Geochim. Cosmochim. Acta* 265, 242–258. doi: 10.1016/j.gca.2019.08.044

Konecke, B. A., Fiege, A., Simon, A. C., Parat, F., and Stechern, A. (2017). Co-variability of S6+, S4+, and S2- in apatite as a function of oxidation state: implications for a new oxybarometer. *Am. Mineral.* 102, 548–557. doi: 10.2138/am-2017-5907

Kovacs, I., Hidas, K., Hermann, J., Sharygin, V., Szabó, C., and Ntaflos, T. (2007). Fluid induced melting in mantle xenoliths and some implications for the continental lithospheric mantle from Minusinsk region (Khakasia, southern Siberia). *Geol. Carpathica* 58, 211–228.

Lee, C.-T. A., Luffi, P., Chin, E. J., Bouchet, R., Dasgupta, R., Morton, D. M., et al. (2002). Copper systematics in arc magmas and implications for crust-mantle differentiation. *Science* 336, 64–68. doi: 10.1126/science.1217313

Lee, C.-T. A., Luffi, P., Le Roux, V., Dasgupta, R., Albarède, F., and Leeman, W. P. (2010). The redox state of arc mantle using Zn/Fe systematics. *Nature* 468, 681–685. doi: 10.1038/nature09617

Li, Y., and Audétat, A. (2012). Partitioning of V, Mn, Co, Ni, Cu, Zn, As, Mo, Ag, Sn, Sb, W, Au, Pb, and Bi between sulfide phases and hydrous basanite melt at upper mantle conditions. *Earth Planet. Sci. Lett.* 355-356, 327–340. doi: 10.1016/j.epsl.2012.08.008

Lindsley, D. H., Kesson, S. E., Hartzman, M. J., and Cushman, M. K. (1974). "The stability of armalcolite: experimental studies in the system MgO-Fe-Ti-O," in *Proceedings of the 11 Lunar and Planetary Science Conference*, (New York, NY: Pergamon Press Inc), 521–534.

Lorand, J.-P., and Luguet, A. (2016). "Chalcophile and siderophile elements in mantle rocks: trace elements controlled by trace minerals," in *Highly Siderophile and Strongly Chalcophile Elements in High-Temperature Geochemistry and*

Cosmochemistry. Reviews in Mineralogy and Geochemistry 81, eds J. Harvey, and J. M. D. Day, (Chantilly, VA: The Mineralogical Society of America).

Medvedev, A. Y. (1996). Synthetic armalcolite and pseudobrookite. *Mineral. Mag.* 60, 347–353. doi: 10.1180/minmag.1996.060.399.09

Matjuschkin, C., Blundy, J. D., and Brooker, R. A. (2016). The effect of pressure on sulfur speciation in mid-to deep-crustal arc magmas and implications for the formation of porphyry copper deposits. *Contribut. Mineral. Petrol.* 171:66.

Mavrogenes, J. A., and O'Neill, H. S. C. (1999). The relative effects of pressure, temperature and oxygen fugacity on the solubility of sulfide in mafic magmas. *Geochim. Cosmochim. Acta* 63, 1173–1180. doi: 10.1016/s0016-7037(98)00289-0

Mungall, J. E. (2002). Roasting the mantle: slab melting and the genesis of major Au and Au-rich Cu deposits. *Geology* 30, 915–918.

Nash, W. P. (1984). "Phosphate minerals in terrestrial igneous and metamorphic rocks," in *Phosphate Minerals*, eds J. O. Nriagu, and P. B. Moore, (Berlin: Springer-Verlag), 442.

O'Reilly, S. Y., and Griffin, W. L. (2010). "Rates of magma ascent: constraints from mantle-derived xenoliths," in *Timescales of Magmatic Processes: From Core To Atmosphere*, eds A. Dosseto, S. Turner, and J. Van Orman, (Oxford: John Wiley & Sons).

Pankhurst, R. J., Riley, T. R., Fanning, C. M., and Kelley, S. P. (2000). Episodic silicic volcanism in Patagonia and the Antarctic Peninsula: chronology of magmatism associated with the break-up of Gondwana. *J. Petrol.* 41, 605–625. doi: 10.1093/petrology/41.5.605

Piccoli, P. M., and Candela, P. A. (2002). "Apatite in igneous systems," in *Phosphates: Geochemical, Geobiological, and Materials Importance*, eds M. J. Kohn, and J. M. Hughes, (Chantilly, VA: Mineralogical Society of America), 255–292. doi: 10.2138/rmg.2002.48.6

Richards, J. P. (2015). The oxidation state, and sulfur and Cu contents of arc magmas: implications for metallogeny. *Lithos* 233, 27–45. doi: 10.1016/j.lithos.2014.12.011

Rielli, A., Tomkins, A. G., Nebel, O., Brugger, J., Etschmann, B., Zhong, R., et al. (2017). Evidence of sub-arc mantle oxidation by sulphur and carbon. *Geochem. Perspect. Lett.* 3, 124–132. doi: 10.7185/geochemlet.1713

Rivalenti, G., Mazzucchelli, M., Laurora, A., Ciuffi, S. I. A., Zanetti, A., Vannucci, R., et al. (2004). The backarc mantle lithosphere in patagonia, South America. *J. South Am. Earth Sci.* 17, 121–152. doi: 10.1016/j.jsames.2004.05.009

Schalamuk, I. B., Zubia, M., Genini, A., and Fernandez, R. R. (1997). Jurassic epithermal Au-Ag deposits of patagonia, Argentina. *Ore Geol. Rev.* 12, 173–176.

Schilling, M. E., Conceição, R. V., Mallmann, G., Koester, E., Kawashita, K., Hervé, F., et al. (2005). Spinel-facies mantle xenoliths from Cerro Redondo, Argentine Patagonia: Petrographic, geochemical, and isotopic evidence of interaction between xenoliths and host basalt. *Lithos* 82, 485–502. doi: 10.1016/j.lithos.2004.09.028

Sillitoe, R. H. (2008). Major gold deposits and belts of the North and South American cordillera: distribution, tectonomagmatic settings, and metallogenic considerations. *Econ. Geol.* 103, 663–687. doi: 10.2113/gsecongeo.103.4.663

Tang, M., Erdman, M., Eldridge, G., and Lee, C.-T. A. (2018). The redox "filter" beneath magmatic orogens and the formation of continental crust. *Sci. Adv.* 4:eaar4444. doi: 10.1126/sciadv.aar4444

Tassara, S., González-Jiménez, J. M., Reich, M., Saunders, E., Luguet, A., Morata, D., et al. (2018). Highly siderophile elements mobility in the subcontinental lithospheric mantle beneath southern Patagonia. *Lithos* 314-315, 579–596. doi: 10.1016/j.lithos.2018.06.022

Tassara, S., González-Jiménez, J. M., Reich, M., Schilling, M. E., Morata, D., Begg, G. C., et al. (2017). Plume-subduction interaction forms large auriferous provinces. *Nat. Commun.* 8:843. doi: 10.1038/s41467-017-00821-z

Tollan, P., and Hermann, J. (2019). Arc magmas oxidized by water dissociation and hydrogen incorporation in orthopyroxene. *Nat. Geosci.* 12, 667–671. doi: 10.1038/s41561-019-0411-x

Wood, B. J., Bryndzia, L. T., and Johnson, K. E. (1990). Mantle oxidation state and its relationship to tectonic environment and fluid speciation. *Science* 248, 337–345. doi: 10.1126/science.248.4953.337

Zajacz, Z., Candela, P. A., Piccoli, P. M., Wälle, M., and Sanchez-Valle, C. (2012). Gold and copper in volatile saturated mafic to intermediate magmas: solubilities, partitioning, and implications for ore deposit formation. *Geochim. Cosmochim. Acta* 91, 140–159. doi: 10.1016/j.gca.2012.05.033

Conflict of Interest: The authors declare that the research was conducted in the absence of any commercial or financial relationships that could be construed as a potential conflict of interest.

frontiers in Earth Science

ORIGINAL RESEARCH
published: 03 April 2020
doi: 10.3389/feart.2020.00084

Hydrated Peridotite–Basaltic Melt Interaction Part II: Fast Assimilation of Serpentinized Mantle by Basaltic Magma

Anastassia Y. Borisova[1,2]*, *Nail R. Zagrtdenov*[1], *Michael J. Toplis*[3], *Georges Ceuleneer*[1], *Oleg G. Safonov*[2,4,5], *Gleb S. Pokrovski*[1], *Klaus Peter Jochum*[6], *Brigitte Stoll*[6], *Ulrike Weis*[6], *Svyatoslav Shcheka*[7] and *Andrey Y. Bychkov*[2]

[1] Géosciences Environnement Toulouse, GET, Université de Toulouse, CNRS, IRD, UPS, Toulouse, France, [2] Geological Department, Lomonosov Moscow State University, Moscow, Russia, [3] Institut de Recherche en Astrophysique et Planétologie (IRAP) UPS OMP – CNRS – CNES, Toulouse, France, [4] Korzhinskii Institute of Experimental Mineralogy, Chernogolovka, Russia, [5] Department of Geology, University of Johannesburg, Johannesburg, South Africa, [6] Climate Geochemistry Department, Max Planck Institute for Chemistry, Mainz, Germany, [7] Bavarian Research Institute of Experimental Geochemistry and Geophysics (BGI), University of Bayreuth, Bayreuth, Germany

Edited by:
Yigang Xu,
Guangzhou Institute of Geochemistry (CAS), China

Reviewed by:
Benxun Su,
Institute of Geology and Geophysics (CAS), China
Tomoaki Morishita,
Kanazawa University, Japan

***Correspondence:**
Anastassia Y. Borisova
anastassia.borisova@get.omp.eu

Specialty section:
This article was submitted to Petrology,
a section of the journal Frontiers in Earth Science

Received: 16 December 2019
Accepted: 12 March 2020
Published: 03 April 2020

Citation:
Borisova AY, Zagrtdenov NR, Toplis MJ, Ceuleneer G, Safonov OG, Pokrovski GS, Jochum KP, Stoll B, Weis U, Shcheka S and Bychkov AY (2020) Hydrated Peridotite–Basaltic Melt Interaction Part II: Fast Assimilation of Serpentinized Mantle by Basaltic Magma. Front. Earth Sci. 8:84. doi: 10.3389/feart.2020.00084

The most abundant terrestrial lavas, mid-ocean ridge basalt (MORB) and ocean island basalt (OIB), are commonly considered to be derived from a depleted MORB-mantle component (DMM) and more specific, variably enriched mantle plume sources. However, findings of oceanic lavas and mafic cumulates issued from melts, enriched in chlorine and having a radiogenic $^{87}Sr/^{86}Sr$ ratio, can be attributed to an interaction between the asthenosphere-derived melts and lithospheric peridotite variably hydrated due to penetration of hydrothermal water down to and below Moho level. To constrain mechanisms and rates responsible for the interaction, we report results of 15 experiments of reaction between serpentinite and tholeiitic basaltic melt at 0.2–1.0 GPa and 1250–1300°C. Results show that the reaction proceeds via a multi-stage mechanism: (i) transformation of serpentinite into Cr-rich spinel-bearing harzburgite (Fo_{92-95} mol.%) containing pore fluid, (ii) partial melting and dissolution of the harzburgite assemblage with formation of interstitial hydrous melts (up to 57–60 wt% of SiO_2 contents at 0.5 GPa pressure), and (iii) final assimilation of the Cr-rich spinel-bearing harzburgite/dunite and formation of hybrid basaltic melts with 12–13 wt.% of MgO and elevated Cr (up to ∼500 ppm) and Ni (up to ∼200 ppm) contents. Assimilation of serpentinite by basaltic melt may occur under elevated melt/rock ratios (>2) and may lead to chromitite formation. We show that hybrid magmas produced by the progressive assimilation of serpentinized lithospheric mantle may be recognized by high Mg-numbers and high Cr and Ni contents of olivine and pyroxenes, an excess of SiO_2, H_2O, and halogens in the melts, and some unusual isotopic composition (e.g., radiogenic $^{87}Sr/^{86}Sr$, non-mantle $\delta^{18}O$, and low $^3He/^4He$). Our experiments provide evidence that MORB and high-Mg-Cr orthopyroxene-rich cumulates depleted in incompatible elements can be produced from common mid-ocean ridge basaltic melts modified by reaction with hydrated lithospheric peridotite. We established that the rate of assimilation of serpentinized peridotite is controlled by silica diffusion in the reacting hydrous basaltic melt. Our study challenges traditional interpretation of the variations in MORB and OIB chemical and isotopic composition in terms of deep mantle plume source heterogeneities or/and degrees of partial melting.

Keywords: hydrated peridotite, serpentinite, basaltic melt, assimilation, MORB, melt–rock interaction, slow spreading ridges, asthenosphere

INTRODUCTION

Mid-ocean ridge basalt (MORB) and ocean island basalts (OIBs) are considered as products of decompression melting of several asthenospheric sources characterized by contrasted isotopic signatures (e.g., DMM, HIMU, EM-1, and EM-2; e.g., Zindler and Hart, 1986). This paradigm implies that the oceanic basalt composition is some kind of "carbon copy" of their deep mantle sources. However, the occurrence of basaltic glasses and high-Mg cumulates with radiogenic $^{87}Sr/^{86}Sr$ ratios along present-day mid-ocean ridges (e.g., Ross and Elthon, 1993; Nonnotte et al., 2005; van der Zwan et al., 2017) and in ophiolites (Amri et al., 1996; Benoit et al., 1999; Clénet et al., 2010; Lange et al., 2013) suggest more complex mechanisms for the generation of oceanic magmas involving the assimilation of altered lithospheric material. Experimental and melt inclusion studies highlight the important role of basaltic melt-lithospheric rocks reactions on the chemical composition of both mantle rocks and silicate melts (e.g., Morgan and Liang, 2003; Kvassnes and Grove, 2008; France et al., 2010; Van den Bleeken et al., 2010, 2011; Borisova et al., 2012a, 2014). For example, Sr isotope diversity of basalts and mafic cumulates possibly related to assimilation of seawater-altered rocks is common in spreading environment (Michael and Cornell, 1998; Lange et al., 2013; van der Zwan et al., 2017). Magmas resulting from the mixing between "asthenospheric" tholeiites and hydrated "lithospheric" melts of depleted andesitic affinity were proposed as parental for some puzzling occurrences of orthopyroxene-rich primitive cumulates along mid-ocean ridges and in ophiolites (Benoit et al., 1999; Nonnotte et al., 2005). The formation of such hybrid or/and depleted magmas due to assimilation of serpentinized mantle peridotite leads to the formation of the Moho transition zone composed by dunites and chromitites (Borisova et al., 2012a; Zagrtdenov et al., 2018; Rospabé et al., 2019a,b).

Hydrothermal circulation in the oceanic lithosphere near and below the mantle/crust boundary ("petrologic Moho") is recorded in such hydrothermal rocks as mantle diopsidites hosted by peridotites in the shallow mantle section of ophiolites (Python et al., 2007; Akizawa and Arai, 2014) as well as in multiphase inclusions representing fluid phase, not a magma, in chromitite orebodies (Borisova et al., 2012a; Johan et al., 2017). Assimilation of seawater-derived brine or aqueous fluid by mafic rocks, magmas and melts, is recorded also at ultraslow-, slow-, and fast-spreading mid-ocean centers and preshield-stage Loihi Seamount lavas (Hawaii) (Michael and Schilling, 1989; Jambon et al., 1995; Michael and Cornell, 1998; Kent et al., 1999; Dixon and Clague, 2001; Dixon et al., 2008; Klein et al., 2019). Seawater-derived component assimilation, possibly through interaction with serpentine, happens at slow-spreading centers or at small oceanic islands (Simons et al., 2002; Dixon et al., 2008). It is also reported that basaltic glasses, melt inclusions, and the serpentinite-hosted gabbroic veins in the environment of the slow-spreading ridges are affected by assimilation of hydrothermally altered lithosphere enriched in such volatile elements as Cl, H_2O, and atmospheric Ne, Ar isotopes (Stroncik and Niedermann, 2016; Ciazela et al., 2017, 2018; van der Zwan et al., 2017). The shallow depths of the melt- or magma-rock interactions extend to 10 to 13 km, suggesting not only crustal but also upper mantle source of such contamination (van der Zwan et al., 2017). Additionally, serpentinites play an important role during melt–rock interactions of upper mantle, which was thereafter exposed in the detachment faults (e.g., Bach et al., 2004; Sauter et al., 2013; Ciazela et al., 2017), where upper mantle serpentinites may be abundant in the crust of slow- and (mostly) ultraslow-spreading ridges. Indeed, hydrated peridotites, in particular, upper mantle serpentinites are high-Mg rocks variously enriched in refractory elements (Cr, Ni) and fluid-mobile elements (e.g., halogens, H, B, O, He, Ar, As, S, Sb, Sr, and Pb) due to interaction between peridotite and seawater-derived low-to-moderate-temperature hydrothermal fluids (e.g., Guillot et al., 2001; Früh-Green et al., 2004; Bonifacie et al., 2008; Deschamps et al., 2010; Evans et al., 2013; Guillot and Hattori, 2013; Kendrick et al., 2013). These rocks crop out preferentially below the mantle-crust transition zone (Evans et al., 2013) which is locally exposed to the seafloor at mid ocean ridges (e.g., Bach et al., 2004) and may be sampled as upper mantle xenoliths by lavas of such oceanic islands as Canary Islands (Neumann et al., 2015) at possible reaction depths of up to 1.0 GPa pressure.

Although the interaction between dry tholeiitic basalt and anhydrous harzburgite has been investigated experimentally by Fisk (1986), Kelemen et al. (1990), Morgan and Liang (2003), and Van den Bleeken et al. (2010, 2011), the rates and mechanisms of assimilation of the hydrated mantle lithosphere (or serpentinite rocks) by the basaltic magmas and the chemical impact of the hydrated mantle on the composition of oceanic basalts are still unconstrained. Such constraints are important to understand the evolution of the oceanic lithosphere and to reconsider some inferences of geochemists on the nature and composition of mantle sources (Nonnotte et al., 2005; Kendrick et al., 2017). Our experiments were designed to study the reaction processes between moderately differentiated basaltic melt and serpentinite with high melt/rock ratio at pressures of 0.2–1.0 GPa. Our new data contribute to constrain the rate, mechanism and compositional impact of the assimilation of the serpentinized lithospheric mantle by the basaltic magma.

MATERIALS AND METHODS

Starting Materials and Analytical Methods

The MORB used in the experiments is a typical moderately differentiated (8.2 wt.% of MgO) glassy tholeiitic basalt (sample 3786/3) from Knipovich ridge of the Mid Atlantic Ridge dredged during the 38th Research Vessel Adademic Mstislav Keldysh expedition (Sushchevskaya et al., 2000). The serpentinite used as starting material is a homogeneous rock composed by antigorite with accessory Fe-rich oxides, devoid of relics of primary mantle silicates, sampled in Zildat, Ladakh, northwest Himalaya (e.g., Deschamps et al., 2010). The composition of the starting materials is given in **Table 1**. The concentrations of elements in both rocks were measured at the Service d'Analyse des Roches et des Minéraux (SARM, Centre de Recherches Pétrographiques et Géochimiques, Vandoeuvre lès Nancy, France). The rock H_2O concentrations were measured using Karl Fischer titration. Major and trace elements were measured using inductively coupled plasma optical emission spectroscopy (ICP–OES) and ICP–MS, using a method developed at the SARM (Carignan et al., 2001) employing an ICP–OES IRIS Advantage ERS from Thermo Scientific and an ICP–MS x7 from Thermo Scientific.

For the hybrid runs, the serpentinite has been prepared as doubly polished ~1000 μm thick section, thereafter cut to 2.7 mm diameter cylinders by a core drill machine. The MORB glass has been crushed to powder (< 100 μm glass size). Additionally, for the mixed runs at 0.2 GPa pressure, the serpentinite sample has been crushed to powder (<100 μm glass size).

TABLE 1 | Starting material composition.

Sample	Basalt*	TSL-19
SiO_2, wt%	50.31	40.69
TiO_2	1.45	D.L.
Al_2O_3	15.31	0.88
Fe_2O_{3total}	9.9	7.53
MnO	0.17	0.11
MgO	8.21	38.24
CaO	10.29	0.06
Na_2O	3.04	D.L.
K_2O	0.31	D.L.
P_2O_5	0.18	0.05
LOI	-0.22	11.55
Total	98.93	99.1
H_2O total, wt%	0.71	11.91
Ba, ppm	75.8	D.L.
Ce	16.8	D.L.
Cr	275	2417
Dy	5	0.049
Er	3.04	0.042
Eu	1.33	0.008
Gd	4.34	0.023
Hf	2.65	D.L.
Ho	1.12	0.012
La	6.44	D.L.
Lu	0.445	0.009
Nb	7.23	D.L.
Nd	12.4	D.L.
Ni	129	1901
Pr	2.51	D.L.
Rb	7.19	D.L.
Sm	3.75	D.L.
Sr	148	2.349
Tb	0.75	0.005
Th	0.63	D.L.
Tm	0.436	0.007
U	0.79	0.627
Y	29.1	0.266
Yb	2.91	0.05
Zr	94.3	D.L.

**Basalt—mid-ocean ridge basaltic glass (Sushchevskaya et al., 2000) used in the experiments; TSL-19—serpentinite (Deschamps et al., 2010) used in the experiments. D.L.—concentrations are below detection limit.*

Experimental Strategy and Method

The experiments in the system containing basalt and serpentinite were performed at 0.2–1.0 GPa and 1250–1300°C. Although in modern oceanic settings, temperatures of 1050°C are sufficient to initiate reaction of hydrated peridotite with basaltic magma at 0.2 GPa (Borisova et al., 2012a), we chose higher temperatures for the experiments as higher temperatures substantially increase reaction rates of the serpentinite-basaltic melt interactions and ensure conditions corresponding to complete melting of the basalt, consistent with the majority of existing models of basaltic melt extraction from the mantle (Fisk, 1986; Hirschmann et al., 1998; Ulmer, 2001; Morgan and Liang, 2003).

Fifteen experimental runs were performed at 0.2–1.0 GPa with similar serpentinite to basalt ratios (with 12–28 wt% of serpentinite in the mixture), the similar initial bulk water content, and different run duration (**Figure 1** and **Table 2**). Two series of experiments were performed: (a) *hybrid* series with serpentinite cylinder and basaltic powder at 0.2 and 1.0 GPa and (b) *mixed* series composed of intimately and well-mixed serpentinite and basaltic powders uniquely at 0.2 GPa pressure. The experimental design of the hybrid runs included a serpentinite cylinder in the upper part and dry or wet MORB glass powder in the lower part of the $Au_{80}Pd_{20}$ (exceptionally, in one run of the Pt) capsule. The mixed runs were performed with mixtures of basaltic powders and 20 wt% of serpentinite powder in the bulk mixture (**Figure 1** and **Table 2**). The starting components were weighed before runs. The distilled water^{MQ} was mixed with the MORB powder in the experiments with additional water uniquely at 0.5 GPa pressure. The experimental runs were performed at temperature of 1250–1300°C. Because the run duration was shorter than 48 h which is necessary to reach oxygen fugacity equilibrium with a piston-cylinder double-capsule techniques of mineral buffer (Matjuschkin et al., 2015), the redox conditions in our kinetic experiments were controlled by the initial Fe^{2+}/Fe^{3+} ratios in the MORB glass and serpentinite, although more oxidized conditions were established during the runs due to the presence of water and partial H_2

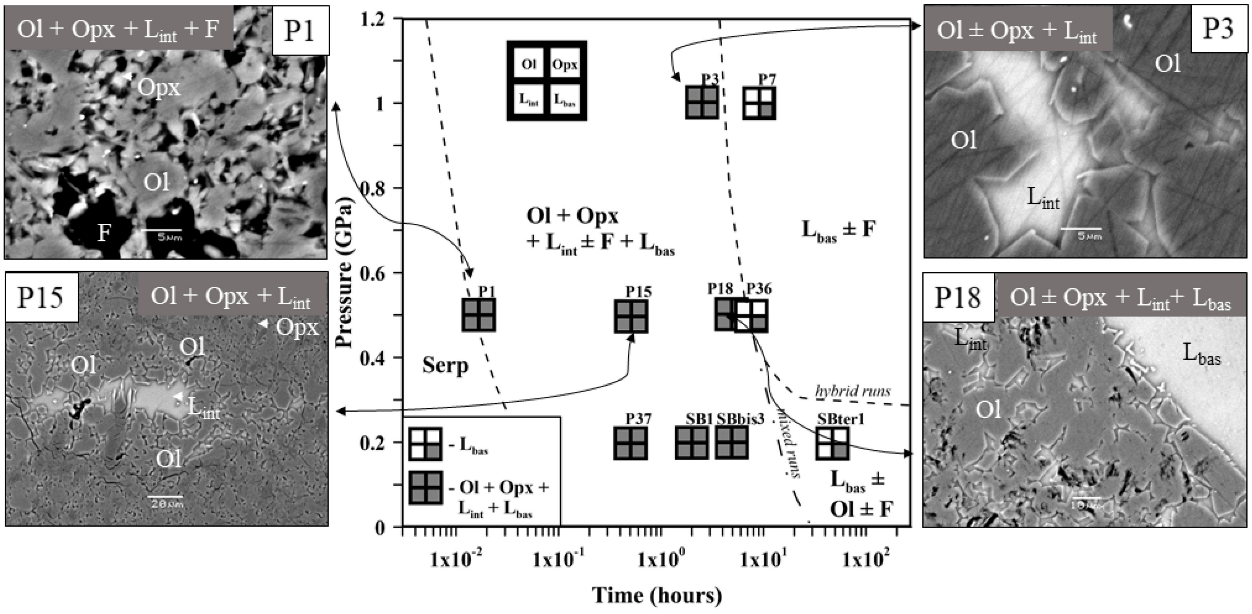

FIGURE 1 | Pressure (in GPa) versus experimental run duration (in hours) diagram in the experimental basaltic melt–serpentinite system (without additional water) showing mineral and glass assemblages produced in hybrid and mixed runs at 1250–1300°C. The diagram and the back-scattered electron images of the samples show the main melt and mineral phases observed after quenching: L_{bas}—zone of hydrous basaltic glass; L_{int}—interstitial glass; Opx—orthopyroxene; Ol—forsteritic olivine; F—fluid; Serp—serpentine, mostly antigorite minerals issued from the starting serpentinite. The run numbers and corresponding run products are given in **Table 2**.

loss to Al_2O_3 pressure media. The Fe^{III}/Fe^{II} ratios in several quenched products were estimated using X-ray absorption near edge structure (XANES) at European Synchrotron Radiation Facility (ESRF) in Grenoble (France). Oxygen fugacity relative to the quartz-fayalite-magnetite (QFM) buffer was calculated based on the obtained ferric iron (Fe^{III}) mole fraction (X_{FeIII}) in the analyzed samples (**Table 2**) using of the FeO^{total} contents in the predominant basaltic melt and model of Borisov et al. (2018). The redox conditions in the shortest runs (<4 h) were estimated from the olivine-chromite assemblages using equations of Ballhaus et al. (1991) and from mole fraction of ferric iron Fe^{III} obtained by XANES at corresponding temperatures to range from QFM(+1.5) (for P10) to QFM(+3.6) (for P1) (**Figure 1** and **Table 2**).

Two piston-cylinder systems were used in our experiments. Experiments (P1–P10) used the end-loaded Boyd-England piston-cylinder apparatus at the Korzhinskii Institute of Experimental Mineralogy, Chernogolovka, Russia. Standard talc-Pyrex cells 3/4 inch in diameter, equipped with tube graphite heaters, and inserts made of MgO ceramics were used as pressure-transmitting medium. The pressure at elevated temperatures was calibrated against two reactions of brucite = periclase + H_2O and albite = jadeite + quartz equilibria. A pressure correction (12%) was introduced for the friction between the cell and hard-alloy vessel. To minimize the friction, a Pb foil and molybdenum disulfide (MoS_2) lubricant were used. $Au_{80}Pd_{20}$ capsules with starting mixtures were mounted in the central parts of the cells. The temperature in the upper part of the capsules was controlled to be accurate to ±1°Ñ using a MINITHERM controller via a $W_{95}Re_5/W_{80}Re_{20}$ thermocouple insulated by mullite and Al_2O_3 without pressure correction. For the Pyrex-bearing assemblies, the sample was heated to 550–600°C at low confining pressure (0.15–0.2 GPa) for a few minutes in order to soften the Pyrex glass; subsequently, both temperature and pressure were increased almost simultaneously up to the desired run conditions. The samples were maintained at run conditions during desired durations (**Table 2**). The experiments were quenched by switching off electricity. The quench rate was 100–300°Ñ/min.

The experiments (P15–P26) used the "Max Voggenreiter" end-loaded Boyd-England piston-cylinder apparatus at the Bavarian Research Institute of Experimental Geochemistry and Geophysics (BGI), Bayreuth, Germany. Talc cells 3/4 inch in diameter with Pyrex sleeves were used. A tapered graphite furnace was inserted in each cell. Alumina (Al_2O_3) spacers were used as pressure-transmitting medium. An $Au_{80}Pd_{20}$ capsule loaded with starting materials was set in the central part of the assembly. A 20% pressure correction was applied for the friction between the talc cell and pressure vessel. A molybdenum disulfide (MoS_2) lubricant was introduced to minimize the friction. The temperature in the upper part of the capsules was controlled by a EUROTHERM (2404) controller via either $W_3Re_{97}/W_{25}Re_{75}$ (type D) or $Pt_6Rh_{94}/Pt_{30}Rh_{70}$ (type B) thermocouple accurate to ±0.5°C. The sample was compressed to 0.5 GPa during a period of 20 min and then heated up to the run temperature (1300°C) at a rate of 100°C/min. The samples were maintained at run conditions during desired durations (**Table 2**). The experiments were quenched by switching off electricity. We have applied

TABLE 2 | Conditions and products of the experimental interaction between basaltic melt and hydrated peridotite at 0.2 1.0 GPa.

N°	Run	Pressure (GPa)	Temperature (°C)	Capsule material	Time (h)	Percentage of the starting components (wt%)			H_2O* (wt%) (α_{H2O})	Run products with phase proportions (wt%)	Resulting oxygen fugacity QFM $(X_{Fe_{III}})^{XANES\$\$}$	Kd
						Serpentinite[a]	Basalt[$]	Water[$]				
1	P37	0.2	1250	$Au_{80}Pd_{20}$	0.5	28.2	71.8	–	–	L bas (72.8) + L int (0.4) + Ol (17.0) + Opx (6.8) + Cpx + ChrMgt (0.0) + F (3.0)	–	–
2	SB1[$$$]	0.2	1250	$Au_{80}Pd_{20}$	2	19.95	80.05	–	–	Ol (39.6) + Cpx (22.3) + Chr (0.8) + L_{int} (34.0) + F (3.3)	–	–
3	SBbis3[$$$]	0.2	1250	$Au_{80}Pd_{20}$	5	19.95	80.05	–	–	Ol + L_{bas} + F	–	–
4	SBter1[$$$]	0.2	1250	$Au_{80}Pd_{20}$	48	19.95	80.05	–	–	L_{bas} + F	–	–
5	P1	0.5	1300	$Au_{80}Pd_{20}$	0.02	19.2	80.8	–	2.8	L_{int} + Ol + Serp + Opx + Cpx + Chr + L_{bas}	0.14–0.19 QFM (2.9 – 3.6)	0.36 ± 0.05 –
6	P15	0.5	1300	$Au_{80}Pd_{20}$	0.5	15.7	84.3	–	2.2	L_{int} (3) + Ol (13) + Opx (3) + ChrMgt + L_{bas} (81)	–	–
7	P10	0.5	1300	Pt	2.6	12.9	87.1	–	1.8	L_{int} + Ol + Cpx + Chr + L_{bas}	QFM (1.5 – 3.0) 0.35 – 0.43	–
8	P18	0.5	1300	$Au_{80}Pd_{20}$	5.0	13.4	86.6	–	1.8	L_{int} (2) + Ol (11) + Opx (2) + Chr + L_{bas} (85)	–	–
9	P36	0.5	1250	$Au_{80}Pd_{20}$	8.0	14.6	85.4	–	2.0	L_{bas}		–
10	P20	0.5	1300	$Au_{80}Pd_{20}$	0.5	14.6	77.6	7.8	(1)*	L_{int} (2) + Ol (11) + Opx (3) + Chr + L_{bas} (84) + F	–	–
11	P21	0.5	1300	$Au_{80}Pd_{20}$	2.5	11.8	78.7	9.5	(1)	L_{int} (2) + Ol (11) + Opx (3) + Chr + L_{bas} (85) + F	–	–
12	P26	0.5	1300	$Au_{80}Pd_{20}$	5.0	13	80.6	6.4	(1)	L_{int} (0.3) + Ol (4) + Opx (0.8) + Chr + L_{bas} (94) + F	–	–
13	P3	1.0	1300	$Au_{80}Pd_{20}$	2.5	15.3	84.7	–	2.1	L_{int} (3) + Ol (11) + Opx (4) + ChrMgt + L_{bas} (83)	– 0.13 QFM (2.5)	0.33 ± 0.05 –
14	P7	1.0	1300	$Au_{80}Pd_{20}$	9.0	15.9	84.1	–	2.2	L_{bas}		
15	P12	1.0	1300	$Au_{80}Pd_{20}$	3.0	13.4	79.3	7.3	(1)	L_{bas} + F	0.21	

[a] *Weight percent of the serpentine in the system is calculated as mass of serpentine divided by total mass of the all components: ($M_{Serp}/(M_{Serp} + M_{MORB})$ for P1, P15, P10, P18, P25, P3, P7 or $M_{Serp}/(M_{Serp} + M_{MORB} + M_{H2O})$ for P20, P21, P26, P12, where M_{Serp}, M_{MORB}, and M_{H2O} are mass of serpentine, basaltic glass, and additional water, respectively.* [b] *"L_{int}" = interstitial glass; "L_{bas}" = hydrous basaltic glass; "Serp" = serpentine; "Ol" = olivine; "Opx" = orthopyroxene; "Cpx" = clinopyroxene; "Amph" = amphibole; "Chr" = chromite; "ChrMgt" = chromiferous magnetite; "F" = water bubble(s).* [$] *"Basalt" = Mid Atlantic Ridge basaltic glass; "Water"—additional water added to the starting system.* [$$] *QFM = oxygen fugacity expressed in log units compared to the quartz-fayalite magnetite (QFM) mineral redox buffer according to Ballhaus et al. (1991).* [$$$] *Mixed runs performed at 0.2 GPa. $(X_{Fe_{III}})^{XANES}$—molar fraction of Fe^{3+} compared to the bulk Fe in the sample measured by XANES. Kd are theoretical FeO–MgO partition coefficient between olivine and co-existing melt (Toplis, 2005) compared to the experimental FeO–MgO partition coefficient between olivine and co-existing melt (0.23 ± 0.10) taking into consideration of Fe^{II} and Fe^{III} in the melt with assumed $[X_{Fe_{III}}] = 0.19$ in the melt.; H_2O wt% = 2 is suggested for the 0.5–1.0 GPa runs. *Calculated maximal H_2O content in the basaltic melt due to the water liberation from the reacting serpentinite. Water activity equal to 1 suggests the basaltic melt saturation with water fluid and the presence of the water fluid at the run conditions of 0.5–1.0 GPa pressure. The solid phase proportions were calculated based on the mass balance consideration.*

decompression during periods from 20 min to 2 h. The rate of quenching to the ambient temperature was ∼300°C/min.

Five experiments (P36, P37, SB1, SBbis3, and SBter1) were carried out at pressure of 0.2–0.5 GPa and a temperature of 1250°C using an internally heated gas pressure vessel at the Korzhinskii Institute of Experimental Mineralogy, Chernogolovka, Russia. The pressure in the system was created by pure Ar gas. The system was heated by a furnace with two windings (to minimize the thermal gradient). The temperature was set and measured by a TRM-101 OVEN controller through two S-type ($Pt_{90}Rh_{10}$ vs Pt_{100}) thermocouples. The thermocouples were mounted at the top and close to the bottom of the run hot spot to monitor the temperature gradient. The duration of experiment was from 0.5 to 48 h (**Table 2**). The experiments were quenched by switching off the furnace. The pressure during the quench was maintained constant down to 550°C, and then slowly released. The cooling rate from 1250 to 1000°C was 167°C/min, and then 90°C/min down to 550°C. After the runs, the capsule was mounted in epoxy, cut in two parts using a diamond saw, and then polished using *SiC* sand papers and diamond pastes.

To calculate phase proportions, we have used the PYTHON language code. At the first step, the initial MORB glass was introduced instead of L_{bas} and L_{int}. On the second step, the basaltic and interstitial glasses (L_{bas} and L_{int}, respectively) were distinguished as two phases.

Scanning Electron Microscope (SEM) and Electron Microprobe Analysis (EPMA)

Major and minor element analyses of minerals and glasses and the experimental sample imaging were performed at the Géosciences Environnement Toulouse (GET, Toulouse, France) laboratory using a scanning electron microscope (SEM) JEOL JSM-6360 LV with energy-dispersive X-ray spectroscopy (EDS), coupled with the automatic analyzer of particles by the program "Esprit." The main experimental phases (oxides, silicates, and glasses) in the samples have been identified by EDS microprobe technique at GET (Toulouse, France) (Borisova et al., 2012b). Major and minor element compositions of the crystals and glasses were analyzed using CAMECA SX-Five microprobe at the Centre de Microcaractérisation Raimond Castaing (Toulouse, France). Electron beam of 15 kV accelerating voltage, and of 20 nA current was focused or defocused on the sample to analyze minerals or glasses, respectively. The following synthetic and natural standards were used for calibration: albite (Na), corundum (Al), wollastonite (Si, Ca), sanidine (K), pyrophanite (Mn, Ti), hematite (Fe), periclase (Mg), Ni metal (Ni), and Cr_2O_3 (Cr). Element and background counting times for most analyzed elements were 10 and 5 s, respectively, whereas peak counting times were 120 s for Cr and 80–100 s for Ni. Detection limits for Cr and Ni were 70 and 100 ppm, respectively. The silicate reference materials of Jarosewich et al. (1980) as well as MPI-DING glasses of ultramafic to mafic composition (GOR132-G, GOR128-G, KL2-G, and ML3B-G of Jochum et al., 2006) were analyzed as unknown samples to additionally monitor the analysis accuracy. The silicate reference material analysis allowed to control precision for the major and minor (e.g., Cr, Ni in glasses) element analyses to be in the limit of the analytical uncertainty (related to the count statistics). The accuracy estimated on the reference glasses ranges from 0.5 to 3% (1σ RSD = relative standard deviation), depending on the element contents in the reference glasses.

H_2O contents of glasses were estimated based on the *in situ* electron probe analyses of the major element oxides. The 0.5–1.0 GPa glasses were analyzed following simplified "by difference method" without bracketing. The uncertainty of the water contents generally varies between 10 and 50%. The 0.2 GPa glasses were analyzed by using bracketing mode (Borisova et al., 2020).

X-Ray Absorption Near Edge Structure (XANES) Spectroscopy

Iron redox state in selected quenched glasses was determined from Fe K-edge (∼7.1 keV) XANES spectra acquired at the FAME beamline (Proux et al., 2005) of the ESRF. The beamline optics incorporates a Si(220) monochromator with sagittal focusing allowing an energy resolution of ∼0.5 eV at Fe K-edge and yielding a flux of >1012 photons/s and a beam spot of about 300 × 200 μm. XANES spectra were acquired in fluorescence mode in the right-angle geometry using a 30-element solid-state germanium detector (Canberra). Energy calibration was achieved using a Fe metal foil whose K-edge energy was set to 7.112 keV as the maximum of the spectrum first derivative. Iron-bearing oxides and silicates with different Fe redox and coordination environment, diluted by mixing with boron nitride to obtain Fe concentrations of a few wt%, were measured similarly to the glasses to serve as reference compounds.

Iron redox state in the glasses was determined by fitting the XANES pre-edge region (7.108–7.120 keV) according to the protocols developed in Muñoz et al. (2013) and using a background polynomial and two pseudo-Voight functions to determine the energy position of the pre-edge peak centroid, which is a direct function of the Fe^{III}/Fe^{II} ratio both in crystalline and glass silicate samples (Wilke et al., 2001, 2005). Ferric iron (Fe^{III}) mole fraction (X_{FeIII}) in the starting basalt, and sample P3 was determined using the calibration established for basaltic glasses (Wilke et al., 2005), while sample P1 that showed a mixture of glass and crystals was processed using the calibration established for Fe minerals (Wilke et al., 2001). The results are reported in **Table 2**. The uncertainties of X_{FeIII} determination for dominantly glassy samples are 0.05 in absolute value, while those for glass-crystal mixtures are typically 0.07 of the value.

Laser Ablation Inductively Coupled Plasma Mass Spectrometry

Major and trace element concentrations were determined by LA-ICP-MS at the Max Planck Institute for Chemistry, Mainz, using a New Wave 213 nm Nd:YAG laser UP 213, which was combined with a sector-field ICP-MS Element2 (Thermo Scientific) (Jochum et al., 2007, 2014). Ablation took place in the New Wave Large Format Cell under He atmosphere. Spot analyses were performed in low mass resolution mode using crater sizes of 30 μm (lines of spots) and 8 μm (single spots), and a pulse repetition rate of 10 Hz at a fluence of about 6.5 J/cm^2 (lines of spots) and 8.3 J/cm^2 (single spots). Isotopes used for analysis are the following: ^{7}Li, ^{23}Na, ^{25}Mg, ^{27}Al, ^{29}Si, ^{31}P, ^{39}K, ^{43}Ca, ^{47}Ti, ^{53}Cr, ^{55}Mn, ^{57}Fe, ^{62}Ni, ^{85}Rb, ^{88}Sr, ^{89}Y, ^{90}Zr, ^{93}Nb, ^{137}Ba, ^{139}La, ^{140}Ce, ^{141}Pr, ^{146}Nd, ^{147}Sm, ^{151}Eu, ^{157}Gd, ^{159}Tb, ^{163}Dy, ^{165}Ho, ^{167}Er, ^{169}Tm, ^{173}Yb, ^{175}Lu, ^{178}Hf, ^{232}Th, and ^{238}U. Data reduction was performed by calculating the ion intensities of each isotope relative to the intensity of ^{43}Ca. The NIST SRM 610 silicate glass (for trace and major elements except Mg, K, Fe) and the basaltic glass GSE-1G (Mg, K, Fe) were used for calibration. Major element concentrations were calculated to a total oxide content of 99 wt%. The repeatability (RSD) of the measurements is about 1–3% (30 μm measurements) and 5–10% (8 μm). The detection limits (3 σ definition) for the 30 μm measurements vary between about 0.001 and 1 ppm (Jochum et al., 2007, 2014). They are about a factor of four higher for the 8 μm analyses. Measurement accuracy was tested with GSE-1G. The concentration values agree within about 5% (30 μm) and 10% (8 μm) of the reference values (GeoReM database) (Jochum et al., 2006).

RESULTS OF EXPERIMENTS ON BASALTIC MELT–SERPENTINITE INTERACTION

Experimental Sample Description

The first group of experiments was conducted at 0.5 GPa and 1300°C with duration up to 8 h (**Tables 2–4** and **Supplementary Table S1**). Products of the shortest run P1 (1 min at the run temperature) which was considered as a zero-time experiment, the quenched basaltic glass zone and a zone replacing serpentinite (former serpentinite zone) are present. The former serpentinite zone contains fine-grained (5–10 μm in size) aggregates of olivine Fo_{95}, enstatite (Mg# = 95), chromite (Cr# = 89), and interstitial glass of basaltic andesite composition (**Figure 1**). Chromite crystals (a few micrometers in size) are disseminated within this zone.

Samples P15 and P10 were kept for 0.5 and 2.6 h, respectively, at run conditions. Distinct quenched melt zone and the former serpentinite zone are also present in this sample. The melt zone consists of hydrous basaltic glass. The former serpentinite zone shows 5–20 μm size aggregate of forsteritic olivine Fo_{93} and enstatite Mg# = 97 (P15) or accessory clinopyroxene Mg# = 81 (P10) (**Figure 1**). It is associated with interstitial glass of basaltic andesite to andesitic composition and chromiferous magnetite (P15) or chromite (P10). Chromiferous magnetite and chromite are clustered in two large ($n \times 100$ μm) areas (P15) or disseminated in the olivine-rich zone (P10).

Sample P18 provides an information about 5 h lasting basaltic melt–serpentinite interaction. The sample shows a hydrous basaltic zone and former serpentinite zone. The former serpentinite zone consists of two areas. The outer area of nearly 200 μm width contains olivine, interstitial basaltic glass, and disseminated chromite (grain size of a few micrometers). The inner area consists of forsteritic olivine Fo_{93}, enstatite (Mg# = 97), and contains magnetite aggregate (∼20 × 40 μm) (**Figure 1**).

P36 is the longest (8 h) experiment of the series at 0.5 GPa. Serpentinite is completely dissolved in the basaltic melt, and the run products are represented by homogeneous basaltic glass with 11.5 wt% MgO.

P20, P21, and P26 runs were performed with an additional water and run duration of 0.5, 2.5, and 5.0 h, respectively (**Table 2** and **Supplementary Table S1**). The run products are composed of hydrous basaltic zone and former serpentinite zone where forsteritic olivine Fo_{91-94}, enstatite (Mg# = 93–96) and chromite are associated with interstitial glass of basaltic andesite to andesite composition (Mg# = 51–67). Numerous bubbles in the basaltic glass reflect saturation with the aqueous fluid at the run conditions.

The second series of experiments has been performed at 1.0 GPa and 1300°C. Experiment P3 with duration 2.5 h shows basaltic glass zone and the former serpentinite zone where forsteritic olivine Fo_{92}, enstatite (Mg# = 96), and Cr-bearing magnetite are associated with interstitial glass of basaltic composition (**Figure 1**). The 9 h long run without additional water (P7) and 3 h long run with additional water (P12) contain uniquely hydrous basaltic glasses with 13.0 wt% MgO.

Thus, at 0.5–1.0 GPa pressure range, the initial stage of basaltic melt–serpentinite reaction generates two contrasting zones: an olivine-rich zone composed of mostly harzburgite (forsteritic olivine Fo_{93-95} and enstatite Mg# = 93–95) with an outer dunite portion, and a reacting basaltic zone. These zones are similar to those produced in the anhydrous peridotite-basalt systems at 0.1 MPa–0.8 GPa (Fisk, 1986; Morgan and Liang, 2003). An addition of water at 1.0 GPa at the conditions of the basaltic melt saturation with water fluid phase likely decreases the timescale required for the serpentinite assimilation from 9 h in the P7 run to 3 h in the P12 run (see **Table 2**).

Additionally, the hybrid run P37 sample is represented by predominant basaltic glass of L_{bas} (72.8 wt% in the sample) with assemblage of interstitial glass (L_{int}, 0.4 wt%), forsteritic olivine (17.0), residual orthopyroxene (6.8), and accessory clinopyroxene and chromiferous magnetite with pores of fluid (3.0) (**Table 2**). The mixed sample number SB1 obtained at 0.2 GPa is represented by polyhedral olivine phenocrystals in matrix. In the matrix, this sample contains assemblage of clinopyroxene microphenocrysts, rims of the olivine phenocrysts, and interstitial felsic glasses. Oxide minerals are represented by chromite microphenocrysts. The sample SBter1 is represented by homogeneous basaltic glass formed by complete hybridation of the starting basaltic liquid with serpentinite, whereas the sample SBbis3 contains residual crystallized aggregate of olivine. It is worth noting that the current experiments with predominant proportion of basaltic melt (72–88 wt%) longer than 5–8 h at 0.2–1.0 GPa produce the total assimilation of the serpentinite zone by the basaltic melt (**Figure 1**), resulting in homogeneous Mg-rich basaltic glasses.

Summary on the Melt Composition

The olivine-rich zones host glass pockets of 10–200 μm in size. The composition of the interstitial glasses produced in the

TABLE 3 | Composition of mineral and glass phases from the 0.5–1.0 GPa basaltic melt–serpentinite reaction experiments.

Exp[a]	Phase[b]	SiO_2 (wt%)	TiO_2 (wt%)	Al_2O_3 (wt%)	Cr_2O_3 (wt%)	FeO_{tot}[c] (wt%)	MnO (wt%)	MgO (wt%)	CaO (wt%)	NiO (wt%)	Na_2O (wt%)	K_2O (wt%)	P_2O_5 (wt%)	Cl (wt%)	Total (wt%)	H_2O (wt%)	Cr (ppm)	Ni (ppm)	Mg# [d]	Cr# [e]
P1	L bas (36)	52.8 ± 3.1	1.46 ± 0.14	16.39 ± 1.69	0.03 ± 0.02	7.3 ± 1.17	0.13 ± 0.04	4.75 ± 2.46	8.74 ± 1.61	D.L.	2.55 ± 0.67	0.36 ± 0.07	0.18 ± 0.03	0.7 ± 0.49	95.35	4.7	209 ± 147	D.L.	50.84 ± 9.09	–
	L int (13)	56.3 ± 3.3	1.37 ± 0.2	17.3 ± 1.76	0.02 ± 0.01	5.28 ± 1.65	0.12 ± 0.05	3.42 ± 1.79	6.73 ± 0.4	D.L.	2.99 ± 1.31	0.36 ± 0.1	0.18 ± 0.04	–	94.04	6.0	112 ± 93	D.L.	51.6 ± 12.46	–
	Ol (14)	42.7 ± 1	D.L.	0.45 ± 0.44	0.2 ± 0.23	4.34 ± 0.91	0.12 ± 0.03	50.82 ± 1.91	0.29 ± 0.25	0.35 ± 0.02	D.L.	D.L.	D.L.	–	99.24	–	1358 ± 1550	2721 ± 191	95.41 ± 1.02	–
	Opx (7)	58.9 ± 0.8	D.L.	1.33 ± 0.88	0.22 ± 0.05	3.56 ± 0.37	0.17 ± 0.03	33 ± 2.37	2.24 ± 1.43	0.15 ± 0.02	0.38 ± 0.19	0.1 ± 0.08	D.L.	–	100.0	–	1488 ± 314	1181 ± 165	94.46 ± 1.13	–
	Chr (1)	D.L.	0.17	1.86	21.57	42.68	0.14	14.4	D.L.	0.36	D.L.	D.L.	D.L.	–	94.31	–	147556	2790	50.01	88.61
P15	L bas (163)	50.8 ± 0.9	1.28 ± 0.09	13.01 ± 0.74	0.07 ± 0.01	8.27 ± 0.23	0.16 ± 0.04	10.92 ± 1.04	8.69 ± 0.39	D.L.	2.39 ± 0.12	0.27 ± 0.05	0.13 ± 0.04	0.02 ± 0.01	95.99	4.0	467 ± 97	D.L.	70.07 ± 2	–
	L int (4)	60.3 ± 1.7	0.67 ± 0.16	12.88 ± 1.65	0.09 ± 0.04	9.57 ± 1.3	0.19 ± 0.05	1.78 ± 0.24	7.16 ± 0.56	D.L.	1.76 ± 0.61	0.21 ± 0.11	0.06 ± 0.03	0.02	94.66	5.3	595 ± 278	D.L.	24.95 ± 2.03	–
	Ol (11)	42.1 ± 1.1	D.L.	0.2 ± 0.2	0.22 ± 0.17	6.89 ± 3.69	0.12 ± 0.04	49.33 ± 2.49	0.13 ± 0.08	0.46 ± 0.08	D.L.	D.L.	D.L.	–	99.46	–	1477 ± 1189	3607 ± 666	92.71 ± 3.97	–
	Opx (13)	57.8 ± 1.5	D.L.	0.81 ± 0.34	0.26 ± 0.12	2.7 ± 0.28	D.L. ± 0.03	37.2 ± 1.13	0.2 ± 0.13	0.17 ± 0.07	0.13 ± 0.11	D.L.	D.L.	–	99.28	–	1791 ± 789	1313 ± 536	96.6 ± 0.97	–
	ChrMgt (2)	D.L.	0.36 ± 0.18	1.02 ± 1.07	0.6 ± 0.77	84.67 ± 2.96	0.19 ± 0.03	4.82 ± 1.39	D.L.	0.65 ± 0.05	D.L.	D.L.	D.L.	–	92.3	–	4071 ± 5283	5116 ± 400	26.95 ± 7.06	20.7 ± 13.34
P18	L bas (122)	49.1 ± 4.3	1.21 ± 0.12	14.12 ± 1.31	0.06 ± 0.01	7.4 ± 0.68	0.14 ± 0.04	12.17 ± 1.33	7.97 ± 0.7	D.L.	2.59 ± 0.28	0.28 ± 0.05	0.12 ± 0.03	–	95.1	4.9	417 ± 101	D.L.	74.31 ± 2.56	–
	L int (5)	49.9 ± 1.7	1.43 ± 0.15	16.07 ± 1.82	0.05 ± 0.02	6.22 ± 0.44	0.13 ± 0.04	7.38 ± 3.6	9.05 ± 0.81	D.L.	3.08 ± 0.35	0.36 ± 0.06	0.13 ± 0.03	–	93.8	6.2	330 ± 111	D.L.	64.8 ± 11.65	–
	Ol (3)	42.6 ± 1.4	D.L.	0.08 ± 0.01	0.09 ± 0.02	6.28 ± 0.14	0.11 ± 0.02	49.32 ± 0.41	0.15 ± 0.01	0.38 ± 0.02	D.L.	D.L.	D.L.	–	99.0	–	643 ± 151	2960 ± 161	93.34 ± 0.09	–
	Opx (4)	56.3 ± 1.4	D.L.	0.9 ± 0.6	0.25 ± 0.03	3.88 ± 0.33	0.1 ± 0.02	37.09 ± 1.4	0.66 ± 0.34	0.14 ± 0.03	D.L.	D.L.	D.L.	–	99.3	–	1728 ± 221	1084 ± 272	97.14 ± 1.03	–
	Mgt (2)	0.2	0.73 ± 0.09	7.17 ± 0.09	0.78 ± 0.2	72.16 ± 0.01	D.L.	9.19 ± 0.06	D.L.	0.65 ± 0.02	D.L.	D.L.	D.L.	–	90.9	–	5323 ± 1374	5073 ± 139	48.31 ± 0.46	6.78 ± 1.72

(Continued)

TABLE 3 | Continued

Exp[a]	**Phase**[b]	**SiO_2 (wt%)**	**TiO_2 (wt%)**	**Al_2O_3 (wt%)**	**Cr_2O_3 (wt%)**	**FeO_{tot}[c] (wt%)**	**MnO (wt%)**	**MgO (wt%)**	**CaO (wt%)**	**NiO (wt%)**	**Na_2O (wt%)**	**K_2O (wt%)**	**P_2O_5 (wt%)**	**Cl (wt%)**	**Total (wt%)**	**H_2O (wt%)**	**Cr (ppm)**	**Ni (ppm)**	**Mg# [d]**	**Cr# [e]**
P36	L bas (21)	50.6 ± 0.3	1.36 ± 0.03	13.45 ± 0.13	0.07	8.07 ± 0.13	0.16 ± 0.03	11.5 ± 0.29	9.16 ± 0.14	0.02 ± 0.01	2.89 ± 0.14	0.29 ± 0.05	0.14 ± 0.02	–	97.72	2.2	513 ± 22	D.L.	71.73 ± 0.74	–
P3	L bas (151)	49.6 ± 7.2	1.34 ± 0.21	13.47 ± 2.11	0.06 ± 0.01	8.03 ± 1.17	0.16 ± 0.05	10.4 ± 1.78	9.27 ± 1.37	D.L.	2.66 ± 0.45	0.28 ± 0.06	0.14 ± 0.04	0.02 ± 0.01	95.48	4.5	405 ± 100	D.L.	68.65 ± 7.59	–
	L int (16)	49.9 ± 1.5	1.51 ± 0.27	14.2 ± 1.78	0.08 ± 0.03	8.74 ± 0.75	0.17 ± 0.05	9.95 ± 4.82	10.36 ± 1.68	D.L.	2.44 ± 0.31	0.27 ± 0.07	0.15 ± 0.04	–	97.72	2.3	516 ± 234	D.L.	64.76 ± 7.32	–
	Ol (17)	43.2 ± 1.4	D.L.	0.97 ± 0.83	0.07 ± 0.03	7.39 ± 1.42	0.15 ± 0.03	45.91 ± 2.51	0.81 ± 0.7	0.36 ± 0.05	D.L.	D.L.	D.L.	–	98.84	–	508 ± 181	2522 ± 1013	91.72 ± 1.53	–
	Opx (11)	54.2 ± 0.8	0.19 ± 0.13	3.08 ± 1.53	0.24 ± 0.06	4.48 ± 0.54	0.14 ± 0.03	34.3 ± 2.84	1.7 ± 0.86	0.16 ± 0.03	0.41 ± 0.31	0.05 ± 0.03	D.L.	–	98.95	–	1609 ± 390	1238 ± 264	96.09 ± 2.38	–
	ChrMgt	0.6 ± 0.1	2.24 ± 0.14	17.9 ± 0.01	2.69 ± 0.27	57.52 ± 0.6	0.15	11.72 ± 0.32	D.L.	–	D.L.	D.L.	D.L.	–	92.84	–	18371 ± 1858	–	53.55 ± 1.35	9.14 ± 0.85
P7	L bas (75)	50.6 ± 5.9	1.22 ± 0.15	12.78 ± 1.48	0.07 ± 0.01	8.02 ± 0.93	0.16 ± 0.03	12.96 ± 1.52	8.78 ± 1.03	D.L.	2.49 ± 0.29	0.27 ± 0.04	0.16 ± 0.03	–	97.54	2.5	508 ± 62	D.L.	73.68 ± 4.84	

[a] *The experiment number, conditions are given in the* ***Table 2****.* [b] *The produced mineral and melt phases. Bracketed numbers correspond to the number of analyses.* L_{bas} *and* L_{int} *are compositions of the basaltic and interstitial glasses correspondingly; Ol—olivine, Opx—orthopyroxene, Chr—chromite, ChrMgt—chromiferous magnetite, Mgt—magnetite.* [c] *All iron content is recalculated as iron total (*FeO_{tot}*).* [d] *Magnesium number [100Mg/(Mg +* Fe^{2+}*)] in atoms per formula unit. In case of glasses iron total is taken* [e] *Chromium number [100Cr/(Cr + Al)] in atoms per formula unit. D.L. corresponds to values below detection limit.*

TABLE 4 | Average major and trace element composition of the 0.5–1.0 GPa homogeneous samples obtained by LA-ICP-MS.

Sample	SiO_2, wt%	TiO_2	Al_2O_3	FeO	MgO	MnO	CaO	Na_2O	K_2O	P_2O_5
P7 (47)[a]	51.14 ± 0.37	1.24 ± 0.02	12.63 ± 0.23	8.97 ± 0.15	12.64 ± 0.18	0.16 ± 0.01	9.09 ± 0.15	2.67 ± 0.05	0.26 ± 0.01	0.22 ± 0.01
P36 (43)	51.90 ± 0.49	1.26 ± 0.02	13.49 ± 0.38	8.87 ± 0.17	10.85 ± 0.59	0.16 ± 0.01	9.31 ± 0.22	2.68 ± 0.07	0.27 ± 0.01	0.20 ± 0.01
	Li, ppm	**Cr**	**Ni**	**Rb**	**Sr**	**Y**	**Zr**	**Nb**	**Ba**	**La**
P7 (47)	5.92 ± 0.29	505.9 ± 10.07	204.6 ± 29.37	6.99 ± 0.22	138.03 ± 3.26	24.84 ± 0.59	8.74 ± 2.15	8.21 ± 0.20	75.38 ± 2.12	6.68 ± 0.20
P36 (43)	16.79 ± 0.77	511.6 ± 38.6	136.9 ± 30.2	7.09 ± 0.22	141.2 ± 2.62	25.8 ± 0.86	92.94 ± 2.58	8.85 ± 0.30	76.93 ± 1.70	6.64 ± 0.20
ppm	**Ce**	**Pr**	**Nd**	**Sm**	**Eu**	**Gd**	**Tb**	**Dy**	**Ho**	**Er**
P7 (47)	16.36 ± 0.33	2.36 ± 0.08	11.43 ± 1.1	3.39 ± 0.23	1.19 ± 0.07	4.04 ± 0.21	0.68 ± 0.04	4.40 ± 0.24	0.93 ± 0.06	2.67 ± 0.20
P36 (43)	16.63 ± 0.38	2.42 ± 0.08	11.51 ± 0.37	3.48 ± 0.16	1.23 ± 0.07	4.24 ± 0.21	0.71 ± 0.04	4.72 ± 0.20	0.98 ± 0.05	2.88 ± 0.19
ppm	**Tm**	**Yb**	Lu	**Hf**	**Th**	**U**	**$(La/Sm)_n$**	**$(La/Yb)_n$**		
P7 (47)	0.39 ± 0.03	2.57 ± 0.16	0.39 ± 0.03	2.38 ± 0.10	0.60 ± 0.03	0.21 ± 0.02	1.28 ± 0.08	1.87 ± 0.11		
P36 (43)	0.40 ± 0.03	2.67 ± 0.14	0.41 ± 0.03	2.53 ± 0.11	0.63 ± 0.04	0.21 ± 0.02	1.23 ± 0.06	1.79 ± 0.10		

[a] *The experiment number, conditions are given in the* ***Table 2****. Bracketed numbers correspond to the number of analyses. The average composition and the glass homogeneity is represented as 1 σ std. deviation. La/Sm and La/Yb are normalized to the composition of the primitive mantle (Lyubetskaya and Korenaga, 2007).*

shortest hybrid runs at 0.5–1.0 GPa varies from basaltic, basaltic andesite to andesitic (**Figure 2**). The interstitial dacitic melts even richer in silica (up to 66–71 wt%) were produced at 0.2 GPa pressure compared to those obtained in the 0.5–1.0 GPa pressure (**Figure 2**) and are discussed elsewhere (Borisova et al., 2020). In this work, we pay more attention to the mechanisms and to the rates of assimilation relevant to the magmas interacting with hydrated mantle lithosphere in oceanic setting. The interstitial melts produced at 0.2–1.0 GPa are formed close to equilibrium with olivines of the olivine-rich zones (**Figure 3**). The major element composition of the basaltic melts produced due to the bulk serpentinite dissolution in the longest experiments (48 h at 0.2 GPa, 8 h at 0.5 GPa, and 3 h at 1.0 GPa pressure) indicates a strong contribution of the serpentinite on the basalt chemistry. Indeed, the final products of the kinetic series at 0.2–1.0 GPa are represented by homogeneous Mg-rich basaltic glasses (50–52 wt% SiO_2, 12–13 wt.% MgO) with ∼500 ppm Cr and 140–200 ppm Ni (**Tables 3**, **4** and **Supplementary Table S1**). They contrast with the starting MORB (50 wt% SiO_2, MgO = 8.2 wt.%, Cr = 275 ppm, Ni = 129 ppm) due to the complete dissolution of the Mg, Cr and Ni-enriched serpentinite (**Figures 2**, **3**). The homogeneous basaltic glasses present lower TiO_2 contents (1.22–1.36 wt%) and similar primitive-normalized $(La/Sm)_n$ (1.1–1.5) and $(La/Yb)_n$ (1.6–2.0) ratios compared to those of the starting basaltic melt (1.45 wt%, 1.1 and 1.6, respectively) due to the low content of these elements in the serpentine (**Table 4**). Thus, the chemical impact of serpentinite on the final basaltic melt as a result of the bulk assimilation is a dilution in incompatible elements (e.g., Ti) contents and an enrichment in compatible Cr, Ni, and Mg elements, as well as a slight enrichment in Si contents.

MECHANISM AND RATE OF THE HYDRATED MANTLE ASSIMILATION

Mechanism of the Basaltic Melt-Hydrated Peridotite Reaction

Hybrid and mixed experiments on identical materials with high basaltic melt to serpentinite rock ratio (>2) performed at different run durations allowed determination of the reaction mechanism and the assimilation rate. The transformation of serpentinite to dehydrated harzburgite with pore fluid is demonstrated in the zero-time experiment at 1300°C and 0.5 GPa (**Figure 1** and **Table 2**). The serpentinite in the shortest runs produces forsteritic olivine (Fo_{91-95}), enstatite (Mg# = 94–97), and chromite and/or chromiferous magnetite with Cr# = 7–89 and Mg# = 27–54 (**Figure 1** and **Table 2**), similarly to the results of Chepurov et al. (2016). The phase composition diagram and MgO–SiO_2 plot (**Figures 1**, **3**) suggest that the basaltic melt–serpentinite reaction at 0.2–1.0 GPa is controlled by the following stages: (1) transformation of serpentinite to chromite-bearing harzburgite (crystallization of forsteritic olivine and enstatite with accessory chromite and liberation of pore fluid), (2) incongruent partial melting of the harzburgite and formation of olivine-rich zones with hydrous interstitial melts. Subsequently, the mechanism involves (3) formation of external

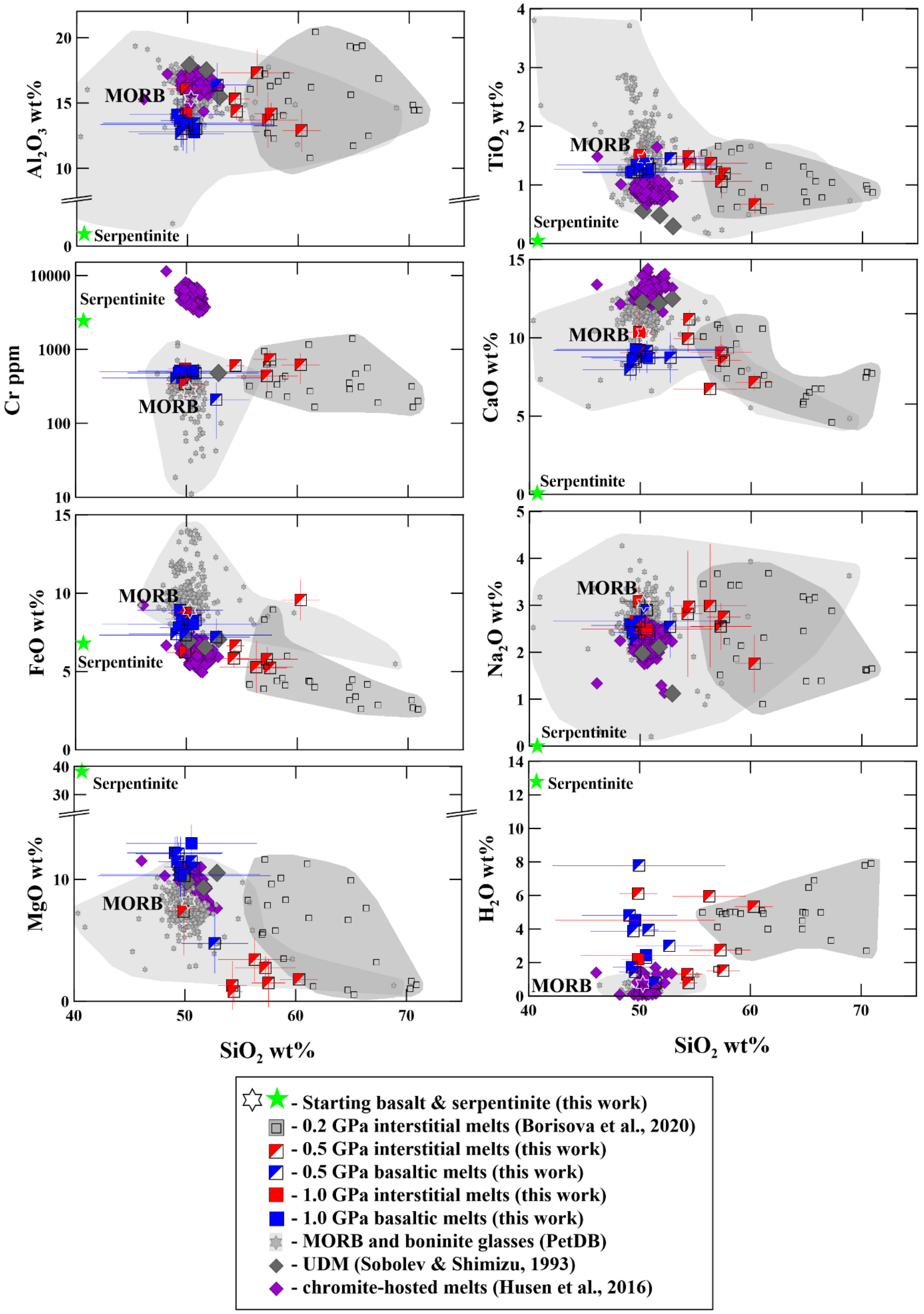

FIGURE 2 | Al_2O_3, TiO_2, FeO, MgO, CaO, and Na_2O (in wt%), Cr (ppm), and H_2O (in wt%) contents versus SiO_2 contents (in wt%) in the experimental glasses. Composition of the experimental glasses produced from 0.2 to 1.0 GPa is compared to the starting basalt (MORB) and the serpentinite compositions as well as to the compositional fields of natural tholeiitic and oceanic boninitic glasses (from database of PetDB, Lehnert et al., 2000), ultra-depleted melts marked as UDM Sobolev and Shimizu (1993), and chromite-hosted melts (Husen et al., 2016) which are differently depleted MORB melts. The recalculated melts obtained experimentally at 0.2 GPa pressure are after Borisova et al. (2020). H_2O contents in the experimental glasses are values calculated from the EPMA. All experimental data are available in **Table 3** and **Supplementary Table S1**.

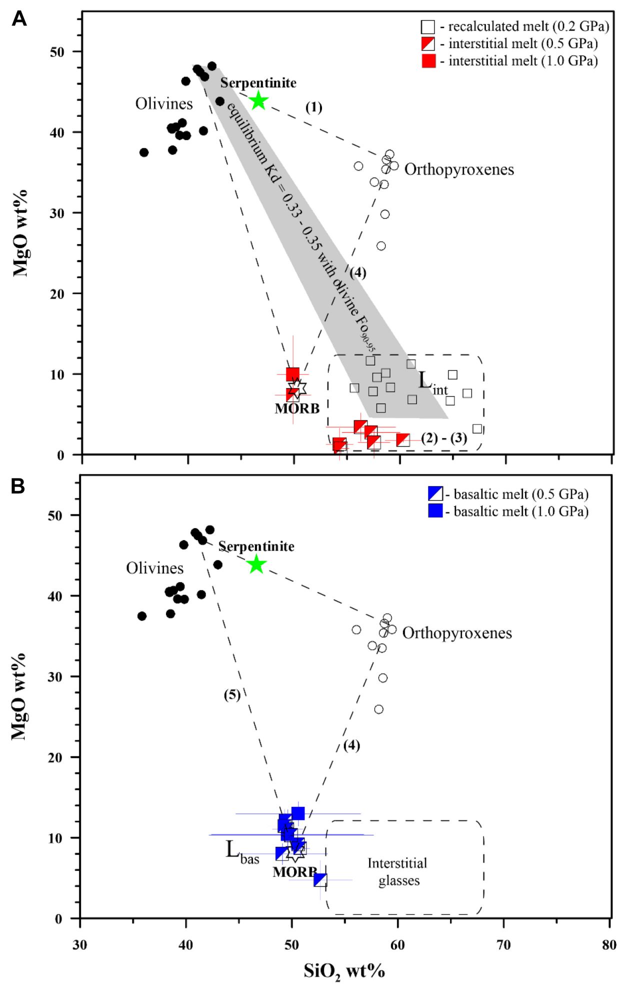

FIGURE 3 | (A,B) Mechanism of the basaltic melt interaction with serpentinite. Five steps of the interaction have been distinguished: (1) dehydration and transformation of serpentinite to Cr-rich spinel-bearing harzburgite (crystallization of olivine and orthopyroxene) with appearance of pore fluid, (2) incongruent melting of the harzburgite and formation of associated hydrous interstitial melts in harzburgite/dunite, (3) progressive formation of external dunite zone due to orthopyroxene dissolution and diffusive exchange between the external basaltic melt and interstitial melts and (4) dissolution of the dunite in the basaltic melt, and finally (5) bulk dissolution of the dunite and formation of hybrid basaltic melts. L_{int} and L_{bas} are interstitial and basaltic melts, respectively (see **Table 2**). Equilibrium Kd are calculated as theoretical FeO–MgO partition coefficient between olivine (Fo_{90-95} mol%) and co-existing interstitial melt of 57–62 wt% SiO_2 at 0.5 GPa pressure according to Toplis (2005). The recalculated melts obtained experimentally at 0.2 GPa pressure are after Borisova et al. (2020). All experimental data are available in **Table 3** and **Supplementary Table S1**.

chromite-bearing dunite zone due to incongruent dissolution of orthopyroxene associated with diffusive exchange between the reacting basaltic melt and the interstitial melts, (4) partial dissolution of the chromite-bearing dunite in the initial basaltic melt, and finally (5) the total assimilation of the chromite-bearing dunite and formation of the high-Mg hydrous hybrid basaltic melt (**Tables 2, 3**). Moreover, the homogeneous hybrid basaltic melts produced in the longest experiments at 0.2–1.0 GPa are enriched in Mg and Cr due to the total assimilation of serpentinite (**Table 4**). Tholeiitic basaltic melts reacting with and assimilating the hydrous peridotite become eventually saturated with olivine, chromite, and orthopyroxene. We suggest that the reaction of such depleted basaltic melt with a peridotite would produce chromite-bearing harzburgite through reactive porous flow. The mechanism observed in our work contrasts with reactive fractionation reported by Van den Bleeken et al. (2010, 2011) at 0.65–0.80 GPa in dry conditions. These authors observed plagioclase and orthopyroxene crystallization and formation of plagioclase-bearing peridotite due to reactive porous flow of dry tholeiitic basaltic melt through anhydrous peridotite at 1170–1320°C.

Fractional crystallization of the hybrid, depleted, and chromite-saturated basaltic melts can produce chromitites. Indeed, according to the recently proposed model of the chromitite genesis, the bulk serpentinite assimilation by MORB basaltic melt is the main factor responsible for the massive chromite crystallization (Borisova et al., 2012a) at the oceanic Moho mantle-crust transition zone. Our experiments demonstrate that formation of the hybrid mid-ocean ridge basaltic melt saturated with chromite is possible at conditions of predominant proportion of basaltic melt (above 70 wt%) and, therefore, due to high melt/rock ratio (>2) at 0.2–1.0 GPa pressure. The main physico-chemical parameters controlling the chromite crystallization are the presence of aqueous fluid or/and hydrous basaltic melts into the reactive system (Borisova et al., 2012a; Johan et al., 2017; Zagrtdenov et al., 2018). The fluid presence at 0.2 GPa pressure is also necessary condition for the chromite concentrating by a physical, not a chemical process due to surface tension of the fluid, which is sufficient to maintain dispersed chromite crystals inside the fluid upon the chromite crystallization (Matveev and Ballhaus, 2002). Additionally, an initial stage of the basaltic melt reaction with dehydrated serpentinite may result in formation of chromite-bearing harzburgite and dunite. The first direct evidence that the initial stage really happens at the 0.2 GPa mantle-crust transition zone is occurrence of chromite-hosted silica-rich inclusions of the Oman ophiolite chromitite ore bodies (Rospabé et al., 2019b).

Assimilation Rate of the Hydrated Mantle Lithosphere

The calculated average rate of the serpentinite assimilation by the basaltic melt in the experiments without additional water is 4.3×10^{-10} m^2/s (**Table 5**). It is surprisingly similar to the assimilation rate by basaltic melt in the runs with an additional water at conditions of the melt saturation with an aqueous fluid ($\sim 4.0 \times 10^{-10}$ m^2/s). **Figure 4** demonstrates that the serpentinite assimilation rate by dry basaltic melt measured at 0.5 GPa is progressively decreasing during the experimental run. This may be explained by approaching equilibrium, in accordance with principles of the chemical kinetics. The calculated rates are at least one order of magnitude higher compared to 10^{-12}–10^{-11} m^2/s for the basalt interacting with anhydrous harzburgite at 0.6 GPa (Morgan and Liang, 2003). The assimilation rate estimated in our work is comparable to the silica diffusivity in a hydrous

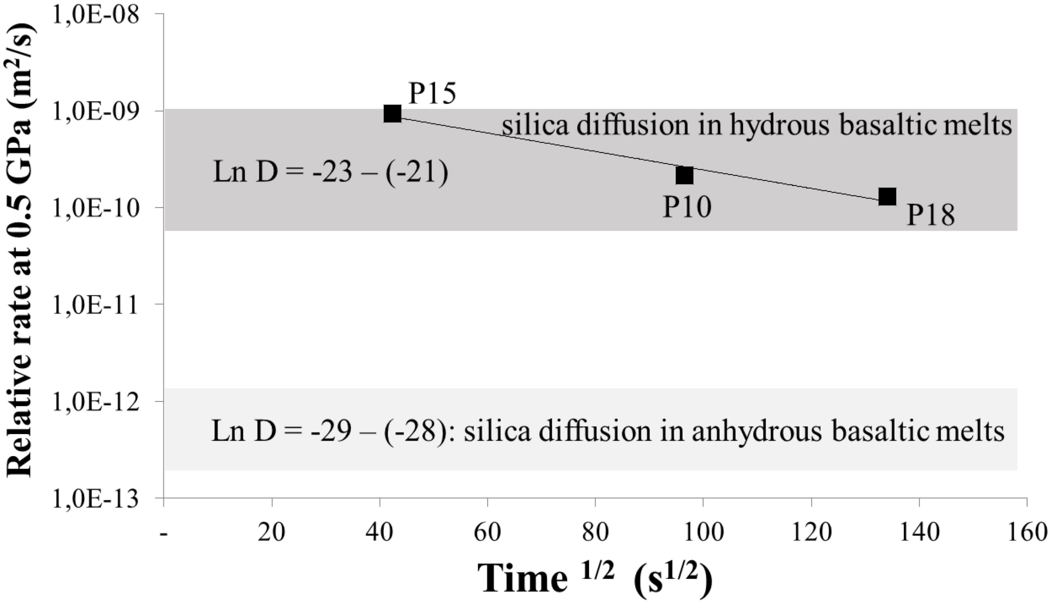

FIGURE 4 | "Relative" rates (in m^2/s) of the serpentinite assimilation by the basaltic melt at 1300°C and 0.5 GPa versus the run duration (in $s^{1/2}$). **Table 5** demonstrates the applied calculation method for the "relative dissolution rate."

basaltic melt (Zhang et al., 2010). Similarly, the reaction rate established by Morgan and Liang (2003) in anhydrous system is mostly comparable to the silica diffusivity in dry basaltic melt. Since both reaction rates are controlled by the silica diffusion, the difference in the reaction rates is related to the well-known promoting effect of H_2O on the silica diffusion in silicate melts (e.g., Zhang et al., 2010 and the references therein). Thus, the serpentinite assimilation by basaltic magma may proceed at least 10 times faster than the formation of dunitic reaction margins (i.e., "dyke walls") in the oceanic lithosphere during transport of dry basaltic melt (Morgan and Liang, 2003) at 0.6–0.8 GPa. Additionally, the newly produced hybrid basaltic melts which become highly saturated with olivine, chromite and, likely, in orthopyroxene would produce plagioclase-free chromite-bearing harzburgite through reactive porous flow in a peridotite. This process may be expressed in nature by formation of chromite-bearing harzburgitic rather than dunitic channels of depleted hybrid magmas enriched in Si, Mg, Cr, and H_2O.

Comparison to Chemistry of Oceanic Magmas and Glasses

Figure 2 illustrates a huge range of the major elements, water and Cr contents in natural MORB, depleted basaltic, and oceanic boninite glasses at wide range of SiO_2 (40–69 wt.%) contents taken from the PetDB database (Lehnert et al., 2000). These compositional variations in the oceanic melts are generally attributed to varying partial melting and fractional crystallization of basaltic and boninite magmas as well as to the reactive basaltic melt percolation through anhydrous peridotite (e.g., Van den Bleeken et al., 2010, 2011). However, the compositional similarity of the experimental glasses produced due to serpentinite assimilation by basaltic melt to the compositional field of the natural oceanic glasses indicates that the composition of the oceanic magmas may also be controlled by the melt reaction with hydrated peridotite during the magma percolation to the seafloor. The elevated water contents in the experimental liquids related to the serpentinite dehydration at magmatic conditions is a main difference between the experimental liquids and natural glasses. This difference may be explained by the natural basaltic melt degassing upon its residence and transport to the surface. Indeed, the highest known water contents of the Kane Megamullion south of the Kane Fracture Zone along the Mid-Atlantic Ridge were recorded in MORB samples (up to 1.8 wt% in glass, and up to 2.7 wt% in bulk rocks) (Ciazela et al., 2017). These MORB magmas are considered to assimilate significant volume of the host serpentinite at lithospheric conditions, whereas most MORB glasses sampled at the surface are degassed.

It is now established that hydrothermal circulation during oceanic spreading reaches mantle peridotite at and below the petrologic Moho (Python et al., 2007; Rospabé et al., 2017, 2019a,b). The serpentinized peridotite or/and dehydrated serpentinite mantle are characterized by an excess of H_2O, Cl (e.g., Bonifacie et al., 2008), ^4He, ^{36}Ar (Kendrick et al., 2013), and radiogenic $^{87}Sr/^{86}Sr$ (e.g., Harvey et al., 2014). The oceanic melts affected by assimilation of serpentinized mantle thus may be recognized by an excess of Si, Cr, Mg, H_2O, Cl, and radiogenic $^{87}Sr/^{86}Sr$ ratio compared to those of typical MORB. It should be noted that the highest measured Cr contents in the chromite-hosted melt inclusions of Husen et al. (2016) are overestimated due to secondary fluorescence effects of nearby chromite (Borisova et al., 2018), whereas these effects are absent during electron microprobe analysis (EPMA) of natural glasses without any trace of chrome-rich minerals. The hybrid oceanic

TABLE 5 | Calculation of assimilation rate at 0.5–1.0 GPa and 1300°C.

N°	Pressure (GPa)	Additional water (wt.%)	Duration (s)	Run duration ($s^{1/2}$)	Volume difference* (mm^3)	Volume difference (%)	Linear difference (μm)	Linear rate1 ($\mu m/s^{1/2}$)	Linear rate2 ($\mu m^2/s$)	Relative rate (m^2/s)	Ln(Average rate) (m^2/s)
P15	0.5	–	1800	42.43	2.210	53.9	1302.6	30.7	9.43E + 02	9.43E-10	
P10	0.5	–	9300	96.44	2.834	69.2	1415.1	14.7	2.15E + 02	2.15E-10	
P18	0.5	–	18000	134.16	3.602	85.1	1532.9	11.4	1.31E + 02	1.31E-10	
Avr.	0.5	–	–	–	–	–	–	–	–	4.30E-10	−21.6
P20	0.5	7.8	1800	42.43	1.830	43.3	1223.1	28.8	8.31E + 02	8.31E-10	
P21	0.5	9.5	9000	94.87	3.295	80.6	1488.0	15.7	2.46E + 02	2.46E-10	
P26	0.5	6.4	18000	134.16	2.195	51.9	1299.7	9.7	9.38E + 01	9.38E-11	
Avr.	0.5	–	–	–	–	–	–	–	–	3.90E-10	−21.7
P3	1.0	–	9000	94.87	1.318	32.2	1096.5	11.6	1.34E + 02	1.34E-10	−22.7

**Volume calculated as cylinder volume based on initial 3D measurements of the serpentinite disc shape and based on measurements of 2D dimensions of the residual serpentinite using SEM in the polished sections. The volume difference is calculated as (V_{int} − V_{exp})/V_{int}, where V_{exp} is the volume after experimentation and V_{int} is the initial volume. Volumes have been calculated from the serpentinite mass and density for the initial volume (V_{int}) and the 2D size measured using SEM after experimentation (V_{exp}). The uncertainty on the assimilation rate (relative rate) is in the limit of 15 rel.%. Avr.—average rate values.*

magmas thus may be distinguished from the original MORB melts by non-mantle isotopic compositions of O, H, Cl, He, Ne, and Ar. For example, elevated Cl contents and atmospheric Ne and Ar in the Mid-Atlantic Ridge basaltic glasses (Stroncik and Niedermann, 2016) are explained by the shallow-level assimilation of a seawater-sourced component. Low $^3He/^4He$ ratios of the Southwest Indian Ridge MORB interpreted by Georgen et al. (2003) as recycled lithospheric material in the upper mantle source region, may be ascribed to the assimilation of the serpentinized lithospheric mantle by the oceanic tholeiitic basalt. Our data confirm the hypothesis of Benoit et al. (1999) and Nonnotte et al. (2005), based on $^{87}Sr/^{86}Sr$–$^{143}Nd/^{144}Nd$ ratios, that petrogenesis of orthopyroxene-rich primitive and depleted oceanic cumulates from the Mid Atlantic Ridge (DSDP Site 334) and at the periphery of the Maqsad paleo-diapir in the Oman ophiolite may be due to hybridization (or mixing) between tholeiitic basaltic melts and liquids issued from melting of the serpentinized lithospheric mantle. Similarly, the radiogenic $^{87}Sr/^{86}Sr$ coupled with an excess of H_2O, SiO_2, halogens, ^4He, ^{36}Ar in oceanic basalts, related cumulates, and associated mantle peridotites is undisputable evidence for their origin due to serpentinization of the mantle lithosphere (Neumann et al., 2015) and the basaltic melt reactions with the serpentinized mantle rather than due to partial melting of deep-seated serpentinized mantle (DMM, HIMU, e.g., Kendrick et al., 2017).

The effect of the altered lithosphere assimilation is likely widespread given the elevated chlorine contents (>50 ppm) and the resulting high Cl/K ratios (>0.09) in the MORB glasses well above Cl of 50 ppm content and global mantle Cl/K of 0.09, respectively (Stroncik and Niedermann, 2016; van der Zwan et al., 2017). Clinopyroxene-melt thermobarometry yields lower crustal-upper mantle crystallization/assimilation depths of 10–13 km. The Cl-excess is observed in both slow-spreading and fast-spreading ridges (van der Zwan et al., 2017 and the references therein). The mechanism of such Cl contamination process may be either assimilation of the country rocks containing pore brine fluid, or brine in fluid inclusions or partial melting of the altered lithosphere, summarized by van der Zwan et al. (2017) to the "assimilation of hydrothermally altered lithosphere." Recent investigation of MOR gabbro hosted by the Kane Megamullion serpentinized mantle supports the existence of the basaltic melt reaction with the serpentinizeed mantle enriching the final melt in water (up to 2.7 wt% in bulk rocks), triggering sulfide saturation, clinopyroxene crystallization before plagioclase, and lowering solidus temperature down to 840°C. The effect of the melt–rock interaction allows even larger amount of melt to react with the channels or dyke walls (Ciazela et al., 2017, 2018). These facts and the well-documented contact metamorphic rock consisting of antigorite, tremolite, chlorite, and prehnite suggest that the mafic melt–serpentinite reaction in fact takes place (Ciazela et al., 2017, 2018), especially in slow-spreading ridges (van der Zwan et al., 2017).

Additionally, ultra-depleted MORB and related variously depleted melts are produced beneath mid-ocean ridges, likely at 0.5–2.0 GPa pressure in assemblage with forsteritic olivine (Fo_{82-91} mol.%) according to Ross and Elthon (1993), Sobolev and Shimizu (1993), and Husen et al. (2016). Routinely, origin

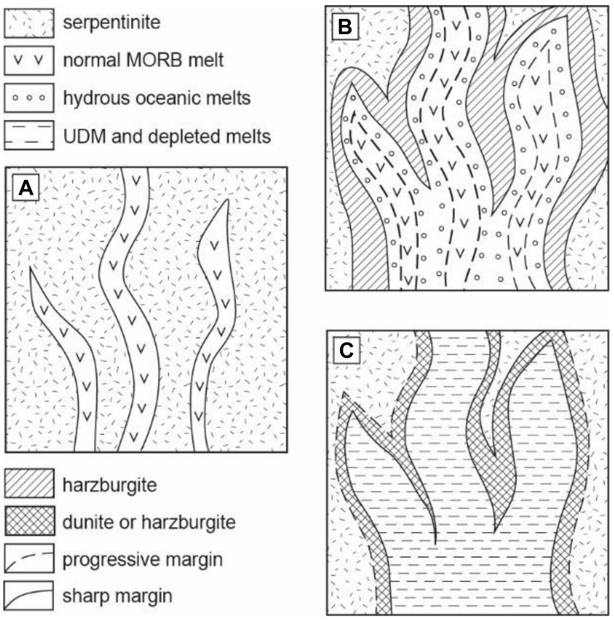

FIGURE 5 | Model of the reaction between "normal" oceanic basaltic melt and the hydrated (serpentinized) mantle lithosphere. **(A)** The initial stage of the mafic melt percolation into the hydrated mantle and formation of contact metamorphic harzburgite containing pore fluid; **(B)** formation of harzburgite wall rocks in assemblage with interstitial hydrous silica-enriched (basaltic to dacitic) melts and diffusive homogenization between the initial oceanic basaltic (e.g., MORB, OIB) melt and the produced hydrous silica-enriched melts. At this stage, formation of peridotite xenoliths containing silica-rich inclusions is highly probable. **(C)** The final production of variously depleted hybrid melts locally associated with the chromite-bearing dunite/harzburgite. The bulk assimilation of serpentinite by basaltic melt may happen at conditions of high melt/rock ratio and the predominant proportion of basaltic melt above 70 wt% into the hybrid system.

of such ultra-depleted and differently depleted MORB melts has been attributed to an effect of critical (continuous) melting with formation of lherzolite/harzburgite residue. Chemical similarity of our experimental Cr-Mg-H_2O-rich melts and associated high-Mg silicates such as forsteritic olivine (Fo_{91-95} mol.%) to those associated to forsteritic olivine (Fo_{82-91} mol.%) (e.g., Sobolev and Shimizu, 1993; Husen et al., 2016) implies that origin of some part of these variously depleted oceanic basaltic melts may be attributed to the reaction between tholeiitic basaltic melt and the serpentinized mantle rather than to fractional "dynamic" melting of mantle peridotite.

Integrated Model of Basaltic Melt–Hydrated Peridotite Reaction

It is likely that the serpentinized lithosphere assimilation may be stronger along slow- and ultraslow-spreading ridges due to faults rooting deeper, providing pathway for hydrothermal fluids (e.g., Mével and Cannat, 1991; van der Zwan et al., 2017 and the references therein), although there are clear evidence for elevated concentrations of Cl in the MORB magmas of fast-spreading ridges (e.g., France et al., 2009) and in small oceanic island magmas (e.g., Dixon et al., 2008 and the references therein). Several examples suggest that the assimilation is favorable in the slow-spreading settings where the source of the Cl contamination lies deep in the magmatic system, although Cl excess in magmas and evidence for the assimilation of the hydrothermally altered lithosphere are observed in all types of ridges, whatever their spreading rate (Ciazela et al., 2017; van der Zwan et al., 2017).

Our experimental work on basaltic melt–serpentinite interaction provides convincing evidence that several types of the oceanic lavas and cumulates can be produced by reaction of a typical mid-ocean ridge basaltic melt with serpentinized lithospheric mantle. Hybrid experiments suggest multi-stage reactions with serpentinized mantle (**Figure 5**): (i) an initial stage of primitive basalt percolation into the serpentinized mantle; (ii) serpentinite dehydration and transformation to chromite-bearing harzburgite containing pore fluid and generation of hydrous interstitial melts variously enriched in silica; and (iii) the final production of hybrid melts depleted in incompatible elements in association with chromite-bearing harzburgite or dunite due to progressive incongruent dissolution of orthopyroxene and reaction with basaltic melt at 0.2–1.0 GPa pressure. Since the observed major and trace element composition of the produced melts depends on the reaction pressure and duration (e.g., **Figures 1–3**), our data infer that chemical evolution of the oceanic basaltic magmas depends on (1) the depth of their interaction with the overlying oceanic lithospheric mantle serpentinized by seawater-derived fluids and (2) the rate of the basaltic melt transport from their upper mantle source, i.e., how long the oceanic melts interacted with the serpentinized lithospheric mantle.

CONCLUSION

(1) The hybrid and mixed experiments performed at 0.2–1.0 GPa pressures on interaction between basaltic melt and serpentinite provide convincing evidence that generation of depleted MORB melts, high-Mg-Cr cumulates, chromitites, and oceanic boninites and andesites can be reliably explained by the efficient reaction of initially anhydrous basaltic melts with the serpentinized lithospheric mantle. Our data infer that chemical evolution of the oceanic magmas depends on which depth and how long the oceanic basaltic melts interacted with the hydrated mantle lithosphere. Our work determines physical-chemical conditions at which reaction of the hydrated peridotite (or serpentinite) with basaltic liquid can lead to massive chromite crystallization at 0.2 GPa pressure according to model of Borisova et al. (2012a).

(2) The effect of the reaction of tholeiitic basaltic melt with hydrous peridotite contrasts strongly with that observed on anhydrous peridotite at 0.65–0.80 GPa by Van den Bleeken et al. (2010, 2011). The main difference is the total assimilation of hydrous harzburgite by the basaltic magma and a complete absence of plagioclase in the reacted harzburgite. That is likely due to the effect of elevated water contents into the hybrid systems suppressing crystallization of plagioclase. Tholeiitic basaltic melts reacting with and

assimilating the hydrous peridotite become more saturated with olivine, chromite, and orthopyroxene and may produce chromite-bearing harzburgite upon reactive melt transport in the upper mantle.

(3) The rate of the bulk serpentinized peridotite assimilation by tholeiitic basaltic melt ($4.0–4.3 \times 10^{-10}$ m^2/s) is controlled by the silica diffusion in hydrous basaltic melts. The calculated rates of the serpentinite assimilation are at least one order of magnitude higher than $10^{-12}–10^{-11}$ m/s^2 for dry basaltic melt interacting with anhydrous harzburgite and producing dunite channels due to reactive porous flow of the basaltic melt (Morgan and Liang, 2003). The bulk assimilation of serpentinite by basaltic melt may happen at conditions of high melt/rock ratio (>2) and the predominant proportion of basaltic melt above 70 wt% in the hybrid system.

(4) Our study challenges the routine interpretation of variations in chemical and isotopic composition of oceanic lavas (e.g., MORB and OIB) in terms of deep mantle plume source heterogeneities or/and mechanism of partial melting.

DATA AVAILABILITY STATEMENT

All datasets generated for this study are included in the article/**Supplementary Material**.

AUTHOR CONTRIBUTIONS

ABo, MT, GC, and OS developed the conceptual idea of the study. ABo, NZ, and SS prepared and conducted high T-P runs at BGI. NZ, OS, and ABy prepared and performed experiments at IEM. GP and NZ carried out XAS measurements. KJ, BS, and UW performed LA-ICP-MS analyses. ABo and NZ performed microanalytical measurements and mapping using EPMA. ABo and GC developed geological applications. All authors contributed to data interpretation and manuscript writing.

FUNDING

This work was supported by the Institut Carnot ISIFoR, Deutsche Forschungsgemeinschaft (DFG - German Research Foundation), the University of Bayreuth, and AST Planets of the Observatoire Midi-Pyrénées. This study was partially fulfilled under the Research Program AAAA-A18-118020590148-3 of the Korzhinskii Institute of Experimental Mineralogy RAS (OS).

ACKNOWLEDGMENTS

We thank the editor YX, and the reviewers TM and BS for comments and suggestions, which helped to improve the manuscript. We acknowledge the access to the experimental facilities of the Bavarian Research Institute of Experimental Geochemistry and Geophysics (BGI) and to the European Synchrotron Radiation Facility (ESRF). We thank C. McCammon, H. Keppler, and N. Dubrovinskaia for advice and assistance with the experiments, M. Munoz for help with the XANES data analyses, and Z. Morgan, Y. Liang, and M. Rabinowicz for discussions on the basalt-peridotite reactions that helped improve this article.

SUPPLEMENTARY MATERIAL

The Supplementary Material for this article can be found online at: https://www.frontiersin.org/articles/10.3389/feart.2020.00084/full#supplementary-material

REFERENCES

Akizawa, N., and Arai, S. (2014). Petrology of mantle diopsidite from Wadi Fizh, northern Oman ophiolite: Cr and REE mobility by hydrothermal solution. *Island Arc* 23, 312–323. doi: 10.1111/iar.12074

Amri, I., Benoit, M., and Ceuleneer, G. (1996). Tectonic setting for the genesis of oceanic plagiogranites: evidence from a paleo-spreading structure in the Oman ophiolite. *Earth Planet. Sci. Lett.* 139, 177–194. doi: 10.1016/0012-821x(95)00233-3

Bach, W., Garrido, C. J., Paulick, H., Harvey, J., and Rosner, M. (2004). Seawater-peridotite interactions: first insights from ODP Leg 209, MAR 15°N. *Geochem. Geophys. Geosyst.* 5:Q09F26. doi: 10.1029/2004GC000744

Ballhaus, C., Berry, R. F., and Green, D. H. (1991). High pressure experimental calibration of the olivine-orthopyroxene-spinel oxygen geobarometer: implications for the oxidation state of the upper mantle. *Contrib. Mineral. Petrol.* 107, 27–40. doi: 10.1007/bf00311183

Benoit, M., Ceuleneer, G., and Polvé, M. (1999). The remelting of hydrothermally altered peridotite at mid-ocean ridges by intruding mantle diapirs. *Nature* 402, 514–518. doi: 10.1038/990073

Bonifacie, M., Busigny, V., Mével, C., Philippot, P., Agrinier, P., Jendrzejewski, N., et al. (2008). Chlorine isotopic composition in seafloor serpentinites an high-pressure metaperidotites. Insights into oceanic serpentinization and subduction processes. *Geochim. Cosmochim. Acta* 72, 126–139. doi: 10.1016/j.gca.2007.10.010

Borisov, A., Behrens, H., and Holtz, F. (2018). Ferric/ferrous ratio in silicate melts: a new model for 1 atm data with special emphasis on the effects of melt composition. *Contrib. Mineral. Petrol.* 173:98.

Borisova, A. Y., Ceuleneer, G., Kamenetsky, V., Arai, S., Béjina, F., Abily, B., et al. (2012a). A new view on the petrogenesis of the Oman ophiolite chromitites from microanalyses of chromite-hosted inclusions. *J. Petrol.* 53, 2411–2440. doi: 10.1093/petrology/egs054

Borisova, A. Y., Faure, F., Deloule, E., Grégoire, M., Béjina, F., de Parseval, P. H., et al. (2014). Lead isotope signatures of Kerguelen plume-derived olivine-hosted melt inclusions: constraints on the ocean island basalt petrogenesis. *Lithos* 198, 153–171. doi: 10.1016/j.lithos.2014.03.022

Borisova, A. Y., Pokrovski, G. S., Pichavant, M., Freydier, R., and Candaudap, F. (2010). Arsenic enrichment in hydrous peraluminous melts: insights from LA-ICP-MS and in situ X-ray absorption spectroscopy. *Am. Mineral.* 95, 1095–1104. doi: 10.2138/am.2010.3424

Borisova, A. Y., Toutain, J.-P., Stefansson, A., Gouy, S., and de Parseval, P. (2012b). Processes controlling the 2010 Eyjafjallajökull explosive eruption. *J. Geophys. Res.* 117:B05202. doi: 10.1029/2012JB009213

Borisova, A. Y., Zagrtdenov, N. R., Toplis, M. J., Bohrson, W. A., Nedelec, A., Safonov, O. G., et al. (2020). Hydrated peridotite – basaltic melt interaction Part

I: planetary felsic crust formation at shallow depth. Special Volume on magma-rock and magma-mush interactions as fundamental processes of magmatic differentiation. *Front. Earth Sci.* (in press).

Borisova, A. Y., Zagrtdenov, N. R., Toplis, M. J., Donovan, J. J., Llovet, X., Asimow, P. D., et al. (2018). Secondary fluorescence effects in microbeam analysis and their impacts on geospeedometry and geothermometry. *Chem. Geol.* 490, 22–29. doi: 10.1016/j.chemgeo.2018.05.010

Carignan, J., Hild, P., Mevelle, G., Morel, J., and Yeghicheyan, D. (2001). Routine analyses of trace elements in geological samples using flow injection and low pressure on-line liquid chromatography coupled to ICP-MS: a study of geochemical reference materials BR. DR-N, UB-N, AN-G and GH, Geostand. *Geoanal. Res.* 25, 187–198. doi: 10.1111/j.1751-908x.2001.tb00595.x

Chepurov, A., Turkin, A., and Dereppe, J.-M. (2016). Interaction of serpentinite and chromite as a possible formation mechanism of subcalcic chromium garnet in the upper mantle: an experimental study. *Eur. J. Miner.* 28, 329–336. doi: 10.1127/ejm/2016/0028-2517

Ciazela, J., Dick, H. J. B., Koepke, J., Pieterek, B., Muszynski, A., Botcharnikov, R., et al. (2017). Thin crust and exposed mantle control sulfide differentiation in slow-spreading ridge magmas. *Geology* 45, 935–938. doi: 10.1130/g39287.1

Ciazela, J., Koepke, J., Dick, H. J. B., Botcharnikov, R., Muszynski, A., Lazarov, M., et al. (2018). Sulfide enrichment at an oceanic crust-mantle transition zone: Kane Megamullion (23°N, MAR). *Geochim. Cosmochim. Acta* 230, 155–189. doi: 10.1016/j.gca.2018.03.027

Clénet, H., Ceuleneer, G., Pinet, P., Abily, B., Daydou, Y., Harris, E., et al., (2010). Thick sections of layered ultramafic cumulates in the Oman ophiolite revealed by an airborne hyperspectral survey: petrogenesis and relationship to mantle diapirism. *Lithos* 114, 265–281. doi: 10.1016/j.lithos.2009.09.002

Deschamps, F., Guillot, S., Godard, M., Chauvel, C., Andreani, M., and Hattori, K. (2010). In situ characterization of serpentinites from forearc mantle wedges: timing of serpentinization and behavior of fluid-mobile elements in subduction zones. *Chem. Geol.* 269, 262–277. doi: 10.1016/j.chemgeo.2009.10.002

Dixon, J., Clague, D. A., Cousens, B., Monsalve, M. L., and Uhl, J. (2008). Carbonatite and silicate melt metasomatism of the mantle surrounding the Hawaiian plume: evidence from volatiles, trace elements, and radiogenic isotopes in rejuvenated-stage lavas from Niihau, Hawaii. *Geochem. Geophys. Geosyst.* 9:Q09005. doi: 10.1029/2008GC002076

Dixon, J. E., and Clague, D. A. (2001). Volatiles in basaltic glasses from Loihi seamount, Hawaii : evidence for a relatively dry plume component. *J. Petrol.* 42, 627–654. doi: 10.1093/petrology/42.3.627

Evans, B. W., Hattori, K., and Baronnet, A. (2013). Serpentinites: what, why, where? *Elements* 9, 99–106.

Fisk, M. R. (1986). Basalt magma interaction with harzburgite and the formation of high-magnesium andesites. *Geophys. Res. Lett.* 13, 467–470. doi: 10.1029/gl013i005p00467

France, L., Ildefonse, B., and Koepke, J. (2009). Interactions between magma and hydrothermal system in Oman ophiolite and in IODP Hole 1256D: fossilization of a dynamic melt lens at fast spreading ridges. *Geochem. Geophys. Geosyst.* 10:GC002652.

France, L., Koepke, J., Ildefonse, B., Cichy, S. B., and Deschamps, F. (2010). Hydrous partial melting in the sheeted dike complex at fast spreading ridges: experimental and natural observations. *Contrib. Mineral. Petrol.* 160, 683–704. doi: 10.1007/s00410-010-0502-6

Früh-Green, G. L., Connolly, J. A. D., Plas, A., Kelley, D. S., and Grobéty, B. (2004). "Serpentinization of oceanic peridotites: implications for geochemical cycles and biological activity," in *The Subseafloor Biosphere at Mid-Ocean Ridges*, Vol. 144, eds W. S. Wilcock, et al. (Washington, D. C: American Geophysical Union) doi: 10.1029/144GM08

Georgen, J. E., Kurz, M. D., Dick, H. J. B., and Lin, J. (2003). Low 3He/4He ratios in basalt glasses from the western Southwest Indian Ridge (10°-24°E). *Earth Planet. Sci. Lett.* 206, 509–528. doi: 10.1016/s0012-821x(02)01106-8

Guillot, S., and Hattori, K. (2013). Serpentinites: essential roles in geodynamics, arc volcanism, sustainable development and the origin of life. *Elements* 9, 95–98. doi: 10.2113/gselements.9.2.95

Guillot, S., Hattori, K. H., de Sigoyer, J., Nägler, T., and Auzende, A.-L. (2001). Evidence of hydration of the mantle wedge and its role in the exhumation of eclogites. *Earth Planet. Sci. Lett.* 193, 115–127. doi: 10.1016/s0012-821x(01)00490-3

Harvey, J., Savov, I. P., Agostini, S., Robert, A., Cliff, R. A., and Walshaw, R. (2014). Si-metasomatism in serpentinized peridotite: the effects of talc-alteration on strontium and boron isotopes in abyssal serpentinites from Hole 1268a, ODP Leg 209. *Geochim. Cosmochim. Acta* 126, 30–48. doi: 10.1016/j.gca.2013.10.035

Hirschmann, M. M., Baker, M. B., and Stolper, E. M. (1998). The effect of alkalis on the silica content of mantle-derived melts. *Geochim. Cosmochim. Acta.* 62, 883–902.

Husen, A., Kamenetsky, V. S., Everard, J. L., and Kamenetsky, M. B. (2016). Transition from ultra-enriched to ultra-depleted primary MORB melts in a single volcanic suite (Macquarie Island, SW Pacific): implications for mantle source, melting process and plumbing system. *Geochim. Cosmochim. Acta* 185, 112–128. doi: 10.1016/J/gca.2016.02.031

Jambon, A., Deruelle, B., Dreibus, G., and Pineau, F. (1995). Chlorine and bromine abundance in MORB: the contrasting behaviour of the Mid-Atlantic Ridge and East Pacific Rise and implications for chlorine geochemical cycle. *Chem. Geol.* 126, 101–117. doi: 10.1016/0009-2541(95)00112-4

Jarosewich, E. J., Nelen, J. A., and Norberg, J. A. (1980). Reference samples for electron microprobe analysis. *Geostand. Newslett.* 4, 43–47.

Jochum, K. P., Stoll, B., Herwig, K., and Willbold, M. (2007). Validation of LA-ICP-MS trace element analysis of geological glasses using a new solid-state 193 nm Nd:YAG laser and matrix-matched calibration. *J. Anal. At. Spectrom.* 22, 112–121. doi: 10.1039/b609547j

Jochum, K. P., Stoll, B., Herwig, K., Willbold, M., Hofmann, A. W., Amini, M., et al. (2006). MPI-DING reference glasses for in situ microanalysis: new reference values for element concentrations and isotope ratios. *Geochem. Geophys. Geosyst.* 7, 1–44.

Jochum, K. P., Stoll, B., Weis, U., Jacob, D. E., Mertz-Kraus, R., and Andreae, M. O. (2014). Non-matrix-matched calibration for the multi-element analysis of geological and environmental samples using 200 nm femtosecond LA-ICP-MS: a comparison with nanosecond lasers. *Geostand. Geoanal. Res.* 38, 265–292. doi: 10.1111/j.1751-908x.2014.12028.x

Johan, Z., Martin, R. F., and Ettler, V. (2017). Fluids are bound to be involved in the formation of ophiolitic chromite deposits. *Eur. J. Mineral.* 29, 543–555. doi: 10.1127/ejm/2017/0029-2648

Kelemen, P. B., Joyce, D. B., Webster, J. D., and Holloway, J. R. (1990). Reaction between ultramafic rock and fractionating basaltic magma II. Experimental investigation of reaction between olivine tholeiite and harzburgite at 1150-1050°C and 5kb. *J. Petrol.* 31, 99–134. doi: 10.1093/petrology/31.1.99

Kendrick, M. A., Hémond, C., Kamenetsky, V. S., Danyushevsky, L., Devey, C. W., Rodemann, T., et al. (2017). Seawater cycled throughout Earth's mantle in partially serpentinized lithosphere. *Nat. Geosci.* 10, 222–228. doi: 10.1038/NGEO2902

Kendrick, M. A., Honda, M., Pettke, T., Scambelluri, M., Phillips, D., and Giuliani, A. (2013). Subduction zone fluxes of halogens and noble gases in seafloor and forearc serpentinites. *Earth Planet. Sci. Lett.* 365, 86–96. doi: 10.1016/j.epsl.2013.01.006

Kent, A. J. R., Clague, D. A., Honda, M., Stolper, E. M., Hutcheon, I. D., and Norman, M. C. (1999). Widespread assimilation of seawater-derived component at Loihi Seamount, Hawaii. *Geochim. Cosmochim. Acta* 63, 2749–2761. doi: 10.1016/s0016-7037(99)00215-x

Klein, F., Grozeva, N. G., and Seewald, J. S. (2019). Abiotic methane synthesis and serpentinization in olivine-hosted fluid inclusions. *PNAS* 116, 17666–17672. doi: 10.1073/pnas.1907871116

Kvassnes, A. J. S., and Grove, T. L. (2008). How partial melts of mafic lower crust affect ascending magmas at oceanic ridges. *Contrib. Mineral. Petrol.* 156, 49–71. doi: 10.1007/s00410-007-0273-x

Lange, A. E., Nielsen, R. L., Tepley, F. J. I. I. I., and Kent, A. J. R. (2013). Diverse Sr isotope signatures preserved in mid-oceanic-ridge basalt plagioclase. *Geology* 41, 279–282. doi: 10.1130/g33739.1

Lehnert, K., Su, Y., Langmuir, C., Sarbas, B., and Nohl, U. (2000). A global geochemical database structure for rocks. *Geochem. Geophys. Geosyst.* 1:1012. doi: 10.1029/1999GC000026

Lyubetskaya, T., and Korenaga, J. (2007). Chemical composition of Earth's primitive mantle and its variance: 1, Method and results. *J. Geophys. Res.* 112:B03211. doi: 10.1029/2005JB004223

Matjuschkin, V., Brooker, R. A., Tattitch, B., Blundy, J. D., and Stamper, C. C. (2015). Control and monitoring of oxygen fugacity in piston cylinder experiments. *Contrib. Mineral. Petrol.* 169:9. doi: 10.1007/s00410-015-1105-z

Matveev, S., and Ballhaus, C. (2002). Role of water in the origin of podiform chromitite deposits. *Earth Planet. Sci. Lett.* 203, 235–243. doi: 10.1016/s0012-821x(02)00860-9

Mével, C., and Cannat, M. (1991). "Lithospheric stretching and hydrothermal processes in oceanic gabbros from slow-speading ridges," in *Ophiolite Genesis and Evolution of the Oceanic Lithosphere*, eds T. J. Peters, A. Nicolas, and R. Coleman (Cham: Springer), 293–312. doi: 10.1007/978-94-011-3358-6_16

Michael, P. J., and Cornell, W. C. (1998). Influence of spreading rate and magma supply on crystallization and assimilation beneath mid-ocean ridges: evidence from chlorine and major element chemistry of mid-ocean ridge basalts. *J.Geophys. Res.* 103, 18325–18356. doi: 10.1029/98jb00791

Michael, P. J., and Schilling, J. G. (1989). Chlorine in mid-ocean ridge magmas: evidence for assimilation of seawater-influenced components. *Geochim. Cosmochim.Acta* 53, 3131–3143. doi: 10.1016/0016-7037(89)90094-x

Morgan, Z., and Liang, Y. (2003). An experimental and numerical study of the kinetics of harzburgite reactive dissolution with application to dunite formation. *Earth Planet. Sci. Lett.* 214, 59–74. doi: 10.1016/s0012-821x(03)00375-3

Muñoz, M., Vidal, O., Marcaillou, C., Pascarelli, S., Mathon, O., Farges, F., et al. (2013). Iron oxidation state in phyllosilicate single crystals using Fe-K pre-edge and XANES spectroscopy: effects of the linear polarization of the synchrotron X-ray beam. *Am. Miner.* 98, 1187–1197. doi: 10.2138/am.2013.4289

Neumann, E. R., Abu El-Rus, M. A., Tiepolo, M., Ottolini, L., Vannucci, R., and Whitehouse, M. (2015). Serpentinization and deserpentinization reactions in the upper mantle beneath Fuerteventura revealed by peridotite xenoliths with fibrous orthopyroxene and mottled olivine. *J. Petrol.* 56, 3–31. doi: 10.1093/petrology/egu069

Nonnotte, P., Ceuleneer, G., and Benoit, M. (2005). Genesis of andesitic-boninitic magmas at mid-ocean ridges by melting of hydrated peridotites: geochemical evidence from DSDP Site 334 gabbronorites. *Earth Planet. Sci. Lett.* 236, 632–653. doi: 10.1016/j.epsl.2005.05.026

Proux, O., Biquard, X., Lahera, E., Menthonnex, J. J., Prat, A., Ulrich, O., et al. (2005). FAME: a new beamline for X-ray absorption investigations of very diluted systems of environmental, material and biological interests. *Phys. Scripta.* 115, 970–973.

Python, M., Ceuleneer, G., Ishida, Y., Barrat, J.-A., and Arau, S. (2007). Oman diopsidites: a new lithology diagnostic of very high temperature hydrothermal circulation in mantle peridotite below oceanic spreading centers. *Earth Planet. Sci. Lett.* 255, 289–305. doi: 10.1016/j.epsl.2006.12.030

Rospabé, M., Benoit, M., Ceuleneer, G., Kaczmarek, M.-A., and Hodel, F. (2019a). Melt hybridization and metasomatism triggered by syn-magmatic faults within the Oman ophiolite: a clue to understand the genesis of the dunitic mantle-crust transition zone. *Earth Planet. Sci. Let.* 516, 108–121. doi: 10.1016/j.epsl.2019.04.004

Rospabé, M., Ceuleneer, G., Benoit, M., Abily, B., and Pinet, P. (2017). Origin of the dunitic mantle-crust transition zone in the Oman ophiolite: the interplay between percolating magmas and high-temperature hydrous fluids. *Geology* 45, 471–474. doi: 10.1130/g38778.1

Rospabé, M., Ceuleneer, G., Granier, N., Arai, S., and Borisova, A. Y. (2019b). Multi-scale development of a stratiform chromite ore body at the base of the dunitic mantle-crust transition zone (Maqsad diapir, Oman ophiolite): the role of repeated melt and fluid influxes. *Lithos* 350–351:105235. doi: 10.1016/j.lithos.2019.105235

Ross, K., and Elthon, D. (1993). Cumulates from strongly depleted mid-ocean-ridge basalt. *Nature* 365, 826–829. doi: 10.1038/365826a0

Sauter, D., Cannat, M., Rouméjon, S., Andreani, M., Birot, D., Bronner, A., et al. (2013). Continuous exhumation of mantle-derived rocks at Southwest Indian Ridge for 11 million years. *Nat. Geosci.* 6, 314–320. doi: 10.1038/ngeo1771

Simons, K., Dixon, J. E., Schilling, J. G., Kingsley, R., and Poreda, R. (2002). Volatiles in basaltic glasses from the Easter-Salas y gomez seamount chain and easter microplate: implications for geochemical cycling of volatile elements. *Geochem. Geophys. Geosyst.* 3:1039.

Sobolev, A. V., and Shimizu, N. (1993). Ultra-depleted primary melt included in an olivine from the Mid-Atlantic ridge. *Nature* 363, 151–154. doi: 10.1038/363151a0

Stroncik, N. A., and Niedermann, S. (2016). Atmospheric contamination of the primary Ne and Ar signal in mid-ocean ridge basalts and its implications for ocean crust formation. *Geochim. Cosmichim. Acta* 172, 306–321. doi: 10.1016/j.gca.2015.09.016

Sushchevskaya, N. M., Tsekhonya, T. I., Kononkova, N. N., Tcherkashov, G. A., Bogdanov, Y. A., and Belyatsky, B. V. (2000). Magmatism of Mona and Knipovich ridges from spreading zones of polar Atlantic Ocean. *Russ. J. Geosci.* 2, 243–267. doi: 10.2205/2000es000043

Toplis, M. J. (2005). The thermodynamics of iron and magnesium partitioning between olivine and liquid: criteria for assessing and predicting equilibrium in natural and experimental systems Contrib. *Mineral. Petrol.* 149, 22–39. doi: 10.1007/s00410-004-0629-4

Ulmer, P. (2001). Partial melting in the mantle wedge - the role of H2O in the genesis of mantle-derived 'arc-related' magmas. *Phys. Earth Planet Inter.* 127, 215–232.

Van den Bleeken, G., Müntener, O., and Ulmer, P. (2010). Reaction processes between tholeiitic melt and residual peridotite in the uppermost mantle: an experimental study at 0.8 GPa. *J. Petrol.* 51, 153–183. doi: 10.1093/petrology/egp066

Van den Bleeken, G., Müntener, O., and Ulmer, P. (2011). Melt variability in percolated peridotite: an experimental study applied to reactive migration of tholeiitic basalt in the upper mantle. *Contrib. Mineral. Petrol.* 161, 921–945. doi: 10.1007/s00410-010-0572-5

van der Zwan, F. M., Devey, C. W., Hansteen, T. H., Almeev, R. R., Augustin, N., Frische, M., et al. (2017). Lower crustal hydrothermal circulation at slow-spreading ridges: evidence from chlorine in Arctic and South Atlantic basalt glasses and melt inclusions. *Contrib. Mineral. Petrol.* 172:97.

Wilke, M., Farges, F., Petit, P., Brown, G. Jr., and Martin, F. (2001). Oxidation state and coordination of Fe in minerals: an Fe K-XANES spectroscopic study. *Am. Mineral.* 86, 714–730. doi: 10.2138/am-2001-5-612

Wilke, M., Partzsch, G., Bernhardt, R., and Lattard, D. (2005). Determination of the iron oxidation state in basaltic glasses using XANES at the K-edge. *Chem. Geol.* 220, 143–161. doi: 10.1016/j.chemgeo.2005.03.004

Zagrtdenov, N. R., Ceuleneer, G., Rospabé, M., Borisova, A., Toplis, M. J., Benoit, M., et al. (2018). Anatomy of a chromitite dyke in the mantle/crust transition zone of the Oman ophiolite. *Lithos* 312-313, 343–357. doi: 10.1016/j.lithos.2018.05.012

Zhang, Y., Ni, H., and Chen, Y. (2010). Diffusion data in silicate melts. *Rev. Mineral. Geochem.* 72, 311–408. doi: 10.1515/9781501508394-009

Zindler, A., and Hart, S. (1986). Chemical geodynamics. *Annu. Rev. Earth Planet. Sci.* 14, 493–571.

Conflict of Interest: The authors declare that the research was conducted in the absence of any commercial or financial relationships that could be construed as a potential conflict of interest.

frontiers
in Earth Science

ORIGINAL RESEARCH
published: 10 June 2020
doi: 10.3389/feart.2020.00175

Felsic Melt and Gas Mobilization During Magma Solidification: An Experimental Study at 1.1 kbar

Mattia Pistone[1,2]*, Lukas P. Baumgartner[1], Florence Bégué[1], Paul A. Jarvis[3], Elias Bloch[1], Martin Robyr[1], Othmar Müntener[1], Thomas W. Sisson[4] and Jon D. Blundy[5]

[1] Institute of Earth Sciences, University of Lausanne, Lausanne, Switzerland, [2] Department of Geology, University of Georgia, Athens, GA, United States, [3] Section of Earth and Environmental Sciences, University of Geneva, Geneva, Switzerland, [4] US Geological Survey, Menlo Park, CA, United States, [5] School of Earth Sciences, University of Bristol, Bristol, United Kingdom

Melt and gas transfer processes are essential to the formation and growth of the Earth's crust and for sustaining volcanic activity. These processes also play a major role in magma fractionation at shallow depths (<10 km) where magmas stall rheologically and solidify. In this scenario, the conditions of melt and gas mobilization during progressive cooling of crystal mushes down to their solidus remain poorly understood. We present experimental data (at 1.1 kbar) showing how a combination of temperature and crystal content control the ability of melt and gas to escape from cooling and solidifying hydrous silicic magmas with initial crystal volume fractions (Φ) of 0.6, 0.7, and 0.8, and for temperature snapshots of 850, 800, and 750°C. Microstructural observations and chemical data show that the amount of extracted melt increases by 70% from 850 to 750°C and by 40% from $\Phi = 0.6$ to 0.8 at 750°C, due to the formation of interconnected crystal frameworks, gas expansion in constricted pore space, and filter pressing during cooling. As a result, our experiments suggest that melt and gas extraction from cooling mushes increases in proximity to their solidus and can operate efficiently at $0.6 < \Phi < 0.93$. These observations shed light on maximum estimates of the segregation of gas-rich, crystal-poor magmas (0.02 m/year at 850°C to 9 m/year at 750°C) to form felsic dykes or eruptible systems feeding volcanoes.

Keywords: melt, gas, magma, cooling, filter pressing

Edited by:
Chiara Maria Petrone,
Natural History Museum,
United Kingdom

Reviewed by:
Silvio Mollo,
Sapienza University of Rome, Italy
Olivier Bachmann,
ETH Zürich, Switzerland

***Correspondence:**
Mattia Pistone
Mattia.Pistone@uga.edu

Specialty section:
This article was submitted to
Petrology,
a section of the journal
Frontiers in Earth Science

Received: 25 March 2020
Accepted: 06 May 2020
Published: 10 June 2020

Citation:
Pistone M, Baumgartner LP, Bégué F, Jarvis PA, Bloch E, Robyr M, Müntener O, Sisson TW and Blundy JD (2020) Felsic Melt and Gas Mobilization During Magma Solidification: An Experimental Study at 1.1 kbar. Front. Earth Sci. 8:175. doi: 10.3389/feart.2020.00175

INTRODUCTION

Crystal fractionation does not depend solely upon gravitational separation of crystals from melt due to density differences (Wager et al., 1960; McKenzie, 1984; Spiegelman et al., 2001; Connolly et al., 2009; Schmidt et al., 2012); in crystal-rich magmas, other processes may operate. Bowen (1928), for example, avers that "the squeezing out of silicate melt residues by forces external or internal to crystal mushes may be the most important of all." In the Earth's shallow crust (<10 km; <2.5 kbar) where most of the erupting silicic magma reservoirs are located (Huber et al., 2019; Zhang et al., 2020), cooling magmas tend to be volatile-saturated (6–8 wt% H_2O; Hui et al., 2009) and become crystal-rich (crystal fraction $\Phi > 0.4$; Marsh, 1981; Dufek and Bachmann, 2010; Huber et al., 2010a), becoming extremely viscous over a very small temperature (T) range as they approach their solidus (Holtz and Johannes, 1994; Holtz et al., 2001; Pistone et al., 2013).

These factors impede any gravitational segregetation of crystals from melt, yet there is clear field evidence for such segregation in natural rocks (Holness, 2018). Instead, these near-solidus systems are capable of releasing high-silica melt (formed during crystallization at low-pressure; Gualda and Ghiorso, 2013) through porous flow (Olsen et al., 2004) to form crystal-poor, evolved magmas of rhyolitic composition that are capable of eruption at the surface (Hildreth, 1981, 2004; Marsh, 1981; Bachmann and Bergantz, 2004; Hildreth and Wilson, 2007; Dufek and Bachmann, 2010; Waters and Lange, 2017).

Using phase equilibria constraints in P–T–H_2O space, most felsic magmas have initial H_2O contents ranging from 5–7 wt% at 4 kbar to 4–5 wt% at 3 kbar and 2–4 wt% at 1 kbar at T = 750–900°C (Clemens and Wall, 1981; Clemens et al., 1986; Webster et al., 1987; Whitney, 1988; Johnson and Rutherford, 1989; Dall'Agnol et al., 1994; Scaillet and Pichavant, 1994; Scaillet et al., 1995a,b). During magma cooling, extraction of hydrous silicic magmas is most likely at crystal fractions ranging between 0.5 and 0.7 (Dufek and Bachmann, 2010). This physical condition is then enhanced by the time spent by crystallizing magmas at conditions optimized for melt extraction: the longer magma spends at such conditions, the greater the amount of extracted residual melt (Huber et al., 2009; Dufek and Bachmann, 2010; Hartung et al., 2019). The competition between the rate of heat loss and the rate of latent heat release due to crystallization during progressive cooling and solidification of magmas exerts an important control on the extraction of interstitial melts (Huber et al., 2009; Caricchi and Blundy, 2015; Lee et al., 2015).

The process of melt transfer from large-volume melt domains to nearly solidified ones is similar to models of filter pressing (Robin, 1979; Sawyer and Robin, 1986; Brown et al., 1995). However, in a rheologically locked magma undergoing solidification, the diminished volume fraction of residual melt concentrates dissolved volatiles and favors exsolution of gaseous bubbles (Bacon, 1986; Sisson and Bacon, 1999; Masotta et al., 2010) and supercritical fluids or brines (Driesner, 2007; Driesner and Heinrich, 2007; Blundy et al., 2015; Afanasyev et al., 2018), a process known as (isobaric) second or resurgent boiling (e.g., Candela and Blevin, 1995; Candela, 1997; Su et al., 2016). Bubble growth is a function of many factors (Gonnermann and Manga, 2007, and references therein). At constant pressure, bubble growth is controlled by the balance between the rate of diffusion of H_2O molecules toward the bubble-melt interface and the rate of viscous deformation of the surrounding melt (Proussevitch et al., 1993; Proussevitch and Sahagian, 1998; Liu and Zhang, 2000). Where the rate of deformation exceeds the rate of diffusion, growth is described as diffusion-limited, whereas the inverse is viscosity-limited (Navon et al., 1998; Colucci et al., 2015). Gas exsolution at low pressures (P < 4 kbar) causes the mush to expand, whereas its high viscosity (10^5 to 10^{18} Pa s; Sparks et al., 2019) resists inflation, along with the contribution of rigid reservoir/conduit walls that play in the background. In this scenario, gradients in Φ and vesiculation drive the melt toward regions of lower Φ, T, and P (Huber et al., 2010b; Parmigiani et al., 2016; Huber and Parmigiani, 2018). Under these conditions, felsic magmas become H_2O-saturated and, thus, the presence of exsolved gas within the interstitial melt is likely. Indeed, field examples of plutonic felsic rocks with vuggy porosity, such as spherical vesicles, angular diktytaxitic voids, and miarolitic cavities, indicate the migration of intergranular melt and gas between interlocking crystals that act as a filter in solidifying mushes (**Figure 1**; Candela and Piccoli, 1995; Candela, 1997). Melt and supercritical fluid percolation generates out-of-equilibrium textures (e.g., Grosse et al., 2010; Vigneresse, 2015; Lissenberg and MacLeod, 2016; McCarthy and Müntener, 2016; Pistone et al., 2020). In cooling magmas emplaced in the shallow crust, melt and gas segregation can produce internal geochemical heterogeneities with macrorhythmic sequences of inter- and cross-connected melanocratic, mesocratic, and leucocratic units with vuggy porosity (**Figures 1A–C**), "foamy" rocks produced as a result of magma decompression following dyking and brecciation of pluton peripheries in contact with brittle country rocks (**Figures 1D,E**), and coarse-grained comb-layered pegmatite pods (**Figure 1F**) produced by "swinging eutectic point" (Balashov et al., 2000), adiabatic drop in pressure (Shannon et al., 1982), and chemical undercooling (Pistone et al., 2016) occurring rapidly with no achievement of chemical and textural equilibrium (e.g., Fenn, 1977; Webber et al., 1997; Nabelek et al., 2010).

One relatively rapid melt extraction mechanism in the upper crust that has been proposed over the last decades is gas filter pressing (Anderson et al., 1984; Bacon, 1986; Sanders, 1986; Sisson and Bacon, 1999; Pistone et al., 2015), which can produce overlying pegmatites and aplites from extracted gas-rich melts (Sisson and Bacon, 1999; Hartung et al., 2017). Gas filter pressing is probably the dominant process by which highly evolved melts segregate from crystal mush to form aplitic dikes in granitic plutons and accounts for the production of voluminous, crystal-poor rhyolites (Sisson and Bacon, 1999). Gas filter pressing operates in crystal-rich systems ($\Phi \geq 0.6$) below the maximum packing fraction of bubbles and crystals ($\sim$0.74; Pistone et al., 2015), in agreement with experimental observations of melt percolation down a pressure gradient along grain boundaries at maximum crystal volume fractions of 0.85–0.9 (Dell'Angelo and Tullis, 1988). Above the maximum packing fraction of solid minerals and expanding bubbles, the mush tends to fracture; gas escapes through open cracks (Parmigiani et al., 2014; Oppenheimer et al., 2015; Pistone et al., 2015). The residual melt remains trapped within the crystal framework and is forced to crystallize and solidify.

To date, field observations offer only the terminal snapshot of the sequence of the dynamic processes that lead to melt extraction. Conversely, the most recent models (Degruyter et al., 2019, and references therein) shed light on the change of the local pore pressure during gas exsolution in cooling magmas, without simulating the actual transport of melt and exsolved fluids during second boiling. What remains unclear is how melt and gas are extracted at the microscale during cooling of hydrous magmas. To address this, our study aims to quantify how Φ and T control the mobilization of volatile-rich melts during mush solidification. We achieve this through high-temperature and -pressure experiments, observing how microstructural textures of crystal-rich magmas control melt segregation, supported by petrological modeling based on Rhyolite-MELTS (Gualda et al., 2012).

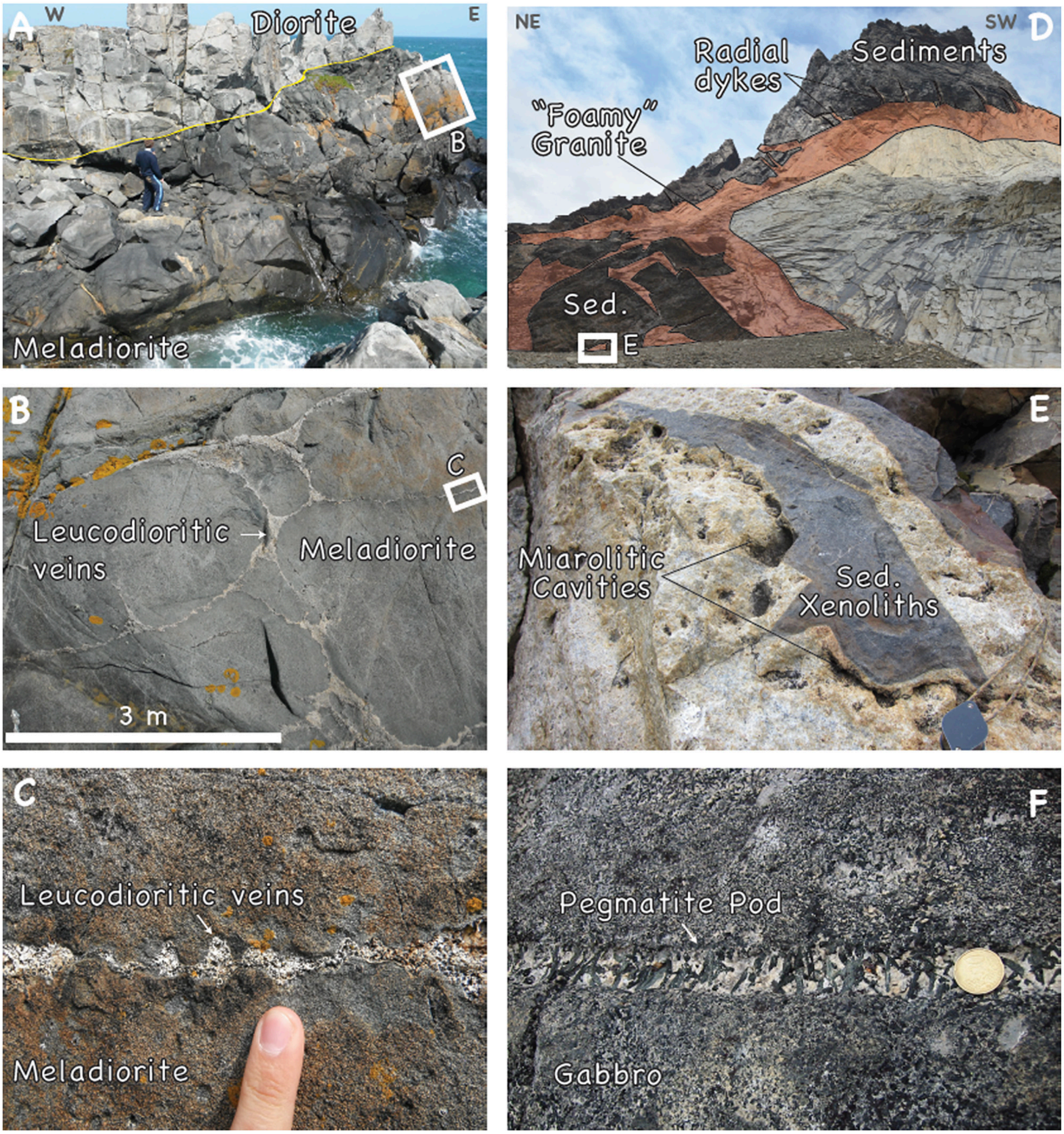

FIGURE 1 | Examples of melt and gas segregation within cooling magmas. **(A–C)** Outcrops of the Beaucette Marina battery of the gabbro-dioritic Bordeaux Group (North-Guernsey Intrusive Complex, Armorican Massif; Caroff et al., 2011) show a cumulative macrorhythmic sequence of meladiorite and diorite rocks. The meladiorite unit consists of alternating dark and few cm-thick mesocratic layers and is veined by leucocratic diorite with vuggy porosity, forming an inter- and cross-connected network of cm-thick sheets. **(D)** Image of the ca. 900 m high N-W cliff of the Cerro Nido el Condor (Patagonia, Chile) showing outcrop of the frontal part of the Torres del Paine igneous complex. The "foamy" granite from Unit I (Michel et al., 2008) is accumulated at the front and is enriched in miarolitic cavities. Note ubiquitous radial diking, and brecciation at the bottom of the laccolith. **(E)** Close-up on one of the dikes from the bottom of the Unit I, where both sedimentary xenoliths and magma solidification act as a barrier to gas and melt movements following dike emplacement. **(F)** Coarse pegmatite pods with hornblende and feldspar minerals arranged in a comb layer (a variant of unidirectional solidification texture or UST) with respect to the equigranular host gabbro from the Val Fredda Complex (Blundy and Sparks, 1992) of the Tertiary Adamello Batholith (Alps, Italy).

MATERIALS AND METHODS

Material Preparation and Synthesis

The preparation of the materials followed the approach of Pistone et al. (2016). We use samples of F dacite, which is the equivalent to the natural sample JM101 (dacite/tonalite from Adamello batholith, Italy; Blundy and Sparks, 1992). Samples were prepared by mixing dried, fine-grained (∼1 μm) oxides and hydroxides in appropriate proportions before the addition of a known volume of quartz crystals that had been fired for 5 h in a one-atmosphere muffle furnace at 1,000°C. Quartz crystals (DORSILIT 2500: SiO_2 = 98.90 wt%; Al_2O_3 = 0.41 wt%; Fe_2O_3 = 0.02 wt%; TiO_2 = 0.04 wt%; minor trace elements; Alberto Luisoni AG, Switzerland) had aspect ratios between 1.0 and 3.5, and three-dimensional grain size distributions with a mean diameter of 68 μm and positive skewness of 0.37, checked using the Malvern Laser Diffraction Grain Sizer at the Limno-Geology Laboratory, ETH-Zurich. Quartz particles were selected to ensure no reaction with the melt in which they resided (Pistone et al., 2012). Aliquots of F dacite glass were mixed with quartz particles to create additional starting materials of different crystallinity: F50 = 0.5 crystal fraction (Φ), F60 = 0.6, F70 = 0.7, and F80 = 0.8. The crystal-glass mixtures were pressed into cylindrical stainless steel canisters (110 mm long, 35 mm inner diameter, 3 mm wall thickness) lined with a thin (25 μm) molybdenum foil to avoid chemical contamination, using a uniaxial cold press. The canisters were stored at 110°C for 24 h, then arc-welded shut. The tightness of the seal was checked by weight after immersion in a water bath under vacuum. The canisters were then hot isostatically pressed (HIP) for 24 h in a large capacity (170 mm in diameter; 500 mm high), internally heated pressure vessel at 1.8 kbar and 1,200°C (Sinter-HIP-Kompaktanlage, ABRA Fluid AG: Rock Deformation Laboratory of ETH-Zurich). The chosen *P* and *T* conditions ensured the generation of chemically homogeneous glass and complete dissolution of H_2O in the melt phase (i.e., water-undersaturated melt). The maximum temperature difference across the sample was 18°C as monitored by three C-type thermocouples placed at the bottom and top and in the middle of the pressure vessel. Samples were then cooled at 60°C/min to a temperature of 100°C above the glass transition temperature (i.e., viscosity equivalent to 10^{12} Pa s) to prevent crystallization; followed by slower cooling (0.6°C/min) to room temperature to obtain thermally relaxed glasses. The confining pressure was decreased by 37.6 bar/min during rapid cooling, and by 1.3 bar/min during slow cooling. Comparison of canister weights showed less than 0.5% change in mass, suggesting H_2O loss during synthesis is negligible. Cores of 2-mm diameter and 2- to 4-mm length were then drilled from each synthesized sample, and the top and bottom faces were ground flat and parallel. The compositions of the starting materials are reported in Pistone et al. (2016) and are presented in the **Supplementary Material**.

High-Pressure and High-Temperature Experiments

To simulate melt and gas mobilization upon magma cooling, three high-temperature (*T* = 750, 800, and 850°C), 1.1-kbar pressure experiments were conducted on a suite of pre-synthesized, H_2O- and crystal-rich glasses (dacite with 4.2 wt% H_2O in the glass, and Φ = 0.6, 0.7, 0.8). The experimental pressure was chosen within the range of emplacement depth of the plutonic systems reported in **Figure 1** (0.75 ± 0.25 kbar for the laccolith of Torres del Paine; Putlitz et al., 2001; Baumgartner et al., 2007, 2014; Leuthold et al., 2014; 3–4 kbar for the Plutonic Complex of Guernsey; D'Lemos, 1987; de Bremond, d'Ars et al., 1992) and consistent with some natural cases of erupting systems with very shallow pre-eruptive residence (∼1 kbar in Taupo Volcanic Zone; Bégué et al., 2014; Gualda et al., 2018). Also, to generate the initial gas phase within the cooling system, the chosen pressure (0.7 kbar lower than the pressure for material synthesis) allowed the achievement of water-saturation conditions during experiments (0.1–0.2 wt% H_2O in excess in the starting melt composition prior to crystallization, calculated using the model of Papale et al., 2006). The different Φ values bracketed the initial crystallinities of natural plutonic gas-saturated mushes; each experiment at specific *T* represents a snapshot of the state of the mush along its cooling path. Three sandwiched samples were inserted into 4-mm diameter Au capsule, crimpled and welded before experiments. Using vertical, hydrothermal cold-seal pressure vessels (University of Lausanne), samples were first pressurized to 1.1 kbar at room temperature, with pressure monitored using both an IMS digital pressure sensor and a Heise 3-kbar bourdon-tube gauge (±5 bar). Then, *T* was increased at a rate of 30°C/min up to the target temperature. Experiments were run for 8 days at constant *P*–*T* and H_2O-saturated conditions (∼4.1 wt% H_2O in the starting melt prior to crystallization at all studied temperatures; Papale et al., 2006) above the wet granite solidus (∼710°C at 1.1 kbar; Tuttle and Bowen, 1958; Holtz et al., 2001). Experiments run between 750 and 850°C at 1.1 kbar allowed equivalent conditions of initial melt viscosity ($\Delta \log\eta_{melt} < 0.5$ and, thus, allowed comparison of processes simulated in the experimental runs at different *T* (Holtz et al., 2001; see also **Supplementary Material**). We did not simulate magma cooling by changing *T* with a specific cooling rate; rather the different temperatures used span those occurring in natural gas-saturated mushes approaching their solidus. Temperature was monitored with an N-type thermocouple (±2°C) connected to a Eurotherm 815/831 controller. Based on temperature calibration at room pressure prior to the high-pressure and high-temperature experiments, no *T* gradients were found in the sample placed in the center of an isothermal 30-mm hot zone. Experiments were terminated by turning off the furnace power and using conventional compressed air quenches (quench rate of ∼4°C/s). Quenching to the solidus (at which the sample microstructure freezes) was thus completed in 15, 30, and 50 s from 750, 800, and 850°C, respectively. Cooling to room *T* was then followed by slow depressurisation and sample recovery.

Microstructural Analysis

Both starting materials and recovered samples were explored using X-ray computed tomography (CT) using a spatial resolution of 6 μm/pixel at 40 kV, 200 A, and 800 ms exposure time with a SkyScan 1173 (University of Lausanne). Under these acquisition conditions, quartz and glass were easily resolvable phases. The higher X-ray attenuation of the glass was largely due to its Fe content. Tomographic 3D renderings were inspected using the IDL-based Blob3D software (Ketcham, 2005a,b) to quantify the spatial distribution and first-order volume fraction of each phase, with an uncertainty of 0.005 in volume fraction. Three-dimensional tomographic analysis is used to capture the bulk microstructural features of the samples, including glass, pre-existing quartz, and vesicle spatial distribution.

In order to image microstructural details at higher spatial resolution (<6 μm/pixel), samples were also inspected using a FEG-EPMA. Samples were cut in half to form a peripheral and a central portion (**Figures 2**, **3**); both portions were impregnated in epoxy, polished, and carbon-coated for analytical inspection. Backscatter electron (BSE) images were acquired at 15-kV accelerating voltage and 1.5-nA beam current. BSE images with a spatial resolution of 1-μm were used to estimate the volume fractions of glass, vesicles, and minerals in the different portions of run products using the image processing software JMicro-Vision® v1.2.7 (Roduit, 2011), with an uncertainty of 0.002 in volume fraction based on inspections of three representative 200 × 200 μm areas for each sample. The vesicle size distribution (VSD), based on Feret's radius, was carried out using the Java 8 Fiji software (Schindelin et al., 2012). The Feret's radius is the half of the maximum distance or caliper between two parallel lines tangential to the particle outline and is used to particles of low aspect ratio (<3) and as long as particle morphology is not largely irregular (Liu et al., 2015). Study of the VSD allowed exploration of the different processes that lead to bubble growth: Ostwald ripening (Stoffregen, 1996; Lautze et al., 2011), H_2O diffusion (Zhang et al., 2000) or physical gas coalescence (Castro et al., 2012). The BSE analysis was used to capture the differences in glass volume fraction between peripheral and central sections of the run products and, thus, to evaluate the movement of residual melt in the synthetic crystal mush at high *P*–*T* conditions.

Chemical Analysis of Glass

A major challenge with glass analyses is alkali loss (Morgan and London, 1996), a very common problem that can be minimized by using a large beam diameter and low beam current on the electron probe micro-analyser (EPMA). However, the available surface of inclusion- and bubble-free glass precluded the use of a defocused beam almost everywhere throughout the experimental run products. Hence, we had to adjust our analytical conditions using a low accelerating voltage and 3–5-μm beam size for the chemical analyses of the experimental glasses. We used two EPMA instruments: a JEOL JXA-8350F HyperProbe (FEG-EPMA; University of Lausanne) and a CAMECA SX Five EPMA (University of Massachusetts in Amherst, MA, United States). The chemical analysis revealed that the experimental glasses are highly heterogeneous as a consequence of the different processes simulated experimentally: vesiculation, crystallization, and melt segregation.

The JEOL JXA-8350F HyperProbe (FEG-EPMA; University of Lausanne) is capable of in-situ quantitative microanalyses at high spatial resolution (<1 μm). Glasses were analyzed at 15 kV, 1.5 nA and 10-μm beam diameter and 7 kV, 1.5 nA, and 5- to 3-μm beam diameter due to the restricted amount of available glass. The counting time on the peak and background positions was 30 and 15 s for Al, Ti, Ca, Mg, and Mn and 10 and 5 s for Si, Fe, Na, K, and P, respectively. Natural and synthetic standards were used and data were ZAF-corrected (Armstrong, 1988). The FEG-EPMA standardization using a small beam diameter (<5-μm) at 7 kV included the analysis of hydrous glasses with known water content (H_2O = 5.7 wt%; Müntener et al., 2001) to monitor any alkali loss. Using these secondary standard glasses let us assume that no alkali loss occurred during FEG-EPMA analysis with a 5-μm beam. At 7 kV, neither Mn or P were analyzed (<0.05 wt% total). Analyses at 15 kV targeted only large glass pools located in the vesicle- and glass-rich regions away from the solidification fronts. The analyses in the run product at 750°C were almost exclusively located in the "glass coronae" around the vesicles and using 10-μm beam size did not yield reliable data, which were discarded (**Supplementary Material**). The analyses at 7 kV targeted the "glass channels" where melt percolation occurred within the areas affected by crystallization fronts during experiments. The two sets of analyses display a major difference in alkali content (especially Na), which is high in the glass-rich areas devoid of plagioclase and remote (>10-μm) from vesicles (**Supplementary Material**). Glass major element compositions and related uncertainties are in the **Supplementary Material**. Newly formed minerals (quartz, plagioclase, hornblende, and oxide) were qualitatively analyzed using an SDD EDS detector (spectral resolution of 129 eV on Mn) at 15 kV, 1.5 nA, and ∼1-μm beam diameter.

Further glass analyses in representative "glass channels" in samples with Φ = 0.6 and Φ = 0.7 at 750°C were carried out using the CAMECA SX Five EPMA (University of Massachusetts in Amherst, MA) at 15 kV, 2 nA, and ∼5- to 10-μm beam diameter. The counting time on the peak and background positions was 30 and 15 s for Al, Ti, Ca, Mg, and Mn, and 10 and 5 s for Si, Fe, Na, K, and P, respectively. We used two glass standards of rhyolitic (USNM 72854 VG-568 from the Smithsonian Institution), haplogranitic (HGGB-3 glasses from Pistone et al., 2012), and dacitic composition (F0 from Pistone et al., 2016) and data were ZAF-corrected. This EPMA analysis helped to show that the FEG-EPMA analysis of the experimental glasses in F60, F70, and F80 at 7 kV were affected by alkali migration due to electron charge with an overall alkali loss of up to 50%. This alkali loss at low voltage and reduced beam size modified the number of counts for Si during analysis.

Estimation of H_2O Content and Calculation of Melt Viscosity

H_2O content in the glass phase was estimated using the volatile-by-difference method (Devine et al., 1995) for both the 7- and 15-kV sets of analyses, with limited uncertainty (<1 wt%) for H_2O contents between 4.5 and 7.2 wt%. This method was applied by calibrating the analytical reproducibility at the chosen FEG-EPMA (7 and 15 kV, respectively) and EPMA analytical conditions (15 kV) with hydrous felsic glasses of similar H_2O content (samples B659 and B736 from Müntener et al., 2001; F0 from Pistone et al., 2017; samples HGGB-3

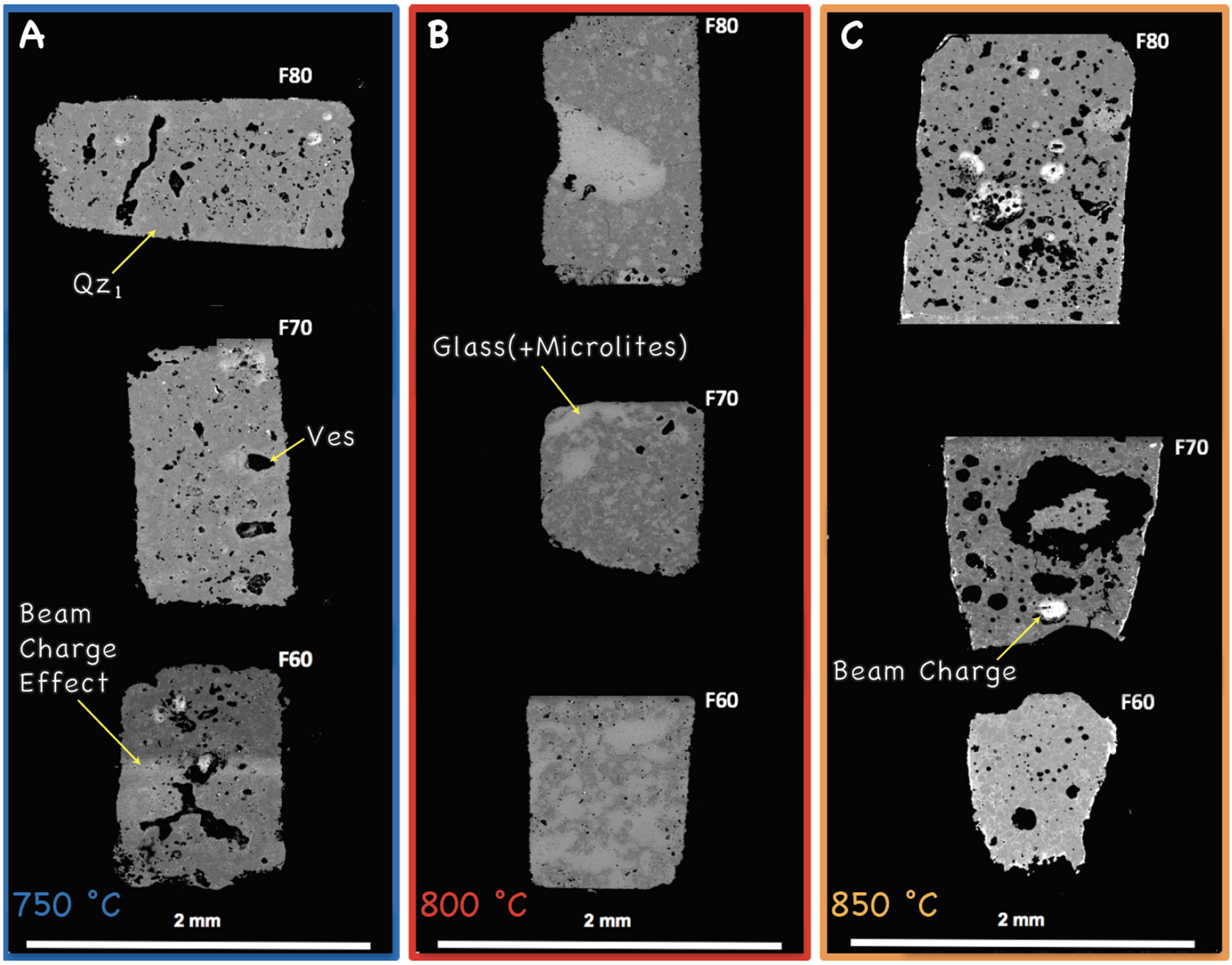

FIGURE 2 | FEG-probe-based BSE images of peripheral sections of all crystal-bearing samples from experiments at: **(A)** 750, **(B)** 800, and **(C)** 850°C. Acronyms are: Qz_1 = pre-existing quartz (dark gray); Ves = vesicle (black objects, sometimes filled with whitish material that produces electron charging); Glass = residual glass (least dark gray phase) that can be populated with microlites.

from Pistone et al., 2012). Most of the results agree with H_2O-saturation concentrations calculated using Papale et al. (2006) for the run pressure and temperatures. However, apparent H_2O contents appreciably exceeding H_2O-saturation values were determined for most analyses of 750°C glasses, even for analyses at 15 kV (summation deficits to as great as 9.7 wt%). These high apparent concentrations were determined in 10-μm thick glass halos around vesicles and in widespread glass domains populated by potential cavitation nuclei or "nanobubbles"; the latter were not observable at the analytical spatial resolution of the BSE images, but inferred from the "foggy" aspect of the residual glass using optical microscopy. Glass adjacent to bubbles can hydrate during quench-cooling to room temperature, and the electron beam's X-ray excitation volume may intersect nanobubbles in "foggy" glass domains. Analyses near bubble walls and in "foggy" glass domains of 750°C runs were therefore excluded. Hydration during quenching, alkali-loss during analysis, and overlap with sub-surface bubbles cannot be ruled out entirely for the accepted analyses of glasses synthesized at 750°C, so the values calculated for their viscosities and saturation overpressures are minima and maxima, respectively.

Melt viscosities at P–T conditions were estimated using the model of Hui et al. (2009) with $\log\eta_{melt}$ variations of maximum 0.2 with H_2O contents ranging between 4.5 and 7.2 wt%, as estimated with the volatile-by-difference method applied to 15-kV data (marked in yellow in the analytical data summary table of the **Supplementary Material**), in line with calculations from solubility modeling (Papale et al., 2006).

Rhyolite-MELTS Crystallization Simulations

Crystallization paths of hydrous dacite from 850 to 750°C at 1.1 kbar were simulated using Rhyolite-MELTS (Gualda et al., 2012) to reconstruct the sequence of crystallization of the major phases (hornblende, plagioclase, and quartz) and volume percentage of excess H_2O-rich bubbles at the different temperatures in the experimental samples. Rhyolite-MELTS software currently lacks

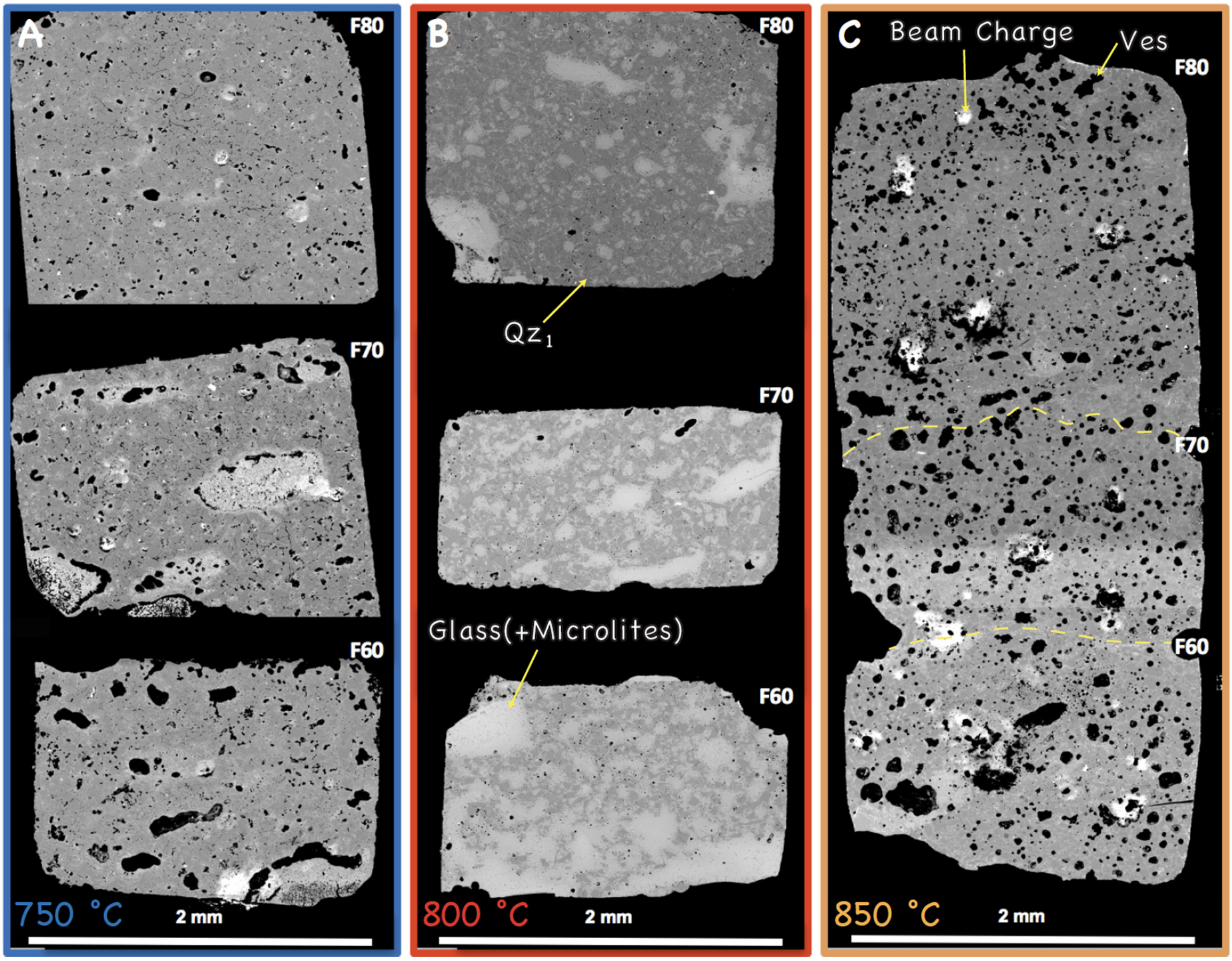

FIGURE 3 | FEG-probe-based BSE images of central sections of all crystal-bearing samples from experiments at: **(A)** 750, **(B)** 800, and **(C)** 850°C. Yellow dashed lines divide the domains of run products F60, F70, and F80 after the experiment run at 850°C. See acronyms from **Figure 2**.

a thermodynamic model for simulating amphibole crystallization in silicate melts, and phases such as pyroxenes are calculated. However, this did not affect the purpose of our simulations here, as melt compositions calculated by Rhyolite-MELTS were not directly considered. Calculations of melt crystallization were run using starting compositions in a near-fractional crystallization style; i.e., the chemical composition of the starting material for the simulation is the measured composition of the glass from the previous crystallization stage at the specified temperature. Starting conditions and results of each simulation are reported in the **Supplementary Material**.

H_2O Diffusion and Bubble Growth

The characteristic timescales for diffusion (τ_d) and viscous deformation or relaxation (τ_v) are:

$$\tau_d = \frac{r^2}{D_{H_2O}} \qquad (1)$$

$$\tau_v = \frac{\eta_{melt}}{\Delta P_g} \qquad (2)$$

where r is the bubble radius, D_{H_2O} the H_2O diffusion coefficient or diffusivity (Zhang et al., 2000), η_{melt} the melt viscosity, and ΔP_g the gas overpressure. D_{H_2O} in rhyolitic melts with H_2O content <7.7 wt% in the T range 403–1629°C and at P < 19 kbar is estimated using the model of Ni and Zhang (2008):

$$\ln\left(\frac{D_{H_2O}}{X}\right) = 13.47 - 49.996X + 7.0827\sqrt{X} + 1.8875P - \frac{9532.3 - 91933 + 13403\sqrt{X} + 3625.6P}{T} \qquad (3)$$

where X is the mole fraction of H_2O on a single oxygen basis, T temperature in K, and P pressure in GPa. ΔP_g is estimated using the equation of state for H_2O reported in Pitzer and Sterner (1994) in the JavaScript-based Fugacity Calculator: https://www.esci.umn.edu/people/researchers/withe012/fugacity.htm.

To determine whether diffusion- or viscosity-limited, the non-dimensional Péclet number (*Pe*), combining Eqs 1 and 2, must be determined (Navon and Lyakhovsky, 1998; Navon et al., 1998):

$$Pe = \frac{\tau_d}{\tau_v} = \frac{\Delta P_g r^2}{\eta_{\text{melt}} D_{H_2O}} \tag{4}$$

In our experiments gas exsolution occurs under conditions of $Pe < 1$, therefore the rate of expansion is unimportant relative to that of diffusive mass transfer. The H_2O diffusion length scale (l) from melt to gas bubble was determined using $l = \sqrt{t \times D_{H_2O}}$, with t as the experiment timescale.

RESULTS

Collectively, the experiments display a sequential record of microstructural changes toward the solidus in a T–Φ space (**Figures 2**, **3**). Visual inspection of the central sections of the samples shows that, as also observed in nature (**Figure 1**), none of the samples achieved textural equilibrium due to rapid crystallization and vesiculation (Anderson et al., 1984; Sanders, 1986; Sisson and Bacon, 1999). Degassing occurred in all experiments with many vesicles found trapped between mineral clusters and in direct contact with surfaces of newly formed minerals. Using three-dimensional image analysis and two-dimensional analysis of vesicle modal abundance, we observe how the distribution of both glass (including hornblende and oxides, which are not resolvable at the spatial resolution of the microtomography) and vesicles changes as the experimental system approaches the solidus (**Figure 4**).

Here we report the observations of the different phase (glass, minerals, and vesicles) proportions and changes as a function of initial crystallinity, sample portion (central versus peripheral section), and temperature (**Figure 4**). The vesicle volume fraction in sample F80 slightly increases from central to peripheral sections in the T range from 800 and 750°C. At 850°C the vesicle content from central to peripheral sections of the cylindrical materials is more variable, with F70 displaying the largest increase in vesicle abundance in the peripheral section (**Figures 4B,C**) where large (up to 500-μm wide) tubular and connected vesicles are found (**Figure 2C**). In both central and peripheral sections of the cylindrical materials we observe the vesicle content decrease from 850 to 800°C and then its increase from 800 to 750°C, except for the case of sample F70 whose vesicle content decreases at 850°C (**Figures 4B,C**). This non-linear change of the vesicle content is a function of both SiO_2 increase in the residual melt during moderate crystallization from 850 to 800°C and during extensive crystallization from 800 to 750°C, and non-equilibrium processes, which include relatively rapid crystallization at the chosen temperatures and melt and vesicle movement during the experiments. At constant P, both SiO_2 increase in melt composition and T decrease concomitantly increase H_2O solubility in the residual melt due to retrograde or inverse volatile solubility with lowering T (Fogel and Rutherford, 1990; Paillat et al., 1992; Blank et al., 1993; Lowenstern, 2001).

At 850 and 800°C, the vesicle content tends to remain unchanged in both central and peripheral sections of each sample, whereas, at 750°C, vesicle abundance increases by up to 50% at largest crystallinity (Φ = 0.8; **Figures 4B,C**). Initial crystallinity increases from 2 to 20% in run products at T = 850°C, whereas it increases by 45% in F60, by 11% in F70, and by 5% in F80 at 750°C, based on the comparison between the 3D renderings of the run products at 850 and 750°C, respectively (**Figure 4A**). At 800°C the initial crystallinity does not vary (<2%) by either partial mineral resorption as observed at 850°C or the formation of new minerals as observed at 750°C (**Figure 4**). The total glass abundance decreases by 10% (in F70 and F80) to 70% (in F60) from 850 to 750°C (**Figure 4A**). Glass modal proportion increases from 20% (in F60 and F70) to 50% (in F80) from central and peripheral section of samples at 750°C (**Figures 4B,C**). Limited glass volume fraction increase is observed between central and peripheral section of samples at 850°C (<5%) or no increase at all at 800°C (**Figures 4B,C**). Analysis of the VSD shows a narrow distribution of Feret's radius centered around 5- to 10-μm (**Supplementary Material**) unlike that expected for Ostwald ripening, which would exhibit a smaller, broader peak (Stoffregen, 1996).

Detailed microstructural inspection of representative sample regions at microscopic scale reveals key features at specific T and initial Φ conditions (**Figures 5–7**). Fractures seen in all samples are produced at the end of the experiment during either sample cooling, recovery, or preparation prior to analysis.

At 850°C (**Figure 5**), vesicles are sub-rounded and surrounded by newly-formed quartz grains (Qz_2) that are 20-μm across and roundish and, thus, devoid of asperities such as those of the pre-existing quartz (70-μm across, Qz_1). Quartz of round shape is typically formed in H_2O-saturated felsic melts (Cabane et al., 2001). Hornblende needles (10-μm long) and tabular plagioclase (40-μm long) are primarily found in vesicle-free regions. Glass-rich regions are free of vesicles and newly-formed minerals (**Figure 5**). Melt viscosity is homogeneously distributed in the sample, with $\log\eta_{\text{melt}} = 3.5 \pm 0.2$ (**Figure 5**).

At 800°C (**Figure 6**), new quartz (Qz_2), plagioclase, and microscopic oxides form on pre-existing quartz (Qz_1). The presence of oxides "coating" quartz and plagioclase favors round vesicles (10-μm diameter) to adhere to the mineral surface, in agreement with previous experimental observations (Hurwitz and Navon, 1994; Laporte, 1994; Navon and Lyakhovsky, 1998; Navon et al., 1998). Glass is populated by oxides (1-μm) and hornblende needles that, at Φ = 0.6, form an alignment texture within glass regions of 10- to 30-μm size (**Figure 6A**). At Φ = 0.8, plagioclase is abundant (**Figure 6C**). Both vesicles and glass are found within the glass-rich portions of the starting materials, which were sealed by the progression of crystallization and gas exsolution (**Figure 6C**). Glass could not be analyzed due to a lack of crystal-free spots; thus, no $\log\eta_{\text{melt}}$ estimations are presented.

At 750°C (**Figure 7**), new quartz (Qz_2), plagioclase, oxide, and hornblende adhering to pre-existing quartz (Qz_1) are widespread. Quartz and plagioclase are arranged in unidirectional solidification textures (USTs; Shannon et al., 1982) that also entrap 3-μm diameter vesicles (**Figure 7C**). In places, these textures end with new 50-μm quartz grown from the USTs (**Figure 7B**). The glass region is constricted by large vesicles (20 μm) and hornblende needles, aligned

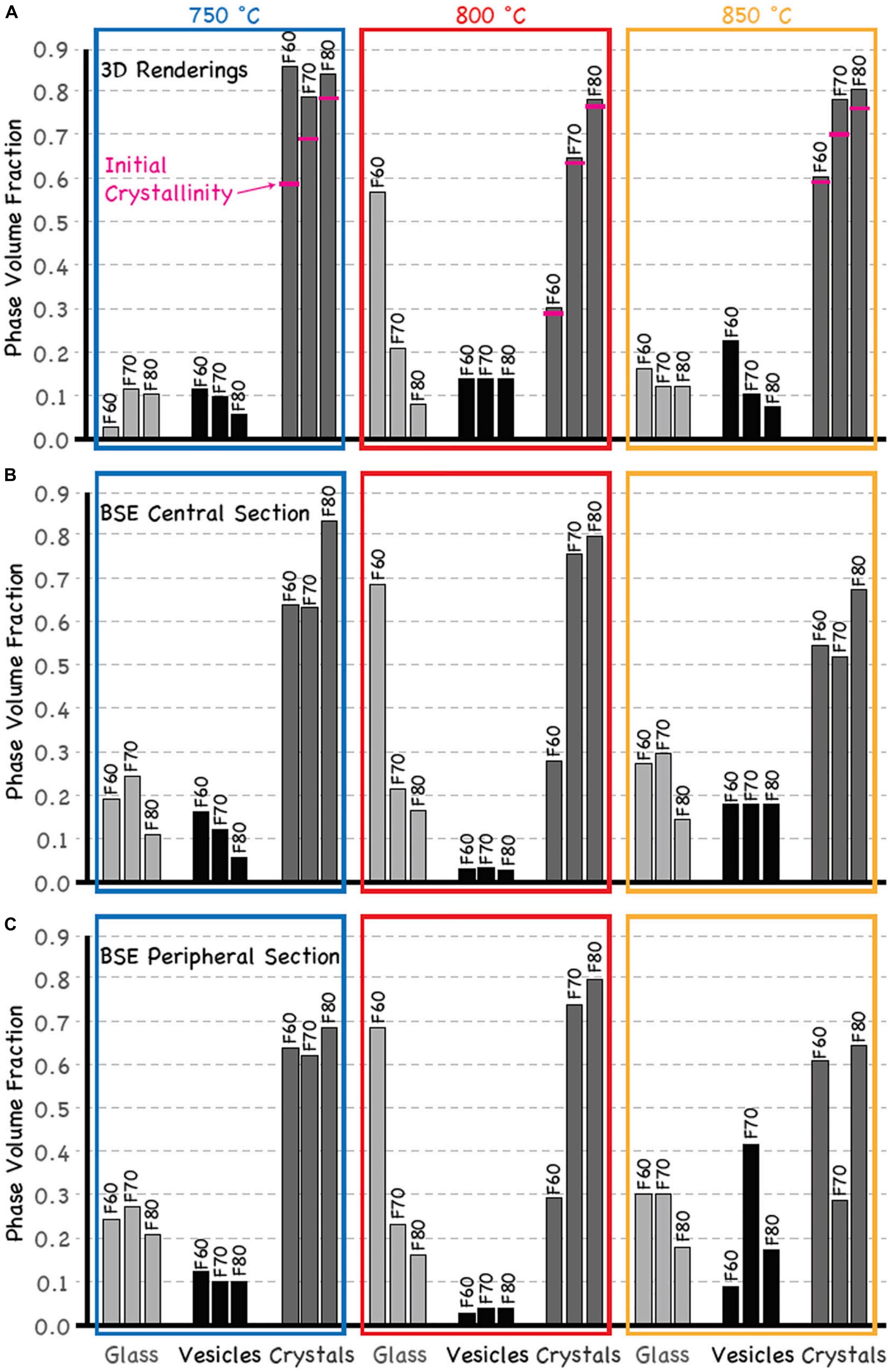

FIGURE 4 | Total volume fractions of phases: **(A)** in each tomographic 3D rendering, **(B)** in each BSE central section, and **(C)** in each BSE peripheral section of the experimental specimens. Volume fraction uncertainties (2σ) are 0.005, 0.002, and 0.002, respectively. Horizontal pink bars indicate initial level of crystallinity in the run products analyzed using X-ray tomographic microscopy.

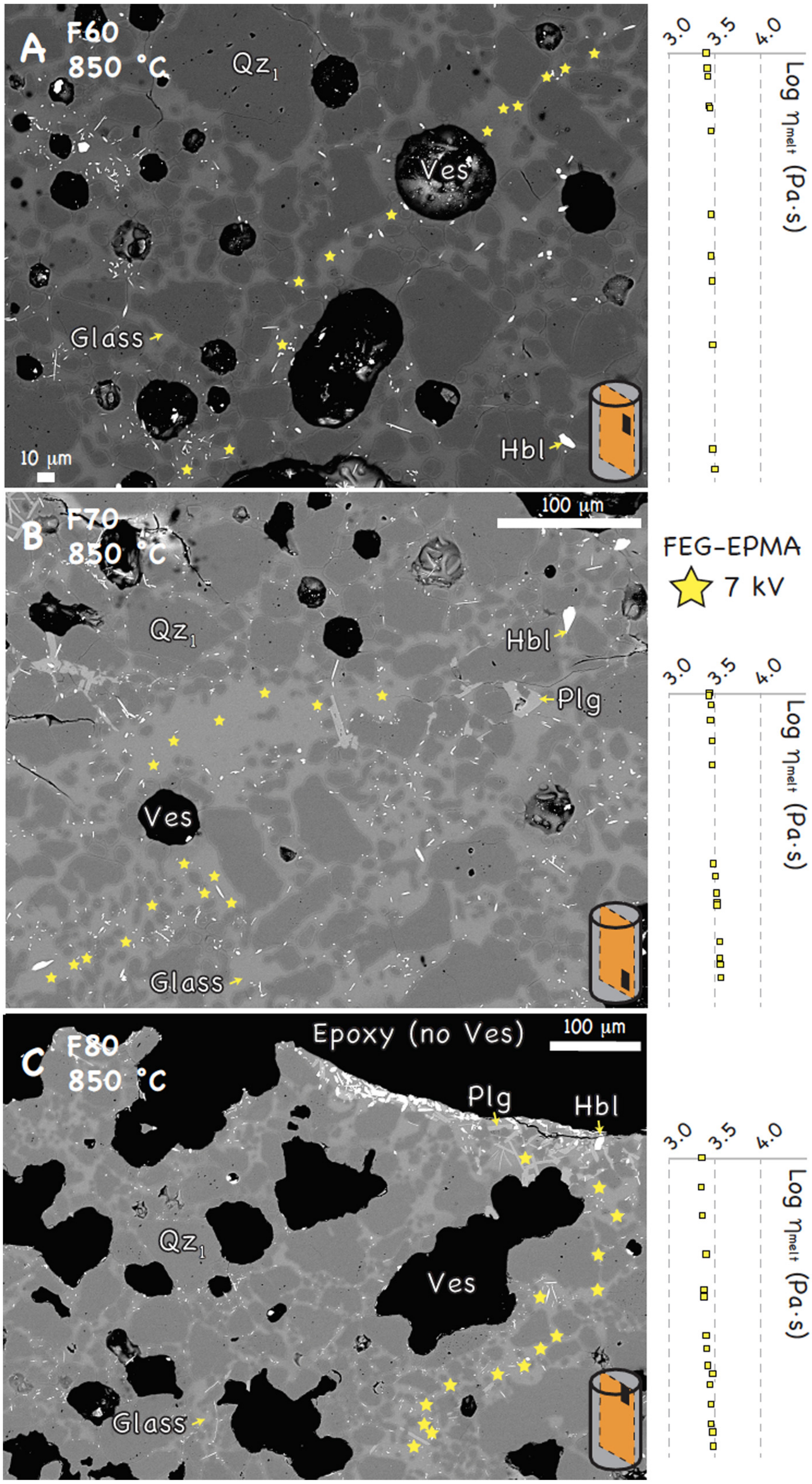

FIGURE 5 | FEG-probe-based BSE images of selected portions within the central polished sections of: **(A)** F60, **(B)** F70, and **(C)** F80 at 850°C. Error bars corresponding to 2σ are smaller than symbols. Acronyms are for: Qz_1 = pre-existing quartz (dark gray); Plg = plagioclase (light gray); Hbl = hornblende (white elongated phase); Ves = vesicle (black objects, sometimes filled with whitish material that produces electron charging); Glass = residual glass (least dark gray phase). Sketches of cylindrical samples (light gray) show the location of the sample portion (black rectangles) inspected in the sample central section (orange plane).

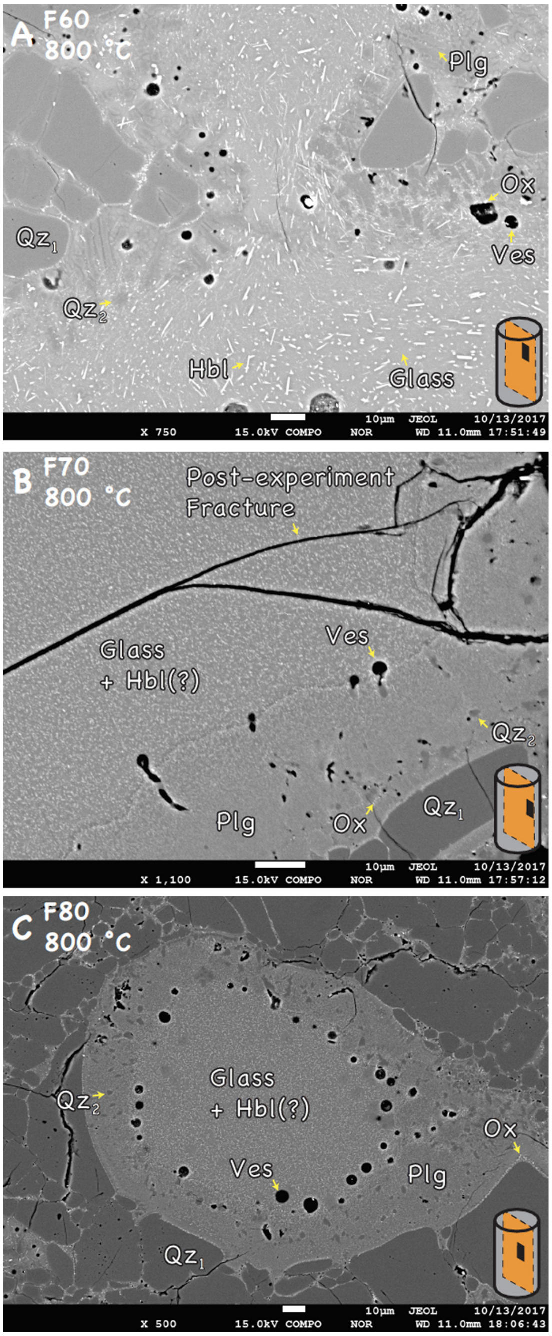

FIGURE 6 | FEG-probe-based BSE images of selected portions within the central polished sections of: **(A)** F60, **(B)** F70, and **(C)** F80 at 800°C. See acronyms from **Figure 5**, plus Ox = oxide (white round phase). Sketches of cylindrical samples (light gray) show the location of the sample portion (black rectangles) inspected in the sample central section (orange plane).

perpendicularly to the USTs (**Figure 7B**). Pre-existing quartz is surrounded by a micrographic texture of ~1-µm oxides and hornblende (**Figures 7B,C**). Logη_{melt} decreases by ~0.5 from crystal-rich and bubble-poor regions to low crystallinity bubble-rich regions within the same sample, especially in specimen F60 (**Figure 7A**). Moreover, samples with high crystallinity (F70 and F80) display calculated logη_{melt} of 3.5–4.0, which is 0.5 orders of magnitude (**Figure 7**) lower than the value obtained for the low crystallinity samples (F60).

At each T, bubble growth was driven by H_2O diffusion, with an initially high D_{H_2O} ($4 \cdot 10^{-11}$ m^2/s at 4.2 wt% H_2O) that increased with increasing H_2O in the residual melt (10^{-10} m^2/s at 5–7 wt% H_2O) during crystallization. In agreement with previous studies (Lyakhovsky et al., 1996), high D_{H_2O} leads to large H_2O diffusion distances (~8 mm > sample length and diameter) in the range of T and run duration of our experiments. There is no evidence of physical interconnectivity of vesicles (**Figures 5–7**), which suggests that bubbles formed by H_2O diffusion only. Locally, H_2O in the glass exceeds H_2O-saturation conditions (>5–7 wt% H_2O at experimental P-T; Papale et al., 2006; **Supplementary Material**), either in the 10-µm thick glass halos around vesicles due to H_2O resorption from bubbles during cooling (McIntosh et al., 2014) or in glass portions suggested to be populated by "nanobubbles" (Davydov et al., 2005). The volume fraction of new minerals increases with decreasing initial Φ at all T. This is due to the fact that samples with low crystallinity (F60) display larger amount of residual melt that degas and crystallize with respect to the high-crystallinity systems (F70 and F80).

Rhyolite-MELTS calculations predict that the starting melt would crystallize plagioclase at 850°C, followed by quartz at 800°C (**Figure 8A**). Solidification fronts from 850 to 750°C would thus be driven by: (i) initial homogenous nucleation of hornblende, plagioclase, and limited quartz, (ii) heterogeneous growth of hornblende, quartz, and plagioclase upon pre-existing quartz, and (iii) increase of vesicle content (**Figure 8A**). These calculations provide minimum mineral fractions in the absence of amphibole, which increases H_2O in the melt and, thus, leads to less extensive crystallization, as observed in our experiments. Overall, the volume fraction of vesicles tends to decrease from the sample center toward its periphery at highest crystallinity (**Figures 4B,C**).

DISCUSSION

The microstructures produced experimentally are the consequence of undercooled partial crystallization of magma that lead to enhanced differentiation of the interstitial melt (from dacite to rhyolite) and disequilibrium rock textures. Both microstructural and chemical analyses demonstrate that *in situ* melt differentiation is driven by vapor-saturated magma crystallization and physical migration of the residual melt, as a result of pressure gradient caused by gas exsolution.

Φ and T govern melt and gas expulsion from the magma during solidification. The reduction of pore space by "crystal zipping" (**Figures 7B,C**), driven by the advancement of solidification fronts (Marsh, 1995), forces both melt and bubbles to migrate toward the crystal-poor regions and to be segregated toward the sample periphery (**Figure 8B**). We quantify the outward movement of melt by measuring the final volume fraction of glass/melt in both the central and peripheral sections of the sample, $X_{f(central)}$ and $X_{f(peripheral)}$, respectively, where the

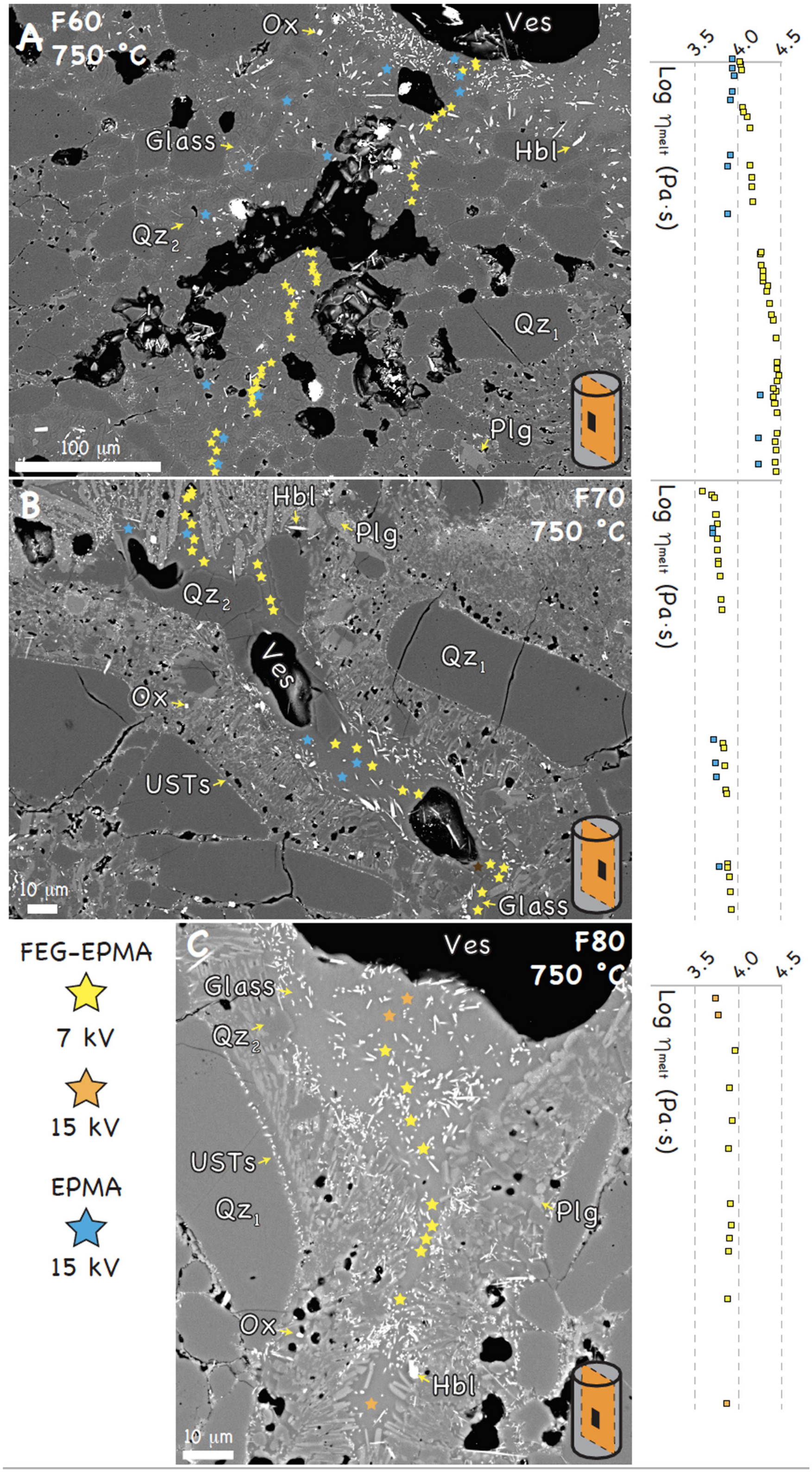

FIGURE 7 | FEG-probe-based BSE images of selected portions within the central polished sections of: **(A)** F60, **(B)** F70, and **(C)** F80 at 750°C. Error bars corresponding to 2σ are smaller than symbols. See acronyms from **Figures 5, 6**, plus USTs = unidirectional solidification textures, consisting of plagioclase and quartz (Qz_2) aligned perpendicular to the surface of the pre-existing quartz minerals (Qz_1). Sketches of cylindrical samples (light gray) show the location of the sample portion (black rectangles) inspected in the sample central section (orange plane).

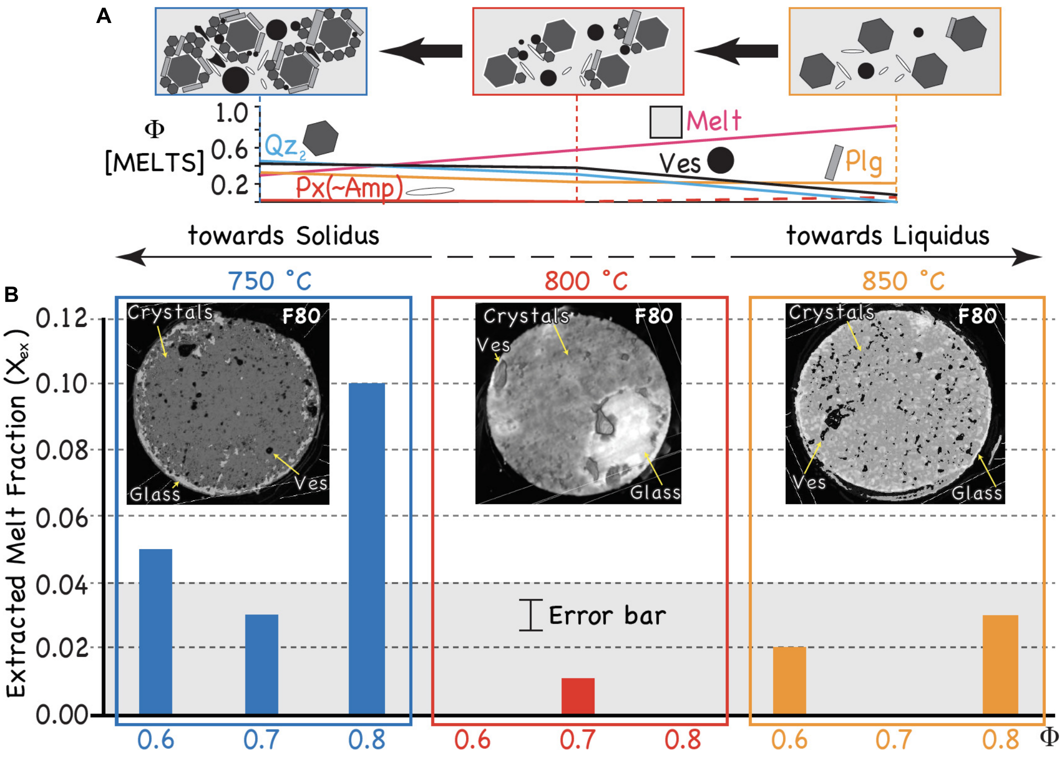

FIGURE 8 | (A) Volume fraction variation of the major phases at different *T*, based on crystallization simulations using Rhyolite-MELTS. **(B)** Extracted melt fraction (X_{ex}) as a function of *T* and Φ, with representative X-ray tomographic projections (6 μm/pixel spatial resolution; top-viewed) taken in the middle portion of each sample that show the distribution of glass (light gray), vesicles (black), and crystals (dark gray). The gray area indicates the volume fractions of residual rhyolitic melt observed in natural enclaves in volcanic rocks (after Bacon, 1986).

peripheral section is located at 1 mm radial distance. We then define the quantity X_{ex} to be

$$X_{ex} = X_{f(\text{peripheral})} - X_{f(\text{central})} \tag{5}$$

and note that the larger the value of X_{ex}, the greater the volume of outward melt transport. We observe that $X_{ex} \leq 0.03 \pm 0.01$ at 850 and 800°C, and $X_{ex} \leq 0.10 \pm 0.01$ at 750°C. At 750°C, crystallization produces a continuous network of minerals upon the pre-existing quartz grains and enhances the *P* increase during gas expansion in the constricted channels (**Figure 7B**). Concurrent pore restriction by crystallization and volume expansion upon H_2O exsolution by diffusion into bubbles leads to highly efficient extraction of large melt fraction by gas filter pressing. Conversely, in the runs at 800 and 850°C, appreciable melt volume extraction occurs at $\Phi \geq 0.8$ due to: gas expansion in absence of melt pore restriction caused by crystallization at 850°C (**Figure 5C**), and limited crystallization without extensive gas exsolution at 800°C (**Figure 6C**). Both cases make evident the limited effectiveness of melt extraction driven by exsolved gas (**Figure 8B**).

The volumetric estimates of extracted melt in our experiments are in line with similar estimates determined using mass balance calculations and textural observations of rinds and cores of glass-bearing andesitic enclaves in volcanic rocks (Bacon, 1986). Specifically, Bacon (1986) showed that the extraction of 0.02–0.04 volume fraction of rhyolitic melt is required to produce the chemical discrepancies between cores and rinds of andesitic inclusions. A few millimeters thick glass linings in vesicles and the rhyolitic glass-filled vesicles found in rinds testify to the migration of interstitial melt from core to margin of the enclaves by gas filter pressing (Anderson et al., 1984), similar to what observed in this study (**Figure 8B**).

In previous experiments simulating gas filter pressing in the absence of concurrent crystallization (Pistone et al., 2015), melt extraction was efficient for $0.6 \leq \Phi \leq 0.74$. Our new study shows how melt and gas extraction proceeds in more complex systems undergoing crystallization. Very evolved, H_2O-rich (5–7 wt% H_2O) melts with $\eta_{melt} \leq 10^4$ Pa s (**Figures 5, 7**) are highly mobile and their migration is efficient even at $\Phi > 0.8$, below the maximum crystallinity preserving melt connectivity in volatile-rich systems ($\Phi = 0.89$–0.93; Faul, 2001; Cheadle et al., 2004; Rosenberg and Handy, 2005). The presence of continuous chains of minerals formed at the solidification fronts (Philpotts et al., 1998, 1999; Philpotts and Dickson, 2000) builds a strong network that is key to promoting melt extraction by gas filter pressing.

IMPLICATIONS

Microstructural and chemical results can be extrapolated to melt and gas movements during magma cooling, for example of a granitic pluton in the upper crust. We can constrain the operating timescale for gas and melt extraction prior to complete solidification of the host mush. Below the melt connectivity transition (Rosenberg and Handy, 2005), we first estimate melt permeability in our quartz-rich magmas (κ) with melt fraction (X_f; **Figure 8**) and average mineral size (R) at the specific T (Richter and McKenzie, 1984):

$$\kappa = \frac{X_f^3 R^2}{A(1 - X_f^2)} \tag{6}$$

where the permeability coefficient $A = 50$ (McKenzie, 1984; Jackson et al., 2003; Bachmann and Bergantz, 2004; Pistone et al., 2015) for $0.07 < X_f < 0.1$ (in the presence of gas bubbles) and R ranging from 70 μm (initial quartz size) at 850°C to 150 μm (due to overgrowth of new quartz and plagioclase) at 750°C. κ ranges from $3{\cdot}10^{-13}$ m^2 at 850°C to $8{\cdot}10^{-12}$ m^2 at 750°C. Here we assume magmatic suspensions containing a monodisperse distribution of crystal size. As magmas contain crystals of different size and shape (i.e., polydisperse suspensions), which both tend to reduce the permeability with respect to monodisperse systems (Bachmann and Bergantz, 2004; Rust and Cashman, 2011), the volumetric rates of melt extraction calculated here for each mineral size (70–150 μm) are maxima.

The velocity (v) of melt and gas migration out of the crystal network can be estimated using Darcy's law:

$$v = \frac{\kappa}{\eta_{\text{melt}}} \times \frac{1}{X_f} \frac{\Delta P_g}{x} \tag{7}$$

$\Delta P_g / x$ is the gas pressure gradient to move melt from the sample center to its periphery (x = 1-mm radius distance) and is calculated based on the difference between experimental P and gas saturation P. From 850 to 750°C, $\Delta P_g / x$ changes from 0.001 to 0.12 kbar/m. Hence, at 1.1 kbar, the extraction of the same amount of H_2O-rich (4–7 wt%) melt ($X_f = 0.1$) occurs at ∼1 to ∼3 μm/day at 850°C (with $\eta_{\text{melt}} = 10^4$ to 10^5 Pa·s) and ∼80 to ∼800 μm/day at 750°C (with $\eta_{\text{melt}} = 10^5$ to 10^6 Pa·s), respectively.

Assuming natural magmas have a phenocryst size of ∼3 to 10 mm (**Figure 1**), Eqs 6 and 7 predict expulsion velocities of melt and gas to increase from ∼1 to ∼8 m/year. These are, however, likely to be maximum estimates, as real magmas could attain, for equivalent Φ timescales that are several orders of magnitude slower at slower cooling rates, and bulk expansion of melt and crystals could minimize melt migration (Sisson and Bacon, 1999). The timescales of extraction of viscous felsic melt from highly crystallized magmas are broadly constrained from months to thousands of years (Huber et al., 2012; Wilson and Charlier, 2016; Gualda et al., 2018). Viable processes that can speed up melt extraction are: (i) volume contraction of magma of up to 20% upon cooling and solidification, which leads to constrictional volume that drives expulsion of residual melts (John and Blundy, 1993; John and Stünitz, 1997), (ii) diking into brittle country rocks or pre-existing magmas (Mahood and Cornejo, 1992) that triggers pluton decompression at its margins leading to magma brecciation and removal or "unzipping" of the melt (**Figures 1D,E**), and (iii) eruptions that rapidly evacuate magma reservoirs, similar to that observed during drilling into magma, where the melt (from a high-P region) invades the drill hole (low-P) within few minutes (Hardee et al., 1981; Helz, 1984). The cooling of gas-saturated magmas in proximity to their solidus has the potential to account for the extraction of interstitial melts by gas filter pressing that form pegmatitic caps or become eruptible magmas feeding volcanoes.

CONCLUSION

We present the first experimental study to show melt segregation driven by gas filter pressing from crystal mushes at conditions relevant to the Earth's shallow crust. Through the use of conventional high-temperature and high-pressure experiments combined with high-spatial resolution techniques and Rhyolite-MELTS simulations, we have illustrated the physical conditions that allow gas-driven filter pressing to be an efficient process for melt extraction from near-solidus systems. Specifically, we have determined the effectiveness of gas-driven filter pressing to expel the silicic melt out of the crystal framework as a function of crystallinity and temperature conditions that bracket solidification of natural mushes. The results from our study are of prime importance for understanding the modality of the generation and extraction of volatile-rich crystal-poor magmas. At a more fundamental level, we document and explain how second boiling at the microscopic level affects the macroscopic dynamics of melt and gas mobilization. The cooling of volatile-saturated magmas in proximity to their solidus could represent a critical stage for silica-rich interstitial melts driven by gas filter pressing to be extracted and form pegmatitic caps or become eruptible magmas feeding volcanoes.

Large-scale magmatic reservoirs should be characterised by slow kinetics of crystallization and rate of gas exsolution (Sisson and Bacon, 1999), which were not simulated in our experiments. There is still need to investigate which short timescale process (years to decades) would speed up extraction and accumulation of large melt lenses (10–1000 km^3; Bachmann and Bergantz, 2004; Bachmann and Huber, 2019) of the size required for large volcanic eruptions (Volcanic Explosivity Index >4; Newhall and Self, 1982). Using the present-day high-resolution local seismic tomography (cell volume of 125 km^3; e.g., Miller and Smith, 1999), there is little geophysical evidence for the presence of crystal-poor bodies of large volume. Their "absence" could be related to long-term storage of melt-rich lenses within large long-lived mush zones with massive thermal inertia that favor slow cooling (Huber et al., 2009; Morse, 2011), as well as to sufficiently fast extraction and eruption of these melt lenses before complete solidification. Further effort is therefore required for scaling up the experimental results to magmatic reservoirs in the Earth's crust.

DATA AVAILABILITY STATEMENT

All datasets presented in this study are included in the article/**Supplementary Material**.

AUTHOR CONTRIBUTIONS

MP and EB conceived and carried out the high-temperature and high-pressure experiments (with technical guidance and assistance from LB and TS). MP performed all the chemical and microstructural analyses (with technical guidance and assistance from MR) and computational calculations and prepared the manuscript. The quantitative information was finalized by MP and PJ. MP and FB explored the link between experiments and natural scenarios. LB, OM, TS, and JB provided critical guidance during the preparation of the manuscript, and all authors were instrumental in the resulting manuscript.

FUNDING

The SNSF PZ00P2_168166 (Ambizione Fellowship) grant and the UGA Presidential Funds to MP supported this research. ERC Advanced Grant CRITMAG to JB and NERC grant NE/K500823/1 to PJ supported fieldwork in Guernsey Island. LB and FB aknowledge support by SNF grants 200020_172513 and 200021_153094. TS was supported by a fellowship from the Herbette foundation.

ACKNOWLEDGMENTS

We ackowledge the support of M. Jercinovic (University of Massachussets in Amherst, MA) and A. van Lankvelt (CAMECA) during FEG-EPMA analyses. We also thank C. R. Bacon, M. A. Clynne (USGS), and Dante Canil (University of Victoria) for their insightful analysis and feedback on an earlier version of the manuscript. In memoriam to A. T. Anderson Jr. who first proposed gas filter pressing as a viable mechanism of melt egress from cooling magmas.

SUPPLEMENTARY MATERIAL

The Supplementary Material for this article can be found online at: https://www.frontiersin.org/articles/10.3389/feart.2020.00175/full#supplementary-material

REFERENCES

Afanasyev, A., Blundy, J., Melnik, O., and Sparks, R. S. J. (2018). Formation of magmatic brine lenses via focussed fluid-flow beneath volcanoes. *Earth Planet. Sci. Lett.* 486, 119–128. doi: 10.1016/j.epsl.2018.01.013

Anderson, A. T. Jr., Swihart, G. H., Artioli, G., and Geiger, C. A. (1984). Segregation vesicles, gas filter-pressing, and igneous differentiation. *J. Geol.* 92, 55–72. doi: 10.1086/628834

Armstrong, J. T. (1988). “Quantitative analysis of silicate and oxide materials: comparison of Monte Carlo, ZAF, and (-(-z procedures,” in *Microbeam Analysis*, ed. D. E. Newbury (San Francisco, CA: San Francisco Press, Inc), 239–246.

Bachmann, O., and Bergantz, G. (2004). On the origin of crystal-poor rhyolites: extracted from batholithic crystal mushes. *J. Petrol.* 45, 1565–1582. doi: 10.1093/petrology/egh019

Bachmann, O., and Huber, C. (2019). The Inner Workings of Crustal Distillation Columns; the Physical Mechanisms and Rates Controlling Phase Separation in Silicic Magma Reservoirs. *J. Petrol.* 60, 3–18. doi: 10.1093/petrology/egy103

Bacon, C. R. (1986). Magmatic inclusions in silicic and intermediate volcanic rocks. *J. Geophys. Res.* 91, 6091–6112.

Balashov, N., Zaraisky, G. P., and Seltmann, R. (2000). Fluid-magmatic interaction and oscillation phenomena during granite melt crystallization with water-fluoride fluid gain-loss. *Petrologiya* 8, 563–585.

Baumgartner, L. P., Bodner, R., Leuthold, J., Müntener, O., and Putlitz, B. (2014). “The torres del paine intrusion as a model for a shallow magma chamber,” in *Proceedings of the EGU General Assembly Conference*, Vienna.

Baumgartner, L. P., Michel, J., Putlitz, B., Leuthold, J., Müntener, O., Robyr, M., et al. (2007). “Field guide to the Torres del Paine Igneous Complex and its contact aureole: field guide book GEOSUR 2007, Bolletino de Geofisica, GEOSUR 2007,” in *Proceedings of the International Congress on the Southern Hemisphere*, Santiago, 185.

Bégué, F., Gualda, G. A. R., Ghiorso, M. S., Pamukcu, A. S., Kennedy, B. M., Gravley, D. M., et al. (2014). Phase-equilibrium geobarometers for silicic rocks based on rhyolite-MELTS. Part 2: application to Taupo Volcanic Zone rhyolites. *Contrib. Mineral. Petrol.* 168:1082.

Blank, J. G., Stolper, E. M., and Carroll, M. R. (1993). Solubilities of carbon dioxide and water in rhyolitic melt at 850 °C and 750 bars. *Earth Planet. Sci. Lett.* 119, 27–36. doi: 10.1016/0012-821x(93)90004-s

Blundy, J. D., Mavrogenes, J., Tattitch, B., Sparks, R. S. J., and Gilmer, A. (2015). Generation of porphyry copper deposits by gas-brine reaction in volcanic arcs. *Nat. Geosci.* 8, 235–240. doi: 10.1038/ngeo2351

Blundy, J. D., and Sparks, R. S. J. (1992). Petrogenesis of mafic inclusions in granitoids of the Adamello Massif, Italy. *J. Petrol.* 33, 1039–1104. doi: 10.1093/petrology/33.5.1039

Bowen, N. L. (1928). *The Evolution of the Igneous Rocks*. Mineola, NY: Dover Publication.

Brown, M., Averkin, Y. A., and McLellan, E. L. (1995). Melt segregation in migmatites. *J. Geophys. Res.* 100, 15655–15679. doi: 10.1029/95jb00517

Cabane, H., Laporte, D., and Provost, A. (2001). Experimental investigation of the kinetics of Ostwald ripening of quartz in silicic melts. *Contrib. Mineral. Petrol.* 150, 361–373. doi: 10.1007/s004100100296

Candela, A. (1997). A review of shallow, ore-related granites: textures, volatiles, and ore metals. *J. Petrol.* 38, 1619–1633. doi: 10.1093/petroj/38.12.1619

Candela, A., and Blevin, L. (1995). Do some miarolitic granites preserve evidence of magmatic volatile phase permeability? *Econ. Geol.* 90, 2310–2316. doi: 10.2113/gsecongeo.90.8.2310

Candela, P. A., and Piccoli, P. M. (1995). “Model ore-metal partitioning from melts into vapor and vapor/brine mixtures,” in *Magmas, Fluids, and Ore Deposits*, ed J. F. H. Thompson, Min. Ass. Can., 23, 101–127.

Caricchi, L., and Blundy, J. D. (eds) (2015). “Experimental petrology of monotonous intermediate magmas,” in *Chemical, Physical and Temporal Evolution of Magmatic Systems* (London: Geological Society of London Publications), 105–130. doi: 10.1144/sp422.9

Caroff, M., Coint, N., Hallot, E., Hamelin, C., Peucat, J.-J., and Charreteur, G. (2011). The mafic-silicic layered intrusions of Saint-Jean-du-Doigt (France) and North-Guernsey (Channel Islands), Armorican Massif: gabbro–diorite layering and mafic cumulate–pegmatoid association. *Lithos* 125, 675–692. doi: 10.1016/j.lithos.2011.03.019

Castro, J. M., Burgisser, A., Schipper, C. I., and Mancini, S. (2012). Mechanisms of bubble coalescence in silicic magmas. *Bull. Volcanol.* 74, 2339–2352. doi: 10.1007/s00445-012-0666-1

Cheadle, M. J., Elliott, M. T., and McKenzie, D. (2004). Percolation threshold and permeability of crystallizing igneous rocks: the importance of textural equilibrium. *Geology* 32, 757–760.

Clemens, J. D., Holloway, J. R., and White, A. J. R. (1986). Origin of an A-type granite: experimental constraints. *Am. Mineral.* 71, 317–324.

Clemens, J. D., and Wall, J. (1981). Origin and crystallization of some peraluminous (S-type) granitic magmas. *Can. Mineral.* 19, 111–131.

Colucci, S., Battaglia, M., and Trigila, R. (2015). A thermodynamical model for the surface tension of silicate melts in contact with H_2O gas. *Geochim. Cosmochim. Acta* 175, 113–127. doi: 10.1016/j.gca.2015.10.037

Connolly, J., Schmidt, M., Solferino, G., and Bagdassarov, N. (2009). Permeability of asthenospheric mantle and melt extraction rates at mid-ocean ridges. *Nature* 462, 209–212. doi: 10.1038/nature08517

Dall'Agnol, R., Scaillet, B., and Pichavant, M. (1994). Phase relations of amphibole-biotite bearing granites. I. Effects of a(H_2O) under oxidizing conditions. *Terra Abstr.* 6:13.

Davydov, M. N., Kendrinskii, K., Chernov, A. A., and Takayama, K. (2005). Generation and evolution of cavitation in magma under dynamic unloading. *J. Appl. Mech. Tech. Phys.* 46, 208–215. doi: 10.1007/s10808-005-0036-2

de Bremond, d'Ars, J., Martin, H., Auvray, B., and Lecuyer, C. (1992). Petrology of a magma chamber: the Plutonic Complex of Guernsey (Channel Islands, UK). *J. Geol. Soc.* 149, 701–708. doi: 10.1144/gsjgs.149.5.0701

Degruyter, W., Parmigiani, A., Huber, C., and Bachmann, O. (2019). How do volatiles escape their shallow magmatic hearth? *Philos. Trans. R. Soc. A* 377:20180017. doi: 10.1098/rsta.2018.0017

Dell'Angelo, L. N., and Tullis, J. (1988). Experimental deformation of partially melted granitic aggregates. *J. Metamorph. Geol.* 6, 495–515. doi: 10.1111/j.1525-1314.1988.tb00436.x

Devine, J. D., Gardner, J. E., Brack, H. P., Layne, G. D., and Rutherford, M. J. (1995). Comparison of microanalytical methods for estimating H_2O contents of silicic volcanic glasses. *Am. Mineral.* 80, 319–328. doi: 10.2138/am-1995-3-413

D'Lemos, R. S. (1987). *Relationships between the Cobo Granite and the Bordeaux Diorite Complex, Guernsey*. Ph.D. dissertation, University of Bristol, Bristol.

Driesner, T. (2007). The system H2O-NaCl. Part II: correlations for molar volume, enthalpy, and isobaric heat capacity from 0 to 1000 (C, 1 to 5000 bar, and 0 to 1 XNaCl. *Geochim. Cosmochim. Acta* 71, 4902–4919. doi: 10.1016/j.gca.2007.05.026

Driesner, T., and Heinrich, C. A. (2007). The system H_2O_NaCl. Part I. Correlation formulae for phase relations in temperature–pressure–composition space from 0 to 1000 (C, 0 to 5000 bar, and 0 to 1 XNaCl. *Geochim. Cosmochimica Acta* 71, 4880–4901. doi: 10.1016/j.gca.2006.01.033

Dufek, J., and Bachmann, O. (2010). Quantum magmatism: magmatic compositional gaps generated by melt-crystal dynamics. *Geology* 38, 687–690. doi: 10.1130/g30831.1

Faul, U. H. (2001). Melt retention and segregation beneath mid-ocean ridges. *Nature* 410, 920–923. doi: 10.1038/35073556

Fenn, M. (1977). The nucleation and growth of alkali feldspars from hydrous melts. *Can. Mineral.* 15, 135–161.

Fogel, R. A., and Rutherford, M. J. (1990). The solubility of carbon dioxide in rhyolitic melts: a quantitative FTIR study. *Am. Mineral.* 75, 1311–1326.

Gonnermann, H. M., and Manga, M. (2007). The fluid mechanics inside a volcano. *Annu. Rev. Fluid Mech.* 39, 321–356. doi: 10.1146/annurev.fluid.39.050905.110207

Grosse, P., Toselli, A. J., and Rossi, J. N. (2010). Petrology and geochemistry of the orbicular granitoid of Sierra de Velasco (NW Argentina) and implications for the origin of orbicular rocks. *Geol. Mag.* 147, 451–468. doi: 10.1017/s0016756809990707

Gualda, G. A. R., and Ghiorso, M. S. (2013). Low-pressure origin of high-silica rhyolites and granites. *J. Geol.* 121, 537–545. doi: 10.1086/671395

Gualda, G. A. R., Ghiorso, M. S., Lemons, R. V., and Carley, T. L. (2012). Rhyolite-MELTS: a modified calibration of MELTS optimized for silica-rich, fluid-bearing magmatic systems. *J. Petrol.* 53, 875–890. doi: 10.1093/petrology/egr080

Gualda, G. A. R., Gravley, D. M., Conner, M., Hollmann, B., Pamukcu, A. S., Bégué, F., et al. (2018). Climbing the crustal ladder: magma storage-depth evolution during a volcanic flare-up. *Sci. Adv*. 4:eaap7567. doi: 10.1126/sciadv.aap7567

Hardee, H. C., Dunn, J. C., Hills, R. G., and Ward, R. W. (1981). Probing the melt zone of Kilauea Iki Lava Lake, Kilauea Volcano, Hawaii. *Geophys. Res. Lett.* 8, 1211–1214. doi: 10.1029/gl008i012p01211

Hartung, E., Caricchi, L., Floess, D., Wallis, S., Harayama, S., Kouzmanov, K., et al. (2017). Evidence for residual melt extraction in the Takidani Pluton, Central Japan. *J. Petrol.* 58, 763–788. doi: 10.1093/petrology/egx033

Hartung, E., Weber, G., and Caricchi, L. (2019). The role of H_2O on the extraction of melt from crystallising magmas. *Earth Planet. Sci. Lett.* 508, 85–96. doi: 10.1016/j.epsl.2018.12.010

Helz, R. T. (1984). In situ fractionation of olivine tholeiite: Kilauea Iki lava lake, Hawaii. *Geol. Soci. Am. Abstr. Programs* 16, 536–537.

Hildreth, W. (1981). Gradients in silicic magma chambers: implications for lithospheric magmatism. *J. Geophys. Res.* 86, 10153–10192. doi: 10.1002/9781118782057.ch3

Hildreth, W. (2004). Volcanological perspectives on Long Valley, Mammoth Mountain, and Mono Craters: several contiguous but discrete systems. *J. Volcanol. Geotherm. Res.* 136, 169–198. doi: 10.1016/j.jvolgeores.2004.05.019

Hildreth, W., and Wilson, C. J. N. (2007). Compositional zoning of the Bishop Tuff. *J. Petrol.* 48, 951–999. doi: 10.1093/petrology/egm007

Holness, M. B. (2018). Melt segregation from silicic crystal mushes: a critical appraisal of possible mechanisms and their microstructural record. *Contrib. Mineral. Petrol.* 173:48. doi: 10.1007/s00410-018-1465-2

Holtz, F., and Johannes, W. (1994). Maximum and minimum water contents of granitic melts: implications for chemical and physical properties of ascending magmas. *Lithos* 32, 149–159. doi: 10.1016/0024-4937(94)90027-2

Holtz, F., Johannes, W., Tamic, N., and Behrens, H. (2001). Maximum and minimum water contents of granitic melts generated in the crust: a reevaluation and implications. *Lithos* 56, 1–14. doi: 10.1016/s0024-4937(00)00056-6

Huber, C., Bachmann, O., and Dufek, J. (2010a). The limitations of melting on the reactivation of silicic mushes. *J. Volcanol. Geotherm. Res.* 195, 97–105. doi: 10.1016/j.jvolgeores.2010.06.006

Huber, C., Bachmann, O., and Dufek, J. (2012). Crystal-poor versus crystal-rich ignimbrites: a competition between stirring and reactivation. *Geology* 40, 115–118.

Huber, C., Bachmann, O., and Manga, M. (2009). Homogenization processes in silicic magma chambers by stirring and mushification (latent heat buffering). *Earth Planet. Sci. Lett.* 283, 38–47. doi: 10.1016/j.epsl.2009.03.029

Huber, C., Bachmann, O., and Manga, M. (2010b). Two competing effects of volatiles on heat transfer in crystal-rich magmas: thermal insulation versus defrosting. *J. Petrol.* 51, 847–867. doi: 10.1093/petrology/egq003

Huber, C., and Parmigiani, A. (2018). A physical model for three-phase compaction in silicic magma reservoirs. *J. Geophys. Res. Solid Earth* 123, 2685–2705. doi: 10.1002/2017JB015224

Huber, C., Townsend, M., Degruyter, W., and Bachmann, O. (2019). Optimal depth of subvolcanic magma chamber growth controlled by volatiles and crust rheology. *Nat. Geosci.* 12, 762–768. doi: 10.1038/s41561-019-0415-6

Hui, H. J., Zhang, Y. X., Xu, Z. J., Del Gaudio, P., and Behrens, H. (2009). Pressure dependence of viscosity of rhyolitic melts. *Geochim. Cosmochim. Acta* 73, 3680–3693. doi: 10.1016/j.gca.2009.03.035

Hurwitz, S., and Navon, O. (1994). Bubble nucleation in rhyolitic melts: experiments at high pressure, temperature, and water content. *Earth Planet. Sci. Lett.* 122, 267–280. doi: 10.1016/0012-821x(94)90001-9

Jackson, M. D., Cheadle, M. J., and Atherton, M. P. (2003). Quantitative modeling of granitic melt generation and segregation in the continental crust. *J. Geophys. Res.* 108:2332. doi: 10.1029/2001JB001050

John, B. E., and Blundy, J. D. (1993). Emplacement-related deformation of granitoid magmas, southern Adamello Massif, Italy. *Geol. Soc. Am. Bull.* 105, 1517–1541. doi: 10.1130/0016-7606(1993)105<1517:erdogm>2.3.co;2

John, B. E., and Stünitz, H. (1997). "Magmtic fracturing and small-scale melt segregation during pluton emplacement: evidence from the Adamello Massif (Italy)," in *Granite: From Segregation of Melt to Emplacement Fabrics*, eds J. L. Bouchez, D. H. W. Hutton, and W. E. Stephens (Berlin: Kluwer Academic Publishers), 55–74. doi: 10.1007/978-94-017-1717-5_4

Johnson, M. C., and Rutherford, M. R. (1989). Experimentally determined conditions in the Fish Canyon Tuff, Colorado, magma chamber. *J. Petrol.* 30, 711–737. doi: 10.1093/petrology/30.3.711

Ketcham, R. A. (2005a). Computational methods for quantitative analysis of three-dimensional features in geological specimens. *Geosphere* 1, 32–41.

Ketcham, R. A. (2005b). Three-dimensional textural measurements using high-resolution X-ray computed tomography. *J. Struct. Geol.* 27, 1217–1228. doi: 10.1016/j.jsg.2005.02.006

Laporte, D. (1994). Wetting behavior of partial melts during crustal anatexis: the distribution of hydrous silicic melts in polycrystalline aggregates of quartz. *Contrib. Mineral. Petrol.* 116, 486–499. doi: 10.1007/bf00310914

Lautze, N. C., Sisson, T. W., Mangan, M. T., and Grove, T. L. (2011). Segregating gas from melt: an experimental study of the Ostwald ripening of vapor bubbles in magmas. *Contrib. Mineral. Petrol.* 161, 331–347. doi: 10.1007/s00410-010-0535-x

Lee, C.-T. A., Morton, D. M., Farner, M. J., and Moitra. (2015). Field and model constraints on silicic melt segregation by compaction/hindered settling: the role of water and its effect on latent heat release. *Am. Mineral.* 100, 1762–1777. doi: 10.2138/am-2015-5121

Leuthold, J., Müntener, O., Baumgartner, L. P., and Putlitz, B. (2014). Petrological constraints on the recycling of mafic crystal mushes and intrusion of braided sills in the Torres del Paine Mafic Complex (Patagonia). *J. Petrol.* 55, 917–949. doi: 10.1093/petrology/egu011

Lissenberg, J. C., and MacLeod, C. J. (2016). A reactive porous flow control on mid-ocean ridge magmatic evolution. *J. Petrol.* 57, 2195–2220. doi: 10.1093/petrology/egw074

Liu, E. J., Cashman, K. V., and Rust, A. C. (2015). Optimising shape analysis to quantify volcanic ash morphology. *GeoResJ* 8, 14–30. doi: 10.1016/j.grj.2015.09.001

Liu, Y., and Zhang, Y. (2000). Bubble growth in rhyolitic melt. *Earth Planet. Sci. Lett.* 181, 251–264. doi: 10.1016/s0012-821x(00)00197-7

Lowenstern, J. B. (2001). Carbon dioxide in magmas and implications for hydrothermal systems. *Mineralium Depos.* 36, 490–502. doi: 10.1007/s001260100185

Lyakhovsky, V., Hurwitz, S., and Navon, O. (1996). Bubble growth in rhyolitic melts: experimental and numerical investigation. *Bull. Volcanol.* 58, 19–32. doi: 10.1007/s004450050122

Mahood, G. A., and Cornejo, C. (1992). Evidence for ascent of differentiated liquids in a silicic magma chamber found in a granitic pluton. *Tran. R. Soc. Edinburgh Earth Sci.* 83, 63–69. doi: 10.1017/s0263593300007756

Marsh, B. D. (1981). On the crystallinity, probability of occurrence, and rheology of lava and magma. *Contrib. Mineral. Petrol.* 78, 85–98. doi: 10.1007/bf00371146

Marsh, B. D. (1995). Solidification fronts and magmatic evolution. *Mineral. Mag.* 60, 5–40. doi: 10.1180/minmag.1996.060.398.03

Masotta, M., Gaeta, M., Gozzi, F., Marra, F., Palladino, D., and Sottili, G. (2010). The Tufo Giallo della Via Tiberina eruptions (Sabatini Volcanic District, Roman Province): insights on H_2O- and temperature-zoning in magma chambers. *Lithos* 118, 119–130. doi: 10.1016/j.lithos.2010.04.004

McCarthy, A., and Müntener, O. (2016). Comb layering monitors decompressing and fractionating hydrous mafic magmas in subvolcanic plumbing systems (Fisher Lake, Sierra Nevada, USA). . *J. Geophys. Res.* 121, 8595–8621. doi: 10.1002/2016jb013489

McIntosh, I. M., Llewellin, E. W., Humphreys, M. C. S., Nichols, A. R. L., Burgisser, A., Schipper, C. I., et al. (2014). Distribution of dissolved water in magmatic glass records growth and resorption of bubbles. *Earth Planet. Sci. Lett.* 401, 1–11. doi: 10.1016/j.epsl.2014.05.037

McKenzie, D. (1984). The generation and compaction of partially molten rock. *J. Petrol.* 25, 713–765. doi: 10.1093/petrology/25.3.713

Michel, J., Baumgartner, L., Putlitz, B., Schaltegger, U., and Ovtcharova, M. (2008). Incremental growth of the Patagonian Torres del Paine laccolith over 90 k.y. *Geology* 36, 459–462.

Miller, D. S., and Smith, R. B. (1999). P and S velocity structure of the Yellowstone volcanic field from local earthquake and controlled source tomography. *J. Geophys. Res.* 104, 15105–15121. doi: 10.1029/1998jb900095

Morgan, G. B., and London, D. (1996). Optimizing the electron microprobe analysis of hydrous alkali aluminosilicate glasses. *Am. Mineral.* 81, 1176–1185. doi: 10.2138/am-1996-9-1016

Morse, S. A. (2011). The fractional latent heat of crystallizing magmas. *Am. Mineral.* 96, 682–689. doi: 10.2138/am.2011.3613

Müntener, O., Kelemen, B., and Grove, T. L. (2001). The role of H_2O during crystallization of primitive arc magmas under uppermost mantle conditions and genesis of igneous pyroxenites: an experimental study. *Contrib. Mineral. Petrol.* 141, 643–658. doi: 10.1007/s004100100266

Nabelek, I., Whittington, A. G., and Sirbescu, M. L. C. (2010). The role of H_2O in rapid emplacement and crystallization of granite pegmatites: resolving the paradox of large crystals in highly undercooled melts. *Contrib. Mineral. Petrol.* 160, 313–325. doi: 10.1007/s00410-009-0479-1

Navon, O., Chekhmir, A., and Lyakhovsky, V. (1998). Bubble growth in highly viscous melts: theory, experiments, and autoexplosivity of dome lavas. *Earth Planet. Sci. Lett.* 160, 763–776.

Navon, O., and Lyakhovsky, V. (1998). "Vesiculation processes in silicic magmas," in *The Physics of Explosive Volcanic Eruptions, Geological Society of London*, Vol. 145, eds J. S. Gilbert and R. S. J. Sparks (London: Geological Society of London Publications), 27–50. doi: 10.1144/gsl.sp.1996.145.01.03

Newhall, C. G., and Self, S. (1982). The volcanic explosivity index (VEI) an estimate of explosive magnitude for historical volcanism. *J. Geophys. Res.* 87, 1231–1238.

Ni, H., and Zhang, Y. (2008). H_2O diffusion models in rhyolitic melt with new high pressure data. *Chem. Geol.* 250, 68–78. doi: 10.1016/j.chemgeo.2008.02.011

Olsen, S. N., Marsh, B. D., and Baumgartner, L. P. (2004). Modelling mid-crustal migmatite terrains as feeder zones for granite plutons: the competing dynamics of melt transfer by bulk versus porous flow. *Trans. R. Soc. Edinburgh Earth Sci.* 95, 49–58. doi: 10.1017/s0263593300000912

Oppenheimer, J., Rust, A. C., Cashman, K. V., and Sandnes, B. (2015). Gas migration regimes and outgassing in particle-rich suspensions. *Front. Phys.* 3:60. doi: 10.3389/fphy.2015.00060

Paillat, O., Elphick, S. C., and Brown, W. L. (1992). The solubility of water in NaAlSi3O8 melts: a re-examination of Ab-H_2O phase relationships and critical behaviour at high pressures. *Contrib. Mineral. Petrol.* 112, 490–500. doi: 10.1007/bf00310780

Papale, P., Moretti, R., and Barbato, D. (2006). The compositional dependence of the saturation surface of $H_2O + CO_2$ fluids in silicate melts. *Chem. Geol.* 229, 78–95. doi: 10.1016/j.chemgeo.2006.01.013

Parmigiani, A., Faroughi, S., Huber, C., Bachmann, O., and Su, Y. (2016). Bubble accumulation and its role in the evolution of magma reservoirs in the upper crust. *Nature* 532, 492–495. doi: 10.1038/nature17401

Parmigiani, A., Huber, C., and Bachmann, O. (2014). Mush microphysics and the reactivation of crystal-rich magma reservoirs. *J. Geophys. Res. Solid Earth* 119, 6308–6322. doi: 10.1002/2014JB011124

Philpotts, A. R., Brustman, C., Shi, J., Carlson, W. D., and Denison, C. (1999). Plagioclase-chain networks in slowly cooled basaltic magma. *Am. Mineral.* 84, 1819–1829. doi: 10.2138/am-1999-11-1209

Philpotts, A. R., and Dickson, L. D. (2000). The formation of plagioclase chains during convective transfer in basaltic magma. *Nature* 406, 59–61. doi: 10.1038/35017542

Philpotts, A. R., Shi, J., and Brustman, C. (1998). Role of plagioclase crystal chains in the differentiation of partly crystallized basaltic magma. *Nature* 395, 343–346. doi: 10.1038/26404

Pistone, M., Arzilli, F., Dobson, K. J., Cordonnier, B., Reusser, E., Ulmer, P., et al. (2015). Gas-driven filter pressing in magmas: insights into in-situ melt segregation from crystal mushes. *Geology* 43, 699–702. doi: 10.1130/g36766.1

Pistone, M., Blundy, J. D., Brooker, R. A., and Eimf. (2016). Textural and chemical consequences of interaction between hydrous mafic and felsic magmas: an experimental study. *Contrib. Mineral. Petrol.* 171:8. doi: 10.1007/s00410-015-1218-4

Pistone, M., Caricchi, L., Ulmer, P., Burlini, L., Ardia, P., Reusser, E., et al. (2012). Deformation experiments of bubble- and crystal-bearing magmas: rheological and microstructural analysis. *J. Geophys. Res.* 117:B05208. doi: 10.1029/2011JB008986

Pistone, M., Caricchi, L., Ulmer, P., Reusser, E., and Ardia. (2013). Rheology of volatile-bearing crystal mushes: mobilization vs. viscous death. *Chem. Geol.* 345, 16–39. doi: 10.1016/j.chemgeo.2013.02.007

Pistone, M., Racek, M., and Štípska. (2020). Effects of diffusion of water and migration of melts in crustal rocks: an experimental study. *Chem. Geol.* 540:119548. doi: 10.1016/j.chemgeo.2020.119548

Pistone, M., Whittington, A. G., Andrews, B., and Cottrell, E. (2017). Crystal-rich lava dome extrusion during vesiculation: an experimental study. *J. Volcanol. Geotherm. Res.* 347, 1–14. doi: 10.1016/j.jvolgeores.2017.06.018

Pitzer, K. S., and Sterner, S. M. (1994). Equations of state valid continuously from zero to extreme pressures for H_2O and CO_2. *J. Chem. Phys.* 101, 3111–3116. doi: 10.1063/1.467624

Proussevitch, A., Sahagian, D. L., and Anderson, A. T. (1993). Dynamics of diffusive bubble growth in magmas: isothermal case. *J. Geophys. Res.* 98, 22283–22307. doi: 10.1029/93jb02027

Proussevitch, A. A., and Sahagian, D. L. (1998). Dynamics and energetics of bubble growth in magmas: analytical formulation and numerical modeling. *J. Geophys. Res.* 103, 18223–18251. doi: 10.1029/98jb00906

Putlitz, B., Baumgartner, L. P., Oberhaensli, R., Diamond, L., and Altenberger, U. (2001). "The Torres del Paine Laccolith (Chile); intrusion and metamorphism," in *Proceedings of the XI Annual V. M. Goldschmidt*, Virginia, NV.

Richter, F. M., and McKenzie, D. P. (1984). Dynamical models for melt segregation from a deformable matrix. *J. Geol.* 92, 729–740. doi: 10.1086/628908

Robin, Y. F. (1979). Theory of metamorphic segregation and related processes. *Geochim. Cosmochim. Acta* 43, 1587–1600. doi: 10.1016/0016-7037(79)90179-0

Roduit, N. (2011). *JMicroVision: Image Analysis Toolbox for Measuring and Quantifying Components of High-Definition Images. Version 1.2.7.* Available online at: http://www.jmicrovision.com (accessed May 2011).

Rosenberg, C., and Handy, M. (2005). Experimental deformation of partially melted granite revisited: implications for the continental crust. *J. Metamorph. Geol.* 23, 19–28. doi: 10.1111/j.1525-1314.2005.00555.x

Rust, A. C., and Cashman, K. V. (2011). Permeability controls on expansion and size distributions of pyroclasts. *J. Geophys. Res.* 116, 1–17.

Sanders, I. S. (1986). Gas filter-pressing origin for segregation vesicles in dykes. *Geol. Mag.* 123, 67–72. doi: 10.1017/s0016756800026546

Sawyer, E. W., and Robin, Y. (1986). The sub-solidus segregation of layer-parallel quartz-feldspar veins in greenschist to upper amphibolite facies metasediments. *J. Metamorph. Geol.* 4, 237–260. doi: 10.1111/j.1525-1314.1986.tb00350.x

Scaillet, B., and Pichavant, M. (1994). Phase relations of amphibole-biotite bearing granites. II: effects of fO_2. *Terra Nova* 6:42.

Scaillet, B., Pecher, A., Rochette, P., and Champenois, M. (1995a). The Gangotri granite (Garhwal Himalaya): laccolithic emplacement in an extending collisional belt. *J. Geophys. Res.* 100, 585–607. doi: 10.1029/94jb01664

Scaillet, B., Pichavant, M., and Roux, J. (1995b). Experimental crystallization of leucogranite magmas. *J. Petrol.* 36, 664–706.

Schindelin, J., Arganda-Carreras, I., Frise, E., Kaynig, V., Longair, M., Pietzsch, T., et al. (2012). Fiji: an open-source platform for biological-image analysis. *Nat. Methods* 9, 676–682.

Schmidt, M. W., Forien, M., Solferino, G., and Bagdassarov, N. (2012). Settling and compaction of olivine in basaltic magmas: an experimental study on the time scales of cumulate formation. *Contrib. Mineral. Petrol.* 164, 959–976. doi: 10.1007/s00410-012-0782-0

Shannon, J. R., Walker, B. M., Carten, R. B., and Geraghty, E. P. (1982). Unidirectional solidification textures and their significance in determining relative ages of intrusions at the Henderson Mine, Colorado. *Geology* 10, 293–297.

Sisson, T. W., and Bacon, C. R. (1999). Gas-driven filter pressing in magmas. *Geology* 27, 613–616.

Sparks, R. S. J., Annen, C., Blundy, J. D., Cashman, K. V., Rust, A. C., and Jackson, M. D. (2019). Formation and dynamics of magma reservoirs. *Philos. Trans. R. Soc. A* 377:20180019. doi: 10.1098/rsta.2018.0019

Spiegelman, M., Kelemen, B., and Aharonov, E. (2001). Causes and consequences of flow organization during melt transport: the reaction infiltration instability in compactible media. *J. Geophys. Res.* 106, 2061–2077. doi: 10.1029/2000jb900240

Stoffregen, R. (1996). Numerical simulation of mineral-water isotope exchange via Ostwald ripening. *Am. J. Sci.* 296, 908–931. doi: 10.2475/ajs.296.8.908

Su, Y., Huber, C., Bachmann, O., Zajacz, Z., Wright, H., and Vazquez, J. (2016). The role of crystallization-driven exsolution on the sulfur mass balance in volcanic arc magmas. *J. Geophys. Res.* 121, 5624–5640. doi: 10.1002/2016jb013184

Tuttle, O. F., and Bowen, N. L. (1958). Origin of granite in the light of experimental studies in the system $NaAlSi_3O_8$-$KAlSi_3O_8$–SiO_2–H_2O. *Geol. Soc. Am. Mem* 74, 1–153. doi: 10.1130/MEM74

Vigneresse, J.-L. (2015). Textures and melt-crystal-gas interactions in granites. *Geosci. Front.* 6, 635–663. doi: 10.1016/j.gsf.2014.12.004

Wager, L. R., Brown, G. M., and Wadsworth, W. J. (1960). Types of igneous cumulates. *J. Petrol.* 1, 73–85. doi: 10.1093/petrology/1.1.73

Waters, L. E., and Lange, R. A. (2017). Why aplites freeze and rhyolites erupt: controls on the accumulation and eruption of high-SiO_2 (eutectic) melts. *Geology* 45, 1019–1022. doi: 10.1130/g39373.1

Webber, K. L., Falster, A. U., Simmons, W., and Foord, E. E. (1997). The role of diffusion-controlled oscillatory nucleation in the formation of line rock in pegmatite-aplite dikes. *J. Petrol.* 38, 1777–1791. doi: 10.1093/petroj/38.12.1777

Webster, J. D., Holloway, J. R., and Hervig, R. L. (1987). Phase equilibria of a Be, U and F-enriched vitrophyre from Spor Mountain, Utah. *Geochim. Cosmochim. Acta* 51, 389–402. doi: 10.1016/0016-7037(87)90057-3

Whitney, J. (1988). The origin of granite: the role and source of water in the evolution of granitic magmas. *Geol. Soc. Am. Bull.* 100, 1886–1897. doi: 10.1130/0016-7606(1988)100<1886:toogtr>2.3.co;2

Wilson, C. J. N., and Charlier, B. L. A. (2016). The life and times of silicic volcanic systems. *Elements* 12, 103–108. doi: 10.2113/gselements.12.2.103

Zhang, C., Li, X., Almeev, R. R., Horn, I., Behrens, H., and Holtz, F. (2020). Ti-in-quartz thermobarometry and TiO2 solubility in rhyolitic melts: new experiments and parametrization. *Earth Planet. Sci. Lett.* 538:116213. doi: 10.1016/j.epsl.2020.116213

Zhang, Y., Xu, Z., and Behrens, H. (2000). Hydrous species geospeedometer in rhyolite: improved calibration and application. *Geochim. Cosmochim. Acta* 64, 3347–3355. doi: 10.1016/s0016-7037(00)00424-5

Conflict of Interest: The authors declare that the research was conducted in the absence of any commercial or financial relationships that could be construed as a potential conflict of interest.

frontiers
in Earth Science

ORIGINAL RESEARCH
published: 14 July 2020
doi: 10.3389/feart.2020.00277

Phlogopite-Olivine Nephelinites Erupted During Early Stage Rifting, North Tanzanian Divergence

Céline Baudouin[1] and Fleurice Parat[2]*

[1] *Centre de Recherches Pétrographiques et Géochimiques, UMR 7358 CNRS-UL, Vandæuvre-lés-Nancy, France,*
[2] *Géosciences Montpellier, UMR 5243 – CC 60 – Université de Montpellier, Montpellier, France*

The North Tanzanian Divergence (NTD, eastern branch of the East African Rift) corresponds to an early stage of continental breakup. In the southern NTD, two quaternary volcanoes of the Manyara-Balangida rift (Labait, Kwaraha) have erupted primary nephelinite lavas (Mg# = 79–57) that allow characterization of their deep mantle source and the alkaline magmas that percolated through the lithosphere during rift initiation. Nephelinites are olivine- and clinopyroxene-rich, and contain up to 4 vol% magmatic phlogopite that crystallized as a liquidus phase with olivine and clinopyroxene. The presence of hydrous mineral (phlogopite) phenocrysts in Kwaraha and Labait lavas strongly suggests that the alkaline melts were H_2O-bearing at the time of phlogopite crystallization (1.57–2.12 wt% H_2O in phlogopite), demonstrating that phlogopite may have influenced the partitioning of water between the silicate melt and anhydrous silicate minerals (<1 ppm wt H_2O clinopyroxene, 1–6 ppm wt H_2O in olivine). Geochemical modeling indicates that the nephelinite magmas resulted from a low degree of partial melting (0.2–1%) of a carbonate-rich (0.3%) garnet peridotite containing ∼2 vol% phlogopite. We estimate the depth of partial melting based on primary melt compositions and empirical relations, and suggest that melting occurred at depths of 110–130 km (4 GPa) for craton-edge lavas (Kwaraha volcano) and 150 km (5 GPa) for on-craton lavas (Labait volcano), close to or below the lithosphere-asthenosphere boundary in agreement with the presence of deep refractory mantle xenoliths in Labait lavas. The depth of melting becomes gradually deeper toward the southern NTD: highly alkaline magmas in the north (Engaruka-Natron Basin) are sourced from amphibole- and CO_2-rich peridotite at 75–90 km depth, whereas magmatism in the south (south Manyara Basin) is sourced from deep phlogopite- and CO_2-rich garnet-peridotite beneath the Tanzania craton (e.g., at the on-craton Labait volcano). Percolation of deep asthenospheric CO_2-rich alkaline magmas during their ascent may have produced strong heterogeneities in the thick sub-continental lithospheric mantle by inducing metasomatism and phlogopite crystallization in glimmerite lithologies.

Keywords: nephelinites, rift, partial melting, alkaline magmatism, metasomatism

Edited by:
Anastassia Borisova,
Centre National de la Recherche Scientifique (CNRS), France

Reviewed by:
Marlina A. Elburg,
University of Johannesburg, South Africa
Stephen Foley,
Macquarie University, Australia

***Correspondence:**
Céline Baudouin
baudouin.geol@gmail.com

Specialty section:
This article was submitted to Petrology, a section of the journal Frontiers in Earth Science

Received: *26 March 2020*
Accepted: *17 June 2020*
Published: *14 July 2020*

Citation:
Baudouin C and Parat F (2020) Phlogopite-Olivine Nephelinites Erupted During Early Stage Rifting, North Tanzanian Divergence. Front. Earth Sci. 8:277. doi: 10.3389/feart.2020.00277

INTRODUCTION

Silica-undersaturated magmas are abundant in continental rifts, including highly alkaline lavas such as melilitite, nephelinite, basanite, and phonolite. Low-silica lavas are commonly CO_2-rich and have been described as the product of CO_2-bearing mantle domains (e.g., Brey, 1978; Dasgupta et al., 2007) associated with carbonatite, suggesting a cogenetic origin (Woolley and Kjarsgaard, 2008). The oldest volcanism of the East African Rift (EAR, ∼45 Ma) occurred in Ethiopia associated with the propagation of the EAR toward the south (Ebinger et al., 2000) and produced abundant highly alkaline rocks and carbonatites (e.g., Pouclet et al., 1981; Foley et al., 2012). Melilitites and nephelinites were erupted at the tip of the propagating rift and around the Tanzanian craton (i.e., Tanzania, Uganda; Foley et al., 2012). In northern Tanzania, primitive lavas, erupted generally in monogenetic volcanic fields (e.g., the Engaruka-Natron monogenetic field), are characterized by small eruptive volumes, little fractional crystallization during ascent, relatively high ascent rates, and xenolith-bearing lavas (Mattsson et al., 2013).

Primary alkaline lavas erupted on and at the edge of the Tanzanian craton sampled mantle xenoliths that indicate the presence of heterogeneous sub-cratonic lithospheric and asthenospheric mantle domains related to metasomatism by carbonated (Jones et al., 1983; Rudnick et al., 1993; Lee and Rudnick, 1999; Foley et al., 2012) and/or H_2O-rich fluids (Dawson and Smith, 1988; Koornneef et al., 2009). The xenolith data suggest that primary lavas originate from deep asthenospheric mantle processes. Furthermore, alkaline lavas are volatile-rich (e.g., Ivanikov et al., 1998; Keller et al., 2006; Métrich and Wallace, 2008; Hudgins et al., 2015) and could only derive from deep, low-degree partial melting of H_2O-CO_2-bearing peridotites. The depth of origin, degree of partial melting, and mantle source control the alkalinity of the primary melt (e.g., Maaløe et al., 1992; Rogers et al., 1992). The diversity of alkaline lavas (melilitite, nephelinite, and basanite) erupted in the North Tanzanian Divergence (NTD) clearly indicates partial melting at various levels in the sub-cratonic lithosphere and asthenosphere (e.g., Rosenthal et al., 2009; Foley et al., 2012; Mana et al., 2015). Further differentiation by fractional crystallization, liquid immiscibility, and assimilation produced Mg-rich nephelinite, Mg-poor nephelinite, and carbonatite at different levels in the mantle and continental crust during ascent (Klaudius and Keller, 2006; Zaitsev et al., 2012; Baudouin et al., 2016).

In this paper, we performed a petrological and geochemical investigation of the most primitive lavas of the NTD, i.e., nephelinites from the Manyara basin (Kwaraha and Labait volcanoes) to determine the mantle conditions of silica-undersaturated magma genesis at the first stage of continental break-up. We discuss the presence of magmatic phlogopite in terms of alkaline magma composition and crystallization environment of these magmas, and model the partial melting of a deep metasomatized mantle source of the highly alkaline magmas beneath the eastern part of the Tanzanian Craton.

Geological Background

The EAR is divided into two branches which correspond to different stages of plate boundary extension, from rift initiation (eastern branch initiation: Manyara-Balangida basin, Tanzania, and western branch initiation: Toro-Ankole basin, Uganda) to oceanic stage in the Afar Triple Junction. In the eastern branch, volcanism began 30 Ma in northern Kenya, 15 Ma in central Kenya, and 6 Ma in northern Tanzania (Mana et al., 2012, 2015). The north Tanzanian rift splays to form the NTD, which includes large volcanic complexes (e.g., Ngorongoro, Meru, and Kilimanjaro) and small volcanic cones (e.g., Lashaine, Olmani) (Dawson et al., 1970, 1997; Jones et al., 1983). The southern NTD is divided into three rift areas: Eyasi, Manyara-Balangida, and Pangani, from west to east (Le Gall et al., 2008; **Figure 1**). The Eyasi and Pangani fault systems are amagmatic and represent rift propagation from the Natron basin to the western and eastern parts of the NTD, respectively. The Manyara-Balangida basin, representing southward rift propagation, lies along the rift escarpment and includes two volcanic centers (Hanang and Kwaraha volcanoes, **Supplementary Figures A1, A2**) surrounded by small volcanic cones (Labait and Sora Hill, respectively, Dawson, 2008). East of the Manyara basin, several volcanic centers have erupted relatively evolved nephelinite lavas, whereas small volcanic cones in the Monduli-Meru area have erupted primitive lavas. The most primitive lavas were erupted at Kwaraha and the small cones around Hanang and Meru. We sampled Labait and Kwaraha for this study (**Figure 1**).

Labait volcano (4°34′12″ S, 35°26′04″ E, near Hanang volcano) is a small olivine melilitite cone (Dawson et al., 1997; **Figure 1**). Eruptions at Labait occurred at 0.4 ± 0.2 Ma (Rudnick et al., 1999). Labait lavas carried abundant mantle xenoliths including spinel phlogopite harzburgites, garnet lherzolite-harzburgites, dunites, and glimmerite xenoliths (Lee and Rudnick, 1999; Koornneef et al., 2009). The presence of phlogopite-bearing xenoliths (lherzolite and glimmerite) strongly suggests the presence of H_2O-rich fluids within the lithosphere. Models of water diffusion profiles in mantle olivines indicate high ascent rates ($4–28\ m{\cdot}s^{-1}$) and a low lithospheric mantle water content (<50 ppm wt H_2O) (Hui et al., 2015). Isotopic data from Labait olivine nephelinites indicate that cratonic or craton-margin lithosphere is present beneath Labait, with a slightly different signature compared to the lithospheric mantle (MacDonald et al., 2001; Aulbach et al., 2008).

Kwaraha volcano (4°13′45″ S, 35°48′53″ E) consists of Quaternary (1.5–0.7 Ma; Dawson, 2008) Mg-rich nephelinite agglomerates, tuffs, and lavas (Dawson et al., 1997). Tuff cones, craters, and a calciocarbonatite lava flow are distributed around the main edifice. Kwaraha lavas are derived from a source with similar isotopic ratio than the Proterozoic Mozambique mobile belt (low $^{87}Sr/^{86}Sr$; Paslick et al., 1996; MacDonald et al., 2001). Small parasitic cones produced lavas with melilitite to nephelinite compositions (Dawson et al., 1997) that are more mafic than those of the main edifice, and may represent the parental melt (Dawson et al., 1997; Dawson, 2008). We studied 10 parasitic cones including Sora Hill (Kw2) and Haindadonga cones (Kw3) (Dawson et al., 1997; **Figure 1**).

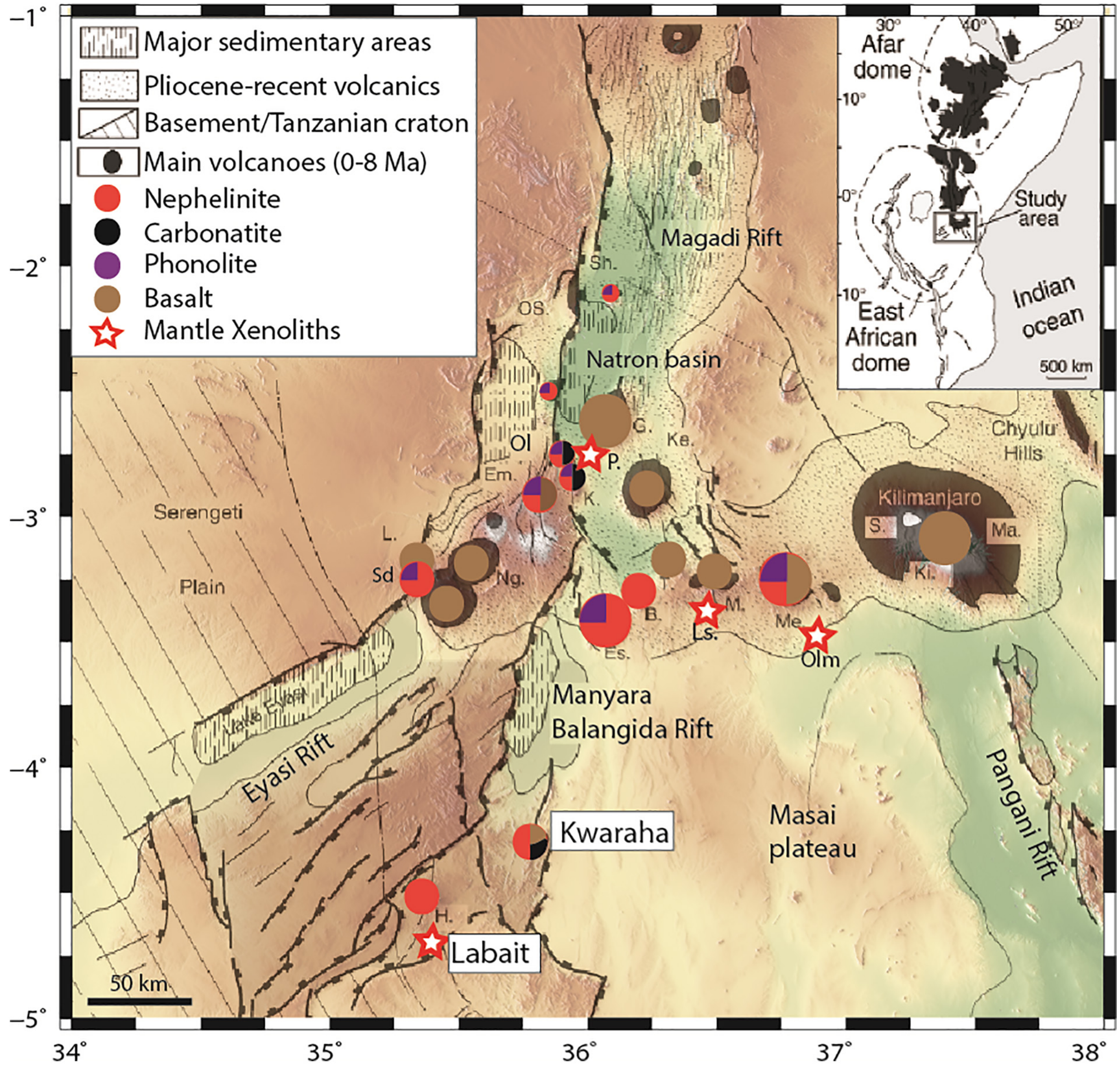

FIGURE 1 | Main structural and magmatic features of the North Tanzanian Divergence, and the locations of Labait and Kwaraha. Proportions of symbol colors represent relative eruptive volumes of magma composition for single volcano (nephelinite, phonolite, carbonatite, basalt). Volcano names are abbreviated as: B., Burko; Em., Embagai; Es., Essimingor; G., Gelai; H., Hanang; K., Kerimasi; Ke., Ketumbeine; Ki., Kibo; L., Lemagrut; M., Monduli; Ma., Mawenzi; Me., Meru; Ng., Ngorongoro; Ol., Oldoinyo Lengai; OS., Ol Donyo Sambu; P., Pello Hill; Sd., Sadiman; S., Shira; Sh., Shombole; T., Tarosero. Map modified after Le Gall et al. (2008).

MATERIALS AND METHODS

Major and Volatile Element Analyses

Whole-rock major element compositions were measured by inductively coupled plasma optical emission spectroscopy (iCap 6500 Thermo Fisher) at the Service d'Analyse des Roches et des Minéraux (SARM) at the Centre de Recherches Pétrographiques et Géochimiques (Nancy, France) following the protocol established by Carignan et al. (2001). One gram of whole-rock powder was dissolved with HNO_3 and the mixture (with $LiBO_2$) was fused. The reference standard was SLRS-5 and errors are estimated to be <2% (1σ).

Complementary whole-rock analyses has been performed by wide-angle X-ray fluorescence using sequential spectrometer Bruker S4 Pioneer at the analytical services of the Instituto Andaluz de Ciencias de la Tierra (IACT, University of Granada, Spain) using Rh X-ray tube (160 kV, 159 mA). Rock powders (1 g) are weighed with di-lithium tetraborate flux, and then the mixture is fused at 1000°C for 15 min. The concentrations of major elements in the samples are measured by comparing the X-ray intensity for each element with nine reference geological standard samples. Whole-rock sulfur and carbon contents were determined for each sample via elemental analyser, F and Cl contents were determined by wet precipitation-ferrithiocyanate spectrophotometry using a Varian Cary 50 spectrophotometer. High LOI (up to 8 wt%), and CO_2 content (up to 4.6 wt%) in nephelinitic lavas are due to the presence of small size secondary minerals within the groundmass from hydrothermal alteration (i.e., calcite, zeolite). Such minerals are common in nephelinites as reported at Mount Etinde (Cameroon; Etame et al., 2012), Engaruka volcanic field (Neukirchen et al., 2010), Cape Verde (Mourão et al., 2012), and as well worldwide nephelinites and melilitites (Georoc database[1]; **Supplementary Table A1**).

Mineral major and volatile element concentrations were determined via electron microprobe (Cameca XS100 at Geoscience Montpellier, France). Analyses were performed with an accelerating voltage of 20 keV, a 10 nA beam current, and a focused (1 μm) beam. The counting time was fixed at 20 and 40 s for major and volatile element (S, Cl) analyses, respectively. The standards used for major and volatile element analyses were wollastonite for Si and Ca, Al_2O_3 for Al, TiO_2 for Ti, forsterite for Mg, hematite for Fe, orthoclase for K, albite for Na, apatite for P, native metal for Ni, Mn, and Cu, barite for S and Ba, fluorite for F, and chlorapatite for Cl.

Trace Element Analyses

Whole-rock trace element analyses of lavas from Kwaraha and related small volcanic cones (samples Kw1–Kw8), and Labait were performed by ICP mass spectrometry (ICP-MS) after HNO_3 and HF digestion of 0.1 g of sample powder in a Teflon-lined vessel at 180°C and 200 psi for 30 min, evaporation to dryness, and subsequent dissolution in 100 mL of 4 vol% HNO_3. Triplicate measurements were performed with a NexION 300d (Perkin Elmer) ICP-MS at the Instituto Andaluz de Ciencias de la Tierra (University of Grenada) using Rh as an internal standard, and using multi-element calibration solutions for external calibration. Analytical precision was better than ± 5% for concentrations > 10 ppm. Whole-rock analyses of samples Kw10, Kw11, and Kw12 were performed using a quadrupole 7700x ICP-MS at the Analyse des Eléments en Trace dans l'Environnement (AETE platform, OSU-OREME, University of Montpellier) where 0.1 g of whole-rock powder was dissolved with acid (HF-HNO_3). Blanks spiked with In and Bi were prepared to monitor instrumental drift. Solutions were analyzed at a final dilution factor of 4000. The sensitivity of the ICP-MS in this configuration was 200×10^6 /ppm ^{115}In. Analytical accuracy was estimated from measurements of international rock standards UBN and BEN for both analytical procedures (**Supplementary Table A1**).

Mineral trace element concentrations were determined by laser ablation ICP-MS at AETE using a GeoLas Q+ Excimer CompEx 102. A 26 and 56 μm diameter laser beam was used for apatite and silicate minerals, respectively, with a laser repetition rate of 6–10 Hz and laser power of 0.5 mJ (5 $J{\cdot}cm^{-2}$). The spot size was chosen as a compromise between signal intensity and the size of the minerals of interest in the samples. Concentrations were calibrated with glass standard NIST612 and SiO_2 and CaO concentrations previously determined by electron microprobe. The BIR-1 standard was used as an external standard. Glitter Software (Griffin et al., 2008) was used to process the raw data files (signal intensity vs. time) into elemental concentrations. This allows precise selection of blanks and signals, and rapid visualization of the intensity data. Instrumental drift was compensated by internal standard calculations using Glitter; no other drift corrections were performed.

Water Content Analyses

The water contents of clinopyroxene and olivine (ol) were determined using Fourier transform infrared (FTIR) spectroscopy. Handpicked minerals were prepared as doubly polished sections with thicknesses between 140 and 325 μm. The hydrogen concentration was measured in transmission mode at the Laboratory Charles Coulomb (University of Montpellier, France). For olivine crystals, FTIR analyses were performed in the center of crystals far from iddingsite rims. Unpolarized infrared spectra were acquired using a Bruker IFS 66v coupled with a Hyperion optical microscope. A Globar light source and a Ge-KBr beam splitter were used to generate unpolarized mid-infrared radiation (4000–400 cm^{-1}). Water contents were calculated by integration of spectra between 3770 and 3000 cm^{-1} for clinopyroxene and between 3610 and 3000 cm^{-1} for olivine (for the detailed analytical method, see Denis et al., 2015). Water concentrations were calculated using the calibration of Paterson (1982), considering the water concentration as a function of the density of clinopyroxene ($\chi_{clinopyroxene}$(Kw3) = 2707 ppm wt H_2O, $\chi_{clinopyroxene}$(Kw5) = 2737 ppm wt H_2O) and olivine (χ_{ol}(Kw) = 2605–2612 ppm wt H_2O, χ_{ol}(Lab) = 2587 ppm wt H_2O). Errors on water contents due to the calibration (Paterson, 1982) and uncertainties on the sample thickness and background correction are ± 15% (Denis et al., 2015). The integrated unpolarized absorbances normalized to 1 cm sample thickness are also reported to use alternative mineral-specific FTIR calibrations.

The water content of phlogopite from sample Kw3 was measured on mineral separates by Karl-Fischer titration (KFT) using air as the transporting gas and muscovite as a standard (σ = 0.1 wt% H_2O) at the University of Hannover (Behrens et al., 1996). Whole rock H_2O content were measured by Karl Fischer titration at SARM. Standard solutions were used to check the accuracy of spectrophotometry analyses, and standard deviations are less than 5%.

RESULTS

All samples from Kwaraha (lava flows) and Labait (scoria) have microlitic porphyric textures with large phenocrysts of olivine and clinopyroxene (>1 mm) (**Figure 2**). Following the nomenclature of Le Bas (1989), the bulk rock compositions of Kwaraha lavas and Labait scoria are foidites with compositions between melilitite and nephelinite, similar to nephelinites reported in north Tanzania (**Figure 3**; Dawson et al., 1970, 1997; Mana et al., 2012). Because of the similar mineral assemblages and chemical compositions of all samples, as well the absence of melilite minerals, we refer to them herein as nephelinites.

---

[1] http://georoc.mpch-mainz.gwdg.de/georoc/

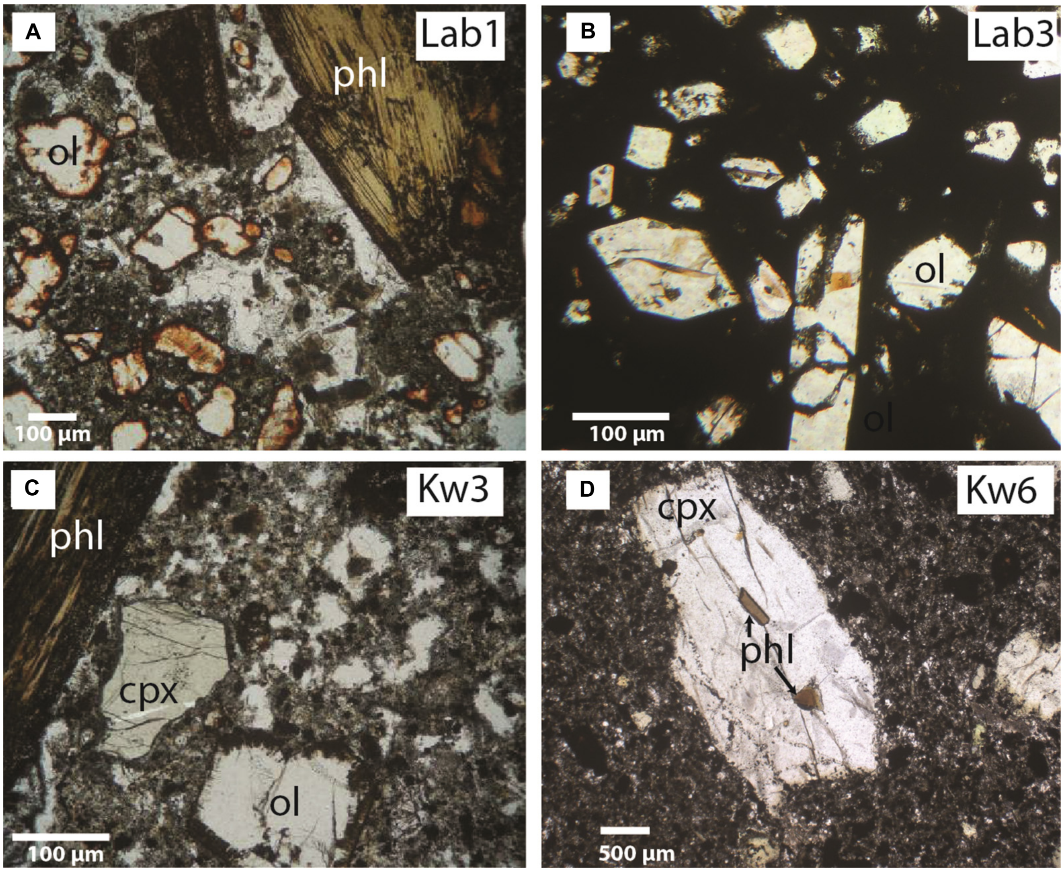

FIGURE 2 | Representative microphotographs of sampled lavas: nephelinites from **(A,B)** Labait (Lab1, Lab3), **(C,D)** Kwaraha (Kw3, Kw6) Abbreviations: ol, olivine; phl, phlogopite; clinopyroxene, cpx.

Labait Volcano

Petrography and Mineral Chemistry

Nephelinites from Labait volcano have microlitic textures with olivine phenocrysts (15–30 vol%, 0.5–4 mm) set in a groundmass of clinopyroxene, magnetite (magnesioferrite, Ti-magnetite) (<1 vol%), and pyrrhotite. Olivine rims are often transformed into iddingsite. Rare phlogopite phenocrysts (0.5–1 vol%, ~1 mm) are present in samples Lab1 (**Figure 2**) and Lab2. Olivines have high forsterite (Fo) and NiO contents in Lab1 (Fo_{91} to Fo_{81}, 0.37–0.18 wt% NiO) and Lab3 (Fo_{89} to Fo_{87}, 0.45–0.24 wt% NiO) lavas (**Supplementary Figures A3, A4** and **Table 2**). Phenocrysts are normally zoned with decreasing MgO and NiO contents (Fo_{91} to Fo_{85}) and increasing CaO contents (0.04–0.61 wt%) from core to rim. One olivine from Lab1 with the lowest Fo content has reverse zoning with increasing Fo content toward the rim (Fo_{83} to Fo_{88}). The water content in olivine (Lab1) ranges from 2.5 to 6.6 ppm wt H_2O (**Figure 5** and **Table 4**).

Small clinopyroxene crystals (<30 mm) are present in the groundmass and have diopsidic compositions ($En_{40}Wo_{49}Fs_{11}$) with relatively low Mg# (78–79) (**Supplementary Figure A5**), high TiO_2 contents (2.5–3 wt%), low Na_2O (0.7–0.9 wt%) and Al_2O_3 contents (1.4–2 wt%), and very low Cr_2O_3 contents (<0.01 wt%).

Phlogopite phenocrysts (Mg# = 83–86) have relatively low F (0.2–0.8 ± 0.2 wt%), TiO_2 (3.6–3.7 wt%) and Al_2O_3 contents (12.2–12.4 wt%) (**Figure 6**). Trace element concentrations are 0.1–2.9 ppm La, 841–9359 ppm Ba, 97–267 ppm Rb, and 32–1395 ppm Sr (**Table 3** and **Figure 7**), and normalized trace element patterns display positive Zr-Hf anomalies.

Nepheline is present in the groundmass as Fe-rich microcrystals (10–20 µm, 2.3–3.4 wt% FeO). Labait lavas contain oxide phases including magnetite (7.3–8.6 wt% TiO_2, 0.8–1.2 wt% MgO), Cr-magnetite (30–50 wt% Cr_2O_3, 3.5–7.5 wt% TiO_2), Mg-magnetite (8.9–9.4 wt% TiO_2, 15–17.4 wt% MgO), and perovskite (55.2 wt% TiO_2) (**Supplementary Table A1** and **Supplementary Figure A6**). Rare apatite crystals are fluorapatites (3–4 wt% F) with low Cl (<0.02 wt%) and SO_3 contents (0.02–0.09 wt%). Sulfides are Ni-rich pyrrhotites (5.7 wt% Ni, 0.06 wt% Cu, 37.6–38.8 wt% S, Pd/Ir = 2–41) with chalcopyrite rims (0.2 wt% Ni, 31.5 wt% Cu, 34.7 wt% S) (**Supplementary Table A1**).

Whole Rock Geochemistry

Nephelinites have very high Mg# ($[Mg/(Mg + Fe_{tot})] \times 100$) values ranging from 76.5 to 79.3 (MgO = 24.8–28.3 wt%), variable peralkaline indices (Na + K/Al = 0.7–1.2) and K_2O/Na_2O ratios

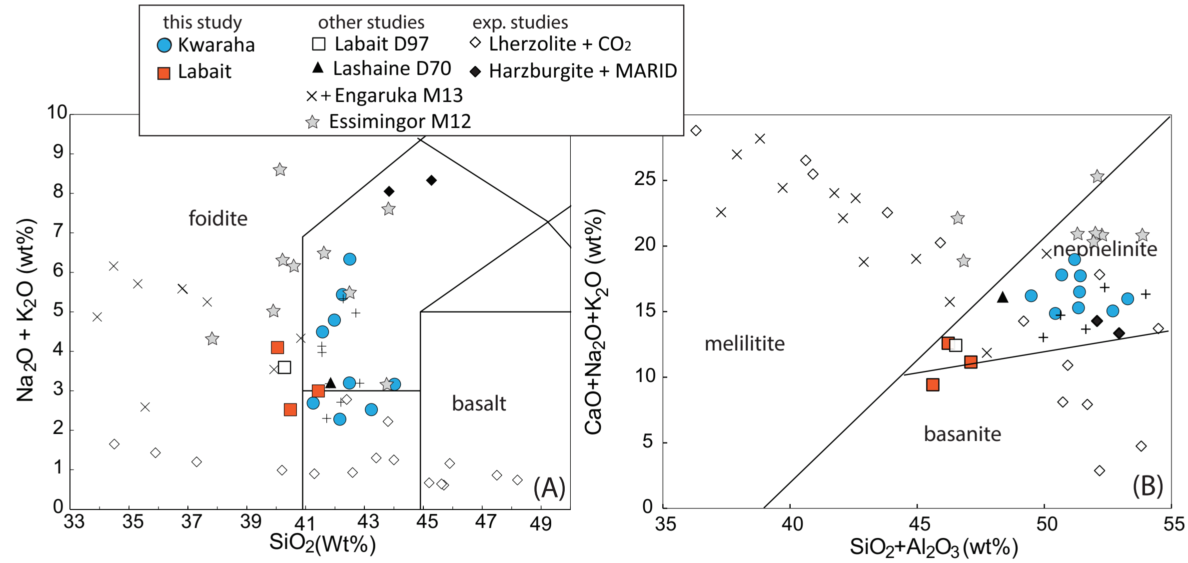

FIGURE 3 | Geochemical classification of sampled lavas from Kwaraha (circles) and Labait (squares). **(A)** Alkali vs. silica composition **(B)** melilitite-nephelinite-basanite classification (Le Bas, 1989). Whole rock data are recalculated anhydrous to 100%. We also reported literature data from Labait and Lashaine (triangle) lavas (Dawson et al., 1970, 1997, respectively), Essimingor lavas (gray stars; Mana et al., 2012), melilitites (plus) and nephelinites (cross) from Engaruka volcanic field (Mattsson et al., 2013). Experimental melt compositions from partial melting of lherzolite + CO_2 (open diamonds; Dasgupta et al., 2007) and Harzburgite + MARID (black squares; Förster et al., 2018) are also reported.

(0.7–1.1), low CaO contents (5–7.4 wt%), and moderate Al_2O_3 contents (5.4–6.1 wt%) (**Figure 4** and **Table 1**). Lavas have variable whole-rock volatile concentrations: 0.7–4.6 wt% CO_2, 2.12–2.54 wt% H_2O, 200–360 ppm S, 1100–1700 ppm F, and 44–71 ppm Cl. No correlations are observed amongst the volatiles. The high CO_2 content of Lab1 and Lab2 samples is related the occurrence of calcite in cracks, whereas no calcite or secondary phases within the groundmass has been observed in Lab3 nephelinitic sample (0.7 wt% CO_2). This sample (Lab3) is considered as fresh sample and whole rock data will be favored for models.

Labait lavas have high incompatible element concentrations up to 300 times chondritic rare earth element (REE) values with a high fractionation of light REEs (LREEs) compared to heavy REEs (HREEs) (La/Sm = 8.2–8.8, La/Yb = 69.1–71.7) (**Figure 8** and **Table 1**). Lavas have high large ion lithophile element (LILE) concentrations (e.g., 551–621 ppm Ba), and relatively low high field strength element (HFSE) contents (e.g., 168–178 ppm Zr) (**Figure 8**). Trace element patterns have negative K and Zr-Hf anomalies (**Figure 5**), high Zr/Hf (42.6–46), Ce/Y (8.4–8.7), Nb/U (52.2–53.9), and Rb/Sr ratios (0.05–0.08), and low Zr/Nb (2–2.3) and Ba/Rb ratios (8.5–13.3). Labait lavas are characterized by high Cr (495–1126 ppm) and Ni contents (827–1000 ppm).

Phlogopite-Bearing Xenoliths

Mantle xenoliths from Labait volcano have been studied previously by Rudnick et al. (1993) and Koornneef et al. (2009). We report here additional geochemical data for phlogopite-bearing mantle xenoliths: phlogopite-bearing lherzolites and glimmerites.

Phlogopite-bearing lherzolites (i.e., Labx6, **Table 2**) have porphyroclastic textures with 71–93 vol% olivine (Fo_{85} to Fo_{93}), 1–10 vol% clinopyroxene, (Mg# = 78–91), 11–24 vol% orthopyroxene (Mg# = 86–91), and 1–2 vol% Cr spinel [Cr# = 82–94; Cr# = Cr/(Cr+Al)] (Koornneef et al., 2009; Hui et al., 2015). Phlogopites occur as phenocrysts (0.1–1 mm), either disseminated throughout the sample or associated with spinel. They have high Mg# (90–92.6) and relatively high Al_2O_3 (14.6–15.8 wt%), TiO_2 (3.5–6.4 wt%), and Cr_2O_3 contents (0.17–1.86 wt%) (**Table 2** and **Figure 6**). Phlogopites have relatively low F (0.3–1.2 wt%) and very low Cl contents (<0.04 wt%). They have low REE (0.02–0.2 ppm La, <0.01 ppm Yb) and high LILE concentrations (1267–4310 ppm Ba, 178–274 ppm Rb, 30–33 ppm Sr) (**Table 3** and **Figure 7**).

Glimmerites (Labx7) contain 99 vol% phlogopite (<1% oxides). Phlogopites have low Mg# (83.7–84) and relatively low Al_2O_3 (12.9–13.2 wt%) and Cr_2O_3 contents (0.51–0.57 wt%) (**Table 2** and **Figure 6**). Phlogopites have low F (0.2–0.8 ± 0.2 wt%) and very low Cl contents (<0.03 wt%). They have low Ba (842–934 ppm), very low REE (<0.02 ppm La), and high Rb concentrations (323–358 ppm Rb) (**Table 3**).

Kwaraha Volcano

Petrography and Mineral Chemistry

Lavas sampled from small volcanic cones around Kwaraha volcano are nephelinites (*n* = 9, **Figure 3**) and one carbonatite (Kw1) was sampled from the main volcanic center. The nephelinites have microlitic textures and contain phenocrysts of

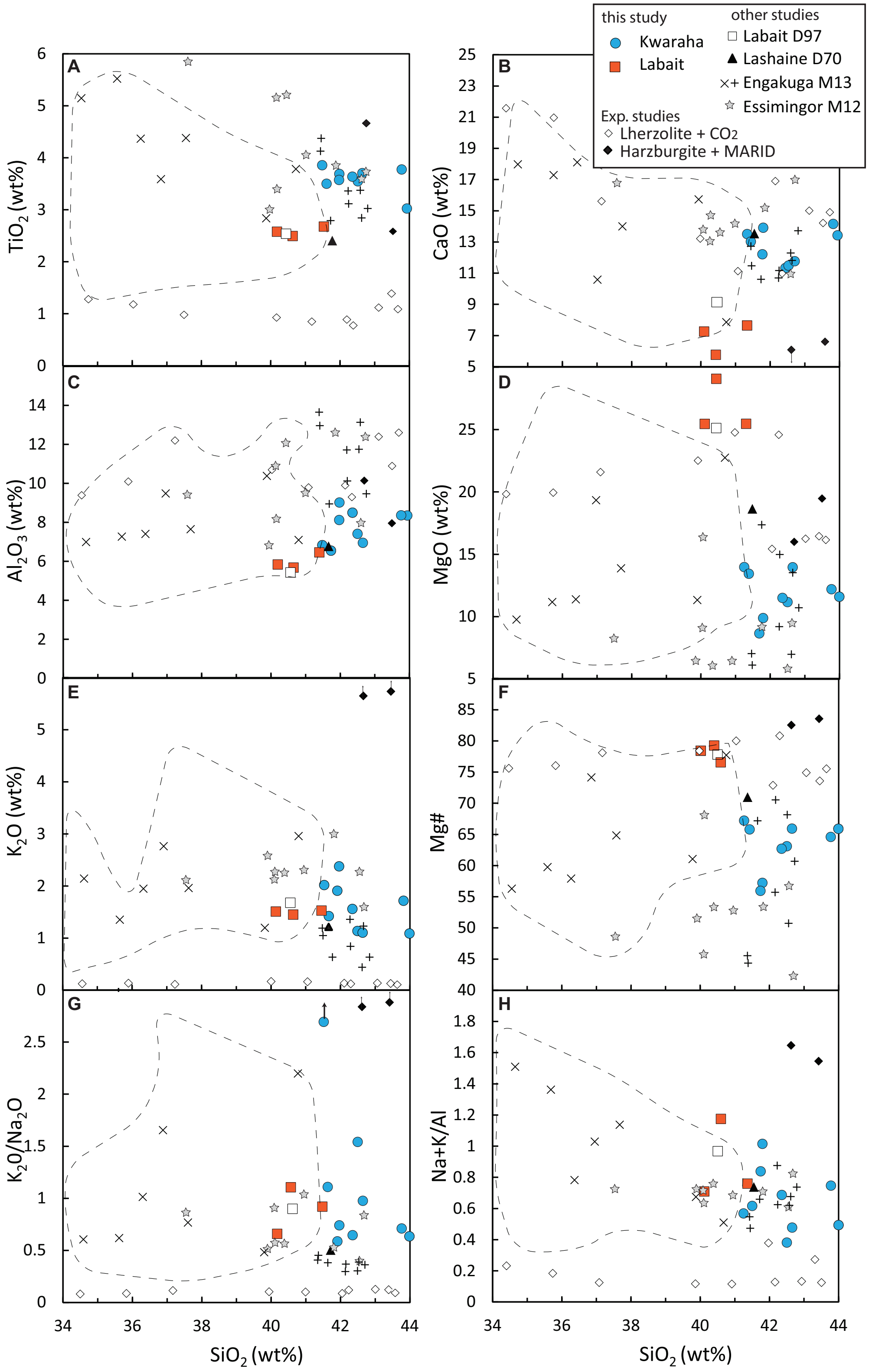

FIGURE 4 | Major element variation diagrams of sampled lavas from Kwaraha and Labait **(A)** TiO_2, **(B)** CaO, **(C)** Al_2O_3, **(D)** MgO, **(E)** K_2O, **(F)** Mg#, **(G)** K_2O/Na_2O, and **(H)** Na + K/Al vs. SiO_2 content. Continental melilitite compositions (dashed line) are from the Georoc database (http://georoc.mpch-mainz.gwdg.de/georoc/). All other symbols are as in **Figure 3**.

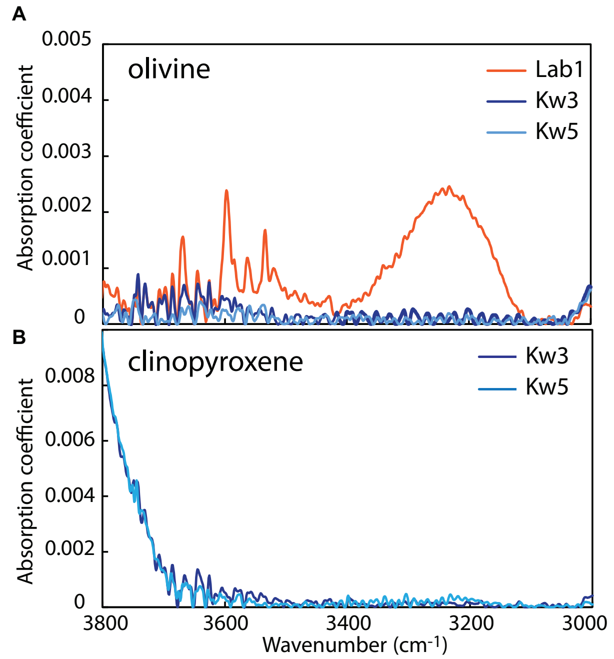

FIGURE 5 | Representative FTIR spectra of unoriented **(A)** olivine (4 ppm H_2O for Lab1 and < 1 ppm H_2O for Kw3, Kw5) and **(B)** clinopyroxene (<1 ppm H_2O for Kw3, Kw5) from Labait and Kwaraha lavas. All spectra are normalized to 1 cm thickness.

olivine (2–13 vol%, 0.2–7 mm), clinopyroxene (4–12 vol%, 0.2–8 mm), phlogopite (0–4 vol%, 0.2–10 mm), and magnetite (1–5 vol%, 0.5 mm) (**Figure 2**). Olivine, clinopyroxene, nepheline, and rare apatite occur as microcrystals in the groundmass.

Olivines from Kwaraha lavas have high Fo (Fo_{86} to Fo_{81}) and NiO contents (0.23–0.04 wt%) (**Supplementary Figure A4**). Olivine phenocrysts are normally zoned with decreasing MgO and NiO contents (Fo_{86} to Fo_{82} and 0.2–0.05 wt%, respectively) and increasing CaO contents from core to rim (0.17–0.83 wt%). Olivine water contents are very low, <2 ppm wt H_2O (**Table 4**).

Clinopyroxene phenocrysts have diopsidic compositions ($En_{35-48}Wo_{47-52}Fs_{2-16}$) with high Mg# (90–77), although rare clinopyroxene have low Mg# (63–74). High-Mg# clinopyroxene phenocrysts have 16.4–13.4 wt% MgO, 3.5–0.3 wt% Al_2O_3 (Al^{VI}/Al^{IV} = 0.89–0.56), and up to 1.1 wt% Cr_2O_3 (**Supplementary Figure A5**). REE patterns are concave, and enriched in LREEs compared to HREEs (2–60 ppm La, 0.02–0.5 ppm Lu, La/Yb = 4–19) (**Supplementary Figure A7**). Trace element analyses show relatively low Zr (12–480 ppm) and Sr contents (100–870 ppm) (**Supplementary Figure A7** and **Table 3**). Low-Mg# clinopyroxene have very low Cr_2O_3 contents (<0.01 wt%), high Na_2O contents (0.94–0.96 wt% Na_2O), and are enriched in REEs compared to high-Mg# clinopyroxene (**Supplementary Figure A7**). Clinopyroxene from Kwaraha (Kw3, Kw5) are dry, with <2 ppm wt H_2O (**Figure 5** and **Table 4**).

Phlogopite is present in almost all Kwaraha samples. Phlogopites occurring as inclusions in clinopyroxene and as interstitial phenocrysts have the same composition (Mg# = 79–83, 3.1–3.6 wt% TiO_2, 13.5–14.1 wt% Al_2O_3) (**Figures 2, 6**). They have very low F contents (0.2–0.7 ± 0.2 wt%) and phlogopite from Kw3 contains 1.57–2.12 wt% H_2O (KFT analyses). Phlogopites have variable REE (2.7–6.8 ppm La), HFSE (1.2–27.5 ppm Zr), and LILE contents (25–176 ppm Sr) (**Figure 7** and **Table 3**).

In the groundmass, nepheline microcrystals have homogeneous compositions (39.5–40.5 wt% SiO_2, 10.75–11 wt% Na_2O, 1.6–1.7 wt% FeO) (**Supplementary Table A1**). Three Fe-Ti oxide phases were identified as Ti-magnetite (18.1–18.6 wt% TiO_2, 4.5–5.6 wt% MgO), magnetite (0.03 wt% TiO_2, 0.1–0.2 wt% MgO), and rare Cr-magnetite (42.55 wt% Cr_2O_3) (**Supplementary Table A1**). Magnetites have low HFSE contents (7–75 ppm Nb, 16–39 ppm Zr). Apatite is F-rich (3–4 wt%) and Cl- (<0.02 wt%) and SO_3-poor (0.01–0.07 wt%).

Whole Rock Geochemistry

Kwaraha silicate lavas have relatively low Mg# values ranging from 67 to 56 (MgO = 15.4–9.6 wt%). These lavas have variable peralkaline indices (Na + K/Al = 0.4–1), alkali contents ($Na_2O + K_2O$ = 2.2–6.2 wt%), and K_2O/Na_2O ratios (0.6–1.5) (**Figure 4**), and very high CaO (10.7–14.4 wt%) and moderate Al_2O_3 contents (7.4–10.1 wt%). They have variable whole-rock volatile concentrations: 0.1–2.7 wt% CO_2, 100–300 ppm S, 1400–2600 ppm F, and 33–1150 ppm Cl.

Kwaraha lavas have high incompatible element concentrations up to 350 times chondritic values. REE patterns show LREE enrichments compared to HREEs (68.2–82.2 ppm La, 0.18–0.24 ppm Lu, La/Sm = 6.9–9.7, La/Yb = 46.1–62.4) (**Figure 5A**). These lavas have high LILE (673–1225 ppm Ba, 643–1009 ppm Sr) and relatively low HFSE contents (168–259 ppm Zr) (**Figure 8B**). Trace element concentrations show negative K and Zr-Hf anomalies (**Figure 5B**), high Zr/Hf (39.2–45), Ce/Y (6.05–7.53), Nb/U (45.8–52), and Rb/Sr ratios (0.04–0.12), and low Zr/Nb (1.9–2.8) and Ba/Rb ratios (10.3–33.9). Kwaraha parasitic cones (Kw2 to Kw12) are characterized by relatively low Cr (110–367 ppm) and Ni contents (60–145 ppm).

DISCUSSION

Nephelinites erupted at Labait and Kwaraha volcanoes are among the less-differentiated and more-mafic magmas of the NTD. The high Mg# and Cr and Ni contents of olivine-bearing lavas (Mg# = 56–79, 110–1126 ppm Cr, 60–1000 ppm Ni, **Table 1**) are characteristic of primary lavas associated with rifting close to the craton (e.g., Rogers et al., 1992; Rosenthal et al., 2009; Foley et al., 2012; Baasner et al., 2016).

In the following sections, we discuss the mantle partial melting environment leading to the genesis of silica-undersaturated alkaline magmas, the role of volatiles (H_2O, CO_2) in magma differentiation and metasomatism, and the interaction between magmas and the Tanzanian lithospheric mantle. We conclude with a comparison of the characteristics of magmatism during the early stages of rift initiation in the western and

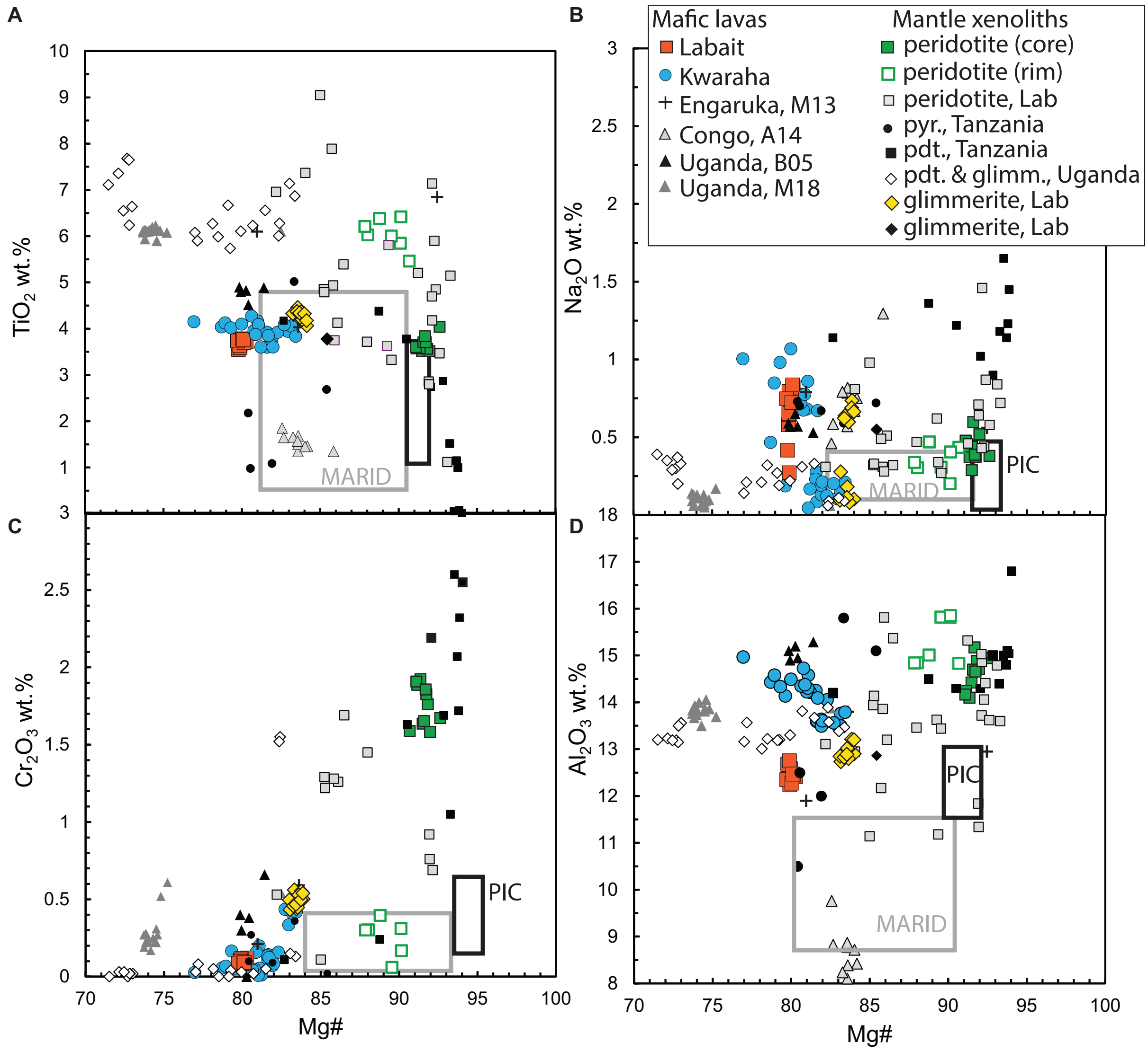

FIGURE 6 | Phlogopite compositions **(A)** TiO_2 **(B)** Na_2O, **(C)** Cr_2O_3 and **(D)** Al_2O_3 vs. Mg# from Kwaraha (blue circles) and Labait lavas (orange close squares), and glimmerite (Labx7, orange diamonds) and lherzolite xenoliths (Labx6, open orange squares). Literature data are also reported for lavas from: Engaruka (Tanzania; Mattsson et al., 2013); Nyiragongo volcano (Congo; Andersen et al., 2014); Fort Portal (Uganda; Bailey et al., 2005); Bunyaruguru volcanic field (Uganda; Muravyeva and Senin, 2018) and xenoliths from Labait (Tanzania; Lee and Rudnick, 1999; Koornneef et al., 2009) and north Tanzania (Dawson and Smith, 1988, 1992) and from Bunyaruguru volcanic field (Uganda; Muravyeva and Senin, 2018). Gray and black rectangles for phlogopite composition in MARID and PIC, respectively, from Dawson and Smith (1977); Jones et al. (1982), Kramers et al. (1983); Waters (1987), and Grégoire et al. (2002). Lab: Labait; pyr: pyroxenite; pdt: peridotite.

eastern branches of the EAR (e.g., Uganda-Rwanda and north Tanzania, respectively).

Phlogopite-Bearing Primary Alkaline Magma

Primary magmas as product of partial melting of mantle peridotite are very rare at the Earth surface as the composition of magmas can be modified in their source deeper in the mantle by crystallization and/or during ascent by interaction with or assimilation of lithospheric mantle (Huppert and Sparks, 1985; Streck et al., 2007). The compositional range observed in Labait and Kwaraha nephelinites may suggest olivine accumulation (<10%ol; Mg# = 76–79) (**Table 1** and **Figure 4**) and fractional crystallization during ascent (Kwaraha lavas with Mg# < 65), respectively (e.g., Frey et al., 1978). However, the lavas erupted at Labait and Kwaraha volcanoes are the more primitive magmas of the southern part of the NTD (i.e., Mg# > 65) and their major and trace element composition is consistent with experimental primary alkaline melt from partial melting of mantle peridotite (**Table 1** and **Figures 3**, **4**, 8; e.g., Mattsson et al., 2013; Green and Falloon, 2015).

In nephelinites, olivine and clinopyroxene are the liquidus phases and coexist with phlogopite phenocrysts. The presence

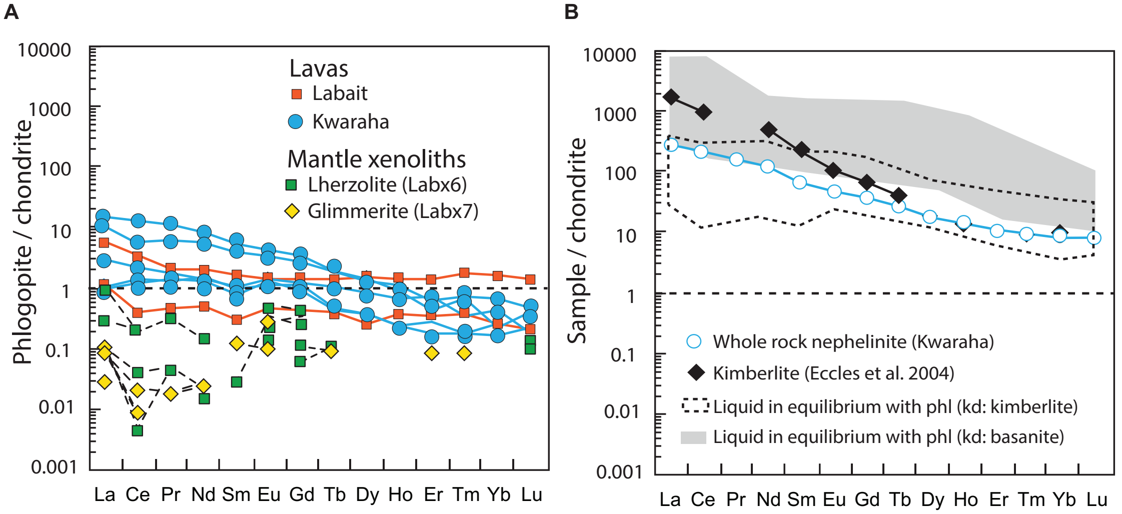

FIGURE 7 | (A) Chondrite-normalized REE patterns of phlogopite from Kwaraha and Labait lavas and lherzolite (Labx6) and glimmerite xenoliths (Labx7). **(B)** Representative chondrite-normalized whole-rock REE pattern of Kwaraha lavas, and the silicate liquids in equilibrium with phlogopite (phl) calculated using partition coefficients for kimberlite (Fujimaki et al., 1984) and basanite (Adam and Green, 2006). The chondrite-normalized REE pattern of kimberlite (Eccles et al., 2004) is shown for comparison with the calculated liquids. Chondrite and primitive mantle values from Sun and McDonough (1989).

of phlogopite in nephelinite lavas carrying phlogopite-bearing mantle xenoliths has led to the consideration that phlogopites are xenocrysts assimilated from the lithospheric mantle (e.g., Johnson et al., 1997; Lloyd et al., 2002). However, our analyses of phlogopite crystals in lavas and mantle xenoliths show that they have different major and trace element compositions, suggesting different crystallization environments. Phlogopite from Labait lavas have lower Mg# and Cr_2O_3 and Al_2O_3 contents, and higher trace element concentrations than phlogopite from glimmerite (igneous rocks mainly composed of mica) and phlogopite-bearing peridotite mantle xenoliths from the NTD (Mg# = 79–83 and 90–93, respectively, **Table 2** and **Figure 6**), suggesting that they crystallized early from primary trace-element-rich magmas. In Kwaraha nephelinites, phlogopites occur as inclusions in clinopyroxene and as phenocrysts in the groundmass (**Figure 2**) and all phlogopites have the same range of composition with high Mg# (up to Mg# = 83) suggesting an early crystallization (**Figure 2D**). The variable phlogopite compositions in Kwaraha lavas (Mg# = 83–76, **Figure 6**) correspond to their crystallization from slightly more evolved magmas with higher Al_2O_3 and trace element concentrations than phlogopite from Labait.

Using available experimentally determined partition coefficients ($D^{mineral/melt} = X^{mineral}/X^{melt}$, where X is the concentration of a given element in each phase) between phlogopite and alkaline and potassic magmas (i.e., basanite, kimberlite, lamproite; Fujimaki et al., 1984; Schmidt et al., 1999; Adam and Green, 2006, respectively), the calculated silicate liquid compositions in equilibrium with phlogopite from Kwaraha and Labait have high REE (**Figure 7B**) and trace element concentrations similar to the whole-rock nephelinite compositions. This suggests that early phlogopite crystallization occurred at the liquidus with clinopyroxene and olivine, possibly from primitive K-rich silicate liquid. These observations agree with partial melting and phase equilibria experiments in which phlogopite crystallized with clinopyroxene at high pressure (1–5 GPa) in potassic magma (Parat et al., 2010; Förster et al., 2018).

We note that the early crystallization of phlogopite in alkaline magmas may have slightly lowered the potassium content of these magmas during crystallization (5 vol% phlogopite corresponds to ~0.5 wt% K_2O). Therefore, their primary magma may have had a composition close to that of potassic melt produced by incongruent melting of a mica + amphibole + rutile + ilmenite + diopside assemblage and harzburgite at 5 GPa, which provides all the constituents for rapid growth of phlogopite and clinopyroxene (Förster et al., 2018). The high CaO contents of nephelinite NTD magmas may be related to the presence of clinopyroxene and lherzolite, rather than harzburgite, in their mantle source.

Crystallization Environment and Volatile Concentrations

Temperature, pressure, and volatile contents are key parameters controlling phase equilibria, mineral, melt, and gas compositions, and further magmatic evolution including fractional crystallization, immiscibility, and degassing processes (e.g., Carmichael and Ghiorso, 1990; Toplis and Carroll, 1995; Berndt et al., 2005). The composition of clinopyroxene in mafic magmas is strongly dependent on melt composition, pressure, and temperature during crystallization, and can be used as a geothermobarometer (e.g., Putirka, 2008; Masotta et al., 2013). Clinopyroxene and their associated bulk nephelinites have Kd (Fe^{2+}/Mg) values ranging from 0.2 to 0.41 for Kwaraha, suggesting that clinopyroxene are near equilibrium with the silicate liquid and thus suitable for calculation of the pressure

TABLE 1 | Major, volatile and trace element concentrations of the nephelinitic lavas.

Sample	Lab1	Lab2	Lab3	Kw2	Kw3	Kw4	Kw5	Kw6	Kw8	Kw10	Kw11	Kw12
SiO_2 (wt.%)	40.42	40.12	41.71	43.95	41.47	44.43	42.31	42.58	41.93	41.90	41.60	42.79
TiO_2	2.76	2.79	2.47	3.27	3.68	3.01	3.81	3.50	3.22	3.48	3.39	3.30
Al_2O_3	5.37	5.18	6.09	8.48	7.55	9.10	8.97	10.08	8.83	9.28	7.49	7.42
Fe_2O_3	14.66	15.06	13.58	14.81	15.90	12.94	16.17	15.07	14.12	14.79	15.42	14.71
MnO	0.22	0.21	0.19	0.23	0.22	0.20	0.25	0.25	0.22	0.23	0.22	0.21
MgO	28.28	24.81	24.91	12.78	15.44	12.63	10.92	9.66	13.00	12.56	15.05	15.22
CaO	5.00	7.11	7.36	13.68	12.30	14.40	10.77	12.61	13.55	12.75	13.81	12.68
Na_2O	1.22	2.50	1.63	0.85	0.56	1.87	3.56	3.64	2.65	2.64	1.22	1.46
K_2O	1.34	1.65	1.49	1.30	2.23	1.19	2.63	2.13	1.83	1.70	1.19	1.61
P_2O_5	0.74	0.58	0.48	0.65	0.64	0.24	0.61	0.49	0.64	0.66	0.60	0.58
F (ppm)	1500	1700	1100	–	1900	1600	1400	2100	–	2000	2200	2600
Cl (ppm)	44	71	49	–	33	660	1150	550	–	99	89	72
S (ppm)	260	200	200	270	222	148	140	220	300	100	100	100
Total	100	100	100	100	100	100	100	100	100	100	100	100
Mg#	79.26	76.54	78.42	63.1	65.81	65.9	57.22	55.95	64.59	62.7	65.91	67.21
Cr (ppm)	756	495	1126	294	366	246	141	110	334	247	368	335
Ni	827	1000	890	125	143	102	60	64.6	90.4	74.9	145	121
Cu	117	118	115	171	168	150	262	219	173	182	198	193
Cs	0.21	0.15	2.62	0.26	0.28	0.27	0.44	0.36	0.34	0.27	0.24	0.11
Rb	44.9	51	64.7	48.4	74.3	36.1	58.5	45.4	61.3	41.9	48	67.2
Ba	595	621	551	775	801	1225	673	1166	812	854	750	689
Th	7.34	8.37	7.99	7.83	8.06	8.51	9.7	9.79	10.7	9.73	9.89	8.99
U	1.48	1.73	1.45	1.7	1.72	1.68	2.01	2.05	2.02	2.22	4.59	1.89
Nb	78.9	90.4	78.3	86	82.4	81	104	107	101	102	87.3	95.7
Ta	5.4	5.13	4.8	5.96	5.7	5.49	7.45	7.73	6.94	5.41	5.42	6.02
La	64.9	68.3	62.7	68.2	68.2	69.2	76.6	76.8	82.2	75.7	80.8	77.9
Ce	123	120	111	128.6	130.2	130.5	144.8	142.8	152	130.2	132.5	128
Pb	2.99	3.85	7.04	3.06	4.16	4.5	8.09	6.22	8.31	9.8	5.35	0.64
Pr	13.7	13.4	12.5	14.4	14.9	14.8	16.3	15.8	16.7	14.6	14.1	13.8
Sr	840	754	853	1009	643	1108	811	931	989	934	937	867
Nd	49.7	49.6	46.3	53.7	55.9	54.9	59.9	58.9	60.9	54.1	51.6	50.6
Zr	178	183	168	180	207	226	255	259	220	255	168	190
Hf	4.16	3.97	3.94	4.47	4.97	5.28	6.52	6.43	5.34	5.68	4.14	4.63
Sm	7.91	7.73	7.34	9.13	9.76	9.57	10.65	10.27	10.47	8.96	8.35	8.33
Eu	2.14	2.27	2.1	2.53	2.64	2.71	2.84	2.91	2.86	2.75	2.51	2.45
Gd	6.07	7.81	7.37	7.15	7.48	7.45	8.37	8.08	7.96	9.49	8.83	8.81
Tb	0.787	0.799	0.77	0.941	0.99	1.012	1.12	1.103	1.077	1.041	0.936	0.953
Dy	3.34	3.54	3.47	4.34	4.51	4.62	5.25	5.19	5.22	4.91	4.41	4.52
Y	14.2	14.3	13.1	19.8	19.8	20.3	23.3	23.6	23.4	21.2	17.6	19.3
Ho	0.55	0.58	0.57	0.78	0.79	0.81	0.91	0.93	0.93	0.84	0.75	0.78
Er	1.26	1.31	1.25	1.81	1.71	1.9	2.06	2.08	2.01	1.94	1.71	1.8
Tm	0.16	0.16	0.15	0.25	0.22	0.26	0.28	0.3	0.29	0.25	0.22	0.23
Yb	0.91	0.96	0.91	1.47	1.35	1.5	1.66	1.62	1.68	1.5	1.29	1.42
Lu	0.14	0.13	0.12	0.2	0.19	0.22	0.24	0.24	0.24	0.21	0.18	0.2

*Mg# = Mg/(Mg+Fe)*100; bdl, below detection limit.*

and temperature conditions during their crystallization. This is corroborated by clinopyroxene trace element concentrations, which indicate equilibrium with the whole rock based on experimental partition coefficients for alkaline magmas (Adam and Green, 2006; **Supplementary Figure A8**). Assuming clinopyroxene-melt equilibrium and using the thermobarometer of Masotta et al. (2013; σ = 50°C, 150 MPa), we estimate the temperature and pressure during crystallization to have been 1170–1290°C and 200–1080 MPa for Kwaraha lavas (**Supplementary Figure A9**). Simonetti et al. (1996) proposed a correlation between the Al^{VI}/Al^{IV} ratio of clinopyroxene and their crystallization pressure, and the high clinopyroxene Al^{VI}/Al^{IV} ratios (0.89–0.56) from Kwaraha are consistent with crystallization at 1000 MPa.

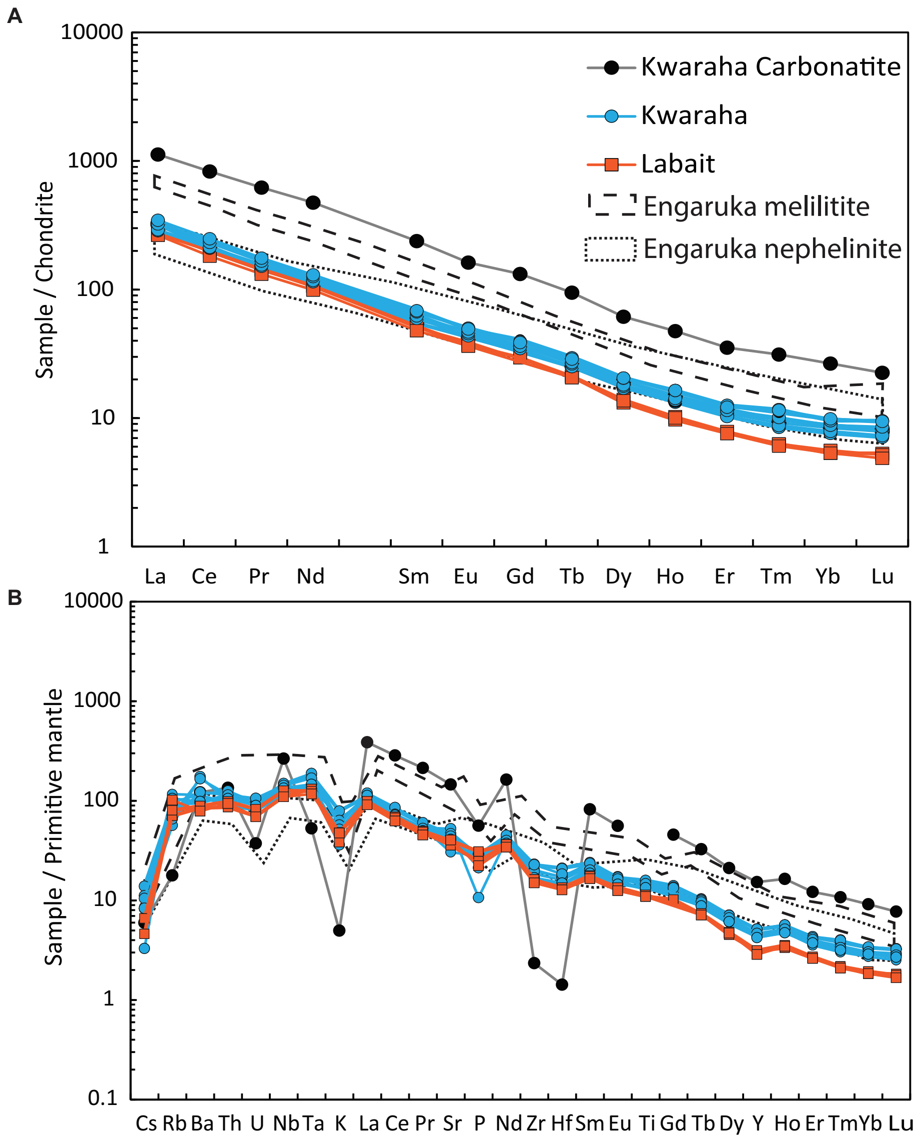

FIGURE 8 | (A) Chondrite-normalized REE contents and **(B)** primitive mantle-normalized trace element compositions of Kwaraha and Labait nephelinites (symbols as in **Figures 3**, **4**) and the Kwaraha carbonatite (black circles). Primitive mantle and chondrite values from Sun and McDonough (1989). Engaruka melilitites and Engaruka nephelinites from Mattsson et al. (2013) are also reported.

Volatiles such as CO_2 and H_2O affect the conditions of partial melting (e.g., Dasgupta et al., 2007; Baasner et al., 2016), play a fundamental role during magmatic evolution and ascent, and control eruptive style (e.g., Oppenheimer et al., 2003; Berndt et al., 2005). The presence of phlogopite in Kwaraha and Labait lavas suggests that the silicate melts were H2O-bearing at the time of phlogopite crystallization (1.57–2.12 wt% H2O in phlogopite, KFT method). However, the abundant water in crystal lattice of phlogopite (OH site) prevents us from quantifying precisely the amount of water present in the melt (i.e., non-Henrian behavior). In experimental study, hydroxyl-rich phlogopite with 4.3 wt.% H_2O crystallized from hydrous melt with 3.1 wt.% H_2O at 1250°C and 3 GPa (Condamine et al., 2016; calculated $D_{H2O} = 1.4$), suggesting that 1.12–1.4 wt.% H_2O may have been present in the melt at the time of phlogopite crystallization.

Only nominally anhydrous minerals (NAMs) such as olivine and clinopyroxene incorporate trace concentrations of hydrogen that can be used to determine the H_2O content of the silicate melt during their crystallization ($D^{clinopyroxene/melt} = 0.01–0.013$, $D^{olivine/melt} = 0.0013$; Aubaud et al., 2004; Hauri et al., 2006). The measured water contents are very low: < 1 ppm wt H_2O in clinopyroxene and olivine from Kwaraha lavas (**Figure 5**) and 3–6 ppm wt H_2O in olivine from Labait. Using the partition

TABLE 2 | Representative major element compositions of minerals.

Sample	Lab3	Lab1	Labx6	Labx7	Kw3	Kw3	Kw3	Kw5	Kw11	Kw11
Mineral	**ol**	**phl**	**phl**	**phl**	**phl**	**ol**	**cpx**	**cpx**	**cpx**	**cpx**
SiO_2	41.17	39.97	38.50	38.57	38.30	40.96	52.12	52.97	53.50	50.15
TiO_2	0.07	3.26	3.52	4.23	3.61	0.06	0.85	0.58	0.55	1.50
Al_2O_3	0.03	12.43	14.71	13.21	14.03	0.03	2.03	1.33	1.37	2.39
FeO	11.12	8.89	3.48	7.33	7.69	11.35	5.49	4.34	3.96	9.09
MnO	0.19	0.04	0.03	0.03	0.04	0.19	0.11	0.07	0.06	0.20
MgO	46.42	19.77	22.33	21.38	20.02	46.69	15.04	16.22	15.85	11.68
CaO	0.53	0.01	0.01	0.02	0.05	0.29	23.53	23.31	22.32	23.03
Na_2O	0.00	0.76	0.52	0.69	0.08	0.00	0.84	0.66	0.88	0.94
K_2O	0.00	9.89	10.44	10.05	10.68	0.01	0.00	0.01	0.00	0.01
Cr_2O_3	0.05	–	1.58	0.51	–	0.07	0.03	0.49	1.11	0.00
NiO	0.18	–	–	–	–	0.25	0.01	0.01	0.05	0.00
F	–	0.78	0.39	0.23	0.42	–	–	–	–	–
Total	99.78	95.84	95.51	96.25	94.92	99.90	100.05	99.97	99.64	99.01
Mg#	88.1	79.8	92.0	83.9	82.2	87.8	82.9	86.9	87.7	69.6
Numbers of ions on the basis of										
	4O	**24O**				**4O**	**6O**			
Si	1.02	5.68	5.48	5.54	5.50	1.01	1.91	1.94	1.96	1.90
Al^{IV}	–	2.08	2.47	2.24	2.38	–	0.09	0.06	0.04	0.10
Al^{VI}	–	0.00	0.00	0.00	0.00	–	0.00	0.00	0.02	0.00
Al tot	0.00	–	–	–	–	0.00	–	–	–	–
Ti	0.00	0.35	0.50	0.61	0.39	0.00	0.02	0.02	0.02	0.04
Fe^{2+}	–	–	–	–	–	–	0.07	0.06	0.11	0.20
Fe^{3+}	–	–	–	–	–	–	0.10	0.07	0.01	0.08
Fe tot	0.18	1.06	0.41	0.88	0.92	0.23	–	–	–	–
Mn	0.00	0.00	0.00	0.00	0.00	0.00	0.00	0.00	0.00	0.01
Mg	1.78	4.19	4.74	4.58	4.29	1.72	0.82	0.88	0.87	0.66
Ca	0.00		0.00			0.01	0.92	0.91	0.88	0.93
Na	–	0.21	0.14	0.19	0.02	–	0.06	0.05	0.06	0.07
K	–	1.79	1.86	1.84	1.96	–	–	–	–	–
Ni	0.01	–	–	–	–	0.00	–	–	–	–
Cr	–	–	0.18	0.06	–	–	0.00	0.01	0.03	0.00
OH	–	3.65	3.82	3.90	3.81	–	–	–	–	–
F	–	0.35	0.18	0.10	0.19	–	–	–	–	–
Total	3	19.36	19.78	19.94	19.43	3	4	4	4	4

ol olivine, cpx clinopyroxene, phl phlogopite.

coefficients of Hauri et al. (2006), the water content in the nephelinite melt was 0.2–0.5 and <0.01 wt% H_2O during olivine and clinopyroxene crystallization, respectively (**Table 4**). However, calculated H_2O melt content for Labait is up to 0.5 wt% H_2O, consistent with the estimation from xenoliths suggesting that they were carried by H_2O-poor mafic magmas (Hui et al., 2015). It should be noted that these partition coefficients were determined for ol-clinopyroxene-melt equilibria in basaltic melt, and that no experimental data exists for potassic melts bearing hydrous minerals. The presence of phlogopite may have strongly influenced the distribution of water between anhydrous minerals and the melt, with H_2O being preferentially incorporated into phlogopite, and our estimated water contents in the melt should be considered minimum values. Petrographic observations strongly suggest an early crystallization of phlogopite, before clinopyroxene, whereas both phlogopite and NAMs data allow us to discuss the H_2O content in primary magmas. In the primary alkaline melt, water content was high enough to allow phlogopite crystallization and stabilize this hydrous mineral through all the magmatic stage. Due to uncertainties on distribution of water in NAMS in presence of hydrous minerals, we can assume that calculated H_2O content from NAM's mineral is a minimal value. Based on experimental data, H_2O content of the melt during phlogopite crystallization could have reached 1.4 wt% H_2O at $P > 3$ GPa (Condamine et al., 2016). Although primary melts from Labait and Kwaraha are hydrated, the water content was probably not high enough to favor phlogopite crystallization over olivine (Foley, 1993).

CO_2 contents in silicate melts are generally investigated through melt inclusion studies (e.g., Métrich and Wallace, 2008; Hudgins et al., 2015; Baudouin et al., 2018). The lack of melt inclusions in minerals from Labait and Kwaraha lavas prevents

TABLE 3 | Trace element compositions of minerals.

Sample	**Lab1**	**Lab1**	**Labx6**	**Labx7**	**Kw3**	**Kw3**	**Kw3**	**Kw5**	**Kw5**	**Kw11**	**Kw11**
mineral	**ol**	**phl**	**phl**	**phl**	**Phl**	**ol**	**cpx**	**cpx**	**cpx**	**cpx**	**cpx**
Cs	0.01	3.32	3.27	1.89	1.94	0.01	0.18	0.01	0.01	< 0.01	<0.01
Rb	0.06	558	204	347	314	0.09	0.5	0.03	0.03	< 0.01	<0.01
Ba	0.14	2383	3095	911	2014	0.11	3.45	0.11	0.1	0.06	0.05
Th	0.00	0.01	0.00	–	–	0.00	0.21	0.01	0.04	0.02	0.02
U	0.02	1.5	–	–	0.09	–	< 0.01	–	–	–	< 0.01
Nb	0.36	15.8	22.05	9.93	6.67	0.05	2.62	0.92	0.4	0.19	0.28
Ta	0.02	1.42	2.74	0.81	0.47	0.00	0.34	0.13	0.14	0.04	0.02
La	0.01	48.6	0.07	0.02	0.62	0.01	49.8	4.57	4.75	3.29	8.12
Ce	0.09	29.3	0.126	0.014	0.11	0.01	148	16.0	15.5	11.0	17.5
Pr	0.00	5.61	–	–	0.04	0.00	24.3	2.69	2.6	1.87	2.33
Sr	0.08	418	33.2	25.9	142	0.02	790	216	155	124	303
Nd	0.03	26.5	0.01	0.01	0.22	0.04	127	12.7	12.6	9.33	10.1
Zr	0.55	49.2	18.08	5.42	8.72	0.73	419	320	110	49.2	110
Hf	0.01	0.9	0.45	0.196	0.12	0.01	23.9	9.62	5.65	2.41	4.13
Sm	0.01	6	–	–	0.05	0.02	31.2	2.72	3.07	2.49	1.94
Eu	0.01	2.66	0.01	0.02	0.04	0.01	10.7	0.86	0.91	0.72	0.60
Gd	0.07	10.8	0.01	0.02	0.23	0.08	23.2	2.34	2.65	2.02	1.63
Tb	0.01	2.21	–	–	0.04	0.00	3.66	0.29	0.33	0.26	0.23
Dy	0.01	13.9	–	–	0.31	0.05	16.1	1.71	1.91	1.32	1.10
Y	0.13	141	0.20	0.06	3.76	0.45	58.4	6.26	6.08	4.62	4.09
Ho	0.01	3.75	–	–	0.09	0.02	2.66	0.29	0.28	0.20	0.17
Er	0.01	12.7	–	–	0.30	0.05	6.04	0.73	0.63	0.42	0.43
Tm	0.00	2.11	–	–	0.05	0.02	0.76	0.12	0.08	0.05	0.06
Yb	0.04	10.9	–	–	0.31	0.13	2.56	1.27	0.47	0.32	0.43
Lu	0.01	1.63	–	–	0.04	0.04	0.49	0.28	0.07	0.05	0.09

Ol, olivine; cpx, clinopyroxene; phl, phlogopite.

TABLE 4 | Water contents in olivine and cpx, and those calculated for their associated parental melts.

Sample	**Mineral**	**ppm wt H_2O**	**$H/10^6$ Si**	**Area[a]**	**Melt[b] (wt% H_2O)**
Lab1	Olivine	5.3	86.472	44.8	0.41
Lab1	Olivine	2.5	41.14	18.4	0.19
Lab1	Olivine	5.5	89.17	47.2	0.42
Lab1	Olivine	4.3	70.655	32.4	0.33
Lab1	Olivine	4.9	80.375	39.6	0.38
Lab1	Olivine	6.6	108.09	67.2	0.51
Lab1	Olivine	5.9	96.529	54.4	0.45
Kw3	Olivine	1.2	19.262	6.7	0.09
Kw3	Olivine	1.7	27.859	9.3	0.13
Kw5	Olivine	0.7	11.619	4.6	0.05
Kw5	Olivine	0.6	10.429	4.3	0.05
Kw3	Clinopyroxene	0.5	7.93	3.7	0.004
Kw3	Clinopyroxene	1.7	26.988	10.3	0.013
Kw3	Clinopyroxene	1.5	25.028	9.6	0.012
Kw5	Clinopyroxene	0.4	7.02	3.3	0.004
Kw5	Clinopyroxene	0.4	6.35	3.1	0.004
Kw5	Clinopyroxene	0.3	5.703	2.8	0.003

[a] *Integrated unpolarized absorbance normalized to 1 cm thickness.* [b] *Melt water content calculated using $D^{olivine/melt}$ and $D^{clinopyroxene/melt}$ from Aubaud et al. (2004) and Hauri et al. (2006).*

us from precisely constraining the CO_2 content of the nephelinite magmas. However, northern Tanzania contains some of the most concentrated carbonatite magmatism on Earth (e.g., Dawson, 2012) and the occurrence of calciocarbonatite lava (Kw1) at Kwaraha volcano strongly suggests the presence of abundant CO_2 in the primary alkaline magmas. CO_2 solubility in alkaline magmas (e.g., melilitite, phonolite) was experimentally calibrated at 1.5–2 GPa, and strongly depends on the ratio of non-bridging oxygens to tetrahedrally coordinated anions (NBO/T) in the melt (Brooker et al., 2001; Moussallam et al., 2015). Based on the observed compositions of nephelinite lavas (NBO/T = 1.4–1.67 for Labait and 0.93–1.26 for Kwaraha), their CO_2 solubilities (i.e., the maximum amount of CO_2 that can be dissolved in the magma) range from 7.5 to 15.8 wt% CO_2 (**Supplementary Figure A10**). The primary magma from Labait evolved to a Mg-poor nephelinitic liquid containing up to 6 wt% CO_2 at 800 MPa (Hanang volcano; Baudouin et al., 2018); CO_2 contents of Labait nephelinites may indicate that fractional crystallization and immiscibility buffered the CO_2 content during differentiation ($<$6 wt% CO_2).

Partial Melting of Metasomatized Deep Mantle

Alkaline mafic lavas such as melilitites and nephelinites represent more primitive magmas erupted in intracontinental settings, and are characterized by silica-undersaturation and very high Mg contents (Dasgupta et al., 2007; Foley et al., 2012). Their high incompatible element concentrations and strong REE fractionations (Ivanikov et al., 1998; Platz et al., 2004; Keller et al., 2006) have been proposed to result from very low degrees of partial melting of CO_2-bearing lherzolite (Green and Falloon, 1998; Foley et al., 2009, 2012; Foley and Fischer, 2017) or the partial melting of peridotite with contributions from recycled oceanic crust (e.g., Hofmann, 1988) or pyroxenite (Eggler and Holloway, 1977; Dasgupta et al., 2007; Baasner et al., 2016).

Around the Tanzanian craton, nephelinite volcanoes are concentrated at the propagating tips of the rift and mafic and carbonate-rich alkaline melts are associated with thick lithosphere (Foley and Fischer, 2017). The presence of deep garnet-bearing mantle xenoliths in Labait scories indicate that partial melting occurred at least at 150 km (Lee and Rudnick, 1999).

Geochemical modeling results of the partial melting of mantle peridotite to produce Labait and Kwaraha nephelinite magmas corroborate the presence of refractory HREE-rich minerals such as garnet in the mantle source (**Figure 9**). Trace elements such as Y and Rb are compatible in garnet and phlogopite, respectively, which can account for the high Ce/Y ($>$5) and Rb/Sr ratios in the nephelinite melt (Rogers et al., 1992; Platz et al., 2004; Mana et al., 2015). Partial melting of a garnet peridotite with 62% olivine, 16% opx, 12% clinopyroxene and 10% garnet (theoretical mineral assemblage in mantle from Sun and McDonough, 1989) produces melts with high Ce/Y ($\sim$3), low Rb/Sr ($<$0.04), and low Zr/Hf ratios that cannot represent the composition of nephelinite (i.e., Ce/Y $>$ 5, Rb/Sr $>$ 0.04, Zr/Hf = 39.2–46). The high Rb/Sr ratios ($>$0.04) in the nephelinites strongly suggest a contribution of phlogopite (Rogers et al., 1992; Platz et al., 2004), whereas their high Zr/Hf ratios indicate the contribution of a carbonated source (Rudnick et al., 1993). We modeled the partial melting of carbonatite-free and carbonated (0.3 and 1% carbonatitic component) garnet-rich and phlogopite-bearing peridotite mantle (62% olivine, 16% opx, 10% clinopyroxene, 10% garnet, 2% phlogopite, proportion modified from Sun and McDonough, 1989), as well as a natural garnet-bearing xenolith from Lashaine volcano in the north part of the NTD (Gibson et al., 2013).

The best fit to the observed data suggests that nephelinites result from a very low degree of partial melting ($<$1%) with non-modal fractional melting (**Figure 9** and **Supplementary Figure A11**). The low volumes of melts ($<$1%) is generally assume to be motionless in the mantle rocks due to their small permeability and wetting angle characteristics (Maumus et al., 2004). However, recent study based on physical properties and melt-rock reaction suggest that small volume of melts (i.e., 0.75%) could be extracted from the mantle (Soltanmohammadi et al., 2018). The extraction of low volume melt will be effective for a melt with high content in alkaline and volatile elements (Keller and Katz, 2016; Soltanmohammadi et al., 2018), the volatile content being a key parameter to enhance the melt extraction process due to their effect on the melt viscosity properties (Condamine and Médard, 2014; Gardès et al., 2020). In Labait and Kwahara lavas, early phlogopite crystallization suggests that the primary magmas have higher K content than the erupted lavas (nephelinites), and high volatile contents, especially in CO_2, allowing low melt volume 0.5–1 vol% to be extracted from the mantle (Keller and Katz, 2016; Gardès et al., 2020).

Small amounts of carbonate in the source reproduce the high Zr/Hf fractionation observed in Labait lavas (Zr/Hf = 42.6–46) (**Figure 8**). The trace element variability of lavas from Labait and Kwaraha may suggest that the lavas originate from different degrees of partial melting (0.2–1%) and/or variable carbonate components in their mantle sources (0.3%, **Figure 9B**). The mantle source may be homogeneous (i.e., phlogopite-bearing lherzolite) or mixed heterogeneous source (i.e., 90% phlogopite-free lherzolite + 10% phlogopite-pyroxenite), as suggested by isotopic signatures (Paslick et al., 1996; Aulbach et al., 2011), both leading to similar trace element characteristics in primary melts. It should be noted that pyroxene and phlogopite (i.e., mica pyroxenite) as main component of the mantle source would lead to the genesis of highly alkaline melt with trace element content higher than those reported in Labait and Kwaraha lavas.

Using the empirical equation of Albarède (1992), calibrated for partial melting producing basaltic melts, the SiO_2 and MgO contents of the primary melts suggest that the melting pressure was 110–130 km (3.7–4.3 GPa) for Kwaraha, and 150 km (5 GPa) for Labait, below or close to the lithosphere-asthenosphere boundary (LAB at 146 km close to the Tanzanian craton beneath Labait and 135 km beneath Kwaraha, Craig et al., 2011; **Figure 10**). The depth and temperature of partial melting are consistent with (i) the presence of garnet in the mantle source ($>$90 km; McKenzie and O'Nions, 1991; Sato et al., 1997), (ii) the presence of mantle xenoliths equilibrated at 100–147 km depth (3.2–4.9 GPa; Lee and Rudnick, 1999), and

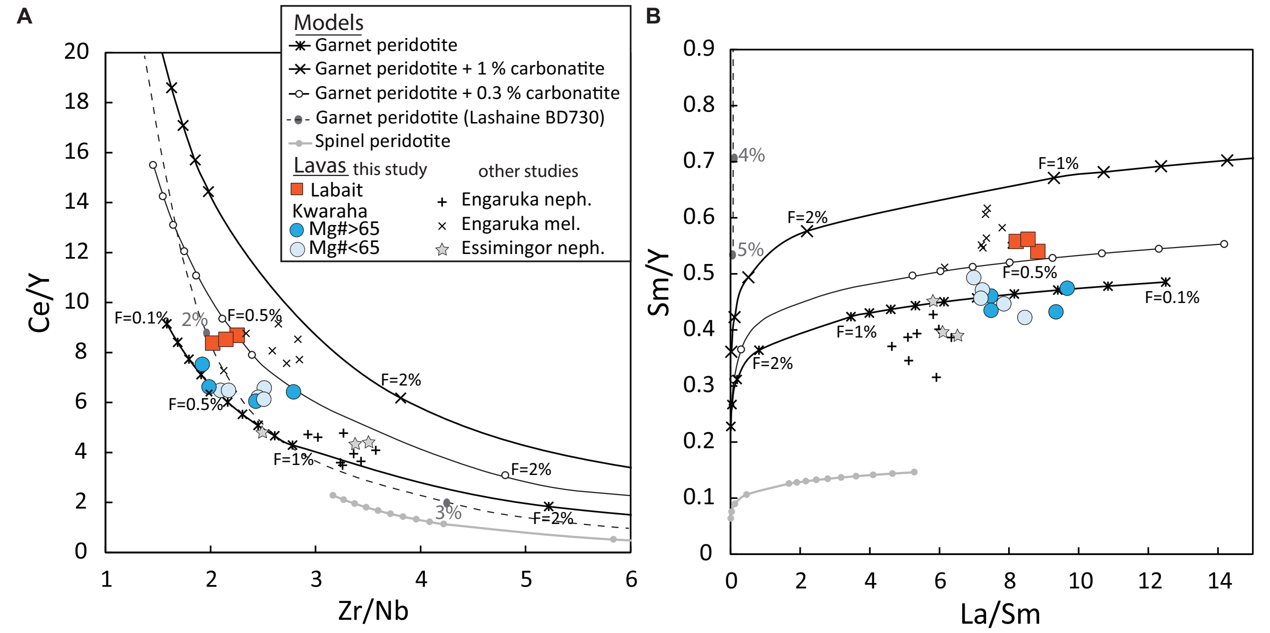

FIGURE 9 | Geochemical model of primary mantle melting for Kwaraha and Labait lavas using **(A)** Ce/Y vs. Zr/Nb ratios and **(B)** Sm/Y vs. La/Sm ratios. Partial melting of a garnet peridotite (62% olivine, 16% opx, 10% clinopyroxene, 10% garnet, and 2% phlogopite), spinel peridotite and garnet peridotites with the addition of 0.3 and 1% carbonatite (Kw1 composition) was modeled with no modal fractional melting. Partial melting of a garnet-bearing xenolith from Lashaine volcano (sample BD730 from Gibson et al., 2013) has also been modeled. The degree of melting (F) is indicated for each composition. Nephelinites (neph.) and melilitites (mel.) from Engaruka-Natron basin (Mattsson et al., 2013) and nephelinites from Essimingor (Mana et al., 2012) are also reported. Mafic nephelinites from Kwaraha (Mg# > 65) are reported in blue circles, and less mafic lavas from Kwaraha (Mg# < 65, **Table 1**) are reported in light blue circles.

(iii) magnetolleruric data by Selway et al. (2014) suggesting that beneath Labait, the geotherm was initially cratonic at 44 mW/m^2, before been impacted by the plume ascent, increasing the mantle temperature of 300°C at 5 GPa, which may lead to melting of fertile lherzolite (**Figure 10**).

The presence of phlogopite in Kwaraha and Labait magmas indicates that the asthenospheric mantle source is hydrated, which may considerably decrease the solidus temperature (e.g., Green et al., 2014). The water content of the nephelinite magma estimated from the water content of olivine and clinopyroxene was 0.2–0.5 wt% H_2O (**Table 4**). Considering 1% partial melting, the garnet-rich and phlogopite-bearing peridotite source may have contained around 300 ppm H_2O (Novella et al., 2015; Demouchy and Bolfan-Casanova, 2016).

Most of the experimental studies performed to determine the depth of partial melting and the composition of primitive alkaline magmas have been carried out in K- and H_2O-free systems, that are not relevant for our phlogopite-bearing magmas (CMAS-CO_2; **Figure 10**; e.g., Green and Falloon, 1998; Gudfinnsson and Presnall, 2005). On the other hand, the experiments that investigated the partial melting in the presence of K_2O and water for alkaline magmas in the KMASH system at $P < 4.5$ GPa and $T < 1300$°C (phl = phl+grt+melt; Yoder and Kushiro, 1969; Sato et al., 1997; Trønnes, 2002), KCMASH system at 3.5–17 GPa and $T < 1400$°C (phl+cpx = phl+cpx+grt+ol+melt; Luth, 1997) and KNCMASH system at 4–9.5 GPa and $T < 1200$°C (phl+cpx+opx = amph+grt+ol+melt; Konzett and Ulmer, 1999) were not performed to account for the presence of garnet (gt) and phlogopite (phl) in lherzolite. Recently, experiments by Condamine et al. (2016) show that melting of phlogopite-garnet lherzolite leads to the reaction phl+cpx+grt = olivine+opx+melt at 3 GPa and 1300°C and forms foiditic to trachy-basaltic melts (44–47 wt% SiO_2, Na_2O+K_2O = 5.2–11.3 wt%) for various degree of melting (F = 0.008–0.255) and alkaline contents. However, the experimental melts from partial melting of phlogopite-bearing lherzolite have higher alkali and silica contents compared to the nephelinite magmas. Similarly, partial melting of water- and carbonate-bearing and phlogopite-free lherzolite (Dasgupta et al., 2007) and carbonate-bearing and phlogopite-rich MARID (Mica-Amphibole-Rutile-Ilmenite-Diopside; Förster et al., 2018) or potassium enriched pyrolite (Foley et al., 2009) at 3–5 GPa do not reproduce the K_2O, CaO, and TiO_2 concentrations of nephelinite magmas (**Figures 3**, 4).

The presence of carbon in mantle source is an important parameter to consider for partial melting at the lithosphere-asthenosphere boundary because (i) it induces a decrease of the solidus temperature of peridotite (Dasgupta et al., 2007) and (ii) below 5 GPa (below LAB), carbon is stable as graphite and it will be oxidized at 4–5 GPa to produce carbonate melt (redox melting, **Figure 10**; Green and Falloon, 1998; Stagno et al., 2013; Hammouda and Keshav, 2015). Experiments of partial melting of CO_2- and phlogopite-bearing garnet peridotite at high pressure (>4–5 GPa) would help to better understand the

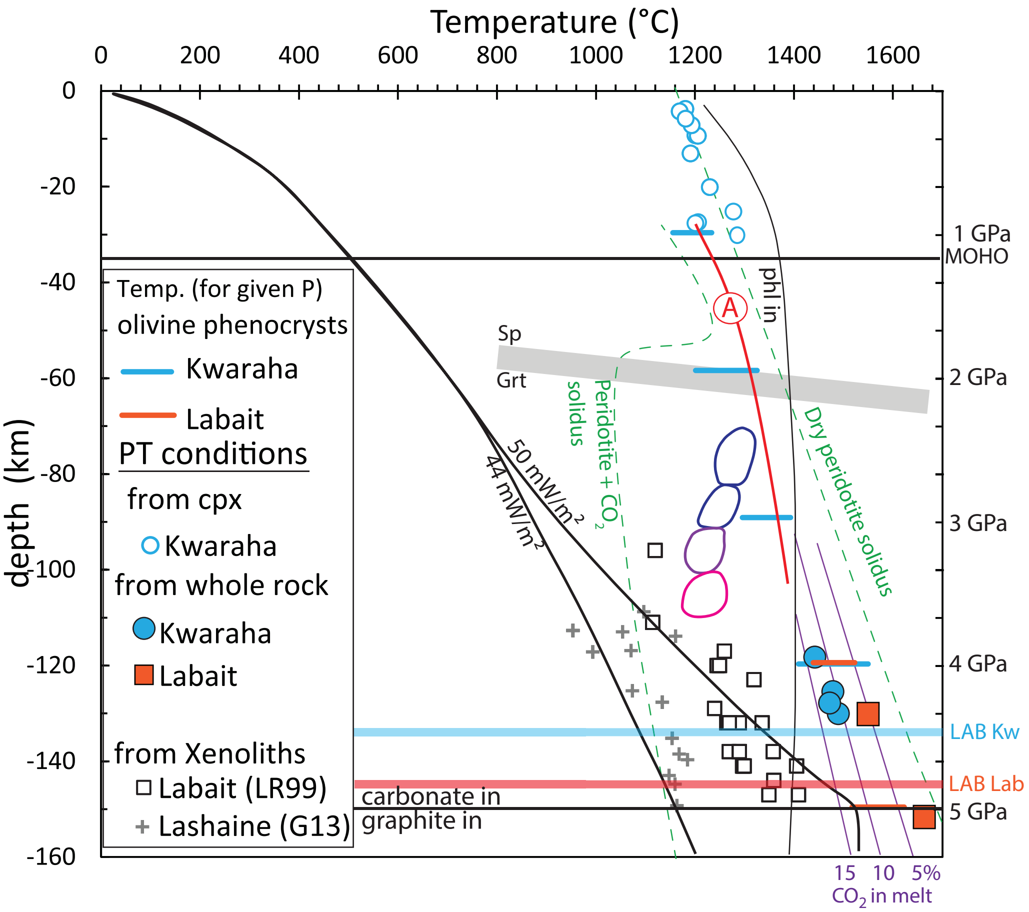

FIGURE 10 | P-T conditions of clinopyroxene crystallization calculated from the clinopyroxene-liquid thermobarometer (Putirka, 2008) for Kwaraha (Mg# > 65) and P-T conditions of partial melting (Albarède, 1992) for Kwaraha and Labait lavas. P-T conditions for Labait and Lashaine mantle xenoliths are from Lee and Rudnick (1999) LR99 and Gibson et al. (2013) G13, respectively. Crystallization temperatures of olivine are represented by color bars (blue: Kwaraha, and orange; Labait; calculation from Putirka, 2008). We include the dry peridotite and peridotite+CO_2 solidi and melt CO_2 isopleths with CO_2 content in weight percent from Dasgupta et al. (2013), the spinel-garnet boundary from Lee et al. (2000), and the lithosphere-asthenosphere boundary (LAB) from Craig et al. (2011). The curve of phlogopite stability (phl) correspond to experiments (KMASH) from Yoder and Kushiro (1969); Sato et al. (1997), and Trønnes (2002). The reaction (A) F-phl+cpx+grt = ol+opx+melt has been determined from melting experiments of phlogopite-garnet peridotite by Condamine et al. (2016). Cratonic geotherm (44 mW/m^2) and geotherm modified by plume thermal anomaly are also reported (Selway et al., 2014), as well as the different melt types produced by low partial melting of CMAS ± H_2O and CO_2: Colored balloons represent P and T conditions of partial melting for basanite (blue balloon), nephelinite, melilitite, and leucitite melt compositions (pink balloon) (Frey et al., 1978; Adam, 1990; Green and Falloon, 1998).

melting conditions of primary nephelinite melt as observed at Labait and Kwaraha volcanoes in the southern part of the NTD.

Melt-Rock Interaction and Lithospheric Metasomatism

Percolation of CO_2- and water-bearing alkaline nephelinite magmas from the LAB through the lithospheric mantle may have induced metasomatism and phlogopite crystallization in garnet and spinel lherzolite and glimmerite lithologies. The large variety of mantle xenoliths sampled by nephelinite lavas at Labait and other localities of NTD strongly indicates that the lithospheric mantle beneath the Tanzanian Craton edge is highly heterogeneous, including fertile and refractory mantle peridotite (i.e., Cr spinel with high Cr#; Cr# up to 94), and metasomatized amphibole- and/or phlogopite-bearing peridotite (Dawson and Smith, 1988; Lee and Rudnick, 1999; Koornneef et al., 2009; Gibson et al., 2013; Baptiste et al., 2015).

The study of magmatic phlogopite in nephelinite and mantle phlogopite in xenoliths from Labait and Kwaraha corroborates previous studies that established the nature and the timing of the metasomatism events. Xenoliths from Labait, Lashaine, Pello hill, and Eledoi (Natron basin) suggest the percolation of a H_2O-rich metasomatic agent within the lithospheric mantle and the presence of heterogeneous lithosphere related to different metasomatic events (Jones et al., 1983; Dawson and Smith, 1988; Rudnick et al., 1993; Koornneef et al., 2009; Baptiste et al., 2015). NAMS minerals in lithospheric peridotites have a low water content (<50 ppm wt H_2O whole rock peridotite; Baptiste et al., 2015; Hui et al., 2015) although the presence of hydrous minerals as amphibole and phlogopite indicates the presence of K_2O-MgO-H_2O-rich silicate melt in the lithosphere. The composition of phlogopite in mantle xenoliths from Labait (i.e., glimmerite, core, and rim of phlogopite in lherzolite, **Figure 6**) indicate at least 3 metasomatic events within the continental lithosphere. Multiple stage of metasomatism in the lithosphere beneath Labait have already been suggested from textural, chemical and isotopic data (Koornneef et al., 2009): Phlogopite, Cr-rich diopside and spinel pockets were produced by an old metasomatism event (i.e., Pan-African Orogeny, 610–650 Ma) associated with a liquid rich in Ni, Cr, Na, K, H_2O, Ba, Fe, Ti. Glimmerite lithologies could be formed by recent metasomatism (rift event) and melt differentiation in veins in the lithosphere, induced by the percolation of nephelinite liquid rich in K, Fe, Ti, and poor in Cl, Mg, Al, Ba (**Figure 10** and **Table 3**). Rift related metasomatism event was previously suggested as anhydrous from textural observation for a spinel lherzolite (Koornneef et al., 2009). However, it can be noted that glimmerite xenoliths (or glimmerite) have been poorly sampled and represent only 2% of Labait xenoliths (Koornneef et al., 2009). This may lead to a sample bias for phlogopite interpretation and hydrous metasomatism.

Alkaline Magmatism During Early Rifting of the East African Rift

Early rifting of the EAR is divided into two branches with opposite rift propagations: rifting in the eastern NTD propagated from north (north and central Kenya, 30–15 Ma) to south (northern Tanzania, <6 Ma; Ebinger et al., 2000; Mana et al., 2015; Furman et al., 2016), whereas rifting in the western part of the Tanzanian Craton propagated from south (Kivu, 8–12 Ma) to north (Toro-Ankole, 0.05 Ma; Ebinger, 1989; Furman, 2007). Both branches have produced highly alkaline, alkaline, and sub-alkaline volcanism along their rift axes (Furman, 2007; Dawson, 2008; Mana et al., 2015; Pouclet et al., 2016). The diversity of erupted lavas in terms of their differentiation (melilitite/basalt to phonolite or trachyte) is linked to fractional crystallization, immiscibility, and assimilation during ascent through the sub-continental lithosphere and continental crust (e.g., Mollel et al., 2009; Dawson, 2012; Mana et al., 2015; Baudouin et al., 2016, 2018), whereas the diversity in terms of magmatic series is related to deep melting processes and the specific mantle sources.

In the NTD, volcanism of different alkalinities occurs along two perpendicular axes (**Figure 1**): the N-S axis erupted highly alkaline magmas such as nephelinite (e.g., Oldoinyo Lengai-Labait; this study; Mana et al., 2012; Mattsson et al., 2013), whereas the W-E axis erupted dominantly alkaline magmas (Essimingor-Kilimanjaro; Nonnotte et al., 2011; Mana et al., 2012, 2015) and sub-alkaline magmas in the western part close to the Tanzanian Craton (i.e., Ngorongoro-Olmoti; Nonnotte, 2007; Mollel et al., 2008, 2009). Although there is a clear correlation between the alkalinity of magmas and their geographical alignment, we found no obvious correlations between eruptive age, alkalinity, depth of partial melting, or mantle source.

Along the N-S axis of the NTD, highly alkaline magmas are the product of very low degrees of partial melting (<1%; this study; Mattsson et al., 2013) of different mantle sources at various depths. From north to south, the depth of partial melting increases and the mantle sources change from (1) CO_2-rich amphibole-lherzolite at shallow depth (∼75–90 km) in the Engaruka-Natron basin (Oldoinyo Lengai; Mattsson et al., 2013), to (2) amphibole-bearing garnet lherzolite at intermediate depth (∼110–140 km at Burko; Mana et al., 2012), and finally to (3) CO_2-rich phlogopite-bearing garnet lherzolite near or below the LAB at 150–160 km depth (Labait; this study; Dawson et al., 1997). The estimated depth of partial melting in the southern part of the NTD is well supported by the presence of deep refractory mantle xenoliths in Labait lavas (>150 km, **Figure 10**; Lee and Rudnick, 1999) and the thick cratonic lithosphere (on-craton eruption; e.g., Dawson et al., 1997; Craig et al., 2011). Alkaline and sub-alkaline magmas erupted along the W-E axis are related to high degrees of partial melting (2–6%) of amphibole-bearing garnet lherzolite at 85–140 km (Nonnotte, 2007; Mana et al., 2015). They erupted at the craton-edge where asthenospheric upwelling may have proceeded to shallow levels, leading to common alkali basalts similar to those observed north of the NTD in central Kenya, which represents a more mature stage of rifting (e.g., Ebinger et al., 2000; Roex et al., 2001).

The relationships between magmatism and rift dynamics observed in the eastern EAR are similar to those observed in the western EAR despite their opposite rift propagations. In the western EAR, magmatism evolved from basalt-basanite at Kivu (south) to K-nephelinite at Toro-Ankole (north) during early stage rifting (Pouclet et al., 1981, 2016; Chakrabarti et al., 2009; Rosenthal et al., 2009) are also associated with peridotite, pyroxenite and glimmerite xenoliths (Muravyeva and Senin, 2018). Alkaline rocks are potassic, attesting to the presence of a potassium-rich mantle source beneath the western part of the Tanzanian Craton (up to 7 wt% K_2O in melt; Pouclet et al., 1981; Rogers et al., 1998). Primary magmas from the north of the western rift originate from the greatest melting depths (>140 km in the presence of phlogopite at Toro-Ankole), and the depth of melting becomes gradually shallower toward the south of the western branch (<90 km in the presence of both amphibole and phlogopite), similar to the observed depth-of-melting in the east branch of EAR (Rosenthal et al., 2009; Foley et al., 2012). The mantle source of potassic magmatism has been characterized as two metasomatic assemblages of phlogopite-clinopyroxenite and a carbonate-rich garnet-free assemblage resulting from kimberlitic-like melt impregnation and crystallization (e.g., Rosenthal et al., 2009; Foley et al., 2012). The asthenospheric source beneath the West branch of EAR is CO_2-rich and highly metasomatized leading to the genesis of ultramafic and potassic primary melt (Foley et al., 2012; Foley and Fischer, 2017).

The low volume of highly alkaline volcanism in both the western and eastern rift branches may be related to the low degrees of partial melting and the deep thermal anomaly beneath the thick cratonic lithosphere (e.g., Ebinger and Sleep, 1998). The occurrence of thin, rifted lithosphere in close proximity to thick cratonic heterogeneous lithosphere may generate melting at shallow depth, likely related to rift propagation and/or the plume-related thermal anomaly. The most likely mechanism for producing sub-cratonic lithospheric heterogeneities is the accumulation of low-degree partial melts from the convecting depleted asthenospheric mantle (e.g., this study, McKenzie, 1989; Lee and Rudnick, 1999; Vauchez et al., 2005; Baptiste et al., 2015; Chin, 2018).

The variability of the mantle sources of potassic and alkaline volcanism between the western and eastern branches of the EAR may also reflect different sub-cratonic lithospheric lithologies beneath the Paleoproterozoic and Neoproterozoic belts underlying the western and eastern branches, respectively (e.g., Corti et al., 2007; Katumwehe et al., 2015).

CONCLUSION

Volcanoes of the Manyara-Balangida rift, associated with early rifting in the East African Rift (northern Tanzania), have erupted primary nephelinites composed of olivine, clinopyroxene, and up to 4 vol% phlogopite. Trace models of Kwaraha and Labait lavas from a low degree of partial melting (0.2–1%) of a garnet-phlogopite-bearing peridotite with a carbonate-rich component (0.3%), consistent with others northern Tanzania lavas. The presence of garnet-bearing mantle xenoliths and the primary melt compositions indicate that melting occurred at depths ≥150 km, below the lithosphere-asthenosphere boundary. The partial melting at the earliest stage rifting is the deepest source reported for East branch of East African Rift. The percolation of deep, CO_2-rich and H_2O-bearing highly alkaline magmas may have produced strong heterogeneities through metasomatism process in the thick sub-continental Tanzanian lithospheric mantle. H_2O-bearing magmas percolation has induced phlogopite crystallization in spinel lherzolite and glimmerite lithology weakening the rheology of the Tanzanian lithosphere. These compositional changes are thus major parameters that have influenced the rift propagation near the craton edge, and should be taken into account to explain tectonic deformation at the surface.

DATA AVAILABILITY STATEMENT

The datasets presented in this study can be found online at https://tel.archives-ouvertes.fr/tel-01563231/.

AUTHOR CONTRIBUTIONS

CB carried out the microprobe, icpms, and FTIR analyses. CB and FP contributed to the interpretations and writing. All authors contributed to the article and approved the submitted version.

FUNDING

This research was financially supported by the ANR project CoLiBrEA CTN°LS 104568 and the HATARI project (Tellus-RIFT INSU).

ACKNOWLEDGMENTS

We thank the reviewers for their suggestions and helpful remarks. This work is a part of CB thesis (Baudouin, 2016). We thank Tanzania COSTECH and the French Embassy for help for Research Permits, and the University of Dar es Salaam for their help during field sampling.

SUPPLEMENTARY MATERIAL

The Supplementary Material for this article can be found online at: https://www.frontiersin.org/articles/10.3389/feart.2020.00277/full#supplementary-material

REFERENCES

Adam, J. (1990). The geochemistry and experimental petrology of Sodic alkaline basalts from Oatlands, Tasmania. *J. Petrol.* 31, 1201–1223. doi: 10.1093/petrology/31.6.1201

Adam, J., and Green, T. (2006). Trace element partitioning between mica- and amphibole-bearing garnet lherzolite and hydrous basanitic melt: 1. Experimental results and the investigation of controls on partitioning behaviour. *Contrib. Mineral. Petrol.* 152, 1–17. doi: 10.1007/s00410-006-0085-4

Albarède, F. (1992). How deep do common basaltic magmas form and differentiate? *J. Geophys. Res. Solid Earth* 97, 10997–11009.

Andersen, T., Elburg, M. A., and Erambert, M. (2014). Extreme peralkalinity in delhayelite-and andremeyerite-bearing nephelinite from Nyiragongo volcano, East African Rift. *Lithos* 206, 164–178. doi: 10.1016/j.lithos.2014.07.025

Aubaud, C., Hauri, E. H., and Hirschmann, M. M. (2004). Hydrogen partition coefficients between nominally anhydrous minerals and basaltic melts. *Geophys. Res. Lett.* 31:L20611.

Aulbach, S., Rudnick, R. L., and McDonough, W. F. (2008). Li-Sr-Nd isotope signatures of the plume and cratonic lithospheric mantle beneath the margin of the rifted Tanzanian craton (Labait). *Contrib. Mineral. Petrol.* 155, 79–92. doi: 10.1007/s00410-007-0226-4

Aulbach, S., Rudnick, R. L., and McDonough, W. F. (2011). Evolution of the lithospheric mantle beneath the East African Rift in Tanzania and its potential signatures in rift magmas. *Geol. Soc. Am. Spec. Pap.* 478, 105–125. doi: 10.1130/2011.2478(06)

Baasner, A., Médard, E., Laporte, D., and Hoffer, G. (2016). Partial melting of garnet lherzolite with water and carbon dioxide at 3 GPa using a new melt extraction technique: implications for intraplate magmatism. *Contrib. Mineral. Petrol.* 171, 1–23.

Bailey, K., Lloyd, F., Kearns, S., Stoppa, F., Eby, N., and Woolley, A. (2005). Melilitite at fort portal, Uganda: another dimension to the carbonate volcanism. *Lithos* 85, 15–25. doi: 10.1016/j.lithos.2005.03.019

Baptiste, V., Tommasi, A., Vauchez, A., Demouchy, S., and Rudnick, R. L. (2015). Deformation, hydration, and anisotropy of the lithospheric mantle in an active rift: constraints from mantle xenoliths from the North Tanzanian Divergence of the East African Rift. *Tectonophysics* 639, 34–55. doi: 10.1016/j.tecto.2014.11.011

Baudouin, C. (2016). *Volcanisme Alcalin Associé À L'initiation de la Rupture Continentale: Rift East Africain, Tanzanie, Bassin de Manyara*. Doctoral dissertation, University of Montpellier, Montpellier.

Baudouin, C., Parat, F., Denis, C. M., and Mangasini, F. (2016). Nephelinite lavas at early stage of rift initiation (Hanang volcano, North Tanzanian Divergence). *Contrib. Mineral. Petrol.* 171, 1–20.

Baudouin, C., Parat, F., and Michel, T. (2018). CO2-rich phonolitic melt and carbonatite immiscibility in early stage of rifting: melt inclusions from Hanang volcano (Tanzania). *J. Volcanol. Geother. Res.* 358, 261–272. doi: 10.1016/j.jvolgeores.2018.05.019

Behrens, H., Romano, C., Nowak, M., Holtz, F., and Dingwell, D. B. (1996). Near-infrared spectroscopic determination of water species in glasses of the system MAlSi3O8 (M = Li, Na, K): an interlaboratory study. *Chem. Geol.* 128, 41–63. doi: 10.1016/0009-2541(95)00162-x

Berndt, J., Koepke, J., and Holtz, F. (2005). An experimental investigation of the influence of water and oxygen fugacity on differentiation of MORB at 200 MPa. *J. Petrol.* 46, 135–167. doi: 10.1093/petrology/egh066

Brey, G. (1978). Origin of olivine melilitites–chemical and experimental constraints. *J. Volcanol. Geother. Res.* 3, 61–88. doi: 10.1016/0377-0273(78)90004-5

Brooker, R. A., Kohn, S. C., Holloway, J. R., and McMillan, P. F. (2001). Structural controls on the solubility of CO2 in silicate melts: part II: IR characteristics of carbonate groups in silicate glasses. *Chem. Geol.* 174, 241–254. doi: 10.1016/s0009-2541(00)00318-1

Carignan, J., Hild, P., Mevelle, G., Morel, J., and Yeghicheyan, D. (2001). Routine analyses of trace elements in geological samples using flow injection and low pressure on-line liquid chromatography coupled to ICP-MS: a study of geochemical reference materials BR, DR-N, UB-N, AN-G and GH. *Geostand. Newsl.* 25, 187–198. doi: 10.1111/j.1751-908x.2001.tb00595.x

Carmichael, I. S., and Ghiorso, M. S. (1990). The effect of oxygen fugacity on the redox state of natural liquids and their crystallizing phases. *Rev. Mineral. Geochem.* 24, 191–212. doi: 10.1515/9781501508769-011

Chakrabarti, R., Basu, A. R., Santo, A. P., Tedesco, D., and Vaselli, O. (2009). Isotopic and geochemical evidence for a heterogeneous mantle plume origin of the Virunga volcanics, Western rift, East African Rift system. *Chem. Geol.* 259, 273–289. doi: 10.1016/j.chemgeo.2008.11.010

Chin, E. J. (2018). Deep crustal cumulates reflect patterns of continental rift volcanism beneath Tanzania. *Contrib. Mineral. Petrol.* 173:85.

Condamine, P., and Médard, E. (2014). Experimental melting of phlogopite-bearing mantle at 1 GPa: implications for potassic magmatism. *Earth Planet. Sci. Lett.* 397, 80–92. doi: 10.1016/j.epsl.2014.04.027

Condamine, P., Médard, E., and Devidal, J. L. (2016). Experimental melting of phlogopite-peridotite in the garnet stability field. *Contrib. Mineral. Petrol.* 171:95.

Corti, G., van Wijk, J., Cloetingh, S., and Morley, C. K. (2007). Tectonic inheritance and continental rift architecture: numerical and analogue models of the East African Rift system. *Tectonics* 26:TC6006.

Craig, T. J., Jackson, J. A., Priestley, K., and McKenzie, D. (2011). Earthquake distribution patterns in Africa: their relationship to variations in lithospheric and geological structure, and their rheological implications. *Geophys. J. Int.* 185, 403–434. doi: 10.1111/j.1365-246x.2011.04950.x

Dasgupta, R., Hirschmann, M. M., and Smith, N. D. (2007). Partial melting experiments of peridotite + CO2 at 3 GPa and genesis of alkalic ocean island basalts. *J. Petrol.* 48, 2093–2124. doi: 10.1093/petrology/egm053

Dasgupta, R., Mallik, A., Tsuno, K., Withers, A. C., Hirth, G., and Hirschmann, M. M. (2013). Carbon-dioxide-rich silicate melt in the Earth's upper mantle. *Nature* 493, 211–215. doi: 10.1038/nature11731

Dawson, J. B. (2008). *The Gregory Rift Valley and Neogene-Recent Volcanoes of Northern Tanzania*. London: Geological Society of London.

Dawson, J. B. (2012). Nephelinite–melilitite–carbonatite relationships: evidence from pleistocene–recent volcanism in northern Tanzania. *Lithos* 152, 3–10. doi: 10.1016/j.lithos.2012.01.008

Dawson, J. B., James, D., Paslick, C., and Halliday, A. M. (1997). Ultrabasic potassic low-volume magmatism and continental rifting in north-central Tanzania: association with enhanced heat flow. *Russ. Geol. Geophys.* 38, 69–81.

Dawson, J. B., Powell, D. G., and Reid, A. M. (1970). Ultrabasic xenoliths and lava from the Lashaine volcano, northern Tanzania. *J. Petrol.* 11, 519–548. doi: 10.1093/petrology/11.3.519

Dawson, J. B., and Smith, J. V. (1977). The MARID (mica-amphibole-rutile-ilmenite-diopside) suite of xenoliths in kimberlite. *Geochim. Cosmochim. Acta* 41, 309–323. doi: 10.1016/0016-7037(77)90239-3

Dawson, J. B., and Smith, J. V. (1988). Metasomatised and veined upper-mantle xenoliths from Pello Hill, Tanzania: evidence for anomalously-light mantle beneath the Tanzanian sector of the East African Rift Valley. *Contrib. Mineral. Petrol.* 100, 510–527. doi: 10.1007/bf00371380

Dawson, J. B., and Smith, J. V. (1992). Olivine-mica pyroxenite xenoliths from northern Tanzania: metasomatic products of upper-mantle peridotite. *J. Volcanol. Geother. Res.* 50, 131–142. doi: 10.1016/0377-0273(92)90041-b

Demouchy, S., and Bolfan-Casanova, N. (2016). Distribution and transport of hydrogen in the Lithospheric mantle: a review. *Lithos* 240, 402–425. doi: 10.1016/j.lithos.2015.11.012

Denis, C. M., Alard, O., and Demouchy, S. (2015). Water content and hydrogen behaviour during metasomatism in the uppermost mantle beneath Ray Pic volcano (Massif Central, France). *Lithos* 236, 256–274. doi: 10.1016/j.lithos.2015.08.013

Ebinger, C. J. (1989). Tectonic development of the western branch of the East-African rift system. *Geol. Soc. Am. Bull.* 101, 885–903. doi: 10.1130/0016-7606(1989)101<0885:tdotwb>2.3.co;2

Ebinger, C. J., and Sleep, N. H. (1998). Cenozoic magmatism throughout east Africa resulting from impact of a single plume. *Nature* 395, 788–791. doi: 10.1038/27417

Ebinger, C. J., Yemane, T., Harding, D. J., Tesfaye, S., Kelley, S., and Rex, D. C. (2000). Rift deflection, migration, and propagation: linkage of the Ethiopian and Eastern rifts, Africa. *Geol. Soc. Am. Bull.* 112, 163–176. doi: 10.1130/0016-7606(2000)112<163:rdmapl>2.0.co;2

Eccles, D. R., Heaman, L. M., Luth, R. W., and Creaser, R. A. (2004). Petrogenesis of the late cretaceous northern Alberta kimberlite province. *Lithos* 76, 435–459. doi: 10.1016/j.lithos.2004.03.046

Eggler, D. H., and Holloway, J. R. (1977). Partial melting of peridotite in the presence of H2O and CO2: principles and review. *Magma Genesis* 96, 15–36.

Etame, J., Suh, C. E., Gerard, M., and Bilong, P. (2012). Phillipsite formation in nephelinitic rocks in response to hydrothermal alteration at Mount Etinde, Cameroon. *Geochemistry* 72, 31–37. doi: 10.1016/j.chemer.2011.08.002

Foley, S. F. (1993). An experimental study of olivine lamproite: first results from the diamond stability field. *Geochim. Cosmochim. Acta* 57, 483–489. doi: 10.1016/0016-7037(93)90448-6

Foley, S. F., and Fischer, T. P. (2017). An essential role for continental rifts and lithosphere in the deep carbon cycle. *Nat. Geosci.* 10, 897–902. doi: 10.1038/s41561-017-0002-7

Foley, S. F., Link, K., Tiberindwa, J. V., and Barifaijo, E. (2012). Patterns and origin of igneous activity around the Tanzanian craton. *J. Afr. Earth Sci.* 62, 1–18. doi: 10.1016/j.jafrearsci.2011.10.001

Foley, S. F., Yaxley, G. M., Rosenthal, A., Buhre, S., Kiseeva, E. S., Rapp, R. P., et al. (2009). The composition of near-solidus melts of peridotite in the presence of CO2 and H2O between 40 and 60 kbar. *Lithos* 112, 274–283. doi: 10.1016/j.lithos.2009.03.020

Förster, M. W., Preleviæ, D., Schmück, H. R., Buhre, S., Marschall, H. R., Mertz-Kraus, R., et al. (2018). Melting phlogopite-rich MARID: lamproites and the role of alkalis in olivine-liquid Ni-partitioning. *Chem. Geol.* 476, 429–440. doi: 10.1016/j.chemgeo.2017.11.039

Frey, F. A., Green, D. H., and Roy, S. D. (1978). Integrated models of basalt petrogenesis: a study of quartz tholeiites to olivine melilitites from south eastern Australia utilizing geochemical and experimental petrological data. *J. Petrol.* 19, 463–513. doi: 10.1093/petrology/19.3.463

Fujimaki, H., Tatsumoto, M., and Aoki, K. I. (1984). Partition coefficients of Hf, Zr, and REE between phenocrysts and groundmasses. *J. Geophys. Res. Solid Earth* 89, B662–B672.

Furman, T. (2007). Geochemistry of East African Rift basalts: an overview. *J. Afr. Earth Sci.* 48, 147–160. doi: 10.1016/j.jafrearsci.2006.06.009

Furman, T., Nelson, W. R., and Elkins-Tanton, L. T. (2016). Evolution of the East African rift: drip magmatism, lithospheric thinning and mafic volcanism. *Geochim. Cosmochim. Acta* 185, 418–434. doi: 10.1016/j.gca.2016.03.024

Gardès, E., Laumonier, M., Massuyeau, M., and Gaillard, F. (2020). Unravelling partial melt distribution in the oceanic low velocity zone. *Earth Planet. Sci. Lett.* 540:116242. doi: 10.1016/j.epsl.2020.116242

Gibson, S. A., McMahon, S. C., Day, J. A., and Dawson, J. B. (2013). Highly refractory lithospheric mantle beneath the Tanzanian craton: evidence from Lashaine pre-metasomatic garnet-bearing peridotites. *J. Petrol.* 54, 1503–1546. doi: 10.1093/petrology/egt020

Green, D. H., and Falloon, T. J. (1998). "Pyrolite: a Ringwood concept and its current expression," in *The Earth's Mantle: Composition, Structure, and Evolution*, ed. I. Jackson, (Cambridge: Cambridge University Press), 311–378. doi: 10.1017/cbo9780511573101.010

Green, D. H., and Falloon, T. J. (2015). Mantle-derived magmas: intraplate, hot-spots and mid-ocean ridges. *Sci. Bull.* 60, 1873–1900. doi: 10.1007/s11434-015-0920-y

Green, D. H., Hibberson, W. O., Rosenthal, A., Kovács, I., Yaxley, G. M., Falloon, T. J., et al. (2014). Experimental study of the influence of water on melting and phase assemblages in the upper mantle. *J. Petrol.* 55, 2067–2096. doi: 10.1093/petrology/egu050

Grégoire, M., Bell, D., and Le Roex, A. (2002). Trace element geochemistry of phlogopite-rich mafic mantle xenoliths: their classification and their relationship to phlogopite-bearing peridotites and kimberlites revisited. *Contrib. Mineral. Petrol.* 142, 603–625. doi: 10.1007/s00410-001-0315-8

Griffin, W. L., Powell, W. J., Pearson, N. J., and O'Reilly, S. Y. (2008). GLITTER: data reduction software for laser ablation ICP-MS. Laser Ablation-ICP-MS in the earth sciences. *Mineral. Assoc. Canada Short Course Ser.* 40, 204–207.

Gudfinnsson, G. H., and Presnall, D. C. (2005). Continuous gradations among primary carbonatitic, kimberlitic, melilititic, basaltic, picritic, and komatiitic melts in equilibrium with garnet lherzolite at 3–8 GPa. *J. Petrol.* 46, 1645–1659. doi: 10.1093/petrology/egi029

Hammouda, T., and Keshav, S. (2015). Melting in the mantle in the presence of carbon: review of experiments and discussion on the origin of carbonatites. *Chem. Geol.* 418, 171–188.

Hauri, E. H., Gaetani, G. A., and Green, T. H. (2006). Partitioning of water during melting of the Earth's upper mantle at H2O-undersaturated conditions. *Earth Planet. Sci. Lett.* 248, 715–734. doi: 10.1016/j.epsl.2006.06.014

Hofmann, A. W. (1988). Chemical differentiation of the Earth: the relationship between mantle, continental crust, and oceanic crust. *Earth Planet. Sci. Lett.* 90, 297–314. doi: 10.1016/0012-821x(88)90132-x

Hudgins, T. R., Mukasa, S. B., Simon, A. C., Moore, G., and Barifaijo, E. (2015). Melt inclusion evidence for CO2-rich melts beneath the western branch of the East African Rift: implications for long-term storage of volatiles in the deep lithospheric mantle. *Contrib. Mineral. Petrol.* 169:46.

Hui, H., Peslier, A. H., Rudnick, R. L., Simonetti, A., and Neal, C. R. (2015). Plume-cratonic lithosphere interaction recorded by water and other trace elements in peridotite xenoliths from the Labait volcano, Tanzania. *Geochem. Geophys. Geosyst.* 16, 1687–1710. doi: 10.1002/2015gc005779

Huppert, H. E., and Sparks, R. S. J. (1985). Cooling and contamination of mafic and ultramafic magmas during ascent through continental crust. *Earth Planet. Sci. Lett.* 74, 371–386. doi: 10.1016/s0012-821x(85)80009-1

Ivanikov, V. V., Rukhlov, A. S., and Bell, K. (1998). Magmatic evolution of the melilitite–carbonatite–nephelinite dyke series of the Turiy Peninsula (Kandalaksha Bay, White Sea, Russia). *J. Petrol.* 39, 2043–2059. doi: 10.1093/petroj/39.11-12.2043

Johnson, L. H., Jones, A. P., Church, A. A., and Taylor, W. R. (1997). Ultramafic xenoliths and megacrysts from a melilitite tuff cone, Deeti, northern Tanzania. *J. Afr. Earth Sci.* 25, 29–42. doi: 10.1016/s0899-5362(97)00060-2

Jones, A. P., Smith, J. V., and Dawson, J. B. (1982). Mantle metasomatism in 14 veined peridotites from Bultfontein Mine, South Africa. *J. Geol.* 90, 435–453. doi: 10.1086/628695

Jones, A. P., Smith, J. V., and Dawson, J. B. (1983). Glasses in mantle xenoliths from Olmani, Tanzania. *J. Geol.* 91, 167–178. doi: 10.1086/628754

Katumwehe, A. B., Abdelsalam, M. G., and Atekwana, E. A. (2015). The role of pre-existing Precambrian structures in rift evolution: the Albertine and Rhino grabens, Uganda. *Tectonophysics* 646, 117–129. doi: 10.1016/j.tecto.2015.01.022

Keller, J., Zaitsev, A. N., and Wiedenmann, D. (2006). Primary magmas at Oldoinyo Lengai: the role of olivine melilitites. *Lithos* 91, 150–172. doi: 10.1016/j.lithos.2006.03.014

Keller, T., and Katz, R. F. (2016). The role of volatiles in reactive melt transport in the asthenosphere. *J. Petrol.* 57, 1073–1108. doi: 10.1093/petrology/egw030

Klaudius, J., and Keller, J. (2006). Peralkaline silicate lavas at Oldoinyo Lengai, Tanzania. *Lithos* 91, 173–190. doi: 10.1016/j.lithos.2006.03.017

Koornneef, J. M., Davies, G. R., Döpp, S. P., Vukmanovic, Z., Nikogosian, I. K., and Mason, P. R. (2009). Nature and timing of multiple metasomatic events in the sub-cratonic lithosphere beneath Labait, Tanzania. *Lithos* 112, 896–912. doi: 10.1016/j.lithos.2009.04.039

Konzett, J., and Ulmer, P. (1999). The stability of hydrous potassic phases in lherzolitic mantle—an experimental study to 9.5 GPa in simplified and natural bulk compositions. *J. Petrol.* 40, 629–652. doi: 10.1093/petroj/40.4.629

Kramers, J. D., Roddick, J. C. M., and Dawson, J. B. (1983). Trace element and isotope studies on veined, metasomatic and "MARID" xenoliths from Bultfontein, South Africa. *Earth Planet. Sci. Lett.* 65, 90–106. doi: 10.1016/0012-821x(83)90192-9

Kushiro, I. (1969). Clinopyroxene solid solutions formed by reactions between diopside and plagioclase at high pressures. *Mineral. Soc. Amer. Spec. Pap.* 2, 179–191.

Le Bas, M. J. (1989). Nephelinitic and basanitic rocks. *J. Petrol.* 30, 1299–1312. doi: 10.1093/petrology/30.5.1299

Le Gall, B., Nonnotte, P., Rolet, J., Benoit, M., Guillou, H., Mousseau-Nonnotte, M., et al. (2008). Rift propagation at craton margin: distribution of faulting and volcanism in the North Tanzanian Divergence (East Africa) during Neogene times. *Tectonophysics* 448, 1–19.

Lee, C. T., and Rudnick, R. L. (1999). "Compositionally stratified cratonic lithosphere: petrology and geochemistry of peridotite xenoliths from the Labait volcano, Tanzania," in *Proceedings of the VIIth International Kimberlite Conference*, Vol. 1, Cape Town, 503–521.

Lee, W. J., Huang, W. L., and Wyllie, P. (2000). Melts in the mantle modeled in the system CaO–MgO–SiO2–CO2 at 2.7 GPa. *Contrib. Mineral. Petrol.* 138, 199–213. doi: 10.1007/s004100050557

Luth, R. W. (1997). Experimental study of the system phlogopite-diopside from 3.5 to 17 GPa. *Am. Min.* 82, 1198–1209. doi: 10.2138/am-1997-11-1216

Lloyd, F. E., Woolley, A. R., Stoppa, F., and Eby, G. N. (2002). Phlogopite-biotite parageneses from the K-mafic-carbonatite effusive magmatic association of Katwe-Kikorongo, SW Uganda. *Mineral. Petrol.* 74, 299–322. doi: 10.1007/s007100200008

Maaløe, S., James, D., Smedley, P., Petersen, S., and Garmann, L. B. (1992). The Koloa volcanic suite of Kauai, Hawaii. *J. Petrol.* 33, 761–784. doi: 10.1093/petrology/33.4.761

MacDonald, R., Rogers, N. W., Fitton, J. G., Black, S., and Smith, M. (2001). Plume–lithosphere interactions in the generation of the basalts of the Kenya Rift, East Africa. *J. Petrol.* 42, 877–900. doi: 10.1093/petrology/42.5.877

Mana, S., Furman, T., Carr, M. J., Mollel, G. F., Mortlock, R. A., Feigenson, M. D., et al. (2012). Geochronology and geochemistry of the Essimingor volcano: melting of metasomatized lithospheric mantle beneath the North Tanzanian Divergence zone (East African Rift). *Lithos* 155, 310–325. doi: 10.1016/j.lithos.2012.09.009

Mana, S., Furman, T., Turrin, B. D., Feigenson, M. D., and Swisher, C. C. (2015). Magmatic activity across the East African North Tanzanian Divergence Zone. *J. Geol. Soc.* 172, 368–389. doi: 10.1144/jgs2014-072

Masotta, M., Mollo, S., Freda, C., Gaeta, M., and Moore, G. (2013). Clinopyroxene–liquid thermometers and barometers specific to alkaline differentiated magmas. *Contrib. Mineral. Petrol.* 166, 1545–1561. doi: 10.1007/s00410-013-0927-9

Mattsson, H. B., Nandedkar, R. H., and Ulmer, P. (2013). Petrogenesis of the melilititic and nephelinitic rock suites in the Lake Natron–Engaruka monogenetic volcanic field, northern Tanzania. *Lithos* 179, 175–192. doi: 10.1016/j.lithos.2013.07.012

Maumus, J., Laporte, D., and Schiano, P. (2004). Dihedral angle measurements and infiltration property of SiO2-rich melts in mantle peridotite assemblages. *Contrib. Mineral. Petrol.* 148, 1–12. doi: 10.1007/s00410-004-0595-x

McKenzie, D. (1989). Some remarks on the movement of small melt fractions in the mantle. *Earth Planet. Sci. Lett.* 95, 53–72. doi: 10.1016/0012-821x(89)90167-2

McKenzie, D., and O'Nions, R. K. (1991). Partial melt distributions from inversion of rare earth element concentrations. *J. Petrol.* 32, 1021–1091. doi: 10.1093/petrology/32.5.1021

Métrich, N., and Wallace, P. J. (2008). Volatile abundances in basaltic magmas and their degassing paths tracked by melt inclusions. *Rev. Mineral. Geochem.* 69, 363–402. doi: 10.1515/9781501508486-011

Mollel, G. F., Swisher, C. C., Feigenson, M. D., and Carr, M. J. (2008). Geochemical evolution of Ngorongoro Caldera, Northern Tanzania: implications for crust–magma interaction. *Earth Planet. Sci. Lett.* 271, 337–347. doi: 10.1016/j.epsl.2008.04.014

Mollel, G. F., Swisher, C. C., McHenry, L. J., Feigenson, M. D., and Carr, M. J. (2009). Petrogenesis of basalt–trachyte lavas from Olmoti Crater, Tanzania. *J. Afr. Earth Sci.* 54, 127–143. doi: 10.1016/j.jafrearsci.2009.03.008

Mourão, C., Mata, J., Doucelance, R., Madeira, J., Millet, M. A., and Moreira, M. (2012). Geochemical temporal evolution of Brava Island magmatism: constraints on the variability of Cape Verde mantle sources and on carbonatite–silicate magma link. *Chem. Geol.* 334, 44–61. doi: 10.1016/j.chemgeo.2012.09.031

Moussallam, Y., Morizet, Y., Massuyeau, M., Laumonier, M., and Gaillard, F. (2015). CO2 solubility in kimberlite melts. *Chem. Geol.* 418, 198–205. doi: 10.1016/j.chemgeo.2014.11.017

Muravyeva, N. S., and Senin, V. G. (2018). Xenoliths from Bunyaruguru volcanic field: some insights into lithology of East African Rift upper mantle. *Lithos* 296, 17–36. doi: 10.1016/j.lithos.2017.10.023

Neukirchen, F., Finkenbein, T., and Keller, J. (2010). The Lava sequence of the East African Rift escarpment in the Oldoinyo Lengai–Lake Natron sector, Tanzania. *J. Afr. Earth Sci.* 58, 734–751. doi: 10.1016/j.jafrearsci.2010.06.002

Nonnotte, P. (2007). *Etude Volcano-Tectonique de la Zone de Divergence Nord Tanzanienne (Terminaison Sud du Rift Kenyan). Caractérisation Pétrologique et Géochimique du Volcanisme Récent (8 Ma–Actuel) et du Manteau Source. Contraintes de Mise en Place*. Doctoral dissertation, Université de Bretagne occidentale, Brest.

Nonnotte, P., Benoit, M., Le Gall, B., Hémond, C., Rolet, J., Cotten, J., et al. (2011). Petrology and geochemistry of alkaline lava series, Kilimanjaro, Tanzania: new constraints on petrogenetic processes. *Geol. Soc. Am. Spec. Pap.* 478, 127–158. doi: 10.1130/2011.2478(07)

Novella, D., Bolfan-Casanova, N., Nestola, F., and Harris, J. W. (2015). H2O in olivine and garnet inclusions still trapped in diamonds from the Siberian craton: implications for the water content of cratonic lithosphere peridotites. *Lithos* 230, 180–183. doi: 10.1016/j.lithos.2015.05.013

Oppenheimer, C., Pyle, D. M., and Barclay, J. (2003). *Volcanic Degassing*. London: Geological Society of London.

Parat, F., Holtz, F., René, M., and Almeev, R. (2010). Experimental constraints on ultrapotassic magmatism from the Bohemian Massif (durbachite series, Czech Republic). *Contrib. Mineral. Petrol.* 159, 331–347. doi: 10.1007/s00410-009-0430-5

Paslick, C. R., Halliday, A. N., Lange, R. A., James, D., and Dawson, J. B. (1996). Indirect crustal contamination: evidence from isotopic and chemical disequilibria in minerals from alkali basalts and nephelinites from northern Tanzania. *Contrib. Mineral. Petrol.* 125, 277–292. doi: 10.1007/s004100050222

Paterson, M. S. (1982). The determination of hydroxyl by infrared absorption in quartz, silicate glasses, and similar materials. *Bull. Soc. Fr. Minéral. Crist.* 105, 20–29. doi: 10.3406/bulmi.1982.7582

Platz, T., Foley, S. F., and André, L. (2004). Low-pressure fractionation of the Nyiragongo volcanic rocks, Virunga Province, D.R. Congo. *J. Volcanol. Geother. Res.* 136, 269–295. doi: 10.1016/j.jvolgeores.2004.05.020

Pouclet, A., Bellon, H., and Bram, K. (2016). The Cenozoic volcanism in the Kivu rift: assessment of the tectonic setting, geochemistry, and geochronology of the volcanic activity in the South-Kivu and Virunga regions. *J. Afr. Earth Sci.* 121, 219–246. doi: 10.1016/j.jafrearsci.2016.05.026

Pouclet, A., Menot, R. P., and Piboule, M. (1981). Discriminant factor-analysis applied to central Africa rift lavas (Zaire, Rwanda, Uganda). *C. R. Acad. Sci. II* 292:679.

Putirka, K. D. (2008). Thermometers and barometers for volcanic systems. *Rev. Mineral. Geochem.* 69, 61–120. doi: 10.1515/9781501508486-004

Roex, A. P., Späth, A., and Zartman, R. E. (2001). Lithospheric thickness beneath the southern Kenya Rift: implications from basalt geochemistry. *Contrib. Mineral. Petrol.* 142, 89–106. doi: 10.1007/s004100100273

Rogers, N. W., Hawkesworth, C. J., and Palacz, Z. A. (1992). Phlogopite in the generation of olivine-melilitites from Namaqualand, South Africa and implications for element fractionation processes in the upper mantle. *Lithos* 28, 347–365. doi: 10.1016/0024-4937(92)90014-p

Rogers, N. W., James, D., Kelley, S. P., and De Mulder, M. (1998). The generation of potassic lavas from the eastern Virunga province, Rwanda. *J. Petrol.* 39, 1223–1247. doi: 10.1093/petroj/39.6.1223

Rosenthal, A., Foley, S. F., Pearson, D. G., Nowell, G. M., and Tappe, S. (2009). Petrogenesis of strongly alkaline primitive volcanic rocks at the propagating tip of the western branch of the East African Rift. *Earth Planet. Sci. Lett.* 284, 236–248. doi: 10.1016/j.epsl.2009.04.036

Rudnick, R. L., Ireland, T. R., Gehrels, G., Irving, A. J., Chesley, J. T., and Hanchar, J. M. (1999). "Dating mantle metasomatism: U–Pb geochronology of zircons in cratonic mantle xenoliths from Montana and Tanzania," in *Proceedings of the 7th International Kimberlite Conference*, Vol. 2, Cape Town, 728–735.

Rudnick, R. L., McDonough, W. F., and Chappell, B. W. (1993). Carbonatite metasomatism in the northern Tanzanian mantle: petrographic and geochemical characteristics. *Earth Planet. Sci. Lett.* 114, 463–475. doi: 10.1016/0012-821x(93)90076-l

Sato, K., Katsura, T., and Ito, E. (1997). Phase relations of natural phlogopite with and without enstatite up to 8 GPa: implication for mantle metasomatism. *Earth Planet. Sci. Lett.* 146, 511–526. doi: 10.1016/s0012-821x(96)00246-4

Schmidt, K. H., Bottazzi, P., Vannucci, R., and Mengel, K. (1999). Trace element partitioning between phlogopite, clinopyroxene and leucite lamproite melt. *Earth Planet. Sci. Lett.* 168, 287–299. doi: 10.1016/s0012-821x(99)00056-4

Selway, K., Yi, J., Karato, S. I. (2014). Water content of the Tanzanian lithosphere from magnetotelluric data: implications for cratonic growth and stability. *Earth Planet. Sci. Lett.* 388, 175–186. doi: 10.1016/j.epsl.2013.11.024

Simonetti, A., Shore, M., and Bell, K. (1996). Diopside phenocrysts from nephelinite lavas, Napak Volcano, eastern Uganda; evidence for magma mixing. *Can. Mineral.* 34, 411–421.

Soltanmohammadi, A., Gregoire, M., Rabinowicz, M., Gerbault, M., Ceuleneer, G., Rahgoshay, M., et al. (2018). Transport of volatile-rich melt from the mantle transition zone via compaction pockets: implications for mantle metasomatism and the origin of alkaline lavas in the Turkish–Iranian plateau. *J. Petrol.* 59, 2273–2310. doi: 10.1093/petrology/egy097

Stagno, V., Ojwang, D. O., McCammon, C. A., and Frost, D. J. (2013). The oxidation state of the mantle and the extraction of carbon from Earth's interior. *Nature.* 493, 84–88. doi: 10.1038/nature11679

Streck, M. J., Leeman, W. P., and Chesley, J. (2007). High-magnesian andesite from Mount Shasta: a product of magma mixing and contamination, not a primitive mantle melt. *Geology* 35, 351–354.

Sun, S. S., and McDonough, W. S. (1989). Chemical and isotopic systematics of oceanic basalts: implications for mantle composition and processes. *Geol. Soc. Lond. Spec. Publ.* 42, 313–345. doi: 10.1144/gsl.sp.1989.042.01.19

Toplis, M. J., and Carroll, M. R. (1995). An experimental study of the influence of oxygen fugacity on Fe-Ti oxide stability, phase relations, and mineral—melt equilibria in ferro-basaltic systems. *J. Petrol.* 36, 1137–1170. doi: 10.1093/petrology/36.5.1137

Trønnes, R. G. (2002). Stability range and decomposition of potassic richterite and phlogopite end members at 5–15 GPa. *Mineral. Petrol.* 74, 129–148. doi: 10.1007/s007100200001

Vauchez, A., Dineur, F., and Rudnick, R. (2005). Microstructure, texture and seismic anisotropy of the lithospheric mantle above a mantle plume: insights from the Labait volcano xenoliths (Tanzania). *Earth Planet. Sci. Lett.* 232, 295–314. doi: 10.1016/j.epsl.2005.01.024

Waters, F. G. (1987). A suggested origin of MARID xenoliths in kimberlites by high pressure crystallization of an ultrapotassic rock such as lamproite. *Contrib. Mineral. Petrol.* 95, 523–533. doi: 10.1007/bf00402210

Woolley, A. R., and Kjarsgaard, B. A. (2008). Paragenetic types of carbonatite as indicated by the diversity and relative abundances of associated silicate rocks: evidence from a global database. *Can. Mineral.* 46, 741–752. doi: 10.3749/canmin.46.4.741

Yoder, H. S., and Kushiro, I. (1969). Melting of a hydrous phase: phlogopite. *Am. J. Sci.* 267, 558–582.

Zaitsev, A. N., Marks, M. A. W., Wenzel, T., Spratt, J., Sharygin, V. V., Strekopytov, S., et al. (2012). Mineralogy, geochemistry and petrology of the phonolitic to nephelinitic Sadiman volcano, Crater Highlands, Tanzania. *Lithos* 152, 66–83. doi: 10.1016/j.lithos.2012.03.001

frontiers
in Earth Science

ORIGINAL RESEARCH
published: 15 September 2020
doi: 10.3389/feart.2020.554598

Magma Reservoir Formation and Evolution at a Slow-Spreading Center (Atlantis Bank, Southwest Indian Ridge)

Marine Boulanger[1]*, *Lydéric France*[1], *Jeremy R.L. Deans*[2], *Carlotta Ferrando*[1,3], *C. Johan Lissenberg*[4] and *Anette von der Handt*[5]

[1] Université de Lorraine, CNRS, CRPG, Nancy, France, [2] School of Biological, Environmental, and Earth Sciences, University of Southern Mississippi, Hattiesburg, MS, United States, [3] Dipartimento di Scienze Della Terra, Università Degli Studi di Pavia, Pavia, Italy, [4] School of Earth and Ocean Sciences, Cardiff University, Cardiff, United Kingdom, [5] Department of Earth Sciences, University of Minnesota, Minneapolis, MN, United States

Edited by:
Frank John Spera,
University of California, Santa Barbara,
United States

Reviewed by:
Henry J. B. Dick,
Woods Hole Oceanographic
Institution, United States
Michael Perfit,
University of Florida, United States
Jon Blundy,
University of Bristol, United Kingdom

***Correspondence:**
Marine Boulanger
marineb@crpg.cnrs-nancy.fr

Specialty section:
This article was submitted to
Petrology,
a section of the journal
Frontiers in Earth Science

Received: *22 April 2020*
Accepted: *21 August 2020*
Published: *15 September 2020*

Citation:
Boulanger M, France L, Deans J. R. L.,
Ferrando C, Lissenberg C. J. and
von der Handt A (2020).
Front. Earth Sci. 8:554598.
doi: 10.3389/feart.2020.554598

Several ODP-IODP expeditions drilled oceanic core complexes interpreted as exhumed portions of lower crust close to the ridge axis, and provide the community with invaluable sampling opportunity for further constraining magmatic processes involved in the formation of the slow-spreading lower oceanic crust. ODP Hole 735B presents the most primitive lithologies sampled at Atlantis Bank oceanic core complex (Southwest Indian Ridge) in a ~250 m thick section that was previously interpreted as a single crustal intrusion. We combined detailed structural and petrographic constraints with whole rock and *in situ* mineral analyses of this section in order to precisely determine the processes of emplacement, crystallization, and melt migration within the lower crust. The lower half of the unit is comprised of alternating olivine gabbros and troctolites showing intrusive contacts, magmatic fabrics, and crystal-plastic fabrics. Such structures and primitive lithologies are lacking in the upper half, rather uniform, gabbroic sequence. Whole rock compositions highlight the cumulative character of both lower and upper units and a great compositional variability in the lower sequence, whereas the upper sequence is homogeneous and differentiates up-section. *In situ* analyses of mineral phases document magma emplacement processes and provide evidence for ubiquitous reactive porous flow (RPF) during differentiation. We show that the whole section, and related geochemical unit, constitutes a single magmatic reservoir, in which the lower unit is formed by stacked primitive sills formed by repeated recharge of primitive melts and melt-present deformation. Recharge led to partial assimilation of the crystallizing primitive cumulates, and hybridization with their interstitial melts. Hybrid melts were progressively collected in the overlying mushy part of the reservoir (upper unit), whereas the sills' residual hybrid melts differentiated by RPF processes under a predominantly crystallization regime. Similarly, hybrid melts' evolution in the upper unit was governed by upward RPF, and progressive differentiation and accumulation of evolved melts at the top of the reservoir. Our results provide the community with the first integrated model for magma reservoir formation in the lower slow-spreading oceanic crust that can potentially be applied to other magmatic lower crust sections.

Keywords: Atlantis Bank, lower oceanic crust, magma intrusion, crystal mush, reactive porous flow, assimilation-fractional crystallization

INTRODUCTION

Slow-spreading ridges represent more than 50% of the global oceanic ridge system (spreading rates <40 mm year^{-1}, Dunn, 2015) and are characterized by both heterogeneous crustal structure (e.g., oceanic core complexes or OCCs) and composition. Most of this heterogeneity can be linked to uneven distribution of melt generation within the mantle below the ridge axis (e.g., Tucholke and Lin, 1994; Dunn et al., 2005; Rubin and Sinton, 2007; Dunn, 2015 and references therein). Uneven melt supply results in the formation of intermittent and discontinuous magma reservoirs within the crust (e.g., Dick et al., 2003; Carbotte et al., 2015), contrasted reservoir geometry (axial magma chamber or sill intrusions; Jian et al., 2016; Canales et al., 2017), and variable depth of melt emplacement which can range between 2 and 16 km depth below seafloor (Dunn et al., 2005; Singh et al., 2006; Canales et al., 2017; Bennett et al., 2019). The common thread running through all processes that potentially govern magma accretion at spreading ridges is the importance of melt migration mechanisms involved. Among them, reactive porous flow (RPF) tend to be considered ubiquitous during the evolution of gabbroic magma reservoirs, since crystal mushes forming porous and permeable frameworks constitute the principal medium of the magma plumbing system (Lissenberg et al., 2019 and references therein).

Long *in situ* sections of lower slow-spreading oceanic crust have been sampled by deep drilling in OCCs. These structures form during asymmetric spreading at the ridge axis and associated exhumation of both lower oceanic crust and upper mantle (e.g., Dick et al., 1991b; Escartín et al., 2003; Ildefonse et al., 2007). Two drilled holes have reached more than 1,400 mbsf (meters below sea floor), one in the Atlantis Massif OCC on the Mid-Atlantic Ridge (MAR, IODP Hole U1309D), and the other in the Atlantis Bank OCC on the Southwest Indian Ridge (SWIR, ODP Hole 735B). Their study enabled to characterize the modes of magma emplacement and evolution at these locations, but only at a large scale (Dick et al., 2000; John et al., 2004; Grimes et al., 2008; Godard et al., 2009; Dick et al., 2019a). The crust appears highly heterogeneous in both complexes and lacks any systematic downhole variations in modal compositions, or clear lateral continuity as evidenced from multiple drill holes, for example, at Atlantis Bank (Dick et al., 2000; MacLeod et al., 2017; Dick et al., 2019a). Despite the disparities between the ODP Hole 735B and IODP Hole U1309D, similar types of magma emplacement mechanisms have been inferred, which suggests a continuity of processes for the accretion of slow-spreading lower oceanic crust (Blackman et al., 2006; Dick et al., 2019a; Dick et al., 2019b). Whole rock compositions, together with the lack of modal downhole variations, led Godard et al. (2009) to interpret the cumulate sequence sampled in Atlantis Massif as the result of multiple magma intrusions. Upward differentiation trends on >200 m thicknesses have been identified in ODP Hole 735B based on whole rock major element compositions (Dick et al., 2000; Natland and Dick, 2002), and *in situ* mineral compositions (Dick et al., 2002). These trends are interpreted as the result of cyclic major magmatic events that formed by multiple intrusions and differentiated *in situ* during large-scale upward percolation of melts (Dick et al., 2000; Dick et al., 2019a). In addition, detailed studies of individual samples collected in drilled cores from Atlantis Massif and Atlantis Bank enabled workers to find evidence for extensive melt-rock or melt-mush reactions (e.g., in olivine-rich troctolites from Hole U1309D, Suhr et al., 2008; Drouin et al., 2009; Ferrando et al., 2018; or in gabbroic samples from Hole 735B, Robinson et al., 2000; Natland and Dick, 2001; Dick et al., 2002; Gao et al., 2007), suggesting that these processes likely play a substantial role in the differentiation of melts in the lower crust (Lissenberg and MacLeod, 2016; Dick et al., 2019a).

Here, we integrate structural, petrographic and high-resolution geochemical data of a ~250 m section from ODP Hole 735B characterized as a single intrusion by Dick et al. (2000) and Natland and Dick (2002). We reconstruct the different steps of evolution of this magma reservoir, leading to the first detailed reservoir model for a slow-spreading lower oceanic crust section. We particularly focused on the impact of RPF processes on the reservoir by using modeling and the assimilation-fractional crystallization (AFC) equation of DePaolo (1981). The novelty of our approach here is to consider an entire sample suite interpreted as representative of an entire reservoir for the study of RPF, instead of individual samples as considered in previous studies on the lower (slow-spreading) oceanic crust.

GEOLOGICAL SETTING

The Atlantis Bank OCC is located on the eastern flank of the Atlantis II Transform Fault ~95 km south of the ultra-slow SWIR (Dick et al., 1991b—**Figure 1**). The ~2 km uplift of lower crust lithologies at Atlantis Bank is the consequence of a ~1 km flexural uplift due to detachment faulting, exacerbated by transform-parallel normal faulting on the eastern flank of the structure. The latter event is linked to a change of spreading direction at the ridge axis between 19.5 and ~7.5 Ma (Baines et al., 2003, Baines et al., 2007). The OCC is mainly composed of gabbroic lithologies, bordered to the East by extrusive lithologies (dikes and pillow lavas) and to the West by mantle lithologies affected by variable degrees of serpentinization (Dick et al., 2000; MacLeod et al., 2017; Dick et al., 2019b). The top of the structure is defined by a 4 km-wide and ~8.5 km-long horizontal platform at ~700 m depth below sea level, in which three deep holes have been drilled by the ODP/IODP consortium (MacLeod et al., 2017).

The deepest and most studied core so far is ODP Hole 735B, which reached a total depth of 1,508 mbsf, and recovered ~1,300 m of gabbroic lithologies. The 735B drilled cores are composed of 68% olivine gabbros, 23% oxide and oxide-bearing gabbros, in addition to 5% troctolites and troctolitic gabbros (1.9% troctolites *sensu stricto*, Dick et al., 2019a) and 4% gabbros *sensu stricto* (MacLeod et al., 2017). Some minor

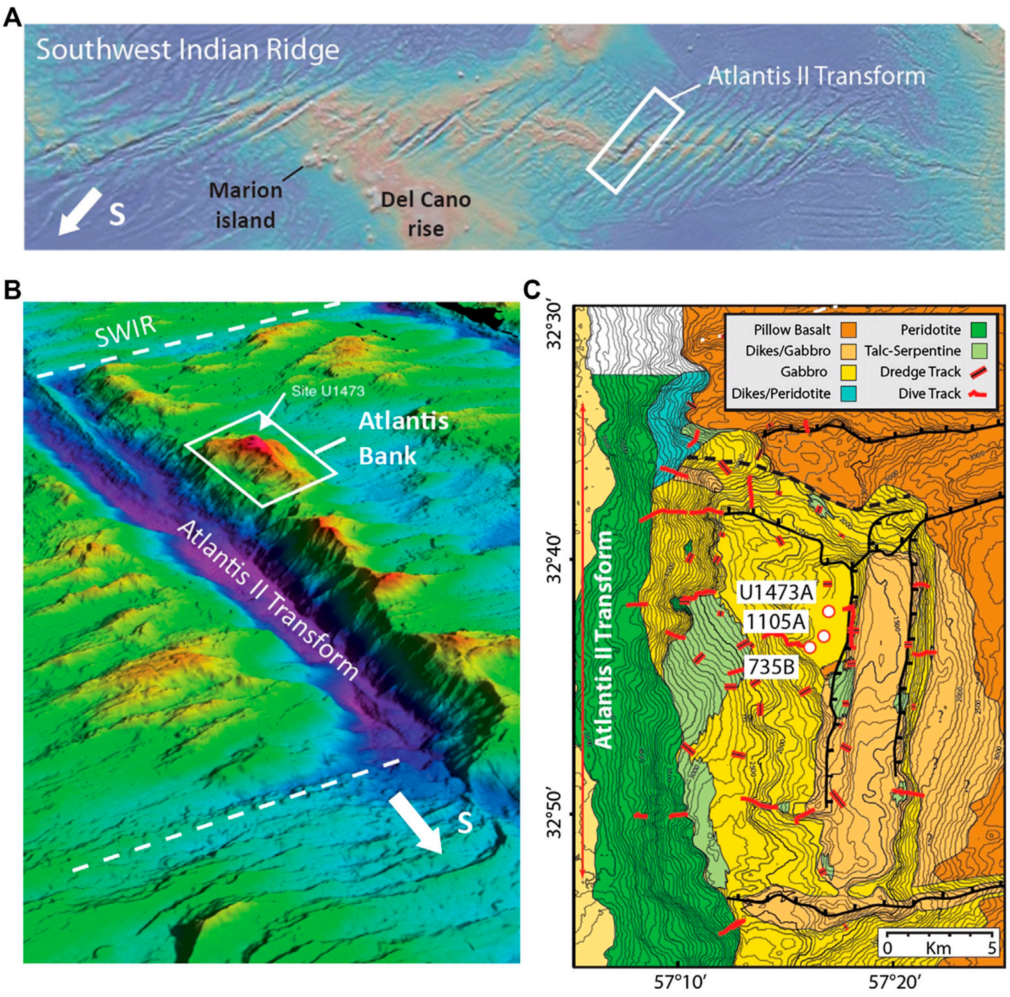

FIGURE 1 | (A) Location map of the Atlantis II Transform on the Southwest Indian Ridge, **(B)** 3D bathymetric map of the Atlantis II Transform and location of the Atlantis Bank Oceanic Core Complex (IODP Publications), and **(C)** geological map of the Atlantis Bank oceanic core complex and location of ODP Holes 735B and 1105A, and IODP Hole U1473A (modified from Dick et al., 2019b).

lithologies such as diabase dikes and felsic veins were also recovered (Dick et al., 2000). Whole rock and *in situ* major element compositions indicate three to five upward differentiation trends (**Figure 2**). Each trend has been interpreted as the signature of individual intrusions, potentially crosscutting each other, and emplaced during large magmatic events by multiple intrusions (Dick et al., 2000; Dick et al., 2002; Dick et al., 2019a). In this study we focus on the second unit from the top (274–53 mbsf), which contains some of the most primitive lithologies in the hole (Mg# = molar ratio Mg/[Mg + Fe_{tot}] × 100, of Ti-poor lithologies ranging between 74.5 and 86.8—MacLeod et al., 2017). The selected unit is relatively fresh and one of the least deformed of the drilled section, and presents the entire compositional range of rocks recovered in Hole 735B. U-Pb zircon dates suggest intrusion of the series ranging from 11.974 to 11.926 Ma (Rioux et al., 2016).

The intrusion has been described as two separate units (V and VI) during ODP Leg 118 and Leg 176 (Dick et al., 1991a; Dick et al., 2000). The upper unit, Unit V, is a massive 108.3 m-long olivine gabbro unit. The lower unit, Unit VI, is described as a 153.6 m-long "lower compound olivine gabbro," including more than 200 distinct igneous intervals (Dick et al., 2000). In detail, Unit VI is composed of four interleaved subunits of olivine gabbros or troctolites, crosscut by various amounts of "synkinematic" oxide gabbros (Dick et al., 2000). Oxide-rich lithologies are often associated with strain localization (Natland et al., 1991; Dick et al., 2000), and are more common in Unit VI. The intrusion is bordered at the top by a 50.5 m-long massive oxide gabbro unit (Unit IV) and at the bottom by a 63 m-long evolved gabbroic unit (Unit VII).

METHODS

The structure and textures of Unit V and VI from ODP Hole 735B were re-described at the Kochi Core Center, Japan. Igneous

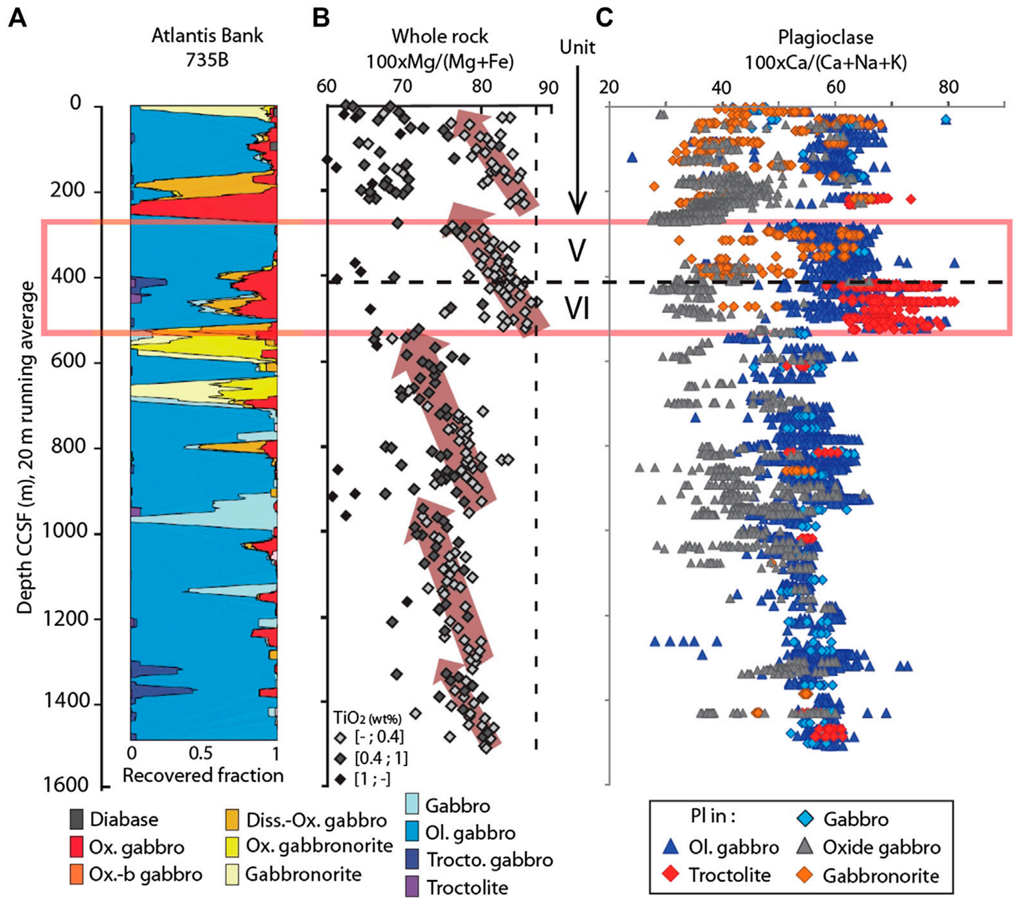

FIGURE 2 | Comparison between **(A)** the lithostratigraphic variations of Hole 735B with relative abundances averaged over 20 m (from Macleod et al., 2017), **(B)** the corresponding shipboard X-ray fluorescence (XRF) whole rock gabbro Mg# trends (modified from Dick et al., 2000), and **(C)** *in situ* plagioclase An content (data from Dick et al., 2002).

contacts used here were initially defined and delineated by the Shipboard Scientific Party (Dick et al., 1999), and are defined by changes in mineral proportion and/or grain size; sheared contacts are also observed. Magmatic fabrics are defined by a shape preferred orientation of igneous phases like plagioclase, pyroxene, and/or olivine with no to little internal crystal-plastic strain and no recrystallization. Crystal-plastic fabrics are defined by a shape preferred orientation of porphyroclasts and neoblasts with internal crystal-plastic strain. The level of fabric development of each fabric type is based on a qualitative ranking system plotted as a thickness corrected running average developed by the Shipboard Scientific Party (following Dick et al., 1999—**Figure 3**). Magmatic fabrics range from no alignment, rank of 0, to almost all phases aligned, rank of 3. Crystal-plastic fabrics range from no alignment, rank of 0, to porphyroclastic (close to equal proportion of porphyroclasts and neoblasts), rank of 3, to ultramylonite, rank of 5.

In total, 95 gabbroic lithologies (characterized as olivine gabbros and troctolites by Dick et al., 1999) were resampled to get representative samples exhibiting the entire range of compositional variation observed in the available whole rock data (**Supplementary Table S1**; **Figure 2**). Only rocks characterized as olivine gabbros and troctolites were sampled in order to focus on the early and intermediate stages of the magmatic differentiation. We excluded oxide gabbros also present in the lower ~150 m of the sequence that are associated with highly differentiated, late-stage melts, as emphasized by MacLeod et al. (2017) and supported by the experimental work of Koepke et al. (2018). In addition, many oxide gabbros present evidence for late emplacement by deformation-assisted intrusion of an oxide-bearing melt in a more primitive gabbroic host in disequilibrium (Koepke et al., 2018 and references therein). We also excluded samples presenting strong crystal-plastic deformation or alteration features that might have disrupted their initial magmatic geochemical signatures. The mineral mode of 50 of the samples was determined by using the ImageJ software on thin section scans (Schneider et al., 2017; http://imagej.nih.gov/ij/).

Major element contents of minerals from 78 samples were quantified by Electron Probe Micro Analyzer at Laboratoire Magmas et Volcans (Clermont-Ferrand, France) and the University of Minnesota (United States). The thin sections

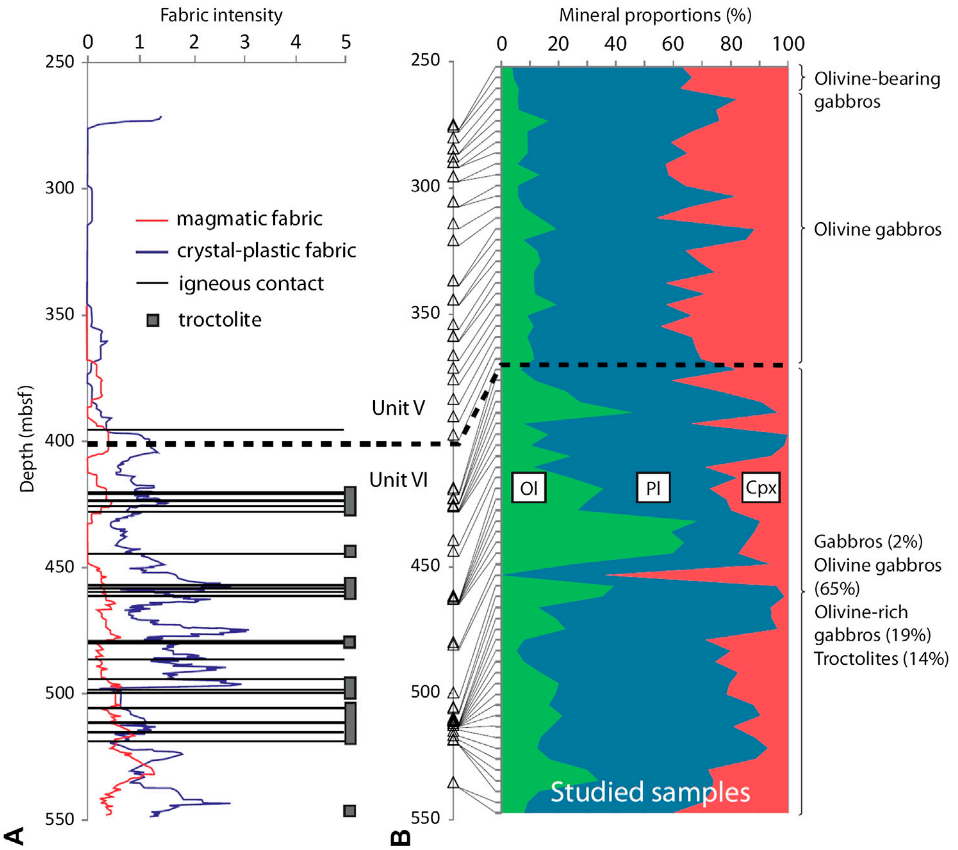

FIGURE 3 | (A) Downhole distribution of fabric intensity for the section studied. Red line is magmatic fabric intensity (0–3); blue line is crystal-plastic fabric intensity (0–5). The fabric intensity is a qualitative scale developed by Shipboard Scientific Party (1999) and the intensity is plotted as a thickness-corrected running average. The horizontal black lines represent igneous contacts (Natland and Dick, 2002; their **Table 1**). The gray boxes are the location of troctolites. **(B)** Location at depth of the samples collected in Units V and VI (units' name after Dick et al., 2000) with their corresponding modal compositions. The black dotted line represents the approximate transition between the Lower and the Upper unit.

analyzed were selected according to their lack of alteration or strong crystal plastic deformation, and for sampling at regular intervals of <5 m on average between each group of samples. In order to get the entire compositional variability of minerals from the selected samples, when possible at least three grains of the main constituting minerals were analyzed in on average 5 representative areas of the thin section. For each grain, core and rim (geometrical) were analyzed. At Clermont-Ferrand, we used a Cameca SX100 equipped with four wavelength-dispersive X-ray spectrometers. Analyses were performed with a 15 kV accelerating potential and a focused beam using a 15 nA beam current. Counting times were of 10 or 20 sec on peak and also for background. At Minnesota, we used a JEOL JXA-8900 equipped with four wavelength-dispersive X-ray spectrometers. Analyses were performed with a 15 kV accelerating potential, a beam current of 20 nA, and beam diameters of 10 µm for clinopyroxene, 5 µm for plagioclase, and 1 µm for olivine. Counting times were of 10 s on peak and off peak for all elements. The data and associated analytical errors are available in **Supplementary Material** (see details and calibration standards for each element in **Supplementary Table S2**).

Mineral trace elements of 24 samples were analyzed *in situ* with a ThermoFinnigan Element2 XR inductively coupled plasma mass spectrometer (eXtended Range—ICP-MS) coupled with a laser ablation (LA) system Téledyne G2 at Géosciences Montpellier (AETE-ISO regional facility of the OSU OREME, Montpellier University, France). Where possible, the same analytical strategy as for major element measurements regarding the selection of samples and the location of *in situ* analyses was followed. Signal acquisition was made in Time Resolved Acquisition, counting 120 sec for the background, and 60 sec for the sample measurement. The frequency of the laser was of 10 Hz, with an energy density of ~6.2 J cm^2. Ablation experiments were conducted under helium which was mixed with argon before entering the plasma. Clinopyroxenes (Cpx) were analyzed with a laser spot size of 77 µm, while a spot size of 102 µm was used for olivines (Ol) and plagioclases (Pl). Data were processed using the GLITTER software (van Achterbergh et al., 2001). All measured concentrations were calibrated using the synthetic glass NIST 612 with the values of Pearce et al. (1997). The internal standards used for the minerals are ^{43}Ca for Cpx, and ^{29}Si for Pl and Ol, with the values previously analyzed in the same minerals by Electron Probe Micro Analyzer. An average of the values analyzed by LA-ICP-MS for the standard reference basalt BIR-1G is available in **Supplementary Table S3**, together with all trace elements data and associated errors.

RESULTS

Although whole rock geochemical trends suggest a first-order relative continuity of compositions (e.g., Mg#—**Figure 2**), the section can be divided in two distinct units based on structural, lithological, and geochemical criteria. In the following we refer to the Upper unit and to the Lower unit, which together correspond to the ensemble formed by Unit V and Unit VI as described by Dick et al. (2000). We first describe the structural and petrographic variations and then describe the compositional variations in each unit.

Structure and Petrographic Variations

The Lower unit (~400–530 mbsf) is heterogeneous and presents numerous igneous contacts recovered at different depths all along the section. Intrusive contacts separate subunits whose thicknesses range from meters to tens of meters. Lithologies range from the more primitive troctolites and olivine-rich gabbros to olivine gabbros and olivine-bearing gabbros (**Figure 3B**). Oxide gabbros are also present within this unit, and are associated with deformed areas present throughout the interval. The presence of igneous contacts is very frequently associated with the presence of troctolites *sensu lato* (i.e., Ol-rich lithologies—**Figure 3A**). Within each subunit defined by the igneous contacts, the transition between lithologies is gradational. The modal proportion of Ol tends to decrease (from 69 to 4%) and proportions of Cpx increase (from 1 to 64%) toward the top of each subunit. This is especially the case for one subunit located at ~510 mbsf and described in Hole 735B cores 90R-2 and 90R-3 (see **Supplementary Figure S1**). From bottom to top of the subunit, the modal composition of lithologies progressively change from troctolites with <5% interstitial Cpx and up to ~25% Ol, to Ol gabbros with up to 40% Cpx and <5% Ol. Samples' textures are subophitic to granular with grain size varying from medium-to coarse-grained. All lithology types may record a crystal-plastic fabric at all intensity ranks, and whose intensity is highly variable with depth (**Figure 3A**; **Supplementary Figure S2**). The sampled lithologies representing the primary magmatic background of the sequence show magmatic fabrics whose intensity and orientation vary along the section. A maximum intensity of ~2 is reached at the bottom of the sequence, at about 530 mbsf (**Figure 3A**). No clear systematics between the orientation and intensity of the magmatic fabric, and depth can be observed. Common mineral textures in the Lower unit are rounded Ol chadacrysts in poikilitic Pl or Cpx in troctolites (**Figure 4D**), Pl crystals presenting discordant polysynthetic twins on their irregular grain boundaries in poikilitic Cpx (**Figures 4A–C**), and/or Pl crystals with similar irregular grain boundaries and complex optical zoning in Ol gabbros (green arrows, **Figures 4B–D**). Such textures have previously been interpreted as evidence for RPF (e.g., Lissenberg and MacLeod, 2016), and are better developed in samples with magmatic fabrics in Ol gabbros. Sparse minerals presenting intragrain deformation, such as tapered twins in Pl and subgrain development in Ol are also locally observed in the samples.

The Upper unit, ~274–400 mbsf, is composed of Ol gabbros with rather homogeneous modal compositions (**Figure 3B**), and on average 60% Pl, 30% Cpx, and 10% Ol. The highest crystal-plastic fabric ranks are at the bottom of the unit near the contact with the Lower unit, with a maximum of ~2 at 367 mbsf; the rest of the unit is almost devoid of crystal-plastic and magmatic fabrics. No igneous contacts were observed in this unit. At the very top of the unit at ~ 275 mbsf, the Ol proportions decrease down to 4% with the presence of more differentiated Ol bearing gabbros (**Figure 3B**) and the return of crystal-plastic fabric between 271 and 273 mbsf. The initial description by Dick et al. (2000) characterized these last samples as felsic veins, due to the presence of several areas of conjugated veins filled with felsic material crosscutting the primary gabbroic lithology. Closer to the veins, minerals present interaction textures with amphibole rims around Cpx, mostly dissolved Ol grains and strongly zoned Pl. Similar lithologies have been reported from Atlantis Bank IODP Hole U1473A; those are referred to as "felsic rocks with diffused boundaries (vein-D)" by Nguyen et al. (2018), and interpreted as felsic melt infiltration into solidifying gabbros. More generally in olivine gabbros, mineral textures such as intergrown Cpx, Cpx with symplectite textures, Pl crystals with discordant polysynthetic twins on irregular grain boundaries and/or complex optical zoning are common (**Figures 4A,B**). Again, such textures are interpreted as evidence for RPF (e.g., Lissenberg and MacLeod, 2016), and minerals presenting intragrain deformation, such as tapered twins in Pl and subgrain development in Ol are also locally observed, but are less common compared to the observations made in the Lower unit. In closing, the Upper unit is homogeneous, lacking strong magmatic, and crystal-plastic fabrics along with intrusive contacts compared with the Lower unit (**Figure 3A**).

Whole Rock and *In Situ* Geochemical Compositions

The 154 whole rock compositions used herein for the Upper and Lower units are from the Shipboard Scientific Party of Leg 118 (1989), Dick et al. (1999), Dick et al. (1991a), Hart et al. (1999), Hertogen et al. (2002), Holm (2002), and Niu et al. (2002), with four additional unpublished ones analyzed at SARM-CRPG (CNRS, Nancy, France). The rare earth element (REE) compositions of both Ol gabbros and troctolites are all depleted relative to an average primitive MORB from the Atlantis Bank area (value in **Supplementary Table S4**) and span similar compositional ranges. The La_N contents of Ol gabbros vary between 0.12 and 1.09 and between 0.10 and 0.74 for troctolites, and the Lu_N contents vary between 0.07 and 0.81 for Ol gabbros and between 0.1 and 0.86 for troctolites (see **Supplementary Table S1**). Likewise, samples of both lithologies present weak to strong positive Eu anomalies, which vary between 0.41 and 2.93 with an average of 1.60 for Ol gabbros and 1.89 for troctolites. Both units present Ol gabbro and troctolite samples with weak to strong cumulative signatures in REE, a geochemical cumulate character of the lithologies that was

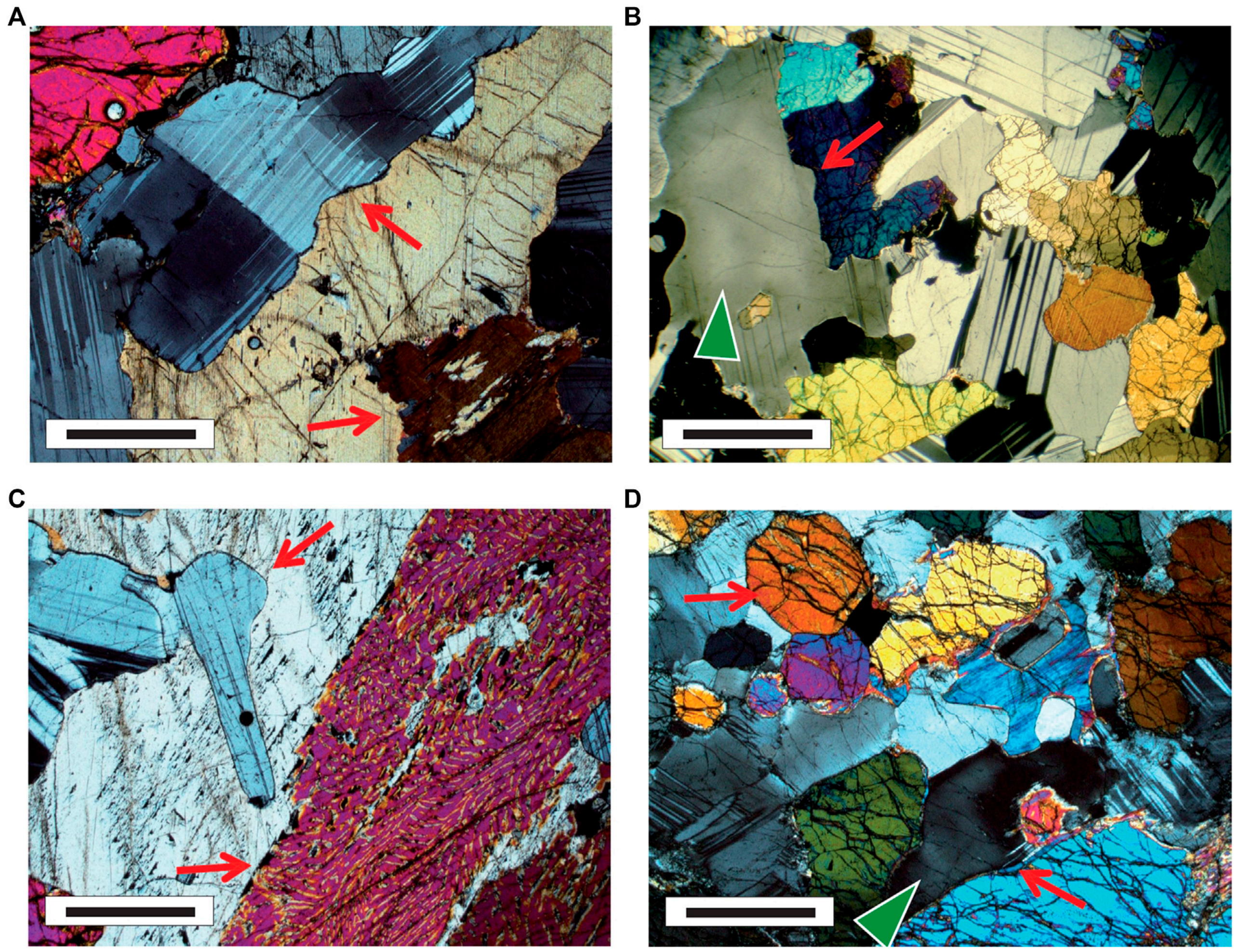

FIGURE 4 | Microphotographs in polarized light of samples from the Upper unit **(A,B)** and the Lower unit **(C,D)**. Scale bar: 500 µm. All samples have magmatic fabrics and crystal-plastic fabrics ranks of 0. **(A)** Sample 735B-60R-4, 115 cm (295.38 mbsf): plagioclase grain presenting irregular grain boundaries (top red arrow) and clinopyroxenes intergrowth (bottom arrow). **(B)** Sample 735B-72R-3, 0 cm (358.5 mbsf): plagioclase grain presenting complex zoning (green arrow) and irregular grain boundaries (red arrow). **(C)** Sample 735B-81R-5, 7 cm (439.24 mbsf): plagioclase grain with irregular grain boundaries (top arrow) engulfed in a clinopyroxene crystal presenting symplectite textures (bottom arrow). **(D)** Sample 735B-83R-7, 130 cm (462.55 mbsf): Rounded-shape olivine crystals (top arrow) and plagioclase presenting complex zoning (bottom arrows).

also identified by Dick et al. (2000) and Dick et al. (1991a). Compatible element contents (e.g., Cr) and Mg# recorded in the Lower unit reach higher values compared to the Upper unit, with Cr contents up to 3,670 ppm and Mg# up to 86.8 in the Lower unit, whereas in the Upper unit the values reach up to 900 ppm Cr and 82.9 in Mg# (**Figure 5**). This highlights a more primitive character recorded in lithologies below ~400 mbsf. Compositions are also more variable in the Lower unit, with, for example, variation ranges in Cr contents of ~3,500 ppm in the Lower unit and of only ~750 ppm in the Upper unit, and lower minimum Cr contents reached in the Lower unit. The Upper unit, in contrast, shows a progressive upward decrease in Mg# (ranging between 82.8 and 67) and relatively uniform compositions through depth in compatible and incompatible trace elements, except in the very top ~50 m of the unit where, for example, the Cr contents decrease from ~380 to ~25 ppm (**Figure 5B**).

In situ mineral major and compatible trace element compositions of the samples collected in depth along the section (**Figure 3**) are consistent with whole rock data. The maximum *in situ* An content of Pl (An content = molar ratio Ca/[Ca + Na + K] × 100), Fo content of Ol (Fo = molar ratio Mg/[Mg + Fe + Mn] × 100) and of Mg# and Cr contents of Cpx are higher in the Lower unit compared to the corresponding maximum values in the Upper unit (**Figure 6**). The same parameters are also more heterogeneous in the Lower unit regardless of the lithology considered (troctolite or Ol gabbro). In addition, the compositional variability recorded in a single sample or at the same depth is much greater in the Lower unit compared to the Upper one. For example, the Cpx Cr contents range between 1,880 and 8,520 ppm at 462 mbsf (variation of 6,640 ppm), when on average at a single depth the Cr content only varies ~1,500 ppm in the Upper unit. In the upper ~20 m of

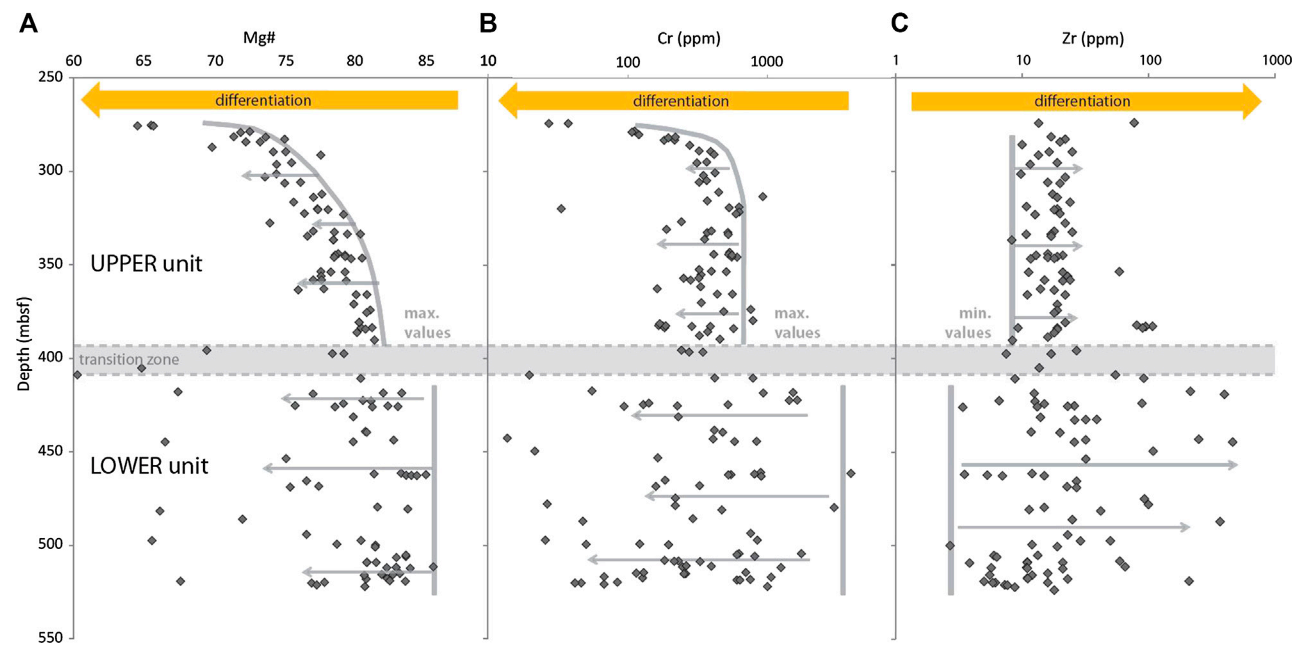

FIGURE 5 | Downhole evolution of whole rock Mg# (**A**—molar ratio Mg/[Mg + Fe_{tot}] × 100), Cr content (**B**—in ppm) and Zr content (**C**—in ppm) in Hole 735B Upper and Lower unit. Gray trends represent the more primitive values (maximum or minimum values) and gray arrows the schematic extent of differentiation at a given depth.

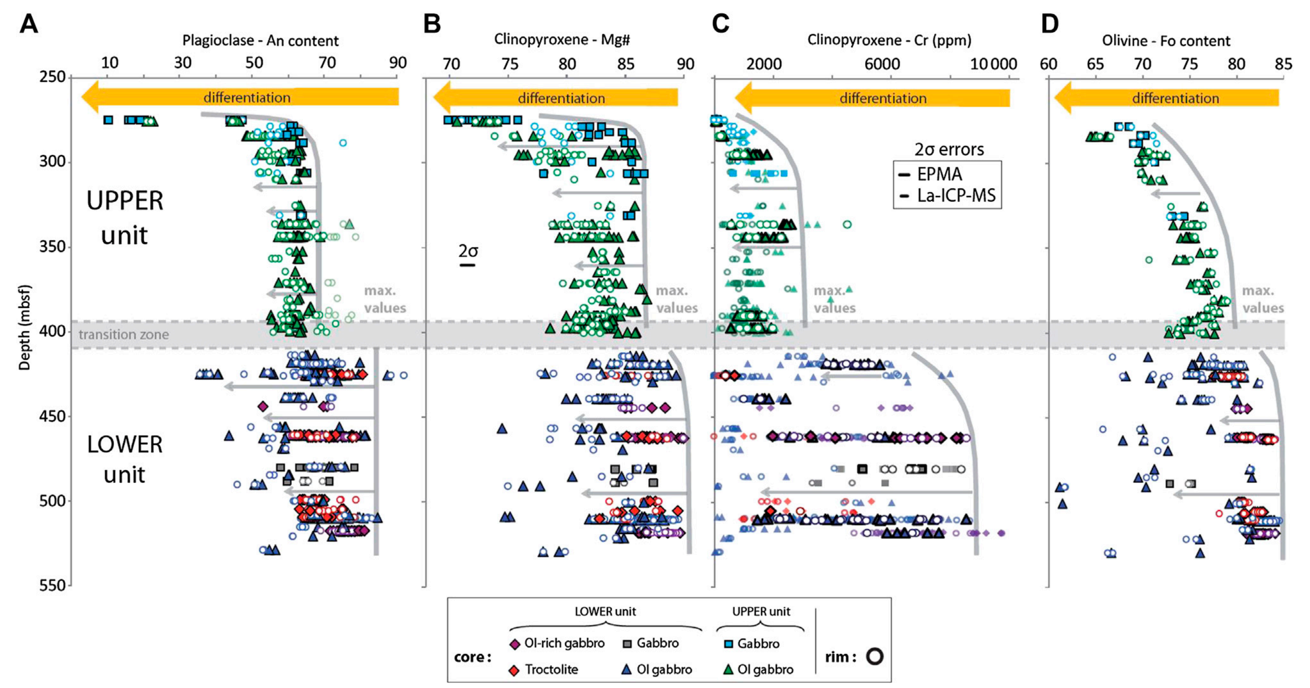

FIGURE 6 | Downhole composition evolution along Hole 735B Upper and Lower unit of *in situ* **(A)** plagioclase An content, **(B)** clinopyroxene Mg#, and **(C)** clinopyroxene Cr content (in ppm). Gray trends represent the maximum values and gray arrows the schematic extent of differentiation at a given depth. The light green rims with the high An contents (right to the gray trend) in **(A)** present in the Upper unit are very local <10 µm An-rich rims discussed in *Model of Emplacement and Evolution of the Magma Reservoir*. Average 2*σ* error values indicated in **(B,C)**, inferior to the symbols' size in **(A,D)**.

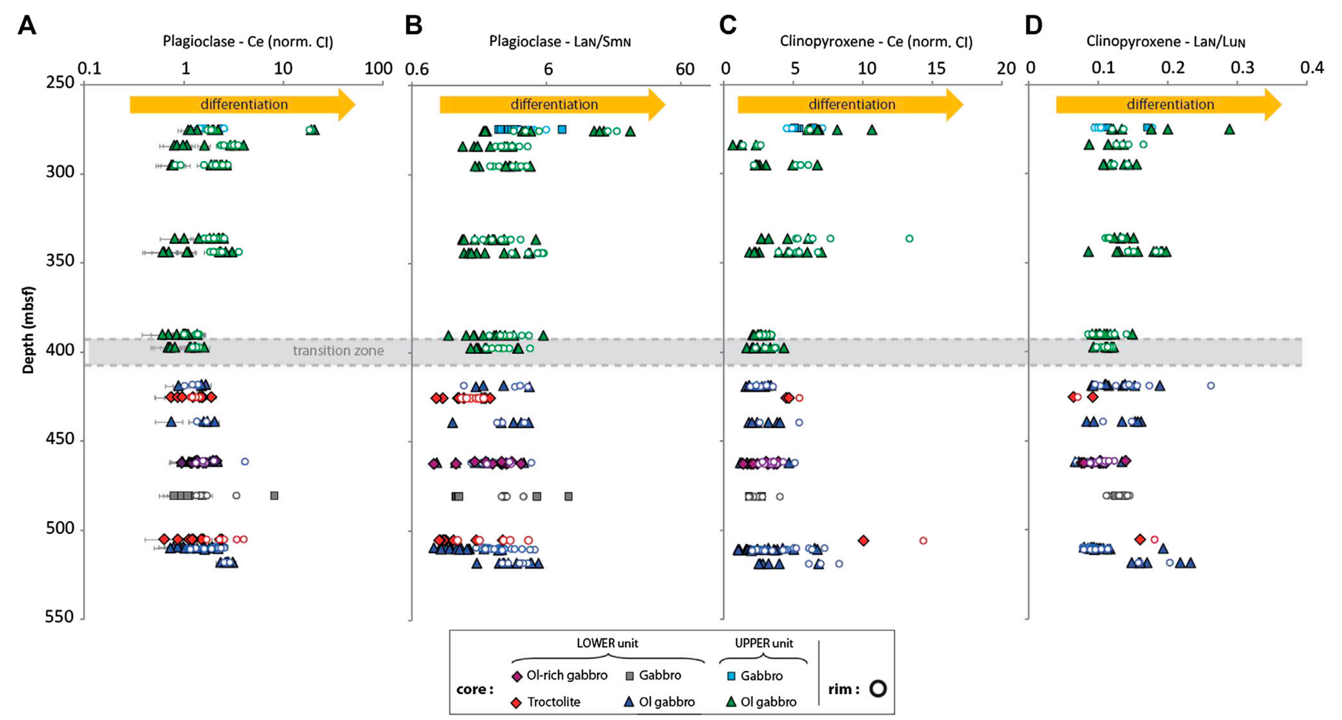

FIGURE 7 | Downhole composition evolution along Hole 735B Upper and Lower unit of *in situ* **(A)** plagioclase Ce content, **(B)** plagioclase ratio La (Light REE) on Sm (Middle REE), **(C)** clinopyroxene Ce content, and **(D)** clinopyroxene ratio La (Light REE) on Lu (Heavy REE). Normalization values ($_N$) for CI chondrites after McDonough and Sun (1995). Average 2σ error within the symbols' size on every plot except **(A)**.

the Upper unit, the Cpx Mg# and Cr contents and the Pl An content drop to the lowest values recorded in the section (**Figure 6**). The compositions fall down to 61.9 Mg#, no Cr, and 10.4 An contents (and 0.2 Or component) in the Ol gabbros crosscut by felsic veins with diffuse boundaries. No clear systematic zoning of the minerals is observed in major and compatible elements in the Lower unit. In the Upper unit below ~320 mbsf, no clear systematic zoning is observed, although on average minerals' Cpx rims have slightly lower Mg# (82.4) than cores (83.3). Above ~320 mbsf, more systematic zoning is observed, with Cpx rims showing lower Mg# and Cr contents (<~82 and ~1,020 ppm, respectively) compared to cores (up to 86.6 and ~1,800 ppm, respectively—**Figure 6**). The same tendencies cannot be observed for Pl. Some Pl grains present, at the very grain boundary, 5–10 μm wide An-rich rims with contents varying between 67 and 79 (**Figure 6**). These An-rich rims are only observed in the bottom half of the Upper unit.

In situ mineral REE compositions and fractionations are not correlated with depth in the Lower and Upper units. Pl Ce_N contents vary between 0.6 and 4 all along the section, only one analysis in the Lower unit reaches 8.2, and in the Upper unit the shallowest samples associated with felsic material present Pl Ce_N contents reaching up to 20.5 ppm (**Figure 7A**). The same tendency can be described for the Cpx Ce_N contents, which vary between 0.7 and 8.2 ppm in both units. Locally the compositions can reach up to 14 ppm, such as in the troctolite sample located at 505 mbsf (**Figure 7C**). The fractionation ranges between light REE and middle REE in Pl and light REE and heavy REE in Cpx are also very similar between the Upper and the Lower unit. Pl La_N/Sm_N ratios vary between 0.9 and 6 through the entire section (and reach up to 36.7 for the samples associated with felsic material, **Figure 7B**), with slightly higher lower bound for the Upper unit (lowest La_N/Sm_N of 1.1). The same tendency can be described for Cpx, with La_N/Lu_N ratios varying between 0.07 and 0.23 through the entire section (and reaching up to 0.29 for the samples associated with felsic material, **Figure 7D**). Incompatible elements are on average more enriched in mineral rims (**Figure 7** and **8**). This is the case, for example, for Ti in Cpx (average core to rim varies from 4,310 to 5,000 ppm) and La in Pl (0.59–0.62 ppm), or Ce in both minerals (2.09–2.49 ppm, and 1.26–1.36 ppm). Cpx Ti contents increase to higher contents for a given Mg# in the most primitive minerals of the Lower unit (and especially the rims, with Mg# > 85, up to 1.8 wt% TiO_2) compared to the minerals in the Upper unit (**Figure 8A**). Oppositely, REE content in Pl varies within similar ranges of compositions for the Upper and Lower units despite significant differences in the minerals' major element contents, as already described above. The Pl La_N content ranges between 0.58 and 4.35 in the Lower unit for an average mineral's An content of 69.3 (ranging between 10 and 78.9), and ranges between 0.58 and 4.6 in the Upper unit for an average mineral's An content of 55.4 (ranging between 35.6 and 87.7, **Figure 8B**).

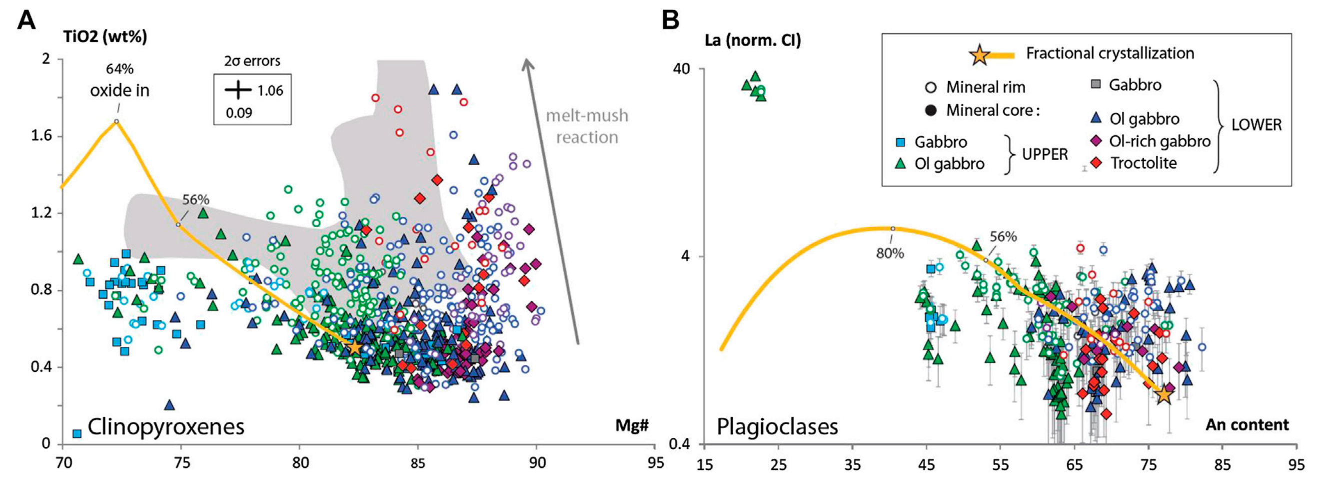

FIGURE 8 | (A) TiO$_2$ concentrations in clinopyroxenes plotted against the minerals' Mg#. Gray area from Yang et al. (2019). **(B)** Chondrite-normalized La concentrations in plagioclases plotted against the minerals' An contents. Normalization values after McDonough and Sun (1995). Average 2σ error on the An contents smaller than the symbols' size. The orange trend corresponds to the evolution by fractional crystallization of an average primitive MORB composition for the Atlantis Bank area determined by MELTS (details in the **Supplementary Material**).

DISCUSSION

Model of Emplacement and Evolution of the Magma Reservoir

In the Lower unit (~125 m thick) the lithologies range from the most primitive troctolites to Ol gabbros and gabbros. There is no systematic distribution of the lithologies with depth along the entire unit, which appears highly heterogeneous. A total of 20 intrusive contacts were identified and are almost always associated with the presence of troctolites (**Figure 3A**). Apart from the sharp transitions between troctolites and more evolved lithologies marked by intrusive contacts, the rest of the sequence is characterized by gradual transitions between the different lithology types within subunits. More specifically, we observed a progressive transition from troctolite to Ol gabbro between two intrusive contacts at ~510 mbsf, where the Cpx content of the samples progressively increases from the bottom toward the upper contact (see *Structure and Petrographic Variations* and **Supplementary Figure S1**). Magmatic fabrics of different intensities are also described at various depths within the unit, but no systematic pattern in their distribution or orientation has been identified (e.g., Deans and Yoshinobu, 2019). The whole rock and *in situ* analyzes also confirm the heterogeneous character of the Lower unit, which presents very large variations in major and both compatible and incompatible trace elements. Again, there is no clear systematic pattern between the compositions recorded in the samples and depth. The most primitive signatures (e.g., higher bound of the compositional ranges in whole rock or Cpx Mg#, Pl An contents, Ol Fo contents, or Cpx Cr contents—**Figures 5** and **6**) vary in depth, but do not show a progressive evolution up/down section. The extent of differentiation per sample or at each depth is also variable along the unit.

Altogether, the Lower unit most likely formed from emplacement of sills (~6 m thick in average) at the bottom of the intrusion forming a thick crystal mush and potentially crosscutting one another during emplacement, as indicated by the presence of intrusive contacts and the strong variability in compositions recorded. A sill-like geometry of the intrusions is favored according to seismic observations of such features in the oceanic crust (e.g., Marjanović et al., 2014; Canales et al., 2017; Carbotte et al., 2020), field observations and previous drilled section observations (e.g., Bédard and Hébert, 1996; Boudier et al., 1996; Kelemen et al., 1997; Lissenberg et al., 2004; Sanfilippo and Tribuzio, 2011; Coogan, 2014). In that case, the magmatic fabric would result mainly from crystal orientation due to local flow within each sill (Deans and Yoshinobu, 2019), hence explaining the lack of orientation systematics for the magmatic fabrics in the section. Similar processes producing magmatic fabrics have been described for Atlantis Bank gabbros and quantified by electron backscatter diffraction (EBSD) measurements on a smaller scale by Boulanger et al. (2018). Each sill would have then evolved from bottom to top to various extents, according to the gradual transitions between lithologies and the variable extent of the compositional ranges recorded at depth. Finally, the cumulative geochemical signatures of the lithologies (whole rock REE contents, see *Whole Rock and in situ Geochemical Compositions*) indicate that melt at some point was extracted from the crystallizing mushes.

In contrast, the Upper unit is homogeneous. The unit is composed of Ol gabbro except in the top ~20 m of the sequence which is composed of Ol-bearing gabbro. No igneous contacts or pervasive fabrics are observed; only weak magmatic and crystal-plastic fabrics appear between ~350 and 400 mbsf (**Figure 3A**). Whole rock and *in situ* analyses confirm the homogeneity of the unit, but show more systematic evolution tendencies with depth. Whole rock compositions present progressive upward differentiation trends, as evidenced by the progressive decrease in whole rock Mg# (**Figure 5A**), and are not correlated with depth below 290 mbsf (e.g., Cr and Zr—**Figures 5B,C**). Most of the mineral compositions show the same homogeneity with depth (e.g., Pl An contents and Mg# of Cpx cores), even though Ol Fo content, and Cpx rims present a progressively more differentiated character up section. Cpx rims are the last to form in the lithologies, as Cpx is mostly interstitial and hence is the last phase to appear on the liquidus during crystallization; also, given their diffusion rates at magmatic temperature (Dohmen et al., 2007), Ol Mg-Fe contents are likely reequilibrated with the evolving interstitial melt upon differentiation, the same melt that crystallizes the late Cpx. Together with the observed discrepancies between most of the *in situ* analyses and the progressive upward differentiation trend observed in whole rock Mg#, these observations on Ol and Cpx suggest a progressive accumulation and crystallization of evolved, interstitial melts toward the top of the unit. Only the top ~20 m of the section record a much stronger differentiated character of the lithologies (very low Pl An contents down to 10, whole rock and Cpx Mg# down to 65 and 70, respectively—**Figures 6A,B**). The uppermost two samples (275 mbsf) have crosscutting felsic veins which infiltrate the host Ol-bearing gabbro. This interaction with differentiated late-stage melts may account for the local highly evolved compositions of these samples, which have the lowest whole rock Mg# of the section (down to 65, **Figure 5A**).

Altogether, the Upper unit most likely formed during a common magmatic event, and by upward differentiation and accumulation of evolved melts toward the top of the homogeneous mushy reservoir. The homogeneity of the unit suggests crystallization from a single magma batch emplaced within the crust, or multiple incoming melts with similar compositions. The only anomalous features are the very thin, high An content rims that are locally observed at grain boundaries (max 10 μm), and sometimes associated with thin amphibole blebs; those are mostly present in the lower half of the unit (see *Whole Rock and in situ Geochemical Compositions*). The observation that those An-rich zones are restricted to very narrow grain boundaries suggests a late-stage origin, perhaps by hydrous partial melting, a hypothesis supported by the work on similar features in oceanic gabbros from various settings (e.g., Koepke et al., 2005a; Koepke et al., 2005b; Koepke et al., 2007). Hence, these features likely formed at lower temperatures and thus are considered out of the scope here for our reconstruction of the emplacement and primary magmatic evolution processes of the magma reservoir(s), and will thus not be further discussed herein.

The combined observation of structures, textures and geochemical compositions of the gabbroic sequence reveals critical differences in the melt emplacement dynamics that formed the Lower and the Upper units. The question arising from this observation relates to the link between the two units and the chronology of their emplacement and evolution. Two scenarios are possible: one involves first the formation of the Upper unit by crystallization of a large magma reservoir at depth, then intruded by sills at the bottom of the homogeneous gabbroic sequence. In that case, no direct link between the two units in terms of evolution of the compositions can be drawn. The second scenario involves first stacking of primitive sills, thereby forming the Lower unit, and a subsequent, progressive collection of melts from the sills toward the top of the sequence and formation of the Upper unit. This second option implies a genetic link between melts forming the Lower and Upper units. Previous studies of Hole 735B, based on whole rock and *in situ* geochemical compositions of the lithologies, favor the common origin for Upper and Lower unit (e.g., Dick et al., 2000; Natland and Dick, 2002). They interpret the entire section as a "form of cyclic intrusion that differentiated *in situ* as the magma worked its way upward" (Dick et al., 2000), and an intrusion that was "repetitively injected by comparatively primitive magma" (Natland and Dick, 2002). Other arguments and discussions will be developed in the following sections that tend to favor this last hypothesis (see *Origin and Evolution of Melts Within the Upper Unit*).

Role of Reactive Porous Flow in the Formation and Evolution of the Reservoir

Although the two units record different dynamics of magma emplacement, textures and chemistry in both units indicate common, if not ubiquitous occurrence of RPF, regardless of the lithology considered (see *Structure and Petrographic Variations*, **Figure 4**). The same type of textures, such as rounded Ol grains, irregular Pl grains or intergrown Cpx, have been previously described in Hole 735B and in other gabbroic sections sampled in modern slow-spreading oceanic crust (Lissenberg and MacLeod, 2016 and references therein). They have been interpreted as the result of RPF processes and partial assimilation of crystals during percolation of melt(s) through the permeability of a mush. Together with fractional crystallization (FC), RPF processes are increasingly considered as the predominant processes governing melt differentiation within the lower crust (Lissenberg et al., 2019). Here the implication of RPF is clear from the textures presented above, and in order to test if RPF had also an impact on the chemistry of minerals, we hereafter compare the measured compositions with FC and AFC models. The AFC model of DePaolo (1981) has been commonly used for the study of lower oceanic crust samples as a simplified analogue to the complex RPF processes (Coogan et al., 2000; Kvassnes, 2003; Borghini and Rampone, 2007; Gao et al., 2007; Lissenberg et al., 2013; Sanfilippo et al., 2014; Ferrando et al., 2018). The novelty of our approach resides in our consideration of a sample suite interpreted as representative of an entire magmatic reservoir instead of individual samples, hence helping to better assess the impact of RPF on the differentiation process.

We first modeled the evolution by FC at crustal pressure (0.2 GPa) of a parental melt composition using the rhyolite-MELTS model (Ghiorso and Gualda, 2015; Gualda and Ghiorso, 2015—details in **Supplementary Table S4**). In order to determine the REE evolution of the melt (and its equilibrium minerals), we used the Rayleigh equation for FC. The phase proportions and partition coefficients were computed at each temperature step of the MELTS model using the composition-dependent models of Sun and Liang (2013, 2014) for Ol, Sun et al. (2017) for Pl, and Wood and Blundy (1997) for Cpx. The major and trace element compositions of the starting melt were taken to be an average of the most primitive MORBs sampled in the vicinity of Atlantis Bank (from Coogan et al., 2004—details in **Supplementary Table S4**), and which represent the most likely candidate for the composition of the parental melt forming the section. The results show that Cpx Ti contents and Mg# expected after FC are both lower than the actual content of the minerals from both the Lower and the Upper unit (**Figure 8A**). These geochemical signatures have already been interpreted as evidence for the occurrence of RPF in lower oceanic crustal sections (e.g., Lissenberg and Dick, 2008; Lissenberg and MacLeod, 2016; Leuthold et al., 2018). High-Mg# and Ti Cpx were also identified by Yang et al. (2019) in the products of interaction experiments between MORB-type melts and a troctolite analog (**Figure 8A**). They are interpreted as having crystallized from an interstitial high-Ti melt whose major element contents (Mg#) were buffered by dissolution of primitive Ol from the mush analog, hence increasing the melt Mg content. Regarding the composition of Pl obtained after FC, the An contents of the minerals are consistent with the data for both the Lower and Upper units (all ranging between An ~78 and 45). However, the associated La_N contents of the same Pl grains show a progressive increase during FC that is not observed in the natural rock record. For the highest An contents from the Lower unit, the La_N contents of the Pl are up to four times higher than the expected value for FC. Conversely, for the Upper unit, almost all the La_N contents range below the expected value at given An contents after an evolution by FC (**Figure 8B**). Hence, the majority of both Pl and Cpx signatures fail to be reproduced by FC alone. Together with the characteristic textures observed throughout the section, this result suggests that RPF processes strongly impact the evolution of the Lower and the Upper unit of the reservoir. In the following, we test this hypothesis and attempt to define the reactions involved.

Evolution of Melts Within the Lower Unit

The widespread involvement of RPF in the evolution of the Lower unit is supported by the pervasive reactive textures found in the samples, and by the major and minor element compositional trends that fail to be reproduced by simple FC models. In order to better constrain the reactions involved, and the extent of RPF in the sequence, we modeled the evolution of the minerals' REE contents after both FC (following the procedure described before) and AFC, and compared them with the natural compositions recorded in our samples. We focused on Pl compositions as this mineral is the most abundant in all samples (58% on average—**Figure 3B**), and Pl is less subject to post-crystallization reequilibration than Ol due to slower diffusion

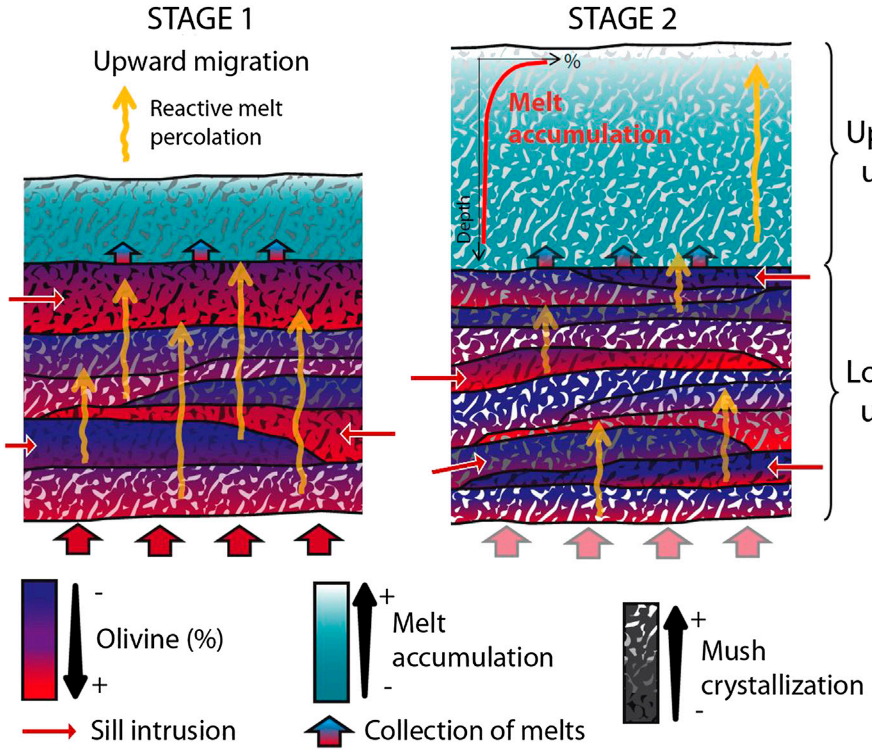

FIGURE 9 | Model of formation of the magma reservoir implying the intrusion of sills in the Lower unit, and progressive extraction and collection of melts in the Upper unit of the reservoir (after *Model of Emplacement and Evolution of the Magma Reservoir*). Widespread occurrence of reactive textures suggests the implication of reactive porous flow processes in both units, and accumulation of melts at the top of the intrusion (after *Role of Reactive Porous Flow in the Formation and Evolution of the Reservoir*). See the text for more discussion.

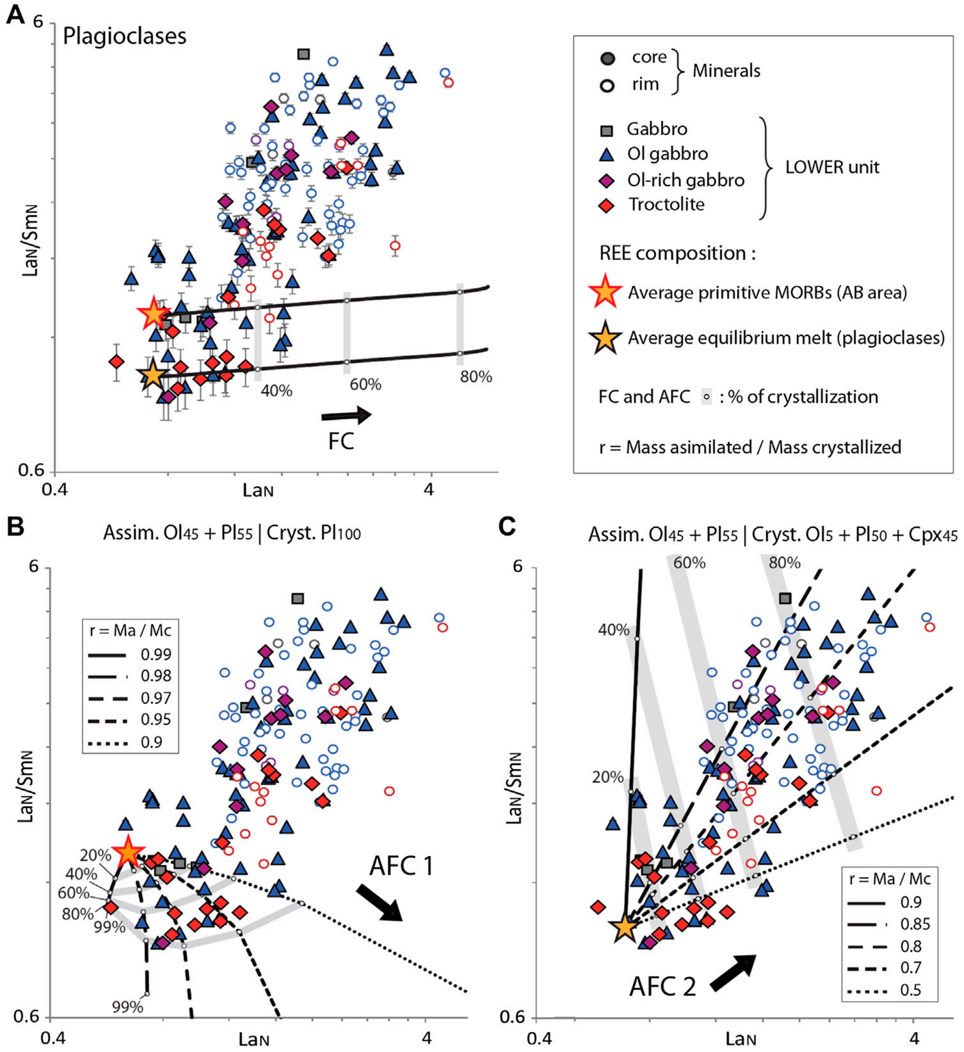

FIGURE 10 | La_N/Sm_N ratio vs. La_N analyzed in plagioclases from the Lower unit of ODP Hole 735B [N = normalized to an average primitive MORB composition of the Atlantis Bank area, computed after the MORB data from Coogan et al. (2004)]. **(A)** Modeling of the plagioclase compositions expected after Fractional Crystallization (FC) from two different parental melts, the average primitive MORB of the Atlantis Bank area (star with red rim), and the melt in equilibrium with the plagioclase presenting the more depleted La compositions and the lower La/Sm ratios (star with black rim). The error bars on the sample analyses represent a 1σ error on the values. **(B)** Modeling of the plagioclase compositions expected after Assimilation-Fractional Crystallization (AFC1) of a troctolitic matrix (45% olivine + 55% plagioclase) by the average primitive MORB-type melt (star with red rim) with crystallization of plagioclase exclusively. **(C)** Modeling of the plagioclase compositions expected after Assimilation-Fractional Crystallization (AFC2) of a troctolitic matrix (45% olivine + 55% plagioclase) by the melt in equilibrium with the more depleted plagioclases (star with black rim) with crystallization of a gabbroic assemblage (5% olivine + 50% plagioclase + 55% clinopyroxene). Details in **Supplementary Material**.

of the REE (e.g., Cherniak, 2003; Spandler and O'Neill, 2010). Cpx is classically used for such models, but the very low amount of Cpx in troctolites and its interstitial position in our Ol-rich samples seems to point to a relatively late stabilization in comparison to the large Pl laths. Pl are thus more likely to record the early stages of evolution than Cpx and to cover the entire reservoir evolution history, and they are therefore used herein to track RPF. Light REE and heavy REE are usually used to highlight incompatible element fractionations, however as HREE are strongly depleted in Pl, we will hereafter rather consider light REE and middle REE (La/Sm).

The REE evolution by FC was modeled following the same approach as the one presented above (*Model of Emplacement and Evolution of the Magma Reservoir* and further details in **Supplementary Table S4**). The global partition coefficient of the crystallized mass was thus calculated for each increment of fractionation with composition-dependent models (Wood and Blundy, 1997; Sun and Liang, 2013; Sun and Liang, 2014; Sun et al., 2017), and was then used to determine the composition of the crystallizing minerals. Two initial REE contents were considered, first the same average composition of primitive MORB-type melts from the Atlantis Bank area as used before (see *Model of Emplacement and Evolution of the Magma Reservoir*), and second the average composition of melts in equilibrium with the Pl crystals which have the lowest La contents and La/Sm ratios of the unit, i.e., the most primitive signatures. To obtain the composition of these equilibrium melts we used the partition coefficient model of Sun et al. (2017) for each mineral at a chosen temperature of 1,100°C. The FC results for both starting melt compositions show that the evolution by FC fails to reproduce the REE compositional ranges of Pl, and more specifically the progressive increase of fractionation between more to less incompatible REE that we quantify with the La/Sm ratio (**Figure 10A**).

To test the RPF hypothesis and to better constrain the reactions involved, we applied the AFC model (DePaolo, 1981) to simulate an evolution by assimilation of a preexisting crystal matrix by a disequilibrium melt, and simultaneous crystallization of a new generation of minerals. The input parameters of the model are the composition of the percolating melt, the type, composition and proportion of assimilated phases, and the mineral species crystallized during the reaction (**Supplementary Table S5**). The output parameters obtained by fitting the trace elements of natural samples will be the proportions of crystallizing minerals and the *r* value (*r* = Mass assimilated/Mass crystallized ratios). We first determined the type of reaction involved, i.e., the nature of the assimilated and crystallized phases, using the textural evidences for RPF found in the Lower unit (**Figure 4**). Dissolution features can be found for Ol and Pl crystals, such as irregular Pl grain boundaries and complex optical zoning due to the presence of "ghost" Pl cores remnants, or numerous roundish Ol chadacrysts in Pl and/or Cpx oikocrysts (see *Structure and Petrographic Variations* and **Supplementary Figure S3**), suggesting Pl and Ol are involved in the assimilation step of the reaction. Conversely, the presence of Pl overgrowths, the very interstitial character of Cpx in some samples, the lack of Cpx core relicts and the occurrence of Pl and Cpx oikocrysts containing dissolved Ol and/or Pl chadacrysts suggest that both Pl and Cpx crystallized during the reaction. These observations are also consistent at a larger scale with the changes of the modal compositions and the progressive increase in Cpx abundances toward the top of the sills from the Lower unit (**Figure 3B**; **Supplementary Figure S1**). The general reaction considered here based on petrographic constraints is as follow (LU for Lower unit):

$$\mathrm{Ol}_1^{\mathrm{LU}} + \mathrm{Pl}_1^{\mathrm{LU}} + \mathrm{melt}_1^{\mathrm{LU}} \rightarrow \mathrm{Ol}_2^{\mathrm{LU}} + \mathrm{Pl}_2^{\mathrm{LU}} + \mathrm{Cpx}^{\mathrm{LU}} + \mathrm{melt}_2^{\mathrm{LU}} \qquad (1)$$

The composition of the assimilated phases was chosen to represent a relatively primitive crystal mush composed of Ol and Pl. We selected the composition of minerals determined by MELTS after ~12% FC from the average primitive MORB of the Atlantis Bank area, which corresponds to crystallization of 45% Ol and 55% Pl. This ratio is in rather good agreement with the dissolved Pl/Ol ratios determined by Yang et al. (2019) and the faster dissolution of Pl compared to Ol suggested by Donaldson (1985). The equation itself is also consistent with AFC equations previously established from lower oceanic crust samples (e.g., Lissenberg and Dick, 2008; Leuthold et al., 2018). In addition, we used the REE partition coefficients calculated for the average compositions of Ol, Pl, and Cpx analyzed in the Lower unit using the composition-dependent models described above at 1,100°C. The same two melt REE compositions considered in the FC models were tested here as the reactive melt composition in the AFC model.

We first tested an AFC model considering **reaction 1**, with percolation of a melt with the composition of the average primitive equilibrium melt through the troctolitic mush (AFC2—**Figure 10C**). One of the outputs of the AFC model that can be obtained by fitting the mineral trace element contents is the proportion of the crystallizing phases; the best fit (5% Ol, 50% Pl, and 45% Cpx) is consistent with the average modal composition of Ol gabbros. With this balance, the model manages to reproduce the entire compositional range recorded in the samples for Mass assimilated/Mass crystallized ratios of 0.5–0.99, and especially matches the increase of fractionation between more to less incompatible REEs (AFC2—**Figure 10C**). The lack of systematic variation of La or La/Sm with depth through the Lower unit (both high and low values at each depths) also highlight that the RPF process is widespread and of variable extent at depth. The variations in Mass assimilated/Mass crystallized ratios (*r* values in **Figure 9**) potentially highlight a progressive change of the RPF dynamics. A decrease of *r* value might reflect a progressive closure of the crystal matrix porosity during the reaction, and the promotion of crystallization over assimilation due to a decrease of the percolating melt flow. The variations might also reflect the heterogeneous character of the reaction in space, and the presence of areas with enhanced percolation or areas of preferred crystallization. Intervals of enhanced percolation may directly correlate to areas of textural equilibrium or melt-present deformation. Cheadle et al. (2004) demonstrated that a cumulate pile is permeable down to very low porosities, on the order of 5%, if the cumulate minerals are in textural equilibrium. Textural equilibrium may cease during RPF reactions, leading to the closure of the cumulate pile to incoming melts. Melt-present deformation is also likely to play a role in the permeability of a cumulate pile demonstrated by models by Zimmerman et al. (1999) and Bruhn et al. (2000) that show deformed samples have a higher permeability compared to undeformed samples, and that melt in pockets once interconnected by shearing can flow through pores based on imposed stress fields. We therefore suggest that melt-present deformation increased the permeability of the cumulate pile and also provided a stress field to help move melt through the system.

Even though this specific AFC2 model manages to reproduce the entire compositional range of the Lower unit, we observed that the modal compositions of the lithologies recovered are highly heterogeneous (see *Structure and Petrographic Variations* and **Figure 3B**). The type of reactive textures encountered is also correlated to the modal composition of the sample considered. The Ol crystals which are the most heavily rounded, which we interpret as being dissolved, are found in the Ol-rich lithologies, together with resorbed Pl grains, poikilitic Pl, and rarer poikilitic Cpx (**Figure 4**). The texture of these samples indicates that Pl is the main phase to crystallize during the AFC process in those specific Ol-rich samples. In addition, the percolating melt composition is taken in AFC2 as the average primitive equilibrium melt of the unit, and the use of an equilibrium melt instead of a natural melt composition for the reaction can be challenged. Hence, we run an additional model in which the initial primitive melt involved in the reaction had the composition of the average primitive MORB from the Atlantis Bank area. The Pl in equilibrium with this melt shows similar La_N contents but higher La_N/Sm_N compared to the most primitive Pl analyzed in the unit. In agreement with the characteristic textures of Ol-rich lithologies described above, a model of extensive Ol and Pl assimilation and Pl-only crystallization was tested (AFC1—**Supplementary Table S5**).

$$Ol_1^{LU} + Pl_1^{LU} + melt_1^{LU} \rightarrow Pl_2^{LU} + melt_2^{LU} \quad (2)$$

This reaction leads to variable increases in the La_N content of Pl coupled to a decrease in the La_N/Sm_N ratios that enables the reproduction of the most depleted and fractionated primitive Pl compositions (AFC1—**Figure 10B**). The occurrence of **reaction 2** is supported by the textures of the Ol-rich lithologies and by the modal contents in Pl of some of these lithologies, which exceeds 80% at different depths within the Lower unit (**Figure 3B**). Other lithologies that are the most common in the Lower unit require the involvement of widespread **reaction 1** for their formation in order to explain the entire compositional range of the section. AFC1 is here considered to be effective for the most primitive lithologies, and thus to proceed first, when AFC2 that reproduced most of the Lower unit plutonic rocks, is proposed to proceed following AFC1.

The exact composition and origin of the initial reactive melt entering the system is difficult to determine. However, according to the model of emplacement determined for the Lower unit (see *Model of Emplacement and Evolution of the Magma Reservoir*), the presence of this reactive melt is likely linked to the intrusion of sills at depth and the cyclic input of new primitive MORB-type melts in the system, leading to an evolution of the Lower unit governed by RPF processes and the initial reaction between primitive melts and Ol-Pl crystal matrices. Some late Ti-rich melts are also likely involved in the formation of the high-Mg# Cpx presenting the highest Ti contents of the unit (>1 wt%), and are probably genetically related to the late formation of the oxide gabbros that are restricted to the Lower unit (see *Methods* and *Model of Emplacement and Evolution of the Magma Reservoir*). Interstitial Ti-rich melt generation and collection to form oxide gabbros may also be enhanced by focused deformation. Melt-present deformation is likely to lead to enhanced crystal-liquid separation through forced melt removal leading to increased differentiation (differentiation by deformation; Bowen, 1920; Dick et al., 2000) forming Fe-Ti enriched fluids. This forced differentiation may explain the higher proportion of oxide gabbros in the Lower unit, which has an abundant record of high temperature deformation, compared to the Upper unit, which has a lack of high temperature deformation.

Origin and Evolution of Melts Within the Upper Unit

The first order petro-structural observations, and related geochemical constraints at Hole 735B (e.g., **Figure 2**) have led Dick et al. (2000) and Natland and Dick (2002) to propose that the Lower and Upper units are genetically related. Also, both the more primitive character of the Lower unit and the widespread evidence for melt extraction observed in this unit, together with the more evolved character of the Upper unit (**Figures 5** and **6**), suggest that melt(s) feeding the Upper unit may originate from the Lower unit (see *Model of Emplacement and Evolution of the Magma Reservoir*). In order to test this hypothesis, we determined whether, geochemically, the parental melt(s) of the Upper unit could indeed originate from the Lower unit, and if so, at which stage of evolution melt extraction from the Lower unit occurred. Mineral major element compositions of the Upper unit are more differentiated, with a maximum Pl An content of 63 (excluding the late-stage high-An rims that are locally observed and attributed to hydrous partial melting; see *Whole Rock and in situ Geochemical Compositions*), whereas the more primitive An contents recorded in the Lower unit reach up to 87.7. After an evolution by FC, Pl An contents of 63 would correspond to 50% crystallization of the average primitive MORB-type melt determined by MELTS (same model described previously), the most likely parental melt to feed the Lower unit. However, we determined earlier that RPF is the dominant process during the evolution of the Lower unit, which precludes the collection of a melt in the upper reservoir after just extensive FC.

A key observation to quantify the process that links the Upper unit to the Lower unit is the decoupling between the major and compatible element contents of minerals with their REE contents (**Figures 6** and **7**). The most depleted Pl Ce contents in the Upper unit are similar to those in the Lower unit (**Figure 7A**), when a marked step is observed between the two units for major and compatible element contents of minerals (**Figure 6**). The only difference in terms of REE compositions between the calculated parental melts of the two units is the slightly stronger fractionation (represented by the La/Sm ratio of Pl and the La/Lu ratio of Cpx, **Figures 7B,D**) recorded in the Upper unit (see comparison between the Upper and Lower units compositions in **Figure 11B**). We proposed earlier for the evolution of the Lower unit a first step of reaction involving stronger assimilation of the initial Ol-Pl matrix by a MORB-type primitive melt, followed by the average reaction of assimilation and crystallization of an Ol gabbro assemblage (*Evolution of Melts Within the Lower Unit*). We can go further in this reasoning, and assume that a chronological decoupling occurs between the assimilation and the crystallization phase of the reaction in the Lower unit. Such decoupling was already considered by Lissenberg and Dick (2008) for the oceanic environment, based on the work of Edwards and Russell (1998) and Reiners et al. (1995). A major consequence of this decoupling is the conservation or even increase of the melt fraction in the system during the first step of reaction by predominant assimilation that would favor remobilization of material, potentially solids but mostly melt.

Based on the general reaction established for the Lower unit, we tested if a first step of preferential assimilation could lead to the formation of a melt with a composition consistent with the one that fed the Upper unit (see *Evolution of Melts Within the Lower Unit*; **Figure 11A**). We computed by mass balance the theoretical compositions of hybrid melts by using the composition of the average primitive MORB, from which

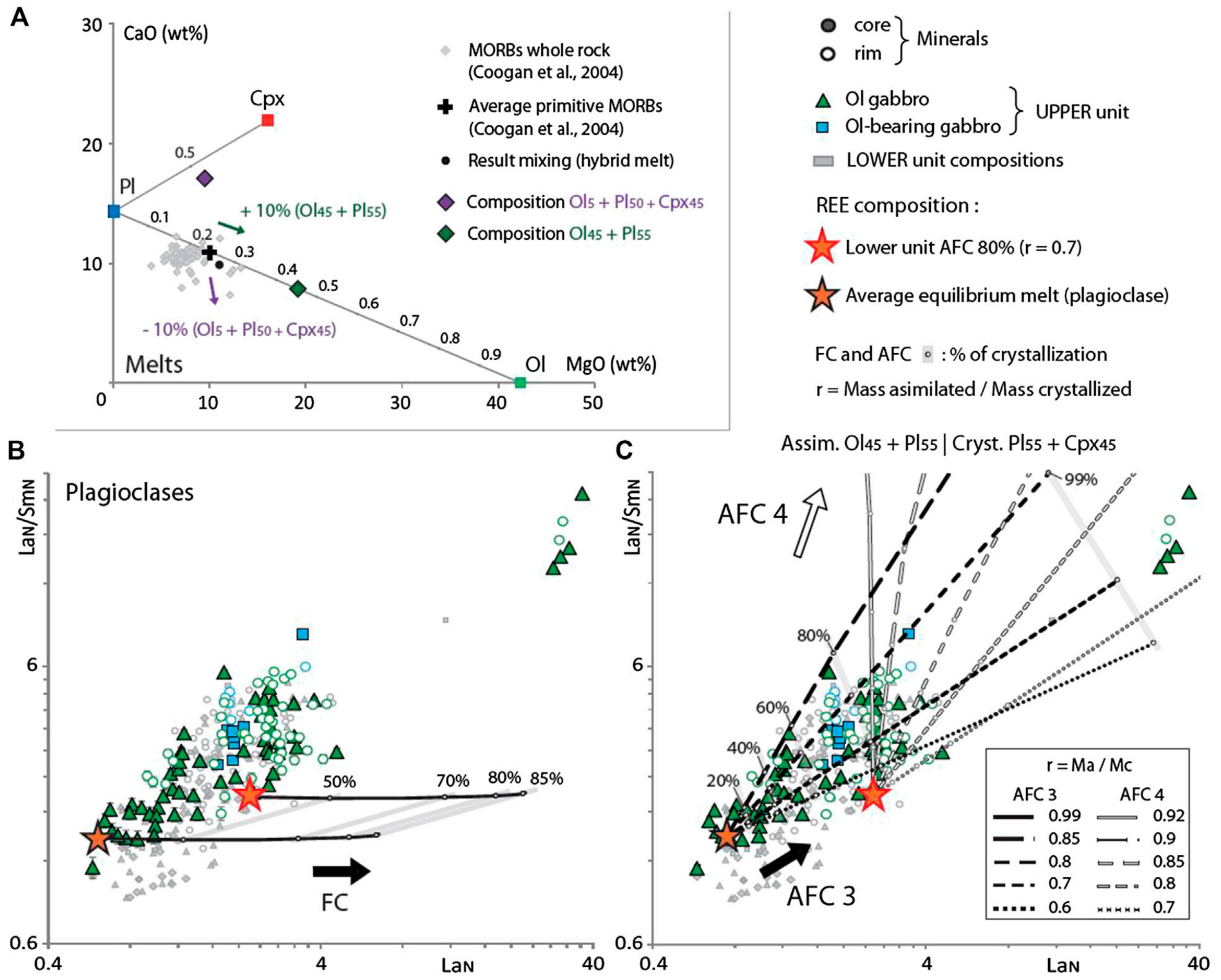

FIGURE 11 | (A) Evolution of the composition in CaO (wt%) and MgO (wt%) of a primitive MORB-type melt after 1) assimilation of a troctolitic component with 55% plagicolase (Pl) and 45% olivine (Ol) (green arrow and diamond), and 2) crystallization of a gabbroic assemblage (5% Ol + 50% Pl + 45% clinopyroxene—Cpx, purple arrow and diamond). Black line: Mixing line between the Pl and Ol or Pl and Cpx end member compositions. **(B,C)** La$_N$/Sm$_N$ ratio vs. La$_N$ analyzed in Pl from the Upper unit of ODP Hole 735B [*N* = normalized to the average primitive MORB composition of the Atlantis Bank area, computed after the MORB data from Coogan et al. (2004)]. **(B)** Modeling of the plagioclase compositions expected after Fractional Crystallization (FC) from two different parental melts, the melt in equilibrium with the plagioclase presenting the more depleted La compositions and the lower La/Sm ratios (star with black rim), and a residual melt obtained with the second AFC model (star with red rim—AFC2 in **Figure 13**). The error bars on the sample analyses represent a 1σ error on the values. The gray symbols represent the composition of the plagioclase analyzed in the Lower unit. **(C)** Modeling of the plagioclase compositions expected after Assimilation-Fractional Crystallization (AFC) of a troctolitic matrix (45% Ol + 55% Pl) by the equilibrium melt (AFC3) and the residual melt (AFC4) with crystallization of a gabbro assemblage (55% Pl and 45% Cpx). Details in **Supplementary Material**.

variable proportions of the Ol-Pl assemblage were added (=assimilation of 45% Ol and 55% Pl) and from which variable proportions of the gabbroic assemblage were removed (=crystallization of 5% Ol, 50% Pl, and 45% Cpx). The mineral compositions used for calculations are the average compositions of minerals from the Lower unit (**Figure 11A**). This equivalent reaction results in hybrid melt compositions that are, for example, slightly enriched in Mg and depleted in Ca relative to the initial primitive MORB (**Figure 11A**). In order to determine if these melts can account for the melt that fed the Upper unit, we modeled their FC by MELTS (**Supplementary Table S4**) and compared the obtained minerals compositions to the ones of the natural samples. The rationale behind this comparison is to verify if the first phases to crystallize in the Upper unit (i.e., the most primitive Ol and Pl) can crystallize from such hybrid melts.

The best fit to the compositions of the natural samples was obtained by an equivalent 10% assimilation of the Ol-Pl matrix by the primitive MORB melt, and 10% crystallization of the gabbroic assemblage (FC of the hybrid melt at 1,150°C, 0.2 GPa, and [H_2O] = 0.2 wt%). The model shows that the compositions of Ol and Pl crystallizing from the hybrid melt are Fo75.5 and An65.8, respectively, when the corresponding compositions in natural samples from the Upper unit are Fo76 and An63

(**Figure 7**). The results of the model therefore matches the composition of both Ol and Pl, but fail to reproduce the composition of natural Cpx that are enriched in Mg compared to the first Cpx that crystallize directly from the hybrid melt (Mg# of 85 and 79.8, respectively). Cpx usually crystallizes later than Ol and Pl in the crystallization sequence of primitive MORB-type melts in the lower crust, which is supported here by the more interstitial textures of Cpx in Ol gabbros from the Upper unit. The discrepancy between the Cpx compositions likely means that FC is not the predominant process governing the evolution of the Upper unit and that RPF must also be considered, as already suggested by the mineral textures and the geochemical signatures of the Upper unit (see *Model of Emplacement and Evolution of the Magma Reservoir*). In addition, Cpx Mg# can increase during RPF processes as the Mg content of a melt increases by assimilation of Ol as mentioned earlier (Lissenberg and Dick, 2008; Yang et al., 2019). The differentiation processes of the Upper unit will be further quantified in the following.

The associated evolution of the hybrid melt's REE contents expected after an increased assimilation stage (equivalent to M assimilated/M crystallized = 1) would also explain the decoupling observed between major and trace elements in the section. Higher assimilation of REE-poor materials (Ol + Pl) associated to smaller fractions of gabbros crystallized, imply relatively stable REE contents of the melt during the reaction despite the simultaneous noticeable changes in the major element contents of the same melt (Yang et al., 2019). This effect could also explain the relatively constant range of La compositions at variable An contents from the Lower to the Upper unit. For example, at low An contents the La concentrations in the Pl is very low compared to the contents expected after FC (down to 0.58 La_N—**Figure 8B**). However, determining a precise parental melt REE composition for the Upper unit is elusive as the construction of the Lower unit by several sill intrusions, recharge stages, and various amounts of RPF implies a great compositional variability of the melts extracted from the Lower unit. In addition, variable extents of mixing between recharge melts and hybrid melts are likely, especially considering the relatively major element homogeneous character and the lack of igneous contacts in the Upper unit.

We then constrained the evolution of melts collected in the Upper unit following their extraction from the Lower unit. We first modeled evolution by FC (following the method used for FC in *Evolution of Melts Within the Lower Unit*) of two different starting REE compositions to account for the variability suggested above. The first one is the melt in equilibrium with the average composition of the most primitive Pl of the Upper unit (lower La_N contents and lower La_N/Sm_N ratios), and the second is a melt composition resulting from the average AFC model applied to the Lower unit (**Supplementary Table S5**). Both FC models fail to reproduce the compositional range recorded in the Upper unit, and especially the increase of fractionation between more to less incompatible REE that we quantified with the La_N/Sm_N ratio (**Figure 11B**). We then applied two AFC models involving interactions between the latter melts, and an Ol-Pl matrix of the Upper unit (~1:1 identical to **reactions 1** and **2**) with the following reaction (UU for Upper unit):

$$Ol^{UU} + Pl_1^{UU} + melt_1^{UU} \rightarrow Pl_2^{UU} + Cpx^{UU} + melt_2^{UU} \qquad (3)$$

We followed the same reasoning for the determination of the models input and output parameters as described for the study of the Lower unit. We considered both Pl and Cpx crystallization in **reaction 3** as the mineral textures described in the Upper unit are similar to those of the Lower unit. Conversely, Ol crystallization was not considered in **reaction 3** as the Upper unit is more evolved compared to the Lower unit and the Ol content tend to slightly decrease toward the top of the section. The best fit of the model results to the REE compositions of the natural samples was obtained for 55 and 45% crystallization of Pl and Cpx, respectively. The AFC model involving the equilibrium melt reproduces the entire compositional range of the Upper unit, with ratios of mass assimilated/mass crystallized varying between 0.6 and 0.99 (AFC3—**Figure 11C**). However, a contribution of melts that previously experienced various steps of evolution by AFC in the Lower unit and that display more enriched and fractionated signatures cannot be excluded. RPF processes involving such melts (e.g., AFC4 in **Figure 11C**) also reproduce part of the compositional range recorded in the Upper unit with *r* ratios varying in this case between 0.7 and 0.92. Overall, RPF processes are the predominant processes governing the evolution of the Upper unit, and shape the rock textures, crystal morphologies and compositions, and the modal proportions of rocks.

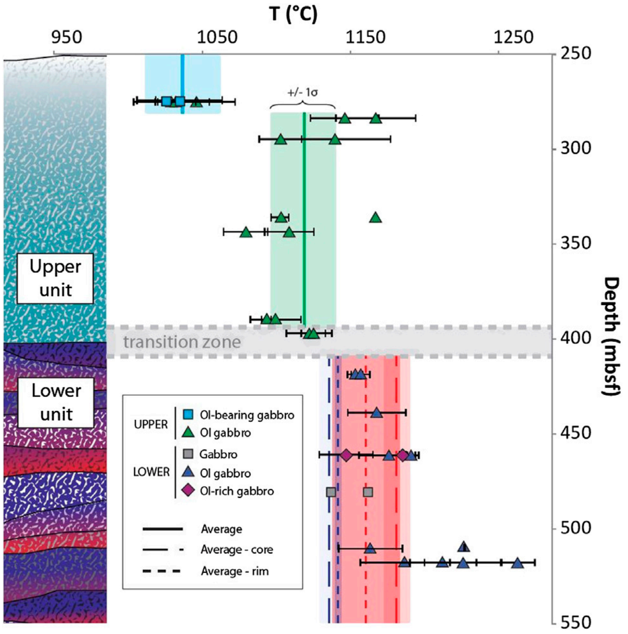

FIGURE 12 | Estimated equilibrium temperatures between Pl and Cpx with the thermometer of Sun and Liang (2017) represented with depth. Left: representation of the reservoir structure. Solid and dotted lines represent the average temperatures for lithologies with >5% Cpx in the Upper and Lower unit. 1σ errors (error bars and shaded areas) given by the model.

Temperature Constraints on the Evolution of the Reservoir

We estimated the range of temperature experienced by the reservoir during its formation and evolution by applying the REE-in-plagioclase-clinopyroxene thermometer of Sun and Liang (2017). We determined equilibrium temperatures of Pl and Cpx pairs based on 1) core-core or rim-rim compositions analyzed in the same area of a thin section (32 pairs in total for 15 different samples) and 2) minerals' core and rim average compositions per lithology and per unit (see **Supplementary Table S6**). The temperatures obtained by the two approaches for the Ol-rich lithologies from the Lower unit, the Ol-bearing gabbros and Ol gabbro from the Upper unit corresponds to each other (**Figure 12**). However, the temperatures for the Ol gabbro samples from the Lower unit range between 1,150 and ~1,260°C, whereas the temperatures obtained with the average compositions are of only ~1,140°C. This discrepancy emphasizes that average compositions are not completely irrelevant but need to be checked with spot analyses, especially for lithologies like the Lower unit Ol gabbros which present a wide compositional variability in major elements. The final results show a temperature range of ~230°C (1,260°C at the bottom of the Lower unit and 1,026°C at the top of the Upper unit) corresponding to the differentiation of the primitive melt down to the temperature range of Ti-rich melts, which later likely segregate and form the oxide gabbros not studied here. The lowest values determined herein correspond to the highest temperatures of formation of the oxide gabbros, as, for example, determined experimentally by Koepke et al. (2018) in a temperature range of 1,050–850°C. Eventually, the variations of the depth-record of temperature are consistent with the composition-record as more evolved compositions are associated with lower temperature estimates, and ultimately with the reservoir model developed here.

Implications for the Slow-Spreading Lower Oceanic Crust

Hidden Primitive Cumulates and Differentiation of Primitive MORB

The more primitive average bulk composition of the lower crust *in situ* section drilled at the Atlantis Massif OCC (MAR—IODP Hole U1309D) is considered as one of the main differences with the crustal sections drilled at Atlantis Bank. The estimated bulk composition of the plutonic section drilled at Hole U1309D is close to the composition of primary MORB magmas (average bulk crust Mg# of 72.9–76, Godard et al., 2009). This led Godard et al. (2009) to suggest that no significant fraction of evolved melt escaped the magmatic system sampled at Atlantis Massif. At Atlantis Bank, Dick et al. (2000) and Kvassnes (2003) suggest that the average bulk composition of the cumulate sequence from ODP Hole 735B (and later from IODP Hole U1473A, Dick et al., 2019a) is too evolved with respect to the composition of primary MORB melts (bulk Mg# of 69.2 for Hole 735B and of 71 for Hole U1473A, Dick et al., 2000). Dick et al. (2000) first infer the presence of a significant mass of "missing" primitive cumulates lying either out of the section or further deep in Atlantis Bank to account for this difference. The cumulate sequences drilled at Atlantis Bank would then represent already differentiated melts originating from a first step of crystallization at depth, and the theoretical cumulate series that crystallized from the most primitive melts would be absent or at least truncated in the drilled series. This model would also explain the major lack of primitive lithologies drilled at Atlantis Bank such as dunites or troctolites, with troctolites being found only locally in Hole 735B (Dick et al., 2000; MacLeod et al., 2017). Although primitive cumulates are clearly missing when considering the entire ODP Hole 735B drilled at Atlantis Bank, we may wonder if such primitive cumulates are also missing at the scale of the reservoir studied herein. Indeed, we do find primitive cumulates that crystallized in the Lower unit from primitive MORB-type melts. Strikingly, those lithologies were later partially to totally assimilated by reactive percolating melts, and are thus hard to identify. In order to test if the reservoir studied herein is a suitable candidate to represent a lower crust section that record all the key processes related to crustal differentiation, and thus if its bulk composition is similar to primitive MORBs, we quantified this bulk composition.

We approximated the bulk composition of the reservoir, and thus of the Upper and Lower units together, by following the same computation method as Dick et al. (2000). We used the same average bulk composition per lithology and revised interval dimensions by rock type focused on the studied intrusion, after the lithology intervals provided by MacLeod et al. (2017). All lithologies, including oxide gabbros, were considered. The results show that the computed bulk composition of the reservoir is more primitive than the bulk composition of Hole 735B previously determined by Dick et al. (2000), and is comparable to primary MORBs (**Table 1**). The Mg# of the reservoir is 72.8, when the value is 72.3 for the primary MORB and of 69.2 for the bulk of Hole 735B. The reservoir bulk composition is also very close to that of Hole U1309D bulk gabbroic composition, which has a Mg# of 73.2. The Ca# are more dispersed, with a Ca# of 73.1 for the reservoir comprised between the Ca# of the primary MORB and of the bulk Hole U1309D (71.2 and 76.4, respectively). Hence, only regarding the section of Hole 735B representing the reservoir studied herein (Upper and Lower units; **Figure 8**), no missing primitive cumulate series is required. This result is noteworthy and highlights that one should not always expect large primitive cumulate series (e.g., dunite, troctolite) to be widespread in lower crust sections from slow-spreading centers. Instead, sparse troctolites with abundant olivine gabbros could represent the most primitive cumulates that were partially consumed by RPF. Our new reservoir model also highlights that the scarcity of troctolites is likely related to widespread RPF that occurs since the first stages of the crystallization process, with Ol + Pl assemblages being consumed by the reactions. This supports the suggestion made by Dick et al. (2019b) for the entire Hole 735B that at least some of the Ol gabbro result from melt interaction processes with more primitive cumulates.

The reservoir model presented herein eventually covers most of the differentiation sequence of primitive MORB-type melts in a slow-spreading environment, apart from the ultimate stages of

TABLE 1 | Results of bulk rock mass balance calculations for the reservoir of Hole 735B (Mg# = 100 × Mg/(Mg + Fe_{tot}) with Fe_{tot} as ferrous iron. Ca# = 100 × Ca/(Ca + Na). Average primitive MORB after Coogan et al. (2004).

	SiO_2	TiO_2	Al_2O_3	FeO	Fe_2O_3	FeO_{tot}	MnO	MgO	CaO	Na_2O	K_2O	P_2O_5	Mg#	Ca#
Hole 735B reservoir	50.12	0.76	16.50	5.47	1.25	6.47	0.13	9.71	12.75	2.60	0.04	0.02	72.8	73.1
Calculated primary MORB[a]	50.30	0.91	16.40	nd	nd	7.45	nd	10.90	12.50	2.80	0.05	0.05	72.3	71.2
Average primitive MORB	47.86	1.33	16.30	—	10.56	—	0.20	9.84	10.86	2.77	0.10	0.10	64.8	68.4
Bulk Hole 735B[a]	50.60	0.87	16.10	6.19	1.37	7.31	0.14	9.21	12.50	2.80	0.05	0.05	69.2	71.2
Bulk Hole U1309D (BG)[b]	50.18	0.67	16.69	—	7.44	—	0.13	10.26	12.94	2.10	0.03	0.13	73	77
Bulk Hole U1309D (BG:LD)[b]	50.27	0.80	16.65	—	7.34	—	0.12	9.97	12.98	2.22	0.03	0.20	73	76

[a] *Values after Dick et al. (2000).*

[b] *Values after Godard et al. (2009).*

BG, bulk gabbro composition; BG-LD, bulk gabbro composition with additional contribution of leucocratic dykes; nd, not determined.

evolution documented by the oxide gabbros and felsic veins (e.g., Koepke et al., 2018; Nguyen et al., 2018). One of the questions arising is if this reservoir evolution and associated processes impact the differentiation of the MORBs erupted on the seafloor. The reservoir model itself suggests that if MORBs were extracted from such a reservoir, it is highly unlikely they escaped RPF processes as reactions occur everywhere and at each step of evolution of the reservoir. The issue regarding a possible RPF control on MORB major element signatures (initially only interpreted as originating from different crystallization pressures, e.g., Grove et al., 1992; Villiger et al., 2007) was previously addressed by Lissenberg and Dick (2008). The lowering of Ca contents and increase in Al and Mg content suggested during the reactions were also observed experimentally by Yang et al. (2019), and are similar to the major elements evolution modeled herein, for example, to describe the origin of the reactive melts feeding the Upper unit (see *Origin and Evolution of Melts Within the Upper Unit*). In order to test if the RPF process identified herein may be recorded in MORB trace elements from the study area, we compared the computed melt compositions obtained by our AFC models and the natural MORB record at Atlantis Bank and the SWIR (**Figure 13**). We selected the most primitive MORB composition of the Atlantis Bank area (Coogan et al., 2004), and applied the FC and the AFC2 models following the same method used earlier (see *Model of Emplacement and Evolution of the Magma Reservoir* and *Origin and Evolution of Melts Within the Upper Unit*). Similarly to what was shown by Lissenberg and Macleod (2016), we show that FC is unable to reproduce the compositional variability of MORBs, whereas the AFC model matches rather well the observed trend. Altogether, our observations are consistent with a widespread implication of RPF in the lower crustal reservoirs that feed MORBs.

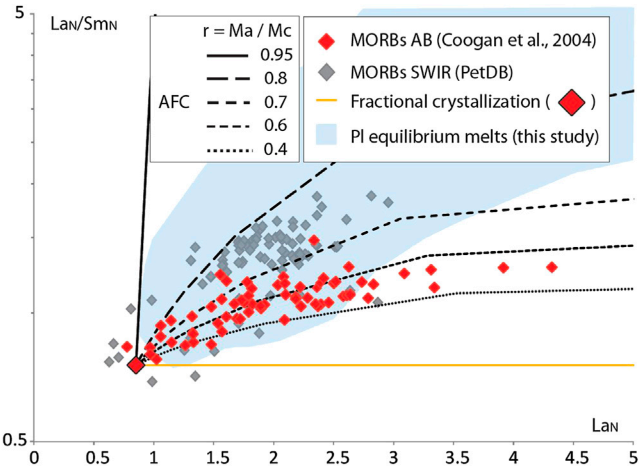

FIGURE 13 | La_N/Sm_N ratio vs. La_N [N = normalized to the average primitive MORB composition of the Atlantis Bank area, computed after the MORB data from Coogan et al. (2004)] of 1) MORBs from the Southwest Indian Ridge between the Gallieni fracture zone and the Rodriguez triple junction (data from PetDB), and MORBs collected in the vicinity of Atlantis Bank (Coogan et al., 2004), 2) the output melt composition from the FC model and the AFC model using the most primitive MORB from the Atlantis Bank area (see *Origin and Evolution of Melts Within the Upper Unit* for details and **Supplementary Table S4**), and 3) the area covered by the compositions of the melts in equilibrium with the analyzed Pl from the studied section, and determined at 1,100°C thanks to the model of Sun et al. (2017).

Cyclicity of Magma Inputs and Time Constraints

The model of reservoir formation proposed herein involves repeated replenishments in the form of small magma intrusions, or sills, during a main magmatic event that led to the formation of the entire unit. Reactive melt percolation appears as the predominant process governing the evolution of melts within the ~200 m-thick reservoir, and hence melt supply during the main magmatic event was likely sustained, preventing advanced crystallization of each small intrusion and allowing large scale porous migration of melts (Dick et al., 2019a). Even though we bring new constraints on the dynamics of magma emplacement and evolution processes, no time constraint is directly provided by our data. Nevertheless, previous studies that have constrained the timescales of igneous processes at oceanic spreading centers can be used to discuss our reservoir model from a timescale perspective.

At fast-spreading centers, cyclic replenishment of magma chambers has been highlighted based on geochemical data (Rannou et al., 2006). In a review of timescale constraints for magmatic systems of fast-spreading ridges, France et al. (2009) highlighted that different cyclicity periods are likely implicated in the evolution of those systems. Those periods vary from long periods (~100 ky) tentatively related to variations in magma supply from the mantle (e.g., Hooft et al., 1997), to short periods (~1 ky) that may correspond to major magma chamber recharges (e.g., Cordier et al., 2012). Small scale mixing processes, and related recharge events that may be associated with eruption triggering are also identified at the

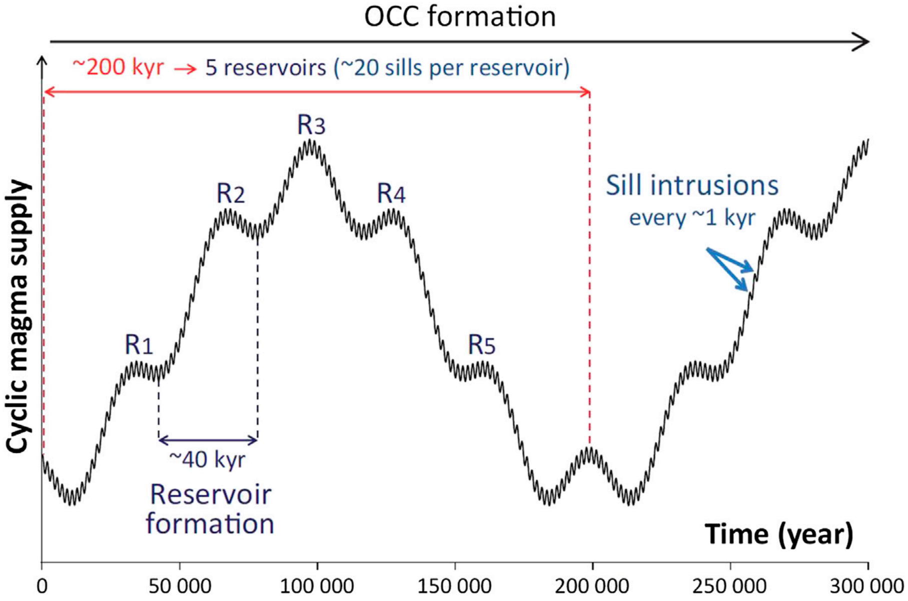

FIGURE 14 | Compilation of the estimated timescales for magma supply below slow-spreading centers, here applied to the Atlantis Bank system and findings on ODP Hole 735B. R, reservoir. See *Cyclicity of Magma Inputs and Time Constraints* for further details and justification.

scale of 1–10 years (e.g., Costa et al., 2010). The same characteristics of periodicity may apply to slow-spreading environments, but would likely be associated with different timescales. Lower melt supply could indeed imply longer periodicity of melt inputs at the ridge axis.

At slow-spreading centers, Lambart et al. (2019) focused on the isotopic composition of minerals sampled at the Atlantis Massif OCC on the MAR to track the composition of primary melts feeding the crust, which is also discussed by Cordier et al. (2010) who studied the trace element composition of MORBs emplaced at the axis of the slow-spreading Central Indian Ridge. In both cases, whether mantle melts are segregated within the crust or emplaced at the surface, they concluded that melt inputs from the mantle take the form of small magma batches resulting from cyclic melt aggregation in the heterogeneous mantle. In addition, by considering the symmetry of melts' compositions to the ridge axis and the time relations given by magnetic microanomalies at the surface, Cordier et al. (2010) determined a timescale of 150–200 kyr for the aggregation process. This timescale would correspond to the order of magnitude for the periodicity of melt intrusions within the lower slow-spreading oceanic crust, and/or magma replenishment in the lower crust reservoirs. At OCCs, beside the overall cooling rates documented by diffusion chronometry or multi-geochronology tools (e.g., Coogan et al., 2007; Grimes et al., 2011), the only time constraints available for magmatic processes are zircon dates of minerals formed in late-stage lithologies crosscutting the gabbroic sequences. This method enables the estimation of the general age of formation of the structures and the relative emplacement age of the various large-scale intrusions identified. For Atlantis Massif, Grimes et al. (2008) determined that the OCC formation ~1.2 Ma ago lasted for at least 100–200 kyr, and that the age peaks of the two major units forming Hole U1309D are separated by 70 ka. In addition, they estimate that based on the number of intrusive contacts in the section and the approximated duration of accretion, the structure potentially formed by on average one sill intrusion (~10 m thick) every ~1 kyr. For Atlantis Bank, Rioux et al. (2016) studied zircon ages of Hole 735B, and Hole 1105A that is the shallowest section (160 m deep) drilled at Atlantis Bank and lies 1.2 km east-northeast of Hole 735B. The formation of the Atlantis Bank batholith ~12 Ma ago (Schwartz et al., 2009; Rioux et al., 2016) is estimated to have lasted at least 214 kyr (Rioux et al., 2016). This time interval is similar to the estimated duration of crustal accretion for Atlantis Massif described above, but also to the magma emplacement time of >210 kyr reported for the MARK area (Grimes et al., 2008 and references therein), the 90–235 kyr crystallization timescale recorded at the Vema section of the MAR (Lissenberg et al., 2009), and the 100–200 kyr timescale established by Cordier et al. (2010) for the mantle melt aggregation process. Rioux et al. (2016) also favor the model of episodic growth and formation of the crust at Atlantis Bank by periodic intrusion of "sub-horizontal sheets" of >250 m thick, corresponding to the entire reservoir studied herein. Altogether, despite the lack of direct time constraints on the different events of formation of the igneous reservoir described herein, and by analogy with fast-spreading ridges where various periods of process cyclicity is suggested (e.g., France et al., 2009), the previous results on slow-spreading ridges led us to propose a similar scenario.

The formation of the ~1,500 m thick OCC section drilled at IODP Hole 735B, and possibly the OCC itself is potentially related to cyclic increase of the mantle melt supply, a process with a likely periodicity of ~200 kyr (**Figure 14**). A shorter timescale of a few tens of ky is thus required for the emplacement of each of the large-scale intrusions or reservoirs (~250 m thick; 5 units representing part or entire reservoirs at Hole 735B). In this perspective, the repetitive injection of primitive melts feeding the lower crust reservoir, and leading to the formation of the ~20 sills (~10 m thick) in the lower part of the reservoir studied herein (**Figure 3** and **9**) seems to recur every ~1 kyr, which is the same timescale considered for the replenishment of fast-spreading lower crust magma chambers. The relatively continuous replenishment leading to protracted RPF within each of the identified sills likely occurs at a smaller timescale. When considering the reservoir studied herein, the temperature estimates document a cooling of ~230°C from the parental magma injection to the temperature range of Ti-rich melts (**Figure 12**; see *Temperature Constraints on the Evolution of the Reservoir*). Given the cooling rates documented by Coogan et al. (2007), this corresponds to ~70 ky suggesting that the various reservoirs (~250 m) intruded each other while melt was still present. Following the same approach we can also estimate the temperature decrease experienced by a given 10 m thick sill in the time lapse preceding the subsequent sill intrusion (~1 ky). In this case it corresponds to a temperature decrease of ~3°C highlighting the potential of interstitial melt percolation from one sill to another upon cooling.

CONCLUSIONS

We combined high-resolution *in situ* analyses together with detailed petrographic and structural characterization of a preserved magmatic unit from ODP Hole 735B. The study enabled the establishment of an integrated mush evolution model of a unit formed in the lower oceanic crust of an OCC at a slow-spread ridge. Both melt emplacement processes by intrusion and migration by RPF contributed to its accretion, and strongly influenced the architecture and composition of the reservoir. The principal characteristics of evolution of the igneous reservoir emphasized by the model are as follows:

(1) The lower half of the reservoir represents the initial emplacement of magmas within the slow-spreading crust by repetitive intrusions and sills stacking during a major magmatic event (~20 sills stacked over ~125 m).
(2) The continuous recharge of the lower half of the reservoir has led to assimilation of early primitive liquidus minerals, and to the formation of hybrid melts, which were progressively collected in an overlying mush constituting the upper half of the reservoir.
(3) The upper half of the reservoir has formed by upward differentiation and progressive accumulation of evolved melts, also a product of RPF, toward to the top of the mushy magmatic unit.

Geochemical modeling of *in situ* incompatible trace element contents enabled the establishment of the strong and ubiquitous involvement of RPF processes in the evolution of the intrusion, and to add further constraints on melt-mush interaction processes that occurred during the evolution of both units. Our results also support models in which MORB melts are affected and record melt-mush interactions and RPF that are identified in the plutonic record. The bulk composition of the studied reservoir is similar to primitive MORBs, and highlight that this specific unit eventually records the entire differentiation series of a slow-spreading center reservoir. Lastly, an attempt to address timescales for the formation of the reservoir is made by comparison with preexisting data and models for magma reservoir at slow-spreading ridges. The igneous reservoir model proposed here opens new perspectives for the comprehension of mush-dominated igneous reservoirs dynamics in the crust and magma accretion at slow-spreading oceanic centers.

DATA AVAILABILITY STATEMENT

All datasets presented in this study are included in the article **Supplementary Material** and/or are available in the OTELo Research Data Repository (FAIR).

AUTHOR CONTRIBUTIONS

LF has designed the project. MB, LF, and JL have described and collected the samples at the Kochi Core Center (Japan). JD has conducted the structural and textural description of the section at the Kochi Core Center (Japan). MB, AH, and CF have analyzed samples and processed the data. MB has conducted the geochemical modeling, written the manuscript, and prepared the figures. All authors have participated to the manuscript preparation. The models were discussed by all authors, who have approved this submitted manuscript.

FUNDING

This research was supported by CNRS-INSU and IODP-France. MB's PhD project was funded by the French Ministry of Research (MESRI). JL was supported by the UK Natural Environment Research Council (NERC Grant NE/I001670/1).

ACKNOWLEDGMENTS

This research used samples and data provided by the Ocean Drilling Program (ODP). ODP was sponsored by the US National Science Foundation (NSF) and participating countries under management of Joint Oceanographic Institutions (JOI), Inc. We acknowledge IODP France funded by CNRS for participating in the funding of this project. The assistance of the staff at the Kochi IODP core repository is gratefully acknowledged. We also express our warm thanks to Jean-Luc Devidal (LMV Clermont-Ferrand) and Olivier Bruguier (Geosciences Montpellier) for their assistance during EPMA and LA-ICP-MS measurements, respectively. This study greatly benefited from thorough reviews by H. J. B. Dick, J. D.

Blundy, M. R. Perfit, and the editor F. J. Spera, whom we gratefully thank. The authors also thank J. H. Bastin, M. Cannat, K. V. Cashman, H. J. B. Dick, M. Godard, C. J. MacLeod, and A. Sanfilippo for constructive discussions. This is CRPG contribution number 2740.

SUPPLEMENTARY MATERIAL

The Supplementary Material for this article can be found online at: https://www.frontiersin.org/articles/10.3389/feart.2020.554598/full#supplementary-material

REFERENCES

Baines, A. G., Cheadle, M. J., Dick, H. J. B., Scheirer, A. H., John, B. E., Kusznir, N. J., et al. (2003). Mechanism for generating the anomalous uplift of oceanic core complexes: Atlantis Bank, southwest Indian Ridge. *Geology* 31, 1105–1108. doi:10.1130/G19829.1

Baines, A. G., Cheadle, M. J., Dick, H. J. B., Scheirer, A. H., John, B. E., Kusznir, N. J., et al. (2007). Evolution of the southwest Indian ridge from 55°45′E to 62°E: changes in plate-boundary geometry since 26 Ma. *Geochem. Geophys. Geosy.* 8, Q06022. doi:10.1029/2006GC001559

Bédard, J. H., and Hébert, R. (1996). The lower crust of the Bay of Islands ophiolite, Canada: petrology, mineralogy, and the importance of syntexis in magmatic differentiation in ophiolites and at ocean ridges. *J. Geophys. Res.* 101, 25105–25124. doi:10.1029/96jb01343

Bennett, E. N., Jenner, F. E., Millet, M.-A., Cashman, K. V., and Lissenberg, C. J. (2019). Deep roots for mid-ocean-ridge volcanoes revealed by plagioclase-hosted melt inclusions. *Nature* 572, 235–239. doi:10.1038/s41586-019-1448-0

Blackman, D. K., Ildefonse, B., John, B., Ohara, Y., Miller, D. J., and Macleod, C. J. (2006). Site U1309. *Proc. Ocean Drill. Progr.* 304/305, 304. doi:10.2204/iodp.proc.304305.103.2006

Borghini, G., and Rampone, E. (2007). Postcumulus processes in oceanic-type olivine-rich cumulates: the role of trapped melt crystallization versus melt/rock interaction. *Contrib. Mineral. Petrol.* 154, 619–633. doi:10.1007/s00410-007-0217-5

Boudier, F., Nicolas, A., and Ildefonse, B. (1996). Magma chambers in the Oman ophiolite: fed from the top and the bottom. *Earth Planet. Sci. Lett.* 144, 239–250. doi:10.1016/0012-821x(96)00167-7

Boulanger, M., France, L., Ildefonse, B., Ghosh, B., Sanfilippo, A., Liu, C. Z., et al. (2018). "Origin of the interlayered series at Atlantis Bank (SWIR): new insights on lower oceanic crust accretion processes," in Goldschmidt2018, Boston, USA, August 2018. Abstract 122.

Bowen, N. L. (1920). Differentiation by deformation. *Proc. Natl. Acad. Sci. U.S.A.* 6, 159. doi:10.1073/pnas.6.4.159

Bruhn, D., Groebner, N., and Kohlstedt, D. L. (2000). An interconnected network of core-forming melts produced by shear deformation. *Nature* 403, 883–886. doi:10.1038/35002558

Canales, J. P., Dunn, R. A., Arai, R., and Sohn, R. A. (2017). Seismic imaging of magma sills beneath an ultramafic-hosted hydrothermal system. *Geology* 45, 451–454. doi:10.1130/G38795.1

Carbotte, S. M., Arnulf, A., Spiegelman, M., Lee, M., Harding, A., Kent, G., et al. (2020). Stacked sills forming a deep melt-mush feeder conduit beneath Axial Seamount. *Geology* 48, 693–697. doi:10.1130/g47223.1

Carbotte, S. M., Smith, D. K., Cannat, M., and Klein, E. M. (2015). Tectonic and magmatic segmentation of the Global Ocean Ridge System: a synthesis of observations. *Geol. Soc. Spec. Publ.* 420, 249–295. doi:10.1144/sp420.5

Cheadle, M. J., Elliott, M. T., and McKenzie, D. (2004). Percolation threshold and permeability of crystallizing igneous rocks: the importance of textural equilibrium. *Geology* 32, 757–760. doi:10.1130/g20495.1

Cherniak, D. J. (2003). REE diffusion in feldspar. *Chem. Geol.* 193, 1–17. doi:10.1016/s0009-2541(02)00246-2

Coogan, L. A. (2014). *The lower oceanic crust*. 2nd Edn. Amsterdam, Netherlands: Elsevier.

Coogan, L. A., Jenkin, G. R. T., and Wilson, R. N. (2007). Contrasting cooling rates in the lower oceanic crust at fast- and slow-spreading ridges revealed by geospeedometry. *J. Petrol.* 48, 2211–2231. doi:10.1093/petrology/egm057

Coogan, L. A., Saunders, A. D., Kempton, P. D., and Norry, M. J. (2000). Evidence from oceanic gabbros for porous melt migration within a crystal mush beneath the Mid-Atlantic Ridge. *Geochem. Geophys. Geosyst.* 1, 2000GC000072. doi:10.1029/2000GC000072

Coogan, L. A., Thompson, G. M., MacLeod, C. J., Dick, H. J. B., Edwards, S. J., Hosford Scheirer, A., et al. (2004). A combined basalt and peridotite perspective on 14 million years of melt generation at the Atlantis Bank segment of the Southwest Indian Ridge: evidence for temporal changes in mantle dynamics? *Chem. Geol.* 207, 13–30. doi:10.1016/j.chemgeo.2004.01.016

Cordier, C., Benoit, M., Hémond, C., Dyment, J., Le Gall, B., Briais, A., et al. (2010). Time scales of melt extraction revealed by distribution of lava composition across a ridge axis. *Geochem. Geophys. Geosyst.* 11, Q0AC06. doi:10.1029/2010GC003074

Cordier, C., Caroff, M., and Rannou, E. (2012). Timescale of open-reservoir evolution beneath the south Cleft segment, Juan de Fuca ridge. *Mineral. Petrol.* 104, 1–14. doi:10.1007/s00710-011-0159-5

Costa, F., Coogan, L. A., and Chakraborty, S. (2010). The timescales of magma mixing and mingling involving primitive melts and melt–mush interaction at mid-ocean ridges. *Contrib. Mineral. Petrol.* 159, 173–194. doi:10.1007/s00410-009-0432-3

Deans, J. R. L., and Yoshinobu, A. S. (2019). Geographically re-oriented magmatic and metamorphic foliations from ODP Hole 735B Atlantis Bank, Southwest Indian Ridge: magmatic intrusion and crystal-plastic overprint in the footwall of an oceanic core complex. *J. Struct. Geol.* 126, 1–10. doi:10.1016/j.jsg.2019.05.001

DePaolo, D. J. (1981). Trace element and isotopic effects of combined warlock assimilation and fractional crystallization. *Earth Planet. Sci. Lett.* 53, 189–202. doi:10.1016/0012-821X(81)90153-9

Dick, H. J. B., Kvassnes, A. J. S., Robinson, P. T., MacLeod, C. J., and Kinoshita, H. (2019a). The Atlantis Bank Gabbro Massif, Southwest Indian Ridge. *Prog. Earth Planet. Sci.* 6, 64. doi:10.1186/s40645-019-0307-9

Dick, H. J. B., Macleod, C. J., Blum, P., Abe, N., Blackman, D. K., Bowles, J. A., et al. (2019b). Dynamic accretion beneath a slow-spreading ridge segment: IODP Hole U1473A and the Atlantis Bank core complex. *J. Geophys. Res. Solid Earth* 124, 12631–12659. doi:10.1029/2018JB016858

Dick, H. J. B., Lin, J., and Schouten, H. (2003). An ultraslow-spreading class of ocean ridge. *Nature* 426, 405–412. doi:10.1038/nature02128

Dick, H. J. B., Meyer, P. S., Bloomer, S., Kirby, S., Stakes, D., and Mawer, C. (1991a). Lithostratigraphic evolution of an in-situ section of oceanic layer 3. *Proc. Ocean Drill. Prog. Sci. Results* 118, 439–538. doi:10.2973/odp.proc.sr.118.128.1991

Dick, H. J. B., Schouten, H., Meyer, P. S., Gallo, D. G., Bergh, H., Tyce, R., et al. (1991b). Tectonic evolution of the Atlantis II fracture zone. *Proc. Ocean Drill. Progr. Sci. Results* 118, 359–398. doi:10.2973/odp.proc.sr.118.156.1991

Dick, H. J. B., Natland, J. H., Alt, J. C., Bach, W., Bideau, D., Gee, J. S., et al. (2000). A long in situ section of the lower ocean crust: results of ODP Leg 176 drilling at the Southwest Indian Ridge. *Earth Planet. Sci. Lett.* 179, 31–51. doi:10.1016/S0012-821X(00)00102-3

Dick, H. J. B., Natland, J. H., Miller, D. J., and Al, E. (1999). Site 735. *Proc. Ocean Drill. Progr.* 176, 1–314. doi:10.2973/odp.proc.ir.176.103.1999

Dick, H. J. B., Ozawa, K., Meyer, P. S., Niu, Y., Robinson, P. T., Constantin, M., et al. (2002). 10. Primary silicate mineral chemistry of a 1.5-km section of very slow spreading lower ocean crust: ODP Hole 753B, Southwest Indian Ridge. *Proc. Ocean Drill. Progr. Sci. Results* 176, 1–61. 10.2973/odp.proc.sr.176.001.2002

Dohmen, R., Becker, H.-W., and Chakraborty, S. (2007). Fe-Mg diffusion in olivine I: experimental determination between 700 and 1,200°C as a function of composition, crystal orientation and oxygen fugacity. *Phys. Chem. Miner.* 34, 389–407. doi:10.1007/s00269-007-0157-7

Donaldson, C. H. (1985). The rates of dissolution of olivine, plagioclase, and quartz in a basalt melt. *Mineral. Mag.* 49, 683–693. doi:10.1180/minmag.1985.049.354.07

Drouin, M., Godard, M., Ildefonse, B., Bruguier, O., and Garrido, C. J. (2009). Geochemical and petrographic evidence for magmatic impregnation in the oceanic lithosphere at Atlantis Massif, Mid-Atlantic Ridge (IODP Hole U1309D, 30°N). *Chem. Geol.* 264, 71–88. doi:10.1016/j.chemgeo.2009.02.013

Dunn, R. A. (2015). "Crust and lithospheric structure - seismic structure of mid-ocean ridges," in *Treatise on geophysics*. New York, NY: Elsevier, 419–451.

Dunn, R. A., Lekić, V., Detrick, R. S., and Toomey, D. R. (2005). Three-dimensional seismic structure of the Mid-Atlantic Ridge (35°N): evidence for focused melt supply and lower crustal dike injection. *J. Geophys. Res. Solid Earth* 110, 1–17. doi:10.1029/2004JB003473

Edwards, B. R., and Russell, J. K. (1998). Time scales of magmatic processes: new insights from dynamic models for magmatic assimilation. *Geology* 26, 1103. doi:10.1130/0091-7613(1998)026<1103:TSOMPN>2.3.CO;2

Escartín, J., Mével, C., MacLeod, C. J., and McCaig, A. M. (2003). Constraints on deformation conditions and the origin of oceanic detachments: the Mid-Atlantic Ridge core complex at 15°45′N. *Geochem. Geophys. Geosyst.* 4, 1067. doi:10.1029/2002GC000472

Ferrando, C., Godard, M., Ildefonse, B., and Rampone, E. (2018). Melt transport and mantle assimilation at Atlantis Massif (IODP Site U1309): constraints from geochemical modeling. *Lithos* 323, 24–43. doi:10.1016/j.lithos.2018.01.012

France, L., Ildefonse, B., and Koepke, J. (2009). Interactions between magma and hydrothermal system in Oman ophiolite and in IODP Hole 1256D: fossilization of a dynamic melt lens at fast spreading ridges. *Geochem. Geophys. Geosyst.* 10, 1–30. doi:10.1029/2009GC002652

Gao, Y., Hoefs, J., Hellebrand, E., von der Handt, A., and Snow, J. E. (2007). Trace element zoning in pyroxenes from ODP Hole 735B gabbros: diffusive exchange or synkinematic crystal fractionation? *Contrib. Mineral. Petrol.* 153, 429–442. doi:10.1007/s00410-006-0158-4

Ghiorso, M. S., and Gualda, G. A. R. (2015). An H_2O-CO_2 mixed fluid saturation model compatible with rhyolite-MELTS. *Contrib. Mineral. Petrol.* 169, 53. doi:10.1007/s00410-015-1141-8

Godard, M., Awaji, S., Hansen, H., Hellebrand, E., Brunelli, D., Johnson, K., et al. (2009). Geochemistry of a long in-situ section of intrusive slow-spread oceanic lithosphere: results from IODP Site U1309 (Atlantis Massif, 30°N Mid-Atlantic-Ridge). *Earth Planet. Sci. Lett.* 279, 110–122. doi:10.1016/j.epsl.2008.12.034

Grimes, C. B., Cheadle, M. J., John, B. E., Reiners, P. W., and Wooden, J. L. (2011). Cooling rates and the depth of detachment faulting at oceanic core complexes: evidence from zircon Pb/U and (U-Th)/He ages. *Geochem. Geophys. Geosyst.* 12 (3), Q0AG01. doi:10.1029/2010GC003391

Grimes, C. B., John, B. E., Cheadle, M. J., and Wooden, J. L. (2008). Protracted construction of gabbroic crust at a slow spreading ridge: constraints from 206Pb/238U zircon ages from Atlantis Massif and IODP Hole U1309D (30°N, MAR). *Geochem. Geophys. Geosyst.* 9, Q08012. doi:10.1029/2008GC002063

Grove, T. L., Kinzler, R. J., and Bryan, W. B. (1992). "Fractionation of mid-ocean ridge basalt (MORB)," in *Mantle flow and melt generation at Mid-Ocean Ridges*. Editors J. P. Morgan, D. K. Blackman, and J. M. Sinton (Washington, DC: AGU Advances), 281–310.

Gualda, G. A. R., and Ghiorso, M. S. (2015). MELTS_Excel: A Microsoft Excel-based MELTS interface for research and teaching of magma properties and evolution. *Geochem. Geophys. Geosyst.* 16, 315–324. doi:10.1002/2014GC005545

Hart, S. R., Blusztajn, J., Dick, H. J. B., Meyer, P. S., and Muehlenbachs, K. (1999). The fingerprint of seawater circulation in a 500-meter section of ocean crust gabbros. *Geochem. Cosmochim. Acta* 63, 4059–4080. doi:10.1016/S0016-7037(99)00309-9

Hertogen, J., Emmermann, R., Robinson, P. T., and Erzinger, J. (2002). Lithology, mineralogy, and geochemistry of the lower ocean crust, ODP Hole 735B, Southwest Indian Ridge. *Proc. Ocean Drill. Prog. Sci. Results* 176, 75. doi:10.2973/odp.proc.sr.176.003.2002

Holm, P. M. (2002). Data report: on the composition of the lower ocean crust-major and trace element analyses of gabbroic rocks from Hole 735B, 500–1500 mbsf. *Proc. Ocean Drill. Prog. Sci. Results* 176, 1–13. doi:10.2973/odp.proc.sr.176.020.2002

Hooft, E. E. E., Detrick, R. S., and Kent, G. M. (1997). Seismic structure and indicators of magma budget along the southern East Pacific Rise. *J. Geophys. Res. Solid Earth* 102 (B12), 27319–27340. doi:10.1029/97JB02349

Ildefonse, B., Blackman, D. K., John, B. E., Ohara, Y., Miller, D. J., MacLeod, C. J., et al. (2007). Oceanic core complexes and crustal accretion at slow-spreading ridges. *Geology* 35, 623–626. doi:10.1130/G23531A.1

Jian, H., Singh, S. C., Chen, Y. J., and Li, J. (2016). Evidence of an axial magma chamber beneath the ultraslow-spreading Southwest Indian Ridge. *Geology* 45, 143–146. doi:10.1130/G38356.1

John, B. E., Foster, D. A., Murphy, J. M., Cheadle, M. J., Baines, A. G., Fanning, C. M., et al. (2004). Determining the cooling history of in situ lower oceanic crust-Atlantis Bank, SW Indian Ridge. *Earth Planet. Sci. Lett.* 222, 145–160. doi:10.1016/j.epsl.2004.02.014

Kelemen, P. B., Koga, K., and Shimizu, N. (1997). Geochemistry of gabbro sills in the crust-mantle transition zone of the Oman ophiolite: implications for the origin of the oceanic lower crust. *Earth Planet. Sci. Lett.* 146, 475–488. doi:10.1016/s0012-821x(96)00235-x

Koepke, J., Berndt, J., Feig, S. T., and Holtz, F. (2007). The formation of SiO_2-rich melts within the deep oceanic crust by hydrous partial melting of gabbros. *Contrib. Mineral. Petrol.* 153, 67–84. doi:10.1007/s00410-006-0135-y

Koepke, J., Botcharnikov, R. E., and Natland, J. H. (2018). Crystallization of late-stage MORB under varying water activities and redox conditions: implications for the formation of highly evolved lavas and oxide gabbro in the ocean crust. *Lithos* 323, 58–77. doi:10.1016/j.lithos.2018.10.001

Koepke, J., Feig, S., and Snow, J. (2005a). Late stage magmatic evolution of oceanic gabbros as a result of hydrous partial melting: evidence from the Ocean Drilling Program (ODP) Leg 153 drilling at the Mid-Atlantic Ridge. *Geochem. Geophys. Geosyst.* 6, Q02001. doi:10.1029/2004GC000805

Koepke, J., Feig, S. T., and Snow, J. (2005b). Hydrous partial melting within the lower oceanic crust. *Terra. Nova.* 17, 286–291. doi:10.1111/j.1365-3121.2005.00613.x

Kvassnes, A. J. S. (2003). The evolution of oceanic gabbros: in situ and ancient examples. PhD thesis. Cambridge (MA): Massachusetts Institute of Technology and Woods Hole Oceanographic Institution.

Lambart, S., Koornneef, J. M., Millet, M.-A., Davies, G. R., Cook, M., and Lissenberg, C. J. (2019). Highly heterogeneous depleted mantle recorded in the lower oceanic crust. *Nat. Geosci.* 12, 482–486. doi:10.1038/s41561-019-0368-9

Leuthold, J., Lissenberg, C. J., O'Driscoll, B., Karakas, O., Falloon, T., Klimentyeva, D. N., et al. (2018). Partial melting of lower oceanic crust gabbro: constraints from poikilitic clinopyroxene primocrysts. *Front. Earth Sci.* 6, 15. doi:10.3389/feart.2018.00015

Lissenberg, C. J., Bédard, J. H., and van Staal, C. R. (2004). The structure and geochemistry of the gabbro zone of the Annieopsquotch ophiolite, Newfoundland: implications for lower crustal accretion at spreading ridges. *Earth Planet. Sci. Lett.* 229, 105–123. doi:10.1016/j.epsl.2004.10.029

Lissenberg, C. J., and Dick, H. J. B. (2008). Melt-rock reaction in the lower oceanic crust and its implications for the genesis of mid-ocean ridge basalt. *Earth Planet. Sci. Lett.* 271, 311–325. doi:10.1016/j.epsl.2008.04.023

Lissenberg, C. J., and MacLeod, C. J. (2016). A reactive porous flow control on mid-ocean ridge magmatic evolution. *J. Petrol.* 57, 2195–2220. doi:10.1093/petrology/egw074

Lissenberg, C. J., MacLeod, C. J., and Bennett, E. N. (2019). Consequences of a crystal mush-dominated magma plumbing system: A mid-ocean ridge perspective. *Philos. Trans. A Math. Phys. Eng. Sci.* 377, 20180014. doi:10.1098/rsta.2018.0014

Lissenberg, C. J., MacLeod, C. J., Howard, K. A., and Godard, M. (2013). Pervasive reactive melt migration through fast-spreading lower oceanic crust (Hess Deep, equatorial Pacific Ocean). *Earth Planet. Sci. Lett.* 361, 436–447. doi:10.1016/j.epsl.2012.11.012

Lissenberg, C. J., Rioux, M., Shimizu, N., Bowring, S. A., and Mevel, C. (2009). Zircon dating of oceanic crustal accretion. *Science* 323, 1048–1050. doi:10.1126/science.1167330

MacLeod, C. J., Dick, H. J. B., Blum, P., Abe, N., Blackman, D. K., Bowles, J. A., et al. (2017). Site U1473. *Proc. Ocean Drill. Progr.* 360. doi:10.14379/iodp.proc.360.103.2017

Marjanović, M., Carbotte, S. M., Carton, H., Nedimović, M. R., Mutter, J. C., and Canales, J. P. (2014). A multi-sill magma plumbing system beneath the axis of the East Pacific Rise. *Nat. Geosci.* 7, 825–829. doi:10.1038/ngeo2272

McDonough, W. F., and Sun, S.-S. (1995). The composition of the earth. *Chem. Geol.* 120, 223–253. doi:10.1016/0009-2541(94)00140-4

Natland, J. H., and Dick, H. J. B. (2001). A brief narrative history of ODP Hole 735B. *Proc. Ocean Drill. Prog. Sci. Results* 176, 1–20. doi:10.2973/odp.proc.sr.176.021.2002

Natland, J. H., and Dick, H. J. B. (2002). Stratigraphy and composition of gabbros drilled in ODP Hole 735B, SWIR: a synthesis of geochemical data. *Proc. Ocean Drill. Prog.Sci. Results* 176, 1–69. doi:10.2973/odp.proc.sr.176.002.2002

Natland, J. H., Meyer, P. S., Dick, H. J. B., and Bloomer, S. H. (1991). Magmatic oxides and sulfides in gabbroic rocks from Hole 735B and the later development of the liquid line of descent. *Proc. Ocean Drill. Prog. Sci. Results* 118, 75–111. doi:10.2973/odp.proc.sr.118.163.1991

Nguyen, D., Morishita, T., Soda, Y., Tamura, A., Ghosh, B., Harigane, Y., et al. (2018). Occurrence of felsic rocks in oceanic gabbros from IODP hole U1473A: implications for evolved melt migration in the lower oceanic crust. *Minerals* 8, 583. doi:10.3390/min8120583

Niu, Y., Gilmore, T., Mackie, S., Greig, A., and Bach, W. (2002). Mineral chemistry, whole-rock compositions, and petrogenesis of Leg 176 gabbros: data and discussion. *Proc. Ocean Drill. Prog. Sci. Results* 176, 1–60. doi:10.2973/odp.proc.sr.176.011.2002

Pearce, N. J. G., Perkins, W. T., Westgate, J. A., Gorton, M. P., Jackson, S. E., Neal, C. R., et al. (1997). A compilation of new and published major and trace element data for NIST SRM 610 and NIST SRM 612 glass reference materials. *Geostand. Newsl.* 21, 115–144. doi:10.1111/j.1751-908X.1997.tb00538.x

Rannou, E., Caroff, M., and Cordier, C. (2006). A geochemical approach to model periodically replenished magma chambers: does oscillatory supply account for the magmatic evolution of EPR 17-19°S? *Geochem. Cosmochim. Acta* 70, 4783–4796. doi:10.1016/j.gca.2006.07.007

Reiners, P. W., Nelson, B. K., and Ghiorso, M. S. (1995). Assimilation of felsic crust by basaltic magma: thermal limits and extents of crustal contamination of mantle-derived magmas. *Geology* 23, 563–566. doi:10.1130/0091-7613(1995)023<0563:aofcbb>2.3.co;2

Rioux, M., Cheadle, M. J., John, B. E., and Bowring, S. A. (2016). The temporal and spatial distribution of magmatism during lower crustal accretion at an ultraslow-spreading ridge: high-precision U-Pb zircon dating of ODP Holes 735B and 1105A, Atlantis Bank, Southwest Indian Ridge. *Earth Planet Sci. Lett.* 449, 395–406. doi:10.1016/j.epsl.2016.05.047

Robinson, P. T., Dick, H. J. B., Natland, J. H., Alt, J. C., Bach, W., Bideau, D., et al. (2000). Lower oceanic crust formed at an ultra-slow-spreading ridge: Ocean Drilling Program Hole 735B, Southwest Indian Ridge. *Geol. Soc. Am. Spec. Pap.* 349, 75–86. doi:10.1130/0-8137-2349-3.75

Rubin, K. H., and Sinton, J. M. (2007). Inferences on mid-ocean ridge thermal and magmatic structure from MORB compositions. *Earth Planet. Sci. Lett.* 260, 257–276. doi:10.1016/j.epsl.2007.05.035

Sanfilippo, A., and Tribuzio, R. (2011). Melt transport and deformation history in a nonvolcanic ophiolitic section, northern Apennines, Italy: implications for crustal accretion at slow spreading settings. *Geochem. Geophys. Geosyst.* 12, 1–34. doi:10.1029/2010GC003429

Sanfilippo, A., Tribuzio, R., and Tiepolo, M. (2014). Mantle-crust interactions in the oceanic lithosphere: constraints from minor and trace elements in olivine. *Geochem. Cosmochim. Acta* 141, 423–439. doi:10.1016/j.gca.2014.06.012

Schneider, C. A., Rasband, W. S., Eliceiri, K. W., and Instrumentation, C. (2017). NIH image to ImageJ: 25 years of image analysis. *Nat. Methods* 9, 671–675. doi:10.1038/nmeth.2089

Schwartz, J. J., John, B. E., Cheadle, M. J., Reiners, P. W., and Baines, A. G. (2009). Cooling history of Atlantis Bank oceanic core complex: evidence for hydrothermal activity 2.6 Ma off axis. *Geochem. Geophys. Geosyst.* 10, Q08020. doi:10.1029/2009GC002466

Shipboard Scientific Party (SSP). (1989). Shipboard Scientific Party 2 HOLE 735A. *Proc. Ocean Drill. Prog. Sci. Results* 118, 89–222. doi:10.2973/odp.proc.ir.118.107.1989

Singh, S. C., Crawford, W. C., Carton, H., Seher, T., Combier, V., Cannat, M., et al. (2006). Discovery of a magma chamber and faults beneath a Mid-Atlantic Ridge hydrothermal field. *Nature* 442, 1029–1032. doi:10.1038/nature05105

Spandler, C., and O'Neill, H. S. C. (2010). Diffusion and partition coefficients of minor and trace elements in San Carlos olivine at 1,300°C with some geochemical implications. *Contrib. Mineral. Petrol.* 159, 791–818. doi:10.1007/s00410-009-0456-8

Suhr, G., Hellebrand, E., Johnson, K., and Brunelli, D. (2008). Stacked gabbro units and intervening mantle: a detailed look at a section of IODP Leg 305, Hole U1309D. *Geochem. Geophys. Geosy.* 9, Q10007. doi:10.1029/2008GC002012

Sun, C., Graff, M., and Liang, Y. (2017). Trace element partitioning between plagioclase and silicate melt: the importance of temperature and plagioclase composition, with implications for terrestrial and lunar magmatism. *Geochem. Cosmochim. Acta* 206, 273–295. doi:10.1016/j.gca.2017.03.003

Sun, C., and Liang, Y. (2013). The importance of crystal chemistry on REE partitioning between mantle minerals (garnet, clinopyroxene, orthopyroxene, and olivine) and basaltic melts. *Chem. Geol.* 358, 23–36. doi:10.1016/j.chemgeo.2013.08.045

Sun, C., and Liang, Y. (2014). An assessment of subsolidus re-equilibration on REE distribution among mantle minerals olivine, orthopyroxene, clinopyroxene and garnet in peridotites. *Chem. Geol.* 372, 80–91. doi:10.1016/j.chemgeo.2014.02.014

Sun, C., and Liang, Y. (2017). A REE-in-plagioclase-clinopyroxene thermometer for crustal rocks. *Contrib. Mineral. Petrol.* 172, 24. doi:10.1007/s00410-016-1326-9

Tucholke, B. E., and Lin, J. (1994). A geological model for the structure of ridge segments in slow spreading ocean crust. *J. Geophys. Res.* 99, 11937–11958. doi:10.1029/94jb00338

van Achterbergh, E., Ryan, C. G., Jackson, S. E., and Griffin, W. L. (2001). "Data reduction software for LA-ICP-MS," in *Laser ablation ICP-MS in Earth science: principles and applications*. Editor P. J. Sylvester (Québec, Canada: Mineralogical Association of Canada), 239–243.

Villiger, S., Müntener, O., and Ulmer, P. (2007). Crystallization pressures of mid-ocean ridge basalts derived from major element variations of glasses from equilibrium and fractional crystallization experiments. *J. Geophys. Res. Solid Earth* 112, 1–18. doi:10.1029/2006JB004342

Wood, B. J., and Blundy, J. D. (1997). A predictive model for rare earth element partitioning between clinopyroxene and anhydrous silicate melt. *Contrib. Mineral. Petrol.* 129, 166–181. doi:10.1007/s004100050330

Yang, A. Y., Wang, C., Liang, Y., and Lissenberg, C. J. (2019). Reaction between MORB magma and lower oceanic crust: an experimental study. *Geochem. Geophys. Geosyst.* 20, 4390–4407. doi:10.1029/2019GC008368

Zimmerman, M. E., Zhang, S., Kohlstedt, D. L., and Karato, S.-i. (1999). Melt distribution in mantle rocks deformed in shear. *Geophys. Res. Lett.* 26, 1505–1508. doi:10.1029/1999gl900259

Conflict of Interest: The authors declare that the research was conducted in the absence of any commercial or financial relationships that could be construed as a potential conflict of interest.

frontiers
in Earth Science

ORIGINAL RESEARCH
published: 09 November 2020
doi: 10.3389/feart.2020.579138

Early-Stage Melt-Rock Reaction in a Cooling Crystal Mush Beneath a Slow-Spreading Mid-Ocean Ridge (IODP Hole U1473A, Atlantis Bank, Southwest Indian Ridge)

Alessio Sanfilippo[1,2,3]*, *Christopher J. MacLeod*[4], *Riccardo Tribuzio*[2,3], *C. Johan Lissenberg*[4] *and Alberto Zanetti*[5]

[1] Dipartimento di Scienze della Terra e dell'Ambiente, Universita' di Pavia, Pavia, Italy, [2] Graduate School of Natural Science and Technology, Kanazawa University, Kanazawa, Japan, [3] Istituto Geoscienze e Georisorse, Pavia, Italy, [4] School of Earth and Environmental Sciences, Cardiff University, Cardiff, United Kingdom, [5] National Research Council, Roma, Italy

OPEN ACCESS

Edited by:
Wendy A. Bohrson,
Colorado School of Mines,
United States

Reviewed by:
Takeshi Kuritani,
Hokkaido University, Japan
Michel Grégoire,
Centre National de la Recherche
Scientifique (CNRS), France

***Correspondence:**
Alessio Sanfilippo
Alessio.sanfilippo@unipv.it

Specialty section:
This article was submitted
to Petrology,
a section of the journal
Frontiers in Earth Science

Received: 01 July 2020
Accepted: 23 September 2020
Published: 09 November 2020

Citation:
Sanfilippo A, MacLeod CJ, Tribuzio R, Lissenberg CJ and Zanetti A (2020) Early-Stage Melt-Rock Reaction in a Cooling Crystal Mush Beneath a Slow-Spreading Mid-Ocean Ridge (IODP Hole U1473A, Atlantis Bank, Southwest Indian Ridge). Front. Earth Sci. 8:579138. doi: 10.3389/feart.2020.579138

Microtextural and chemical evidence from gabbros indicates that melts may react with the crystal framework as they migrate through crystal mushes beneath mid-ocean ridges; however, the importance of this process for the compositional evolution of minerals and melts remains a matter of debate. Here we provide new insights into the extent by which melt-rock reaction process can occur in oceanic gabbros by conducting a detailed study of cryptic reactive melt migration as preserved in an apparently unremarkable, homogeneous olivine gabbro from deep within a section of the plutonic footwall of the Atlantis Bank core complex on the Southwest Indian Ridge (International ocean discovery program Hole U1473A). High-resolution chemical maps reveal that mineral zoning increases toward and becomes extreme within a cm-wide band that is characterized by elevated incompatible trace element concentrations and generates extreme more/less incompatible element ratios. We demonstrate that neither crystallization of trapped melt nor diffusion can account for these observations. Instead, taking the novel approach of correcting mineral-melt partition coefficients for both temperature and composition, we show that these chemical variations can be generated by intergranular reactive porous flow of a melt as it migrated through the mush framework, and whose composition evolved by melt-rock reaction as it progressively localized into a cm-scale reactive channel. We propose that the case reported here may represent, in microcosm, a preserved snapshot of a generic mechanism by which melt can percolate through primitive mafic (olivine gabbro) crystal mushes, and be modified toward more evolved compositions via near-pervasive reactive transport.

Keywords: melt-rock reaction, reactive porous flow, lower oceanic crust, mineral zoning, South West Indian ridge

INTRODUCTION

Seismic investigations of mid-ocean ridges have shown that the large, km-scale melt-filled magma chambers originally inherent in ophiolite-derived models do not exist: at even the most magmatically robust fast-spreading ridges most of the lower ocean crust beneath the ridge axis transmits shear waves and is therefore largely solid, albeit normally with a tiny melt-rich lens or sill ≤10 s of meters thick present at the very top of the lower crust; instead, it is now generally believed that the broader lower crustal region must be comprised of a "crystal mush", apparently consisting of no more than a few percent interstitial melt overall (e.g. Detrick et al., 1987; Sinton and Detrick, 1992). At slower-spreading ridges, below ~50 mm/yr, even this small axial melt lens is not normally observed: detection of a comparable melt body in a few cases (e.g. Sinha et al., 1998) suggests it can exist but instead as a transient feature, although there are some indications that comparable crystal mush is present more widely in the lower crust beneath slower-spreading ridge axes (e.g. Singh et al., 2006). More broadly, the relative paucity of magma, together with observations such as the exposure of plutonic and/or mantle rocks on the seafloor near some slow-spreading mid-ridge axes, all leads to the recognition that melt delivery from the mantle at slower-spreading rates may be restricted in space and time, and is not always sufficient to generate or maintain a continuous magmatic crustal layer (Cannat et al., 2006). In such an environment, extensional tectonic processes are an integral part of the plate spreading process. Although subsequent geophysical experiments have identified small, sill-like melt bodies within the deeper lower crustal region beneath faster-spreading mid-ocean ridges (e.g., Marjanovic et al., 2014), the mechanisms of formation of the crystal mush, and the igneous processes that generate it, are poorly understood. From an igneous perspective, it is however agreed in broad terms that the magmatic lower crustal crystal mush must ultimately form by solidification of successive magma batches that somehow intrude, underplate and dissect existing crystal frameworks. At slower spreading ridges, this accretionary process is likely to be further complicated by physical and chemical interactions between different magmatic intrusions injected into an actively deforming environment (Dick et al., 2019b).

Several authors have suggested that when fresh injections of hot, primitive magma are intruded into a host rock they provide enough heat to melt the host minerals to some degree (Bédard et al., 2000; Leuthold et al., 2014; Coumans et al., 2016). Crustal melts can be produced and assimilated within the actively forming crustal mushes, leading to fundamental changes in melt (e.g., DePaolo, 1981; Solano et al., 2014; Jackson et al., 2018) and crystal compositions (Eason and Sinton, 2009). Furthermore, extensive reaction between interstitial liquid and host may also occur when chemically evolved melts migrate upwards, driven by buoyancy, compaction, deformation, or a combination thereof (Natland and Dick, 2001; Lissenberg et al., 2013, 2019). The equilibration between minerals and migrating melts leads to changes in mineral and melt chemistry at the reaction front, and these reactive melts crystallize new phases around partly resorbed pre-existing minerals, ultimately modifying or even completely replacing the original crystal matrix (Coogan et al., 2000; Lissenberg and Dick, 2008; Suhr et al., 2008; Drouin et al., 2009; Drouin et al., 2010; Sanfilippo et al., 2015; Tamura et al., 2016 Ferrando et al., 2018). Whether leading to partial melting of the host rocks or selective dissolution of a crystal matrix, the assimilation of crustal material in the ascending magmas may be sufficiently efficient (Kvassnes and Grove, 2008; Yang et al., 2019) to potentially control the major- and trace element budgets of the melts erupted at the surface (e.g., Lissenberg and Dick, 2008; Lissenberg and MacLeod, 2016; Sanfilippo et al., 2016; Jackson et al., 2018; Renna et al., 2018; Lissenberg et al., 2019).

Textural evidence for reactive melt migration processes is widely preserved in abyssal and ophiolitic gabbros, and generally includes: 1) large poikilitic clinopyroxene (Cpx) locally containing resorbed olivine (Ol) and plagioclase (PL) chadacrysts (Blackman et al., 2006; Lissenberg and Dick, 2008; Sanfilippo and Tribuzio, 2013; Leuthold et al., 2014; 2018); 2) resorbed cores with higher An compared to the rim compositions in cumulus Pl (Lissenberg et al., 2013, Lissenberg et al., 2019; Lissenberg and MacLeod, 2016); 3) complex intergrowths of irregular Cpx commonly containing small (<100 μm) blebs of magmatic amphibole (Amp), oxides and orthopyroxene (Opx) (Tribuzio et al., 1999; Coogan et al., 2001; Dick et al., 2002; Beard et al., 2004; Lissenberg and MacLeod, 2016); and 4) Cpx-Amp symplectites (Lissenberg and MacLeod, 2016). However, Lissenberg and MacLeod (2016) recently provided evidence for reactive porous flow that was nearly undetectable from a textural perspective. They used Ti–Cr element mapping to show that chemical zoning characterizes the crystals of primitive olivine gabbros that otherwise possess an unremarkable, apparently well-equilibrated cumulus texture, and hypothesized that the chemical changes in minerals from these samples could be produced by reaction with migrating melts. The cryptic nature of the reaction was attributed to the fact that the reacting melt was at relatively high temperature, similar to that at which the original crystal framework was formed, and hence the reaction products were mineralogically similar to the original cumulus assemblage. If reactive melt flow can induce significant geochemical exchange in a cumulate system whilst leaving no characteristic textural signature in its wake, the process may be far more extensive and widespread in mafic cumulate systems than hitherto supposed. However, there is only very limited data to test this.

In this contribution we perform a detailed case-study of cryptic reaction between a crystal matrix and a migrating melt, developing a quantitative understanding of reactive porous flow at high temperatures (>1,050°C). We focus on an apparently mundane, texturally homogeneous olivine-gabbro from the plutonic lower crustal section of the Atlantis Bank oceanic core complex Southwest Indian Ridge; IODP Hole U1473A; (MacLeod et al., 2017). We will demonstrate that this key sample preserves evidence for a number of igneous processes that we argue are of broader significance at mid-ocean ridges and for mafic plutonic systems more generally. For the first time, we integrate high-resolution, thin section-scale chemical maps with detailed *in situ* mineral major- and trace-element analyses, to document a profound–yet petrographically undetectable–variability

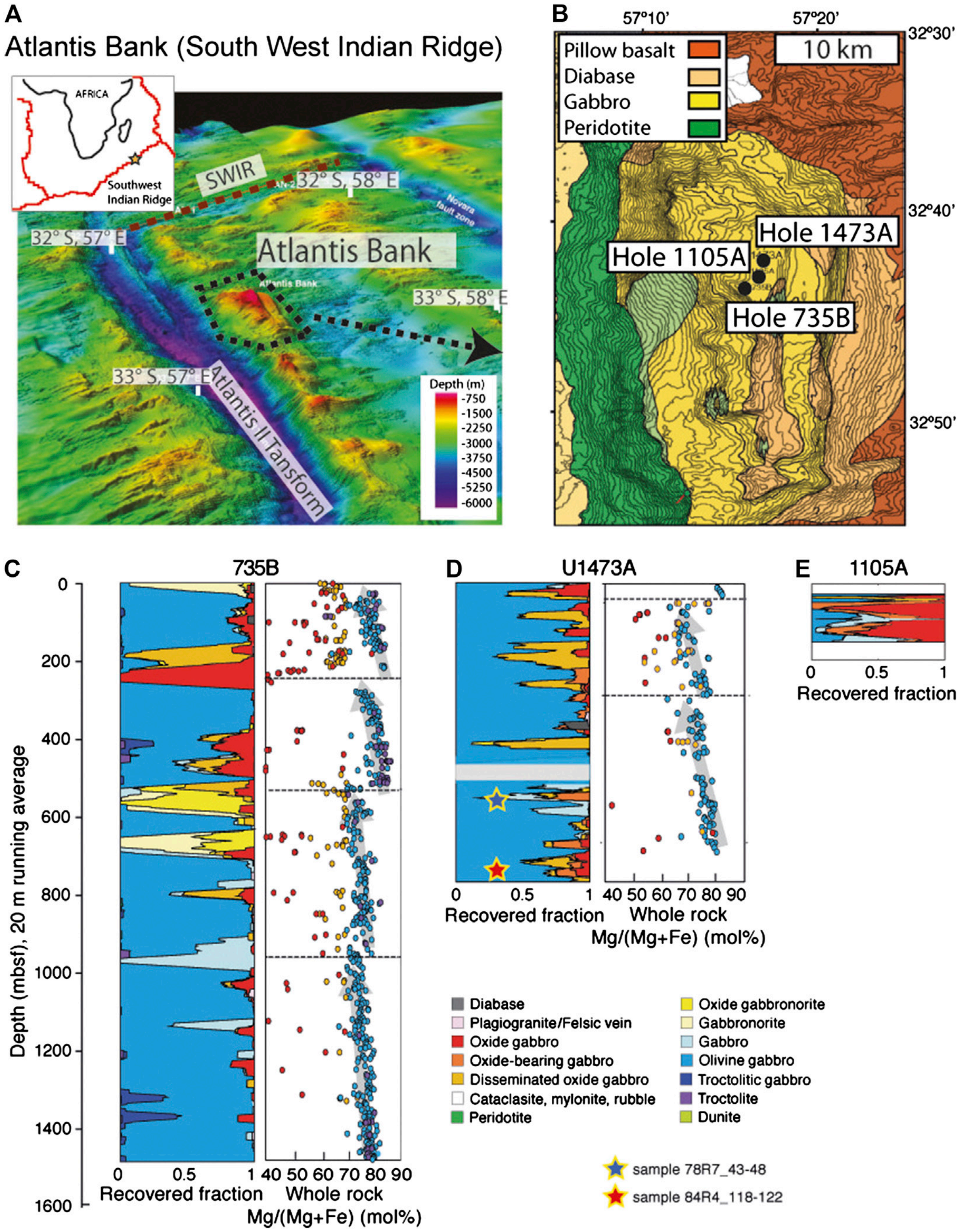

FIGURE 1 | (A) Location and bathymetric map of the Atlantis II Fracture Zone in the Southwest Indian Ridge and **(B)** and detail of the Atlantis Bank core complex showing the location of Holes 1105A, 735B and U1437A **(C)** Stratigraphic columns representing running averages of lithological intervals plotted against depth in Holes 735B, U1473A and 1105A. Whole rock Mg/(Mg + Fe) (mol%) compositions of samples from Hole 735B and U1473A are also reported, defining distinct geochemical units (modified from MacLeod et al., 2017). The location of samples U1473A-78R-7_43–48 and U1473A-84-R4_118–122 is also indicated.

in mineral composition and zoning throughout the sample, localized within a highly modified cm-scale "reaction band" within the sample. We show that the reaction band most likely represents a high local melt flux channel, and demonstrate that the mineral chemical modifications throughout the sample are explained by dissolution-reprecipitation melt-rock reactions that occurred under decreasing temperature conditions as melt migrated through the host crystal framework. If evidence for near-pervasive reactive porous melt migration is preserved in even the most mundane sample of primitive olivine gabbro, which we take as representative of the early-formed crystal mush framework in magma bodies beneath mid-ocean ridges–and this evidence is otherwise invisible without modern high-resolution chemical imaging and mapping–then it follows that reactive porous melt percolation through mushes may be a far more prevalent mechanism of melt transport and modification in the lower ocean crust than presupposed. Our study also highlights that the kind of detailed investigation presented here, integrating high-resolution, thin section-scale chemical maps with chemical profiles, are a first-order necessity to illuminate the chemical evolution of crystal mushes (Lissenberg & MacLeod, 2016), and to allow more meaningful comparison of the natural cases with theoretical models (e.g. Jackson et al., 2018).

LOWER OCEANIC CRUST AT HOLE U1473A, ATLANTIS BANK OCEANIC CORE COMPLEX SOUTHWEST INDIAN RIDGE

The Southwest Indian Ridge (SWIR) is a slow-to ultraslow-spreading mid-ocean ridge, spreading approximately N-S at a full spreading rate of 14 mm/yr. For much of its length the ridge trends SW-NE, oblique to its spreading direction. Between ~52°E and 60°E the Southwest Indian Ridge axis is offset by a series of prominent, long-offset N-S striking transform faults, among which the Atlantis II Transform (at 57°E) has an offset of 200 km. On a transverse ridge east of the transform valley and ~80 km south of the present axis lies the Atlantis Bank (**Figure 1A**), a large oceanic core complex that exposes a tectonic window of deep crustal and lithospheric mantle exhumed in the footwall of an 11–13 Myr old oceanic detachment fault (e.g., Dick et al., 1991; Dick et al., 2000). Atlantis Bank is comprised of a >400 km^2 gabbro massif overlying serpentinized mantle peridotites that crop out along the slopes of the eastern transform wall (Dick et al., 2019a). The shallowest part of Atlantis Bank is at ~700 m water depth and consists of a wave-cut platform rimmed by a thin limestone cap. Here, the top of the basement consists of amphibolitised gabbro mylonite generated by detachment faulting (MacLeod et al., 1998). Previous Ocean Drilling Program (ODP) operations at Atlantis Bank drilled the 1,508 m deep Hole 735B, and 150 m deep Hole 1105A, both recovering long sections of gabbro *sensu lato* (Dick et al., 1991; Dick et al., 2000; Pettigrew et al., 1999). Recently, International Ocean Discovery Program (IODP) Expedition 360 drilled a further deep hole, at Site U1473, located ~2.2 and 1.4 km north-northeast and north of Hole 735B and 1105A respectively (MacLeod et al., 2017; **Figure 1B**).

Eighty-nine cores were drilled at Hole U1473A (32°42.3622S 57°16.6880′E, 710.2 m water depth; MacLeod et al., 2017), supplemented by five further cores during engineering Expedition 362T, to a current total depth of 809.4 m below seafloor (mbsf; Blum et al., 2017). Overall recovery was 44%, relatively low in the upper part of the hole because of the presence of a fault zone, though markedly higher, at ~96%, in the lowermost few hundred meters. Similar to the previous drill holes at Atlantis Bank, the section drilled at IODP Hole U1473A is mainly composed of olivine (Ol) gabbro (Ol > 5 vol%), interspersed with more evolved oxide (Ox)-bearing varieties, and cut by felsic veins and rare diabase dykes (MacLeod et al., 2017; **Figure 1**). Most of the gabbros show textural evidence for crystal-plastic deformation, ranging from hyper-solidus to granulite and amphibolite grade facies, as a consequence of the deformation event related to the detachment faulting and exhumation of the plutonic basement.

The principal lithology is coarse-to medium-grained olivine gabbro (76.5%); only 5.1% of Hole U1473A is gabbro (<5 vol% olivine) *sensu stricto* (MacLeod et al., 2017). Primary magmatic textures throughout the hole are in many instances partially obscured by crystal-plastic deformation, typically expressed in the form of undulose extinction of cumulus phases and/or variable plagioclase neoblast formation, but extending in some instances to the development of mylonitic or ultramylonitic textures (MacLeod et al., 2017). Completely undeformed gabbros are preserved in only a few intervals: from petrographic examination we observe some degree of plagioclase neoblast development at grain boundaries in most of those units previously described as “undeformed” on the basis of macroscopic description (crystal-plastic fabric “0”: MacLeod et al., 2017). In the few samples in which recrystallization is absent in thin section the rocks appear generally equigranular, and with highly variable grain sizes ranging from fine-grained to pegmatitic. Magmatic fabrics are rare but, where visible, are defined by the preferred orientation of Pl and, in some instances, by the occurrence of decimetre-scale igneous layering defined predominantly by grain-size variation.

The Ol-gabbros are interspersed with evolved Ox-bearing (Ox > 1 vol%) lithologies, which include disseminated Ox-gabbro (Ox 1-2 vol%), Ox-bearing gabbro (Ox 2-5 vol%) and Ox-gabbro (Ox > 5 vol%) that constitute 9.5, 3.7, and 3.7% of the hole, respectively. Ox-bearing rocks tend to be slightly more deformed than the host Ol-gabbros and are widespread in the entire section at Hole U1473A (MacLeod et al., 2017), whereas they tend to be highly localized at several deformed horizons in shallower levels of Hole 735B (Ozawa et al., 1991). Finally, different generations of felsic rocks (i.e., leucodiorite, diorite, quartz diorite, trondhjemite, and tonalite) crosscut the Ol-gabbros in the form of irregular patches and veins. The felsic veins locally crosscut the foliation, although they may themselves be internally deformed. Felsic material makes up ~1.5 vol% of the core and tends to be concentrated in specific zones, within which it appears to have been formed either as intrusions of a late-stage melt or by crystallization of melts produced by local gabbro anatexis (e.g., Koepke et al., 2007; Nguyen et al., 2018).

Taken as a whole, the igneous stratigraphic relationships and range of lithologies recovered in Hole U1473A are similar to those encountered in the previous holes at Atlantis Bank, but cannot be compared directly. Altogether, the respective sequences show the absence of any direct correlation or systematic variation, either laterally (on a km-scale) or vertically (on a 100 s of meter scale), indicating that accretion of the lower crust in this region was governed by a complex, continual interplay between magmatic intrusion, crystallization and hyper-solidus to high-temperature sub-solidus deformation. As separately deduced from the plutonic complex sampled at Hole U1309D at Atlantis Massif (Mid-Atlantic Ridge), the only other long section drilled into an oceanic core complex thus far (Blackman et al., 2006; Blackman

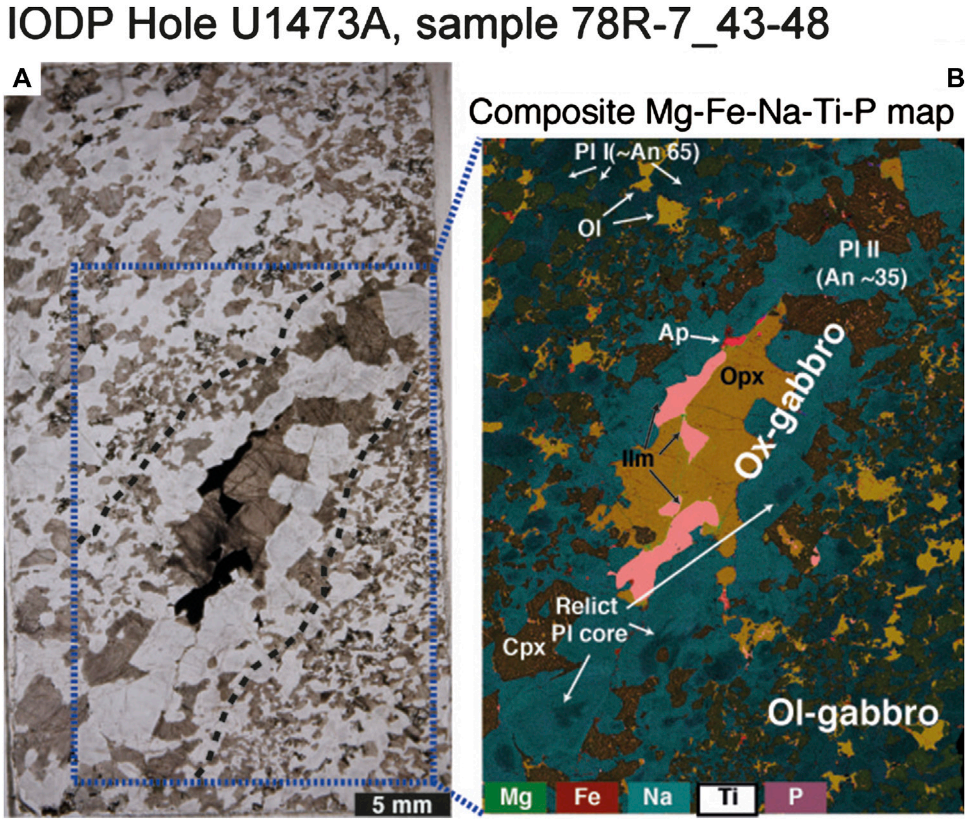

FIGURE 2 | (A) Photomicrograph and **(B)** composite Mg-Fe-Na-Ti-P compositional map of sample U1473A-78R-7_43–48. Dashed black lines contour the Ox-gabbro seam and delineate the boundary between the two regions displaying chemical variation in mineral compositions. Note that plagioclase cores with An compositions comparable to that of the host Ol-gabbro are preserved in the Ox-gabbro. Cpx, clinopyroxene; Ilm, ilmenite; Ol, olivine; Opx, orthopyroxene; Pl, plagioclase.

et al., 2011), the metre-scale heterogeneity in composition and texture suggests that the plutonic lower crust at slow-spreading ridges forms through the successive accretion of episodic “nested” intrusions to form an heterogeneous gabbroic layer (e.g., Cannat and Casey, 1995; Grimes et al., 2011; Rioux et al., 2016).

CHEMICAL EVIDENCE FOR REACTIVE MELT MIGRATION PROCESSES IN THE ATLANTIS BANK LOWER OCEANIC CRUST: PREVIOUS STUDIES

Previous authors have proposed that gabbros from Atlantis Bank experienced some degree of porous melt-crystal interaction (e.g., Dick et al., 1991, Dick et al., 2000; Gao et al., 2007; Lissenberg and MacLeod, 2016; MacLeod et al., 2017). Most obvious evidence for this process is the occurrence of centimetre-to decimetre-scale evolved Ox-rich gabbro patches and veinlets that cross-cut primitive Ol-gabbros, interpreted as localized zones of crystallization of highly evolved, Fe-Ti oxide-saturated melts (Dick et al., 1991; Dick et al., 2000; Ozawa et al., 1991; Natland and Dick 2001). Recently, Lissenberg and MacLeod (2016) used chemical maps and trace element profiles of petrographic thin sections from Hole 735B to propose that some mylonitic Ox-gabbro bands formed by a process of hybridization of a former Ol-gabbro that had been converted into an Ox-rich lithology by melt-rock reaction (see also Ozawa et al., 1991).

The same textural relationships between Ox- and Ol-gabbros are observed in Hole U1473A and the same reactive melt migration processes may also be inferred (see also MacLeod et al., 2017; Dick et al., 2019b). We report by way of example sample 360-U1473A-78R-7, 43–48 cm (**Figure 2**), a typical undeformed olivine gabbro notable in hand specimen principally for containing a narrow (12 mm-wide) band or pocket of coarser-grained Ox-gabbro (**Figure 2A**). Such primitive/evolved mineralogical relationships, with olivine and Fe-Ti oxide in close proximity, are widespread and unremarkable both in the Hole U1473A section (see MacLeod et al., 2017) and in gabbros from elsewhere in Atlantis Bank (Dick et al., 1999; Dick et al., 2019a). The contact between the two lithologies is diffuse, and ill-defined in both hand specimen or petrographic thin section (**Figure 2A**). The compositional difference between the two lithologies becomes obvious only in the combined

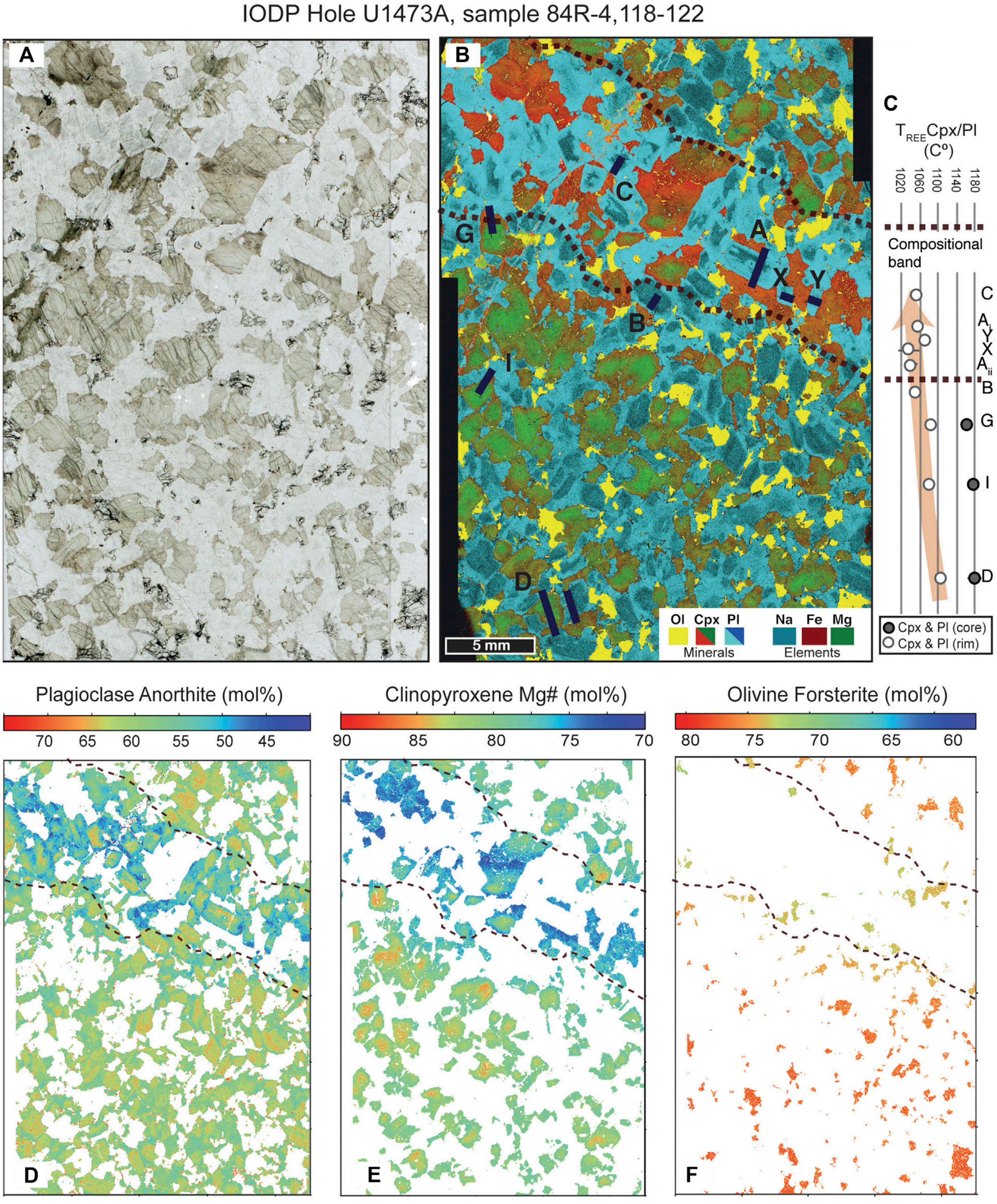

FIGURE 3 | (A) photomicrograph of sample U1473A-84R-4_118–112. The sample has a granular, equilibrated texture, with negligible crystal plastic deformation, and lacking petrographic evidence for mineral reactions. The composite Mg-Fe-Na-Ti element map in **(B)** however reveals a compositional band within which plagioclase and clinopyroxene have more evolved compositions. Corroded plagioclase cores are preserved in the band. **(C)** Variation of the Cpx-Pl equilibration temperatures using the Cpx-PlREE-Y geothermometer of Sun et al. (2017). Note that Cpx-Pl equilibration temperatures tend to decrease toward the compositional band. Core temperatures were not calculated within the band due to the lack of clinopyroxene having core compositions. **(D)** Anorthite maps in plagioclase **(E)** Fo map in olivine and **(F)** Mg# maps in clinopyroxene calculated using the Quack software. Black dashed lines in **(B)**, **(D)**, **(E)** and **(F)** delineate the compositional band. Also indicated in **(B)** are the areas selected for the detailed trace element determination and the geochemical traverses (black lines).

element map (**Figure 2B**; see Cryptic Chemical Variations in an Apparently Homogeneous Olivine-Gabbro below) from which it is evident that the minerals in the Ox-gabbro band have substantially more evolved compositions (Pl An ~35, Cpx Mg# ~65) than the host (Pl An~65, Cpx Mg#~82). However, we note the occurrence of relict, partially resorbed cores of high An plagioclase which, coupled with the gradational decrease of the An content in the Pl of the host Ol-gabbros, is hard to explain by the simple *in situ* crystallization of a melt pocket; instead, it suggests that the Ox-gabbros formed by the migration of chemically evolved (Fe-Ti-rich) melt into an existing crystal matrix of primitive Ol, Pl and Cpx. This deduction is directly comparable to that inferred from previous studies on Ox-gabbros from Hole 735B Ox-gabbros (e.g., Ozawa et al., 1991; Lissenberg and MacLeod, 2016).

Whether reactive porous flow is also a significant process in the Ol-gabbros that are the primary constituent of the section at Atlantis Bank (~77%) and regarded as the primary crystal mush framework, is more difficult to assess. Gao et al. (2007) previously documented strong core–rim enrichment in incompatible elements of Cpx in the Hole 735B Ol-gabbros, which display over-enrichments in highly incompatible trace elements relative to less incompatible trace elements (i.e., Ce to Y; Zr to Nd). These authors showed that enrichments in Zr and LREE are more extreme than those expected in fractional crystallization models, and cannot be explained by crystallization of trapped melt *in situ* (Bedard 1994). Similar trace element zoning patterns were documented by Lissenberg and MacLeod (2016) in a core–rim traverse of a large (8 mm) Cpx from an apparently homogeneous Ol-gabbro. They measured the core–rim distributions of several trace elements (i.e., Cr, Ti, Y, Yb, Nd, Zr, Ce and La), and noted selective over-enrichment from core to rim in La, Zr and Ce (all reaching a factor of ~30x enrichment from core to rim) and, furthermore, strong concomitant increases in Ce/Y and Zr/Nd ratios. Together with the preservation of Mg-Fe chemical zoning, these observations led the same authors to conclude that the grain-scale over-enrichment both in incompatible trace element abundances and trace element ratios in Ol-gabbro resulted from dissolution–reprecipitation reactions between migrating melts and a primitive crystal mush.

CRYPTIC CHEMICAL VARIATIONS IN AN APPARENTLY HOMOGENEOUS OLIVINE-GABBRO

Sample Selection and Analytical Methodology

In this study we hereinafter focus on an apparently unremarkable "typical" coarse-grained olivine gabbro, in which the potentially complicating effects of deformation are absent and which lacks any visible textural evidence of melt-rock interaction. This sample (360-U1473A-84R-4, 118–122 cm; 746 m below seafloor; **Figure 3**) has some of the most primitive mineral compositions encountered at Hole U1473A and contains an extremely low proportion of accessory phases, so much so that it was initially selected for study as a typical representative of the predominant olivine gabbro facies and hence pre-supposed to be the least modified representative of the original cumulate crystal mush. Oxides and apatite are found only as a few <0.1 mm grains, and Amp and Opx are absent completely. Cpx and Pl have sub-ophitic texture, whereas Ol is typically subhedral to interstitial, although a few fine-grained Ol chadacrysts are locally included in Cpx.

We acquired chemical maps of whole thin sections of the sample using a Zeiss Sigma HD field emission gun SEM installed at Cardiff University. This machine is equipped with dual 150-mm^2 Oxford Instruments X-Max^N energy dispersive silicon drift detectors, which enable high count rates (>1,000,000 cps) and rapid acquisition of quantitative element maps of all phases e.g. Pl anorthite and Cpx Mg#, in this case at 10 μm step ("pixel") size. The data were background-corrected using Oxford Instruments AZtec software prior to the production of element maps. Mineral major element compositions (An in Pl, Mg# in Cpx and Fo in Ol) were quantified from the element maps using the approach of Loocke (2016).

Major element compositions of points along a series of detailed mineral transects were separately acquired using a JEOL JXA-8200 electron microprobe located at Dipartimento di Scienze della Terra, Universita' degli Studi di Milano (Italy). Conditions of analyses were 15 kV accelerating voltage and 15 nA beam current. Counting time was 30 s on the peak and 10 s on the backgrounds. Natural standards were utilized and data reduction was carried out using the CITZAF package. Pl, Cpx and Ol compositions as deduced from the element maps (**Figure 3**) differ from the point analyses by ≤ 2% in An, Mg# and Fo.

Trace element compositions of clinopyroxene and plagioclase from these transects were obtained using Laser Ablation Inductively Coupled Plasma Mass Spectrometry (LA-ICP-MS) at C.N.R., Istituto di Geoscienze e Georisorse (Unita' di Pavia; **Supplementary Tables S1 and S2**). The probe consists of a PerkinElmerSCIEX ELAN DRC-e quadrupole mass spectrometer coupled with an UP213 deep-UV YAG Laser Ablation System (New Wave Research, Inc.). The laser was operated at a repetition rate of 10 Hz, with 213 nm wavelength and a fluence of ~9.5 J/cm^2. Helium was used as carrier gas and was mixed with Ar downstream of the ablation cell. Spot diameter ranged from 50 to 100 microns. Data reduction was performed offline using the GLITTER software. For this study, the NIST SRM 610 synthetic glass standards was used as external standard, and CaO as internal standard. Precision and accuracy of the REE concentration values were assessed through repeated analysis of the BCR2-g standard to be better than ±7% and ±10%, respectively, at the ppm concentration level.

Results

High-resolution chemical maps show that Pl and Cpx across the entire thin section exhibit prominent chemical zoning, characterized by an overall decrease in Pl An and Cpx Mg# from the cores to the rims of most minerals (**Figure 3**). Even more noteworthy is that the chemical maps also document an otherwise invisible increase in the extent of zoning toward an inclined, centimetre-wide band, within which Pl is characterized by

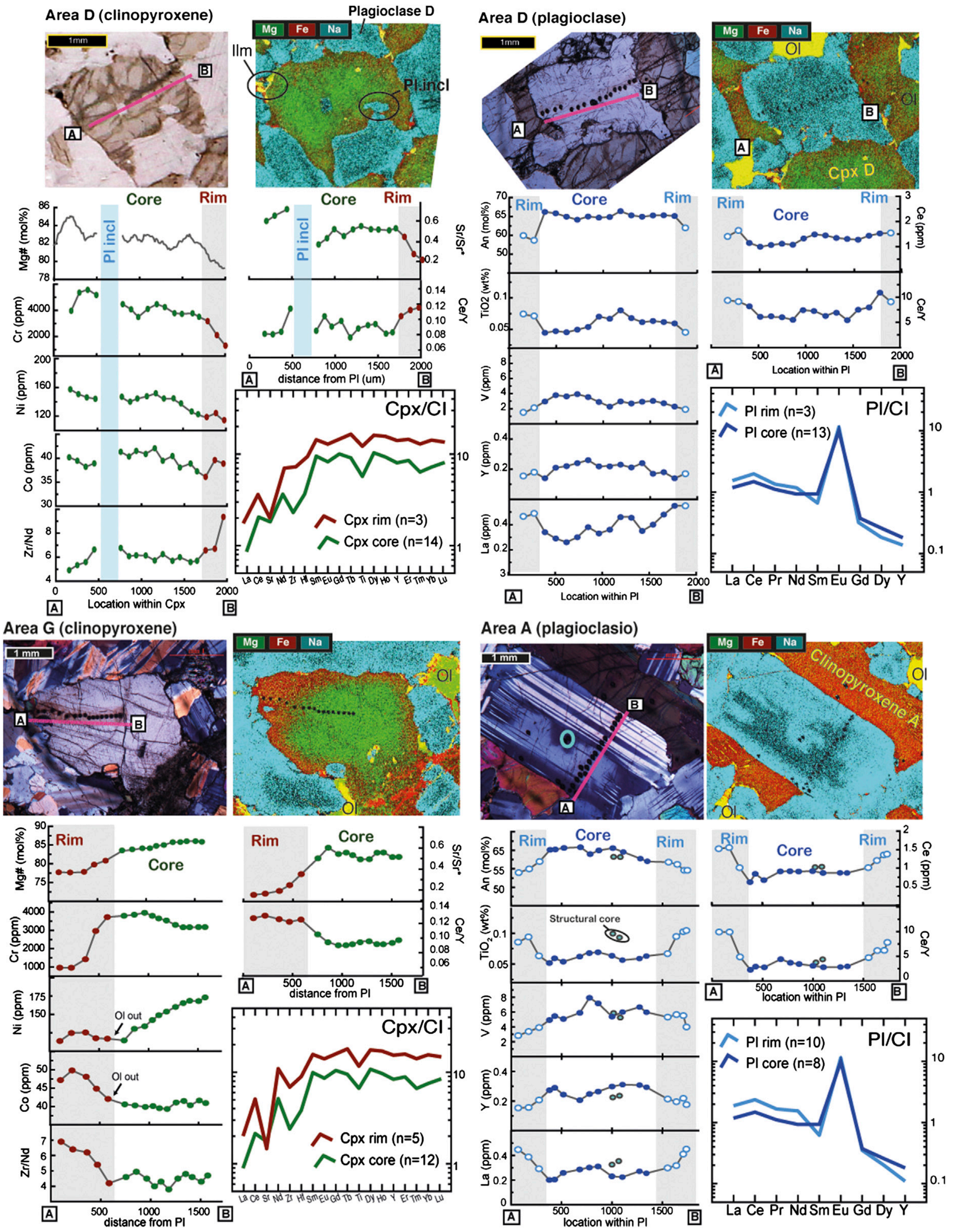

FIGURE 4 | Plagioclase and clinopyroxene geochemical profiles of grains selected in areas A and G (see **Supplementary Material** for the complete dataset). Plagioclase-Rim and clinopyroxene-Rim are defined on the optical and chemical zoning and underlined by a grey background (see text). Photomicrographs show the locations of each point analysis. The CI normalized incompatible trace element patterns of average analyses of Pl- and Cpx-Core (red) and Pl- and Cpx-Rim (green) are also shown. The geochemical profiles include An (mol%), TiO_2 (wt%), V, Y, La, Ce (ppm) and Ce/Y ratio for plagioclase; Mg# (mol%), Cr, Ni, Co (ppm) and Zr/Nd, Sr/Sr* = Sr_N [$\sqrt{(Ce_N x Nd_N)}$], Ce/Y ratios for clinopyroxene.

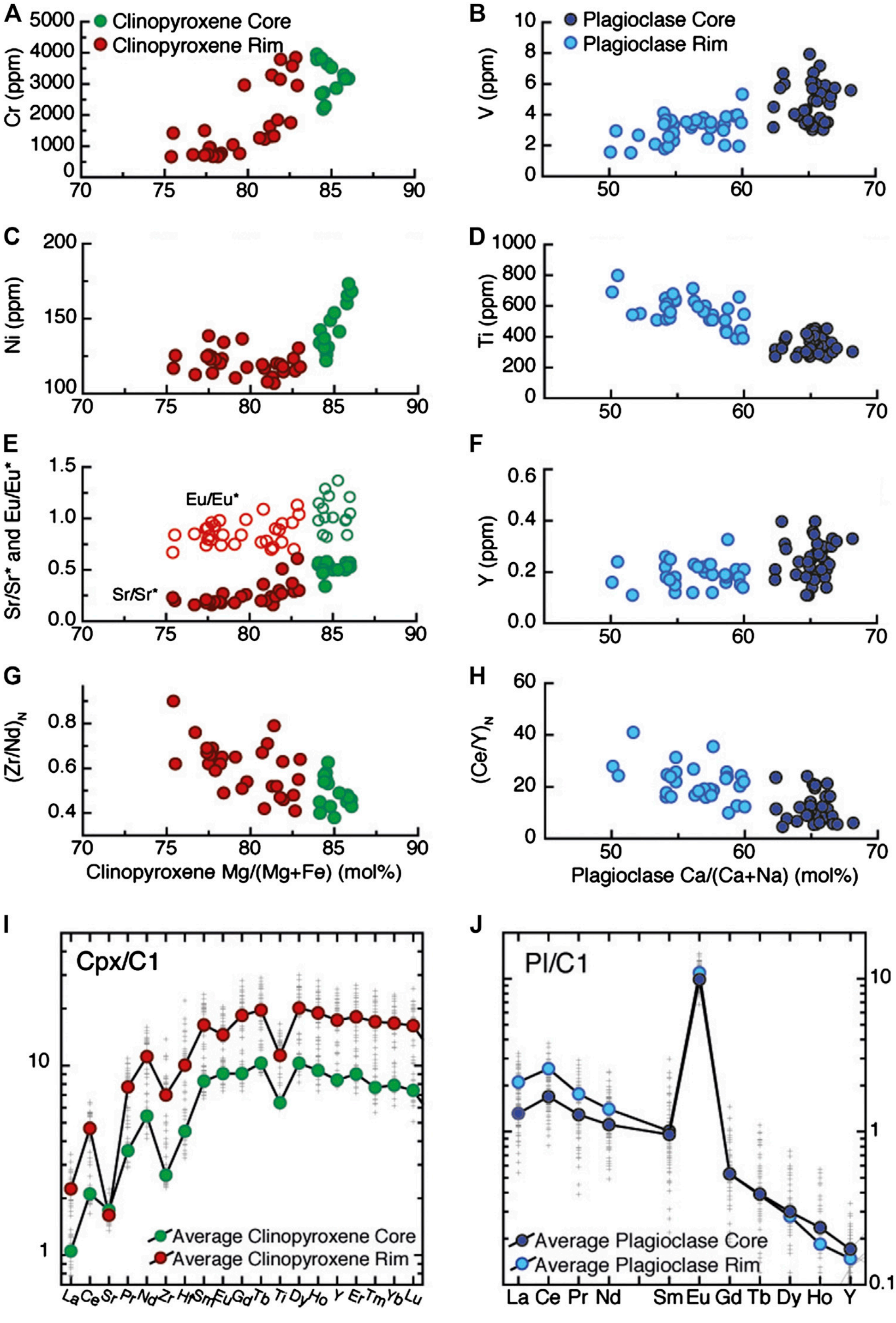

FIGURE 5 | General trace element variability of clinopyroxene and plagioclase from the entire thin section. Clinopyroxene (Cpx) Mg/(Mg + Fe) (mol%) vs. Cr, Ni (ppm), $Sr/Sr^* = Sr_N [\sqrt{(Ce_N x Nd_N)}]$, $Eu/Eu^* = Eu_N [\sqrt{(Sm_N x Gd_N)}]$ $(Zr/Nd)_N$ ratios. Plagioclase (PL) Ca/(Ca + Na) (mol%) vs. V, Ti, Y (ppm) and $(Ce/Y)_N$ ratio. Chondrite (C1)-normalised (Anders and Ebihara, 1982) incompatible trace element patterns of each point (grey cross) and average Cpx-Core and Pl-Core and Cpx-Rim and Pl-Rim are also depicted. The different generations of Pl and Cpx are defined on the basis of the chemical profiles in **Figure 4** and **Supplementary Figure S1**.

irregular, partly corroded An-rich cores surrounded by often euhedral, An-poor rims. As this band is approached Cpx tends to acquire a coarser grain-size and a poikilitic texture, at the same time becoming progressively enriched in Fe. Furthermore, the magnitude of Fe-Mg zoning in Cpx of the Ol gabbro increases toward the band. Intra-grain Mg-Fe zoning is not obvious in Ol from the combined compositional map (**Figure 3A**) for reasons of color scaling, but the transition toward more fayalitic compositions is clearly evident in the specific olivine composition map (**Figure 3E**). In addition, from the same figure it is clear that Ol is progressively less abundant, acquires irregular habits, and finally disappears toward the innermost part of the band. Critically, all of these coupled textural-compositional changes are gradual.

We investigate the variations in trace element concentrations and zoning characteristics of different individual Cpx and Pl grains, chosen on the basis of their location and of their major element chemical zoning characteristics determined from the element maps (**Figure 3B, D**). Cpx and Pl were selected in progressive proximity to the band (see locations in **Figure 3**). Two examples of Cpx and Pl are reported in **Figure 4**, as representative of the chemical zoning in this section; additional transects are reported in **Supplementary Figure S1** and listed in **Supplementary Tables S1 and S2**. The Cpx grains display a strong Fe-Mg zonation, with Mg# ranging from ~87 in the core to ~77 at the rim. The decrease in Mg# is coupled with a decrease in compatible elements such as Cr and Ni (ranging from ~3,500 to 1,000 ppm and from 175 to 125 ppm, respectively) and by corresponding increases in all incompatible elements. This is obvious from the chondrite-normalized (Anders and Ebihara, 1982) patterns depicted in **Figure 4**, which show Cpx rims having sub-parallel trace element patterns at progressively higher absolute concentrations, but a deep negative Sr anomaly compared to the Cpx cores. As typically reported in Cpx from other Ol-gabbros from Hole 735B (Gao et al., 2007; Lissenberg and MacLeod, 2016), a gradual enrichment in incompatible elements is present from the core toward rim, coupled with a concomitant increase in the ratios of more-incompatible/less-incompatible elements: for instance, Cpx cores have low and nearly constant Zr/Nd (~4), and Ce/Y (~0.09) ratios that increase toward the rim at 7 and 1.3, corresponding to core/rim enrichment factors of 1.7 and 1.4, respectively.

Major and trace element zoning is equally well developed and ubiquitous in Pl (**Figure 3B, E**). Plagioclase An content in all selected grains decreases from their cores to their rims. As with Cpx, the major element chemical zoning in Pl is associated with enrichments in the most incompatible elements (e.g., Ti, La or Ce) compared to the least incompatible (i.e., Y). This results in low and constant Ce/Y ratios in the Pl cores (~2.5), which gradually increase by up to 4 times toward the rims (Ce/Y ratios up to 10). As a consequence, the C1-normalized patterns of the Pl cores are relatively flat in LREE, whereas those of Pl rims show positive fractionations in LREE, and lower Gd, Dy and Y, compared to the Pl cores. The only exceptions are two small euhedral Pl grains included in a Cpx within the band, which have no An zoning and show compositions similar to the rims of the other minerals (see area X and Y in **Supplementary Figure S1**).

A generalized view of the chemical characteristics of these minerals is shown in **Figure 5**, in which Pl and Cpx "Rims" represent the spot analyses located within the band and mostly, but not only, localized at the rim of the minerals. Indeed, a fundamental observation is that chemical variations in Cpx and Pl are primarily localized in specific zones within the section (**Figure 3**). Away from the compositional band most of the sample comprises crystals with thin rims of more evolved compositions; in contrast, minerals within the band are mainly composed of this rim composition, with small, often resorbed, cores compositionally similar to the host Ol-gabbro. Hence, what we labeled "Cpx-Cores" correspond to locations having Mg# > 83, and also characterized by high Cr and Ni and low TiO_2 and incompatible trace elements, contrasting with "Cpx-Rims" which are instead characterized by gradually higher incompatible trace element compositions, pronounced negative Sr anomalies, and high Zr/Nd and Ce/Y ratios. Following the same rationale we defined "Pl-Core" as those locations with An > 61, and generally having low Ti, nearly flat LREE, and higher Y concentrations compared to "Pl-Rim".

DISCUSSION

Origin of Trace Element Zoning: Trapped Melt, Diffusion or Reactive Porous Flow?

As more trace element mineral chemical studies of abyssal gabbros are being conducted, it is becoming clear that intra-crystal trace element zoning is a widespread phenomenon. Typically, transitions in composition from core to rim in Cpx are marked by a decrease in compatible elements (e.g. Cr), a deepening of Sr and Eu anomalies, and a general increase in incompatible elements (Coogan et al., 2000; Gao et al., 2007; Drouin et al., 2009; Lissenberg et al., 2013; Sanfilippo et al., 2015; Lissenberg and MacLeod, 2016). At the same time, Pl rims show enrichments in LREE, whereas HREE and Y exhibit slight decreases (Lissenberg et al., 2013; Coogan and O'Hara, 2015).

Several very different processes have been proposed thus far to explain such mineral trace element zoning patterns, with profoundly different implications for magmatic processes and the behavior of melts in igneous systems. They may be broadly summarized as: 1) melt entrapment *in situ*; 2) diffusional re-equilibration; and 3) reactive porous flow. We here examine each of these hypotheses in turn to explore whether they might explain the observations we have documented.

Melt Entrapment

The entrapment of small aliquots of melt within a crystal matrix can generate zoning as a result of the progressive fractional crystallization of trapped melt as the system cools. This zoning is characterized by an increase of incompatible elements from core to rim of a crystal, coupled with a decrease of compatible elements. This process of *in situ* melt entrapment has been traditionally and widely invoked to explain much of the major element chemical zoning in minerals from plutonic crustal rocks (e.g., Meyer et al., 1989; Elthon et al., 1992). Previous authors explored the ability of melt entrapment to account for such strong enrichments in abundances and increases in more incompatible/less incompatible element ratios (e.g. Coogan et al., 2000; Gao et al., 2007; Lissenberg et al., 2013; Sanfilippo et al., 2015). In each case these studies showed that increases e.g. Ce/Y, Zr/Nd from crystal core to rim (see **Figure 4**) are typically too large to be explained by any conventional fractional crystallization mechanism. We test this hypothesis again here for our specific example by exploring whether a fractional crystallization process

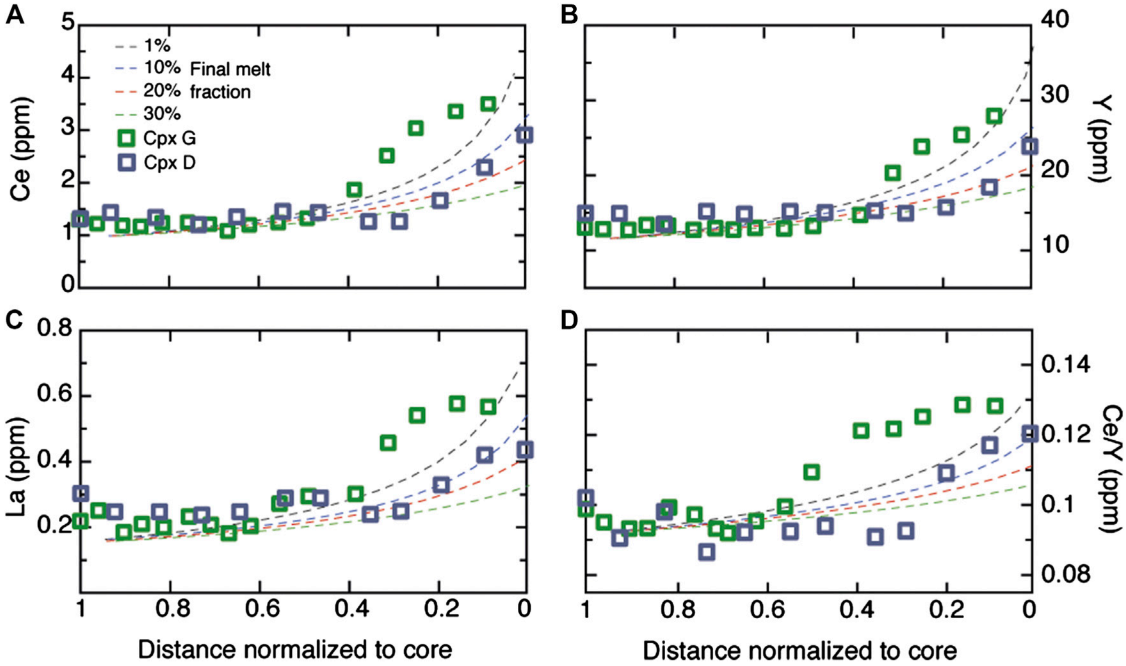

FIGURE 6 | Variation of Ce, La and Y (ppm) and Ce/Y ratio of a clinopyroxene from a ol-gabbros crystallized by a fractional crystallization process are compared to those of clinopyroxene in area G. Distance is normalized to core. The different models refer to different fractional crystallization process scenarios at residual melt fractions varying from 1 to 30% as indicated in the legend. Initial melt is in chemical equilibrium with clinopyroxene core; partition coefficients for La, Ce and Y are calculated using the model of Sun and Liang (2012; 2017) at T~1180°C and are 0.090, 0.154 and 0.598 for clinopyroxene; 0.095, 0.085 and 0.017 for plagioclase and 0.0003, 0.0004 and 0.004 for olivine.

is capable of reproducing the La, Ce and Y variations of the two detailed Cpx profiles we obtained (areas D and G). In **Figure 6** we model the behavior of clinopyroxene during closed-system fractional crystallization of an olivine gabbro with the same proportions as observed in our rock (Ol-Pl-Cpx 0.1:0.5:0.4), assuming a concentric spherical growth of clinopyroxene and crystal growth assumed to be proportional to the crystallization of the melt. The initial melt is in equilibrium with the core composition and the final melt fraction (i.e., the remaining fraction of melt during the crystallization of the rim) was chosen to vary between 1 and 30% to simulate different proportions of melt entrapment. Partition coefficients for Ol, Pl and Cpx are reported in the caption to **Figure 6**. We find that the decrease of melt fraction indeed causes a strong increase both in elemental concentrations and in Ce/Y ratios toward the rim; however, the observed zoning profiles cannot be fitted by any fractional crystallization process in a closed system. In particular, Cpx G, within the compositional band, shows increases in La and Ce concentrations and, in consequence, Ce/Y ratios, that are more rapid than can be accounted for by fractional crystallization. Only the rim composition of Cpx D, far from the band, seems to be intercepted by the fractional crystallization trends. Even so, fractional crystallization cannot account for the steep increase in e.g., Ce/Y between the core composition and the rim of this crystal (normalized distance of ~0.08–0.3; **Figure 6**); furthermore, if the rim data point did record fractional crystallization, it would require a final melt fraction of <10% so to do. In consequence, more than 90% of the initial melt mass needs to have been entrapped in the cumulus matrix to explain such enriched compositions. To test whether the degree of fractionation implied is consistent with the textural and chemical characteristics of our sample we use a *MELTS* calculation (Ghiorso and Sack, 1995) starting with an average melt composition for the Southwest Indian Ridge basalts (Coogan et al., 2004). The *MELTS* model indicates that late-stage phases such as Ti-Fe oxides and orthopyroxene should start to crystallize as early as F~0.85 and, in agreement with experimental results (Feig et al., 2006; Koepke et al., 2018), further shows that these late phases should also be associated with pargasitic amphibole. This contrasts with the mineral assemblage of our sample, in which these interstitial phases are almost completely absent. Furthermore, >90% fractionation crystallization should generate a melt with Mg# of <30 mol%, which is inconsistent with the observed Mg# (~77 mol%) of the Cpx rim in chemical equilibrium with melts having Mg# of >40 mol%. Although we do not dismiss the idea that *in situ* fractional crystallization can locally successfully reproduce–or, more realistically, contribute to–chemical zoning of the Cpx in gabbros (see also Bedard, 1994), this process requires an unfeasibly high amount of melt entrapment, which is markedly at odds with the mineralogy, texture and major element compositions of the evolved melt band in the current sample.

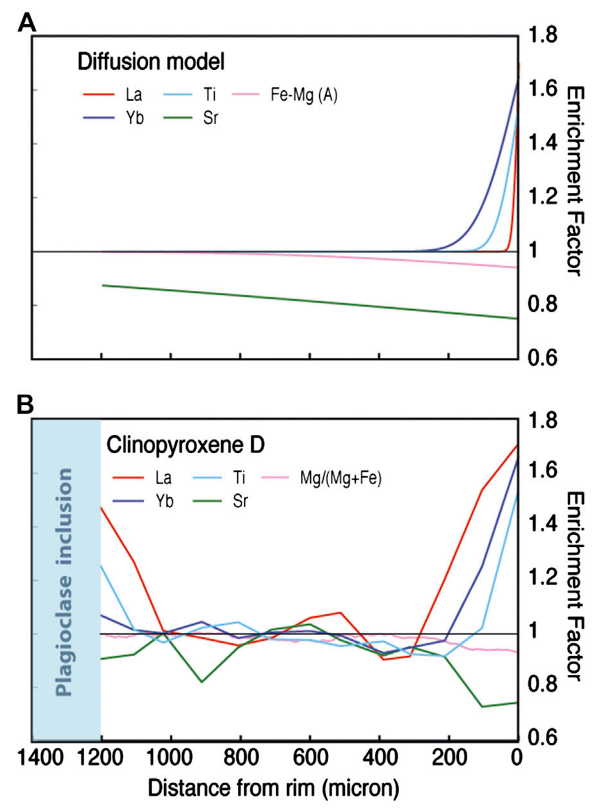

FIGURE 7 | Diffusion model **(A)** compared with trace element profiles of Cpx D **(B)**. Panel **(A)** models the diffusive influx of selected elements into Cpx from a surrounding melt. The resulting compositional profiles track the post-diffusion concentration C relative to the concentrations in the melt C0. An essential characteristic of this and all comparable diffusion models is the contrasting diffusion length generated for different elements. In panel B actual data for the compositional profiles of Cpx D are plotted as the "Enrichment Factor", which is the concentration at a given point of the profile divided by that of the crystal core (here set as the 600–800 μm interval), and directly comparable to C/C0 in Panel **A**. A critical observation in **(B)** is that, in marked contrast to essential requirement of the diffusion model, the different elements in Cpx D co-vary at the same places along the profiles, and that La varies over significantly larger distances than can be accounted for by diffusion.

Diffusion

Diffusion, given sufficient time, is capable of generating significant changes in trace element concentrations in minerals. Furthermore, because different trace elements migrate at different rates, trace elements may become fractionated from one another, effecting changes in their ratios. Some authors have suggested that diffusive re-equilibration may play a dominant role in controlling trace element distributions in oceanic gabbros (Coogan and O'Hara, 2015). Is such diffusion by itself capable of generating the fractionations we observe? In this section we explore whether diffusion can indeed explain the observed zoning in our sample.

We envisage two possible scenarios in which diffusion can play a role. The first is the situation in which evolved melts migrate into and/or become trapped within a more primitive crystal matrix. Over and beyond simple crystallization (see previous section), the melt may also exchange components with the host crystals through diffusive processes: hence, to test this scenario, we assume that the clinopyroxene was initially unzoned and developed zoning as a result of diffusive exchange with a more evolved melt. This scenario was evaluated in detail by Gao et al. (2007) for the example of trace element zoning in clinopyroxene in a gabbroic rock from Atlantis Bank (ODP Hole 735B), and we apply a simplified version of their approach to the geochemical profile of Cpx D in sample 360-U1473A-84R-4, 118–122. In **Figure 7** we present diffusion profiles calculated on the basis of the following constraints: 1) that diffusion occurred at a temperature of 1,100°C: this temperature was calculated from the REE data for the rim of the crystal using the Cpx-Pl$_{\text{REE-Y}}$ geothermometer of Sun et al. (2017; **Supplementary Figure S3**): in a diffusion scenario this represent the equilibrium temperature between melt and mineral, and hence it is the best estimate of the temperature at which the diffusion event took place; and 2) that diffusion operated over a timescale of 26.6 kyr: this we derived by dividing the

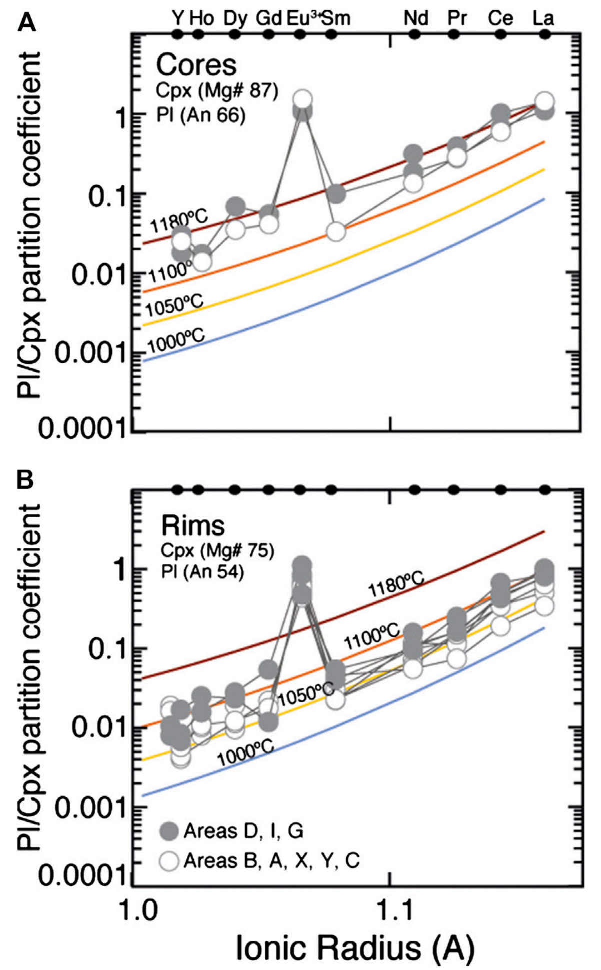

FIGURE 8 | Relationships between the Pl/Cpx trace element (Y and REE) ratios in the different areas of the studied rock and ionic radius. Equilibration temperature contour lines are calculated on the basis of the mineral major element compositions for core **(A)** and rim **(B)** compositions using the Pl/Cpx partitioning model developed by Sun and Liang (2012) and Sun et al. (2017).

temperature interval of 77°C recorded by Cpx D ($\text{Cpx-Pl}_{\text{REE-Y}}$ temperature of 1,177°C for the core and 1,100°C for the rim; **Supplementary Figure S3**) by the cooling rate for Atlantis Bank gabbros (2,898°C/M.yr.; the average of cooling rates determined on 29 samples from ODP Hole 735B by Coogan et al., 2007). Although the use of combined geospeedometers suggests that the cooling rate of the Atlantis Bank decreases exponentially at temperatures <600°C (John et al., 2004), it may considered constant in the temperature interval considered here. Hence, the difference between "core" temperature, at which the Cpx initially crystallized from the melt, and the "rim" temperature provides an upper limit on the duration of the diffusion event. With the duration and temperature of diffusion thus constrained we were able to calculate the diffusion of La, Yb, Ti, Sr and Fe-Mg into the crystal using the Cpx diffusion data of Van Orman et al. (2001); REE, Cherniak and Liang (2012); Ti, Müller et al. (2013; Fe-Mg) and Sneeringer et al. (1984; Sr).

The results of the above modeling, shown in **Figure 7A**, provide a number of clear predictions that can be tested against real-world data (see also Gao et al., 2007). First, the diffusive influx of the REE is limited. This is particularly the case for La, which only diffuses ~20 μm into the Cpx (**Figure 7**). Second, because the diffusivity of the different elements differs substantially, their diffusion distances into Cpx vary significantly relative to one another. For example, among the REE, Yb migrates a factor of seven further into the crystal than La under the conditions modeled here. Fe-Mg, whose interdiffusion in Cpx is rapid (Müller et al., 2013) migrate further again (~1,200 μm), and Sr is affected by diffusion throughout the crystal (**Figure 7**). Diffusion will thereby lead to significant differences in zoning profiles for the different elements, and, consequently, fractionate element ratios significantly. Third, because individual REE have different diffusivities, these elements have different closure temperatures for diffusion (Dodson, 1973). Calculated REE closure temperatures for oceanic gabbros from ODP Hole 735B decrease systematically from 1,287°C for La to 1,135°C for Yb (Gao et al., 2007). Although these closure temperatures will vary depending on the assumed cooling rate, grain size and grain geometry, a decrease in closure temperature from LREE to HREE will be present in any particular diffusion scenario.

These three predictions (**Figure 7A**) can be tested against our observations, which we present in **Figure 7B**. Measured trace element profiles for Cpx D show that: 1) La enrichment occurs over a distance of >300 μm, much higher than that predicted for diffusion (**Figure 7B**); 2) enrichment becomes detectable at very similar distances along the profile for each and all of the elements: strikingly, it is clear that enrichment in the slowest-diffusing element considered here (La) occurs at the same location as the change in Mg#, which diffuses much more rapidly (**Figure 7B**); 3) The different REE all record very similar temperatures. This is illustrated in **Figure 8**, where we plot the ratios of the measured REE + Y concentrations in Pl vs. Cpx against their ionic radii. The observed Kds are compared to the Pl/Cpx Kds computed at major element compositions of Pl and Cpx akin to those of the mineral cores (Pl An 66; Cpx Mg# 87) and rims (Pl An 54; Cpx Mg# 77) and at temperature ranging from 1,180 to 1000°C. The $\text{Kd}^{\text{REE}}{}_{\text{Pl/Cpx}}$ of our Pl/Cpx couples form linear correlations vs. the ionic radii, following those of the trends computed at constant temperatures (see also **Supplementary Figure S2**). Each of these observations allows us to rule out models in which diffusion plays a major control on the trace element concentrations, in keeping with previous deductions from ODP Hole 735B (Gao et al., 2007; Lissenberg and MacLeod, 2016).

A second diffusion scenario is one in which *in situ* fractional crystallization of interstitial melt is followed by sub-solidus diffusion between coexisting Pl and Cpx (Coogan and O'Hara, 2015). Modeling REE to diffusion between coexisting Pl and Cpx down to a closure temperature of 700°C, these authors argue that this scenario is capable of modifying the initial trace element profiles of oceanic cumulus minerals to such an extent that they control the observed variations in incompatible trace element zoning. A number of arguments may be made to show that this cannot be the case for our sample. The first is the REE equilibration temperatures recorded by our sample. We show above that the REE in Cpx D equilibrated at 1,177°C (core) and 1,100°C (rim). Extending this to all data from the sample we calculate REE equilibration temperatures for a series of Cpx-Pl pairs (**Supplementary Figure S1** and **Supplementary Tables S1, S2**), and derive estimates of the closure temperature using the Pl-Cpx trace element thermometer of Sun et al. (2017), calculating temperatures for each area in a traverse across the compositional band (**Figure 3**). Equilibrium temperatures for the selected Pl and Cpx rim couples range between 1,030 (±22)oC and 1,100 (±8)oC (see **Figure 3**). Using the same method we also calculate inferred core Pl and Cpx temperatures using core compositions in each area of the thin section, making the assumption that cores of physically adjacent cumulus minerals were in chemical equilibrium during their formation. Note that core temperatures could not be calculated for those locations within the compositional band because Cpx with "core" compositions do not occur. We find core temperatures to be rather uniform: in the range 1,156 (±5)°C to 1,181 (±12)oC. The relatively high equilibration temperatures of the rims, combined with the (very high) cooling rate of Atlantis Bank gabbros (Coogan et al., 2007), means that the sample did not have enough time at elevated temperatures to have suffered significant sub-solidus diffusion (Fig. 7). The second observation inconsistent with a sub-solidus diffusive control on the trace elements is that the closure temperatures for the different REE are all similar (see above, and **Figure 8)**. Third, sub-solidus diffusion between Cpx and Pl leads to a number of distinct signatures in resulting trace element profiles (Coogan and O'Hara, 2015). Arguably the most obvious of these is that La will diffuse out of Cpx and into adjacent Plag, leading to a distinct decrease in Cpx La when approaching Plag (Coogan and O'Hara, 2015; their **Figure 4**). Cpx D provides an ideal test case for this prediction because, in addition to being in contact with plagioclase at its rim, the traverse also crossed into a plagioclase inclusion. From **Figure 7B** it is evident there is no decrease in La either at the crystal rim or near the inclusion. Rather, we infer that the high La contents of the Cpx close to the Pl inclusion was produced by an igneous process, either melt entrapment or melt-rock reaction (see below). We therefore conclude that the REE distributions in our samples are inconsistent with a sub-solidus diffusive control.

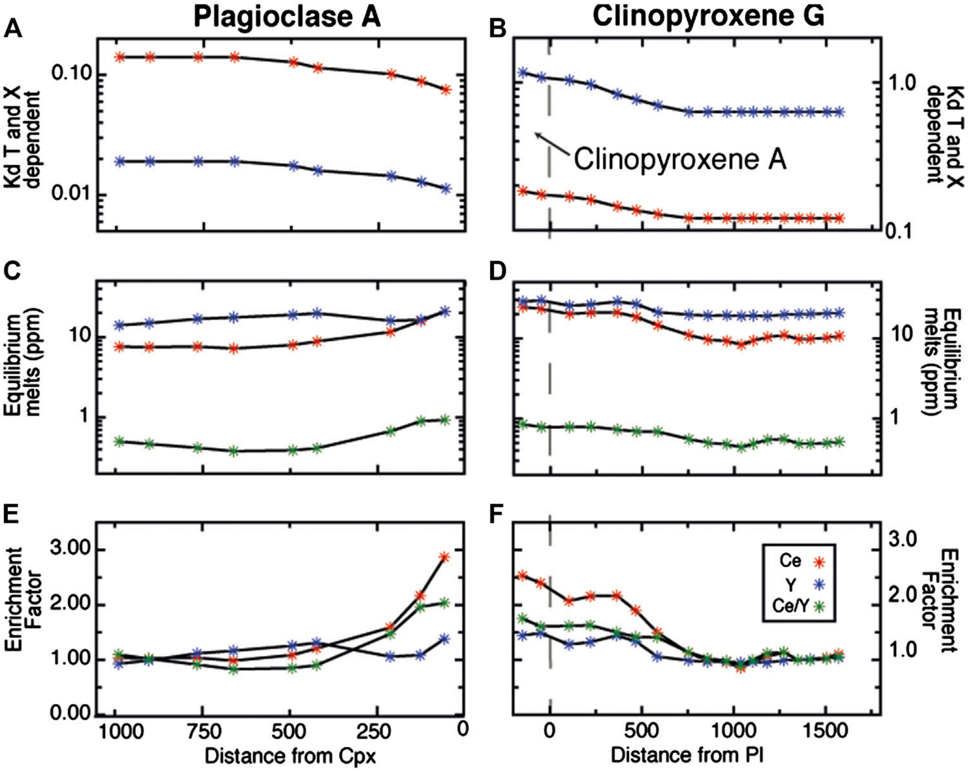

FIGURE 9 | Variation of Ce and Y partition coefficients, Ce, Y (ppm) and Ce/Y ratio, and enrichment factors of the equilibrium melts at each point of the geochemical transects in plagioclase and clinopyroxene from area A and G. The rim compositions of clinopyroxene A are reported as continuous with clinopyroxene G to better represent compositions in textural equilibrium with plagioclase A. Partition coefficients were calculated at specific temperature (inferred from core and rim equilibration temperatures) and compositions (measured) using the parameterization of Sun and Liang (2012) for clinopyroxene and Sun and Liang (2017) for plagioclase (see text for further details). The enriched factor of the equilibrium melts is calculated normalizing the Ce, Y and Ce/Y ratio of each point of the two transects to the average core compositions.

A further, independent, complementary consideration is the spatial distribution of crystal domains enriched in incompatible elements (**Figures 3, 4**). The element maps (**Figures 3B, 4**) reveal a great complexity to the chemical zoning: first, the enriched domains (illustrated by those areas with lower Mg# and An) do not only occur from core to rim but also vary across the sample; second, the enrichment is not necessarily simply related to its location (core to rim) within a single grain: i.e. zoning is not always concentric. For instance, Pl and Cpx from the internal portion of the reactive layer (points X and Y in **Figure 3C**) do not show a well-defined chemical zoning but are instead characterized by rim-like trace element compositions and element ratios (e.g., Ce/Y), and no evidence of intra-grain chemical gradients (**Supplementary Figure S1**). These observations even by themselves are inconsistent with simple diffusion; instead, together with our findings above, they indicate that both the spatial distributions of enrichment (**Figures 3, 4**) and the compositional trends (**Figures 4-6**) must be controlled by magmatic processes.

Reactive Porous Flow

Several previous authors have suggested that assimilation of the pre-existing gabbroic minerals coupled with crystallization of new phases during reactive porous flow (Coogan et al., 2000; Borghini and Rampone, 2007; Gao et al., 2007) is capable of generating a preferential increase in the most incompatible elements (Zr, Hf, LREE) compared to moderately incompatible elements (M-HREE, Y). This process is generally referred to as assimilation-fractional crystallization (AFC). AFC equations proposed by DePaolo (1981) have been employed successfully to reproduce the extent of fractionation in incompatible elements in abyssal gabbros (see also Lissenberg et al., 2013; Sanfilippo et al., 2015; Lissenberg and MacLeod, 2016). To test the hypothesis that chemical changes in the minerals in the band in our sample are produced by a reactive melt migration process we now consider a parameter referred to as the "enrichment factor" (EF; Lissenberg & MacLeod, 2016) as an aid to describing the intra-crystal chemical zonation. In any geochemical transect the EF is calculated as the composition of each point normalized to the crystal core composition. If the mineral-melt partition coefficients remained constant during the crystallization process, the EF of a given element in a mineral equals that of the equilibrium melt $\left(\frac{C^{Sol}_{point\ x}}{C^{Sol}_{Core}} = \frac{C^{Liq}_{point\ x}*Kd}{C^{Liq}_{Core}*Kd}\right)$. Temperature and composition are however known to have a major effect on mineral-melt partitioning; in particular, Sun et al. (2017) have

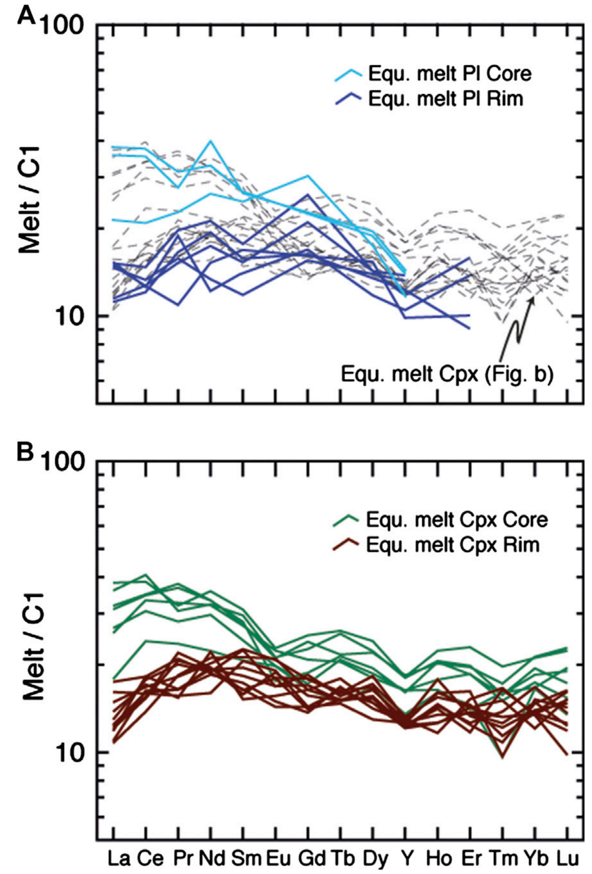

FIGURE 10 | Chondrite (C1)-normalized (Anders and Ebihara, 1982) REE patterns of computed melts in equilibrium with **(A)** plagioclase (PL) and **(B)** and clinopyroxene (Cpx) at each point of the chemical transects in **Figure 9**. Melts in equilibrium with Cpx are also shown in A as dashed gray lines for comparative purposes. Core and rim compositions are distinguished as indicated in **Figure 4** and show a very good consistency.

recently shown that the effect of temperature and composition on REE and Y partitioning in a basaltic system is particularly strong for Pl. This is shown in the **Supplementary Figure S3**, in which the variation in Pl-melt and Cpx-melt partition coefficients at temperatures between 1180° and 1,000°C are calculated using the average composition of Cpx-Core and Pl-Core (An 68, Cpx Mg# 87) and Cpx-Rim and Pl-Rim (An 57, Mg# 71). As discussed above, the REE + Y equilibration temperature reveals a difference of up to 150°C for the Pl and Cpx cores and rims (**Figure 3**).

On the basis of the formulations of Sun and Liang (2017) and Sun et al. (2017), and utilizing their mineral-melt partitioning models, we calculate the melt concentrations of the equilibrium melts at each point on each geochemical transect (**Figure 9**). To calculate the equilibrium melts we derived the mineral-melt partition coefficients from the major element composition and temperature at each point, using representative equilibration temperatures of 1180°C for Cpx-Core and Pl-Core, and 1050°C for Cpx-Rim and Pl-Rim. The results, shown in **Figures 9** and **10**, indicate that the REE and Y compositions of the equilibrium melts along the selected transects for Pl are very consistent with those for Cpx when adjustments of the Kd for temperature and compositions are applied. In addition, the melts in equilibrium with Pl and Cpx Rims have similar EF for Y and Ce and, by consequence, reach similar Ce/Y ratios. We note that when the effect of temperature is considered, Y in the equilibrium melt displays a small, insignificant increase toward the rims of the crystal, whereas Ce increases sharply. Thus, even if the effect of temperature change in mineral-melt partitioning is taken into account, the Ce/Y ratios of the equilibrium melts still increase progressively toward the rims.

We will now explore whether melt-rock reaction can explain these variations. We opted for the assimilation-fractional crystallization (AFC) model based on the equations in DePaolo (1981). This model assumes that a proportion of solid is melted and incorporated into a transient melt that is simultaneously fractionating solid minerals. As assimilant, we used the average composition of Ol, Pl-Core and Cpx-Core at proportions derived from the modal proportions of these minerals in the sample (0.1:0.5:0.4), and a melt in chemical equilibrium with both Cpx- and Pl-Core as the initial melt. Crystallized phases were assumed to be only Pl and Cpx in nearly cotectic proportions (0.6:0.4), to account for the disappearance of Ol toward the compositional band. Mass assimilated vs. mass crystallized ratio was fixed at 0.99, which is consistent with the abundance of Cpx and Pl having “rim” like compositions in the compositional band compared to the less-modified host gabbro, indicating that assimilation and synchronous crystallization of new phases was highly efficient at least in the compositional band (details and parameters in **Supplementary Table S3** of supplements). In addition, the above analysis shows that the effect of temperature on partition coefficients is significant and must therefore be considered explicitly when modeling the evolution of incompatible elements. This being so, we calculate the composition of Cpx and Pl in equilibrium with melt evolving through an AFC process, using Kd that varies both for temperature and for major element composition. First, we derive two end member trends at constant temperature: the “high-T trend”, calculated at temperature of 1180°C and major element compositions of the Cpx and Pl cores; and the “low-T trend”, calculated at 1030°C and major element compositions of the Cpx and Pl rims (see **Supplementary Figure S3**). To bracket the range of possible temperatures derived from the Cpx-REE thermometry above we then consider a model characterized by a gradual decrease in temperature during the AFC process. At each step (arbitrarily fixed at F = 0.1), we decrease the temperature and modify the Pl and Cpx Kd accordingly. We varied the extent of temperature variation, i.e., decrease in temperature during the entire AFC process, progressively from 15°C to 150°C. This parameter, reported as *dT/dF* in **Figure 11** and **Supplementary Table S4**, indicates the magnitude of temperature decrease (°C) for each 1% of AFC process. This changes in response to the overall cooling of the system and, in a single sample, can reasonably be considered to be constant.

The results of our AFC model are shown in **Figure 11**, where the Ce and Y compositions of the Pl, Cpx and melts produced during an AFC process, both at fixed temperature and at varying

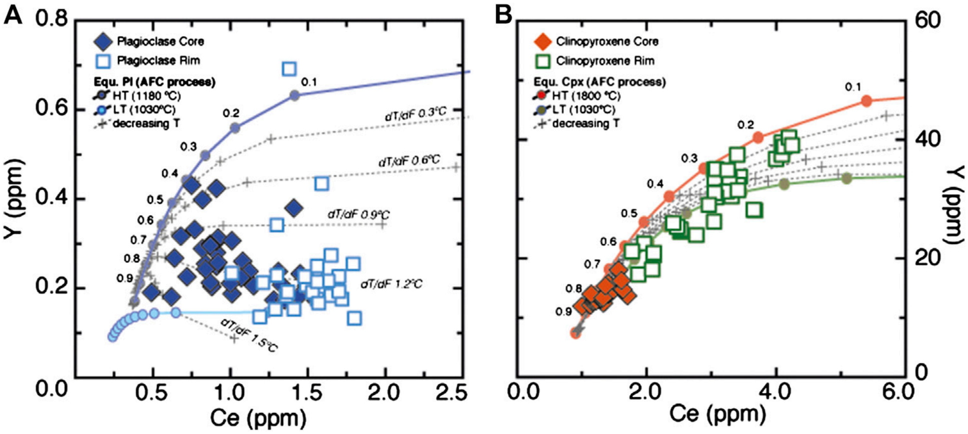

FIGURE 11 | Ce and Y (ppm) variations in plagioclase **(A)** and clinopyroxene **(B)** from our sample. Also shown are the compositions of plagioclase and clinopyroxene in equilibrium with melts produced by the process of assimilation-fractional crystallization (AFC) at different temperature conditions described herein (see text for explanation). Each symbol represents step of F = 0.1 of the AFC process as indicated by the numbers. *dT/dF* indicates the decrease in temperature (°C) at each 1% of the AFC process. Note that the temperature control on Ce/Y covariation is strong because the temperature decrease has a major effect on plagioclase whereas the effect on clinopyroxene is negligible.

temperature (gradually decreasing from 1180°C to 1030°C), are compared to those of our sample. In addition, we plot the trends resulting from fractional crystallization (Melt Entrapment) at temperatures decreasing to the same extent (i.e., 1180°C to 1030°C). Although in our model we focus on Ce and Y alone, these elements can be considered good representatives for the behavior of LREE and (M)HREE, respectively (see also Lissenberg and MacLeod, 2016). The model is satisfactory as the computed Pl and Cpx compositions mimic those in our sample and can potentially explain the relatively low Y at increasing Ce contents of the rim compositions of the selected minerals. The temperature decrease particularly affects the composition of Pl: we find the Pl of our sample is reproduced at 1.3°C of temperature decrease for each 1% of assimilation. This corresponds to an overall temperature decrease of 130°C during the entire process, which is of similar magnitude to the temperature drop estimated on the basis of the REE in Pl-Cpx thermometry in **Figure 3**.

In conclusion, we demonstrate here that neither a process of closed system fractional crystallization with melt entrapment, nor modification by diffusion (be it supra- or subsolidus), can satisfactorily explain the major- and trace element chemical variations of the selected Pl and Cpx grains. Instead, we can successfully account for most of the broad variation in major and trace element compositions in our particular sample by a process of melt-rock reactions, at gradually decreasing temperature conditions, during the migration of an interstitial melt through a host crystal mush framework.

Origin of the “Compositional Band” and Possible Consequence for a Cryptic Reactive Porous Flow Process

The multi-element map (**Figure 3E**) shows the existence of a cm-size band otherwise undetectable on a purely petrological or microstructural basis (**Figure 3A**). Careful observation of this compositional band in petrographic thin section however shows that, in contrast to the remainder of the thin section, most Pl grains are characterized by An-rich cores with irregular shapes surrounded by thick Pl with more evolved, “rim-like” compositions. Chemical zoning is also observed in Cpx approaching the band, although Mg# zoning in Cpx seems smooth compared to other trace elements in the same traverse and corroded cores are not observed. This is potentially related to intercrystalline diffusion of Mg and Fe in Cpx, which may have slightly modified the original zoning due to a very high diffusivity of Fe and Mg in Cpx. In the previous sections we showed that neither melt entrapment nor diffusion can explain the trace element patterns of the selected Pl and Cpx in our sample, favoring the idea that chemical zoning was instead produced by a process of reaction between a former crystal matrix and migrating melt; hence, given that these enriched compositions are not only limited to the rims, but preferentially located toward and within the band, we infer a “replacive” origin for this band. On the basis of the presence within the band of “ghost” cores with compositions similar to those of the cores away from the band, coupled with the chemical dissimilarity between cores and rims, we suggest the band therefore most likely formed by the migration of an exotic melt into and through a pre-existing crystal framework rather than simply being residual liquid of the local crystal mush sucked or pressed out from the adjacent interstices. This process led to the partial to (locally) complete dissolution of a pre-existing Ol, Pl and Cpx framework, recrystallized into a newly formed Pl and Cpx assemblage.

Another fundamental observation is that the equilibration temperature of Pl/Cpx not only drops from core to rim of the same crystal, but that rim temperatures gradually decreases toward the reaction band, with a maximum temperature of 1100°C far from the reactive band and minimum estimate of ~1030°C in its medial portion (**Figure 3**). A reduction in

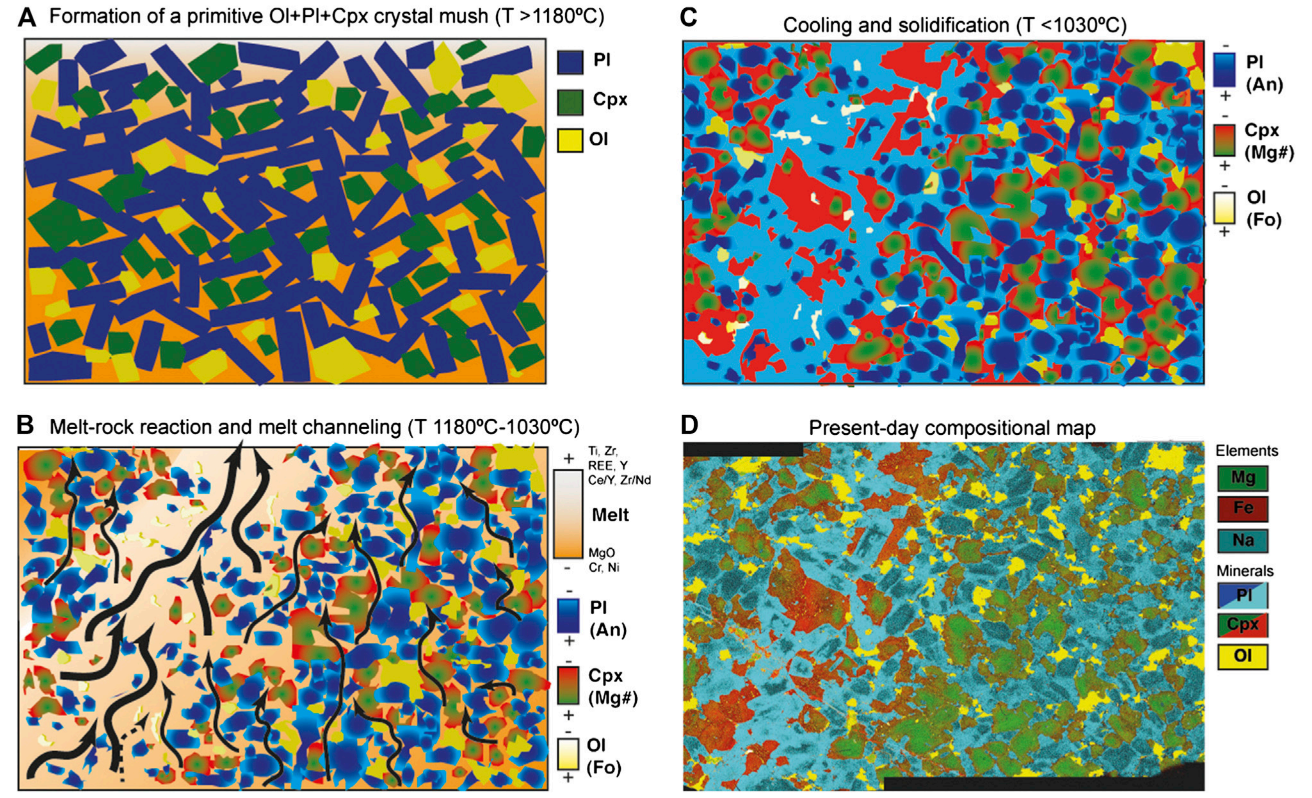

FIGURE 12 | Schematic cartoon representing the textural and chemical evolution of the sample and the formation of the replacive band in three steps (see text for details). The compositional map is also shown for comparative purposes.

equilibration temperature toward the band is consistent with thermodynamic models for reactive migration in porous media, which show that the average temperature of the system is gradually modified at the reaction front as consequence of the physico-chemical re-equilibration between the migrating melt and the crystals (Solano et al., 2014; Jackson et al., 2018). When an intergranular melt migrates through a porous mush the local bulk composition (i.e., the melt + solid compositions at each specific location along the reaction path) becomes more evolved along the melt transport pathway because of the gradual addition of melt, by definition enriched in the more fusible components. As a result, when reactive transport is considered, the temperature gradually decreases relative to the initial value at the migration front and the bulk composition becomes gradually more evolved. Although the major- and trace-element composition of the newly-formed phases and the disappearance of olivine in the reaction band suggest that the interacting melt was more evolved compared to that crystallizing the first generation of Pl and Cpx, the fact that the sample contains only a few grains of Ti-Fe oxide and Fe sulfide and no late-stage phases (amphibole, orthopyroxene or apatite), coupled with the higher An-in-Pl and Mg#-in-Cpx Rim compared to those in Ox-gabbros, indicate that it was nevertheless more primitive than those late-stage percolating melts that generated the Ox-gabbros that are otherwise prevalent throughout the Atlantis Bank gabbroic section (**Figure 1**; e.g., Dick et al., 1999; Pettigrew et al., 1999; MacLeod et al., 2017). We deduce that the Ol-gabbro investigated here provides clear evidence that the primitive crystal mush formed at the earliest stages of generation of the Atlantis Bank lower crust experienced reactive melt migration from the outset, much earlier and not directly related to that associated with the later, much lower temperature Ox-gabbros (**Figure 1**). Instead, we propose that the percolating melt in the present case was the product of partial crystallization of the primitive liquid that formed the initial Ol-Pl-Cpx framework elsewhere in the same crystal mush pile, focused into the reaction band as it migrated, presumably upward, through the gradually cooling mush, most likely in response to compaction.

In **Figure 12** we summarize the processes of formation we deduce for the reaction band, which we conclude may be better described as a "reactive porous flow channel". We envisage this as a three-stage process. First of all a primitive crystal mush framework is formed by crystallization of a basaltic melt at temperature >1180°C, as defined by the equilibration temperatures of the Cpx-Pl mineral cores. The intergranular melts residual from this crystallization event started to migrate upward, likely driven by difference in buoyancy and/or compaction of the underlying cumulate pile. The chemical gradient between melts and crystals provoked interactions and the decrease in temperature conditions, leading to AFC processes and to a sharp increase in incompatible elements in the melt and in the newly formed crystals. As discussed above, the migrating melts were most likely residual after the formation of the primitive crystal mush and became progressively undersaturated in olivine. In the same way as that inferred for replacive dunite channels in a partly molten mantle column (e.g., Spiegelman et al., 2001), the high solubility of olivine within the melt phase caused a positive feedback between dissolution and melt-flux, promoting the progressive focusing of these melts into a more permeable "replacive" channel. Here, most minerals crystallized from the migrating melt, leaving few, partly resorbed cores with original "core-like" compositions. Fast cooling of the gabbroic sequence likely due to exhumation in the detachment fault footwall (see John et al., 2004; Coogan et al., 2007; Rioux et al., 2016) led to the complete solidification of the crystal mush and the final equilibration of the mineral rims at nearly magmatic temperatures (≥1030°C); indeed, fast cooling rates likely inhibited further modifications by sub-solidus diffusion. Taken as a whole, the reactive melt migration process we document in this sample can thereby be regarded in microcosm as a snapshot of a general magmatic differentiation process, potentially occurring in other "homogeneous" olivine gabbros throughout the Atlantis Bank lower crust. By implication, we here demonstrate that interactions and reactions between melts and crystal mush happen from the earliest stages of intrusion and crystallization of the melts into a dynamic magmatic lower crustal system, as an inevitable consequence of the compaction, extraction and upward migration of interstitial melts throughout an early-formed primitive, cooling crystal mush.

SYNTHESIS

In this study we report the occurrence of cryptic reactive melt migration through a primitive crystal mush as preserved in olivine gabbros from deep within the plutonic lower crust of an ultraslow-spreading mid-ocean ridge. High-resolution chemical maps and trace element zoning profiles reveal cryptic chemical variations in the mineral phases, localized in particular in a discrete, cm-scale compositional band. Major- and trace element mineral compositions reveal the occurrence of well-defined Pl and Cpx trace element zoning profiles most likely produced during a process of dissolution-reprecipitation under decreasing temperature conditions. For the first time, we explicitly consider th effect of changes in mineral-melt partitioning that are a direct consequence of this temperature drop, and show that temperature-driven disequilibrium in and by itself is sufficient to account for the chemical changes in the newly-formed minerals and in the equilibrium melts. The preferential occurrence of these relatively more evolved mineral compositions within the compositional band suggests that the latter formed by a process of focusing and transport of interstitial melt through a crystal framework. The cryptic changes toward more evolved compositions and trace-element over-enrichment that are consequence of this process are impossible to detect on textural evidence alone but require sophisticated chemical mapping techniques comparable to those presented herein. It is highly likely, therefore, that melt-rock reaction and reactive porous melt migration similar to that reported here is a far more important mechanism of chemical evolution of igneous rocks than hitherto recognized, and may potentially be responsible for a significant proportion of crystal and melt modification in magma reservoirs.

DATA AVAILABILITY STATEMENT

All datasets presented in this study are included in the article/ **Supplementary Material**.

AUTHOR CONTRIBUTIONS

AS, CM, and RT conceived the project. CM chose the samples and ran the compositional maps, using the approach designed by JL. AS compiled the figures and performed the geochemical models. JL performed the diffusion model. AZ performed the LA-ICP-MS analyses. AS and CM wrote the text with the contribution of all authors.

FUNDING

This work was financially supported by the grant "Contributo a Spedizione oceanografica" of the University of Pavia to AS and RT by the Italian Programma di Rilevante Interesse Nazionale (PRIN_2017KY5ZX8), and by Natural Environment Research Council grant NE/N019199/1 to CJM. AS and RT were further supported by IODP-Italy.

ACKNOWLEDGMENTS

The study uses samples provided by the International Ocean Discovery Program (IODP) (https://www.iodp.org/about-iodp); we thank the captain, the crew, and the staff of the JOIDES Resolution for their work during Expedition 360. The ideas in this study benefited from comments and discussion with all the Expedition 360 scientists. Henry Dick and the igneous petrology group are particularly thanked. Comments from the editor Wendy Bohrson and from two anonymous reviewers greatly improved the quality of the manuscript.

SUPPLEMENTARY MATERIAL

The Supplementary Material for this article can be found online at: https://www.frontiersin.org/articles/10.3389/feart.2020.579138/full#supplementary-material

REFERENCES

Anders, E., and Ebihara, M. (1982). Solar system abundances of the elements. *Geochem. Cosmochim. Acta.* 46, 2363–2380. doi:10.1016/0016-7037(82)90208-3

Beard, J.S., Ragland, P.C., and Rushmer, T. (2004). Hydration crystallization reactions between anhydrous minerals and hydrous melt to yield amphibole and biotite in igneous rocks: description and implications. *J. Geol.* 112, 617–621.

Bedard, J. H. (1994). A procedure for calculating the equilibrium distribution of trace elements among the minerals of cumulate rocks, and the concentration of trace elements in coexisting liquids. *Chem. Geol.* 118, 143–153. doi:10.1016/0009-2541(94)90173-2

Bédard, J. H., Hebert, R., Berclaz, A., and Varfalvy, V. (2000). "Syntexis and the genesis of lower oceanic crust," in *Ophiolites and Oceanic crust: new insights from field studies and the Ocean Drilling Program*. Editors Y. Dilek, E. M. Moores, D. Elthon, and A. Nicolas (Boulder, CO: Geological Society of America), Vol. 349, 105–119.

Blackman, D. K., Ildefonse, B., John, B. E., Ohara, Y., Miller, D. J., and MacLeod, C. J. (2006). "IODP expeditions 304 & 305 characterize the lithology," in *Proceedings of the Integrated Ocean Drilling Program.*, Vol. 304/305. (College Station, TX: Integrated Ocean Drilling Program.

Blackman, D.K., Ildefonse, B., John, B.E., Ohara, Y., Miller, D. J., Abe, N., et al. (2011). Drilling constraints on lithospheric accretion and evolution at Atlantis massif, Mid-Atlantic Ridge 30°N. *J. Geophys. Res.* 116, B07103. doi:10.1029/2010JB007931

Blum, P., MacLeod, C.J., Dick, H.J.B., Abe, N., Blackman, D.K., Bowles, J.A., et al. (2017). "Hole U1473A remediation operations, Expedition 362T," in Proceedings of the International Ocean Discovery Program. *Editors C. J. MacLeod, H. J. B. Dick, P. Blum, and E. Scientists*. (College Station, TX: International Ocean Discovery Program), 11.

Borghini, G., and Rampone, E. (2007). Postcumulus processes in oceanic-type olivine-rich cumulates: the role of trapped melt crystallization versus melt/rock interaction, *Contrib. Mineral. Petrol.* 154, 619–633. doi:10.1007/s00410-007-0217-5

Cannat, M., and Casey, J. F. (1995). "An ultramafic lift at the Mid-Atlantic Ridge: successive stages of Magmatism in serpentinized peridotites from the 15 degree N region," in *Mantle and lower crust exposed in Oceanic Ridges and in Ophiolites*. Editors R. Vissers and A. Nicolas (Norwell, MA: Kluwer), 5–34.

Cannat, M., Sauter, D., Mendel, V., Ruellan, E., Okino, K., Escartin, J., et al. (2006). Modes of seafloor generation at a meltpoor ultraslowspreading ridge. *Geology,* 34 (7), 605–608. doi:10.1130/G22486.1

Cherniak, D. J., and Liang, Y. (2012). Ti diffusion in natural pyroxene, *Geochem. Cosmochim. Acta.* 98, 31–47. doi:10.1016/j.gca.2012.09.021

Coogan, L. A., Jenkin, G. R. T., and Wilson, R. N. (2007). Contrasting cooling rates in the lower oceanic crust at fast- and slow-spreading ridges revealed by geospeedometry. *J. Petrol.* 48 (11), 2211–2231. doi:10.1093/petrology/egm057

Coogan, L. A., and O'Hara, M. J. (2015). MORB differentiation: *In situ* crystallization in replenished–tapped magma chambers. *Geochem. Cosmochim. Acta.* 158, 147–161. doi:10.1016/j.gca.2015.03.010

Coogan, L. A., Saunders, A. D., Kempton, P. D., and Norry, M. J. (2000). Evidence from oceanic gabbros for porous melt migration within a crystal mush beneath the Mid-Atlantic Ridge. *Geochem. Geophys. Geosyst.* 1. doi:10.1029/2000GC000072

Coogan, L.A., Thompson, G., MacLeod, C.J., Dick, H.J.B., Edwards, S.J., Hosford Scheirer, A., et al. (2004). A combined basalt and peridotite perspective on 14 million years of melt generation at the Atlantis Bank segment of the Southwest Indian Ridge: evidence for temporal changes in mantle dynamics? *Chem. Geol.* 207, 13–30.

Coogan, L. A., Wilson, R. N., Gillis, K. M., and MacLeod, C. J. (2001). Near-solidus evolution of oceanic gabbros: insights from amphibole geochemistry. *Geochem. Cosmochim. Acta.* 65, 4339–4357. doi:10.1016/s0016-7037(01)00714-1

Coumans, J. P., Stix, J., Clague, D. A., Minarik, W. G., and Layne, G. D. (2016). Melt-rock interaction near the Moho: evidence from crystal cargo in lavas from near-ridge seamounts. *Geochem. Cosmochim. Acta.* 191, 139–164. doi:10.1016/j.gca.2016.07.017

DePaolo, D. J. (1981). Trace element and isotopic effects of combined wall-rock assimilation and fractional crystallization. *Earth Planet Sci. Lett.* 53, 189–202. doi:10.1016/0012-821x(81)90153-9

Detrick, R. S., Buhl, P., Vera, E., Mutter, J., Orcutt, J., Madsen, J., et al. (1987). Multi-channel seismic imaging of a crustal magma chamber along the East Pacific Rise. *Nature.* 326, 35–41. doi:10.1038/326035a0

Dick, H. J. B., Kvassnes, A. J. S., Robinson, P. T., MacLeod, C. J., and Kinoshita, H. (2019a). The Atlantis Bank gabbro massif, Southwest Indian ridge. *Progress in Earth and Planetary Science.* 6, 64. doi:10.1186/s40645-019-0307-9

Dick, H. J. B., MacLeod, C. J., Blum, P., Abe, N., Blackman, D. K., Bowles, J. A., et al. (2019b). Dynamic accretion beneath a slow spreading ridge segment: IODP hole U1473A and the Atlantis Bank oceanic core complex. *J. Geophys. Res. Solid Earth.* 124, 12631–12659. doi:10.1029/2018JB016858

Dick, H.J.B., Meyer, P.S., Bloomer, S., Kirby, S., Stakes, D., and Mawer, C. (1991). "Lithostratigraphic evolution of an in-situ section of oceanic layer 3," in Proceedings of the Ocean Drilling Program, Scientific Results, 118. Editors R. P. Von Herzen, and P. T. Robinson (Station,TX: Ocean Drilling Program), 439–540.

Dick, H. J. B., Natland, J. H., Alt, J. C., Bach, W., Bideau, D., Gee, J. S., et al. (2000). A long *in-situ* section of the lower ocean crust: results of ODP Leg 176 drilling at the Southwest Indian Ridge. *Earth Planet Sci. Lett.* 179, 31–51. doi:10.1016/s0012-821x(00)00102-3

Dick, H. J. B., Natland, J. H., Miller, D. J., et al. (1999). *Proceedings of the Ocean Drilling Program, initial reports.* College Station, TX: Ocean Drilling Program, 176.

Dick, H. J. B., Ozawa, K., Meyer, P. S., Niu, Y., Robinson, P. T., Constantin, M., et al. (2002). "Primary silicate mineral chemistry of a 1.5-km section of very slow spreading lower ocean crust: ODP Hole 735B, Southwest Indian Ridge," in *Proceedings of the Ocean Drilling Program, scientific results.* Editors J. H. Natland, H. J. B. Dick, D. J. Miller, and R. Von Herzen (College Station, TX: Ocean Drilling Program), 176, 1–60. Available at: <http://www-odp.tamu.edu/publications/176_SR/chap_10/chap_10.htm>.

Dodson, M. H. (1973). Closure temperature in cooling geochronological and petrological systems. *Contrib. Mineral. Petrol.* 40, 259–274. doi:10.1007/bf00373790

Drouin, M., Godard, M., Ildefonse, B., Bruguier, O., and Garrido, C. J. (2009). Geochemical and petrographic evidence for magmatic impregnation in the oceanic lithosphere at Atlantis Massif, Mid-Atlantic Ridge (IODP Hole U1309D, 30°N). *Chem. Geol.* 264, 71–88. doi:10.1016/j.chemgeo.2009.02.013

Drouin, M., Ildefonse, B., and Godard, M. (2010). A microstructural imprint of melt impregnation in slow-spread lithosphere: Olivine-rich troctolites from the Atlantis massif (Mid-Atlantic Ridge 30°N, IODP Hole U1309D). *Geochem. Geophys. Geosyst*, 11, Q06003. doi:10.1029/2009GC002995.

Eason, D. E., and Sinton, J. M. (2009). Lava shields and fissure eruptions of the Western Volcanic Zone, Iceland: evidence for magma chambers and crustal interaction. *J. Volcanol. Geoth. Res.* 186, 331–348. doi:10.1016/j.jvolgeores.2009.06.009

Elthon, D., Casey, J. F., and Komor, S. (1982). Mineral chemistry of ultramafic cumulates from the North Arm Mountain Massif of the Bay of Islands ophiolite: evidence for high pressure crystal fractionation of oceanic basalts. *J. Geophy. Res.* 87, 8717–8734.

Ferrando, C., Godard, M., Ildefonse, B., and Rampone, E. (2018). Melt transport and mantle assimilation at Atlantis Massif (IODP Site U1309): constraints from geochemical modelling. *Lithos*. 323, 24–43.

Gao, Y., Hoefs, J., Hellebrand, E., von der Handt, A., and Snow, J. E. (2007). Trace element zoning in pyroxenes from ODP Hole 735B gabbros: diffusive exchange or synkinematic crystal fractionation?. *Contrib. Mineral. Petrol.* 153, 429–442. doi:10.1007/s00410-006-0158-4

Ghiorso, M. S., and Sack, O. (1995). Chemical mass transfer in magmatic processes. IV. A revised and internally consistent thermodynamic model for the interpolation and extrapolation of liquid-solid equilibria in magmatic systems at elevated temperatures and pressures. *Contrib. Mineral. Petrol.* 119 (2-3), 197–212. doi:10.1007/BF00307281.

Grimes, C. B., Cheadle, M. J., John, B. E., Reiners, P. W., and Wooden, J. L. (2011). Cooling rates and the depth of detachment faulting at oceanic core complexes: evidence from zircon Pb/U and (U-Th)/He ages. *Geochem. Geophys. Geosyst.* 12, 1–24. doi:10.1029/2010GC003391

Jackson, M. D., Blundy, J. D., and Sparks, R. S. J. (2018). Chemical differentiation, cold storage and remobilization of magma in the Earth's crust. *Nature.* 564, 405–409. doi:10.1038/s41586-018-0746-2

John, B. E., D. A., Foster, J. M., Murphy, M.J., Cheadle, A. G., Baines, C. M., Fanning, et al. (2004). Determining the cooling history of in situ lower oceanic crust-Atlantis Bank, SW Indian Ridge, *Earth Planet Sci. Lett.* 222, 154–160. doi:10.1016/j.epsl.2004.02.014

Koepke, J., Botcharnikov, R.E., and Natland, J.H. (2018). Crystallization of late-stage MORB under varying water activities and redox conditions: Implications for the formation of highly evolved lavas and oxide gabbro in the ocean crust. *Lithos.* 323, 58–77. doi:10.1016/j.lithos.2018.10.001

Koepke, J., Berndt, S.T.F., and Holtz, F. (2007). The formation of SiO2 rich melts within the deep oceanic crust by hydrous partial melting of gabbros. *Contrib. Mineral. Petrol.* 153 (1), 67–84. doi:10.1007/s00410-006-0135-y

Kvassnes, A.J.S., and Grove, T. (2008). How partial melts of mafic lower crust affect ascending magmas at oceanic ridge. *Contrib. Mineral. Petrol.* 156, 49–71.

Leuthold, J., Blundy, J. D., Holness, M. B., and Sides, R. (2014). Successive episodes of reactive liquid flow through a layered intrusion (unit 9, Rum Eastern Layered Intrusion, Scotland). *Contrib. Mineral. Petrol.* 168, 1021. doi:10.1007/s00410-014-1021-7.

Leuthold, J., Lissenberg, C. J., O'Driscoll, B., Karakas, O., Falloon, T., Klimentyeva, D. N., et al. (2018). Partial melting of lower oceanic crust gabbro: constraints from poikilitic clinopyroxene primocrysts. *Front. Earth Sci.* 6, 15. doi:10.3389/feart.2018.00015

Lissenberg, C. J., and Dick, H. J. B. (2008). Melt–rock reaction inthe lower oceanic crust and its implications for the genesis of mid-Ocean Ridge Basalt. *Earth Planet Sci. Lett.* 271, 311–325. doi:10.1016/j.epsl.2008.04.023

Lissenberg, C. J., and MacLeod, C. J. (2016). A reactive porous flow control on mid-ocean ridge magmatic evolution. *J. Petrol.* 57, 2195–2220. doi:10.1093/petrology/egw074

Lissenberg, C. J., MacLeod, C. J., and Bennett, E. N. (2019). Consequences of a crystal mush-dominated magma plumbing system: a mid-ocean ridge perspective. *Phil. Trans. R. Soc. A.* 377, 20180014. doi:10.1098/rsta.2018.0014

Lissenberg, C. J., MacLeod, C. J., Howard, K. A., and Godard, M. (2013). Pervasive reactive melt migration through fastspreading lower oceanic crust (Hess Deep, equatorial Pacific Ocean). *Earth Planet Sci. Lett.* 361, 436–447. doi:10.1016/j.epsl.2012.11.012

Loocke, M. P. (2016). The role of the axial melt lens in crustal accretion at fast-spreading mid-ocean ridges. PhD thesis. Cardiff (Wales): Cardiff University, 191.

MacLeod, C. J., Dick, H. J. B., Allerton, S., Robinson, P. T., Coogan, L. A., Edwards, S. J., et al. (1998). Geological mapping of slow-spread lower ocean crust: a deep-towed video and wireline rock drilling survey of Atlantis Bank (ODP Site 735, SW Indian Ridge). *InterRidge News.* 7 (2), 39–43.

C. J., MacLeod, H. J. B., Dick, and P., Blum, and theExpedition 360 Scientists (Editors) (2017). "in Southwest Indian Ridge Lower Crust and Moho." *Proceedings of the International Ocean Discovery Program.* (College Station, TX: International Ocean Discovery Program), 360.

Marjanovic, M., Carbotte, S. M., Carton, H., Nedimovic, M. R., Mutter, J. C., and Canales, J. P. (2014). A multi-sill magma plumbing system beneath the axis of the East Pacific Rise. *Nat. Geosci.* 7, 825–829. doi:10.1038/ngeo2272

Meyer, P.S., Dick, H.J.B., and Thompson, G. (1989). Cumulate gabbros from the Southwest Indian Ridge, 548S, 7816'E: implications for magmatic processes at a slow spreading ridge. *Contrib. Mineral. Petrol.* 103, 44–63.

Müller, T., Dohmen, R., Becker, H. W., ter Heege, J., and Chakraborty, S. (2013). Fe-Mg interdiffusion rates in clinopyroxene: experimental data and implications for Fe-Mg exchange geothermometers. *Contrib. Mineral. Petrol.* 166 (6), 1563–1576. doi:10.1007/s00410-013-0941-y

Natland, J. H., and Dick, H. J. B. (2001). Formation of the lower ocean crust and the crystallization of gabbroic cumulates at a very slowly spreading ridge. *J. Volcanol. Geoth. Res.* 110, 191–233. doi:10.1016/s0377-0273(01)00211-6

Nguyen, D., Morishita, T., Soda, Y., Tamura, A., Ghosh, B., Harigane, Y., et al. (2018). Occurrence of felsic rocks in oceanic gabbros from IODP Hole U1473A: implications for evolved melt migration in the lower oceanic crust. *Minerals.* 8, 583. doi:10.3390/min8120583

Ozawa, K., Meyer, P. S., and Bloomer, S. (1991). Mineralogy and textures of iron-titanium oxide gabbros and associated olivine gabbros from Hole 735B. *Proc. Ocean Drill. Progr. Sci. Results.* 118, 41–73. doi:10.2973/odp.proc.sr.118.125.1991

Pettigrew, T. L., Casey, J. F., Miller, D. J., et al. (1999). *Proceedings of the Ocean Drilling Program, Initial Reports.* College Station, TX: Ocean Drilling Program, 179.

Phipps Morgan, J., and Chen, Y. J. (1993). The genesis of oceanic crust: magma injection, hydrothermal circulation, and crustal flow. *J. Geophys. Res.* 98 (B4), 6283–6297. doi:10.1029/92jb02650

Renna, M. R., Tribuzio, R., Sanfilippo, A., and Thirlwall, M. (2018). Role of melting process and melt–rock reaction in the formation of Jurassic MORB-type basalts (Alpine ophiolites). *Contrib. Mineral. Petrol.* 173 (4), 31. doi:10.1007/s00410-018-1456-3

Rioux, M., Cheadle, M. J., John, B. E., and Bowring, S. A. (2016). The temporal and spatial distribution of magmatism during lower crustal accretion at an ultraslow-spreading ridge: high-precision U-Pb zircon dating of ODP Holes 735B and 1105A, Atlantis Bank, Southwest Indian Ridge. *Earth Planet Sci. Lett.* 449, 395–406. doi:10.1016/j.epsl.2016.05.047

Sanfilippo, A., Morishita, T., Kumagai, H., Nakamura, K., Okino, K., Hara, K., et al. (2015). Hybrid troctolites from mid-ocean ridges: inherited mantle in the lower crust. *Lithos.* 232, 124–130. doi:10.1016/j.lithos.2015.06.025Google Scholar

Sanfilippo, A., Morishita, T., and Senda, R. (2016). Rhenium-osmium isotope fractionation at the oceanic crust-mantle boundary. *Geology.* 44 (2), 167–170. doi:10.1130/G37428.1

Sanfilippo, A., and Tribuzio, R. (2013). Origin of olivine-rich troctolites from the oceanic lithosphere: a comparison between the Alpine Jurassic ophiolites and modern slow spreading ridges. *Ofioliti.* 38, 89–99. doi:10.4454/ofioliti.v38i1.418

Singh, S. C., Crawford, W.C., Carton, H., Seher, T., Combier, V., Cannat, M., et al. (2006). Discovery of a magma chamber and faults beneath a Mid-Atlantic Ridge hydrothermal field. Nature 442, 1029–1032.

Sinha, M. C., Constable, S. C., Peirce, C., White, A., Heinson, G., MacGregor, L. M., et al. (1998). Magmatic processes at slow spreading ridges: implications of the RAMESSES experiment at 57° 45′N on the Mid-Atlantic Ridge. *Geophys. J. Int.* 135, 731–745. doi:10.1046/j.1365-246x.1998.00704.x

Sinton, J. M., and Detrick, R. S. (1992). Mid-ocean ridge magma chambers. *J. Geophys. Res.* 97 (B1), 197–216. doi:10.1029/91jb02508

Sneeringer, M., Hart, S. R., and Shimizu, N. (1984). Strontium and samarium diffusion in diopside. *Geochem. Cosmochim. Acta.* 48, 1589–1608. doi:10.1016/0016-7037(84)90329-6

Solano, J. M. S., Jackson, M. D., Sparks, R. S. J., and Blundy, J. (2014). Evolution of major and trace element composition during melt migration through crystalline mush: implications for chemical differentiation in the crust. *Am. J. Sci.* 314, 895–939. doi:10.2475/05.2014.01

Spiegelman, M., Kelemen, P. B., and Aharonov, E. (2001). Causes and consequences of flow organization during melt transport: the reaction infiltration instability in compactible media, *J. Geophys. Res.* 106, 2061–2077. doi:10.1029/2000JB900240.

Suhr, G., Hellebrand, E., Johnson, K., and Brunelli, D. (2008). Stacked gabbro units and intervening mantle: a detailed look at a section of IODP Leg 305, Hole U1309D. *Geochem. Geophys. Geosyst.* 9. doi:10.1029/2008GC002012

Sun, C., Graff, M., and Liang, Y. (2017). Trace element partitioning between plagioclase and silicate melt: the importance of temperature and plagioclase composition, with implications for terrestrial and lunar magmatism. *Geochem. Cosmochim. Acta.* 206, 273. doi:10.1016/j.gca.2017.03.003

Sun, C., and Liang, Y. (2012). Distribution of REE between clinopyroxene and basaltic melt along a mantle adiabat: effects of major element composition, water, and temperature. *Contrib. Mineral. Petrol.* 163, 807–823. doi:10.1007/s00410-011-0700-x

Sun, C., and Liang, Y. (2017). A REE-in-plagioclase-clinopyroxene thermometer for crustal rocks. *Contrib. Mineral. Petrol.* 172, 24. doi:10.1007/s00410-016-1326-9

Tamura, A., Morishita, T., Ishimaru, S., Hara, K., Sanfilippo, A., and Arai, S. (2016). Compositional variations in spinel-hosted pargasite inclusions in the olivine-rich rock from the oceanic crust-mantle boundary zone. *Contrib. Mineral. Petrol.* 171 (5), 39. doi:10.1007/s00410-016-1245-9

Tribuzio, R., Tiepolo, M., Vannucci, R., and Bottazzi, P. (1999). Trace element distribution within olivine-bearing gabbros from the Northern Apennine ophiolites (Italy): evidence for post-cumulus crystallization in MOR-type gabbroic rocks. *Contrib. Mineral. Petrol.* 134, 123–133. doi:10.1007/s004100050473

Van Orman, J. A., Grove, T. L., and Shimizu, N. (2001). Rare earth element diffusion in diopside: influence of temperature, pressure, and ionic radius, and an elastic model for diffusion in silicates. *Contrib. Mineral. Petrol.* 141 (6), 687. doi:10.1007/s004100100269

Yang, A. Y., Wang, C., Liang, Y., and Lissenberg, C. J. (2019). Reaction between Mid-Ocean Ridge basalt and lower Oceanic crust: an experimental study. *Geochem. Geophys. Geosyst.* 20 (9), 4390–4407. doi:10.1029/2019gc008368

Conflict of Interest: The authors declare that the research was conducted in the absence of any commercial or financial relationships that could be construed as a potential conflict of interest.

frontiers
in Earth Science

ORIGINAL RESEARCH
published: 28 May 2021
doi: 10.3389/feart.2021.640464

Hydrated Peridotite – Basaltic Melt Interaction Part I: Planetary Felsic Crust Formation at Shallow Depth

Anastassia Y. Borisova[1,2]*, Nail R. Zagrtdenov[1], Michael J. Toplis[3], Wendy A. Bohrson[4], Anne Nédélec[1], Oleg G. Safonov[2,5,6], Gleb S. Pokrovski[1], Georges Ceuleneer[1], Ilya N. Bindeman[7,8], Oleg E. Melnik[9], Klaus Peter Jochum[10], Brigitte Stoll[10], Ulrike Weis[10], Andrew Y. Bychkov[2], Andrey A. Gurenko[11], Svyatoslav Shcheka[12], Artem Terehin[5], Vladimir M. Polukeev[5], Dmitry A. Varlamov[5], Kouassi Chariteiro[1], Sophie Gouy[1] and Philippe de Parseval[1]

[1]Géosciences Environnement Toulouse, GET/OMP (CNRS, UT3, IRD, CNES), Toulouse, France, [2]Geological Department, Lomonosov Moscow State University, Vorobievy Gory, Moscow, Russia, [3]Institut de Recherche en Astrophysique et Planétologie (IRAP) UT3, CNRS, Toulouse, France, [4]Department of Geology and Geological Engineering, Colorado School of Mines, Golden CO, United States, [5]Korzhinskii Institute of Experimental Mineralogy, Chernogolovka, Moscow Region, Russia, [6]Department of Geology, University of Johannesburg, Auckland Park, 2006, Johannesburg, South Africa, [7]Department of Sciences, University of Oregon, Eugene, OR, United States, [8]Fersman Mineralogical Museum, Leninsky Prospect 18, Moscow, Russia, [9]Institute of Mechanics, Moscow State University, 1- Michurinskii Prosp, Moscow, Russia, [10]Climate Geochemistry Department, Max Planck Institute for Chemistry, Mainz, Germany, [11]Centre de Recherches Pétrographiques et Géochimiques, UMR 7358, Université de Lorraine, 54501 Vandœuvre-lès-Nancy, France, [12]Bavarian Research Institute of Experimental Geochemistry and Geophysics (BGI), University of Bayreuth, Bayreuth, Germany

Edited by:
Scott Andrew Whattam,
King Fahd University of Petroleum and Minerals, Saudi Arabia

Reviewed by:
Kent Condie,
New Mexico Institute of Mining and Technology, United States
Elena Sizova,
University of Graz, Austria

***Correspondence:**
Anastassia Y. Borisova
anastassia.borisova@get.omp.eu

Specialty section:
This article was submitted to Petrology,
a section of the journal
Frontiers in Earth Science

Received: 11 December 2020
Accepted: 26 January 2021
Published: 28 May 2021

Citation:
Borisova AY, Zagrtdenov NR, Toplis MJ, Bohrson WA, Nédélec A, Safonov OG, Pokrovski GS, Ceuleneer G, Bindeman IN, Melnik OE, Jochum KP, Stoll B, Weis U, Bychkov AY, Gurenko AA, Shcheka S, Terehin A, Polukeev VM, Varlamov DA, Chariteiro K, Gouy S and de Parseval P (2021) Hydrated Peridotite – Basaltic Melt Interaction Part I: Planetary Felsic Crust Formation at Shallow Depth. Front. Earth Sci. 9:640464. doi: 10.3389/feart.2021.640464

Current theories suggest that the first continental crust on Earth, and possibly on other terrestrial planets, may have been produced early in their history by direct melting of hydrated peridotite. However, the conditions, mechanisms and necessary ingredients for this crustal formation remain elusive. To fill this gap, we conducted time-series experiments to investigate the reaction of serpentinite with variable proportions (from 0 to 87 wt%) of basaltic melt at temperatures of 1,250–1,300°C and pressures of 0.2–1.0 GPa (corresponding to lithostatic depths of ~5–30 km). The experiments at 0.2 GPa reveal the formation of forsterite-rich olivine ($Fo_{90–94}$) and chromite coexisting with silica-rich liquids (57–71 wt% SiO_2). These melts share geochemical similarities with tonalite-trondhjemite-granodiorite rocks (TTG) identified in modern terrestrial oceanic mantle settings. By contrast, liquids formed at pressures of 1.0 GPa are poorer in silica (~50 wt% SiO_2). Our results suggest a new mechanism for the formation of the embryonic continental crust via aqueous fluid-assisted partial melting of peridotite at relatively low pressures (~0.2 GPa). We hypothesize that such a mechanism of felsic crust formation may have been widespread on the early Earth and, possibly on Mars as well, before the onset of modern plate tectonics and just after solidification of the first ultramafic-mafic magma ocean and alteration of this primitive protocrust by seawater at depths of less than 10 km.

Keywords: experiment, basaltic melt-serpentinite rock interaction, TTG, ophiolites, Hadean eon, Noachian, Mars, protocrust

INTRODUCTION

The conditions and mechanisms that led to the production of the earliest intermediate to felsic (Si- and Al-enriched) crust on Earth and Mars are the subject of intense debate (Rudnick and Gao, 2003; Harrison, 2009; Reimink et al., 2014, 2016; Sautter et al., 2015, 2016; Burnham and Berry, 2017). There are some indications that this crust was composed of igneous rocks of granitic composition (I-type) and may have been formed in a tonalite-trondhjemite-granodiorite (TTG)-like environment, i.e., by partial melting of a garnet-bearing lower crust, as far back as the geological record goes (e.g., the parental melt of the 4.37–4.02 Ga Jack Hills detrital zircon crystals, Burnham and Berry, 2017). Ancient granodiorite rocks have also been identified on Mars (Sautter et al., 2015; Sautter et al., 2016), indicating that formation of felsic crust occurred on other terrestrial planets even without plate tectonics and subduction. In this context, melting of dry peridotite at shallow depths does not produce appropriate intermediate to felsic melt compositions comparable to that of bulk continental crust (Hirschmann et al., 1998; Rudnick and Gao, 2003; Harrison, 2009; Reimink et al., 2014, 2016; Burnham and Berry, 2017). As a result, most currently accepted models for the generation of felsic crust on the Earth or Mars consider a complex multi-stage process at different depths, which involves extraction of basaltic magma from peridotitic mantle followed by fractional crystallization (Reimink et al., 2014, 2016; Udry et al., 2018) and/or re-melting of hydrated mafic rocks at lithospheric conditions of ≥0.6 GPa (Harrison, 2009; O'Neil and Carlson, 2017). However, specific conditions during the Hadean lead us to envisage petrological mechanisms that are not typical of present-day felsic magma generation (i.e., not involving subduction; see Herzberg et al., 2010; Sautter et al., 2016). For example, the early terrestrial crust of intermediate to felsic composition might have been created by direct melting of a serpentinized (e.g., hydrated) peridotite at shallow depths (Rudnick, 1995; Rudnick and Gao, 2003). A possible present-day analogue is the formation of tonalites-trondhjemites in the shallow mantle beneath oceanic spreading centers (called oceanic plagiogranites in this context) (Coleman and Peterman, 1975; Amri et al., 1996; Amri et al., 2007). Trondhjemite-tonalite veins are common features throughout the cores in the few sites of the Deep Sea Drilling Project, and Ocean Drilling, Integrated Ocean Drilling and International Ocean Discovery Programs (DSDP, ODP, and IODP) where the deep oceanic crust has been drilled along present-day spreading ridges. These rocks have been ascribed to local remelting processes in the presence of hydrothermal fluids along high-temperature normal shear zones. These rocks are not abundant (no more than 1% of the volume of the sections), but their abundance might be underestimated due to poor core recovery in the fault zones (e.g., Pietranik et al., 2017). Their origin is enigmatic, although understanding the origin of TTG rocks situated in modern oceanic lithosphere may open new perspectives on the formation of the first planetary felsic crust.

Rare low-pressure melting experiments (≤1.0 GPa) involving peridotite and low water contents (up to 0.5 wt% in the bulk source) indicate that peridotite-derived partial melts may become enriched in SiO_2 (up to 57 wt%) and other lithophile elements (Al, alkalis), with abundances approaching those of continental crustal rocks (Hirschmann et al., 1998; Ulmer, 2001). The increase in the silica contents of partial melts at low pressures is generally considered to be due to the combined effects of water, alkalis, and low pressure on the structure of the aluminosilicate melt, shifting the olivine-pyroxene cotectics to higher SiO_2 contents through a decrease in the silica activity coefficient (Kushiro, 1968; Hirschmann et al., 1998; Lundstrom, 2000).

As an alternative, or complement to direct hydrous melting of peridotite, a currently untreated question is to what extent the presence of basaltic melt may have an impact on the production of felsic crust. This impact may be direct (through chemical reactions with the host peridotite) or indirect (by providing a heat source). In this respect, experiments that reproduce basaltic melt-peridotite reaction at low pressures (<0.8 GPa) are currently limited to systems undersaturated in aqueous fluid (e.g., Fisk, 1986; Kelemen et al., 1990; Morgan, and Liang, 2003; Van den Bleeken et al., 2010; 2011). Although the experiments show the presence of dry basaltic to andesitic-basaltic melts in association with olivine, no direct data exist concerning the partial melting of hydrated (serpentinized) peridotite (or serpentinite) triggered by the emplacement of basaltic melts at shallow crustal depths (5–15 km). This latter scenario is of primary interest in early Earth history (and possibly also for Mars), because the ultramafic-mafic protocrust formed from the crystallization of a magma ocean was most likely hydrated, either by volatiles released by the magma ocean itself or through interactions with liquid water available on the planetary surface (Albarède and Blichert-Toft, 2007; Elkins-Tanton, 2012). A present-day analogue can be observed at the level of the mantle/petrologic Moho boundary in the oceanic lithosphere (at depths of 6 km), where interactions of basaltic magmas with peridotites produce chromitite-dunite associations (Kelemen et al., 1995; Arai, 1997; Borisova et al., 2012; Zagrtdenov et al., 2018; Rospabé et al., 2019) and serpentinized peridotite (hydrated residual peridotite) undergoes partial melting (Benoit et al., 1999). Furthermore, such shallow conditions of serpentinite melting in the presence of basaltic melt might also occur in mantle plumes (Bindeman, 2008; Reimink et al., 2014, 2016; Borisova et al., 2020a), in Hadean heat-pipe volcanoes (Moore and Webb, 2013) or Hadean proto-rift volcanoes (Capitanio et al., 2020) and/or during meteorite impacts (Marchi et al., 2014).

The above considerations provide a strong motivation for the present study, which aims to directly investigate the generation of intermediate to felsic crust on young terrestrial planets. For this purpose, we have conducted a set of time-series experiments in serpentinite-basalt systems under relatively low pressures (≤1 GPa), corresponding to depths of ≤30 km. Modern (i.e., post-Archean) magmatism near the petrologic Moho in the oceanic lithosphere can then be used as a ground-truth test within its limits.

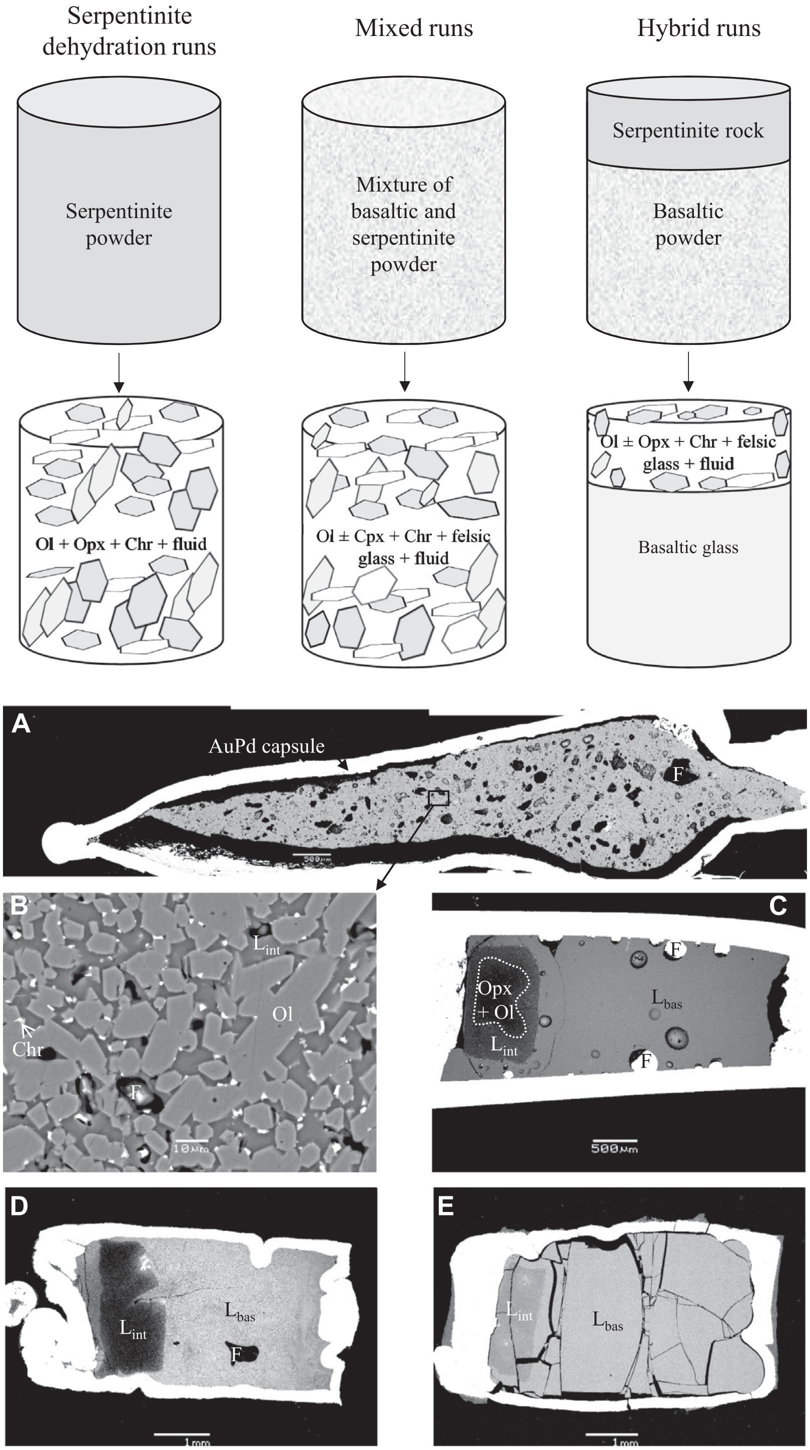

FIGURE 1 | Upper panel: Scheme of time-series runs at 0.2 GPa, showing starting configurations and final products containing felsic glasses. Three types of experiment are described: serpentinite dehydration, and mixed and hybrid runs. Ol, high-Mg olivine; Opx, orthopyroxene; Cpx, clinopyroxene; Chr, chromite or chromiferous magnetite; felsic glass, intermediate to felsic glasses and fluid, aqueous fluid. **Lower panel:** Backscattered electron images of the hybrid and mixed runs at 0.2–1.0 GPa pressures. **(A)** mixed run SB7 at 0.2 GPa; **(B)** zoom on the SB7 with magnification of 1,100; hybrid runs: **(C)** P32 at 0.2 GPa; **(D)** P1 at 0.5 GPa; **(E)** P3 at 1.0 GPa. Mixed samples (SB7) is homogeneous sample with high-Mg olivine and interstitial felsic glasses. Hybrid samples (P32, P1, and P3) contain two zones: olivine-rich zone (the former serpentinite zone) with interstitial felsic melt (L_{int}) and zone of reacting basalt (L_{bas}). Ol, high-Mg olivine; Opx, orthopyroxene; Chr, chromite, and F, aqueous fluid. It should be noted that the homogeneous olivine-rich zone containing high-Mg olivine, chromite, interstitial felsic melt, and aqueous fluid is formed in the mixed run SB7 ($R = 0.25$) at an early stage (in less than 2 h), suggesting early attainment of steady state in this system with a high starting proportion of serpentinite (80 wt%). All details may be found in **Table 1** and **Supplementary Table S2**.

EXPERIMENTAL STRATEGY AND METHODS

Experimental Strategy

To investigate the serpentinite rock-basaltic melt reactions, we have conceived three types of time-series experiments: (i) pure serpentinite dehydration in a basalt-free system, and so-called (ii) “mixed” and iii) “hybrid” experiments in the serpentinite-basalt system as a function of pressure and basalt-to-serpentinite ratio. (**Figures 1A–E**; **Table 1**; **Supplementary Tables S1, S2**). The “mixed” experiments were performed on well-homogenized serpentinite and basaltic powders compressed together, whereas the “hybrid” experiments were performed using cylindrical pieces of serpentinite rock placed in the upper part of the capsule and a basaltic powder in the lower part of the capsule in contact with the base of the serpentinite cylinder (**Figures 1A-E**). These two distinct experimental setups were designed to simulate two principal geological scenarios of basaltic melt emplacement. The mixed experiments (with variable basalt-to-serpentinite mass ratios, $R_{bas/serp}$ or R from 0.25 to 4) simulate the case of efficient fertilization of peridotite in order to achieve a closer approach to equilibrium and obtain stable associations of the minerals and melts produced by the reactions on the relatively short time scales that are accessible experimentally. The hybrid experiments (with generally higher R, from ~3 to ~7) were designed to simulate the process of basaltic melt infiltration into serpentinite rock, that does not necessarily reach equilibrium.

All experiments were conducted using two types of piston cylinder and an internally heated pressure vessel for durations ranging from 1 min to 120 h at pressures of 0.2, 0.5, and 1.0 GPa and temperatures of 1,250 and 1,300°C (see **Supplementary Materials** for details). In modern oceanic settings, temperatures of ~1,050°C are considered to be sufficient to initiate the reaction of serpentinized peridotite with basaltic magma at 0.2 GPa (Borisova et al., 2012). In the present experimental study, however, we chose to use higher temperatures (1,250–1,300°C) since these provide a closer analogue of the thermal conditions of the Hadean and early Martian upper mantle (Herzberg et al., 2010; Sautter et al., 2016). Redox conditions expressed relative to the conventional quartz-fayalite-magnetite f_{O2} buffer [$\Delta QFM = \log_{10} f_{O2}$ (experiment)$-\log_{10} f_{O2}$ (QFM) = +1.8 to +4.6] established in our experiments are comparable to those characteristic of the Jack Hills zircon crystals in equilibrium with the mantle (Trail et al., 2011). In addition, higher temperatures should substantially increase the rates of serpentinite-basaltic melt reactions. On the time scale of laboratory experiments, such conditions correspond to the complete melting of basalt, which is consistent with most existing models of basaltic melt extraction from the mantle and its emplacement in the upper crust (Fisk, 1986; Hirschmann et al., 1998; Ulmer, 2001; Morgan and Liang, 2003).

Experimental Conditions and Starting Materials

To describe mechanisms of the serpentinite dehydration and the serpentinite interaction with basaltic melt, the duration of the experiments varied from 1 min to 120 h. The experiments were performed in two laboratories: Korzhinskii Institute of Experimental Mineralogy (Russia) and Bavarian Research Institute of Experimental Geochemistry and Geophysics (Germany) (**Table 1**; **Supplementary Table S2**). The dehydration runs and the mixed runs were performed for durations of 0.5, 2, 5, and 48 h. The starting basalt used in the hybrid and mixed experiments is an enriched mid-ocean ridge basaltic glass containing 8.2 wt% MgO and 0.7 wt% H_2O (**Supplementary Table S1**) from the Knipovich ridge of the Mid Atlantic Ridge sampled by dredging during the 38th expedition of R/V Akademik Mstislav Keldysh (number 3786/3, Sushchevskaya et al., 2000). The serpentinite (11.9 wt% H_2O) (**Supplementary Table S1**) used as a starting material is from a homogeneous antigorite-dominated sample from Zildat, in the Ladakh area, northwest Himalayas (TSL-19) (Deschamps et al., 2010). This sample has accessory magnetite but no trace of chromite, olivine or orthopyroxene. The serpentinite was prepared either as doubly polished ~1 mm high and ~2.6 mm-diameter cylinders (for hybrid runs) or as serpentinite powder (<100 μm; for mixed runs).

The use of $Au_{80}Pd_{20}$ alloy for the experimental capsule material avoids Fe diffusion into the capsule because of the negligibly small iron solubility at the temperature-pressure-redox conditions of our experiments (Balta et al., 2011). Therefore, the capsules were not pre-doped with Fe. The redox conditions in our experiments were buffered by the initial Fe^{2+}/Fe^{3+} ratios imposed by the starting basaltic glass and serpentinite in the capsule. Note that our run durations (≤48 h) are too short to allow use of a double-capsule technique with common mineral buffers of oxygen fugacity that require longer times to attain equilibrium (Matjuschkin et al., 2015). The redox conditions (i.e., oxygen fugacity, f_{O2}) during the runs are estimated from the compositions of co-existing olivine and chromite using equations of Ballhaus et al. (1991) that yield ΔQFM values of +1.8 to +4.6 (where ΔQFM denotes the $\log f_{O2}$ value relative to the quartz-fayalite-magnetite buffer, **Supplementary Table S2**). Additionally, the Fe^{2+}/Fe^{3+} ratios in several glass run products were derived from XANES (X-ray absorption near edge structure) spectroscopy using the Fe K-edge at the European Synchrotron Radiation Facility (ESRF) in Grenoble, France **(Supplementary Figure S1)**. The Fe^{2+}/Fe^{3+} ratios obtained by XANES correspond to ΔQFM (+1.8 to +3.6) based on model of Borisov et al. (2018) (**Supplementary Table S2**), in excellent agreement with the values estimated from phase composition. The relatively oxidized conditions inferred for our runs are principally the result of the presence of water, although partial H_2 loss through the capsule wall cannot be fully excluded. However, redox potential does not have a significant influence on the concentrations of the major redox-insensitive elements of the felsic crust (predominantly Si, and Al).

We used the law of mass conservation and the minimization code of Oliphant (2006) (version 1.17). Two steps were applied to calculate phase proportions obtained in hybrid runs. In the first step, the initial MORB glass composition was introduced for the compositions of L_{bas} (basaltic liquid) and L_{int} (interstitial felsic liquid) (**Supplementary Tables S1, S2**). In the second step, the basaltic and interstitial glasses (L_{bas} and L_{int}, respectively) were distinguished as different phases. The run products (glasses and minerals) were analyzed for chemical compositions (**Supplementary Tables S3, S4**; **Supplementary Material**) to make reasonable comparison with natural felsic melts and magmas. Furthermore, thermodynamic modelling was performed to constrain the equilibrium compositions of the liquids, minerals as well as fluid produced during serpentinite dehydration and responsible for the felsic melt production (**Supplementary Tables S5–S7**; **Supplementary Material**).

Analytical and Microanalytical Methods

The bulk-rock chemical compositions of the starting serpentinite and basalt samples have been analyzed by inductively coupled plasma-mass spectrometry (ICP-MS) and inductively coupled plasma-optical emission spectroscopy (ICP-OES), using a method developed at the SARM (Nancy, France). Scanning electron microscope (SEM) and electron probe microanalysis and mapping (EPMA) of minerals and glasses were performed at the Géosciences Environnement Toulouse (GET, Toulouse, France) laboratory and at the Centre de Microcaractérisation Raimond Castaing (Toulouse, France). Secondary ion mass spectrometry (SIMS) was applied to measure the H_2O contents at CRPG-CNRS (Nancy, France). Laser ablation-inductively coupled plasma-mass spectrometry (LA-ICP-MS) was applied to analyze major and trace element contents at the Max Planck Institute for Chemistry, (Mainz, Germany). XANES spectroscopy was used to estimate iron redox state in selected experimental glass products from Fe K-edge XANES spectra acquired at the FAME beamline of the European Synchrotron Radiation Facility (ESRF, France). All details of the applied methods may be found in the **Supplementary Material**.

Modelling Approaches

To interpret the experimental and analytical data obtained in this study and to enable comparisons with natural systems, we employed complementary modelling approach. Note that there is no currently available thermodynamic model and associated software tools allowing to directly simulate the aqueous fluid-assisted melting of serpentinite in the presence of basaltic melt at pressures below 1 GPa, that could predict, simultaneously and within the same thermodynamic framework, the compositions of fluid, melts and minerals. By contrast, robust thermodynamic models currently exist for i) hydrous melts and ii) aqueous fluid phase. Therefore, we conducted two types of thermodynamic modelling to better constrain the compositions of the different phases produced in the experiments: i) calculations of liquid and mineral phase proportions and compositions formed at different physical chemical conditions (temperature, pressure, T-P) using MELTS and Magma Chamber Simulator, MCS software and ii) calculations of the equilibrium aqueous fluid composition and major element speciation in the fluid phase to constrain the capacity of the aqueous phase to mobilize and fractionate major elements at the experimental T-P conditions from the initial materials (basalt and serpentinite). All details of the modelling part are reported in **Supplementary Material** and **Supplementary Tables S5–S7**.

RESULTS

Experimental Sample Description

In this section, we describe the results of 23 experimental runs performed at 0.2–1.0 GPa and 1,250–1,300°C to investigate pure serpentinite dehydration and serpentinite-basalt interaction in the mixed and hybrid systems with different durations (1 min–120 h), different proportions of serpentinite (13–100 wt%) and variable basalt-to-serpentinite initial ratios ($R = 0.25–6.5$) in the starting material (**Table 1**; **Supplementary Table S2**).

Dehydration Experiments at 0.2–0.5 GPa

Three experiments on pure serpentinite dehydration (100 wt% serpentinite) at 0.2–0.5 GPa and 1,250°C were performed with different run durations. In experiment P29 (0.5 h duration), we observe a very porous aggregate consisting of enstatite [92–95 Mg# = 100 Mg/(Mg + Fe^{2+})], high-Mg olivine ($Fo_{91–92}$, mol% forsterite) and chromite [69–73 Mg#, and 68–95 Cr# = 100 Cr/(Cr + Al), **Figures 1**, **2**, **Supplementary Tables S2, S3**]. Similarly, in the long-duration experiments P27 and P28 (48 h), the products are represented by a re-crystallized powder containing enstatite, high-Mg olivine and chromite. No trace of silicate glass was found in the run products. In all dehydration experiments at 0.2 and 0.5 GPa, fluid was present, likely produced by serpentinite decomposition.

Mixed Experiments at 0.2 GPa

Based on textural and compositional characteristics, three types of mineral-glass assemblage can be distinguished in nine samples from the mixed experiments on serpentinite-basaltic melt reactions with different proportions of serpentinite ($R = 0.25–4.0$) in the starting material.

1) Most samples of the SB (Serpentinite-Basalt) series with high initial proportions of serpentinite ($R = 0.25–1.0$) are characterized by a homogeneous zone of polyhedral unzoned crystals of high-Mg olivine ($Fo_{90–94}$ mol%) associated with interstitial felsic glasses (SiO_2 = 62–71 wt%) as well as fluid bubbles (**Figures 1A,B**, **2**). Chromite (Cr# = 68–89; Mg# 56–73) is associated with the euhedral olivine grains, and crystals of clinopyroxene (Mg# 58–68) are characteristic of the runs with $R = 1$. **Figures 1A,B**, **2** show that samples SB7, SBbis2, SBter3 with high initial proportions of serpentinite ($R = 0.25$) are characterized by a single zone composed of polyhedral unzoned olivine ($Fo_{90–94}$) and chromite crystals associated with interstitial felsic glasses (L_{int}) and interstitial crystals of chromite and fluid bubbles. Remarkably, the proportions of interstitial melt are high (33–40 wt%).
2) Experiments SB1, SB4, SBbis1, and SBter2, with lower initial proportions of serpentinite ($R = 1–4$), are characterized by polyhedral unzoned olivine

TABLE 1 | Experimental run conditions and the resulting phases with the phase proportions.

№	Run	P	T	Time	Percentage of the starting components (wt%)		R	Resulting experimental phases
		(GPa)	(°C)	(h)	SERP	BAS*	BAS-to-SERP mass ratio	(Phase proportion in wt%)
Serpentinite dehydration experiments								
1	P29	0.2	1250	0.5	100	-	0	Ol (54.1) + Opx (30.4) + Chr (2.6) + F(12.8)
2	P28	0.2	1250	48	100	-	0	Ol + Opx + Chr + F
3	P27	0.5	1250	48	100	-	0	Ol (55.8) + Opx (28.6) + Chr (2.7) + F(12.8)
Mixed experiments								
4	SB1	0.2	1250	2	19.95	80.05	4.0	Ol (39.6) + Cpx (22.3) + Chr (6.8) + L_{int} (34.0) + F (3.3)
5	SB4	0.2	1250	2	49.89	50.11	1.0	Ol + Cpx + Chr + L_{int} + F
6	SB7	0.2	1250	2	80.01	19.99	0.25	Ol (59.2) + Chr (6.5) + L_{int} (33.5) + F (5.9)
7	SBbis3	0.2	1250	5	19.95	80.05	4.0	Ol + L bas + F
8	SBbis1	0.2	1250	5	49.89	50.11	1.0	Ol (37.9) + Cpx (19.3) + Chr (6.7) + L_{int} (39.9) + F (2.1)
9	SBbis2	0.2	1250	5	80.01	19.99	0.25	Ol (59.4) + Chr (6.0) + L_{int} (33.4) + F (6.1)
10	SBter1	0.2	1250	48	19.95	80.05	4.0	L bas + F
11	SBter2	0.2	1250	48	49.89	50.11	1.0	Ol (36.0) + Cpx (22.0) + Chr (7.1) + L_{int} (38.9) + F (2.1)
12	SBter3	0.2	1250	48	80.01	19.99	0.25	Ol (57.5) + Chr (6.0) + L_{int} (35.0) + F (6.5)
Hybrid experiments								
13	P37	0.2	1250	0.5	28.2	71.8	2.5	L bas (72.8) + L int (0.4) + Ol (17.0) + Opx (6.8) + Cpx + ChrMgt (0.0) + F (3.0)
14	P32	0.2	1250	2.5	17.7	82.3	4.6	L bas (72.7)+ L int (8.7) + Ol (10) + Opx (7) + Chr (0.0) + F (1.6)
15	P35	0.2	1250	5	18.8	81.2	4.3	L bas + L int + Ol + Opx + Chr + ChrMgt + Amph + F
16	P33	0.2	1250	48	19.8	80.2	4.1	L bas (57.1) + L int (15.4) + Ol (13.1) + Opx* (0.0) + Chr (6.0) + Amph (6.6) + F (1.7)
17	P42	0.2	1250	120	17.6	82.4	4.7	L bas (~58) + L int (~27.8) + Ol (12.8) + ChrMgt (0.0) + F (1.4)
18	P1	0.5	1300	0.02	19.2	80.8	4.2	L bas + L int + Ol + Opx + Chr + F
19	P15	0.5	1300	0.5	15.7	84.3	5.4	L bas + L int + Ol + Opx + ChrMgt
20	P18	0.5	1300	5	13.4	86.6	6.5	L bas + L int + Ol + Opx + Mgt + Chr
21	P36	0.5	1250	8	14.6	85.4	5.8	L bas (+ F)
22	P3	1.0	1300	2.5	15.3	84.7	5.5	L bas + L int + Ol + Opx + ChrMgt
23	P7	1.0	1300	9	15.9	84.1	5.3	L bas

**P, pressure; T, temperature; SERP, serpentinite; BAS, basalt; L int, interstitial glass; L bas, hydrous basaltic glass; Serp, serpentine minerals; Ol, olivine; Opx, orthopyroxene; Opx*, ferrosilite; Cpx, diopside; Amph, amphibole; Chr, chromite; ChrMgt, chromiferous magnetite.*

phenocrystals. The matrix of these samples contains a clinopyroxene-olivine assemblage with interstitial felsic glasses (L_{int}). Oxide minerals are represented by chromite phenocrysts.

3) Finally, the longest run sample SBter1 (48 h) with the lowest initial proportion of serpentinite (20 wt%) is represented by homogeneous basaltic glass formed by complete hybridization of the starting basaltic liquid with serpentinite. By contrast, the intermediate-duration sample SBbis3 (5 h) is characterized by a residual olivine-rich zone, even though the starting material contains the same proportion of serpentinite as SBter1 (20 wt%).

Hybrid Experiments at 0.2 GPa

The samples from hybrid experiments with low starting proportions of serpentinite (18–28 wt%; R = 2.5–4.7) produced at 0.2 GPa pressure show two distinct zones: a former serpentinite (or olivine-rich) zone and a zone of quenched basaltic melt (**Figures 1C**, **2**; **Table 1**; **Supplementary Tables S2, S3**). The olivine-rich zone in sample P37 shows a core composed of enstatite (Mg# = 96.5 ± 2.1) and high-Mg olivine ($Fo_{93\pm1}$), and a periphery (80–280 µm thick) consisting of olivine and interstitial felsic glass. In sample P32, which was kept for 2.5 h at 1,250°C and 0.2 GPa, the former serpentinite zone has a harzburgitic core (olivine $Fo_{89\pm1}$ and orthopyroxene Mg# = 95 ± 3) and an outer thick rim composed of olivine and interstitial glass. Chromite is localized exclusively in the former serpentinite zone (**Figures 1**, **2**). In sample P35, which was produced after 5 h at 1,250 °C and 0.2 GPa, a large (~200 × 290 µm) aggregate of chromite is observed in the former serpentinite zone at the contact with the hydrous basalt glass. Moving away from the contact to the center of the former-serpentinite zone, pockets of interstitial glass can be found with rare crystals of amphibole and zoned olivine (more magnesian in the core and more ferric at the rim). The abundance of interstitial glass is lower in the olivine-rich area consisting of olivine and enstatite (olivine $Fo_{80\pm7}$ and orthopyroxene Mg# = 92 ± 2). For the experiment conducted for 48 h under these conditions (run P33), the olivine-rich zone comprises euhedral zoned olivine crystals with highly magnesian cores and more ferrous rims associated with interstitial felsic glasses and interstitial crystals of clinopyroxene, amphibole and fluid

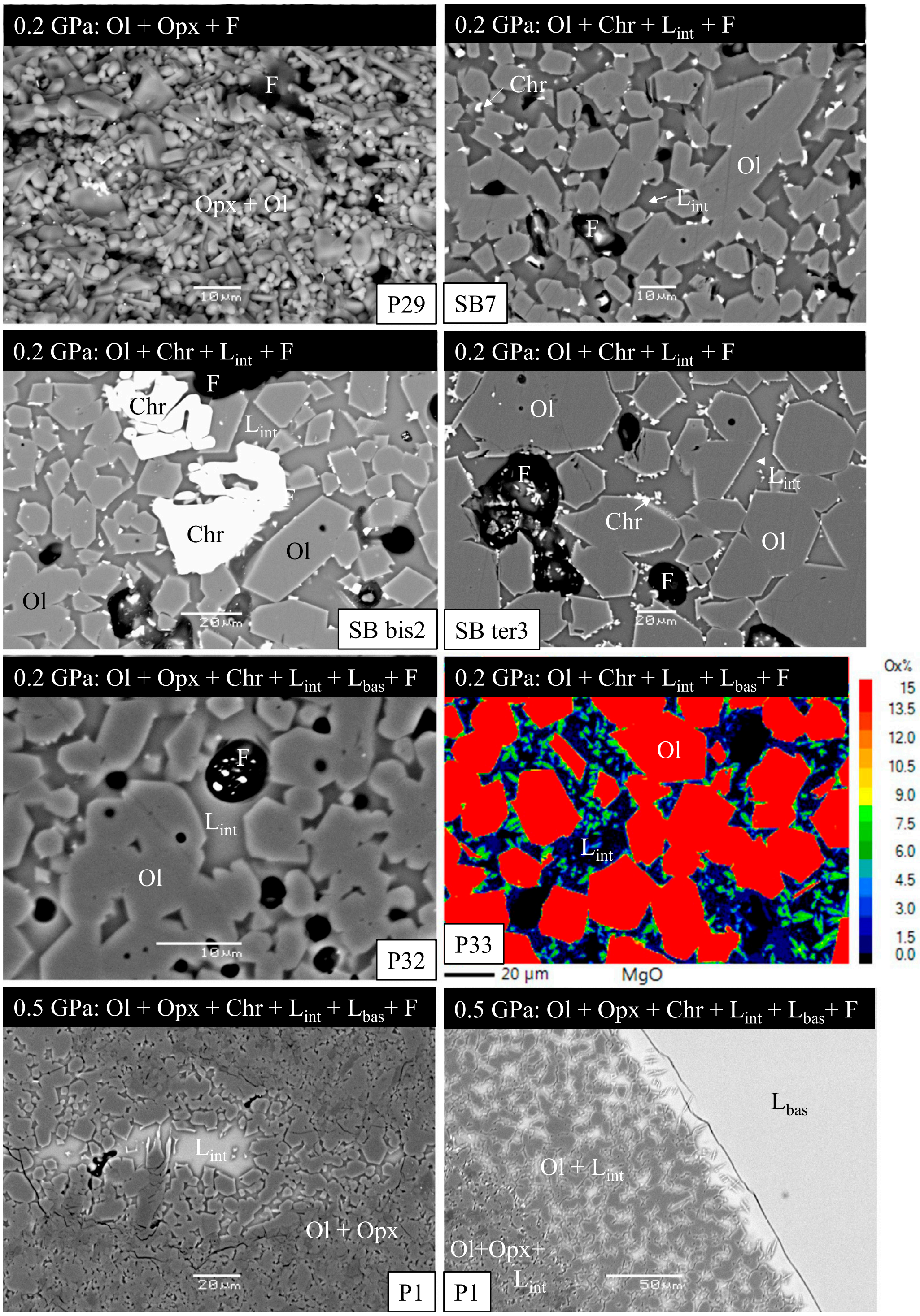

FIGURE 2 | Backscattered electron images and elemental X-ray maps of the hybrid and mixed runs to investigate aqueous fluid-assisted partial melting of peridotite at pressures of 0.2 and 0.5 GPa. The images show mineral, glass and fluid phase associations observed in the capsules, particularly the olivine-rich zones after quenching. Ol, Opx, Chr, L_{int}, L_{bas}, and F on the images stand for olivine, orthopyroxene, chromite, interstitial and basaltic glass, and fluid bubbles, respectively. The run numbers correspond to those used in **Table 1**; **Supplementary Table S2**. (P29) The serpentinite dehydration sample produced at 0.2 GPa displays a single zone represented by enstatite with high-Mg olivine and orthopyroxene. (SB7, SB bis2, and SB ter3) The mixed samples with highest initial proportions of serpentinite (80 wt%; *R* = 0.25) are characterized by a unique polyhedral olivine-rich domain of unzoned crystals of olivine associated with interstitial felsic glass (L_{int}) and fluid bubbles. Chromite is associated with the euhedral olivine grains (high-Mg olivine $Fo_{90–94}$). (P32) The hybrid run sample P32 lasting 2.5 h at 1,250°C and 0.2 GPa (*R* = 4.6) shows a former-serpentinite zone with an inner harzburgite part and an outer olivine-rich part (olivine $Fo_{89±1}$) composed of olivine and interstitial glass. Chromite is localized

(*Continued*)

FIGURE 2 | exclusively in the former-serpentinite zone. (P33) The hybrid P33 run was performed at 0.2 GPa and 1,250°C for 48 h (*R* = 4.1). The olivine-rich zone comprises euhedral zoned crystals of olivine associated with interstitial felsic glasses and interstitial crystals of clinopyroxene, amphibole and fluid bubbles. Chromite and chromiferous magnetite are located in the interstitial zones between the euhedral olivine grains (olivine $Fo_{90\pm4}$) and are also associated with amphibole microcrystals grown around the Cr-rich spinels. (P1) A quenched glass zone and former-serpentinite zone are present in the hybrid sample P1 produced at 0.5 GPa pressure in the shortest duration experiment (1 min, *R* = 4.2). The former-serpentinite zone contains fine-grained (5–10 μm) aggregates of olivine Fo_{95}, enstatite, chromite, and interstitial glass of basaltic andesite composition. Chromite crystals (few microns in size) are disseminated within this zone. The bubbles in the quenched melt zone are evidence for the presence of water fluid during quenching. The textures demonstrate that the formation of the felsic liquids precedes the complete dissolution of orthopyroxene in the olivine-rich zones of the shortest-duration runs at 0.5 GPa. All data on the hybrid and mixed samples may be found in the **Supplementary Tables S2, S3**.

bubbles (**Figure 2**). Chromite and chromiferous magnetite are located in the interstitial zones between the euhedral olivine grains (high-Mg olivine $Fo_{90\pm4}$) and are also associated with amphibole microcrystals grown around the Cr-rich spinels. Only one crystal of ferrous orthopyroxene (hypersthene) is recorded in association with interstitial glass. In sample P42 (120 h), which contains a quenched melt zone of hydrous basaltic glass with rare euhedral olivine, the olivine-rich zone consists of euhedral olivine crystals ($Fo_{92.8\pm0.5}$), chromiferous magnetite and interstitial glass of dacitic composition.

Hybrid Experiments at 0.5 GPa

The following group of samples with low initial proportions of serpentinite (13–19 wt%; *R* = 4.2–6.5) in the starting material was produced at 0.5 GPa and 1,300°C (except P36 at 1,250°C) with run durations from 1 min to 8 h (**Table 1**; **Supplementary Tables S2, S4**). In sample P1 with the shortest run duration (1 min), the quenched glass zone and former-serpentinite zone are both present. The former-serpentinite zone contains fine-grained aggregates (5–10 μm) of high-Mg olivine Fo_{95}, enstatite with Mg# = 95, chromite (Cr# = 89) and an interstitial glass of basaltic andesite composition (**Figures 1D**, **2**). Chromite crystals (a few microns in size) are disseminated within this zone. The bubbles in the quenched melt zone are evidence for the presence of fluid water during quenching. Sample P15 (0.5 h) also shows two distinct zones (quenched basaltic melt zone and olivine-rich zone). The quenched basaltic melt zone consists of hydrous basaltic glass characterized by a high magnesium content (11 wt% MgO). The former serpentinite zone consists of 5–20 μm aggregates of high-Mg olivine Fo_{93} and enstatite with Mg# = 97. These aggregates are associated with an interstitial glass of andesitic composition and chromiferous magnetite. The outer part of this zone is characterized by a layer (~120 μm thick), consisting of olivine crystals and interstitial glass. Chromiferous magnetite is concentrated in two large areas (up to 200 μm and 400 μm in size) or disseminated near these areas. Sample P18 (5 h of interaction) is also characterized by a hydrous basaltic zone and a former-serpentinite zone (**Table 1**; **Supplementary Tables S2, S4**). However, in this case, the olivine-rich zone consists of two areas; the outer area of nearly 200 μm width contains olivine and basaltic interstitial glass with disseminated chromite (a few microns in size), while the inner area is situated 200 μm from quenched basaltic glass. This inner area consists of high-Mg olivine Fo_{93}, enstatite with Mg# = 97 and contains aggregate of magnetite (~20 × 40 μm). For the longest experiment of this series (P36, 8 h), serpentinite has completely dissolved into the basalt melt (**Table 1**; **Supplementary Tables S2, S4**). Run products show a homogeneous basaltic glass with high MgO content (11.5 wt%). More details are reported in Borisova et al. (2020a). Numerous bubbles with dendritic amphibole aggregates are present in the glass, suggesting amphibole growth upon quenching.

Hybrid Experiments at 1.0 GPa

Two experiments with low initial proportions of serpentinite (~15 wt%; *R* = 5.3–5.5) in the starting material were performed at 1.0 GPa and 1,300°C. The run products from experiment P3 (2.5 h) contain a basaltic glass zone and the former-serpentinite zone (**Figure 1E**; **Table 1**; **Supplementary Tables S2, S4**). High-Mg olivine (Fo_{92}), enstatite with Mg# = 96 and chromiferous magnetite are associated with interstitial glass of basaltic composition (up to 51 wt% SiO_2) in the former-serpentinite zone. A longer-duration experiment (P7, 9 h) yields products containing hydrous basaltic glass with 13.0 wt % MgO (**Supplementary Tables S2, S4**). More details are reported in Borisova et al. (2020a).

Summary of the Major Findings From the Whole Series of Experimental Data

1) Highly magnesian olivine ($Fo_{91–92}$, mol% forsterite), orthopyroxene [92–95 Mg# = 100 Mg/(Mg + Fe^{2+})] and chromite [69–73 Mg#, and 68–95 Cr# = 100 Cr/(Cr + Al)] are found in the serpentinite dehydration runs containing only serpentinite as starting material (*R* = 0), but no interstitial glass can be detected **(Figure 3A).**
2) Bulk assimilation of the dehydrated serpentinite by the basaltic melt and production of homogeneous crystal-free hydrous basaltic melts (L_{bas}) are consistently observed in the hybrid and mixed experiments with the highest proportions of basalt and the lowest proportions of serpentinite (*R* ≥ 4, Borisova et al., 2020a) in the starting material and with durations longer than 5 h at pressures of 0.2–1.0 GPa (**Figure 3B**; **Table 1**; **Supplementary Tables S2–S4**).
3) The shortest hybrid runs at pressures of 0.5–1.0 GPa, and in all hybrid runs at 0.2 GPa lasting for 0.5–120 h contain olivine-rich zone composed of high-Mg olivine, Cr-rich spinels and interstitial glasses (L_{int}) (former-serpentinite zone or olivine-rich zone) and zone of hydrous basaltic glass (**Figures 1C–E**; **Figure 2**; **Figure 3B**; **Table 1**; **Supplementary Tables S3, S4**). The infiltration of basaltic melt into serpentinite at high basalt-to-serpentinite ratios (R = 2.5–6.5), as simulated in the hybrid experiments, is able to generate new interstitial melts of intermediate to felsic composition

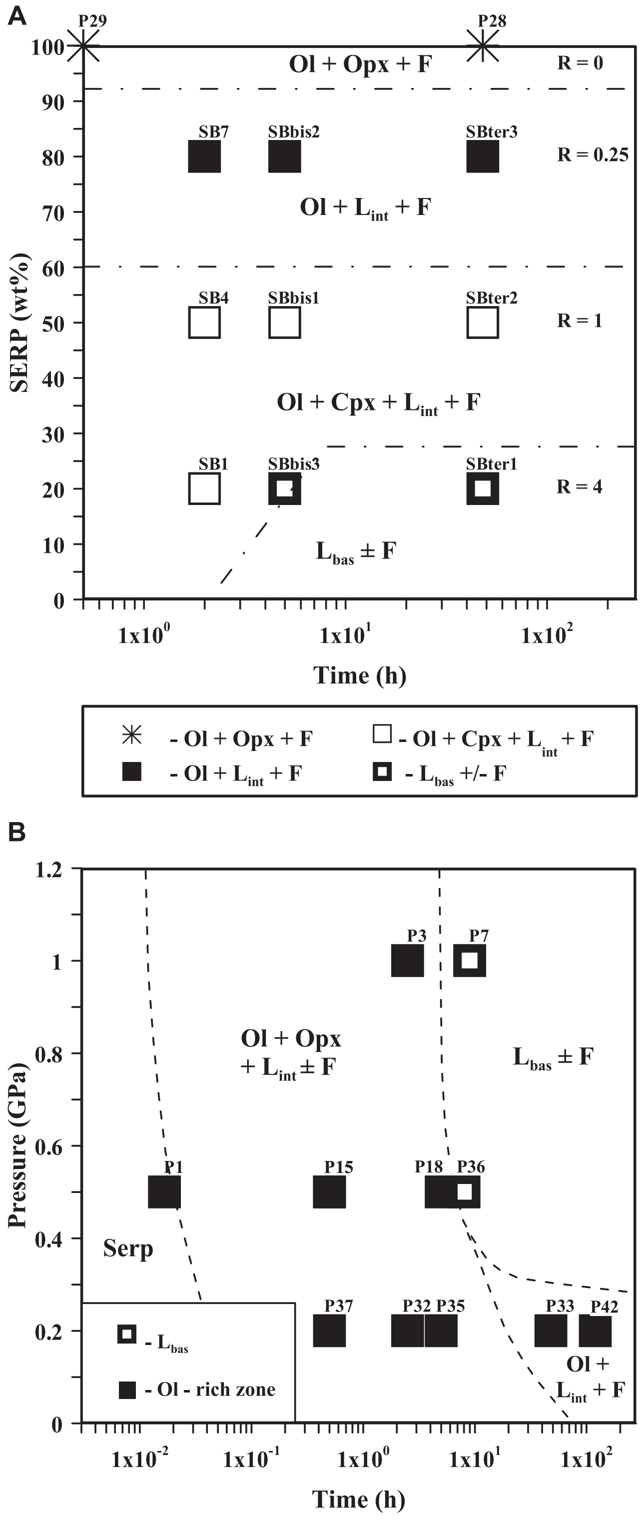

FIGURE 3 | (A) Phase compositions plotted as serpentine (SERP) proportion (in wt%) vs. run duration (h) for the pure serpentinite dehydration experiments (R = 0) and mixed serpentinite-basalt reaction experiments at 0.2 GPa and 1,250°C and basalt-to-serpentinite ratios R = 0.25, 1 and 4. The diagram shows mineral, glass, and fluid phase associations observed after quenching. Ol, Opx, Cpx, L_{int}, L_{bas}, and F stand for olivine, orthopyroxene, clinopyroxene, interstitial glass, basaltic glass, and fluid, respectively. All olivine-rich samples demonstrate the presence of chromite and chromiferous magnetite. The run numbers and corresponding experimental products with their compositions are further detailed in **Supplementary Tables S2–S4**. **(B)** Phase compositions plotted as pressure vs. run duration (h) for the hybrid serpentinite-basalt reaction experiments at 0.2–1.0 GPa and 1,250–1,300°C and R = 2.5–6.5. The diagram shows mineral, glass, and fluid phase associations observed in the olivine-rich zone after quenching. L_{bas} is a unique zone of hydrous basaltic glass, while the olivine-rich zone contains residual serpentine minerals (Serp), predominant magnesian olivine (Ol), and orthopyroxene (Opx) in the interstitial glass (L_{int}), in the presence of fluid (F) bubbles. All olivine-rich samples show the presence of chromite or chromiferous magnetite. R is the ratio of starting basaltic melt to serpentinite rock.

(SiO_2 contents ranging from 57 to 67 wt%) in most hybrid 0.2 GPa experiments. Only two shortest (≤0.5 h) of the 0.5 GPa runs yield interstitial melts of intermediate composition (SiO_2 = 56–60 wt%), whereas the shortest (2.5 h) 1.0 GPa run generates interstitial melt of mafic composition (SiO_2 = 50 wt %). These results are in line with the fact that the combined effects of water, alkalis and low pressure on the structure of the aluminosilicate melt shift the equilibrium olivine-pyroxene cotectics to higher SiO_2 contents (Kushiro, 1968; Hirschmann et al., 1998; Lundstrom, 2000).

4) Finally, a homogeneous and stable olivine-rich zone containing mostly high-Mg olivine (Fo_{90-94}, mol%), chromite (56–73 Mg#, and 68–89 Cr#) and interstitial felsic glass is systematically observed in all mixed (SB series) time-series experiments with low basalt-to-serpentinite ratios (R = 0.25–1.0) in the starting material, suggesting the formation of stable association of olivine, chromite and felsic melts at 0.2 GPa (**Figures 1A,B**, **2**, **3A**, **and 4**; **Supplementary Table S3**).

Interstitial Glass Composition and Equilibration With Minerals

In the hybrid and mixed runs at 0.2–1.0 GPa, the olivine-rich zones host interstitial pockets of glass ranging in size from 10 to 200 μm, showing enrichment in silica (up to 66–71 wt%), aluminum, alkalis and water (**Figures 4**, **5**, **Supplementary Tables S2–S4**). The calculated chromite-olivine pair equilibration temperatures range from 1,222 to 1,261°C (**Supplementary Table S2**), in accordance with the runs temperature of 1,250 °C, confirming an attainment of thermodynamic equilibrium between solid phases during experiments even if Fe-Mg partition coefficients between olivine and the associated felsic melt range from 0.19 to 0.24 in the hybrid runs and from 0.08 to 0.25 in the mixed runs according to model of (Toplis, 2005), indicating a lack of Fe-Mg equilibrium between phases involving the felsic liquid (although such low values as 0.16 have been reported in alkali-rich systems). This variability may be at least partly due to quench artifacts. Indeed, the glass transition temperature of hydrous andesitic

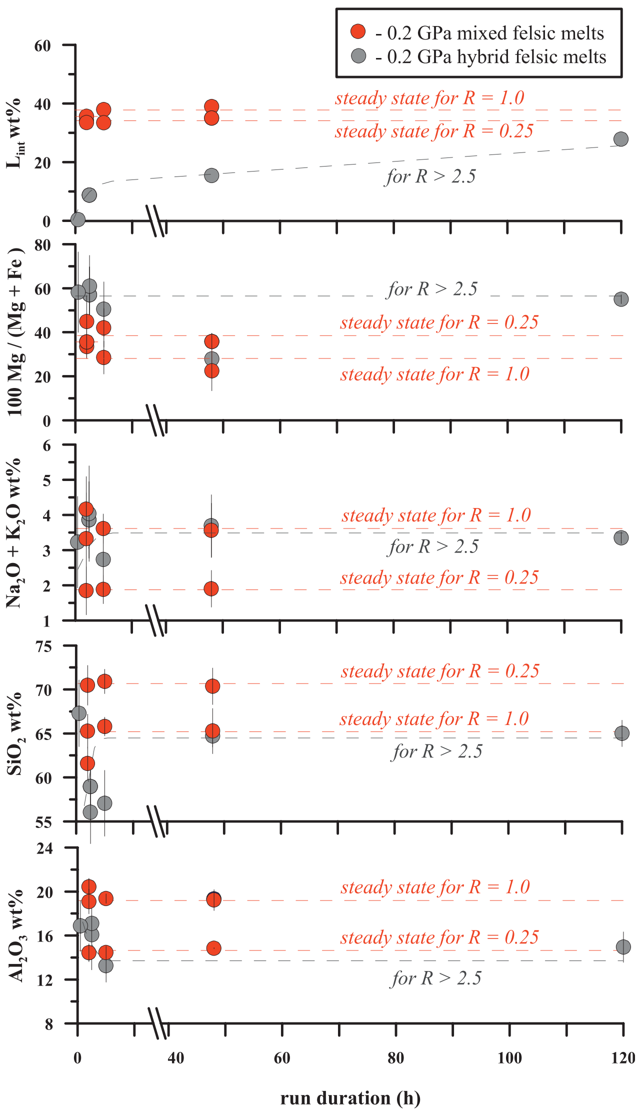

FIGURE 4 | Weight proportion of interstitial felsic melt (in wt%), magnesium index (100 Mg/(Mg + Fe), total alkalis, SiO_2 and Al_2O_3 (in wt%) in the interstitial felsic melts of the time-series experiments vs. run duration (h). The oxide contents are recalculated to 100% on a volatile-free basis. R is the mass ratio of starting basaltic melt to serpentinite rock (basalt-to-serpentinite ratio). The dotted lines indicate compositional tendencies for the felsic melts of the mixed and hybrid runs. The mixed runs for given R values (0.25 and 1.0) are characterized by homogeneous interstitial felsic melts with constant Si, Al, and alkalis, while L_{int} proportions are independent of run duration. We argue for near equilibrium (steady) state of the produced felsic melts in assemblages with high-Mg olivine based on the mixed time-series experiments. Constant concentrations are established very early (in less than 2 h) for *R* = 0.25 and *R* = 1.0 in the mixed runs, suggesting attainment of steady state or thermodynamic equilibrium of the run products. *X* axis scale breaks from 12 to 40.

melts with ~5 wt% H_2O is very low, $T_g \approx 300°C$ (e.g., Deubener et al., 2003). As a result, these melts are particularly sensitive to modification during quenching, thus contributing to the observed Fe-Mg disequilibrium. Hybrid run samples P32, P33, and P42 yield olivine-felsic glass Fe-Mg partition coefficients of 0.24 ± 0.13, close to the theoretical range of 0.31 ± 0.05 (Toplis, 2005) (**Supplementary Table S2**), suggesting that the felsic melts are close to Fe-Mg equilibrium with the associated olivine.

The major element composition of the glass produced in these experiments is mainly controlled by pressure, but also depends on the basalt-to-serpentinite initial ratio (R) in the mixed runs. The glasses produced in the hybrid run lasting 2.5 h at 1.0 GPa are mafic (50 wt% SiO_2), with an average MgO content of 10 wt%, similar to the glasses produced in previous studies of equilibrium partial melting of hydrated peridotite at similar pressures (Ulmer, 2001). By contrast, generally higher SiO_2 (57–71 wt%, recalculated to 100% on a volatile-free basis) contents are found in glasses from all hybrid runs at 0.2 GPa, and from the mixed experiments at 0.2 GPa with the highest proportion of serpentinite (50–80 wt%; *R* = 0.25–1.0), as well as those produced in short (≤0.5 h) runs at 0.5 GPa. For example, the mixed runs with the highest proportion of serpentinite (80 wt%) and low basalt-to-serpentinite initial ratios (*R* = 0.25) produce dacite glasses with up to 70–71 wt% SiO_2 contents (**Figures 4–6, Supplementary Table S3**). Furthermore, the 0.2 GPa glasses are enriched in alkalis (up to 3.9 wt% Na_2O+ K_2O), aluminum (up to 20.4 wt% Al_2O_3) and chromium (up to ~710 Cr ppm) (**Figures 5, 6; Supplementary Tables S3, S4**).

The experimental glass composition obtained in the 0.2 GPa mixed experiments is in an agreement with that obtained through modeling using MELTS at condition of the melts saturation with H_2O fluid (**Figures 5, 6; Supplementary Table S6**). In the modeling, we used mixture of serpentinite with basalt in different proportions comparable to those observed in the mixed experiments (see **Supplementary Material**). The modeled phase proportions (e.g., melt proportions up to 35 wt %, **Supplementary Table S6**) and the mineral compositions are in agreement with those of the experimental ones (melt proportion up to 40 wt%, **Supplementary Table S2**). For example, high-Mg olivine (91–93 mol% Fo), chromite (20–45 mol% of chromite molecule), aqueous fluid and Si-rich liquid (up to 61 wt% SiO_2 on anhydrous basis) appear in equilibrium assemblages at 1,250–1,300°C, 0.2 GPa and ΔQFM+2 to +3 in the models using a mixture of 80–95 wt% serpentinite and 20–5 wt% basalt, respectively. The felsic liquids contain up to 67 wt% SiO_2 if the composition of aqueous fluid is taken into consideration (**Supplementary Table S6**). Additionally, the MELTS liquids modelled at 0.2 GPa (up to 61 wt% SiO_2 on anhydrous basis) are richer in SiO_2 than those modelled at 0.5–0.9 GPa (up to 55–59 wt% SiO_2 on anhydrous basis) (**Supplementary Table S6**), confirming our experimental observations at 0.5 and 1.0 GPa.

To evaluate the result of energy constrained interaction between serpentinite and basalt, we have performed Magma Chamber Simulator (MCS, Bohrson et al., 2014; Bohrson et al., 2020; Heinonen et al., 2020) modeling in the range from 0.1 to 0.5 GPa at condition of the magma saturation with H_2O fluid (**Supplementary Table S7**). The MCS modeled liquid composition is in excellent agreement with that of the experimental felsic melts (**Figures 5, 6**). The only exception is Mg index, but this is likely related to the Fe-Mg re-equilibration of

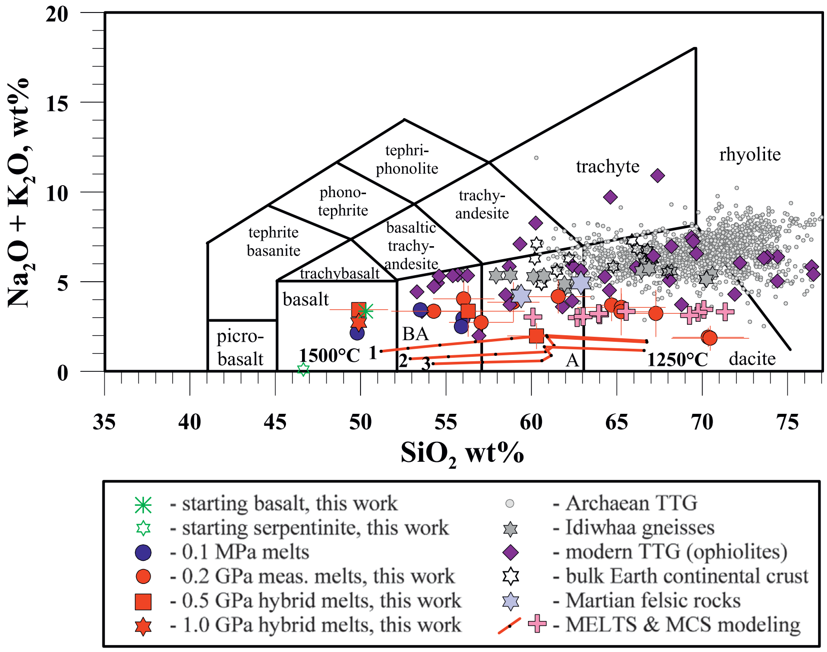

FIGURE 5 | Sum of alkali oxides (in wt%) vs. SiO_2 (in wt%) in interstitial glasses produced during hybrid and mixed runs of serpentinite-basalt interaction plotted in the classification diagram of Le Maitre (2002). The major element compositions of the measured ("meas. melts", red dots are recalculated to 100% on a volatile-free basis). The error bars reflect the felsic glass heterogeneity compared to the mean values. The glass compositions are compared with the starting basalt and serpentinites, the anhydrous 0.1 MPa experimental glasses (Fisk, 1986), modern TTG or plagiogranites in mantle section of ophiolites (Amri et al., 1996, 2007; Shervais, 2008; Xu et al., 2017), the bulk Earth continental crust (Wedepohl, 1995; Rudnick and Gao, 2003), Archaean TTG (Moyen and Martin, 2012), Acasta Gneiss Complex rocks (Idiwhaa gneisses) (Reimink et al., 2016), Martian felsic rocks (Sautter et al., 2016). BA, basaltic andesite; A, andesite. Red lines with black points correspond to the thermodynamic modeling using MELTS of equilibrium liquids coexisting with mixture of 80–95 wt% serpentinite with 20–5 wt% basalt ($R < 1$) at 0.2 GPa and different temperatures ranging from 1,500°C to 1,250°C and redox conditions of ΔQFM+2: 1) 80 wt% serpentinite and 20 wt% basalt ($R = 0.25$); 2) 90 wt% serpentinite and 10 wt% basalt ($R = 0.11$), and 3) 95 wt% serpentinite and 5 wt% basalt ($R = 0.05$) (**Supplementary Table S6**). The compositions modeled at 1,250°C are corrected according to SiO_2 contents of 6 wt% SiO_2 in the aqueous fluid (**Supplementary Tables S5, S6**). Pink crosses correspond to the Magma Chamber Simulator (MCS) modeling results of equilibrium liquid appearing upon the interaction between the serpentinite and basalt at different basalt-to-serpentinite mass ratio, R, different temperatures of the serpentinite rock (1,100–1,300°C) and pressures from 0.1 to 0.5 GPa at conditions of the magma saturation with H_2O fluid (**Supplementary Table S7**).

the experimental liquids with the predominant olivine upon quenching.

DISCUSSION

Felsic Melt Formation

The measured glass compositions vary from basaltic andesite to dacite, which is consistent with the general tendency of olivine-saturated partial melts to become progressively richer in SiO_2 with decreasing pressure and increasing water content (e.g., Hirschmann et al., 1998). Additionally, it is widely known that water fluid expands the thermodynamic stability of forsterite-rich olivine (e.g., Green, 1973; Nicholls et al., 1973) and chromite (Veksler and Hou, 2020). Thus, it is not surprising that high-Mg olivine in association with chromite is recorded in equilibrium with felsic melts of dacitic composition in our low-pressure experiments (0.2 GPa). Most glasses produced at 0.2 GPa are richer in Si, Al, and alkalis than dry glasses produced at 0.1 MPa (Fisk, 1986) as well as nearly dry glasses produced at 0.5 GPa (Kelemen et al., 1995). The hydrous intermediate to felsic melts produced in our experiments are likely formed by the fertilization of olivine-rich zones due to the presence of aqueous fluids produced by the interaction of serpentinite and basaltic melt at 0.2–1.0 GPa. At lower pressures, this process is associated with the incongruent melting of harzburgite producing olivine at the expense of orthopyroxene. Indeed, according to Kushiro (1968), Shaw (1999), Shaw et al. (1998), Lundstrom (2000), Shaw and Dingwell (2008), and Borisova et al. (2020a) silica-rich liquids may be formed via orthopyroxene dissolution during melt-peridotite interactions. The presence of polyhedral and mainly unzoned olivine crystals, co-existing with homogeneous interstitial felsic melt in the olivine-rich zone of the longest runs (**Figure 2**; **Table 1**; **Supplementary Table S2**), supports the growth of new olivine that attains equilibrium with the melt at 1,250°C and 0.2 GPa.

A steady state is established within less than 2 h after the start of reaction in the mixed runs (**Figures 3, 4**). The fluid-present reaction leads to the formation of high-Mg olivine + chromite + felsic melt. Note that the composition of the interstitial felsic melt produced in this way is a function of the basalt-to-serpentinite mass ratio (R). High and constant SiO_2 contents (70–71 wt%,

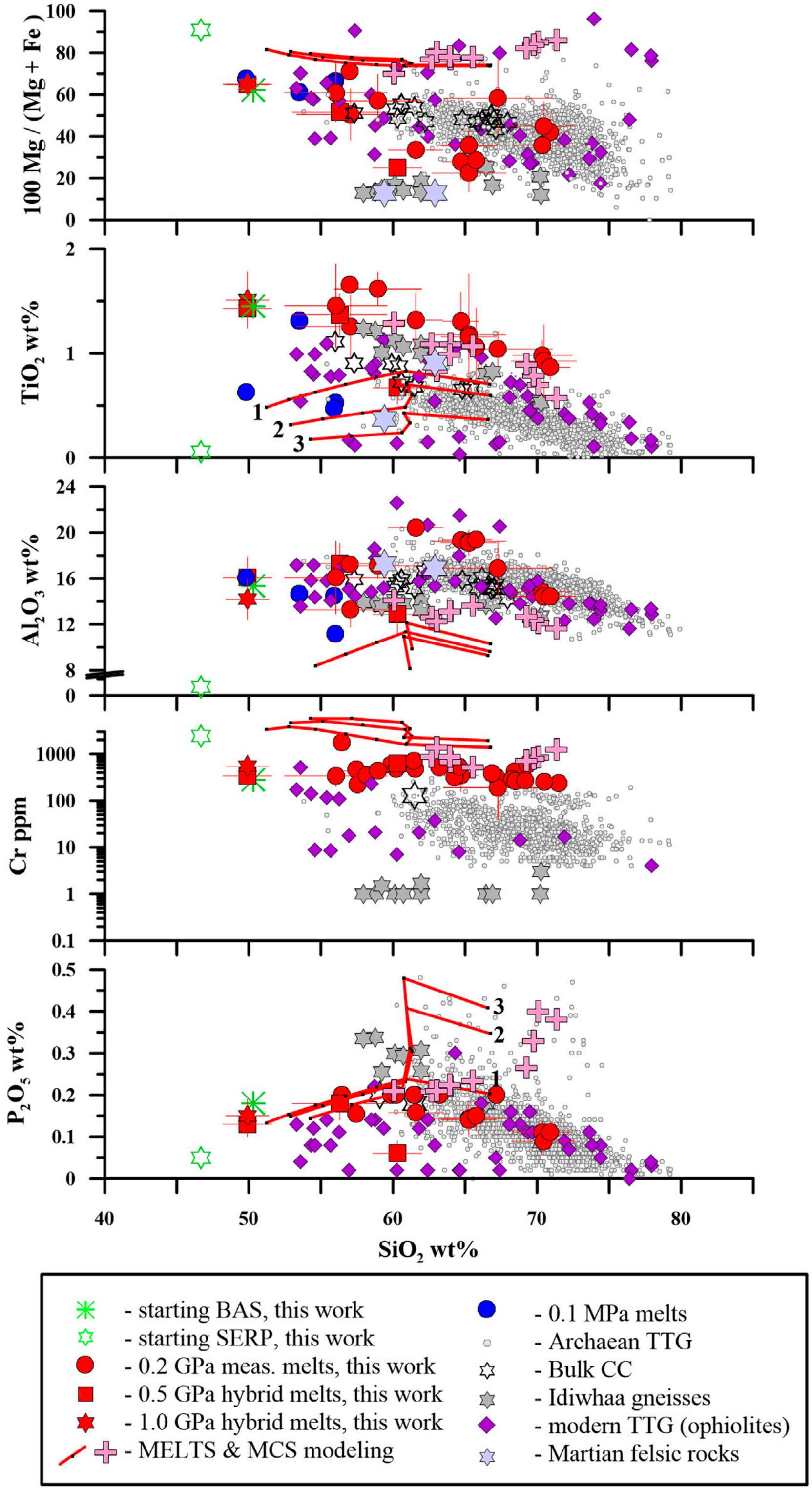

FIGURE 6 | Magnesium index (100 Mg/(Mg + Fe)), major and minor Ti, Al, P oxides (in wt%), and Cr (in ppm) vs. SiO_2 (in wt%) in interstitial glasses produced at 0.2–1.0 GPa during serpentinite-basalt interaction of hybrid and mixed runs. The major element compositions of the measured (meas.) melts are recalculated to 100% on a volatile-free basis. The error bars reflect the felsic glass inter-sample heterogeneity compared to the mean values (**Supplementary Tables S3, S4**). The glass composition is compared to the starting basalt (BAS) and serpentinite (SERP), the anhydrous 0.1 MPa experimental glasses (Fisk, 1986), modern TTG (plagiogranites) in mantle sections of ophiolites (Amri et al., 1996, 2007; Shervais, 2008; Xu et al., 2017), the bulk Earth continental crust (Bulk CC) (Wedepohl, 1995;

(*Continued*)

FIGURE 6 | Rudnick and Gao, 2003), Archaean TTG (Moyen and Martin, 2012), Acasta Gneiss Complex rocks (Idiwhaa gneisses) (Reimink et al., 2016) and Martian felsic rocks (Sautter et al., 2016). Both EPMA and LA-ICP-MS data for the 0.2 GPa felsic melts are used to determine the Cr concentrations of hybrid melts, whereas only EPMA data are used for the P contents (**Supplementary Table S3**). Red lines labelled 1, 2 and 3 with black points correspond to the thermodynamic modeling using MELTS of equilibrium liquids coexisting with mixture of 80–95 wt% serpentinite with 20–5 wt% basalt (*R* < 1) at 0.2 GPa and different temperatures ranging from 1,500°C to 1,250°C and redox conditions of ΔQFM+2: 1) 80 wt% serpentinite and 20 wt% basalt (*R* = 0.25); 2) 90 wt% serpentinite and 10 wt% basalt (*R* = 0.11) and 3) 95 wt% serpentinite and 5 wt% basalt (*R* = 0.05) (**Supplementary Table S6**). The compositions modeled at 1,250°C are corrected according to SiO_2 contents of 6 wt% SiO_2 in the aqueous fluid (**Supplementary Tables S5, S6**). Pink crosses correspond to the Magma Chamber Simulator (MCS) modeling results of equilibrium liquid appearing upon the interaction between the serpentinite and basalt at different basalt-to-serpentinite mass ratio, *R*, different temperatures of the serpentinite rock (1,100–1,300°C) and pressures from 0.1 to 0.5 GPa at conditions of the magma saturation with H_2O fluid (**Supplementary Table S7**).

recalculated to 100% on a volatile-free basis) are observed in the felsic melts at the lowest *R* of 0.25. For the run series with *R* = 1.0, clinopyroxene is an additional stable crystalline phase formed in association with high-Mg olivine, chromite and felsic melt. Remarkably, the proportions of interstitial melt (33–40 wt%), as well as the concentrations of SiO_2, Al_2O_3, and alkalis (Na_2O+ K_2O wt%) in the melt, remain constant over a wide range of R (0.25–1.0) throughout the whole run duration (**Figure 4**). The Mg/(Mg + Fe) index of the melt may be affected by Fe-Mg exchange with olivine and chromite during quenching.

The MCS modeling data demonstrate that i) after the serpentinite addition, SiO_2 content in the equilibrated liquid increases with decreasing pressures (**Supplementary Table S7**). ii) The lower basalt-to-serpentinite (R) mass ratio increases the SiO_2 content in the equilibrated melt (**Figures 5, 6**). In MCS results there is a massive crystallization event following the reaction with serpentinite, but the following crystallization will be discussed in a future paper. iii) The lower the temperature of the serpentinite, the higher the SiO_2 increase in the equilibrated liquid. This is a good outcome since the experiments cannot really realistically reproduce the lower temperature of the serpentinite. iv) Having Cr in the initial serpentinite rock also increases the SiO_2 in the equilibrated liquid. Both thermodynamic models (MELTS and MCS) suggest that the mineral association observed in the 0.2 GPa mixed experiments is near thermodynamic equilibrium.

Aqueous Fluid Composition

In all hybrid and mixed experiments at 0.2 and 0.5 GPa, fluid bubbles are present, likely produced by serpentinite decomposition. Therefore, we conducted thermodynamic modelling of the element solubility in the aqueous fluid phase (**Supplementary Material**), which provides an independent qualitative support for our conclusions drawn from the analysis of the run products described above (e.g., interstitial felsic glasses). Modeling shows that the aqueous fluid generated by serpentinite dehydration in the presence of basaltic melt is systematically enriched in Si, Al, Na, and K (**Supplementary Table S5**) compared to both the initial and reacted serpentinite (olivine-rich zone, see above). The major mineral phases predicted to form at equilibrium are olivine and orthopyroxene, together with minor amounts of clinopyroxene and feldspar-like glass phases, are in good agreement with those observed in most hybrid and mixed experiments. The calculations predict high-Mg olivine ($Fo_{93–96}$ mol%) and orthopyroxene (Mg# 94–96) compositions, which are within the range analyzed in the hybrid run products (**Supplementary Table S3, S4**), suggesting local thermodynamic equilibrium was attained between the fluid and these minerals.

The aqueous fluid in mixed and hybrid experiments is predicted to be enriched in Si (up to 6 wt%), Na (up to 4 wt%), K (up to 0.4 wt%), and Al (up to 0.2 wt%), with other elements being much less abundant (Mg, Ca, Fe typically < ~10 ppm). Increasing the pressure from 0.2 to 1.0 GPa generally results in an increase of all element concentrations in the fluid, in agreement with the increase of water solvent density and water solvation power (e.g., Pokrovski et al., 2013). A similar systematic order of decreasing concentration in the fluid is maintained over the whole range of pressures and basalt-to-serpentinite initial ratios: Si > Na > K > Al >> Fe > Ca > Mg. This finding strongly suggests that intrinsic uncertainties in the thermodynamic model are unlikely to obscure the large amplitude of general trends. The low concentrations of Fe and Ca (typically 100 to 10,000 times less abundant than Si, Na, K or Al), and in particular of Mg (10^6–10^8 less abundant than Si, **Supplementary Table S5**), are in agreement with the typical order of elemental abundance in natural hydrothermal-magmatic fluids of relatively low salinity as inferred from fluid inclusions (e.g., Kouzmanov and Pokrovski, 2012; references therein). This is corroborated by our experimental results, providing evidence for major transfer of Si, Na, K, and Al from basalt and serpentinite to felsic melts. Remarkably, the Si/Mg ratio (~10^6–10^{10}) in the fluid phase predicted by calculations systematically increases by almost 1,000 times with decreasing pressure from 1 to 0.2 GPa (**Supplementary Table S5**). Even though our calculations are semi-quantitative at such extreme conditions for the fluid phase (see **Supplementary Material**), this large relative change is an additional indication that relatively low pressures should favor the enrichment of both fluid and melt phases in Si relative to "mafic" elements (Mg) in water-present systems, thus promoting the formation of felsic (i.e. Si-rich) melts quenched to glasses, as observed in our direct experiments.

Compositional Features of Interstitial Glasses

The intermediate to felsic glasses from the hybrid and mixed runs were analyzed not only for major and minor (Cr, Ni) but also for trace elements (**Supplementary Material**). **Figure 7** demonstrates incompatible trace element compositions (normalized to the primitive mantle) of the interstitial felsic glasses. The positive Pb anomaly relative to light rare earth

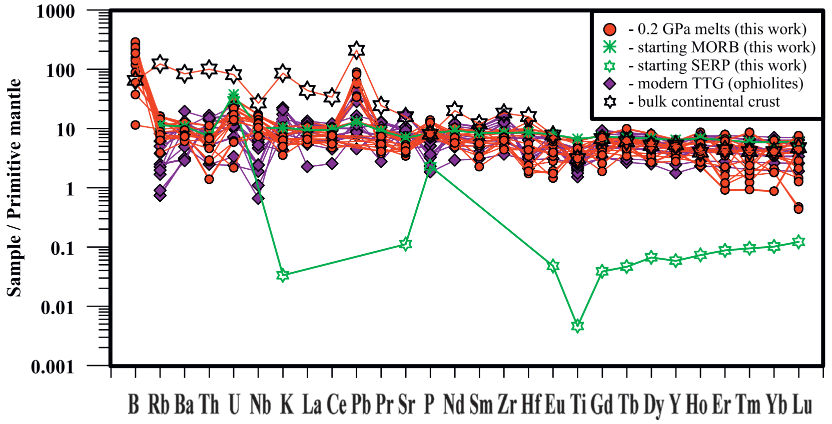

FIGURE 7 | Primitive mantle-normalized trace element abundance patterns of felsic glasses produced at 0.2 GPa during serpentinite-basalt interaction. The primitive mantle composition is after (Sun and McDonough, 1989) and (Lyubetskaya and Korenaga, 2007) for B only. The felsic glass composition is compared to basalt (starting MORB) and serpentinite (starting SERP), modern TTG (Amri et al., 1996, 2007; Shervais, 2008; Xu et al., 2017), the bulk continental crust after Wedepohl (1995).

elements (LREE) observed in felsic glasses is an important signature of typical continental rocks compared to mantle-derived magmas (Rudnick and Gao, 2003). The incompatible trace element patterns of the felsic glasses are nearly identical to those of modern TTG (plagiogranite) rocks found in the mantle sections of ophiolites (Amri et al., 1996; 2007; Shervais, 2008; Xu et al., 2017). The felsic glasses produced in runs at 0.2 GPa have major and trace element contents (Si, Ti, Al, Mg, Ca, Na, K, P, and Cr, REE), as well as Mg/(Mg + Fe), that share some similarities with modern TTG situated in the mantle sections of ophiolites (**Figures 5–7**). The 0.2 GPa intermediate to felsic melts are characterized by lower SiO_2 and Na_2O + K_2O contents and higher Cr contents compared with Archaean TTG rocks (**Figures 5, 6**). The slight enrichment in LREE of the felsic glasses produced in our experiments differs from the strongly fractionated patterns of Archaean tonalite-trondhjemite-granodiorite (TTG) suites (Moyen and Martin, 2012). This is in line with the conditions of shallow felsic crust formation by a mechanism distinct from the “sagduction” or plate subduction operating during the Archaean (Moyen and Martin, 2012). At similar SiO_2 contents, the higher Mg index and Cr contents (up to 1,400 Cr ppm) in the experimental felsic glasses produced at 0.2 GPa contrast strongly with the 4.02 Ga Idiwhaa gneisses, northwest Canada (**Figure 6**), suggesting that the Hadean Acasta Gneiss Complex magmas did not form due to reaction of serpentinite with basaltic melts. Except for fluid-mobile B and Pb, the trace element compositions of the 0.2 GPa interstitial felsic glasses are similar to those of the starting basaltic melt (**Figure 7**). Additionally, hafnium contents (0.5–4.0 ppm Hf) and Lu/Hf ratios [Lu_N/Hf_N = 0.11–2.2, normalized to the primitive mantle composition of Sun and McDonough (1989)] in the 0.2 GPa felsic melts are similar to those of the starting basaltic melt (2.7 ppm and 0.7, respectively), suggesting that the experimental melts might have inherited their trace element and Hf isotope signatures from a precursor basaltic reservoir (**Supplementary Table S3**).

GEOLOGICAL SIGNIFICANCE

Shallow Felsic Crust Production by Melting of Serpentinized Peridotite

Our study provides new insight into potential mechanisms of intermediate to felsic crust formation. Serpentinized peridotites and mafic cumulates are the most abundant constituents of the modern slow-spreading oceanic lithosphere at the level of the Moho mantle-crust boundary (Cannat, 1993). Cyclic magmatic and hydrothermal processes in the modern Earth likely lead to the generation of intermediate to felsic material within the peridotitic lithosphere below spreading centers at high temperature and shallow (<10 km) depths. These processes include repeated intrusions of mantle-derived basaltic magmas (O’Hara and Mathews, 1981; Amri et al., 1996; 2007; Borisova et al., 2012), where reactions are possible between hot basaltic melts and a previously formed cold hydrated ultramafic lithosphere during periods of low magma supply and oceanic water circulation at shallow depth (**Figure 8**). The melting of serpentinized peridotite produced in our experiments leads to the formation of dunite-wehrlite- or chromitite-type rocks (**Figures 1–3A,B**) similar to their natural analogues described in ophiolites (e.g., Dick, 1977; Benoit et al., 1999; Borisova et al., 2020c; Zagrtdenov et al., 2018; Rospabé et al., 2019; Borisova et al., 2020b). Our experimental data thus support an empirical model for the reaction between hydrated mantle and basaltic magma inferred from natural data on chromite-hosted inclusions from the Oman ophiolite (Borisova et al., 2012). The olivine-rich aggregates containing interstitial hydrous silica-saturated liquids are gravitationally unstable, like those obtained in our experiments. This is because of the high density contrast between hydrous felsic melts (<2.4 g/cm^3, **Supplementary Table S6**) and mafic silicate minerals (3.2–3.3 g/cm^3) and chromite (~5.0 g/cm^3), while melt mobility is also favored by low viscosity. With reference to processes occurring at oceanic spreading centers (Amri et al., 1996, 2007; Benoit et al., 1999), which lead to the formation of

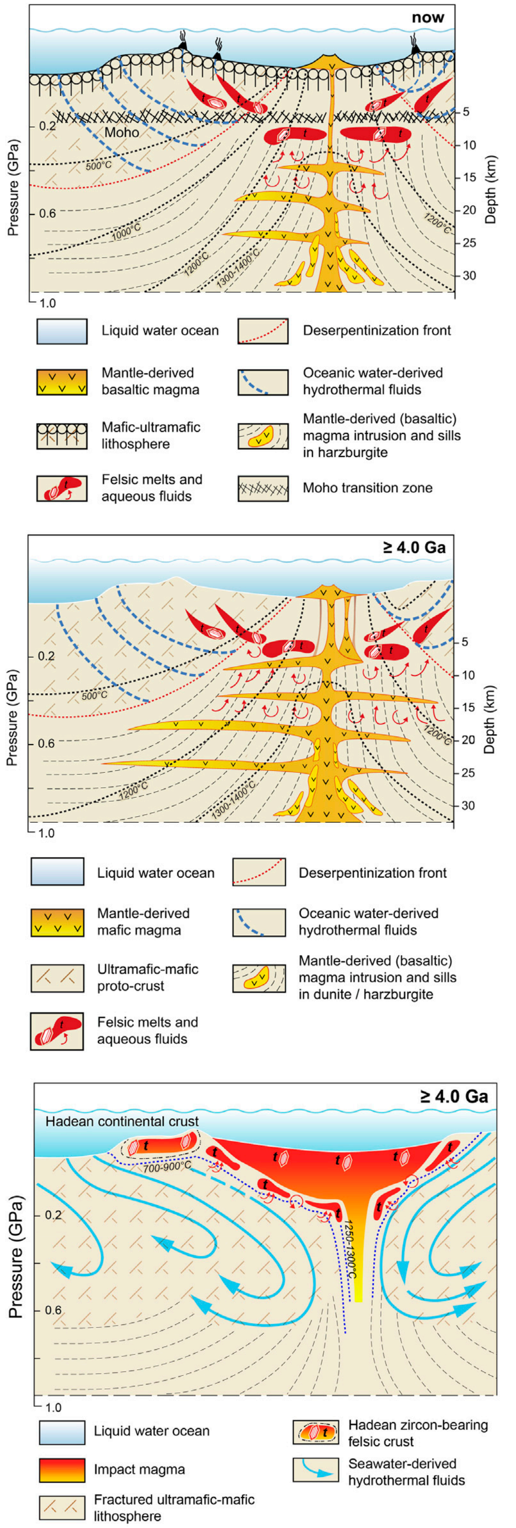

FIGURE 8 | Upper panel: Model for the formation of shallow felsic crust in mantle peridotites of the oceanic lithosphere. Dehydration is initiated by the intrusion of mantle-derived magmas into hydrated (serpentinized) mantle. The released fluid promotes fertilization and partial melting of the peridotite, which leads to production of TTG magmas *(Continued)*

FIGURE 8 | marked as "*t*". The generated melts forms intrusive bodies in the host peridotite and overlying crust at shallow depths <10 km. Black dotted lines correspond to isotherms. The horizontal scale of the model is ~30 km. The depths on the vertical scale are calculated assuming a serpentinite density of 3 g/cm^3. **Middle panel:** Model for the formation of the Hadean felsic crust due to activity of either a heat-pipe or a proto-rift volcanoes. Dehydration is initiated by the intrusion of mantle-derived magmas into (ultra-)mafic protocrust. The released fluids promote partial melting of the peridotite, which produces felsic (e.g., tonalite) magmas marked as "*t*". The generated melts form intrusive bodies in the host peridotite protocrust at shallow depths <10 km. Black dotted lines correspond to isotherms. The horizontal scale of the model is ~30 km. The depths on the vertical scale are calculated assuming a serpentinite density of 3 g/cm^3. **Lower panel:** Model of impact formation of felsic crust on the early Earth and Mars. Impact-induced melting of the hydrated ultramafic-mafic protocrust promotes fertilization and partial melting of the peridotite. The (ultra-) mafic protocrust is hydrated through hydrothermal circulation due to contact with seawater. The partial melting produces intermediate to felsic (tonalite and/or granodiorite) magmas marked as "*t*". The production of intermediate to felsic melts may occur when the predominant proportion of serpentinite in the hybrid system is above 50 wt% (*R* ≤ 1). The generated melts form an impact body at shallow depths <10 km. Blue dotted lines correspond to isotherms. The horizontal scale of the model is ~30 km.

ophiolites, low-density hydrous felsic melts generated below and/or at the Moho transition zone are collected in decimeter to meter sized pods and veins which then progressively coalesce into larger intrusions in the shallow oceanic lithosphere. Alternatively, the felsic melts produced by aqueous fluid-assisted partial melting of peridotite may remain scattered in peridotites at shallow depths <10 km, as shown by olivine-hosted melt inclusions in peridotite xenoliths (Hirschmann et al., 1998). If segregation into intrusions takes place, cooling (e.g., due to hydrothermal circulation) will result in crystallization of these hydrous felsic liquids. In addition to the generation of low-temperature plagiogranite magmas in the oceanic crust due to partial melting of hydrated gabbros (Koepke et al., 2004), we suggest that high-temperature plagiogranites melts and magmas (or high-temperature TTG) may be formed through aqueous fluid-assisted partial melting of serpentinized peridotite.

Implications for the Early Earth

Hydrated peridotite, and its isochemical analogue serpentinite, has been suggested to be a major shallow component of the Hadean and Noachian protocrusts on Earth and Mars (Albarède and Blichert-Toft, 2007; Elkins-Tanton, 2012), being the result of the interaction of seawater-derived fluids with peridotites (Guillot and Hattori, 2013). Indeed, planets like Earth and Mars were massive enough to allow the formation of an early ultramafic (peridotite-like, silica-poor) magma ocean, while the distance from the Sun and the surface temperature were appropriate for the existence of an ocean of liquid water (Valley et al., 2002; Albarède and Blichert-Toft, 2007; Müntener, 2010). It is widely recognized (Albarède and Blichert-Toft, 2007; Elkins-Tanton, 2012) that magma ocean(s) underwent solidification to produce shallow ultramafic-mafic protocrust during the earliest stages of planetary evolution. However, it remains unclear how early Hadean crustal rocks could have generated quartz-normative to quartz-saturated magmas of intermediate to felsic composition. Direct natural evidence for the precursor of Hadean (≥4 Ga) felsic crust is scarce, and remains the subject of intense debate (Wedepohl, 1995; Rudnick and Gao, 2003; Harrison, 2009; Reimink et al., 2014, 2016; Burnham and Berry, 2017; Bell et al., 2018). Investigations of the 4.37–4.02 Ga Jack Hills detrital zircon crystals (JHZ), which are the oldest remnants of primordial felsic magmas on Earth, support the existence of a felsic crust during the earliest stages of the Hadean eon (Cavosie et al., 2006; Harrison, 2009; Burnham and Berry, 2017). Either reworking into younger crust or recycling of the Hadean crust into the mantle have been proposed to explain the lack of remnants of the earliest felsic crust on Earth (O'Neil and Carlson, 2017; Nédélec et al., 2017). However, studies of the Jack Hills zircon crystals allow to infer the presence of an igneous protolith that had experienced low-to-moderate temperature alteration by aqueous fluids, thereby ruling out a sedimentary source (Burnham and Berry, 2017; Whitehouse et al., 2017), although alternative opinions still exist (Harrison, 2009; Bell et al., 2018).

We propose that basaltic melts were introduced in the primitive ultramafic protocrust at the very end of the crystallization of the magma ocean, and/or by heat-pipe volcanoes through a stagnant lid (Moore and Webb 2013), during the earliest stages of Earth evolution, or as proto-rifts at the end of the Hadean (Capitanio et al., 2020). Unfortunately, no traces of Hadean tectonic regimes survived so far. Thus, we propose here that the basaltic melts were intruded into an ultramafic protocrust, initiating dehydration processes. The released fluids promoted fertilization and partial melting of the peridotite, which in turn led to the production of tonalite-granodiorite magmas forming intrusive bodies in the peridotite protocrust at shallow depths <10 km (**Figure 8**). The segregation of felsic melts in the upper protocrust was favored by lithospheric hydraulic fracturing and the low density of the hydrous melts, with high melt proportions (up to 33–40 wt%, **Supplementary Table S2**) corresponding to high liquid volume fractions (φ) of ~37–45 vol%. Alternatively, the generation of such intermediate to felsic melts and magmas at shallow depths within the early ultramafic-mafic protocrust may also have been possible due to impact-induced melting (Marchi et al., 2014), particularly if the proportion of serpentinite was above 50 wt% in the hybrid system ($R \leq 1$). Such melting would have favored intense mixing of shallow hydrated ultramafic and mafic components at high temperature (as modelled in our mixed experiments), well above the liquidus of basalt before the onset of modern plate tectonics (**Figure 8**).

Implications for Early Mars

The proposed mechanism of the aqueous fluid-assisted partial melting of peridotite may have led to the formation of a shallow felsic (continental) crust on other rocky planets such as Mars, provided liquid water or a volatile element-rich magma ocean was present at an early stage of their evolution. The finding of ancient serpentinites at the surface of Mars (Ehlmann et al., 2010) suggests that serpentinite formation and aqueous fluid-assisted melting of serpentinized peridotite may be envisaged during the earliest history of this planet. There is also evidence for a 4.43–4.13 Ga-old granodioritic and/or tonalitic crustal component on early Mars (Sautter et al., 2015; Sautter et al., 2016). These quartz-normative rocks, which are believed to represent the early Martian continental crust, cannot be produced from partial melting of the mantle and subsequent fractional crystallization (Sautter et al., 2015; Sautter et al., 2016). By contrast, recent modeling using the MELTS software (Udry et al., 2018) suggests that the felsic rocks of Gale crater were produced by the accumulation/fractionation of feldspar from basaltic melt; however, these authors make no comparison with modern TTG (plagiogranite) rocks. Our data demonstrated on **Figures 5**, **6** are also in line with our model and suggest that the Noachian granodiorite (felsic) rocks on Mars may have been produced by aqueous fluid-assisted partial melting of peridotite induced by reaction with basaltic melts. Survival of the primary intermediate to felsic liquids and formation of a solid crust may have been possible if the effects of gravitational overturn were limited (Elkins-Tanton, 2012; Bouvier et al., 2018). Thus, the primordial environment of the peridotite protocrust in the presence of mantle-derived (e.g., basaltic) melt at shallow depth is favorable for the production of silica-enriched melts provided liquid water is present in sufficient amounts. The mechanism suggested in our study may thus have led to formation of large volumes of the earliest felsic crust.

CONCLUSION

The proposed mechanism of aqueous fluid-assisted partial melting of peridotite induced by reaction with basaltic melt supports the possibility of felsic crust formation at depths of ≤10 km. The shallow depths of generation of felsic magma proposed in this study imply that the formation of silica-rich crust does not require convergent plate tectonics, in agreement with geodynamic simulations of the hotter mantle on early Earth and Mars (Herzberg et al., 2010; Sautter et al., 2016). The most favorable conditions for felsic crust formation are high-temperature interactions between serpentinized peridotite and basaltic melts at 0.2 GPa and low basalt-to-serpentinite mass ratio (≤1). Such conditions may have occurred in various geologic settings that do not require modern plate tectonics. Such conditions are highly probable at spreading centers, hot spots and Hadean heat-pipe volcanoes or proto-rifts. A felsic crust may also have been formed in a more transient way during intensive impact-induced melting of the ultramafic-mafic protocrust in the presence of a liquid water ocean on early Earth and Mars. Even though the geodynamic and thermal conditions on both planets have changed, small volumes of felsic crust are still forming by this process at modern spreading centers.

DATA AVAILABILITY STATEMENT

The datasets presented in this study can be found in online repositories. The names of the repository/repositories and accession number can be found in the article/**Supplementary Material**, **Supplementary Tables S1–S7**.

AUTHOR CONTRIBUTIONS

ABo, AN, MT, and OS developed the conceptual idea of the study; ABo and NZ, SS prepared and conducted high T-P runs at BGI; NZ, OS, ABy, AT, VP, DV prepared and performed experiments at IEM; NZ, GP, WB, OM conducted thermodynamic modeling; GP, NZ, and AG carried out XAS and SIMS measurements, respectively; KJ, BS, and UW performed LA-ICP-MS analyses. IB performed bulk-rock analyses of serpentinite. ABo, NZ, SG, PP, and KC performed microanalytical measurements and mapping using EPMA; ABo, AN, GC developed geological applications; all authors contributed to data interpretation and manuscript writing.

FUNDING

This work is funded by the Institut Carnot ISIFoR “TRACENEO”, AST “Planets” in Toulouse (France) and Deutsche Forschungsgemeinschaft (DFG, Germany) to ABo and ATUPS (Université Paul Sabatier, Toulouse, France) for providing a travel grant in 2015–2016 to NZ. This research is fulfilled under the Research Program AAAA–A18–118020590148–3 of the Korzhinskii Institute of Experimental Mineralogy RAS and partially supported by the Russian Scientific Foundation (project 18-17-00206 to OS) and (grant 19–17–00200 to ABy). This work was supported by the French National Research Agency (project RadicalS ANR–16–CE31–0017 to GP and AG) and by the Institut Carnot ISIFoR (project OrPet to GP). IB and OM thank RNF Grant (RNF19–17–00241) for support. Funding from the US National Science Foundation to WB supported this work.

ACKNOWLEDGMENTS

This study is in tribute to E.Y. Borisova, E.V. Bibikova and Y.V. Bychkova for their works on zircon-based geochronology and Precambrian geology. The first author ABo dedicates this work to the memory of her brother, I.Y. Borisov. We thank Editors SW and M. Pistone, and eight anonymous reviewers for comments and suggestions, that helped to improve the manuscript. F. Spera, E. Sizova, J. Reimink, M. Belosevic, D. Baratoux and A.V. Sobolev are thanked for helpful discussions. We acknowledge the European Synchrotron Radiation Facility for providing access to beamtime, and O. Proux and M. Muñoz for help with XANES data acquisition and processing. C. McCammon and H. Keppler are thanked for offering access to the Bavarian Research Institute of Experimental Geochemistry and Geophysics (Germany). The English style and grammar were post-edited by M.S.N. Carpenter.

SUPPLEMENTARY MATERIAL

The Supplementary Material for this article can be found online at: https://www.frontiersin.org/articles/10.3389/feart.2021.640464/full#supplementary-material

REFERENCES

Albarède, F., and Blichert-Toft, J. (2007). The split fate of the early earth, Mars, venus, and moon. *C.R. Geosci.* 339, 917–927. doi:10.1016/j.crte.2007.09.006

Amri, I., Benoit, M., and Ceuleneer, G. (1996). Tectonic setting for the genesis of oceanic plagiogranites: evidence from a paleo-spreading structure in the Oman ophiolite. *Earth Planet. Sci. Lett.* 139, 177–194. doi:10.1016/0012-821X(95)00233-3

Amri, I., Ceuleneer, G., Benoit, M., Python, M., Puga, E., and Targuisti, K. (2007). Genesis of granitoid by interaction between mantle peridotites and hydrothermal fluids in oceanic spreading setting in the Oman Ophiolite. *Geogaceta* 42, 23–26.

Arai, S. (1997). Origin of podiform chromites. *J. Asian Earth Sci.* 15, 303–310. doi:10.1016/S0743-9547(97)00015-9

Ballhaus, C., Berry, R. F., and Green, D. H. (1991). High pressure experimental calibration of the olivine-orthopyroxene-spinel oxygen geobarometer: implications for the oxidation state of the upper mantle. *Contrib. Mineral. Petrol.* 107, 27–40. doi:10.1007/BF00310615

Balta, J. B., Beckett, J. R., and Asimow, P. D. (2011). Thermodynamic properties of alloys of gold-74/palladium-26 with variable amounts of iron and the use of Au-Pd-Fe alloys as containers for experimental petrology. *Am. Mineral.* 96, 1467–1474. doi:10.2138/am.2011.3637

Bell, E. A., Boehnke, P., Harrison, T. M., and Wielicki, M. M. (2018). Mineral inclusion assemblage and detrital zircon provenance. *Chem. Geology* 477, 151–160. doi:10.1016/j.chemgeo.2017.12.024

Benoit, M., Ceuleneer, G., and Polve, M. (1999). The remelting of hydrothermally altered peridotite at mid-ocean ridges by intruding mantle diapirs. *Nature* 402, 514–518.

Bindeman, I. N. (2008). “Oxygen isotopes in mantle and crustal magmas as revealed by single crystal analysis,”. *Minerals, inclusions, and volcanic processes,* Reviews in Mineralogy and Geochemistry. Editors K. Putirka and F. Tepley, 69, 445–478. doi:10.2138/rmg.2008.69.12

Bohrson, W. A., Spera, F. J., Ghiorso, M. S., Brown, G. A., Creamer, J., and Mayfield, A. (2014). Thermodynamic model for energy-constrained open system evolution of crustal magma bodies undergoing simultaneous assimilation, recharge, and crystallization: the magma chamber simulator. *J. Petrology* 55, 1685–1717. doi:10.1093/petrology/egu036

Bohrson, W. A., Spera, F. J., Heinonen, J. S., Brown, G. A., Scruggs, M. A., Adams, J. V., et al. (2020). Diagnosing open-system magmatic processes using the Magma Chamber Simulator (MCS): part I- major elements and phase equilibria. *Contrib. Mineralogy Petrology* 175, 104. doi:10.1007/s00410-020-01722-z

Borisov, A. A., and Shapkin, A. I. (1990). New empirical equation rating Fe^{3+}/Fe^{2+} in magmas to their composition, oxygen fugacity, and temperature. *Geochem. Int.* 27, 111–116.

Borisov, A., Behrens, H., and Holtz, F. (2018). Ferric/ferrous ratio in silicate melts: a new model for 1 atm data with special emphasis on the effects of melt composition. *Contrib. Mineral. Petrol.* 173, 98. doi:10.1007/s00410-018-1524-8

Borisova, A. Y., Ceuleneer, G., Kamenetsky, V., Arai, S., Béjina, F., Abily, B., et al. (2012). A new view on the petrogenesis of the Oman ophiolite chromites from microanalyses of chromite-hosted inclusions. *J. Petrology* 53, 2411–2440. doi:10.1093/petrology/egs054

Borisova, A. Y., Gurenko, A. A., Martel, C., Kouzmanov, K., Cathala, A., Bohrson, W. A., et al. (2016). Oxygen isotope heterogeneity of arc magma recorded in plagioclase from the 2010 Merapi eruption (Central Java, Indonesia). *Geochimica et Cosmochimica Acta* 190, 13–34. doi:10.1016/j.gca.2016.06.020

Borisova, A. Y., Martel, C., Gouy, S., Pratomo, I., Sumarti, S., Toutain, J-P., et al. (2013). Highly explosive 2010 Merapi eruption: evidence for shallow-level crustal assimilation and hybrid fluid. *J. Volcanol. Geotherm. Res. Spec. Vol. Merapi Eruption.* 261, 193–208. doi:10.1016/j.jvolgeores.2012.11.002

Borisova, A. Y., Pichavant, M., Beny, J.-M., Rouer, O., and Pronost, J. (2005). Constraints on degassing of dacite magma and regime of the June 15, 1991, climactic eruption of Mount Pinatubo (Philippines): new data on melt and crystal inclusions in quartz. *J. Volcanol. Geotherm. Res.* 145, 35–67. doi:10.1016/j.jvolgeores.2005.01.004

Borisova, A. Y., Pokrovski, G. S., Pichavant, M., Freydier, R., and Candaudap, F. (2010). Arsenic enrichment in hydrous peraluminous melts: insights from LA-ICP-MS and *in situ* X-ray Absorption Spectroscopy. *Am. Mineral.* 95, 1095–1104. doi:10.2138/am.2010.3424

Borisova, A. Y., Zagrtdenov, N. R., Toplis, M. J., Ceuleneer, G., Safonov, O. G., Pokrovski, G. S., et al. (2020a). Hydrated peridotite – basaltic melt interaction Part II: fast assimilation of serpentinized mantle by basaltic magma. *Front. Earth Sci* 8, 84. doi:10.3389/feart.2020.00084

Borisova, A. Y., Jochum, K. P., and Gouy, S. (2020b). Mineralogical and geochemical features of the Allan Hills tephra, South Victoria Land: implications for mid-Pleistocene volcanic activity in Antarctica. *Polar Sci.* 23. doi:10.1016/j.polar.2020.100505

Borisova, A. Y., Bindeman, I. N., Toplis, M. J., Zagrtdenov, N. R., Guignard, J., Safonov, O. G., et al. (2020c). Zircon survival in shallow asthenosphere and deep lithosphere. *Am. Mineral.* 105, 1662–1671. doi:10.3389/feart.2020.00084

Bouvier, L. C., Costa, M. M., Connelly, J. N., Jensen, N. K., Wielandt, D., Storey, M., et al. (2018). Evidence for extremely rapid magma ocean crystallization and crust formation on Mars. *Nature* 558, 586–589. doi:10.1038/s41586-018-0222-z

Brimhall, G. H., and Crerar, D. A. (1987). Ore fluids: magmatic to supergene. *Rev. Mineral.* 17, 235–321. doi:10.1515/9781501508950-010

Bromiley, G., Hilaret, N., and McCammon, C. (2004). Solubility of hydrogen and ferric iron in rutile and TiO_2 (II): implications for phase assemblages during ultrahigh-pressure metamorphism and for the stability of silica polymorphs in the lower mantle. *Geophys. Res. Lett.* 31, L04610. doi:10.1029/2004GL019430

Burnham, A. D., and Berry, A. J. (2017). Formation of the Hadean granites by melting of igneous crust. *Nat. Geosci.* 10, 457–462. doi:10.1038/ngeo2942

Cannat, M. (1993). Emplacement of mantle rocks in the sea-floor at mid-ocean ridges. *J. Geophys. Research-Solid Earth* 98 (B3), 4163–4172. doi:10.1029/92JB02221

Capitanio, F. A., Nebel, O., and Cawood, P. A. (2020). Thermochemical lithosphere differentiation and the origin of cratonic mantle. *Nature* 588, 89–94. doi:10.1038/s41586-020-2976-3

Carignan, J., Hild, P., Mevelle, G., Morel, J., Yeghicheyan, D., Dr-N, Ub-N, et al. (2001). Routine analyses of trace elements in geological samples using flow injection and low pressure on-line liquid chromatography coupled to ICP-MS: a study of geochemical reference materials BR. *Geostand. Geoanal. Res.* 25, 187–198. doi:10.1111/j.1751–908X.2001.tb00595.x

Cavosie, A. J., Valley, J. W., Wilde, S. A., and F., E. I. M. (2006). Correlated microanalysis of zircon: trace element, $\delta^{18}O$, and U-Th-Pb isotopic constraints on the igneous origin of complex >3900 Ma detrital grains. *Geochim. Cosmochim. Acta* 70, 5601–5616. doi:10.1016/j.gca.2006.08.011

Coleman, R. G., and Peterman, Z. E. (1975). Oceanic plagiogranites. *J. Geophys. Res.* 80, 1099–1108. doi:10.1029/JB080i008p01099

Deschamps, F., Guillot, S., Godard, M., and Chauvel, C. (2010). *In situ* characterization of serpentinites from forearc mantle wedges: timing of serpentinization and behavior of fluid-mobile elements in subduction zones. *Chem. Geol.* 269, 262–277. doi:10.1016/j.chemgeo.2009.10.002

Deubener, J., Müller, R., Behrens, H., and Heide, G. (2003). Water and glass transition temperature of silicate melts. *J. Non-Cristalline Sol.* 330, 268–273. doi:10.1016/S0022-3093(03)00472-1

Diakonov, I. I., Pokrovski, G. S., Schott, J., Castet, S., and Gout, R. (1996). An experimental and computational study of Na-Al complexing in crustal fluids. *Geochim. Cosmochim. Acta* 60, 197–211. doi:10.1016/0016-7037(95)00403-3

Dick, H. J. B. (1977). "Evidence of partial melting in the josephine peridotite,". *Magma genesis: proceedings of the American geophysical union chapman conference on partial melting in the earth's upper mantle: state of Oregon department of geology and mineral industries*. Editor H. J. B. Dick, 59–62. doi:10.2475/ajs.277.7.801

Ehlmann, B. L., Mustard, J. F., and Murchie, S. L. (2010). Geologic setting of serpentine deposits on Mars. *Geophys. Res. Lett.* 37, L06201. doi:10.1029/2010GL042596

Elkins-Tanton, L. T. (2012). Magma ocean in the inner Solar system. *Ann. Rev. Earth Planet. Sci.* 40, 113–139. doi:10.1146/annurev-earth-042711-105503

Fisk, M. R. (1986). Basalt magma interaction with harzburgite and the formation of high-magnesium andesites. *Geophys. Res. Lett.* 13, 467–470. doi:10.1029/GL013i005p00467

Ghiorso, M. S., and Sack, R. O. (1995). Chemical mass transfer in magmatic processes IV. A revised and internally consistent thermodynamic model for the interpolation and extrapolation of liquid-solid equilibria in magmatic systems at elevated temperatures and pressures. *Contrib. Mineral. Petrol.* 119, 197–212. doi:10.1007/BF00307281

Govindaraju, K. (1994). Compilation of working values and sample description for 383 geostandards. *Geostand. Newslett.* 18, 1–158. doi:10.1046/j.1365-2494.1998.53202081.x-i1

Green, D. H. (1973). Experimental melting studies on a model upper mantle composition at high pressure under water saturated and water undersaturated conditions. *Earth Planet. Sci. Lett.* 19, 37–53. doi:10.1016/0012-821X(73)90176-3

Guillot, S., and Hattori, K. (2013). Serpentinites: essential roles in geodynamics, arc volcanism, sustainable development, and the origin of life. *Elements* 9, 95–98. doi:10.2113/gselements.9.2.95

Gurenko, A. A., Kamenetsky, V. S., and Kerr, A. C. (2016). Oxygen isotopes and volatile contents of the Gorgona komatiites, Colombia: a confirmation of the deep mantle origin of H_2O. *Earth Planet. Sci. Lett.* 454, 154–165. doi:10.1016/j.epsl.2016.08.035

Harrison, T. M. (2009). The Hadean crust: evidence from > 4 Ga zircons. *Annu. Rev. Earth Planet. Sci.* 37, 479–505. doi:10.1146/annurev.earth.031208.100151

Heinonen, J. S., Bohrson, W. A., Spera, F. J., Brown, G. A., Scruggs, M. A., and Adams, J. V. (2020). Diagnosing open-system magmatic processes using the Magma Chamber Simulator (MCS): part II- trace elements and isotopes. *Contrib. Mineralogy Petrology* 175, 105. doi:10.1007/s00410-020-01718-9

Helgeson, H. C., Kirkham, D. H., and Flowers, G. C. (1981). Theoretical prediction of thermodynamic behavior of aqueous electrolytes at high temperatures and pressures. IV. Calculation of activity coefficients, osmotic coefficients, and apparent molal and standard and relative partial molal properties to 5 kb and 600 °C. *Am. J. Sci.* 281, 1249–1516. doi:10.2475/ajs.281.10.1249

Herzberg, C., Condie, K., and Koregana, J. (2010). Thermal history of the Earth and its petrological expression. *Earth Planet. Sci. Lett.* 292, 79–88. doi:10.1016/j.epsl.2010.01.022

Hirschmann, M. M., Baker, M. B., and Stolper, E. M. (1998). The effect of alkalis on the silica content of mantle-derived melts. *Geochim. Cosmochim. Acta* 62, 883–902. doi:10.1016/S0016-7037(98)00028-3

Holland, T. J. B., and Powell, R. (2011). An improved and extended internally consistent thermodynamic dataset for phases of petrological interest, involving a new equation of state for solids. *J. Metamorphic Geol.* 29, 333–383. doi:10.1111/j.1525-1314.2010.00923.x

Jochum, K. P., Nohl, U., Herwig, K., Lammel, E., Stoll, B., and Hofmann, A. W. (2005). GeoReM: A new geochemical database for reference materials and isotopic standards. *Geostandards Geoanalytical Res.* 29, 333–338. doi:10.1111/j.1751–908X.2005.tb00904.x

Jochum, K. P., Stoll, B., Herwig, K., Willbold, M., Hofmann, A. W., Amini, M., et al. (2006). MPI-DING reference glasses for *in situ* microanalysis: new reference values for element concentrations and isotope ratios. *Geochem. Geophys. Geosystems* 7, Q02008. doi:10.1029/2005GC001060

Jochum, K. P., Stoll, B., Herwig, K., and Willbold, M. (2007). Validation of LA-ICP-MS trace element analysis of geological glasses using a new solid-state 193 nm Nd:YAG laser and matrix-matched calibration. *J. Anal. Spectrom.* 22, 112–121. doi:10.1039/B609547J

Jochum, K. P., Stoll, B., Weis, U., Jacob, D. E., Mertz-Kraus, R., and Andreae, M. O. (2014). Non-matrix-matched calibration for the multi-element analysis of geological and environmental samples using 200 nm femtosecond LA-ICP-MS: a comparison with nanosecond lasers. *Geostandards Geoanalytical Res.* 38, 265–292. doi:10.1111/j.1751–908X.2014.12028.x

Johnson, J. W., Oelkers, E. H., and Helgeson, H. C. (1992). SUPCRT92: A software package for calculating the standard molal thermodynamic properties of minerals, gases, aqueous species, and reactions from 1 to 5000 bar and 0 to 1000 °C. *Comput. Geosci.* 18, 899–947. doi:10.1016/0098-3004(92)90029-Q

Kelemen, P. B., Joyce, D. B., Webster, J. D., and Holloway, J. R. (1990). Reaction between ultramafic rock and fractionating basaltic magma II. Experimental investigation of reaction between olivine tholeiite and harzburgite at 1150-1050°C and 5kb. *J. Petrology* 31, 99–134. doi:10.1093/petrology/31.1.99

Kelemen, P. B., Shimizu, N., and Salters, V. J. M. (1995). Extraction of mid-ocean-ridge basalt from the upwelling mantle by focused flow of melt in dunite channels. *Nature* 375, 747–753. doi:10.1038/375747a0

Koepke, J., Feig, S., Snow, J., and Freise, M. (2004). Petrogenesis of oceanic plagiogranites by partial melting of gabbros: an experimental study. *Contrib. Mineral. Petrol.* 146, 414–432. doi:10.1007/s00410-003-0511-9

Kouzmanov, K., and Pokrovski, G. S. (2012). "Hydrothermal controls on metal distribution in Cu(-Au-Mo) porphyry systems,". *Geology and genesis of geology and genesis of major copper deposits and districts of the world: a tribute to richard H. Sillitoe*. Editors J. W. Hedenquist, M. Harris, and F. Camus (Littleton, CO: Society of Economic Geologists Special Publication), 16, 573–618. doi:10.5382/SP.16.22

Kushiro, I (1968). Compositions of magmas formed by partial zone melting of the Earth's upper mantle. *J. Geophys. Res.* 73, 619–634. doi:10.1029/JB073i002p00619

Le Maitre, R. W. (2002). Igneous rocks. A classification and glossary of terms. *Recommendations of the international union of geological sciences subcommission on the systematics of igneous rocks*. 2nd ed. Cambridge, New York, Melbourne: Cambridge University Press, 236. doi:10.1017/CBO9780511535581

Lundstrom, C. C. (2000). Rapid diffusive infiltration of sodium into partially molten peridotite. *Nature* 403, 527–530. doi:10.1038/35000546

Lyubetskaya, T., and Korenaga, J. (2007). Chemical composition of Earth's primitive mantle and its variance: 1. Method and results. *J. Geophys. Res.* 112, B03211. doi:10.1029/2005JB004223

Marchi, S., Bottke, W. F., Elkins-Tanton, L. T., Bierhaus, M., Wuennemann, K., Morbidelli, A., et al. (2014). Widespread mixing and burial of Earth's Hadean crust by asteroid impacts. *Nature* 511, 578–582. doi:10.1038/nature13539

Martel, C., Dingwell, D. B., Spieler, O., Pichavant, M., and Wilke, M. (2000). Fragmentation of foamed silicic melts: an experimental study. *Earth Planet. Sci. Lett.* 178, 47–58. doi:10.1016/S0012-821X(00)00062-5

Matjuschkin, V., Brooker, R. A., Tattitch, B., Blundy, J. D., and Stamper, C. C. (2015). Control and monitoring of oxygen fugacity in piston cylinder experiments. *Contrib. Mineral. Petrol.* 171, 66. doi:10.1007/s00410-016-1274-4

Moore, W. B., and Webb, A. A. (2013). Heat-pipe earth. *Nature* 501, 501–505. doi:10.1038/nature12473

Morgan, Z., and Liang, Y. (2003). An experimental and numerical study of the kinetics of harzburgite reactive dissolution with application to dunite formation. *Earth Planet. Sci. Lett.* 214, 59–74. doi:10.1016/S0012-821X(03)00375-3

Moyen, J.-F., and Martin, H. (2012). Forty years of TTG research. *Lithos* 148, 312–336. doi:10.1016/j.lithos.2012.06.010

Muñoz, M., Vidal, O., Marcaillou, C., Pascarelli, S., Mathon, O., and Farges, F. (2013). Iron oxidation state in phyllosilicate single crystals using Fe-K pre-edge and XANES spectroscopy: effects of the linear polarization of the synchrotron X-ray beam. *Amer. Miner.* 98, 1187–1197. doi:10.2138/am.2013.4289

Müntener, O. (2010). Serpentine and serpentinization: a link between planet formation and life. *Geology* 38, 959–960. doi:10.1130/focus102010.1

Nédélec, A., Monnereau, M., and Toplis, M. (2017). The Hadean-Archaean transition at 4 Ga: from magma trapping in the mantle to volcanic resurfacing of the Earth. *Terra Nova* 29, 218–223. doi:10.1111/ter.12266

Nicholls, I. A., Ringwood, A. E., O'Neil, J., and Carlson, R. W. (1973). Effect of water on olivine stability in tholeiites and the production of silica-saturated magmas in the island-arc environment. *J. Geology Science* 81, 285–300. doi:10.1086/627871

Oelkers, E. H., Benezeth, P., and Pokrovski, G. S. (2009). "Thermodynamic databases for water-rock interaction,". *Thermodynamics and kinetics of water-rock interactions*. Editors E. H. Oelkers and J. Schott (Mineralogical Society of America and Geochemical Society. Rev. Miner. Geochem.), 70, 1–46. doi:10.2138/rmg.2009.70.1

Oliphant, T. E. (2006). *Guide to NumPy*. USA: Massachusetts Institute of Technology, 261.

O'Hara, M. J., and Mathews, R. E. (1981). Geochemical evolution in an advancing, periodically replenished, periodically tapped, continuously fractionated magma chamber. *J. Geol. Soc.* 138, 237–277. doi:10.1144/gsjgs.138.3.0237

O'Neil, J., and Carlson, R. W. (2017). Building Archean cratons from Hadean mafic crust. *Science* 355, 1199–1202.

Pietranik, A., Storey, C., Koepke, J., Lasalle, S., and EIMF (2017). Zircon record of fractionation, hydrous partial melting and thermal gradients at different depths in oceanic crust (ODP Site 735B, South-West Indian Ocean). *Contrib. Mineral. Petrol.* 172, 10. doi:10.1007/s00410-016-1324-y

Pokrovski, G. S., Borisova, A. Y., and Bychkov, A. Y. (2013). "Speciation and transport of metals and metalloids in geological vapors," in *Book chapter 6 in: thermodynamics of geothermal fluids. Reviews in Mineralogy & Geochemistry*. Editors A. Stefánsson, T. Driesner, and P. Bénézeth, 76, 165–218. doi:10.2138/rmg.2013.76.6

Pokrovski, G. S., Schott, J., Hazemann, J.-L., Farges, F., and Pokrovsky, O. S. (2002). An X-ray Absorption Fine Structure and Nuclear Magnetic Resonance spectroscopy study of gallium-silica complexes in aqueous solution. *Geochimica et Cosmochimica Acta* 66, 4203–4322. doi:10.1016/S0016-7037(02)00973-0

Pouchou, J. L., and Pichoir, F. (1991). "Qualitative analysis of homogeneous or stratified microvolumes applying the model "PAP"," in *Electron probe quantitation*. Editors K. F. J. Heinrich and D. E. (NewburyNew York: Plenum Press). doi:10.1007/978-1-4899-2617-3_4

Proux, O., Biquard, X., Lahera, E., Menthonnex, J-J., Prat, A., Ulrich, O., et al. (2005). FAME: a new beamline for X-ray absorption investigations of very diluted systems of environmental, material and biological interests. *Phys. Scripta* T115, 970–973. doi:10.1238/Physica.Topical.115a00970

Reimink, J. R., Chacko, T., Stern, R. A., and Heaman, L. M. (2014). Earth's earliest evolved crust generated in an Iceland-like setting. *Nature* 7, 529–533. doi:10.1038/NGEO2170

Reimink, J. R., Chacko, T., Stern, R. A., and Heaman, L. M. (2016). The birth of a cratonic nucleus: lithogeochemical evolution of the 4.02-2.94 Ga Acasta Gneiss complex. *Precambrian Res.* 281, 453–472. doi:10.1016/j.precamres.2016.06.007

Robie, R. A., and Hemingway, B. S. (1995). Thermodynamic properties of minerals and related substances at 298.15 K and 1 bar (10^5 Pascals) pressure and at higher temperatures. *U.S. Geol. Surv. Bull.* 2131. doi:10.3133/b213

Rospabé, M., Ceuleneer, G., Granier, N., Arai, S., and Borisova, A. Y. (2019). Multi-scale development of a stratiform chromite ore body at the base of the dunitic mantle-crust transition zone (Maqsad diapir, Oman ophiolite): the role of repeated melt and fluid influxes. *Lithos* 350–351, 10523536. doi:10.1016/j.lithos.2019.105235

Rudnick, R. L., and Gao, S. (2003). Composition of the continental crust, *Treatise Geochem.*, 3, 1–64. doi:10.1029/95RG01302

Rudnick, R. L. (1995). Making continental crust. *Nature* 378, 571–578. doi:10.1038/378571a0

Safonov, O. G., Kosova, S. A., and Van Reenen, D. D. (2014). Interaction of biotite-amphibole gneiss with H_2O-CO_2-(K, Na)Cl fluids at 550 MPa and 750 and 800°C: experimental study and applications to dehydration and partial melting in the middle crust. *J. Petrology* 55, 2419–2456. doi:10.1093/petrology/egu062

Salvi, S., Pokrovski, G. S., and Schott, J. (1998). Experimental investigation of aluminum-silica aqueous complexing at 300°C. *Chem. Geology.* 151, 51–67. doi:10.1016/S0009-2541(98)00070-9

Sautter, V., Toplis, M. J., Beck, P., Mangold, N., Wiens, R., Pinet, P., et al. (2016). Magmatic complexity on early Mars as seen through a combination of orbital, *in-situ* and meteorite data. *Lithos* 254–255, 36–52. doi:10.1016/j.lithos.2016.02.023

Sautter, V., Toplis, M. J., Wiens, R. C., and Cousin, A. (2015). *In situ* evidence for continental crust on early Mars. *Nat. Geosci.* 3, 605–609. 10.1038/ngeo2474

Savin, S. M., and Lee, M. (1988). "Isotopic studies of phyllosilicate," in *Hydrous phyllosilicate (exclusive of micas),* Rev Mineral ***19***. Editor S. W. Bailey (Washington, DC: Mineral Soc Am.), 189–223.

Shaw, C. S. J., and Dingwell, D. B. (2008). Experimental peridotite–melt reaction at one atmosphere: a textural and chemical study. *Contrib. Mineral. Petrol.* 155, 199–214. doi:10.1007/s00410-007-0237-1

Shaw, C. S. J. (1999). Dissolution of orthopyroxene in basanitic magma between 0.4 and 2 GPa: further implications for the origin of Si-rich alkaline glass inclusions in mantle xenoliths. *Contrib. Mineral. Petrol.* 135, 114–132. doi:10.1007/s004100050501

Shaw, C. S. J., Thibault, Y., Edgar, A. D., and Lloyd, F. E. (1998). Mechanisms of orthopyroxene dissolution in silica-undersaturated melts at 1 atmosphere and implications for the origin of silica-rich glass in mantle xenoliths. *Contrib. Mineral. Petrol.* 132, 354–370. doi:10.1007/s004100050429

Shervais, J. W. (2008). "Tonalites, trondhjemites, and diorites of the Elder Creek ophiolite, California: low-pressure slab melting and reaction with the mantle wedge,". *Ophiolites, arcs, and batholiths: a tribute to cliff hopson*. Editors

J. E. Wright and J. W. Shervais (University of Virginia), 438, 113–132. doi:10.1130/2008.2438(03)

Shock, E. L., Sassani, D. C., Willis, M., and Sverjensky, D. A. (1997). Inorganic species in geologic fluids: correlations among standard molal thermodynamic properties of aqueous ions and hydroxide complexes. *Geochim. Cosmochim. Acta.* 61, 907–950. doi:10.1016/s0016-7037(96)00339-0

Shvarov, Y. V. (2015). A suite of programs, OptimA, OptimB, OptimC, and OptimS compatible with the Unitherm database, for deriving the thermodynamic properties of aqueous species from solubility, potentiometry and spectroscopy measurements. *Appl. Geochem.* 55, 17–27. doi:10.1016/j.apgeochem.2014.11.021

Shvarov, Y. V. (2008). HCh: new potentialities for the thermodynamic simulation of geochemical systems offered by Windows. *Geochem. Intern.* 46, 834–839. doi:10.1134/S0016702908080089

Sun, S.-S., and McDonough, W. M. (1989). "Chemical and isotope systematics of oceanic basalts: implications for mantle compositions and processes,". *Magmatism in the ocean basins*. Editors A. D. Saunders and M. J. Norry (London: Geological Society of London), 42, 313–345. doi:10.1144/GSL.SP.1989.042.01.19

Sushchevskaya, N. M., Korago, E. A., Belyatsky, B. V., and Sirotkin, A. N. (2000). Magmatism of mona and Knipovich ridges from spreading zones of polar atlantic ocean. *Russ. J. Geosciences.* 2, 243–267. doi:10.1134/S0016702909100024

Sverjensky, D. A., Shock, E. L., and Helgeson, H. C. (1997). Prediction of the thermodynamic properties of aqueous metal complexes to 1000 degrees C and 5 kb. *Geochim. Cosmochim. Acta.* 61, 1359–1412. doi:10.1016/s0016-7037(97)00009-4

Sverjensky, D. A., Harrison, B., and Azzolini, D. (2014). Water in the deep Earth: the dielectric constant and the solubilities of quartz and corundum to 60 kb and 1200 °C. *Geochim. Cosmochim. Acta.* 129, 125–145. doi:10.1016/j.gca.2013.12.019

Tagirov, B., and Schott, J. (2001). Aluminum speciation in crustal fluids revisited. *Geochim. Cosmochim. Acta.* 65, 3965–3992. doi:10.1016/S0016-7037(01)00705-0

Tanger, J. C., and Helgeson, H. C. (1988). Calculation of the thermodynamic and transport properties of aqueous species at high pressures and temperatures: revised equation of state for the standard partial molal properties of ions and electrolytes. *Am. J. Sci.* 288, 19–98. doi:10.2475/ajs.288.1.19

Toplis, M. J. (2005). The thermodynamics of iron and magnesium partitioning between olivine and liquid: criteria for assessing and predicting equilibrium in natural and experimental systems *Contrib. Mineral. Petrol.* 149, 22–39. doi:10.1007/s00410-004-0629-4

Trail, D., Watson, E. B., and Tailby, N. D. (2011). The oxidation state of Hadean magmas and implications for early Earth's atmosphere. *Nature* 480, 79–82. doi:10.1038/nature10655

Turek, A., Riddle, C., Cozens, B. J., Tetley, N. W., Udry, A., Gazel, E., et al. (1976). Determination of chemical water in rock analysis by Karl Fischer titration. *Chem. Geol. J. Geophys. Res. Planets* 17, 261–267. doi:10.1029/2018JE005602

Udry, A., Gazel, E., and McSween, H. Y. (2018). Formation of evolved rocks at Gale crater by crystal fractionation and implications for Mars crustal composition. *J. Geophys. Res. Plan.* 123, 1525–1540. doi:10.1029/2018JE005602

Ulmer, P. (2001). Partial melting in the mantle wedge – the role of H_2O in the genesis of mantle-derived 'arc-related' magmas. *Phys. Earth Planet. Inter.* 127, 215–232. doi:10.1016/S0031-9201(01)00229-1

Valley, J. W., Peck, W. H., King, E. M., and Wilde, S. A. (2002). A cool early Earth. *Geology* 30, 351–354. doi:10.1130/0091-7613(2002)030<0351:ACEE>2.0.CO;2

Van den Bleeken, G., Müntener, O., and Ulmer, P. (2011). Melt variability in percolated peridotite: an experimental study applied to reactive migration of tholeiitic basalt in the upper mantle. *Contrib. Mineral. Petrol.* 161, 921–945. doi:10.1007/s00410-010-0572-5

Van den Bleeken, G., Müntener, O., and Ulmer, P. (2010). Reaction processes between tholeiitic melt and residual peridotite in the uppermost mantle: an experimental study at 0.8 GPa. *J. Petrol.* 51, 153–183. doi:10.1093/petrology/egp066

Veksler, I. V., and Hou, T. (2020). Experimental study on the effects of H_2O upon crystallization in the Lower and Critical Zones of the Bushveld Complex with an emphasis on chromite formation. *Contrib. Mineralogy Petrology.* 175, 85. doi:10.1007/s00410-020-01733-w

Wedepohl, K. H. (1995). The composition of the continental crust. *Geochim. Cosmochim. Acta* 59, 1217–1232. doi:10.1016/0016-7037(95)00038-2

Westrich, H. R. (1987). Determination of water in volcanic glasses by Karl-Fischer titration. *Chem. Geol.* 63, 335–340. doi:10.1016/0009-2541(87)90170-7

Whitehouse, M. J., Nemchin, A. A., and Pidgeon, R. T. (2017). What can Hadean detrital zircon really tell us? A critical evaluation of their geochronology with implications for the interpretation of oxygen and hafnium isotopes. *Gondwana Res.* 51, 78–91. doi:10.1016/j.gr.2017.07.007

Wilke, M., Farges, F., Petit, P., Brown, G., Jr., and Martin, F. (2001). Oxidation state and coordination of Fe in minerals: an Fe K-XANES spectroscopic study. *Am. Mineral.* 86, 714–730. doi:10.2138/am-2001-5-612

Wilke, M., Partzsch, G., Bernhardt, R., and Lattard, D. (2005). Determination of the iron oxidation state in basaltic glasses using XANES at the K-edge. *Chem. Geol.* 220, 143–161. doi:10.1016/j.chemgeo.2005.03.004

Xu, Y., Liu, C.-Z., Chen, Y., Guo, S., Wang, J.-G., and Sein, K. (2017). Petrogenesis and tectonic implications of gabbro and plagiogranite intrusions in mantle peridotite of the Myitkyina ophiolite, Myanmar. *Lithos* 284-285, 180–193. doi:10.1016/j.lithos.2017.04.014

Zagrtdenov, N. R., Ceuleneer, G., Rospabé, M., Borisova, A. Y., Toplis, M. J., Benoit, M., et al. (2018). Anatomy of a chromite dyke in the mantle - crust transition zone of the Oman ophiolite. *Lithos* 312, 343–357. doi:10.1016/j.lithos.2018.05.012

Zimmer, K., Zhang, Y., Lu, P., Chen, Y., Zhang, G., Dalkilic, M., et al. (2016). A revised and extended thermodynamic dataset software package of SUPCRT92. *Comput. Geosciences* 90, 97–111. doi:10.1016/j.cageo.2016.02.013

Conflict of Interest: The authors declare that the research was conducted in the absence of any commercial or financial relationships that could be construed as a potential conflict of interest.

frontiers | Frontiers in Earth Science

TYPE Original Research
PUBLISHED 17 February 2023
DOI 10.3389/feart.2023.1101331

EDITED BY
Oleg G. Safonov,
Institute of Experimental Mineralogy (RAS), Russia

REVIEWED BY
Alexei Ivanov,
Institute of the Earth's Crust (RAS), Russia
Sebastien Meffre,
University of Tasmania, Australia

*CORRESPONDENCE
Kieran A. Iles,
✉ kieran.iles@helsinki.fi

SPECIALTY SECTION
This article was submitted to Geochemistry,
a section of the journal
Frontiers in Earth Science

RECEIVED 17 November 2022
ACCEPTED 27 January 2023
PUBLISHED 17 February 2023

CITATION
Iles KA, Hergt JM and Woodhead JD (2023), Multi-scale isotopic heterogeneity reveals a complex magmatic evolution: An example from the wallundry suite granitoids of the lachlan fold belt, Australia. *Front. Earth Sci.* 11:1101331.
doi: 10.3389/feart.2023.1101331

Multi-scale isotopic heterogeneity reveals a complex magmatic evolution: An example from the wallundry suite granitoids of the lachlan fold belt, Australia

Kieran A. Iles[1,2]*, Janet M. Hergt[1] and Jon D. Woodhead[1]

[1]School of Geography, Earth and Atmospheric Sciences, The University of Melbourne, Parkville, VIC, Australia,
[2]Department of Geoscience and Geography, University of Helsinki, Helsinki, Finland

Open-system magmatic processes are expected to impart various sorts of isotopic heterogeneity upon the igneous rocks they produce. The range of processes under the "open-system" umbrella (*e.g.*, simple two-component mixing, magma mingling, assimilation with fractional crystallization) cannot usually be uniquely identified using data from a single isotope system. The use of bulk-rock, mineral separate and *in situ* techniques and multiple isotope systems allows the characterization of isotopic variability at different sampling scales, illuminating details of the petrogenesis of a magmatic system. This approach has been applied to granitoids of the Wallundry Suite in the Lachlan Fold Belt, Australia. The Wallundry Suite exhibits variations in mineral assemblage, mineral composition and trends in bulk-rock major and trace element compositions consistent with the involvement of liquid-crystal sorting processes such as fractional crystallization. *In situ* paired O-Hf isotope data from zircon in six samples show an array indicating the isotopic evolution of the melt phase. Similarly, bulk-rock Sr-Nd-Hf isotope arrays support open-system magma evolution. These data combined with the petrographic observations and major and trace element geochemical variations suggest some form of assimilation-fractional crystallization process in the petrogenesis of the Wallundry Suite. Added complexity is revealed by two observations: 1) the isotopic variations are only weakly coupled to the lithology and major element compositions of the samples; and 2) there are distinguishable differences between the Hf isotope compositions of bulk-rock samples and those of the magmatic zircons they host. To varying degrees the rocks consistently show negative $\Delta\varepsilon\mathrm{Hf}^{\text{bulk-zrc}}$ values (i.e., the bulk-rock compositions have less radiogenic Hf isotope values than their coexisting zircons). The preservation of distinctly low Nd and Hf isotope ratios in an Fe-Ti oxide mineral separate suggests that the bulk-rock vs. zircon discrepancy is caused by the presence of unmelted components derived from a contaminant of continental origin (i.e., a rock with low Sm/Nd and Lu/Hf and thus unradiogenic Nd and Hf). Evidently, a complex interplay of assimilation, crystallization and melt segregation is required to account for the data. This investigation demonstrates that such complexity can, nevertheless, be disentangled through comparison of complementary isotope data at multiple sampling scales.

KEYWORDS

high-temperature I-types, assimilation, fractional crystallisation, hf isotopes, disequilibium

1 Introduction

A critical aspect of granitoid research has been identifying sources that contribute to the production of melt in the source region, and processes involved throughout magma evolution until its final crystallisation in the upper crust. Constraining these parameters relies on elucidating the origin of observed mineralogical and geochemical variations, often at different scales (see, for example, Chappell and White, 1974; Reid et al., 1983; Watson and Harrison, 1983; Williams et al., 1983; Chappell, 1984; Gray, 1984; Wyborn and Chappell, 1986; Chappell et al., 1987; Clemens and Vielzeuf, 1987; Chappell and Stephens, 1988; White and Chappell, 1988; Vernon, 1990; Patiño Douce and Johnston, 1991; Vielzeuf and Montel, 1994; Patiño Douce, 1995; Collins, 1996; Sawyer, 1996; Singh and Johannes, 1996; Beard et al., 2005; Brown, 2007; Kemp et al., 2007; Sawyer et al., 2011; Clemens and Stevens, 2012; McLeod et al., 2012; Paterson et al., 2016). The many models for granitoid genesis range from closed-system, single-source (be they crust or mantle) models to open-system, multi-source models. These include crystallisation-differentiation (fractional crystallisation), mixing of pure melts or of (crystal-bearing) magmas, solid entrainment models (i.e., restite unmixing or peritectic assemblage entrainment, PAE), and assimilation through bulk-digestion or coupled to fractional crystallisation (AFC). In different contexts and by different researchers, assorted petrogenetic models are viewed as competing hypotheses, envisaged as complementary processes, or invoked in combination with each other.

Fractional crystallisation has long been regarded as an important process in the evolution of both intrusive and extrusive rocks, and is in many ways the classic form of magmatic differentiation (for a historical overview, see Marsh, 2006; Wilson 1993). Bowen (1947) emphasised the ability of fractional crystallisation to generate a range of compositions from basaltic to granitic along a liquid line of descent. It has also long been recognised that separating a residual granitic liquid from the considerable quantity of crystalline material required to produce it in this fashion is problematic, and many potential mechanisms to achieve this have been proposed (Bowen, 1919; Bowen, 1947; McKenzie, 1985; Marsh, 2006). Marsh (2006) suggested punctuated differentiation, in which extensive settling of phenocrysts (formerly carried by ascending magma) occurs upon emplacement, to segregate relatively large volumes of fractionated liquid. The modelling of Dufec and Buchmann (2010) suggests melt extraction is optimised in particular crystallinity windows (~50–70%) such that a fractionated liquid is likely to escape from a crystalline mush of a distinctly different composition (explaining compositional gaps observed in many volcanic settings). Thus, those authors proposed that fractional crystallisation could produce a step-wise compositional evolution of both volcanic and plutonic rocks, which is consistent with the broadly layered structure of the continental crust.

For virtually as long as fractional crystallisation has been considered an important form of magmatic differentiation, geologists have been cognisant of the possibility that this process may be accompanied by assimilation of the surrounding rocks (McBirney, 1979; Wilson 1993; and references therein). Numerous quantitative models for AFC have been derived (*e.g.*, Allègre and Minister, 1978; Taylor, 1980; DePaolo, 1981; Nielsen, 1989; Hagen and Neumann, 1990; Aitcheson and Forrest, 1994; Bohrson and Spera, 2001; Spera and Bohrson, 2001; Bohrson et al., 2014; Bohrson et al., 2020; Heinonen et al., 2020), showing that isotope systems and some trace elements are likely to be strongly affected by progressive assimilation. A review of the theory and implementation of such models was undertaken by Heinonen et al. (2021), including a comparison of possible outputs for different modelling approaches. Typically (and critically) such models have emphasised departures for trends in isotope-isotope and trace element-isotope space expected to arise through AFC from those expected for simple liquid-crystal sorting or binary mixing. This will especially be the case when magmatic system modelling is thermodynamically constrained and the trace element and isotopic evolutions are tied to phase equilibria modelling, as is the case with the Magma Chamber Simulator (MCS) modelling program (Bohrson et al., 2020; Heinonen et al., 2020).

Regardless of whether any particular model was initially developed to examine intrusive or extrusive samples, fundamentally they describe the evolution of a crystallising magma chamber and may, therefore, be applied to the formation of granitoids. Taylor (1980), for example, modelled Sr and O isotope variations during combined assimilation and fractional crystallisation to the role of such a process in the formation of both the Adamello Massif and the Roccamonfina volcanics. Furthermore, Iles and Heinonen (2022) modelled bulk rock major and trace element trends using the MCS to investigate the formation of the Jindabyne Suite granitoids from Australia.

A large body of literature focussing on Australian granites debates the roles of restite unmixing (a closed-system process) *versus* a whole family of open-system models (i.e., various forms of magma mixing). Fractional crystallisation is viewed as an accompanying process in many magma mixing models concerning the granites of the Lachlan Fold Belt (LFB), Australia (Collins, 1996; Keay et al., 1997; Kemp et al., 2007; Kemp et al., 2009). In contrast, proponents of restite unmixing (White and Chappell, 1977) have seen fractional crystallisation as a complementary process. Chappell et al. (1987) suggested that fractional crystallisation might replace restite unmixing as the differentiation process in a felsic liquid from which essentially all restite has been removed. Furthermore, it was recognised that some magmas (which might include basaltic melts) would leave their source region free of residual solids and ascend through the crust as essentially pure melts (Chappell et al., 1987). The mechanism for producing petrographic and chemical variations in granite (*sensu lato*) suites that result from such cases would be fractional crystallisation.

In this context, few LFB granitoids (those classified as high-temperature I-types according to the scheme of Chappell et al., 1998) have escaped the contention associated with magma mixing *versus* restite unmixing, and are considered to have evolved via fractional crystallisation. One such example from the LFB is the Wallundry Suite. Using these granitoids as an example, this contribution demonstrates what insights into open-system magmatic process can be gained by examining isotopic heterogeneity at the inter-mineral and inter-sample scales. Particularly, this approach can track the interplay between crystallisation and assimilation and probe the physical nature of the assimilant.

The granitoid Wallundry Suite is dominated by the Middledale Gabbroic Diorite (MGD), which hosts the TEMORA 1 and 2 zircon reference materials (Wormald, 1993; Black et al., 2003; Black et al., 2004). The age of the MGD is well established by various studies. Black et al. (2004) showed that although the accepted ages of the TEMORA 1 and 2 zircons (^{206}Pb/^{238}U ages of 416.8 ±1.1 Ma and 416.8 ±1.3 Ma,

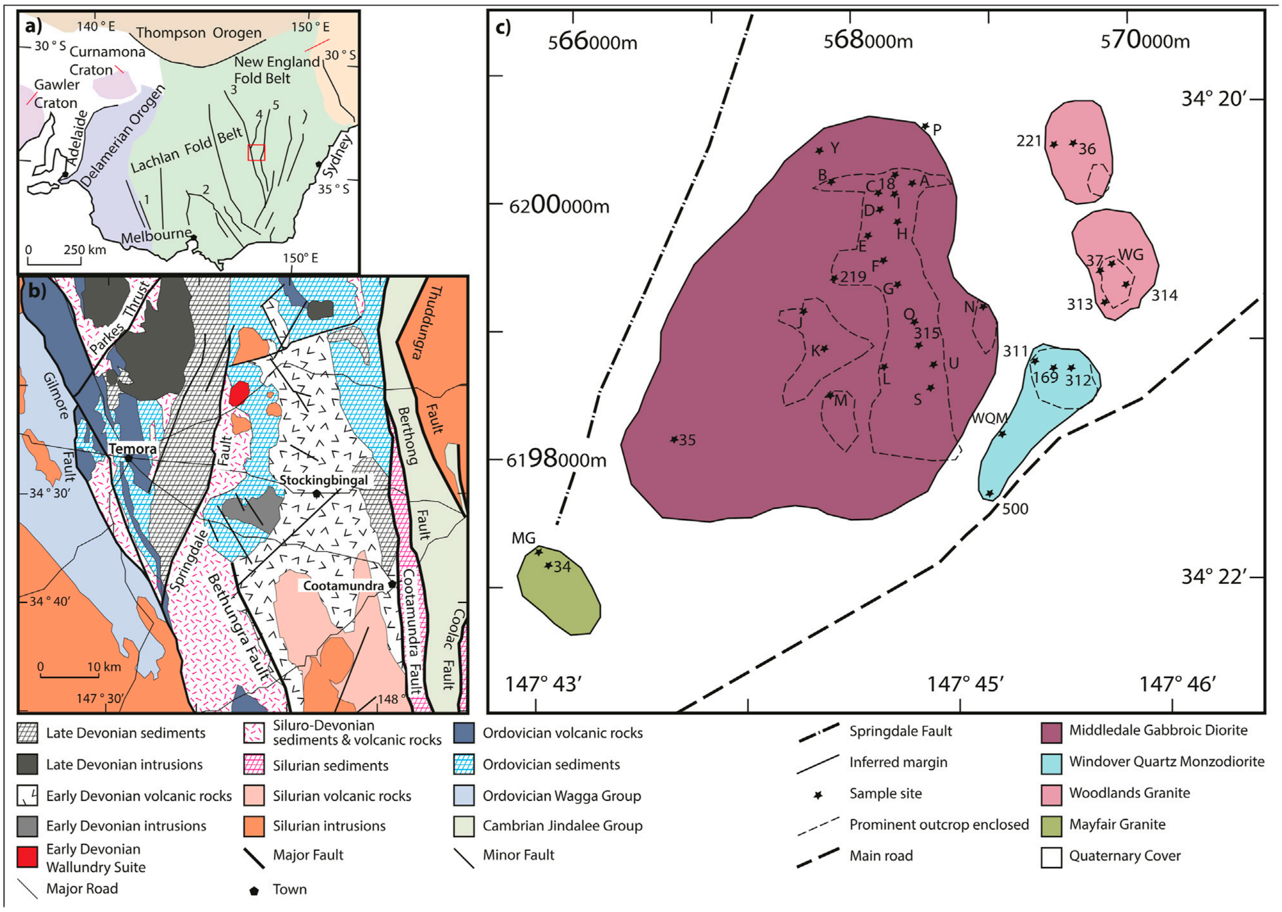

FIGURE 1
Map of the Wallundry Suite, the regional geology and the broad geological setting with southeastern Australia (modified after Figure 1 of Iles et al., 2015). **(A)** Map of the orogenic zones of southeastern Australia, including the Lachlan Fold Belt, which is divided into the Western, Central and Eastern Lachlan by the Stawell-Ararat Fault Zone (1), the Governor Fault Zone (2) and the Gilmore Fault Zone (3). The Parkes Thrust (4) and the Coolac-Narromine Fault Zone (5) bound the region outlined in red, which is expanded in **(B)** to show the regional geological setting of the Wallundry Suite. **(C)** Map of the Wallundry Suite, showing the sample sites from this study (A-P, S, U, Y, WG, WQM and MG) and those from Wormald (1993; numbered sites). The TEMORA 1, two and three sample sites are located to the north of Site A, the east of Site B and the north-east of Site A, respectively, although these boulders are not *in situ*.

respectively, as determined by isotope dilution thermal ionisation mass spectrometry, ID-TIMS) are identical. Iles et al. (2015) confirmed the homogeneity of U-Pb ages (at the precision of ion-microprobe techniques) across the pluton. The best estimate TEMORA 2 age is the chemical abrasion (CA)-ID-TIMS ^{206}Pb/^{238}U age of 417.68 ±0.15 Ma reported by Ickert et al. (2015). The MGD exhibits isotopic heterogeneity for both O (Black et al., 2004; Allen and Campbell, 2012; Hervé et al., 2013; Yakymchuk et al., 2013) and Hf (Woodhead and Hergt, 2005; Iles et al., 2015). Iles et al. (2015) documented zircon O and Hf isotope compositions and covariation in the MGD consistent with variable crustal contamination of a basaltic parent magma, with major and trace element trends attesting to fractional crystallisation. Iles et al. (2015) demonstrated that Zr saturation is reached late in the crystallisation history and the gabbroic samples crystallise zircon in interstitial melt pools aided by late-stage alteration of hornblende. Whereas most previous research focussed on the MGD, its zircon isotope characteristics and zircon formation, here the petrogenesis of the whole Wallundry Suite is investigated by combining petrographic and geochemical observations with Sr-Nd-Hf isotope data. Bulk-rock and mineral isotope analyses serve to explore the ways that assimilation and fractional crystallisation operated to produce petrographic and geochemical variations.

2 Field observations and petrography

The Wallundry Suite, located in NSW, Australia, comprises the MGD, Windover Quartz Monzodiorite (WQM), Woodlands Granite (WG) and Mayfair Granite (MG; Wormald, 1993). This Late Silurian-Early Devonian suite intrudes Late Ordovician to Early Devonian sedimentary formations of the eastern Lachlan Fold Belt (see Figure 1; Black et al., 2003; Wormald and Price, 1988).

The MGD is dominated by subequal amounts of euhedral to anhedral plagioclase and hornblende. Minor amounts of clinopyroxene, magnetite, ilmenite, apatite, titanite and quartz are observed in varying proportions across the pluton. Olivine and orthopyroxene are rarely seen in petrographic thin section. Biotite is also rare, as it has been replaced by chlorite in most samples. Actinolite and, to a lesser extent, epidote are alteration products of

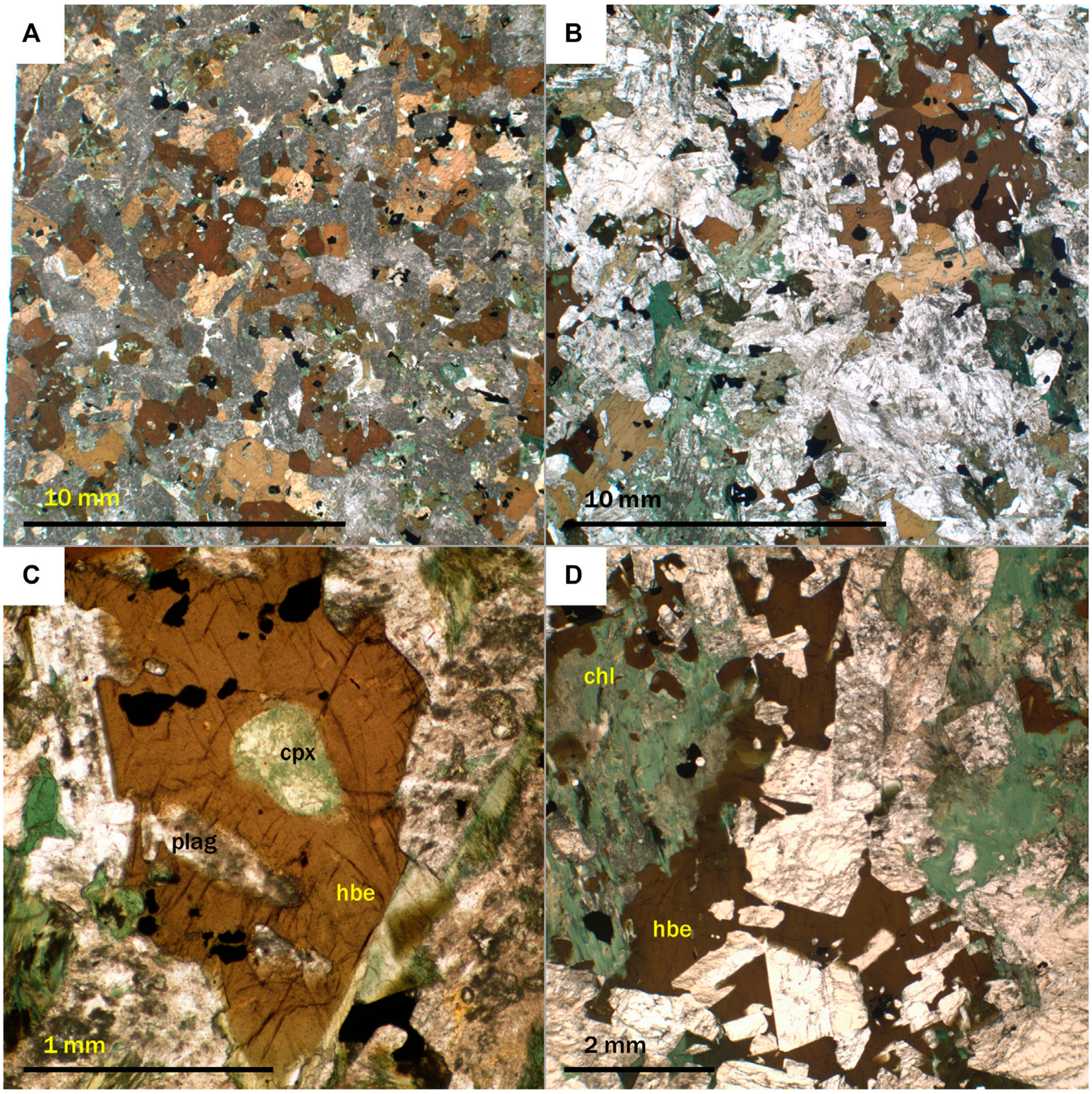

FIGURE 2
Photomicrographs of samples A **(A)**, B **(B)**, F **(C)** and J **(D)** taken in plane-polarised light. Note the smaller grainsize exhibited by sample A (from the northern end of the NNW-trending ridge) compared to sample B (off-ridge, approximately 600 m west). **(A)** Even-grained interlocking anhedral hornblende and plagioclase. **(B)** Patches of hornblende, such as that shown in the top right-hand corner, are common in the medium-coarse-grained samples of the MGD. **(C)** This fine-medium-grained sample (from the ridge, approximately 600 m south of A contains hornblende grains that enclose partially altered clinopyroxene (cpx) and plagioclase (plag). **(D)** Chlorite (chl) has replaced part of a large hornblende that has grown around multiple plagioclase crystals.

hornblende and pyroxene—a feature explored in detail by Iles et al. (2015). Similar mineral assemblages were observed by Black et al. (2003), Black et al. (2004) and Wormald (1993).

The MGD is dominantly medium-grained (2–4 mm), but variations occur such as the contrast between the fine-grained TEMORA 1 host rocks and the coarser-grained host of TEMORA 2 (Black et al., 2004). Samples along a central NNW trending ridge are fine-medium-grained (1–2 mm), whereas samples located topographically lower to the west and east are medium-coarse-grained (2–4 mm). The north of the pluton is generally more mafic than the south, where plagioclase is typically euhedral and has a higher modal abundance. Figure 2 illustrates examples of the textural and mineralogical variations observed in thin sections. The texture of hornblende is also spatially variable. Patches of hornblende that enclose small plagioclase crystals (<1.5 mm) and even smaller clinopyroxene and magnetite crystals (<0.5 mm) become increasingly prominent southwards along the central ridge and away from it into the coarser-grained western and eastern samples. These usually consist of one or two large hornblende crystals (1–6 mm varying in proportion to the average grainsize of the sample) and smaller (~1 mm) crystals of hornblende, actinolite, biotite and chlorite aggregated to form the patch. Textural relationships and mineral chemistry suggest that pyroxenes were the dominant early-crystallising phases, followed by the onset of plagioclase accumulation and later the crystallisation of hornblende (which also partially replaced pyroxene) then biotite (Iles et al., 2015).

The WQM, located to the southwest of the MGD (Figure 1), is fine-medium-grained (~1 mm average grainsize). It exhibits an equigranular fabric of interlocking, quartz, plagioclase and K-feldspar, with minor hornblende, biotite, magnetite and titanite. To the north of the WQM, the WG has a medium-grained, equigranular appearance (most grains are ~2 mm wide). In addition to quartz, plagioclase and K-feldspar, the mineral assemblage consists of magnetite, biotite, chlorite and minor apatite, titanite, epidote and calcite. Examination of petrographic thin section reveals pseudomorphs of biotite and chlorite after hornblende and iddingsite after olivine. A felsic dyke (sample U) that intrudes the southern portion of the MGD is petrographically identical to the WG. In both WQM and WG, there is partial alteration of plagioclase and K-feldspar. The MG is a felsic coarse-grained (3–6 mm, with some K-feldspar up to 15 mm) alkali feldspar granite. Only a highly weathered outcrop could be accessed for this study; however, Wormald (1993) reports that biotite and both primary and secondary muscovite are present, along with zircon, apatite, iddingsite and rutile as accessory phases. Furthermore, 2–4 cm cavities infilled with tourmaline and quartz are also observed in the MG.

3 Analytical methods

Splits of the samples collected for this study (Figure 1) were shared for sample preparation at Geoscience Australia (GA) and the School of Geography, Earth and Atmospheric Sciences at the University of Melbourne (UM). Zircons were extracted from a subset of the samples at GA. For all samples except Sites S, U, and MG, X-ray fluorescence spectroscopy (XRF) at GA was used to acquire bulk-rock major and trace element data. Trace element analyses of these samples were also conducted using an Agilent 7500ce quadrupole inductively-coupled plasma mass spectrometer (ICPMS) at GA. Duplicate trace element data were acquired from the UM splits using an Agilent 7700x quadrupole ICPMS. Based on an assessment of inter-laboratory bias and analytical constraints such as detection limits for some elements (Supplementary Material) the most reliable data have been compiled for use in figures and the discussion. The UM splits were used for bulk-rock isotope analysis and mineral separate geochemical analyses.

The zircon U-Pb geochronology and O-Hf isotope ratio determinations presented in this study were conducted in the same analytical sessions as the study of Iles et al. (2015), wherein the analytical methods are reported in detail. Briefly: zircon U-Pb geochronology was performed using the SHRIMP II at GA; the O isotope compositions of zircons were determined using the SHRIMP II at the Research School of Earth Sciences, Australian National University (ANU); zircon Hf isotope analyses was performed using laser ablation multicollector inductively coupled plasma mass spectrometry (LA-MC-ICPMS) at UM; cathodoluminescence images of zircons were used to guide analytical spot selection and ensure that, following U-Pb analyses, the O isotope then Hf isotope analyses were performed in the same domains for each technique.

Bulk-rock sample dissolution and subsequent element separation chemistry was conducted at UM according to the methods described in Iles et al. (2020); however, the dissolution procedure was simplified in the first run as the samples were prepared without isotopic tracers (i.e., Sr, Nd and Hf isotopes were analysed ‘unspiked’). In addition to the bulk-rock powders, mineral separates of two Wallundry Suite samples (Site J from the MGD and the WG sample) were selected for isotopic analysis. Mineral separation sought to obtain hornblende from Site J, mafic aggregates (clots dominated by chlorite and biotite, likely pseudomorphs after amphibole) from the WG sample, heavy weak-to non-magnetic accessories (zircon removed from the fraction, leaving titanite and epidote) from both, and ilmenite from Site J. Having been crushed, separated by conventional magnetic and heavy liquid techniques and hand-picked, the grains were cleaned by heating in dilute nitric acid and rinsed multiple times in purified water before dissolution. The grains were then prepared for analysis in same way for the powdered samples. Trace element analyses of splits of the dissolved separates were also performed, using the quadrupole ICPMS at UM.

Bulk-rock and mineral separate isotopic analysis was performed using a Nu Plasma MC-ICPMS at UM as described in Iles et al. (2020). External precision (2sd) is ±0.000020 (0.004%, ^{143}Nd/^{144}Nd), 0.2% (^{147}Sm/^{144}Nd), ±0.000015 (0.005%, ^{176}Hf/^{177}Hf), 1% (^{176}Lu/^{177}Hf), ±0.000040 (±0.005%, ^{87}Sr/^{86}Sr) and ±0.5% (^{87}Rb/^{86}Sr). For the analytical sessions in which the samples were analysed, the following isotope ratios were determined for reference materials (with the ranges of literature values given in parentheses): ^{176}Hf/^{177}Hf ratios of 0.282872, 0.282875, 0.282877, 0.282869 and 0.282868 for BCR2 (0.282859–0.282884) and ^{176}Hf/^{177}Hf ratios of 0.283101, 0.283084, 0.283098, 0.283113, 0.283110 and 0.283115 for BHVO-2 (0.283094–0.283118); ^{143}Nd/^{144}Nd ratios of 0.512633 and 0.512621 for BCR2 (0.512624–0.512656) and ratios of 0.512129 and 0.512128 for JNdi-1 (0.512112–0.512123); ^{87}Sr/^{86}Sr ratios of 0.704984 and 0.704978 for BCR2 (0.704995–0.705026). Given the external precision of our measurements, these values are consistent with independent determinations of the reference materials (Bizzarro et al., 2003; Weis et al., 2005; Weis et al., 2007; Chu et al., 2009; Chauvel et al., 2011; Cheong et al., 2013; Li et al., 2016).

4 Results

4.1 Major and trace element geochemistry

When SiO_2 is plotted against MgO, it is clear that, although SiO_2 overall increases as MgO decreases, the majority of samples show little variation in SiO_2 (45.5–49.8 wt%) compared with the changes in MgO content (~3 and 6 wt%). Thus, MgO content provides the better proxy for progressive crystallisation and magma evolution. A general observation from plots of major and trace elements *versus* MgO is that the data form coherent trends and the oxides of mobile elements (K_2O and Na_2O) retain this magmatic coherency and do not show a significant degree of scatter (Figure 3).

Many of the major element variation diagrams show kinked trends (Figure 3). The variation in the major element oxide contents with MgO allows the geochemical data to refine the paragenetic sequence suggested by petrographic evidence. The plot of TiO_2 vs. MgO (Figure 3B) shows that the data define an approximately linear array between 0 and ~4 wt% MgO, and that this divides into two clear groups at higher MgO. Of the two groups, those samples with higher TiO_2 are broadly co-linear with the main array, whereas the samples with lower TiO_2 appear to define a trend of increasing TiO_2 with decreasing MgO. In a number of other variation diagrams (*e.g.*, those illustrating variations in Al_2O_3, CaO, Na_2O, total Fe) there is a clear inflection point at ~3 wt% MgO. Apart from the samples with the highest TiO_2 contents, the variations in TiO_2, Fe_2O_3 and CaO among the most mafic samples (MgO 4–6 wt%) are consistent with the

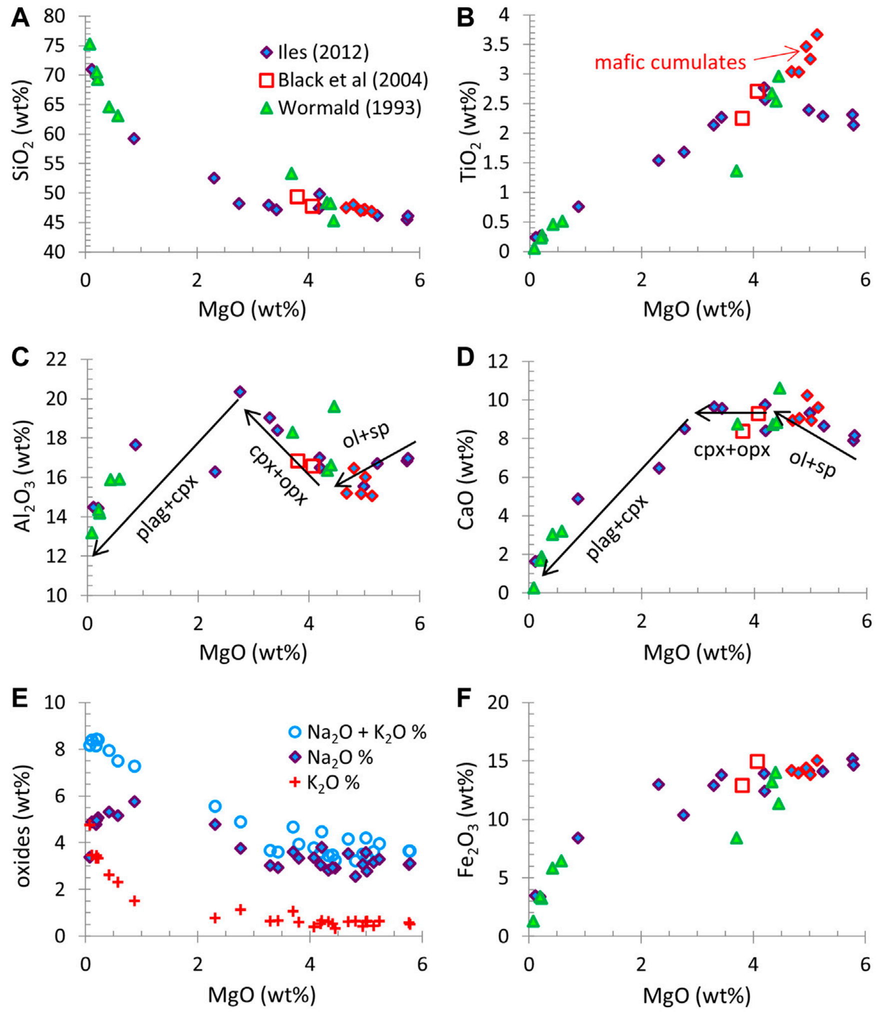

FIGURE 3
Variation diagrams for all Wallundry Suite samples, with elemental oxides plotted against MgO. **(A)** SiO$_2$ varies little for most of the MGD samples, but increases markedly with decreasing MgO for the felsic samples. **(B)** TiO$_2$ shows two trends that intersect at ~4 wt% MgO. **(C)** With decreasing MgO content, Al$_2$O$_3$ begins to increase sharply at ~4 wt% MgO, then decreases from ~3 wt% MgO. As for Al$_2$O$_3$, **(D), (E) and (F)** show that ~3 wt% MgO marks an inflection point for many major elements (Ca, Na, Fe). The trend in K$_2$O is similar to that of SiO$_2$. The five samples with highest TiO$_2$ are shown using a different symbol (diamonds with a heavier red outline) and are believed to represent pyroxene-rich cumulate rocks. The arrows on panel **(D)** illustrate the general shape of a possible liquid line of descent and are labelled with the main phases believed to control the fractional crystallisation assemblage (see text for details).

removal of Mg-rich, Ti-poor minerals. The removal of olivine (reported as a rare occurrence) would change the SiO$_2$ and total Fe contents only subtly, but increase the CaO and TiO$_2$ content of fractionated magmas. At 4 wt% MgO, the replacement of olivine by orthopyroxene (also a rarely observed phase) and appearance of clinopyroxene would generate the inflections illustrated. Assemblages dominated by pyroxene (both clinopyroxene and orthopyroxene) would buffer the CaO content but drive the Al$_2$O$_3$ contents to higher values. At MgO contents below ~3 wt% it is apparent that plagioclase becomes the dominant fractionating phase (both CaO and Al$_2$O$_3$ display a marked decline) but with decreasing MgO, indicating clinopyroxene removal is also important. The total Fe content also decreases at this point, reflecting the more Fe-rich nature of the clinopyroxene being removed, as well as the possible involvement of Fe-bearing oxides. Magnetite is among the opaque oxides observed to occur in these lithologies of intermediate bulk-rock composition.

The above interpretation is consistent with the initial sharp decrease in Ni (not shown) in the most magnesian samples with lower TiO$_2$ contents. The removal of olivine dominated assemblages would be expected to result in the initial sharp decrease in Ni in the fractionated magmas. In addition, although the variations are subtle, it would also appear that Al$_2$O$_3$ decreases in these same samples (Figure 3C), and the behaviour of Cr (~60 ppm in one sample at MgO ~6 wt%, Cr <15 ppm in all others) is consistent with the removal of Cr-bearing spinel. The samples located on an extension of the main TiO$_2$-MgO trend to high MgO contents (beyond ~4 wt%) and elevated TiO$_2$ are interpreted here to represent the accumulation of pyroxene-rich assemblages at the point where olivine is replaced by orthopyroxene (see Figure 3B). This is consistent with the observation that the highest clinopyroxene modes and the rare preservation of orthopyroxene are found in this group of samples.

From ~3 wt% to 0 wt% MgO, the pattern of increasing Na$_2$O changes with values decreasing in the most felsic samples. This is

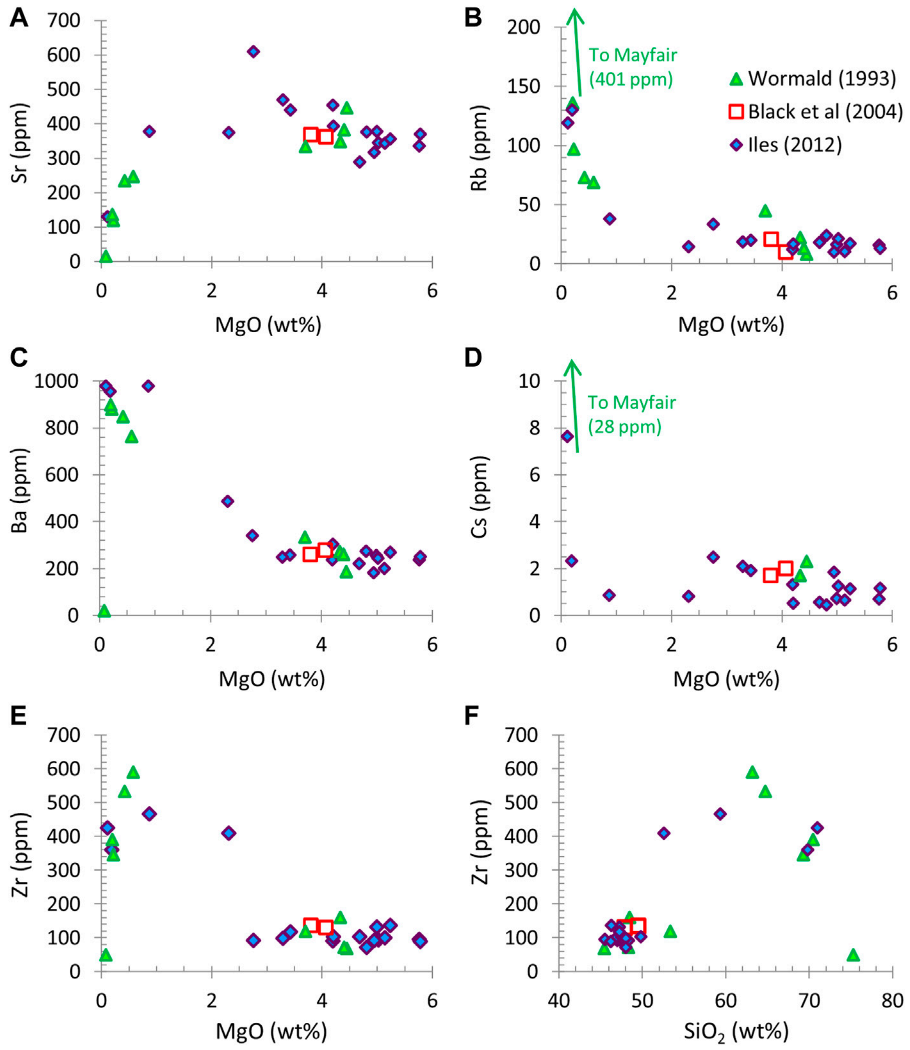

FIGURE 4

Variation diagrams for all Wallundry Suite samples, with trace elements plotted against MgO **(A–E)** or SiO_2 **(F)** **(A)** Sr displays a trend similar to CaO. **(B and C)** Rb and Ba show the least scatter, and have trends similar to K_2O. **(D)** Cs is the most scattered of the LILEs and its trend is similar to that of Rb, but enrichment occurs only in one sample (WQM). **(E and F)** Zr concentration plotted against MgO and SiO_2 respectively. Plotting against MgO shows the uniformity of Zr for a range of mafic compositions (all bar one of the MGD samples). Plotting against SiO_2 and including the data of Wormald (1993) and Black et al. (2004) shows the detail of the variation of Zr in the more felsic samples of the Wallundry Suite.

consistent with the increasing Na content of the plagioclase as fractional crystallisation proceeds and is supported by the variation in plagioclase composition reported by Wormald (1993). In the Na-poor sample 35 (MGD, 2.92 wt% Na_2O, 4.45 wt% MgO) cumulate plagioclase compositions range from An_{60} (core) to An_{53} (rim), whereas sample 312 (WQM, 5.05 wt% Na_2O, 0.50 wt% MgO) contains cores from An_{49} to An_{16} and rims from An_{36} to An_8.

Given the fluid mobility of large ion lithophile elements (LILEs) and the petrographic evidence of alteration, scatter of these elements on variation diagrams might be expected; however, variation diagrams for CaO, Na_2O (mobile elements) as well as K_2O (and other LILEs) *versus* MgO display coherency, and scatter that might have indicated open-system alteration is lacking (Figure 4). Barium and Rb behave in much the same way as the K_2O and are the least scattered LILEs; Cs is generally similar though it preserves more scatter; and, Sr displays a trend very similar to that of CaO with respect to MgO, with a maximum concentration (610 ppm, sample J) and an inflection point at ~3 wt % MgO. Thus, concentrations are preserved on a hand specimen scale despite the local, grain scale redistribution by alteration discussed in Iles et al. (2015).

Figure 4E shows that the majority of the MGD samples have broadly low Zr (88–132 ppm), but the Zr concentration steps up in the most felsic samples (WQM, WG and sample J from the MGD). The variation in Zr concentration in the more felsic samples can be further examined by plotting the data against SiO_2 (Figure 4F). This shows that the Wallundry Suite reaches a maximum Zr concentration in the WQM (sample 169 of Wormald, 1993) then decreases with increasing SiO_2.

4.2 Zircon isotope geochemistry

In addition to the U-Pb ages and O-Hf isotope data for zircons from the four samples reported by Iles et al. (2015), equivalent analyses

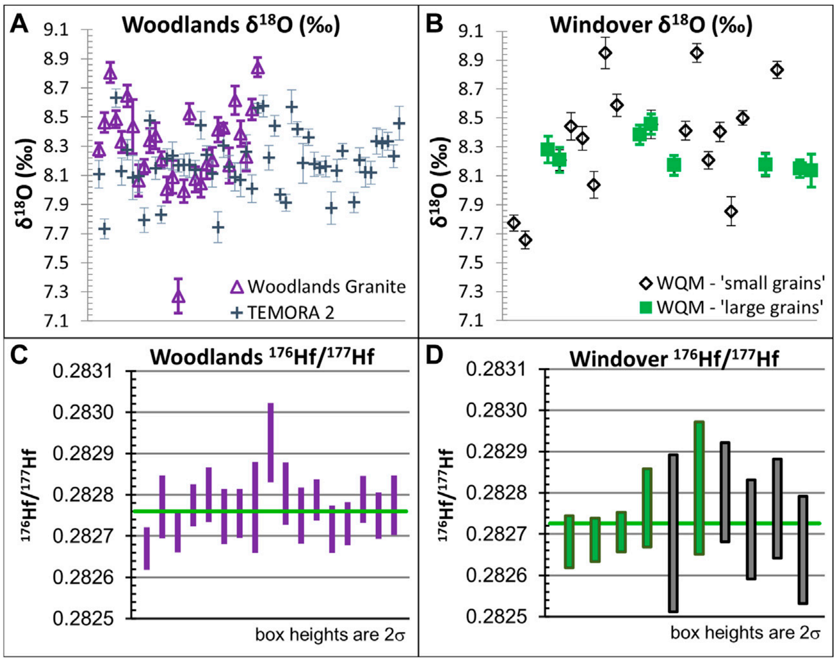

FIGURE 5
(A and B) $\delta^{18}O$ (‰) values of the zircons from the Woodlands Granite (including one outlier, noted in text) and Windover Quartz Monzodiorite (one outlier included and one off scale). Also shown are the 52 analyses of TEMORA 2, used as the calibration reference material for these analyses with a mean δ18O of 8.2‰. **(C and D)** The $^{176}Hf/^{177}Hf$ values of the zircons from the Woodlands Granite and Windover Quartz Monzodiorite (both age populations—large grains in green). Plots were generated using Isoplot of Ludwig (2008).

of zircons from one sample each of the WQM and WG are reported here. Mean $^{206}Pb/^{238}U$ ages of 413.9 ± 2.0 Ma (n = 29) and 412.9 ± 2.0 Ma (n = 29) were determined for zircons from WG and WQM, respectively, which are within uncertainty (quoted at the 95% confidence limits) of the four MGD age determinations reported by Iles et al. (2015). The age for WQM is, however, slightly outside of uncertainty with respect to the accepted ages of the TEMORA 1 and 2 (quoted above; Black et al., 2003; Black et al., 2004). Additionally, a minor inherited population of morphologically distinct zircons ("large grains") with a mean $^{206}Pb/^{238}U$ age of 427.4 ± 4.3 Ma (n = 7) is found in the WQM sample. In contrast to the "small grains" (mostly 50–100 μm long) that define the crystallisation age, the "large grains" are mostly 100–200 μm long and have a uniform dark appearance in CL and higher U concentrations and Th/U ratios (1239–2760 ppm and Th/U = 0.83–1.68 compared to 143–1040 ppm and Th/U =0.32–0.74).

In situ O isotope analysis of zircons from WG yield mean $\delta^{18}O$ values of 8.33 ± 0.23 (1s.d.) for a coherent group (n = 28) and 8.30 ± 0.30 if an anomalously low outlier ($\delta^{18}O = 7.27 \pm 0.12$, 1σ) is included. Analysis of zircons from WQM yields a mean $\delta^{18}O$ value of 8.36 ± 0.28 for a coherent group (n = 26) and 8.25 ± 0.54 if two outliers ($\delta^{18}O = 5.99 \pm 0.08$ and 7.66 ± 0.06, 1σ) are included. Both samples are thus within uncertainty of the coarse-grained MGD samples from Iles et al. (2015). Interestingly, analyses from the 'large grain' group yield $\delta^{18}O$ values showing some of the least deviations from the mean for the sample and, as a consequence, removal of the 'large grain' group does not significantly alter the mean for the WQM (Figure 5). The $\delta^{18}O$ values for the two age groups present in this sample thus are indistinguishable.

For Hf isotope compositions, because sample sizes are smaller and the is greater uncertainty on individual analyses relative to scatter, a more robust measure of central tendency has been used. A weighted mean $^{176}Hf/^{177}Hf$ ratio of 0.282761 ± 0.000021 (95% confidence about the Tukey's biweight mean, n = 17) is preserved in the zircons from WG. This includes one anomalously high outlier, but such values are down-weighted in Tukey's biweight mean. As noted for the O isotope values, the mean $^{176}Hf/^{177}Hf$ ratios of the 'large grain' and 'small grain' groups of WQM are indistinguishable (each 0.28273 ± 0.00010 from five analyses). If the two groups are combined, they yield weighted mean $^{176}Hf/^{177}Hf$ ratio of 0.282726 ± 0.000039 (n = 10). The zircons of the 'large grain' group have higher $^{176}Lu/^{177}Hf$ ratios than those of the 'small grain' group; therefore, the $^{176}Hf/^{177}Hf$ ratios of the two groups diverge slightly after age correction but are still within uncertainty (0.28271 ± 0.00010 for the 'small grains' and 0.282689 ± 0.000099 for the 'large grains'). The O and Hf isotope data discussed above are illustrated in Figure 5. These values correspond to εHf_i of 7.7 ± 0.7 and 6.2 ± 1.4 (95% confidence) for WG and WQM, respectively, using the 416.8 Ma age of Black et al. (2004). Furthermore, the paired O and Hf isotope analyses (outliers excluded for this purpose) for all six zircon populations are plotted in Figure 6, demonstrating the overlap between the coarse-grained MGD samples and the WG and WQM samples in O-Hf isotope space and the contrast between these and the fine-grained MGD sample.

4.3 Bulk-rock isotope geochemistry

The results of the bulk-rock Rb-Sr, Sm-Nd and Lu-Hf isotope analyses are reported in Table 1 and Table 2. Initial isotope ratios have

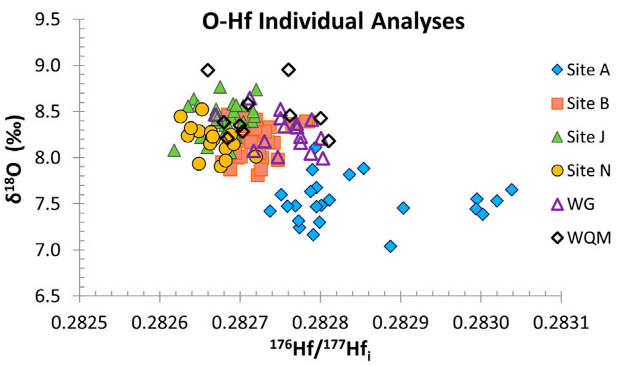

FIGURE 6
The paired $\delta^{18}O$ and $^{176}Hf/^{177}Hf$ data of the zircons from sample Sites A, B, J and N of the Middledale Gabbroic Diorite and from the Woodlands Granite (WG) and the Windover Quartz Monzodiorite (WQM). It is clear that some correlation between the O and Hf isotope compositions exist at the inter-sample scale (Spearman Rank Correlation Coefficient, SRCC, of −0.46 +0.15/-0.13, 95% confidence), and within some samples (WG, SRCC = −0.39 +0.52/−0.35; Site N, SRCC = −0.59 +0.44/−0.24) but not all. Note how most samples, with the single exception of the fine-grained sample from Site A, cluster in O-Hf isotope space. Data from Iles (2012) and Iles et al. (2015), and provided in Supplementary Material.

been calculated using the U-Pb zircon ages of 416.8 Ma for the Wallundry Suite (Black et al., 2004). Plots of the Sr, Nd and Hf isotope compositions of bulk-rock samples (Figure 7) show that the suite forms an array in Sr-Nd-Hf isotope space, which might be expected given the previously described trends in zircon O-Hf isotope space for Wallundry.

The samples appear to form clusters within a broader Nd-Hf isotope array. Samples A, H, L and S from the MGD define a more isotopically primitive group with εHf_i ranging from 7.2 to 9.2 (2 s.d. range) and εNd_i ranging from 3.1 to 5.1. Samples B, J, N and Y from the MGD and the WG, WQM and felsic dyke samples constitute a more evolved group (εHf_i 3.4–6.4 and εNd_i 0.9–2.9) with an internal trend congruent with the overall Nd-Hf trend of the suite. The most evolved sample is the MG, with an εHf_i value of 2.40 ±0.53 and an εNd_i value of −0.89 ±0.38. Although such clustering is not as obvious for the Sr-Nd isotope data, the same division between the two groups defined from the Nd-Hf isotope plot is nevertheless evident in Figure 7A. The evolution of bulk-rock Sr-Nd-Hf isotope compositions does not strongly follow the lithological and chemical evolution of the suite. This is particularly well illustrated by the essentially identical Sr, Nd and Hf isotope compositions of MGD Site N and the WQM sample ($^{87}Sr/^{86}Sr$ of 0.70472, εNd_i of 1.7, εHf_i of 4.2), despite different major element chemistry, petrography and trace element compositions (e.g., 23.5 ppm Rb and 341 ppm Sr for Site N and 121 ppm Rb and 127 ppm Sr for WQM).

4.4 Hf isotope composition of the melt phase

An important and unexpected early observation of this study is the discrepancy between the magmatic zircon Hf isotope compositions and the bulk-rock Hf isotope composition for each of Wallundry Suite samples. This is illustrated in Figure 8. In order to rule out any possible cause resulting from analytical problems, multiple repeat analyses were performed on bulk-rock samples. During these experiments it was confirmed that the observation is genuine (i.e., the phenomenon is not analytically induced) and further noted that the bulk-rock Hf compositions of different aliquots of the same sample varied significantly.

Following the approach described in Iles et al. (2020), the difference between the initial εHf values of the bulk-rock samples and the means of their magmatic zircon populations is represented by their $\Delta\varepsilon Hf^{bulk\text{-}zrc}$ values. Intriguingly, although the low-temperature I-types of Iles et al. (2020) consistently exhibited positive $\Delta\varepsilon Hf^{bulk\text{-}zrc}$ values, the high-temperature I-type Wallundry Suite behaves differently. Although some samples of the Wallundry Suite exhibit greater variability from aliquot to aliquot (poorer reproducibility) than others (2.0ε units for Site J compared to 0.5ε units for Site L), the bulk-rock Hf isotope measurements produce age-corrected εHf_i values that are all within uncertainty of or lower than the εHf_i values of the zircon population. There is no clear relationship between the $\Delta\varepsilon Hf^{bulk\text{-}zrc}$ values and the chemical or petrographic character in the samples. For example, although the largest $\Delta\varepsilon Hf^{bulk\text{-}zrc}$ value occurs in the fine-grained, mafic sample A, the $\Delta\varepsilon Hf^{bulk\text{-}zrc}$ values are smallest among the more isotopically evolved samples, which range from mafic to felsic in composition.

4.5 Geochemistry of mineral separates

That the bulk-rocks and zircons do not preserve the same Hf isotope compositions indicates the presence of inter-mineral isotopic heterogeneity in the samples, a component of which must balance the composition of the zircon. This component would need to be less radiogenic in Hf than the bulk-rock samples. Isotopic analyses of mineral separates from two samples (Site J of the MGD and WG) explore this further, to uncover the identity of the less radiogenic component in the bulk-rock samples. The Sm-Nd and Lu-Hf isotope data are presented in Table 3. Trace element compositions have been included in the Supplementary Material.

In order to assess the possibility that mineral separates contain more than one mineral component, the trace element compositions of the separates were compared with two datasets: 1) LA-ICPMS from hornblende, chlorite, biotite and epidote, thin sections of Wallundry Suite samples (Iles et al., 2015), and 2) a compilation of literature values for hornblende, biotite, titanite, ilmenite, zircon and epidote in other rocks (Luhr and Carmichael, 1980; Bea et al., 1994; Bea, 1996; Bingen et al., 1996; Pan and Fleet, 1996; Ayres and Harris, 1997; Belousova et al., 2002; Hermann, 2002; Jang and Naslund, 2003; Villaseca et al., 2003; Storkey et al., 2005; Tiepolo and Tribuzio, 2005; Bea et al., 2006; Gregory et al., 2009; Acosta-Vigil et al., 2010; Driouch et al., 2010; Nehring et al., 2010; Colombini et al., 2011; Gregory et al., 2012; Starijaš Mayer et al., 2014; Xing et al., 2014). Based on these comparisons (particularly examining REE, Hf and Zr), the hornblende separates from sample J are essentially monomineralic (i.e., minimal contribution from inclusions of other phases), but the pseudomorphs after hornblende from WG are a mixture dominated by chlorite and biotite with a possible minor component similar to the titanite-epidote separate.

The titanite-epidote separate from WG has MREE and HREE abundances similar to the range of published data from titanites,

TABLE 1 Wallundry Suite Rb-Sr and Sm-Nd data acquired by MC-ICPMS. Samples have been age corrected to 416.8 (Black et al., 2004; Iles, 2012). The εNd$_i$ values have been calculated using the modern CHUR values ^{147}Sm/^{144}Nd = 0.1960 and ^{143}Nd/^{144}Nd = 0.512632 (adjusted for La Jolla = 0.511860) of Bouvier et al. (2008). Values in italics are data derived from a trace element run of separate aliquots, paired with ^{87}Sr/^{86}Sr and ^{143}Nd/^{144}Nd determinations made without the use of an isotope spike. Aliquot numbering is in accordance with the numbering used for Lu-Hf determinations in Table 2. Representative values (single analysis or mean of analyses) for each sample are shown in bold.

Unit	Sample	Aliquot	Rb (ppm)	Sr (ppm)	^{87}Rb/^{86}Sr	^{87}Sr/^{86}Sr	^{87}Sr/^{86}Sr$_i$	±2σ	Sm (ppm)	Nd (ppm)	^{147}Sm/^{144}Nd	^{143}Nd/^{144}Nd	^{143}Nd/^{144}Nd$_i$	εNd$_i$	±2σ
Middledale Gabbroic Diorite	**Site A**	**1**	**15.4**	**342**	**0.130**	**0.704919**	**0.70416**	**0.00004**	**7.4**	**27.6**	**0.163**	**0.512738**	**0.512293**	**3.82**	**0.54**
	Site B	**1**	**13.0**	**449**	**0.084**	**0.704945**	**0.70446**	**0.00004**	**5.36**	**22.1**	**0.147**	**0.512619**	**0.512218**	**2.37**	**0.50**
	Site H	**1**	**12.6**	**359**	**0.102**	**0.704442**	**0.70385**	**0.00004**	**3.57**	**15.1**	**0.143**	**0.512723**	**0.512333**	**4.61**	**0.48**
	Site J	1	32.5	535	0.175	0.705809	0.70478		6.07	26.9	0.136	0.512545	0.512173	1.48	
		4	32.6	534	0.176	0.705830	0.70480		6.42	28.3	0.1369	0.512532	0.512159	1.20	
		Mean	**32.5**	**535**	**0.176**	**0.705820**	**0.70479**	**0.00003**	**6.25**	**27.6**	**0.137**	**0.512539**	**0.512166**	**1.34**	**0.32**
	Site L	1	15.3	367	0.120	0.704636	0.70393		10.2	42.8	0.144	0.512678	0.512286	3.69	
												0.512688	0.512296	3.88	
		Mean	**15.3**	**367**	**0.120**	**0.704636**	**0.70393**	**0.00004**	**10.2**	**42.8**	**0.144**	**0.512683**	**0.512291**	**3.79**	**0.48**
	Site N	**1**	**23.5**	**341**	**0.199**	**0.705879**	**0.70472**	**0.00005**	**3.05**	**12.6**	**0.146**	**0.512583**	**0.512183**	**1.69**	**0.51**
	Site S	**1**							**5.25**	**21.7**	**0.1464**	**0.512674**	**0.512275**	**3.47**	**0.38**
	Site Y	**1**							**5.36**	**21.5**	**0.1506**	**0.512606**	**0.512195**	**1.92**	**0.39**
Woodlands Granite	**WG**	1	132	118	3.233	0.723848	0.70497		9.05	44.2	0.124	0.512531	0.512193	1.88	
		5	128	118	3.146	0.723605	0.70522		9.56	42.7	0.1352	0.512531	0.512162	1.27	
		Mean	**130**	**118**	**3.189**	**0.723727**	**0.70510**	**0.00025**	**9.30**	**43.5**	**0.129**	**0.512531**	**0.512178**	**1.58**	**0.31**
Windover Quartz Monzodiorite	**WQM**	1	121	127	2.753	0.720801	0.70472		11.1	52.5	0.128	0.512528	0.512179	1.60	
												0.512543	0.512194	1.89	
		Mean	**121**	**127**	**2.753**	**0.720801**	**0.70472**	**0.00036**	**11.1**	**52.5**	**0.128**	**0.512536**	**0.512186**	**1.74**	**0.46**
Mayfair Granite	**MG**	**1**							1.4	3.4	0.2568	0.512752	**0.512051**	**−0.89**	**0.38**
Unnamed felsic dyke	**Site U**	**1**	**52.8**	**152**	**1.007**	**0.710784**	**0.70490**	**0.00008**	**7.4**	**37.5**	**0.1187**	**0.512484**	**0.512160**	**1.24**	**0.38**

TABLE 2 Wallundry Suite Lu-Hf data acquired by MC-ICPMS. Samples have been age corrected to 416.8 (Black et al., 2004; Iles, 2012). The εHf$_i$ values have been calculated using the modern CHUR values ^{176}Lu/^{177}Hf = 0.0336 and ^{176}Hf/^{177}Hf = 0.282785 of Bouvier et al. (2008). Values in *italics* are data derived from a trace element run of separate aliquots, paired with ^{176}Hf/^{177}Hf determinations made without the use of an isotope spike. Where repeat analyses were made of an aliquot, both isotope ratio determinations are reported, but only the average εHf$_i$ value for the aliquot is shown. Representative values (single analysis or mean of analyses) for each sample are shown in bold.

Unit	Sample	Aliquot	Lu (ppm)	Hf (ppm)	^{176}Lu/^{177}Hf	^{176}Hf/^{177}Hf	^{176}Hf/^{177}Hf$_i$	εHf$_i$	±2σ
Middledale Gabbroic Diorite	**Site A**	*1*	*0.64*	*3.37*	*0.0268*	*0.282933*	*0.282719*	***7.12***	
						0.282938	*0.282729*		
		2	0.63	3.32	0.0268	0.282956	0.282747	7.92	
		3	0.64	3.97	0.0229	0.282919	0.282740	7.70	
		4	0.63	3.67	0.0245	0.282917	0.282725	7.17	
		Mean	**0.63**	**3.58**	**0.0253**	**0.282931**	**0.282734**	**7.48**	**0.30**
	Site B	*1*	*0.37*	*2.09*	*0.0248*	*0.282849*	*0.282655*	*4.70*	
		2	0.35	2.27	0.0222	0.282867	0.282693	**5.93**	
						0.282761	0.282687		
		3	0.36	2.24	0.0227	0.282844	0.282667	5.11	
		Mean	**0.36**	**2.20**	**0.0232**	**0.282852**	**0.282671**	**5.25**	**0.32**
	Site H	*1*	*0.33*	*2.53*	*0.0182*	*0.282874*	*0.282732*	*7.39*	
		2	0.32	2.28	0.0201	0.282935	0.282778	9.03	
		3	0.31	2.19	0.0203	0.282923	0.282765	**8.80**	
						0.282938	0.282780		
		Mean	**0.32**	**2.33**	**0.0196**	**0.282913**	**0.282760**	**8.41**	**0.80**
	Site J	*1*	*0.31*	*2.08*	*0.0211*	*0.282776*	*0.282611*	*3.14*	
		2	0.30	1.53	0.0276	0.282883	0.282668	5.13	
		3	0.30	2.17	0.0199	0.282805	0.282650	4.50	
		4	0.30	1.97	0.0216	0.282837	0.282669	5.16	
		Mean	**0.30**	**1.94**	**0.0225**	**0.282825**	**0.282649**	**4.48**	**0.79**
	Site L	*1*	*0.69*	*4.50*	*0.0218*	*0.282946*	*0.282776*	*8.97*	
		2	0.67	3.71	0.0257	0.282970	0.282769	8.73	
		3	0.68	6.33	0.0154	0.282882	0.282762	**8.47**	
						0.282882	0.282762		
		Mean	**0.68**	**4.85**	**0.0209**	**0.282933**	**0.282769**	**8.73**	**0.31**
	Site N	*1*	*0.28*	*2.19*	*0.0180*	*0.282753*	*0.282612*	*3.17*	
		2	0.28	1.89	0.0207	0.282817	0.282655	4.69	
		3	0.28	2.35	0.0171	0.282789	0.282655	4.70	
		Mean	**0.28**	**2.14**	**0.0186**	**0.282786**	**0.282641**	**4.19**	**0.77**
	Site S	**1**	**0.46**	**3.48**	**0.0190**	**0.282897**	**0.282749**	**8.01**	**0.52**
	Site Y	**1**	**0.43**	**3.40**	**0.0180**	**0.282829**	**0.282689**	**5.88**	**0.52**
Woodlands Granite	**WG**	*1*	*0.85*	*8.66*	*0.0139*	*0.282768*	*0.282660*	*4.84*	
		2	0.85	9.36	0.0130	0.282765	0.282664	**4.99**	
						0.282764	0.282663		
		3	0.85	8.93	0.0135	0.282771	0.282665	5.04	
		4	0.86	9.73	0.0126	0.282764	0.282665	5.05	
		5	0.88	9.85	0.0127	0.282775	0.282675	5.39	

(Continued on following page)

TABLE 2 (*Continued*) Wallundry Suite Lu-Hf data acquired by MC-ICPMS. Samples have been age corrected to 416.8 (Black et al., 2004; Iles, 2012). The εHf$_i$ values have been calculated using the modern CHUR values ^{176}Lu/^{177}Hf = 0.0336 and ^{176}Hf/^{177}Hf = 0.282785 of Bouvier et al. (2008). Values in *italics* are data derived from a trace element run of separate aliquots, paired with ^{176}Hf/^{177}Hf determinations made without the use of an isotope spike. Where repeat analyses were made of an aliquot, both isotope ratio determinations are reported, but only the average εHf$_i$ value for the aliquot is shown. Representative values (single analysis or mean of analyses) for each sample are shown in bold.

Unit	Sample	Aliquot	Lu (ppm)	Hf (ppm)	^{176}Lu/^{177}Hf	^{176}Hf/^{177}Hf	^{176}Hf/^{177}Hf$_i$	εHf$_i$	±2σ
		Mean	**0.86**	**9.30**	**0.0132**	**0.282769**	**0.282666**	**5.06**	**0.24**
Windover Quartz Monzodiorite	**WQM**	*1*	*1.00*	*10.86*	*0.0131*	*0.282735*	*0.282633*	*3.89*	
		2	0.96	9.70	0.0141	0.282752	0.282642	**4.26**	
						0.282754	0.282644		
		3	0.98	10.22	0.0137	0.282756	0.282649	4.47	
		4	0.96	9.51	0.0144	0.282753	0.282641	4.12	
		Mean	**0.97**	**10.07**	**0.0138**	**0.282749**	**0.282641**	**4.20**	**0.27**
Mayfair Granite	**MG**	**1**	**0.14**	**2.58**	**0.0077**	**0.282651**	**0.282591**	**2.40**	**0.53**
Unnamed felsic dyke	**Site U**	**1**	**0.54**	**8.93**	**0.0086**	**0.282726**	**0.282659**	**4.81**	**0.52**

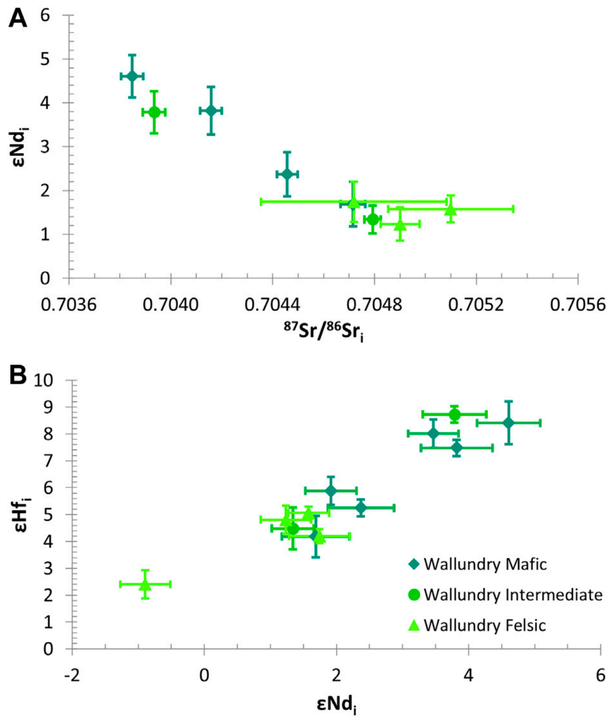

FIGURE 7
Wallundry Suite Sr-Nd-Hf isotope data acquired in this study (Tables 1 and Tables 2). **(A)** εNd$_i$ plotted against ^{87}Sr/^{86}Sr$_i$ for the Wallundry Suite. **(B)** εHf$_i$ plotted against εNd$_i$ for the Wallundry Suite (including the Mayfair Granite, for which Sr isotope data is lacking). Note the weak coupling between the evolution of the isotope compositions and the evolution from mafic to felsic samples.

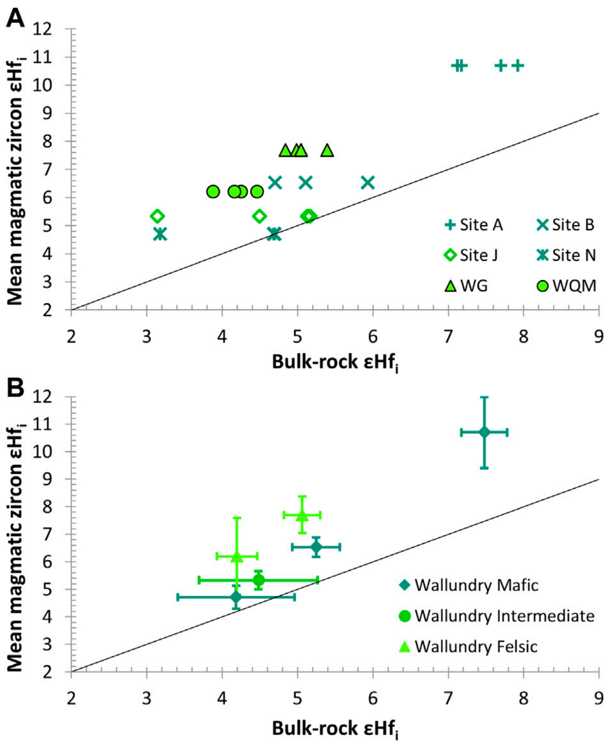

FIGURE 8
Comparison of bulk-rock and magmatic zircon Hf isotope compositions with reference to a 1:1 line. **(A)** Individual bulk-rock initial Hf isotope compositions of Wallundry Suite samples plotted against their weighted mean magmatic zircon compositions. **(B)** Mean bulk-rock εHf$_i$ (and 2σ uncertainty) plotted against weighted mean magmatic zircon εHf$_i$ (and 95% confidence level uncertainty) for the Wallundry Suite.

HREE similar to zircons, and LREE intermediate between titanite and zircon (Supplementary Material); however, the pattern of enrichment of HREE relative to LREE is more consistent with the involvement of zircon or xenotime (albeit very little given the extreme HREE enrichment in xenotime). The higher Zr concentration (13700 ppm) may be due to the inclusion of zircon, but the small amount required to reach that Zr concentration would be insufficient to achieve the observed REE pattern. The presence of a small positive Eu anomaly is not consistent with either titanite or zircon, but could reflect epidote; however, the Ti and REE concentrations are unusually

TABLE 3 Lu-Hf and Sm-Nd isotope data for mineral separates from Site J and the Woodlands Granite (WG). Bulk-rock and magmatic zircon data are included for comparison.

Sample	Phase*	Lu (ppm)	Hf (ppm)	^{176}Lu/^{177}Hf	^{176}Hf/^{177}Hf	εHf$_i$	Sm (ppm)	Nd (ppm)	^{143}Sm/^{144}Nd	^{143}Nd/^{144}Nd	εNd$_i$
Site J	**Bulk-rock_1**	*0.31*	*2.08*	*0.0211*	*0.282776*	**3.14**	*6.07*	*26.91*	*0.136*	*0.512545*	**1.48**
	Bulk-rock_2	0.30	1.53	0.0276	0.282883	**5.13**					
	Bulk-rock_3	0.30	2.17	0.0199	0.282805	**4.50**					
	Bulk-rock_4	0.30	1.97	0.0216	0.282837	**5.16**	6.42	28.34	0.1369	0.512532	**1.2**
	Zircon			0.00094	0.282681	**5.33**					
	Hornblende_1	1.66	9.69	0.0245	0.282856	**5.0**	27.50	89.87	0.1848	0.512670	**1.3**
	Hornblende_2	1.60	7.82	0.0294	0.282863	**3.9**	26.44	86.05	0.1855	0.512695	**1.8**
	Hornblende_3	1.67	7.86	0.0305	0.282867	**3.8**	27.36	89.48	0.1846	0.512674	**1.4**
	Epidote-Titanite_1		1.40				7.26	30.88	0.1420	0.512523	**0.8**
	Epidote-Titanite_2	0.34	12.8	0.00387	0.282691	**4.9**	2.64	12.55	0.1270	0.512533	**1.7**
	Fe-Ti oxide	0.16	9.83	0.0024	0.282285	**-9.1**	2.11	11.10	0.1149	0.511715	**−13.6**
WG	**Bulk-rock_1**	*0.85*	*8.66*	*0.0139*	*0.282768*	**4.84**	*9.05*	*44.25*	*0.124*	*0.512531*	**1.88**
	Bulk-rock_2	0.85	9.36	0.0130	0.282765 0.282764	**4.99**					
	Bulk-rock_3	0.85	8.93	0.0135	0.282771	**5.04**					
	Bulk-rock_4	0.86	9.73	0.0126	0.282764	**5.05**					
	Bulk-rock_5	0.88	9.85	0.0127	0.282775	**5.39**	9.56	42.67	0.1352	0.512531	**1.27**
	Zircon			0.00248	0.28276	**7.70**					
	Chlorite-Biotite_1	1.63	8.26	0.0282	0.282910	**5.9**	3.18	6.52	0.2940	0.512869	**−0.6**
	Chlorite-Biotite_2	2.78	19.22	0.0207	0.282821	**4.8**	9.82	25.53	0.2323	0.512785	**1.1**
	Chlorite-Biotite_3	2.22	21.13	0.0151	0.282778	**4.9**	10.82	29.22	0.2236	0.512751	**0.9**
	Titanite-Epidote	29.8	197.0	0.0216	0.282849	**5.5**					

* Numbers refer to the aliquot numbers used in Tables 1 and Table 2 for bulk-rock powders, and to distinguish different mineral separates.

high and Sr too low for epidote. The small positive Ce anomaly could reflect the involvement of zircon.

The epidote-titanite separates from Site J have similar REE contents and patterns to those acquired via LA-ICPMS for epidote from thin-sections (Supplementary Material), although the relative flatness of the LREE (if not LREE abundance) is more consistent with titanite. Comparison of the trace element compositions for the separates with epidote and titanite compositions on a "spider diagram" highlights departures of the mineral separates from what would be expected for a pure epidote analysis (Supplementary Material). High, Nb, Ta, Zr and Hf and low Pb and Sr could be accounted for by the presence of titanite. Rb and Ba contents are at the upper limits of the ranges for both titanite and epidote.

The Ti concentration measured in the Fe-Ti oxide separate from sample J is ~19 wt%, which is approximately two-thirds of the concentration expected for pure ilmenite, but could reflect hematite-ilmenite solid solution in the grains. Alternatively, minor inclusions have been observed in the ilmenite grains when viewed under reflected light and these may also be responsible for 'diluting' the measured Ti content. Certainly, the Ca concentration of ~8000 ppm (higher than any other trace element measured in this separate) is unusual and is possibly attributed to titanite inclusions. Chalcopyrite is observed in petrographic thin section, sometimes attached to or included in ilmenite; however, the Cu concentration (39 ppm) does not suggest the presence of significant chalcopyrite in the separate. The trace element pattern for the Fe-Ti oxide separate is broadly similar to ilmenite compositions when plotted on a "spider diagram"; however, the separate is enriched in Th, La, Ce and Nd and to a lesser extent Ba, U, Sr and Y (Supplementary Material).

For both samples, the εHf$_i$ values of hornblende (biotite-chlorite pseudomorphs after primary amphibole in the case of WG) and titanite-epidote separates (where available) are bracketed between the zircon LA-ICPMS values and the lowest repeat bulk-rock

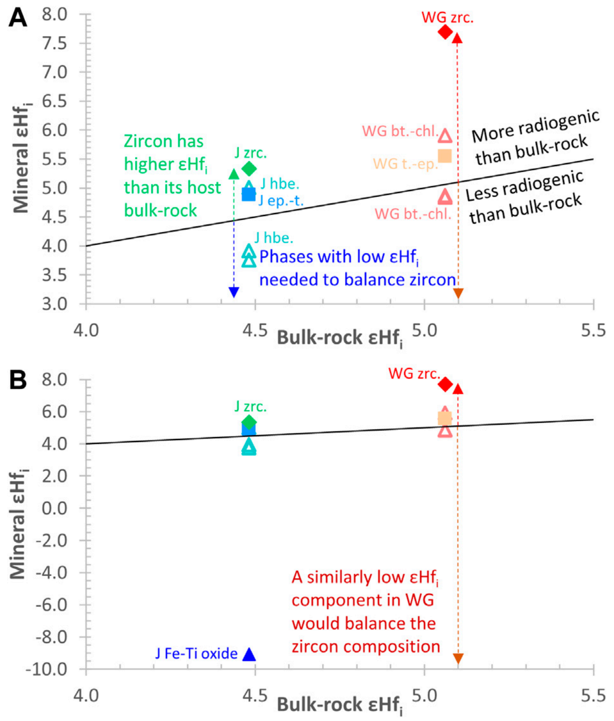

FIGURE 9
Magmatic zircon and mineral separate Hf isotope compositions from the Woodlands Granite and Site J of the MGD plotted against their host bulk-rock compositions. A 1:1 line is shown for reference. **(A)** To balance the radiogenic Hf in magmatic zircon, the bulk-rock samples must contain complementary low εHfi phases, which would plot below the 1:1 line. Among the various mineral separates some capture such a component, while others are intermediate between zircon and bulk-rock. **(B)** The clearest example of a separate with sufficiently low εHfi to balance the contribution of zircon to the bulk-rock Hf budget is the Fe-Ti oxide separate from Site J.

values (Table 3). Similarly, the same mineral separates record εNd$_i$ within one to two ε units of the bulk-rock compositions (one biotite-chlorite separate from WG, which is 1.9 εNd units lower than the lowest bulk-rock analysis, deviates the most). Crucially, one mineral separate, the Fe-Ti oxides from sample J, has Nd and Hf isotope compositions unlike any other analysis. With εHf$_i$ = −9.1 and εNd$_i$ = −13.6, the Fe-Ti oxide phases are distinctly out of equilibrium with the zircon and other melt precipitated phases, and their compositions would account for the discrepancy observed between bulk-rock and zircon Hf isotope compositions (Figure 9).

5 Discussion

5.1 The complex geochemistry of the wallundry suite

Many features of the Wallundry Suite petrography and geochemistry indicate that fractional crystallisation was an important process in the formation of this suite: cumulus-intercumulus relationships between plagioclase and amphiboles (Figure 2D); relicts of early-formed pyroxenes (Figure 2C); inflections and turning points in major and trace elements trends (Figures 3, 4), suggesting sequential appearance of crystallising phases. The isotopic variability exhibited by the magmatic zircon attests to an isotopically evolving melt, suggestive of crustal contamination in the petrogenetic history.

The isotopic similarity of the zircon populations from coarse-grained MGD, WG and WQM samples and the contrast with the more scattered data from the fine-grained, marginal lithology (Site A) could indicate that the dominant compositional group represent a parental magma that underwent fractional crystallisation to produce the range of samples observed, and that Site A represents a portion of the pluton affected by an additional process (such as interaction with meteoric water) that altered the isotope compositions and generated the marked scatter. This would, however, require a process that caused scatter in O-isotopic compositions *and* Hf-isotopic compositions in zircons. Although the presence of strongly sericitised plagioclase in sample A suggests the scatter in O isotopes could be due to alteration processes, such processes would not be expected to generate the observed scatter in the Hf isotope compositions, due to the slow diffusion and effectively immobile nature of Hf (Cherniak et al., 1997). Alternatively, the samples could be part of an assimilation-fractional crystallisation trend in which the low $\delta^{18}O$ and high $^{176}Hf/^{177}Hf$ of the zircons from the fine-grained sample represent a less contaminated (but heterogeneous) melt composition than those represented by the zircon populations, with the higher $\delta^{18}O$ and lower $^{176}Hf/^{177}Hf$, found in the coarser-grained samples. Either of the explanations for the diverse zircon O and Hf isotope compositions of the suite must also account for the apparent entrainment of older zircons into the WQM alone and their remarkable isotopic similarity to the dominant, younger WQM zircons. The older 'large grain' zircon group may have originated from an earlier magmatic pulse from the same source as that which produced the dominant zircon O-Hf isotope compositions of the Wallundry Suite; or their entrainment represents the contamination of the magma that formed the WQM, causing the melt to reach an isotopic composition essentially equivalent (coincidentally) to that of the zircons in the contaminant.

The newly acquired Sr-Nd-Hf bulk-rock isotope data further demonstrate the isotopic variability of the suite, and the correlation between these isotope systems adds to the evidence suggesting progressive evolution of the magma system by assimilation processes (Figure 7). It becomes apparent, however, by comparing the various sources of isotope data with the major and trace element data, that a straightforward combination of assimilation and fractional crystallisation (with isotope and trace element chemistry changing continuously with major element variations) is inadequate to explain the data. Two granitoids (WG and WQM) are isotopically similar to some of the most felsic samples of the MGD, despite being very different chemically. Sample L (52% SiO_2) is isotopically similar to the most mafic samples (A and H, ~47% SiO_2). The MG seems to have evolved both isotopically and chemically, being the most felsic sample and having the lowest εNd$_i$ and εHf$_i$ values. The grouping of samples into 'mafic', 'intermediate' and 'felsic' groups in Figure 7 highlights this apparent decoupling between the evolution of Sr and Nd isotopes and the changes in major element compositions in the suite.

This is also born out in the Hf isotope data. Plotting εHf$_i$ against MgO content (Figure 10A) shows that a wide range of samples have very similar Hf isotope compositions (εHf$_i$ around 4–5), and sample L again plots off-trend as an isotopically primitive but chemically

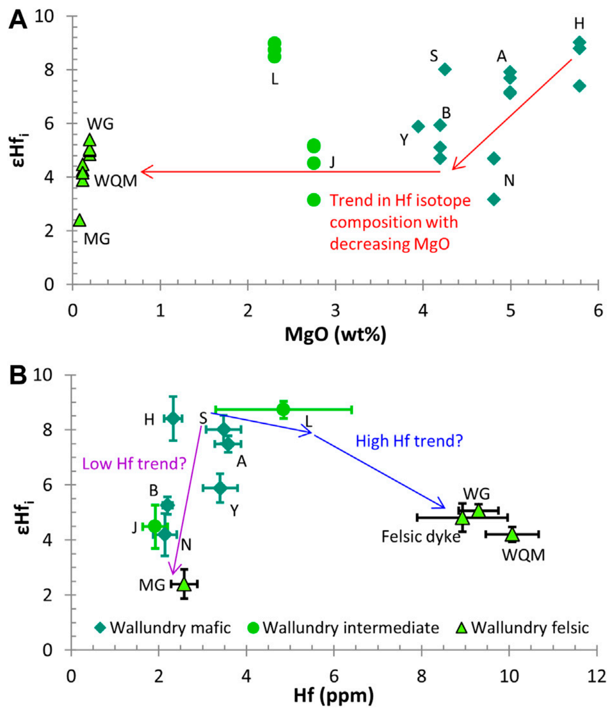

FIGURE 10
(A) The Hf isotope compositions plotted against MgO content. Note that the mafic samples exhibit a wide range of both MgO (a third of the total range) and εHf$_i$ and that in the range of εHf$_i$ = four to six mafic, intermediate and felsic samples are represented. **(B)** The graph of εHf$_i$ *versus* Hf concentration demonstrates that there is no simple relationship between the Hf isotope composition and trace and major element geochemistry. This graph hints at the presence of more than one trend in the evolution of the suite. There is a main "low Hf" trend from mafic, isotopically primitive samples through to the felsic, isotopically evolved Mayfair Granite, but there are also samples with higher Hf concentrations that suggest additional magma evolution pathways.

intermediate composition. A graph of εHf$_i$ *versus* Hf concentration (Figure 10B) hints at the presence of at least two trends. From the most mafic and isotopically primitive samples (A and H) a low Hf trend seems to extend through mafic and intermediate samples to the felsic MG and a high Hf trend seems to extend through sample L and into the other granitoids (WG, WQM and the felsic dyke). Alternatively, the low Hf samples could reflect an AFC trend, with the high Hf samples resulting from later fractional crystallisation of different batches along that trend.

Thus, isotope data combined with major and trace element data point to different degrees of contamination in different samples, different degrees of fractional crystallisation and some decoupling between the two. A possible scenario based on this would be a two-level petrogenetic model. Firstly, assimilation accompanied by some fractional crystallisation occurs below the emplacement level, producing diverse magma batches. Secondary processing via fractional crystallisation alone might occur multiple times as these batches ascend and are emplaced. The somewhat random distribution of granitoids around the gabbro-diorite body, the discovery of a felsic dyke in the south of the MGD that is similar to the WG and hand specimens (albeit not *in situ*) that show mingling textures support intrusion in batches.

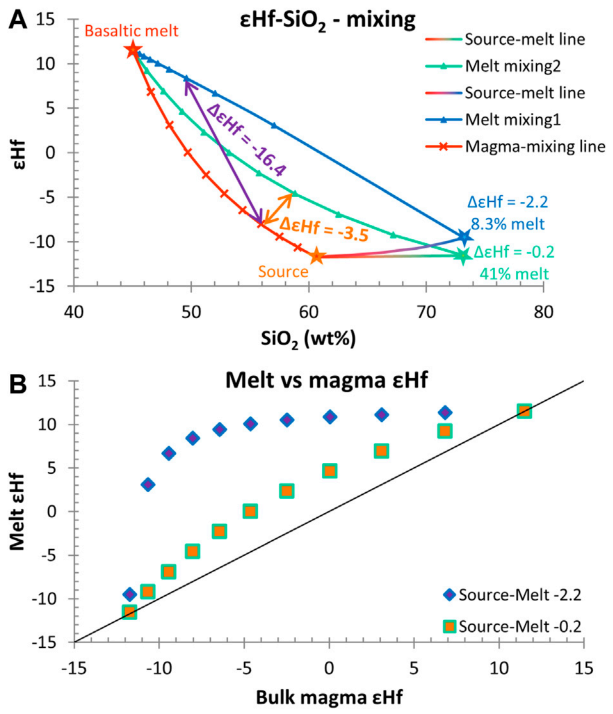

FIGURE 11
Magma-melt relationships for the simple mixing of basaltic melt with bulk incorporation of a partially melted sediment. **(A)** Relationships between mixing endmembers in SiO$_2$-Hf isotope space. Overall the mixture is between basalt and the sediment ("Source"). The sediment has a melt component that can mix with the basaltic melt. Two different possible melts (connected to the bulk-sediment by the "source-melt lines") are shown along with the two different "melt mixing lines" that show the composition of the mixed melt at increments that match those of the overall magma mixing. The compositions of the sedimentary components are modelled by applying the disequilibrium melting approach of Iles et al. (2018) to biotite dehydration (Vielzeuf and Holloway, 1988) of a metapelite (Bea and Montero, 1999). These relationships generate *negative* ΔεHf$_i^{\text{magma-melt}}$ values (mostly) because the sediment is much less radiogenic than the basalt and the mixed magma contains both solid (contaminant restite) and melt components of the sediment whereas the mixed melt only contains the melt component. Note that for very high fractions of sediment in the magma mixture of the second melt case (ΔεHf$^{\text{source-melt}}$ = −0.2, 41% melt) the ΔεHf$_i^{\text{magma-melt}}$ values are very small negative values. **(B)** For the two different melt cases, the relationship between the Hf isotope composition of the magma and its melt is shown, relative to a 1:1 line. Note that the maximum differences between magma and melt are at the intermediate degrees of mixing.

Although such a model mostly reconciles the field observations, petrography and bulk-rock major and trace element data with the bulk-rock isotope data, it does not account for the disequilibrium between bulk-rock and magmatic zircon Hf isotope composition and the intra-sample Nd-Hf isotope heterogeneity. The highly evolved Nd and Hf isotope of the Fe-Ti oxide separate explains why bulk-rock samples would have less radiogenic Hf isotope compositions than the zircon, but also adds complexity to the petrogenesis. With εHf$_i$ = −9.1 and εNd$_i$ = −13.6, the Fe-Ti oxide must be derived from an unmelted (restitic) component of crustal material (possibly sedimentary in origin), which provides strong support for the role of assimilation, but complicating it by requiring that the contaminant is only partially melted and that the solids do not equilibrate with the mixed melt. A petrogenetic model for the Wallundry Suite must, therefore, account for the complex combination of assimilation and fractional crystallisation represented by the trends in major element, trace element and isotope data, the partially molten nature of the contaminant and the mismatch between the bulk and zircon Hf isotope data. This is well beyond the assumptions and framework of classical DePaolo (1981) AFC or EC-AFC (Bohrson and Spera, 2001; Spera and Bohrson, 2001). The diverse options that can be explored with the Magma Chamber Simulator (Bohrson et al., 2014; Bohrson et al., 2020; Heinonen et al., 2020) could potentially address some aspects of the Wallundry Suite petrogenesis; however, MCS does not account for the behaviour of zircon in the magma and wallrock subsystems.

Crucially, the petrogenetic model must address why the Wallundry Suite samples have *negative* $\Delta\varepsilon Hf^{bulk\text{-}zrc}$ values—that is, why would the melt from which zircon crystallises have more radiogenic Hf than the magma dominated by earlier crystallised minerals given that assimilation of common continental crust lithologies (with generally much less radiogenic Hf than the most primitive samples) should cause melt evolution from more radiogenic to less radiogenic Hf isotope compositions? Keeping in mind the evidence (Nd and Hf isotope compositions of the Fe-Ti oxide) that unmelted mature material from continental crustal rocks is present in the samples, this question can be examined through the simplified model illustrated in Figure 11. Setting aside the role of fractional crystallisation, assimilation of partially molten sediment by a basaltic magma is simplified to the three-component mixing of basaltic melt, sedimentary melt and sedimentary restite. The proportion of sedimentary restite relative to sedimentary melt is fixed by the degree of melting, but the ratio of basalt to sedimentary contaminant (melt + restite) is a free parameter. Previous work (Tang et al., 2014; Iles et al., 2017; Iles et al., 2018; Wang et al., 2018; Wolf et al., 2019) has demonstrated that partial melting in the crust may generate melt-restite Hf isotopic disequilibrium; therefore, the sedimentary melt and unmelted components need not have the same isotope composition. With the exception of extreme positive $\Delta\varepsilon Hf^{source\text{-}melt}$ values, a sedimentary restite would be far less radiogenic than basaltic melt, and thus also less radiogenic than a mix between sediment melt and basalt; therefore, the εHf value of a mixed magma (basalt + sedimentary restite + sedimentary melt) would be lower than the εHf value of the mixed melt (basaltic + sedimentary melt). This holds even at $\Delta\varepsilon Hf^{source\text{-}melt}$ ~0, and negative $\Delta\varepsilon Hf^{magma\text{-}melt}$ values will arise also for positive $\Delta\varepsilon Hf^{source\text{-}melt}$ values, as long as the proportion of basaltic melt in the mixture is high enough (the basalt fraction required is dependent on the Hf concentrations of the components and the positive $\Delta\varepsilon Hf^{source\text{-}melt}$ value).

This simplified case provides a conceptual understanding of the way the bulk-rock–zircon Hf isotope discrepancy arises and is tied to the assimilation of a partially molten crustal rock. It does not, however, account for the role of fractional crystallisation. Furthermore, the bulk-rock–zircon discrepancy in the granitic members of the suite is outside of what can be accounted for by this simple mixing because they have higher SiO_2 contents than common sediments (Wyborn and Chappell, 1983; Vielzeuf and Holloway, 1988; Patiño Douce and Johnston, 1991; Turner et al., 1993; Vielzeuf and Montel, 1994). The felsic nature and high Hf concentrations of the WQM and WG, in particular, require that fractional crystallisation be integrated into the model. The following section discusses some additional considerations and constraints on these complexities.

5.2 Constraints of assimilation and fractional crystallisation

Considering the possibility that the mixing illustrated in Figure 11 may be accompanied by crystallisation and, by extension, liquid-crystal sorting, there are various factors that would play a role in the production of the observed bulk-rock vs. zircon Hf isotopic disequilibrium. These are considered here.

One factor already considered in Figure 11 is the melt fraction (f = 0–1) of the contaminant (sedimentary rock in the mixing example). As illustrated, with increasing degree on melting, the degree of magma-melt isotopic disequilibrium decreases (although this will be complicated by disequilibrium in contaminant melting). In the example, for f = 0.41 the maximum $\Delta\varepsilon Hf_i^{magma\text{-}melt}$ value is ~5, whereas the largest $\Delta\varepsilon Hf_i^{bulk\text{-}zrc}$ values recorded by the samples are ~3, suggesting a similar or higher degree of melting of the contaminant is required for the Wallundry Suite. A ratio, R, defines the mass of melt crystallised incrementally during the process relative to the mass of sediment incrementally assimilated, and this would have an important impact on these relationships.

Crystallisation will affect the melt compositional evolution, but the magma trend in Figure 11 will not change unless crystals are removed from the magma. Without crystal segregation, the magma will increase in mass and crystallinity and decrease in melt mass as crystallisation progresses (unless R and f are such that more melt is added from the contaminant than is crystallised at each increment). The melt composition will be affected by the compositions (Hf contents and Hf isotope ratios) of the assimilated melt and the primary magma, as well as by the partitioning behaviour of Hf between the melt and the crystals. Additionally, the partitioning is affected by phase variations in the crystal assemblage and whether or not equilibrium is achieved between melt and unsegregated early crystals (fractional crystallisation of the melt phase could occur via chemical isolation of earlier-formed grains rather than crystal settling).

Although a series of magmas could be produced through assimilation-crystallisation without crystal segregation (and this would be analogous to the mixing relations shown in Figure 11), batches of this magma evolution could subsequently undergo partial segregation. Compositions between the magma trend and the melt trend would represent magma batches that have undergone some degree of melt segregation (simple liquid-crystal fractionation). This would lower the magnitude of melt-magma disequilibrium, since magmas would become more melt rich. Samples would then plot between the 1:1 line and the mixing trends in Figure 11B. Alternatively, any composition along the magma trend could be selected to become the parent magma for fractional crystallisation at the emplacement level to yield chemically evolved compositions (with similar implications for the positions of samples in Figure 11B). Similarly, crystal segregation concurrent with crystallisation adds another layer of complexity to the system evolution and the possible relationships between magma and melt major and trace element and isotope compositions.

Some more specific considerations can also be made. Given the compositions of the Wallundry samples, the primary melt is assumed to be a hot, basaltic melt, in which Zr and Hf bulk partition coefficients (D_{Zr} and D_{Hf}) would be initially below unity (Zr and Hf are incompatible). The AFC process causes Zr concentration in the melt to increase while D_{Zr}<1, but this would eventually lead to Zr saturation, causing the onset of zircon crystallisation and a change in

TABLE 4 Oxygen isotope compositions of zircon populations and bulk-rock samples, and the percent of contaminant present in the sample assuming binary mixing.

Samples	Mean zircon $\delta^{18}O$	1 s.d	2σ ext[a]	Bulk-rock[b] $\delta^{18}O$	Contaminant %[c]	2σ[d]
MGD Site A	7.48	0.24	0.12	7.87	29	17
MGD Site B	8.16	0.19	0.11	8.57	38	19
MGD Site J	8.42	0.18	0.10	8.87	42	20
MGD Site N	8.19	0.21	0.11	8.63	39	19
Woodlands Granite	8.33	0.23	0.12	10.11	57	24
Windover Quartz Monzodiorite	8.36	0.28	0.14	10.20	58	25

[a] The 2σ external precision is calculated by adding in quadrature the 2s.e. Uncertainty of the sample, the 2s.e. Uncertainty in the calibration reference material for the analytical session (2s.e. of TEMORA 2 = 0.06‰), and the 2σ uncertainty in the accepted composition of the reference material (TEMORA 2 $\delta^{18}O$ = 8.20 ±0.03‰).

[b] Bulk-rock $\delta^{18}O$ values have been calculated according to the formula of Valley et al. (2005): δ^{18}Ozircon—δ^{18}Obulk ≈ -0.0612(SiO2) + 2.5, where SiO2 is in wt% for the bulk-rock.

[c] Calculated assuming the bulk-rock is the product of binary mixing between a basaltic melt and a sedimentary contaminant, according to % = 100*(δ^{18}Osample- δ^{18}Omantle)/(δ^{18}Ocontaminant-δ^{18}Omantle).

[d] Calculated by propagating the 2σ uncertainties in the samples and endmembers, with the 2s.d. of the δ18O of mantle-derived zircon (0.6; Valley et al., 2005) used for the mantle endmember.

Zr and Hf partitioning; therefore, it is assumed that both D_{Zr} and D_{Hf} should increase to values greater than one at some point during the AFC process. Zircon crystallisation would act to deplete the melt in Hf. An important effect of the decreasing Hf content is that the melt in the contaminant has more weight in the Hf isotope budget, causing progressively larger decreases in the εHf value of the mixed melt (until the mixed melt approaches the contaminant melt in isotope composition, when the decreases in εHf value become smaller). This highlights both the importance of the role of zircon in future attempts to model this system and the possibility for nuances that cannot be captured in the simple mixing model.

As noted previously the more granitic members of the suite (WG, WQM, the felsic dyke & MG) are too felsic for the mixing model in Figure 11 to account for their compositions. Furthermore, Figure 10 suggests some may belong to a different trend than the MGD, or involve additional fractionation. Two points should be highlighted. Firstly, the magmatic zircon in WQM is much more heterogeneous in Hf isotope composition than the zircon in WG (and in most MGD samples) and is actually within uncertainty of the WG zircon (at the 95% confidence level). Such heterogeneity implies that the sample records a range of melt compositions, and thus should not be modelled as a single contaminated magma and coexisting melt. Secondly, The MG is likely the product of more extensive fractional crystallisation of a contaminated magma or melt, which could be consistent with the low Nd content (~3.4 ppm), high SiO_2 (~75 wt%) and extreme Rb/Sr (26.7; Wormald, 1993).

The oxygen isotope data may provide additional constraints upon the system's evolution. As a first approximation, the oxygen isotope data could be modelled as resulting from binary mixing of mantle-derived and sedimentary endmembers. Assuming a $\delta^{18}O$ value of 5.5‰ for basaltic magma (Eiler, 2001; Valley et al., 2005) and $\delta^{18}O$ = 13.6 ±1.6‰ (2s.d.) for the sedimentary contaminant (the average of metasedimentary rocks associated with the Cooma Granodiorite; Munksgaard, 1988), the proportion of contamination required to produce the oxygen isotope compositions of the bulk-rock samples can be estimated. The oxygen isotope compositions for magmatic zircon from the Wallundry suite are shown in Table 4, as are the corresponding bulk-rock $\delta^{18}O$ values, which range from 7.87 ±0.12‰ to 10.20 ±0.20‰ (2σ external precision; see Table caption for details). As shown in Table 4, the calculated proportion of contaminant involved each sample ranges from 29 ±17% for sample A to 58 ±25% for the WQM sample. It is expected that higher degrees of assimilation will be calculated assuming binary mixing compared with AFC (Taylor, 1980; Aitcheson and Forrest, 1994); therefore, the calculated amounts of assimilation are likely overestimates, particularly for the most evolved samples.

6 Conclusion

Zircon O-Hf and bulk-rock Sr-Nd-Hf isotope data indicate open-system magmatic processes in the formation of the Wallundry Suite. This magmatic system evolved via assimilation and liquid-crystal fractionation processes (i.e., fractional crystallisation and variations thereof) with decoupling between the two at some stages.

Field observations of the Wallundry Suite indicate that it was constructed via multiple magma injections. Petrographic observations in concert with major and trace element data indicate the involvement of fractional crystallisation in generating the different members of the suite (MGD, WQM, WG and MG) and the inter-sample heterogeneity (particularly in the MGD). The zircon O-Hf data demonstrate that the suite underwent some degree of contamination during its formation; however, these data are only weakly related to the lithological and chemical character of the samples. Likewise, the newly acquired bulk-rock Sr-Nd-Hf isotope data indicate different degrees of assimilation of crustal material by a basaltic parent melt and different degrees of fractional crystallisation together produce lithologically similar samples with diverse isotopic compositions, as well as isotopically similar samples with distinct lithologies and chemical compositions.

Comparison of bulk-rock and magmatic zircon Hf isotope compositions permit deeper insights into the magmatic system. The data reveal isotopic disequilibrium that requires that the samples were mixtures of isotopically diverse solids and melts. Particularly, the negative $\Delta\varepsilon Hf^{magma-melt}$ values in the samples led our investigation to uncover details about assimilation that could not be inferred from O-Hf-Sr-Nd-Hf trends. Isotopic analyses of mineral separates demonstrate that the more isotopically evolved component required to account for this disequilibrium between melt (recorded by zircon) and magma (captured by the bulk-rock) was provided by Fe-Ti oxide crystals with Nd-Hf isotope compositions that can only be explained as unmelted mature crustal material. Thus, the isotope data have indicated that the material assimilated by the basaltic parent was only partially melted.

This study illustrates that combined assimilation and fractional crystallisation (with variable degrees of coupling/decoupling) can give rise to highly complex geochemical relationships, especially considering the possibility that the material being assimilated need neither be completely melted nor in isotopic equilibrium. While this potential complexity makes open system processes challenging probe geochemically, we demonstrate that combining bulk-rock, mineral separate and *in situ* zircon isotope data can disentangle this complexity. The comparison of bulk rock and magmatic zircon Hf isotope composition is particularly useful in this regard.

Data availability statement

The original contributions presented in the study are included in the article/Supplementary Material, further inquiries can be directed to the corresponding author.

Author contributions

KI was responsible for data acquisition, analysis and interpretation as well as writing and proofreading the manuscript. JH and JW contributed to the study design, the development of ideas and refinement of interpretation as well as proofreading the manuscript. JW was also responsible in part for the LA-MC-ICPMS Hf isotope data acquisition.

Funding

KI was supported by an Australian Postgraduate Award while undertaking this research as part of his Ph.D. at The University of Melbourne. The preparation and submission of this research article is supported by Academy of Finland grant 333813 awarded to KI.

Acknowledgments

The authors are indebted to the team at Geoscience Australia, coordinated by Keith Sircombe, enabling sample collection, geochemical analysis and zircon geochronology for the undergraduate research project of KI, upon which this study builds. Many thanks also to Ian Williams who was instrumental in acquiring the O isotope data used in this study. We are very grateful to Roland Maas, who played a critical role in the acquisition of the solution mode radiogenic isotope data, which are central to this study. Thanks also are owed to Alan Greig who performed trace element analyses at UM.

Conflict of interest

The authors declare that the research was conducted in the absence of any commercial or financial relationships that could be construed as a potential conflict of interest.

Publisher's note

Supplementary material

The Supplementary Material for this article can be found online at: https://www.frontiersin.org/articles/10.3389/feart.2023.1101331/full#supplementary-material

References

Acosta-Vigil, A., Buick, I. S., Hermann, J., Cesare, B., Rubatto, D., London, D., et al. VI. (2010). Mechanisms of crustal anatexis: A geochemical study of partially melted metapelitic enclaves and host dacite, SE Spain. *J. Petrology* 51, 785–821. doi:10.1093/petrology/egp095

Aitcheson, S. J., and Forrest, A. H. (1994). Quantification of crustal contamination in open magmatic systems. *J. Petrology* 35, 461–488. doi:10.1093/petrology/35.2.461

Allègre, C. J., and Minister, J. F. (1978). Quantitative models of trace element behavior in magmatic processes. *Earth Planet. Sci. Lett.* 38, 1–25. doi:10.1016/0012-821x(78)90123-1

Allen, C. M., and Campbell, I. H. (2012). Identification and elimination of a matrix-induced systematic error in LA-ICP-MS 206Pb/238U dating of zircon. *Chem. Geol.* 332-333, 157–165. doi:10.1016/j.chemgeo.2012.09.038

Ayres, M., and Harris, N. (1997). REE fractionation and Nd-isotope disequilibrium during crustal anatexis: Constraints from himalayan leucogranites. *Chem. Geol.* 139, 249–269. doi:10.1016/s0009-2541(97)00038-7

Bea, F., and Montero, P. (1999). Behavior of accessory phases and redistribution of Zr, REE, Y, Th, and U during metamorphism and partial melting of metapelites in the lower crust: An example from the kinzigite formation of ivrea-verbano, NW Italy. *Geochimica Cosmochimica Acta* 63, 1133–1153. doi:10.1016/s0016-7037(98)00292-0

Bea, F., Pereira, M. D., and Stroh, A. (1994). Mineral/leucosome trace element partitioning in a peraluminous migmatite (a laser ablation-ICP-MS study). *Chem. Geol.* 117, 291–312. doi:10.1016/0009-2541(94)90133-3

Bea, F., Montero, P., and Ortega, M. (2006). A LA-ICP-MS evaluation of Zr reservoirs in common crustal rocks: Implications for Zr and Hf geochemistry, and zircon-forming processes. *Can. Mineralogist* 44, 693–714. doi:10.2113/gscanmin.44.3.693

Bea, F. (1996). Residence of REE, Y, Th and U in granites and crustal protoliths; implications for the chemistry of crustal melts. *J. Petrology* 37, 521–552. doi:10.1093/petrology/37.3.521

Beard, J. S., Ragland, P. C., and Crawford, M. L. (2005). Reactive bulk assimilation: A model for crust-mantle mixing in silicic magmas. *Geology* 33, 681–684. doi:10.1130/g21470ar.1

Belousova, E. A., Griffin, W. L., O'Reilly, S. Y., and Fisher, N. I. (2002). Apatite as an indicator mineral for mineral exploration: Trace-element compositions and their relationship to host rock type. *J. Geochem. Explor.* 76, 45–69. doi:10.1016/s0375-6742(02)00204-2

Bingen, B., Demaiffe, D., and Hertogen, J. (1996). Redistribution of rare Earth elements, thorium, and uranium over accessory minerals in the course of amphibolite to granulite facies metamorphism: The role of apatite and monazite in orthogneisses from southwestern Norway. *Geochimica Cosmochimica Acta* 60, 1341–1354. doi:10.1016/0016-7037(96)00006-3

Bizzarro, M., Baker, J. A., and Ulfbeck, D. (2003). A new digestion and chemical separation technique for rapid and highly reproducible determination of Lu/Hf and Hf isotope ratios in geological materials by MC-ICP-MS. *Geostand. Newsl.* 27, 133–145. doi:10.1111/j.1751-908x.2003.tb00641.x

Black, L. P., Kamo, S. L., Allen, C. M., Aleinikoff, J. N., Davis, D. W., Korsch, R. J., et al. (2003). TEMORA 1: A new zircon standard for phanerozoic U–Pb geochronology. *Chem. Geol.* 200, 155–170. doi:10.1016/s0009-2541(03)00165-7

Black, L. P., Kamo, S. L., Allen, C. M., Davis, D. W., Aleinikoff, J. N., Valley, J. W., et al. (2004). Improved 206Pb/238U microprobe geochronology by the monitoring of a trace-element-related matrix effect; SHRIMP, ID–TIMS, ELA–ICP–MS and oxygen isotope documentation for a series of zircon standards. *Chem. Geol.* 205, 115–140. doi:10.1016/j.chemgeo.2004.01.003

Bohrson, W. A., and Spera, F. J. (2001). Energy-constrained open-system magmatic processes II: Application of energy-constrained assimilation-fractional crystallization (EC-AFC) model to magmatic systems. *J. Petrology* 42, 1019–1041. doi:10.1093/petrology/42.5.1019

Bohrson, W. A., Spera, F. J., Ghiorso, M. S., Brown, G. A., Creamer, J. B., and Mayfield, A. (2014). Thermodynamic model for energy-constrained open-system evolution of crustal magma bodies undergoing simultaneous recharge, assimilation and crystallization: The magma chamber simulator. *J. Petrology* 55, 1685–1717. doi:10.1093/petrology/egu036

Bohrson, W. A., Spera, F. J., Heinonen, J. S., Brown, G. A., Scruggs, M. A., Adams, J. V., et al. (2020). Diagnosing open-system magmatic processes using the magma chamber simulator (MCS): Part I—major elements and phase equilibria. *Contributions Mineralogy Petrology* 175, 104. doi:10.1007/s00410-020-01722-z

Bouvier, A., Vervoort, J. D., and Patchett, P. J. (2008). The Lu-Hf and Sm-Nd isotopic composition of CHUR: Constraints from unequilibrated chondrites and implications for the bulk composition of terrestrial planets. *Earth Planet. Sci. Lett.* 273, 48–57. doi:10.1016/j.epsl.2008.06.010

Bowen, N. L. (1919). Crystallization-differentiation in igneous magmas. *J. Geol.* 27, 393–430. doi:10.1086/622669

Bowen, N. L. (1947). Magmas. *Bull. Geol. Soc. Am.* 58, 263–280. doi:10.1130/0016-7606(1947)58[263:m]2.0.co;2

Brown, M. (2007). Crustal melting and melt extraction, ascent and emplacement in orogens: Mechanisms and consequences. *J. Geol. Soc.* 164, 709–730. London. doi:10.1144/0016-76492006-171

Chappell, B. W. (1984). Source rocks of I- and S-type granites in the Lachlan Fold Belt, southeastern Australia. *Philosophical Trans. R. Soc. Lond.* A310, 693–706. doi:10.1098/rsta.1984.0015

Chappell, B. W., and Stephens, W. E. (1988). Origin of infracrustal (I-type) granite magmas. *Trans. R. Soc. Edinb. Earth Sci.* 79, 71–86. doi:10.1017/s0263593300014139

Chappell, B. W., and White, A. J. R. (1974). Two contrasting granite types. *Pac. Geol.* 8, 173–174.

Chappell, B. W., White, A. J. R., and Wyborn, D. (1987). The importance of residual source material (restite) in granite petrogenesis. *J. Petrology* 28, 1111–1138. doi:10.1093/petrology/28.6.1111

Chappell, B. W., Bryant, C. J., Wyborn, D., White, A. J. R., and Williams, I. S. (1998). High- and low-temperature I-type granites. *Resour. Geol.* 48, 225–235. doi:10.1111/j.1751-3928.1998.tb00020.x

Chauvel, C., Bureau, S., and Poggi, C. (2011). Comprehensive chemical and isotopic analyses of basalt and sediment reference materials. *Geostand. Geoanalytical Res.* 35, 125–143. doi:10.1111/j.1751-908x.2010.00086.x

Cheong, C.-S., Ryu, J.-S., and Jeong, Y.-J. (2013). Simultaneous multiple collector-ICP-MS measurement of Nd isotopic composition and Sm/Nd ratio in geological reference materials by interference corrections and external calibration using matrix-matched standards. *Geosciences J.* 17, 389–395. doi:10.1007/s12303-013-0056-5

Cherniak, D. J., Hanchar, J. M., and Watson, E. B. (1997). Diffusion of tetravalent cations in zircon. *Contributions Mineralogy Petrology* 127, 383–390. doi:10.1007/s004100050287

Chu, Z.-Y., Chen, F.-K., Yang, Y.-H., and Guo, J.-H. (2009). Precise determination of Sm, Nd concentrations and Nd isotopic compositions at the nanogram level in geological samples by thermal ionization mass spectrometry. *J. Anal. Atomic Spectrom.* 24, 1534–1544. doi:10.1039/b904047a

Clemens, J. D., and Stevens, G. (2012). What controls chemical variation in granitic magmas? *Lithos* 134-135, 317–329. doi:10.1016/j.lithos.2012.01.001

Clemens, J. D., and Vielzeuf, D. (1987). Constraints on melting and magma production in the crust. *Earth Planet. Sci. Lett.* 86, 287–306. doi:10.1016/0012-821x(87)90227-5

Collins, W. J. (1996). Lachlan Fold Belt granitoids: Products of three-component mixing. *Trans. R. Soc. Edinb. Earth Sci.* 87, 171–181. doi:10.1017/s0263593300006581

Colombini, L. L., Miller, C. F., Gualda, G. A. R., Wooden, J. L., and Miller, J. S. (2011). Sphene and zircon in the highland range volcanic sequence (miocene, southern Nevada, USA): Elemental partitioning, phase relations, and influence on evolution of silicic magma. *Mineralogy Petrology* 102, 29–50. doi:10.1007/s00710-011-0177-3

DePaolo, D. J. (1981). Trace element and isotopic effects of combined wallrock assimilation and fractional crystallization. *Earth Planet. Sci. Lett.* 53, 189–202. doi:10.1016/0012-821x(81)90153-9

Driouch, Y., Béziat, D., Grégoire, M., Laguenini, F., Ben Abbou, M., Ntarmouchant, A., et al. (2010). Clinopyroxene trace element compositions of cumulate mafic rocks and basalts from the hercynian Moroccan central meseta: Petrogenetic implications. *J. Afr. Earth Sci.* 56, 97–106. doi:10.1016/j.jafrearsci.2009.05.007

Dufec, J., and Buchmann, O. (2010). Quantum magmatism: Magmatic compositional gaps generated by melt-crystal dynamics. *Geology* 38, 687–690. doi:10.1130/g30831.1

Eiler, J. M. (2001). "Oxygen isotope variations in basaltic lavas and upper mantle rocks," in *Stable isotope geochemistry*. Editors J. W. Valley and D. R. Cole (Berlin and Boston: Mineralogical Society of America and The Geochemical Society), 319–364. doi:10.2138/gsrmg.43.1.319

Gray, C. M. (1984). An isotopic mixing model for the origin of granitic rocks in southeastern Australia. *Earth Planet. Sci. Lett.* 70, 47–60. doi:10.1016/0012-821x(84)90208-5

Gregory, C. J., Buick, I. S., Hermann, J., and Rubatto, D. (2009). Mineral-scale trace element and U-Th-Pb age constraints on metamorphism and melting during the Petermann Orogeny (central Australia). *J. Petrology* 50, 251–287. doi:10.1093/petrology/egn077

Gregory, C. J., Rubatto, D., Hermann, J., Berger, A., and Engi, M. (2012). Allanite behaviour during incipient melting in the southern Central Alps. *Geochimica Cosmochimica Acta* 84, 433–458. doi:10.1016/j.gca.2012.01.020

Hagen, H., and Neumann, E.-R. (1990). Modeling of trace-element distribution in magma chambers using open-system models. *Comput. Geosciences* 16, 549–586. doi:10.1016/0098-3004(90)90015-l

Heinonen, J. S., Bohrson, W. A., Spera, F. J., Brown, G. A., Scruggs, M. A., and Adams, J. V. (2020). Diagnosing open-system magmatic processes using the magma chamber simulator (MCS): Part II—trace elements and isotopes. *Contributions Mineralogy Petrology* 175. N.PAG-N.PAG. doi:10.1007/s00410-020-01718-9

Heinonen, J. S., Iles, K. A., Heinonen, A., Fred, R., Virtanen, V. J., Bohrson, W. A., et al. (2021). "From binary mixing to magma chamber simulator: Geochemical modeling of assimilation in magmatic systems," in *Crustal magmatic system evolution*. Editors M. Masotta, C. Beier, and S. Mollo, 151–176.

Hermann, J. (2002). Allanite: Thorium and light rare Earth element carrier in subducted crust. *Chem. Geol.* 192, 289–306. doi:10.1016/s0009-2541(02)00222-x

Hervé, F., Calderón, M., Fanning, C. M., Pankhurst, R. J., and Godoy, E. (2013). Provenance variations in the Late Paleozoic accretionary complex of Central Chile as indicated by detrital zircons. *Gondwana Res.* 23, 1122–1135. doi:10.1016/j.gr.2012.06.016

Ickert, R. B., Mundil, R., Magee, C. W., and Mulcahy, S. R. (2015). The U-Th-Pb systematics of zircon from the bishop tuff: A case study in challenges to high-precision Pb/U geochronology at the millennial scale. *Geochimica Cosmochimica Acta* 168, 88–110. doi:10.1016/j.gca.2015.07.018

Iles, K. A., and Heinonen, J. S. (2022). Modelling the formation of linear geochemical trends using the magma chamber simulator: A case study of the Jindabyne granitoids, Lachlan Fold Belt, Australia. *J. Petrology* 63. doi:10.1093/petrology/egab102

Iles, K. A., Hergt, J. M., Sircombe, K. N., Woodhead, J. D., Bodorkos, S., and Williams, I. S. (2015). Portrait of a reference material: Zircon production in the Middledale gabbroic diorite, Australia, and its implications for the TEMORA standard. *Chem. Geol.* 402, 140–152. doi:10.1016/j.chemgeo.2015.02.036

Iles, K. A., Hergt, J., Woodhead, J., and Williams, I. S. (2017). "Isotopic disequilibrium in S-type granites," in *SGGMP benalla, 2017* (Victoria: Benalla).

Iles, K. A., Hergt, J. M., and Woodhead, J. D. (2018). Modelling isotopic responses to disequilibrium melting in granitic systems. *J. Petrology* 59, 87–113. doi:10.1093/petrology/egy019

Iles, K. A., Hergt, J. M., Woodhead, J. D., Ickert, R. B., and Williams, I. S. (2020). Petrogenesis of granitoids from the Lachlan Fold Belt, southeastern Australia: The role of disequilibrium melting. *Gondwana Res.* 79, 87–109. doi:10.1016/j.gr.2019.08.011

Iles, K. A. (2012). "Petrology, geochemistry and geochronology of the Middledale gabbroic diorite, new south wales, eastern Australia,". *School of Earth Sciences* (Melbourne: The University of Melbourne), 115.

Jang, Y. D., and Naslund, H. R. (2003). Major and trace element variation in ilmenite in the skaergaard intrusion: Petrologic implications. *Chem. Geol.* 193, 109–125. doi:10.1016/s0009-2541(02)00224-3

Keay, S. M., Collins, W. J., and McCulloch, M. T. (1997). A three-component Sr-Nd isotopic mixing model for granitoid Genesis, Lachlan Fold Belt, eastern Australia. *Geology* 25, 307–310. doi:10.1130/0091-7613(1997)025<0307:atcsni>2.3.co;2

Kemp, A. I. S., Hawkesworth, C. J., Foster, J. L., Paterson, B. A., Woodhead, J. D., Hergt, J. M., et al. (2007). Magmatic and crustal differentiation history of granitic rocks from Hf-O isotopes in zircon. *Science* 315, 980–983. doi:10.1126/science.1136154

Kemp, A. I. S., Hawkesworth, C. J., Collins, W. J., Gray, C. M., and Blevin, P. L., EIMF (2009). Isotopic evidence for rapid continental growth in an extensional accretionary orogen: The Tasmanides, eastern Australia. *Earth Planet. Sci. Lett.* 284, 455–466. doi:10.1016/j.epsl.2009.05.011

Li, C.-F., Wang, X.-C., Guo, J.-H., Chu, Z.-Y., and Feng, L.-J. (2016). Rapid separation scheme of Sr, Nd, Pb, and Hf from a single rock digest using a tandem chromatography column prior to isotope ratio measurements by mass spectrometry. *J. Anal. Atomic Spectrom.* 31, 1150–1159. doi:10.1039/c5ja00477b

Ludwig, K. R. (2008). *Isoplot 3.70 - a geochronological toolkit for microsoft* excel. Berkeley, California: Berkeley Geochronology Centre Special Publication No. 4.

Luhr, J. F., and Carmichael, I. S. E. (1980). The colima volcanic complex, Mexico: I. Post-Caldera andesites from volcán colima. *Contributions Mineralogy Petrology* 71, 343–372. doi:10.1007/bf00374707

Marsh, B. D. (2006). Dynamics of magmatic systems. *Elements* 2, 287–292. doi:10.2113/gselements.2.5.287

McBirney, A. R. (1979). "Effects of assimilation," in *Evolution of the igneous rocks: Fiftieth anniversary perspectives*. Editor H. S. Yoder (Princeton University Press).

McKenzie, D. (1985). The extraction of magma from the crust and mantle. *Earth Planet. Sci. Lett.* 74, 81–91. doi:10.1016/0012-821x(85)90168-2

McLeod, C. L., Davidson, J. P., Nowell, G. M., and de Silva, S. L. (2012). Disequilibrium melting during crustal anatexis and implications for modeling open magmatic systems. *Geology* 40, 435–438. doi:10.1130/g33000.1

Munksgaard, N. C. (1988). Source of the cooma granodiorite, new south wales - a possible role of fluid-rock interactions. *Aust. J. Earth Sci.* 35, 363–377. doi:10.1080/08120098808729454

Nehring, F., Foley, S. F., and Hőlttä, P. (2010). Trace element partitioning in the granulite facies. *Contributions Mineralogy Petrology* 159, 493–519. doi:10.1007/s00410-009-0437-y

Nielsen, R. L. (1989). Phase equilibria constraints on liquid lines of descent generated by paired assimilation and fractional crystallization: Trace elements and Sr and Nd isotopes. *J. Geophys. Res.* 94, 787–794. doi:10.1029/jb094ib01p00787

Pan, Y., and Fleet, M. E. (1996). Rare Earth element mobility during prograde granulite facies metamorphism: Significance of fluorine. *Contributions Mineralogy Petrology* 123, 251–262. doi:10.1007/s004100050154

Paterson, S., Memeti, V., Mundil, R., and Žák, J. (2016). Repeated, multiscale, magmatic erosion and recycling in an upper-crustal pluton: Implications for magma chamber dynamics and magma volume estimates. *Am. Mineralogist* 101, 2176–2198. doi:10.2138/am-2016-5576

Patiño Douce, A. E. (1995). Experimental generation of hybrid silicic melts by reaction of high-Al basalt with metamorphic rocks. *J. Geophys. Res.* 100, 15623–15639. doi:10.1029/94jb03376

Patiño Douce, A. E., and Johnston, A. D. (1991). Phase equilibria and melt productivity in the pelitic system: Implications for the origin of peraluminous granitoids and aluminous granulites. *Contributions Mineralogy Petrology* 107, 202–218. doi:10.1007/bf00310707

Reid, J. B., Evans, O. C., and Fates, D. G. (1983). Magma mixing in granitic rocks of the central Sierra Nevada, California. *Earth Planet. Sci. Lett.* 66, 243–261. doi:10.1016/0012-821x(83)90139-5

Sawyer, E. W., Cesare, B., and Brown, M. (2011). When the continental crust melts. *Elements* 7, 229–234. doi:10.2113/gselements.7.4.229

Sawyer, E. W. (1996). Melt segregation and magma flow in migmatites: Implications for the generation of granite magmas. *Trans. R. Soc. Edinb. Earth Sci.* 87, 85–94. doi:10.1017/s0263593300006507

Singh, J., and Johannes, W. (1996). Dehydration melting of tonalites. Part I. Beginning of melting. *Contributions Mineralogy Petrology* 125, 16–25. doi:10.1007/s004100050203

Spera, F. J., and Bohrson, W. A. (2001). Energy-constrained open-system magmatic processes I: General model and energy-constrained assimilation and fractional crystallization (EC-AFC) formulation. *J. Petrology* 42, 999–1018. doi:10.1093/petrology/42.5.999

Starijaš Mayer, B., Krenn, E., and Finger, F. (2014). Microcrystals of Th-rich monazite (La) with a negative Ce anomaly in metadiorite and their role for documenting Cretaceous metamorphism in the Slavonian Mountains (Croatia). *Mineralogy Petrology* 108, 231–243. doi:10.1007/s00710-013-0298-y

Storkey, A. C., Hermann, J., Hand, M., and Buick, I. S. (2005). Using *in situ* trace-element determinations to monitor partial-melting processes in metabasites. *J. Petrology* 46, 1283–1308. doi:10.1093/petrology/egi017

Tang, M., Wang, X.-L., Shu, X.-J., Wang, D., Yang, T., and Gopon, P. (2014). Hafnium isotopic heterogeneity in zircons from granitic rocks: Geochemical evaluation and modeling of "zircon effect" in crustal anatexis. *Earth Planet. Sci. Lett.* 389, 188–199. doi:10.1016/j.epsl.2013.12.036

Taylor, H. P., Jr. (1980). The effects of assimilation of country rocks by magmas on $^{18}O/^{16}O$ and $^{87}Sr/^{86}Sr$ systematics in igneous rocks. *Earth Planet. Sci. Lett.* 47, 243–254. doi:10.1016/0012-821x(80)90040-0

Tiepolo, M., and Tribuzio, R. (2005). Slab-melting during alpine orogeny: Evidence from mafic cumulates of the Adamello batholith (central alps, Italy). *Chem. Geol.* 216, 271–288. doi:10.1016/j.chemgeo.2004.11.014

Turner, S., Foden, J., Sandiford, M., and Bruce, D. (1993). Sm-Nd isotopic evidence for the provenance of sediments from the Adelaide Fold Belt and southeastern Australia with implications for episodic crustal addition. *Geochimica Cosmochimica Acta* 57, 1837–1856. doi:10.1016/0016-7037(93)90116-e

Valley, J. W., Lackey, J. S., Cavosie, A. J., Clechenko, C. C., Spicuzza, M. J., Basei, M. A. S., et al. (2005). 4.4 billion years of crustal maturation: Oxygen isotope ratios of magmatic zircon. *Contributions Mineralogy Petrology* 150, 561–580. doi:10.1007/s00410-005-0025-8

Vernon, R. H. (1990). Crystallization and hybridism in microgranitoid enclave magmas: Microstructural evidence. *J. Geophys. Res.* 95, 17849–17859. doi:10.1029/jb095ib11p17849

Vielzeuf, D., and Holloway, J. R. (1988). Experimental determination of the fluid-absent melting relations in the pelitic system. Consequences for crustal differentiation. *Contributions Mineralogy Petrology* 98, 257–276. doi:10.1007/bf00375178

Vielzeuf, D., and Montel, J. M. (1994). Partial melting of metagreywackes. Part I. Fluid-absent experiments and phase relationships. *Contributions Mineralogy Petrology* 117, 375–393. doi:10.1007/bf00307272

Villaseca, C., Martín Romera, C., De le Rosa, J., and Barbero, L. (2003). Residence and redistribution of REE, Y, Zr, Th and U during granulite-facies metamorphism: Behaviour of accessory and major phases in peraluminous granulites of central Spain. *Chem. Geol.* 200, 293–323. doi:10.1016/s0009-2541(03)00200-6

Wang, D., Wang, X.-L., Cai, Y., Goldstein, S. L., and Yang, T. (2018). Do Hf isotopes in magmatic zircons represent those of their host rocks? *J. Asian Earth Sci.* 154, 202–212. doi:10.1016/j.jseaes.2017.12.025

Watson, E. B., and Harrison, T. M. (1983). Zircon saturation revisited: Temperature and composition effects in a variety of crustal magma types. *Earth Planet. Sci. Lett.* 64, 295–304. doi:10.1016/0012-821x(83)90211-x

Weis, D., Kieffer, B., Maerschalk, C., Pretorius, W., and Barling, J. (2005). High-precision Pb-Sr-Nd-Hf isotopic characterization of USGS BHVO-1 and BHVO-2 reference materials. *Geochem. Geophys. Geosystems* 6. doi:10.1029/2004gc000852

Weis, D., Kieffer, B., Hanano, D., Nobre Silva, I., Barling, J., Pretorius, W., et al. (2007). Hf isotope compositions of U.S. Geological Survey reference materials. *Geochem. Geophys. Geosystems* 8. doi:10.1029/2006gc001473

White, A. J. R., and Chappell, B. W. (1977). Ultrametamorphism and granitoid Genesis. *Tectonophysics* 43, 7–22. doi:10.1016/0040-1951(77)90003-8

White, A. J. R., and Chappell, B. W. (1988). Some supracrustal (S-type) granites of the Lachlan Fold Belt. *Trans. R. Soc. Edinb. Earth Sci.* 79, 169–181. doi:10.1017/s026359330001419x

Williams, I. S., Compston, W., and Chappell, B. W. (1983). Zircon and monazite U-Pb systems and the histories of I-type magmas, Berridale Batholith, Australia. *J. Petrology* 24, 76–97. doi:10.1093/petrology/24.1.76

Wilson, M. (1993)., 150. London, 611–624. doi:10.1144/gsjgs.150.4.0611 Magmatic differentiation*J. Geol. Soc.*

Wolf, M., Romer, R. L., and Glodny, J. (2019). Isotope disequilibrium during partial melting of metasedimentary rocks. *Geochimica Cosmochimica Acta* 257, 163–183. doi:10.1016/j.gca.2019.05.008

Woodhead, J. D., and Hergt, J. M. (2005). A preliminary appraisal of seven natural zircon reference materials for *in situ* Hf isotope determination. *Geostand. Geoanalytical Res.* 29, 183–195. doi:10.1111/j.1751-908x.2005.tb00891.x

Wormald, R. J., and Price, R. C. (1988). Peralkaline granites near Temora, southern New-South-Wales - tectonic and petrological implications. *Aust. J. Earth Sci.* 35, 209–221. doi:10.1080/14400958808527941

Wormald, R. J. (1993). *The petrology and geochemistry of mid to late Paleozoic magmatism in the Temora region, New South Wales. Department of Geology.* Melbourne: La Trobe Univeristy.

Wyborn, L. A. I., and Chappell, B. W. (1983). Chemistry of the ordovician and silurian greywackes of the snowy mountains, southeastern Australia: An example of chemical evolution of sediments with time. *Chem. Geol.* 39, 81–92. doi:10.1016/0009-2541(83)90073-6

Wyborn, D., and Chappell, B. W. (1986). The petrogenetic significance of chemically related plutonic and volcanic rock units. *Geol. Mag.* 123, 619–628. doi:10.1017/s0016756800024134

Xing, C.-M., Wang, C. Y., and Li, C. (2014). Trace element compositions of apatite from the middle zone of the panzhihua layered intrusion, SW China: Insights into the differentiation of a P- and Si-rich melt. *Lithos* 204, 188–202. doi:10.1016/j.lithos.2014.02.009

Yakymchuk, C., Siddoway, C. S., Fanning, C. M., McFadden, R., Korhonen, F. J., and Brown, M. (2013). Anatectic reworking and differentiation of continental crust along the active margin of gondwana: A zircon Hf-O perspective from west Antarctica. *Geol. Soc. Lond. Spec. Publ.* 383, 169–210. doi:10.1144/sp383.7

Frontiers | Frontiers in Earth Science

TYPE Original Research
PUBLISHED 10 August 2023
DOI 10.3389/feart.2023.1186207

How is carbonate crust digested by magma?

Anastassia Y. Borisova[1]* and Wendy A. Bohrson[2]

[1]Géosciences Environnement Toulouse, Observatoire Midi-Pyrénées, Université Toulouse III/CNRS/IRD/CNES, Toulouse, France, [2]Department of Geology and Geological Engineering, Colorado School of Mines, Golden, CO, United States

Magma's volatile budget depends on deep magmatic sources, the degree of differentiation and degassing conditions, and volatile input from the assimilated crust. It is, therefore, important to know the exact mechanism by which the crust is assimilated into magma to understand volatile budgets and eruption behavior. To explore reactions between carbonate, calc–silicate, or skarn xenoliths and basaltic andesite magma, we studied ten calc–silicate xenoliths from the 1994, 1998, 2006, and 2010 Merapi eruptions and four sediment samples of local Javanese carbonate crust. An *in situ* electron probe microanalysis of the 1994–2010 calc–silicate xenolith minerals and glasses suggests that calcite is a minor and metastable mineral phase in association with wollastonite. In addition, carbonate melts quenched to calcic glasses (32 ± 7 wt% SiO_2; 38 ± 3 wt% CaO), similar to experimental glasses produced by crust–melt interaction experiments. Thermodynamic modeling using rhyolite MELTS (version 1.2.0) predicts the production of highly silicic (up to ~84 wt% of SiO_2) and CaO-rich (up to ~25 wt %) melts during partial melting of calc–silicate material. The observed mechanism of calc–silicate xenolith assimilation is the generation of highly silicic (77 ± 4 wt% of SiO_2) melts in association with idiomorphic diopside [$Wo_{49}En_{29}$; 57 ± 3 Mg# = $Mg/(Mg+Fe^{2+})$] and other calcic pyroxenes (Wo_{54-82} En_{2-21}; 16–43 Mg#) due to partial melting of xenolith and incongruent dissolution reactions. We hypothesize that the rate-limiting process is the subsequent mixing of the produced crustal melts with representative resident andesitic melt (average 65 wt% SiO_2) through chemical diffusion, which explains major and volatile (Cl) element contents in the Merapi glass products. In addition to high Sr contents and radiogenic $^{87}Sr/^{86}Sr$ and elevated CO_2, Ba, Co, Cr, Cu, V, Zn, and Zr contents in the magmatic minerals and associated glasses, the recrystallized and residual metamorphic sphene, quartz, garnet, and apatite predicted by rhyolite-MELTS or Magma Chamber Simulator modeling during wallrock melting and residual metastable calcite and wollastonite are important tracers of calc–silicate crust assimilation. The disequilibrium process of calc–silicate crustal assimilation can, thus, be well predicted by dissolution experiments and thermodynamic modeling using rhyolite-MELTS or Magma Chamber Simulator. The rate of calc–silicate crustal assimilation is still unconstrained without adequate high-temperature kinetic time-series experiments. We predict that the crustal assimilation rate is controlled by the Si–Al diffusion and associated convection in the hydrous silicate magma.

KEYWORDS

crustal assimilation, kinetics, mechanism, rate, carbonate crust, calc-silicate xenolith, mineral dissolution, silicic melts

OPEN ACCESS

EDITED BY
Patrizia Fiannacca,
University of Catania, Italy

REVIEWED BY
Rong Xu,
Chinese Academy of Sciences (CAS), China
Saskia Erdmann,
UMR7327 Institut des Sciences de la Terre d'Orléans (ISTO), France

*CORRESPONDENCE
Anastassia Y. Borisova,
✉ anastassia.borisova@get.omp.eu

RECEIVED 14 March 2023
ACCEPTED 28 June 2023
PUBLISHED 10 August 2023

CITATION
Borisova AY and Bohrson WA (2023), How is carbonate crust digested by magma? *Front. Earth Sci.* 11:1186207.
doi: 10.3389/feart.2023.1186207

Introduction

Decarbonation of the arc-crust beneath Merapi may magnify the volcanic CO_2 output and potentially contribute to the volcano's eruption behavior (Borisova et al., 2013, 2016; Erdmann et al., 2014, 2016; Deegan et al., 2023). Numerous experimental works devoted to pure carbonate solubility in mafic melts demonstrated the important role that the addition of carbonate material has on the magma liquidus phase stability field (Freda et al., 2008; Iacono-Marziano et al., 2008, 2009; Mollo et al., 2010). Deegan et al. (2010), Jolis et al. (2013), and Blythe et al. (2015) experimentally studied the interaction of carbonate materials with mafic and alkaline melts at conditions corresponding to the deep crust. They discovered that the direct interaction of carbonates with the silicate melt is rapid (minutes), with the outcome being the formation of Ca-rich carbonate melts. Chadwick et al. (2007) documented the formation of Ca-rich glasses in calc–silicate xenoliths that were assimilated by the 1994–1998 Merapi (Indonesia) magmas. Costa et al. (2013), Borisova et al. (2013; 2016) and Troll et al. (2013) studied the lava, ash, xenolith, and igneous samples of recent Merapi eruptions. Geochemical and detailed *in situ* data on the glasses and minerals confirm an important effect that the crustal level (~200 MPa depths, Borisova et al., 2013; Erdmann et al., 2016) assimilation of crustal calc–silicate xenoliths has on the 2010 basaltic andesite magma. The pre-eruptive saturation of the basaltic andesite magma with aqueous carbonic NaCl–HCl-bearing fluid was suggested to be responsible for the high explosivity of the Merapi volcano in 2010. Both Nadeau et al. (2011; 2013a, b) and Troll et al. (2013) showed that glass inclusions in Merapi's phenocrysts are typically CO_2-rich. Alternatively, it was proposed that an unusually large batch of recharge magma could also have triggered the 2010 eruption (Costa et al., 2013; Jousset et al., 2013).

A mechanism of crustal assimilation has been suggested by Borisova et al. (2013): 1) contact metamorphism of Javanese sediments and formation of calc–silicate skarns like xenoliths in the 1998 and 2006 eruptions; 2) assimilation of the calc–silicate xenoliths through complete digestion, partial melting, or dissolution (partial melting involves reaction of a mineral to silicate melt, whereas mineral dissolution happens in the presence of silicate melt) and generation of calcic melts like those defined by Borisova et al. (2016) (referred to as the 2010 Crustal Assimilant); and 3) effective mixing between hydrous K-rich (resident) melt and the 2010 Crustal Assimilant (CaO up to 10.5 wt% and CaO/Al_2O_3 up to 1.2) melts that are characterized by crustal signatures, followed by crystallization. However, the kinetics (rates and mechanisms) of the assimilation mechanisms occurring in the Merapi pre-eruptive system have not been constrained yet. Mechanisms of xenolith dissolution and/or partial melting in the resident basaltic andesite magma may be recorded through detailed investigation of crustal calc–silicate xenoliths. Finally, Whitley et al. (2020) performed a detailed investigation of the Merapi calc–silicate xenolith production; however, no modeling of partial melting of potential calc–silicate wallrock has been applied. Our work here investigates mechanisms of the crustal assimilation affecting the Merapi basaltic andesite magmas based on detailed petrologic, mineralogical, and geochemical investigations coupled with rhyolite-MELTS thermodynamic modeling (Gualda et al., 2012; Ghiorso and Gualda, 2015). The results demonstrated in this work have implications for explosive volcanism related to crustal carbonate assimilation (e.g., volcanoes Merapi and Kelut, Indonesia).

Geological background

Merapi stratovolcano is located ~30 km north of the city of Yogyakarta, Indonesia. The volcano is composed mainly of basaltic-andesite tephra, pyroclastic flows, lava, and lahar deposits. Since the 19th century, Merapi has erupted every 4–6 years, with most of these eruptions having explosivity indices ≤VEI 2 (Volcanic Explosivity Index), although moderate VEI 1–3 (1832, 1849, 1930, 1961, 2014, and 2018) and large VEI 4 (2010) eruptions have also occurred (https://volcano.si.edu/). The recent activity of Merapi is characterized by 1) recurrent effusive growth of viscous lava domes that collapse to form pyroclastic currents, referred to as the Merapi-type block-and-ash flows (BAFs) (VEI 2) and 2) more exceptional explosive eruptions of the sub-Plinian type (VEI 3–4) associated with columns collapsing into pumice-and-ash pyroclastic flows (Voight et al., 2000). The explosive eruption of 2010 (Costa et al., 2013) marks an important change in Merapi's activity toward more explosive behavior. Today, Merapi has reverted to more typical behavior since, i.e., relatively abundant eruptions at VEI 1–3.

Merapi is located on the carbonate crust of 8–10 km thickness of the Kendeng basin, where Cretaceous to Cenozoic volcanoclastic sediments are overlain by shallow marine limestones, all of which overlie arc and ophiolite basement rocks (Smyth et al., 2005). Recent detailed micro-analytical and experimental data suggest the effects of shallow-level assimilation of the local Javanese sedimentary crust are significant (Chadwick et al., 2007; Deegan et al., 2010; Deegan et al., 2010; Borisova et al., 2013, 2016; Troll et al., 2013). Carbonate crust assimilation can play a key role in producing highly explosive fluid-saturated magmas (Iacono-Marziano et al., 2008, 2009; Deegan et al., 2010; Borisova et al., 2013; Troll et al., 2013). To evaluate the mechanisms and rates of crustal assimilation, we analyzed major, trace, and volatile elements and Sr–Nd–Pb isotopes in the Javanese crust and Merapi xenoliths and their minerals and glasses, using state-of-the-art analytical methods. Based on these data, we propose a mechanism of crustal assimilation preceding and triggering the Merapi eruptions.

Materials and methods

1994–2010 Merapi sample collection

The 1994, 1998, 2006, and 2010 xenolith sample list is shown in Table 1. M94-CS-104 and M94-CS-106 are from the 1994 small-volume Merapi-type BAFs. Samples MXCS-1, MXCS-2, MXCS-4, MXCS-7, and MXCS-9 are from the 1998 BAFs. MXCS-06-KAT2 is a calc–silicate xenolith from the 2006 eruption, and 014-1B is from the 2010 eruption. Samples of the 2010 Merapi xenoliths were collected during the 2015 French expedition (Borisova et al., 2016). LST-1, LST-2, LST-3, and LST-4 are carbonate sediment samples from Parangtritis beach (Java, Indonesia). The sampling locations are shown in the study of Deegan et al. (2010). More details on the samples can be found in the study of Chadwick (2008), Table 2, and Table 3.

TABLE 1 Merapi calc–silicate xenolith location, sampling, and mineralogy details.

Sample:	M94-CS-104	M94-CS-106	MXCS-1	MXCS-2	MXCS-4	MXCS-7	MXCS-9	MXCS-06-KAT2	014-1B (SEMO-3)	LST-1	LST-2	LST-3	LST-4
Rock type:					calc-silicate xenoliths						carbonate sediments		
Figure:	2A			2(B, D)				2(C)	2(E-H)				
Eruption year:	1994	1994	1998	1998	1998	1998	1998	2006	2010	-	-	-	-
Sampling:	(1)	(1)	(1)	(1)	(1)	(1)	(1)	(1)	this work	(2,3)	(2,3)	(2,3)	(2,3)
Mineralogy:													
Cc	+	N.A.	-	N.A.	-	N.A.	N.A.	-	-	+	+	+	+
Larn	+	N.A.	-	N.A.	-	N.A.	N.A.	-	-	N.A.	N.A.	N.A.	-
Srbr	+	N.A.	-	N.A.	-	N.A.	N.A.	-	-	N.A.	N.A.	N.A.	-
Wo	+	N.A.	+	N.A.	-	N.A.	N.A.	+	+	N.A.	N.A.	N.A.	-
Di	-	N.A.	+	N.A.	±	N.A.	N.A.	+	+	N.A.	N.A.	N.A.	-
Heden	-	N.A.	+	N.A.	±	N.A.	N.A.	+	+	N.A.	N.A.	N.A.	-
An	-	N.A.	+	N.A.	+	N.A.	N.A.	-	+	N.A.	N.A.	N.A.	+
Qtz	-	N.A.	-	N.A.	+	N.A.	N.A.	-	-	N.A.	N.A.	N.A.	±
Gross	-	N.A.	-	N.A.	-	N.A.	N.A.	-	-	N.A.	N.A.	N.A.	-
FeTi oxides	±	N.A.	±	N.A.	±	N.A.	N.A.	+	+	N.A.	N.A.	N.A.	-
Sph	-	N.A.	+	N.A.	-	N.A.	N.A.	+	±	N.A.	N.A.	N.A.	-
Sulf	-	N.A.	+	N.A.	-	N.A.	N.A.	-	-	N.A.	N.A.	N.A.	-
Apt	-	N.A.	+	N.A.	-	N.A.	N.A.	+	-	N.A.	N.A.	N.A.	-
Glass	-	N.A.	+	N.A.	-	N.A.	N.A.	+	+	N.A.	N.A.	N.A.	-
Clay	-	N.A.	-	N.A.	-	N.A.	N.A.	+	-	N.A.	N.A.	N.A.	+

References for geographic location: (1) Troll et al. (2013); (2) Deegan et al. (2010); (3) Chadwick (2008). Cc, calcite; Larn, larnite; Srbr, srebrodolskite; Wo, wollastonite; Di, diopside; Hedenb, hedenberite; An, anorthite; Qtz, quartz; Gross, grossular; Sph, sphene; Sulf, sulfides; Apt, apatite; Glass, glasses; Clay, clay minerals. +: present and -: absent in the sample; N.A., not analyzed; (+), irregular presence.

TABLE 2 Volatile, major, and trace element and isotopic composition of the bulk Merapi calc–silicate xenolith and Javanese limestone samples.

Sample	MXCS-1R	MXCS-1C	M-XCS-1	MXCS-2	MXCS-4	MXCS-7R	MXCS-7C	MXCS-9	M-94-CS-104	M94-CS-106	MXCS-06-KAT2	LST-1	LST-2	LST-3	LST-4
SiO_2, wt%	48.11	58.38	52.73	69.44	82.49	53.30	52.61	48.55	48.32	48.27	54.05	0.24	0.19	0.37	46.42
TiO_2	0.50	0.03	0.072	0.49	0.48	0.63	0.17	0.62	0.23	0.31	0.13	D.L.	D.L.	D.L.	0.54
Al_2O_3	10.52	0.63	1.53	12.45	4.55	14.11	5.09	15.77	5.33	9.88	1.56	0.13	0.13	0.18	11.47
Fe_2O_3	11.31	1.67	3.81	4.14	2.75	8.23	3.63	7.80	2.06	3.23	1.73	0.04	0.03	0.06	5.50
MgO	5.84	0.57	1.13	1.76	0.72	3.10	0.86	3.55	0.88	0.89	0.40	0.29	0.28	0.31	2.15
MnO	0.32	0.19	0.24	0.11	0.11	0.25	0.26	0.22	0.078	0.14	0.23	0.00	0.01	0.00	0.19
CaO	21.56	36.75	39.73	8.37	8.52	17.11	34.64	21.70	39.82	35.11	40.21	55.39	55.17	55.00	11.89
Na_2O	0.54	0.02	0.05	1.84	0.16	2.14	0.77	1.15	0.43	0.48	0.32	0.02	0.01	0.02	1.03
K_2O	0.33	0.01	0.02	0.22	0.02	0.83	0.65	0.33	0.16	0.56	0.35	0.01	0.01	0.01	1.06
P_2O_5	0.17	0.03	D.L.	0.11	0.05	0.19	0.04	0.18	0.09	0.10	D.L.	D.L.	D.L.	D.L.	0.13
LOI	0.10	1.17	0.23	−0.13	−0.16	−0.30	0.47	−0.10	1.69	0.49	0.17	43.69	43.71	43.72	19.44
Total	99.29	99.43	99.54	98.79	99.67	99.58	99.18	99.76	99.10	99.46	99.14	99.80	99.52	99.68	99.81
CO_2 total	0.30	0.83	0.29	0.15	0.17	0.25	0.50	0.20	1.16	0.18	0.03	43.68	44.00	43.86	7.79
H_2O total	0.36	0.24	0.26	0.11	0.07	0.13	0.24	0.21	0.60	0.22	0.16	0.32	0.32	0.43	11.78
S total	0.55	<0.01	0.03	0.03	0.01	0.06	0.02	<0.01	0.02	<0.01	<0.01	<0.01	0.02	0.02	0.01
Cl, ppm	175	<20	N.A.	<20	<20	42	29	185	N.A.	N.A.	N.A.	140	22	125	N.A.
As	D.L.	D.L.	D.L.	1.972	5.541	2.915	1.329	1.315	D.L.	3.79	D.L.	D.L.	D.L.	D.L.	3.11
Ba	100.4	1.882	8.1	212.6	171.3	240	110.5	122.9	65.1	326	37.4	2.172	4.374	3.218	106
Be	0.78	D.L.	D.L.	0.779	D.L.	1.056	0.472	1.382	D.L.	1.03	D.L.	D.L.	D.L.	D.L.	0.68
Bi	D.L.	D.L.	D.L.	D.L.	D.L.	D.L.	D.L.	D.L.	D.L.	D.L.	D.L.	D.L.	D.L.	D.L.	0.13
Cd	0.253	0.352	0.43	0.148	0.252	0.182	0.395	0.356	0.39	0.31	0.30	D.L.	D.L.	0.121	0.14
Ce	20.98	5.07	5.94	24.27	30.5	25.52	13.58	26.64	11.2	32.4	9.99	0.541	0.625	0.667	19.8
Co	118.7	59.54	7.03	80.04	86.32	67.89	56.46	72.42	4.76	4.93	3.25	0.617	0.76	0.644	5.73
Cr	49.76	D.L.	7.7	89.05	674.2	79.27	6.809	19.92	22.9	5.6	26.1	5.234	8.375	D.L.	12.3
Cs	0.792	D.L.	0.26	0.52	0.179	2.095	2.45	0.512	0.33	3.68	0.73	D.L.	D.L.	D.L.	1.59
Cu	158.1	D.L.	7.9	19.3	D.L.	244.9	42.03	5.354	19.1	10.5	6.8	D.L.	D.L.	D.L.	45.4
Dy	2.844	2.837	3.78	2.97	3.927	2.713	1.618	3.971	1.46	2.80	1.26	0.157	0.19	0.2	5.22

(Continued on following page)

TABLE 2 (*Continued*) Volatile, major, and trace element and isotopic composition of the bulk Merapi calc–silicate xenolith and Javanese limestone samples.

Sample	MXCS-1R	MXCS-1C	M-XCS-1	MXCS-2	MXCS-4	MXCS-7R	MXCS-7C	MXCS-9	M-94-CS-104	M94-CS-106	MXCS-06-KAT2	LST-1	LST-2	LST-3	LST-4
Er	1.533	1.26	1.79	1.728	2.092	1.666	1.029	2.464	0.886	1.77	0.788	0.09	0.117	0.104	3.34
Eu	1.819	1.73	1.53	0.906	0.948	0.848	0.598	1.063	0.317	0.967	0.696	0.047	0.048	0.053	1.08
Ga	12.03	0.729	1.80	11.31	4.553	16.08	5.427	18.31	6.04	10.9	2.10	D.L.	D.L.	D.L.	12.9
Gd	3.464	3.189	3.64	3.09	3.707	2.886	1.597	3.925	1.43	2.85	1.26	0.181	0.201	0.22	4.37
Ge	1.707	1.152	1.15	1.151	1.401	1.349	0.884	1.411	1.08	0.81	0.50	D.L.	D.L.	D.L.	1.21
Hf	2.194	D.L.	0.34	2.553	6.538	2.345	1.005	3.132	1.23	3.15	0.53	D.L.	D.L.	D.L.	3.02
Ho	0.545	0.503	0.748	0.608	0.761	0.554	0.341	0.846	0.325	0.634	0.291	0.032	0.042	0.038	1.21
In	0.117	D.L.	D.L.	D.L.	D.L.	0.121	D.L.	D.L.	D.L.	D.L.	D.L.	D.L.	D.L.	D.L.	0.09
La	10.18	1.807	2.21	11.36	14.29	11.9	6.297	14.34	5.58	16.4	4.82	0.629	0.771	0.75	8.48
Lu	0.248	0.111	0.161	0.27	0.29	0.288	0.176	0.419	0.128	0.320	0.125	0.01	0.014	0.014	0.555
Mo	0.734	D.L.	D.L.	D.L.	D.L.	1.216	0.695	D.L.	D.L.	0.87	D.L.	D.L.	D.L.	D.L.	0.70
Nb	3.796	0.328	0.54	3.839	5.841	5.132	1.973	2.709	3.08	3.38	1.06	D.L.	D.L.	D.L.	1.41
Nd	12.43	5.697	5.61	13.39	15.92	13.32	7.182	15.96	6.10	14.8	5.48	0.639	0.73	0.766	14.4
Ni	32.5	6.887	13.7	23.71	47.1	41.13	11.63	21.08	8.7	6.0	13.2	D.L.	D.L.	D.L.	11.0
Pb	3.006	0.7216	1.44	7.67	3.9157	6.5409	2.917	3.585	2.13	8.76	3.01	D.L.	D.L.	D.L.	5.98
Pr	2.579	0.854	0.969	2.94	3.656	2.977	1.591	3.456	1.46	3.78	1.31	0.129	0.153	0.156	3.05
Rb	10.66	D.L.	1.12	3.129	0.466	18.97	17.5	6.836	3.79	32.1	10.2	D.L.	D.L.	D.L.	26.6
Sc	13.25	3.45	4.46	11.56	7.01	18.38	3.33	15.54	5.31	3.71	2.77	D.L.	D.L.	D.L.	17.7
Sb	D.L.	D.L.	D.L.	D.L.	0.332	D.L.	D.L.	D.L.	D.L.	0.27	D.L.	D.L.	D.L.	D.L.	0.26
Sm	3.518	2.751	3.09	2.966	3.65	2.933	1.601	3.801	1.45	3.24	1.25	0.144	0.17	0.187	4.04
Sn	0.875	D.L.	0.50	0.749	1.312	0.827	0.5	1.458	D.L.	1.08	0.57	D.L.	D.L.	D.L.	1.18
Sr	681.8	410.2	442	323	154	396.8	222.4	418.9	206	289	190	122.8	176.5	122.4	338
Ta	1.517	0.756	0.05	1.257	1.55	1.06	0.755	0.98	0.19	0.30	0.09	D.L.	D.L.	D.L.	0.14
Tb	0.499	0.492	0.613	0.481	0.634	0.454	0.258	0.635	0.229	0.447	0.187	0.026	0.03	0.032	0.764
Th	3.373	0.263	0.99	3.434	3.953	4.459	2.572	6.882	2.46	7.36	1.08	0.032	0.036	0.04	1.73
Tm	0.228	0.157	0.222	0.256	0.304	0.258	0.166	0.388	0.127	0.277	0.116	0.012	0.017	0.015	0.508
U	1.259	0.116	0.58	0.888	1.083	1.173	0.665	1.822	5.40	2.58	0.43	0.809	0.426	0.519	2.75

(Continued on following page)

TABLE 2 (*Continued*) Volatile, major, and trace element and isotopic composition of the bulk Merapi calc–silicate xenolith and Javanese limestone samples.

Sample	MXCS-1R	MXCS-1C	M-XCS-1	MXCS-2	MXCS-4	MXCS-7R	MXCS-7C	MXCS-9	M-94-CS-104	M94-CS-106	MXCS-06-KAT2	LST-1	LST-2	LST-3	LST-4
V	82.58	4.47	14.0	66	33.1	138.7	25.2	114.9	53.4	32	14.1	2.4	1.956	2.243	62.5
W	N.A.	N.A.	0.58	N.A.	N.A.	N.A.	N.A.	N.A.	0.45	0.70	0.46	D.L.	D.L.	D.L.	0.45
Y	16.97	18.1	23.9	19.05	26.12	16.6	11.1	25.81	10.8	18.0	9.48	1.479	1.957	1.715	32.9
Yb	1.551	0.905	1.30	1.732	1.941	1.774	1.146	2.669	0.820	1.96	0.805	0.071	0.097	0.088	3.53
Zn	113	20.29	42.6	48.13	46.4	104.7	42.91	100.6	20.3	51.0	21.6	D.L.	D.L.	D.L.	71.1
Zr	87.81	3.262	11.4	101.4	298.2	83.84	42.78	122.8	41.3	121	18.5	D.L.	1.111	D.L.	95.8

Sample	MXCS-1R	MXCS-1C	MXCS-2	MXCS-4	MXCS-7R	MXCS-7C	MXCS-9	LST-1	LST-2	LST-3
^{87}Sr/^{86}Sr	0.709376	0.707985	0.705843	0.707387	0.705946	0.705945	0.706840	0.708788	0.708751	0.708789
error (2σ)	0.000016	0.000024	0.000016	0.000010	0.000014	0.000010	0.000006	0.000018	0.000006	0.000020
^{143}Nd/^{144}Nd	0.512555	0.512625	0.512779	0.512503	0.512748	0.512755	0.512778	0.512488	0.512536	0.512379
error (2σ)	0.000018	0.000024	0.000015	0.000009	0.000014	0.000013	0.000010	0.000037	0.000029	0.000049
^{206}Pb/^{204}Pb	18.5576	18.4910	18.6056	18.6388	18.6635	18.6338	18.5802	N.A.	N.A.	N.A.
error (2σ)	0.0033	0.0056	0.0007	0.0010	0.0009	0.0016	0.0009	N.A.	N.A.	N.A.
^{207}Pb/^{204}Pb	15.5310	15.5747	15.5886	15.5243	15.6180	15.6029	15.6012	N.A.	N.A.	N.A.
error (2σ)	0.0031	0.0056	0.0007	0.0009	0.0008	0.0017	0.0010	N.A.	N.A.	N.A.
^{208}Pb/^{204}Pb	38.676	38.863	38.757	38.790	38.937	38.891	38.972	N.A.	N.A.	N.A.
error (2σ)	0.008	0.015	0.002	0.003	0.002	0.005	0.003	N.A.	N.A.	N.A.
^{207}Pb/^{206}Pb	0.83695	0.84230	0.83783	0.83290	0.83683	0.83744	0.83749	N.A.	N.A.	N.A.
error (2σ)	0.00024	0.00026	0.00006	0.00004	0.00004	0.00011	0.00008	N.A.	N.A.	N.A.
^{206}Pb/^{207}Pb	1.19482	1.18722	1.19355	1.20063	1.19498	1.19412	1.19404	N.A.	N.A.	N.A.
error (2σ)	0.00024	0.00026	0.00006	0.00004	0.00004	0.00011	0.00008	N.A.	N.A.	N.A.
^{208}Pb/^{206}Pb	2.08417	2.10184	2.08300	2.08110	2.08628	2.08740	2.08773	N.A.	N.A.	N.A.
error (2σ)	0,00006	0,00006	0,00001	0,00001	0,00001	0,00002	0,00002	N.A.	N.A.	N.A.

D.L., contents below the detection limit; N.A., values not analyzed.

Volatile, major, and trace elements and Sr–Nd–Pb isotopic composition of the bulk xenolith and sediment samples

Volatile concentrations of CO_2 and S were measured at SARM (Service d'Analyse des Roches et des Minéraux, Centre de Recherches Pétrographiques et Géochimiques, Vandoeuvre-ès-Nancy, France) using a Leco SC-144DR sulfur and carbon analyzer, by heating at 1400°C with oxygen flux and infrared (IR) detection. H_2O concentrations were measured using Karl Fischer titration. Major and trace elements were measured by inductively coupled plasma optical emission spectroscopy (ICP–OES) and ICP–MS, using a method developed at SARM (Carignan et al., 2001) employing an ICP–OES IRIS Advantage ERS from Thermo Scientific and an ICP–MS x7 from Thermo Scientific without pre-concentration of rare earth elements (REEs) and U/Th.

For Sr–Nd–Pb isotope measurements at SARM, 100–200 mg of very fine rock powder (particle size <50 mm) was placed into a 15 mL Savillex beaker. A mixture of concentrated sub-boiled HNO_3 (4 mL) and ultrapure HF (1 mL) was added to the powder samples. The solutions were kept at 115°C for 24–48 h, then evaporated, re-filled with concentrated HCl, and heated for 24 h to ensure complete digestion of the powder samples. The samples were then split into two parts and dried prior to purification of the elements.

For chromatographic separation of Pb from the matrix, 1 mL of HBr (0.8 M) was added to the aliquots. The chromatographic micro-column was filled with AG1X8 resin. The matrix was eluted with 0.8 M HBr, and Pb was recovered with 6 M HCl, following a method similar to that in the study of Manhès et al. (1980). Isotopic analysis was conducted using multicollector–inductively coupled plasma–mass spectrometry (MC–ICP–MS) (Micromass IsoProbe) using a Tl (NIST 997) spike to correct instrumental mass bias. Tl and Pb isotope values used for the NIST 981 and NIST 977 reference materials were those obtained by Thirlwall (2002). More details on the method are described by Cloquet et al. (2006).

For Sr and Nd isolation, the samples were diluted with 2 mL of 2 M HNO_3, following the analytical protocol of Pin et al. (1994). An additional stage of further isolation of Nd from Sm was applied using Ln spec resin, following the procedure described by Pin et al. (1994). Strontium isotopes were measured using a thermal ionization mass spectrometer (TIMS; Triton Plus, from Thermo Electron) in the multicollection mode. In addition, five Faraday cups were used to monitor Rb. Sr was loaded onto a Re filament. Internal normalization using $^{86}Sr/^{88}Sr$ (0.1194) and the exponential law were used to correct the instrumental mass bias. NBS 987 was used to control methodological accuracy. The average blanks were negligible compared to the Sr concentration in the samples (average of 300 pg for Sr). Nd isotopes were measured using MC–ICP–MS (Micromass IsoProbe). To control instrumental mass bias, we applied a constant $^{146}Nd/^{144}Nd$ (0.72190) (Luais et al., 1997) and the exponential law. Reference JMC Nd was used to control methodological accuracy. The average blank corresponded to about 100 pg of Nd, which is negligible compared to the Nd concentration of the sample. Results of bulk rock Sr–Nd–Pb isotope analyses are summarized in Table 2 and Figure 1.

Volatile, major, and minor element composition of the xenolith minerals and glasses

Major element analyses of minerals and glasses and backscattered electron images of the samples were performed at the Géosciences Environnement Toulouse (GET, Toulouse, France) laboratory and at the Centre de MicroCaractérisation Raimond Castaing (Toulouse, France). The main phases in the samples were identified using a scanning electron microscope (SEM) JEOL JSM-6360 LV coupled with energy-dispersive X-ray spectroscopy (EDS) (Borisova et al., 2013; Figure 2). The major, minor, and Cl contents of the crystals and glasses were analyzed using a CAMECA SX-Five microprobe. In general, beam conditions were 15 kV accelerating voltage and 10 or 20 nA probe current. For the analysis of glasses, the CAMECA SX-Five was used following the method of Borisova et al. (2010). The beam (15 kV and 10 nA) was set to a 10 μm beam diameter where possible. Sodium was analyzed first to ensure minimal loss during EPMA. These analytical conditions allowed an optimal signal for the major and minor elements, good internal precision, and minimal sodium loss during EPMA. The following synthetic and natural standards were used for calibration: albite (Na), corundum (Al), wollastonite (Si, Ca), sanidine (K), pyrophanite (Mn, Ti), hematite (Fe), periclase (Mg), and tugtupite (Cl). Element and background counting times for most analyzed elements were 10 s (except for 5 s for Na and K) and 5 s, respectively, whereas peak counting time was 120 s for Cl. The detection limit for Cl was 70 ppm. The silicate reference materials of MPI-DING covering ultramafic to felsic compositions (GOR132-G, GOR128-G, KL2-G, ML3B-G, and ATHO-G of the study of Jochum et al. (2006)) were analyzed as unknown samples to monitor analytical accuracy (Borisova et al., 2012, 2010). The estimated accuracy ranges from 0.5% to 3% (1σ RSD = relative standard deviation), depending on the element contents in the reference glasses. Additionally, the analysis of reference silicate material allowed us to estimate the analytical precision for the major and minor elements (e.g., Cl in glasses). The precision estimated in this way is compatible with the microprobe analytical uncertainty (derived from counting statistics).

Thermodynamic modeling by rhyolite-MELTS or Magma Chamber Simulator

Thermodynamic modeling using rhyolite-MELTS (Gualda et al., 2012; Ghiorso and Gualda, 2015) was performed to estimate the compositions of partial melts of representative calc–silicate crust. Rhyolite-MELTS is based on calibrations informed by experiments and constraints from natural silicic magma systems. For detailed model information, see the aforementioned references. Like all thermodynamic models, rhyolite-MELTS results must be carefully assessed to evaluate their applicability to natural systems. This includes comparing the resulting partial melts with compositions of observed products, such as the Si-rich glasses documented in this work.

In the thermodynamic modeling of the wallrock partial melting using rhyolite-MELTS (Gualda et al., 2012; Ghiorso and Gualda, 2015) or Magma Chamber Simulator MCS (Bohrson et al., 2014,

TABLE 3 Average composition of minerals and glasses in the Merapi calc–silicate xenoliths.

Sample:	M94-CS-104	M94-CS-104	M94-CS-104	M94-CS-104	M94-CS-104	MXCS1 and 014-1B	MXCS1	MXCS1 and 014-1B	MXCS1
Phase:	Calcite (3)	Srebrodolskite (2)	Larnite (3)	Wollastonite (8)	Calcic glass (3)	Wollastonite (3)	Hedenbergite (7)	Silicic glass (18)	Diopside (3)
Caption:	Cc	Srbr	Larn	Wo	Ca glass	Wo	Heden	Si glass	Di
Formula:	$CaCO_3$	$Ca_2Fe^{3+}{}_2O_5$	Ca_2SiO_4	$CaSiO_3$	-	$CaSiO_3$	$CaFe_2+Si_2O_6$	-	$CaMgSi_2O_6$
SiO_2	D.L.	0.32 ± 0.08	35.1 ± 0.3	52.0 ± 0.4	31.73 ± 6.80	52.1 ± 0.3	50.6 ± 0.6	76.5 ± 3.5	53.3 ± 0.5
TiO_2	D.L.	D.L.	D.L.	D.L.	D.L.	0.13 ± 0.03	0.06 ± 0.08	0.22 ± 0.10	0.04 ± 0.06
Al_2O_3	D.L.	D.L.	D.L.	D.L.	0.07 ± 0.08	D.L.	0.28 ± 0.07	12.3 ± 3.2	0.4 ± 0.1
FeO_{bulk}	0.07 ± 0.06	50.3 ± 0.3	D.L.	0.2 ± 0.4	0.13 ± 0.08	1.8 ± 0.5	20.5 ± 2.3	1.8 ± 0.8	14.0 ± 1.1
$Fe_2O_{3\ calc}$[a]	-	55.9 ± 0.3	-	0.5 ± 0.7	-	0.01 ± 0.02	0.69 ± 0.67	-	-
MnO	0.08 ± 0.07	0.7 ± 0.4	D.L.	0.07 ± 0.06	0.01 ± 0.02	0.22 ± 0.06	0.43 ± 0.08	0.07 ± 0.06	0.5 ± 0.1
MgO	D.L.	D.L.	D.L.	0.10 ± 0.08	1.15 ± 1.90	0.13 ± 0.01	5.2 ± 1.5	D.L.	10.3 ± 0.6
CaO	59.8 ± 1.3	D.L.	65.1 ± 1.1	48.5 ± 0.5	37.76 ± 3.14	46.9 ± 0.2	23.5 ± 0.4	4.3 ± 2.2	24.1 ± 0.3
Na_2O	D.L.	D.L.	D.L.	D.L.	0.14 ± 0.06	D.L.	0.03 ± 0.03	2.6 ± 0.4	0.02 ± 0.04
K_2O	D.L.	D.L.	D.L.	D.L.	0.03 ± 0.02	D.L.	0.01 ± 0.01	3.1 ± 0.7	0.02 ± 0.01
P_2O_5	D.L.	D.L.	D.L.	D.L.	0.06 ± 0.04	D.L.	D.L.	0.03 ± 0.03	D.L.
Cl	D.L.	D.L.	D.L.	D.L.	D.L.	D.L.	D.L.	0.07 ± 0.04	D.L.
Total	61.1 ± 2.2	92.96 ± 0.01	100.4 ± 0.7	101.6 ± 0.8	71.12 ± 1.81	101.3 ± 0.6	101.4 ± 0.6	101.0 ± 1.1	101.5 ± 0.9
H_2O+CO_2	38.9 ± 2.2.	7.04 ± 0.01	-	-	28.9 ± 1.8	-	-	-	-
Wo[b]	-	-	-	99.4 ± 0.7	-	96.7 ± 0.8	50.3 ± 0.5	-	48.9 ± 0.3
En	-	-	-	0.3 ± 0.2	-	0.37 ± 0.03	15.5 ± 4.2	-	29.0 ± 1.7
Fs	-	-	-	0.4 ± 0.6	-	2.9 ± 0.8	34.2 ± 4.2	-	22.1 ± 1.8
$Mg^{\#}$	-	-	-	22.3 ± 14.4	-	11.5 ± 2.3	30.5 ± 7.9	-	56.7 ± 3.4

The numbers represent the average content (bracketed number is the amount of analytical points per phase) with 2σ standard deviation, reflecting the chemical heterogeneity.

[a] Fe2O3 content is calculated. Fe2O3 content in srebrodolskite is the value calculated from the measured FeO content. Both FeO and Fe2O3 contents are calculated values in pyroxenes based on the chemical formula XY(Si,Al)2O6 (where X represents the ions of Ca, Na, Fe^{2+}, Mg, and Mn and Y represents the ions of Al, Fe^{3+}, and Ti).

[b] Wo is wollastonite, En is enstatite, and Fs is ferrosilite end-members. Mg# is calculated as $Mg/(Mg + Fe^{2+})$ 100, where Mg and Fe^{2+} are ions per formula unit.

D.L. are values below detection limits.

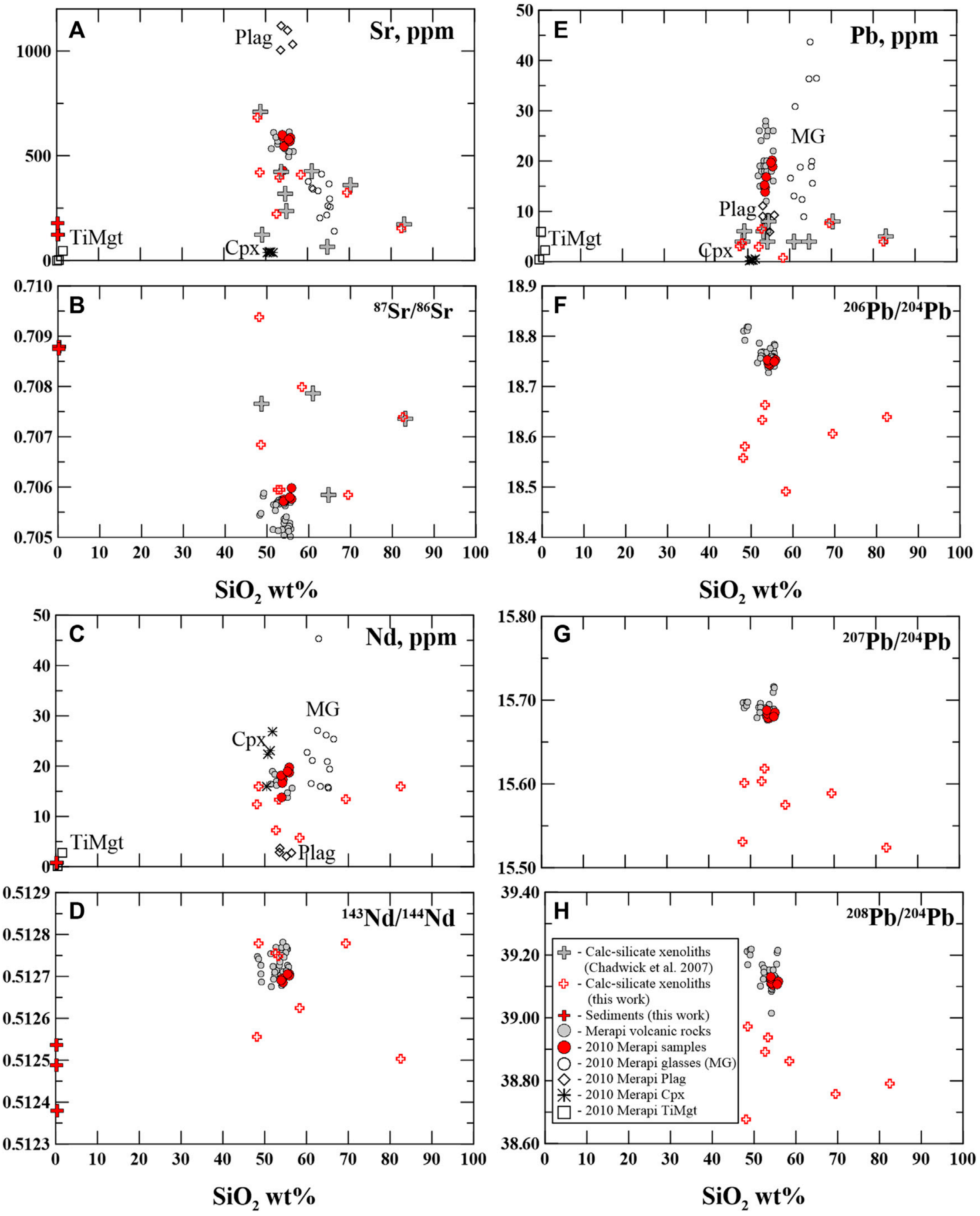

FIGURE 1
(A) Sr (ppm)–SiO_2 (wt%), **(B)** $^{87}Sr/^{86}Sr$–SiO_2 (wt%), **(C)** Nd (ppm)–SiO_2 (wt%), **(D)** $^{143}Nd/^{144}Nd$–SiO_2 (wt%), **(E)** Pb (ppm)–SiO_2 (wt%), **(F)** $^{206}Pb/^{204}Pb$–SiO_2 (wt%), **(G)** $^{207}Pb/^{204}Pb$–SiO_2 (wt%), **(H)** $^{208}Pb/^{204}Pb$–SiO_2 (wt%) in the calc–silicate xenoliths and local Javanese carbonate sediments, the Merapi volcanic rocks, and the 2010 Merapi rocks and matrix glasses. The 2010 Merapi data are according to the study of Borisova et al. (2013), and the previous data on the calc–silicate xenoliths are from the study of Chadwick et al. (2007). Plag - plagioclase, Cpx- clinopyroxene, TiMgt - titanomagnetite. The Merapi volcanic rocks are from the MERAPIDATA database (Borisova et al., 2011).

2020; Heinonen et al., 2020), we used two contrasting compositions (SiO_2-rich and CaO-rich of the 1994–2010 calc–silicate xenoliths Figure 3) from the 1998–2006 Merapi collection (MXCS-1R; MXCS-4, Table 4) as potential crustal contaminants. The bulk compositions (Supplementary Dataset S1) of these two calc–silicate xenoliths underwent equilibrium crystallization (which is the equivalent of equilibrium melting) from the liquidus to the solidus or near solidus. Crystallization/melting occurred in five-degree increments. The resulting partial melts are shown in Figure 4, with the arrow showing the direction of increasing temperature (i.e., wallrock heating). Additional initial conditions include 200 MPa and Fe_2O_3/FeO ratio = 0.24, according to the results of studies of Costa et al. (2013) and Borisova et al. (2013; 2016).

Results

Compositions of the calc–silicate xenoliths and Javanese sediment samples

Javanese carbonate sediments are strongly enriched in volatiles, mostly in CO_2 (8–44 wt%) and H_2O (0.3–11.8 wt%) contents, compared to calc–silicate xenoliths (0.03–1.2 wt% CO_{2total} and 0.1–0.6 wt% H_2O_{total} contents). Both types of rock samples demonstrate similar low chlorine contents, 22–140 ppm for sediments and up to 185 ppm for xenoliths, whereas sulfur contents are extremely low in the sediments (up to 0.02 wt% S) and slightly more elevated in the xenoliths (up to 0.6 wt% S).

Among the major elements, carbonate sediment samples demonstrate an enrichment in calcium (11.9–55 wt% CaO), whereas these rocks are variably depleted in all other major elements: SiO_2 (0.2–46.4 wt%), Al_2O_3 (0.1–12 wt%), MgO (0.3–2.2 wt%), and alkalis (up to 0.02–1.0 wt% Na_2O). Compared to the sediment samples, the calc–silicate xenoliths have higher SiO_2 (48–82 wt%, Figure 1); overlapping Al_2O_3 (0.6–16 wt%), Fe_2O_3 (1.7–11.3 wt%), MgO (0.4–5.8 wt%), alkalis (0.05–2.1 wt% Na_2O and 0.02–0.8 wt% K_2O), TiO_2 (0.03–0.6 wt%), and P_2O_5 (up to 0.2 wt%); and lower CO_2 (up to 1.2 wt%) contents. High SiO_2 and Al_2O_3 contents in the xenoliths (MXCS-4: up to 82 wt% SiO_2 and up to 12.45 wt% Al_2O_3) reflect strong enrichment in silicates due to skarn formation (Burt, 1982).

Javanese sediment samples have higher strontium (122–338 ppm) concentrations compared to other trace elements (2.0–63 ppm V) in these samples. The calc–silicate xenoliths are variably enriched in such trace elements as La (1.8–16.4 ppm), Ce (5–32.4 ppm), Co (up to 119 ppm), Cr (up to 674 ppm), Cu (up to 245 ppm), Ba (up to 326 ppm), Sr (154–682 ppm), Zn (20–113 ppm), and Zr (up to 298 ppm) compared to the sediments.

Figure 1 illustrates that sediments have radiogenic strontium isotope signatures ($^{87}Sr/^{86}Sr$ = 0.70684–0.70879) and low $^{143}Nd/^{144}Nd$ isotope ratios (0.51238–0.51254). The xenolith samples are represented by extremely variable Sr isotope ratios (0.70595–0.70938), whereas the Nd isotope ratio range is more modest, from 0.51250 to 0.51278. Pb isotope ratios are variable: $^{206}Pb/^{204}Pb$ (18.491–18.664), $^{207}Pb/^{204}Pb$ (15.524–15.618), and $^{208}Pb/^{204}Pb$ (38.676–38.972).

Micro-textures, minerals, and glasses in the 1994–2010 calc–silicate xenolith samples

1994 xenolith M94-CS-104 (core)

Figure 2A demonstrates that the investigated sample fragment contains one predominant mineral phase: porous wollastonite. It is important to note that the sample also contains accessory calcite with ≤0.1 wt% MnO, larnite (Larn, Ca_2SiO_4), and srebrodolskite (Srbr, $Ca_2Fe^{3+}{}_2O_5$) (Table 3) in the localized zone of the xenolith edge. In the contact zone between the calcite and wollastonite, the sample contains micro-veins and micro-agglomerates (Figure 2A) of porous calcic glasses (31.7 ± 6.8 wt% SiO_2; 37.8 ± 3.1 wt% CaO).

1998 xenolith MXCS1 (rim)

Figures 2B, D represent the edge zone of the xenolith fragment in contact with the lava. This contact zone contains idiomorphic diopside crystals (Table 3) in association with highly silicic glasses (76.5 ± 3.5 wt% SiO_2) with variable low CaO (4.3 ± 2.2 wt %), low alkalis (2.6 ± 0.4 wt% Na_2O and 3.1 ± 0.7 wt% K_2O), and low MgO (up to 1.3 wt%), FeO (1.8 ± 0.8 wt%), and TiO_2 (0.2 ± 0.1 wt%) contents. These natural silicic glasses are richer in SiO_2 and poorer in Cl contents compared to the 2010 Crustal Assimilant and the groundmass 2006 and 2010 Merapi glasses (Figure 4). The notation of the 2010 Crustal Assimilant (natural high-Ca glasses in the 2010 Merapi pyroclastic lava products) has been introduced to describe a model assimilant composition that interacted with the 2010 Merapi pre-eruptive magma based on the work of Borisova et al. (2013), whereas these natural melts have compositions close to those of the partial melts modeled by MELTS. The natural silicic glasses highly enriched in SiO_2 resemble not only those generated by MELTS during the calc–silicate wallrock partial melting (Supplementary Dataset S1) but also those generated by quartz dissolution in the 1991 Pinatubo basaltic xenoliths (Borisova et al., 2014).

1998 xenolith MXCS4 (core)

The investigated xenolith core contains an assemblage of re-crystallized coarse quartz, anorthite, clinopyroxene, and titanomagnetite identified by using a scanning electron microscope (EDS). The anorthite grains are polyhedral with ~120 dihedral angles or porphyroblastic with abundant inclusions (i.e., typical metamorphic textures). Glass was not detected.

2006 xenolith MXCS06KAT2 (rim)

Another xenolith–lava contact zone is represented by the Merapi calc–silicate xenolith from the 2006 BAF (Figure 2C). It is noticed that the contact zone contains xenomorphic crystals of wollastonite ($Wo_{83\text{-}97}En_{0\text{-}3}$) with up to 0.3 wt% of Al_2O_3 in the groundmass and clusters of euhedral–subhedral individual crystals in highly silicic glass (SiO_2 = 75.2 ± 1.1 wt%, Al_2O_3 = 12.7 ± 0.5 wt%, CaO = 1.7 ± 0.6 wt%, Figure 4). Supplementary Figures A1, A2 demonstrate idiomorphic rims of strongly zoned calcic pyroxenes (CaPx, $Wo_{54\text{-}82}$ $En_{2\text{-}21}$) with compositions (Al_2O_3 0.3–2.0 wt%, Mg# = 13–47) intermediate between hedenbergite and wollastonite at the rims. Moreover, at the xenolith–lava contact, the pyroxene cores are Al-poor augite (Wo_{43} En_{42}, Al_2O_3 = 2.3 wt%) and diopside (Wo_{46} En_{46}, Al_2O_3 = 2.1 wt%) that have high Mg# = 74–76.

2010 xenolith 014-1 B (rim)

Figures 2E–H show that the investigated 2010 Merapi xenolith contains wollastonite associated with silicic glasses and an assemblage of re-crystallized anorthite and diopside clinopyroxene as well as titanomagnetite identified by electron microprobe mapping (EPMA). The anorthite grains are polyhedral with ~120 dihedral angles or porphyroblastic

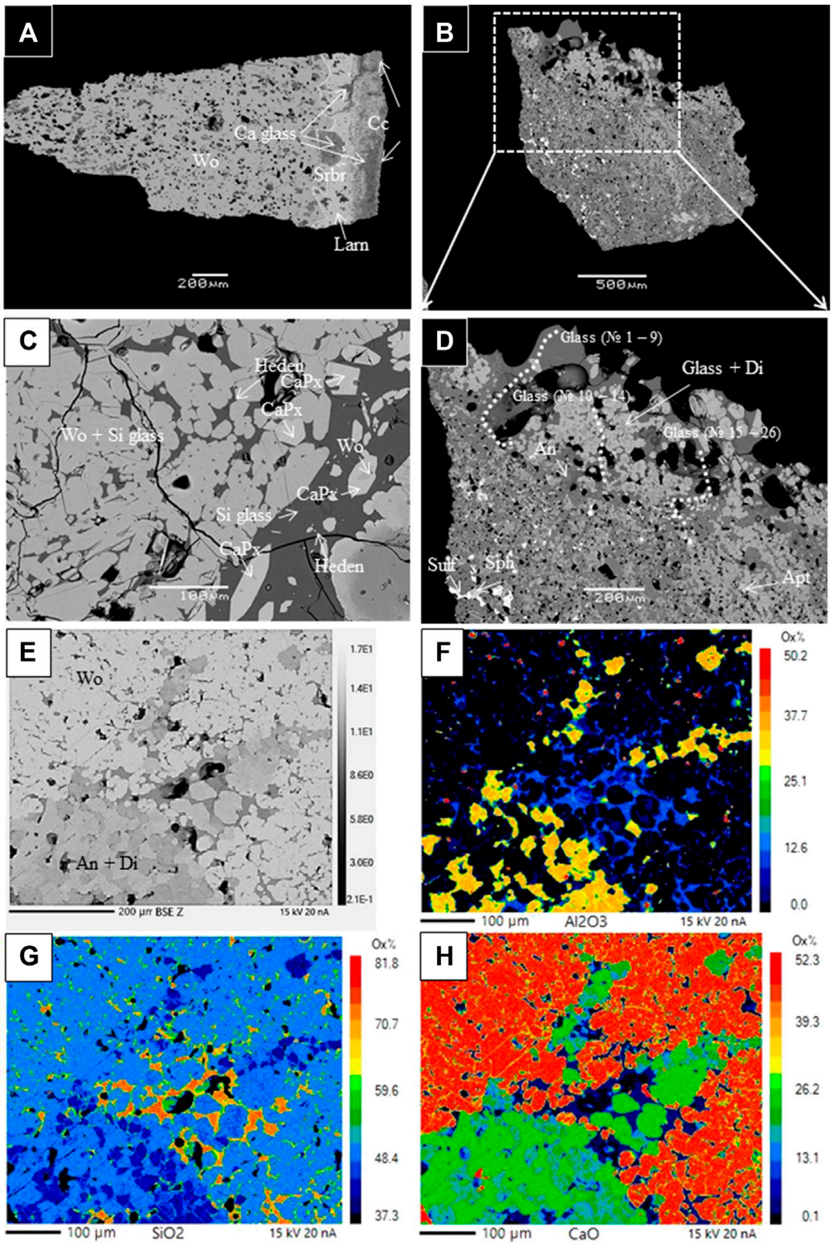

FIGURE 2
Representative backscattered electron images of the 1994–2006 Merapi calc–silicate xenoliths with mineral and glasses phases identified by EDS energy-dispersive X-ray spectroscopy and EPMA. Cc, calcite; Wo, wollastonite; Larn, larnite; Srbr, srebrodolskite; Ca glass, calcic glass; Si glass, silicic glass; Di, diopside, Heden, hedenbergite; An, anorthite; Sulf, sulfide; Sph, sphene; and Apt, apatite. **(A)** M94 CS104 (1994); **(B, D)** MXCS1 (1998); **(C)** MXC06KAT2 (2006); and **(E–H)** 014-1 B (2010).

(i.e., typical metamorphic textures). The presence of silicic glass, detected in an assemblage with massive wollastonite at the rim of the calc–silicate xenolith, suggests production of silica-rich glasses at contact zones between the xenolith and magma.

Partial melt compositions predicted by rhyolite-MELTS modeling

Equilibrium partial melting results using rhyolite-MELTS (version 1.2.0) for two contrasting compositions (SiO_2-rich and CaO-rich, Supplementary Dataset S1 and Table 4) of the calc–silicate xenoliths as the wallrocks from the 1998–2010 Merapi collection (MXCS-1R; MXCS-4, Table 2) are presented in Figure 3 (starting composition) and Figure 4 (modeled partial melt compositions). The SiO_2-rich calc–silicate xenolith, MXCS-4, has a solidus assemblage (~625°C at 200 MPa) of quartz >> garnet >> clinopyroxene > minor feldspar, sphene, and apatite. At its solidus, the assemblage is H_2O-fluid saturated. During partial melting, melts range from ~67 wt% SiO_2 and 12 wt % CaO [at smaller degrees of melt (<1%)] to ~84% SiO_2 at the liquidus. Enriched CaO (>20 wt%) is produced during

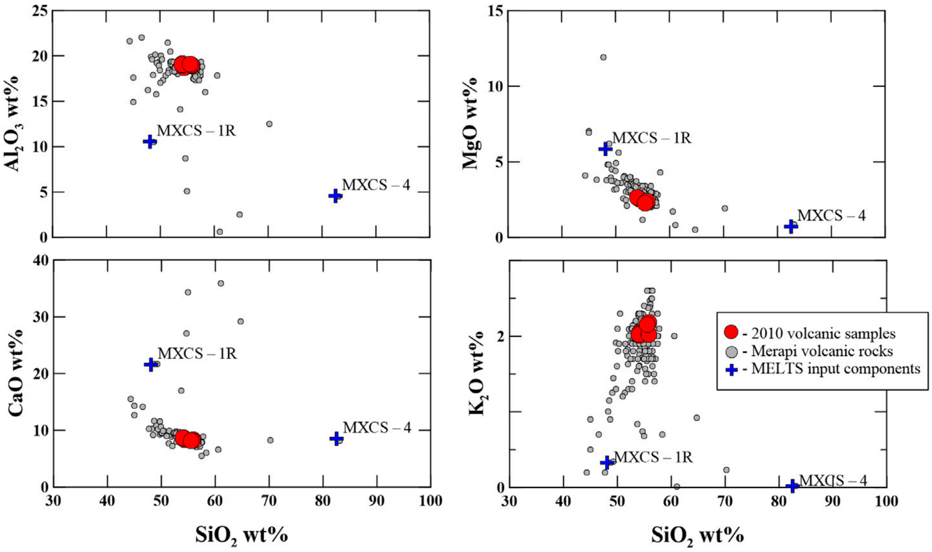

FIGURE 3
The 2010 and other Merapi volcanic rocks and the input component composition used for the thermodynamic modeling of the calc–silicate xenolith partial melting. All details of the thermodynamic modeling (MELTS) are summarized in Table 4 and Supplementary Dataset S1. The Merapi volcanic rocks are from the MERAPIDATA database (Borisova et al., 2011).

equilibrium partial melting between ~790°C (~3.5% partial melt) to ~955°C (25% partial melt). Minerals are consumed in the following order: alkali feldspar (~Or$_{80}$) at ~630°C, the fluid phase at ~650°C, and apatite and garnet between ~815°C and 845°C, followed by sphene (~950°C), plagioclase (~1055°C), and clinopyroxene (~1100°C). Quartz remains the only solid phase above this temperature to the liquidus. See Figure 4 and Supplementary Dataset S1 for more details.

The CaO-rich xenolith, MXCS-1R, is at ~5% melt at ~656°C, where the rhyolite-MELTS run encountered a quadratic error. The conditions of partial melting are well represented by the rhyolite-MELTS results, despite this. The near-solidus assemblage includes clinopyroxene >> garnet > plagioclase > quartz > minor sphene, alkali feldspar, and apatite. This xenolith is not fluid saturated at any point at 200 MPa. During partial melting, SiO$_2$ (wt%) values initiate at ~67.9 (~656°C), increase to a maximum of 72.6 (~766°C), and then, decrease to ~51.7 at the liquidus. CaO (wt%) starts at ~11 at 656°C, increases to a maximum of 25.6 at 886°C (~21% melting), and then, decreases to ~23 wt% at the liquidus. Minerals are consumed in the following order: alkali feldspar (~666°C), quartz (~766°C), sphene and garnet between 856°C and 881°C, apatite (~906°C), and plagioclase (1201°C). Clinopyroxene remains the only phase present to the liquidus. See Figure 4 and Supplementary Dataset S1 for more details.

Discussion

Reaction to produce the calc–silicate crust

Figure 2A demonstrates that the investigated sample fragment, 1994 xenolith M94-CS-104, contains one predominant mineral phase: porous wollastonite formed by regular skarn reaction:

$$CaCO_3^S + SiO_2^F = CaSiO_3^S + CO_2^F, \quad (1)$$

where CaCO$_3^S$ is a calcite molecule, SiO$_2^F$ is SiO$_2$ dissolved in a (an aqueous) fluid (F), CaSiO$_3^S$ is the formed wollastonite mineral, and CO$_2^F$ is the fluid liberated upon reaction. This reaction, also summarized in Figure 5, demonstrates an important flux of silica by shallow aqueous fluid to produce the calc–silicate crust that is enriched in silica relative to the sediments.

Geochemical and mineral tracers of calc–silicate xenolith assimilation

Figure 1 shows that Sr is a unique isotopic tracer of calc–silicate assimilation, whereas Pb isotopes are depleted in the calc–silicate xenoliths compared to the Merapi volcanic rocks. Nd behaves differently depending on the type of the crustal material. As to Sr–Pb isotope signatures, radiogenic Sr and unradiogenic Pb are characteristic features of the Merapi calc–silicate xenoliths (Figure 1). Table 2 also demonstrates that in addition to Sr (up to 682 ppm), trace elements such as Ba (up to 326 ppm), Co (up to 119 ppm), Cr (up to 674 ppm), Cu (up to 245 ppm), V (up to 139 ppm), Zn (up to 105 ppm), and Zr (up to 298 ppm) may be considered as geochemical tracers of calc–silicate crust assimilation. Moderate to strong enrichment of the calc–silicate xenoliths in the trace elements compared to the sediments is likely to be related to aqueous-carbonic fluid reaction at contact metamorphic conditions (Figure 1).

In addition to high Sr contents and radiogenic ^{87}Sr/^{86}Sr, elevated CO$_2$, Ba, Co, Cr, Cu, V, Zn, and Zr contents in the magmatic minerals and associated glasses and re-crystallization/dissolution of wallrock sphene, quartz, garnet, apatite, and ilmenite are predicted

TABLE 4 Composition of calc–silicate wallrocks used for rhyolite-MELTS modeling (or MCS modeling).

Component (MCS models[a])	Input data	Ref	SiO2, wt%	TiO2	Al2O3	Fe2O3tot	FeOtot	FeO[b]	Fe2O3[b]	MgO	MnO	CaO	Na2O	K2O	P2O5	H2O	CO2
WR (M1–M5 M10–M11)	MXCS–4$	C2007	82.49	0.48	4.55	2.75	-	1.02	0.24	0.72	0.11	8.52	0.16	0.02	0.05	0.07	0.17
WR (M6–M9)	MXCS–1R$	C2007	48.11	0.50	10.52	11.31	-	4.18	1.00	5.84	0.32	21.56	0.54	0.33	0.17	0.36	-

All details on the calc–silicate xenoliths MXCS 4 and MXCS 1R may be found in the study of Chadwick et al. (2007).

[a] MCS models according to the study of Borisova et al. (2013; 2016).

[b] FeO and Fe2O3 contents are calculated from either FeOtot or Fe2O3tot contents suggesting FeO/Fe2O3 = 0.24.

by thermodynamic modeling (upon the wallrock melting) and are, thus, important tracers of calc–silicate crust assimilation.

Kinetics of reaction between calc–silicate crust and the Merapi magma

The 1994–2010 Merapi calc–silicate xenoliths are enriched in wollastonite in the core zones and frequently contain calcite as a relic mineral phase (Figure 2A; Deegan et al., 2010). In contrast, the xenoliths' rims are depleted in wollastonite and are commonly enriched in anorthite and diopside. The xenolith samples also contain veins and spherical agglomerates of calcic glasses (31.7 ± 6.8 wt% SiO_2, 37.8 ± 3.1 wt% CaO) (Table 3). This type of natural calcic glass strongly resembles "Ca-rich glasses" (28–38 wt% SiO_2, 27–34 wt% CaO) experimentally produced by Jolis et al. (2013), Deegan et al. (2010), and Blythe et al. (2015) from calcite-enriched material heated with silicate melt at 500 MPa and 1200°C. Moreover, Deegan et al. (2010) reported even more Ca-rich glasses (containing up to 62 wt% CaO) associated with natural wollastonite–calcite in the Merapi xenoliths. We interpret the natural calcic glasses reported in Table 3 to be the result of the reaction between calcite $CaCO_3{}^S$ and $SiO_2{}^{L/F}$ (see Eq. 2; Blythe et al., 2015) rather than the "dissociation" proposed by Deegan et al. (2010). Figure 2A demonstrates the occurrence of calcic glasses in the M94 CS104 xenolith in an assemblage with larnite and wollastonite, whereas the major element composition of the calcic glasses coincides with a calcite–quartz control line, suggesting that the composition of the calcic melt is controlled by the following dissolution reaction:

$$CaCO_3{}^S + SiO_2{}^{L/F} = CaSiO_3{}^L + CO_2{}^F, \quad (2)$$

where $SiO_2{}^{L/F}$ (silicate melt (L) or fluid (F) form of SiO_2) is derived from the magma, F is fluid, and L is the produced Ca–Si-melt.

In the xenolith rim of MXCS1, the observed assemblage of euhedral–subhedral individual crystals of diopside with highly silicic glasses (76.5 ± 3.5 wt% SiO_2, 12.3 ± 3.2 wt% Al_2O_3, 4.3 ± 2.2 wt% CaO) in the 1998 calc–silicate xenoliths (Table 3; Figure 2B) resembles an association of idiomorphic clinopyroxene rims with silicic glasses around quartz xenocrysts produced by dissolution of quartz phenocrysts during the reaction with basaltic magma (Donaldson, 1986; Borisova et al., 2014). We infer, therefore, that the assemblage of silicic glasses and euhedral–subhedral individual crystals of diopside is the result of incongruent dissolution of metamorphic minerals associated with crystallization of calcic clinopyroxenes in the produced highly silicic melts. The incongruent dissolution reaction may be described as follows:

$$CaSiO_3{}^S + SiO_2{}^{L1/S} + MgO^{L1} = CaMgSi_2O_6{}^S, \quad (3)$$

where $CaSiO_3{}^S$ is residual wollastonite, $SiO_2{}^{L1}$ is SiO_2 in the initial melt or solid $SiO_2{}^S$ quartz, MgO^{L1} is MgO components in the initial melt (L_1), and $CaMgSi_2O_6{}^S$ is diopside in the produced highly silicic melt. The mechanism of the crustal assimilation may be first marked by incongruent dissolution of crustal metamorphic minerals with generation of highly silicic (77 ± 4 wt% of SiO_2, 12 ± 3 wt% of Al_2O_3) melts in association with idiomorphic diopside [$Wo_{49}En_{29}$; 57 ± 3 Mg# = Mg/(Mg+Fe^{2+})] or other calcic pyroxenes ($Wo_{54\text{-}82}$ $En_{2\text{-}21}$; 16–43 Mg#).

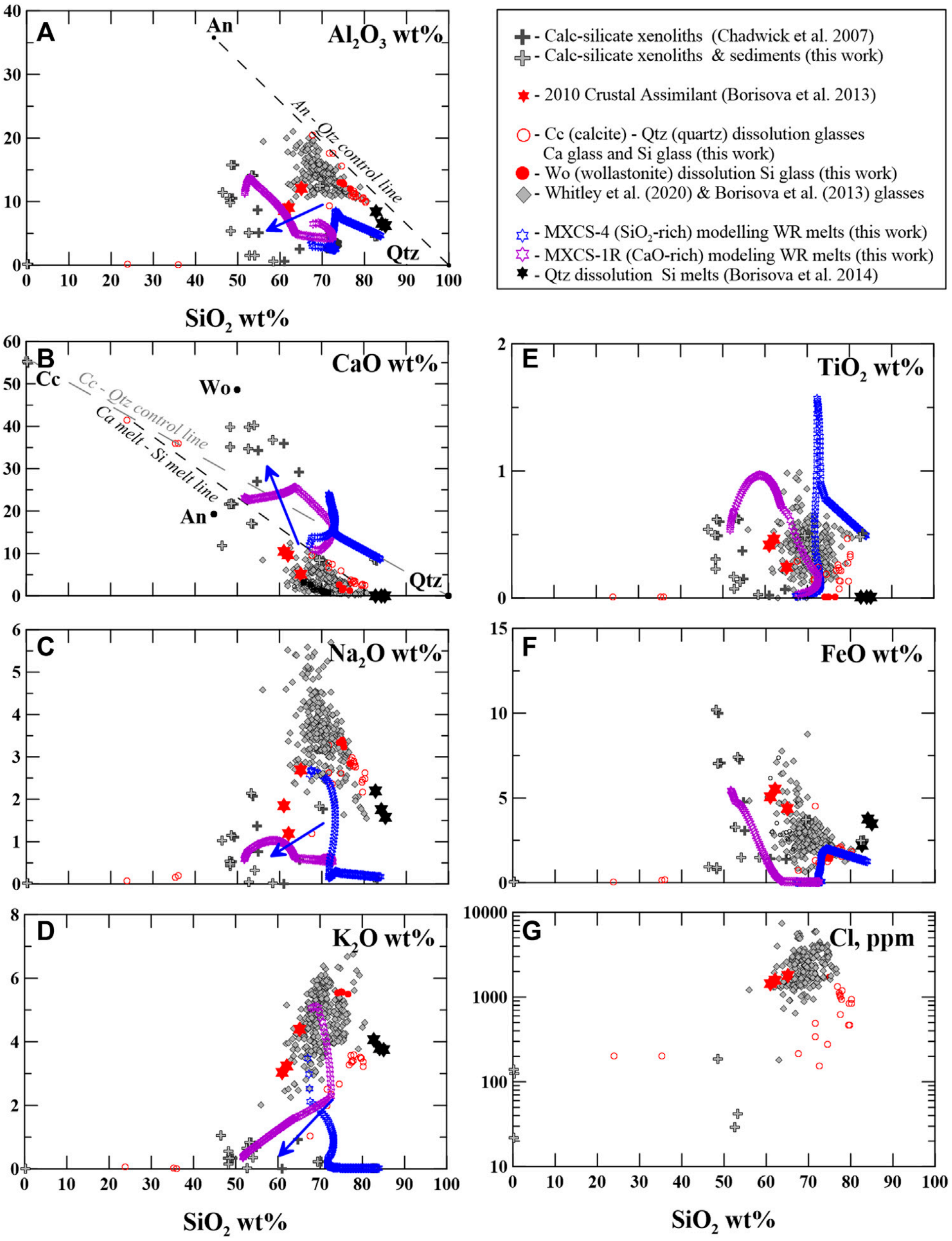

FIGURE 4
(A) Al_2O_3–SiO_2, **(B)** CaO–SiO_2, **(C)** Na_2O–SiO_2, **(D)** K_2O–SiO_2, **(E)** TiO_2–SiO_2, **(F)** FeO–SiO_2, and **(G)** Cl (ppm–SiO_2 (wt%) plotted for the bulk-rock calc–silicate xenoliths and local carbonate sediments, 2006 and 2010 glasses (groundmass), the 2010 Crustal Assimilant glasses compared to the Ca and Si glasses generated by dissolution of calcite, and quartz generated by Woll dissolution. Quartz dissolution glass compositions are from the study of Borisova et al. (2014). The 2006 data are from the study of Costa et al. (2013), and the 2010 data are from the study of Borisova et al. (2013). The MELTS (or MCS) modeling data (see Supplementary Dataset S1) are given for the wallrock melts. The blue arrows indicate the wallrock melt composition trajectories upon the xenolith heating and partial melting (WR). The blue arrows reflect the trends described by the 2010 Crustal Assimilant. An - anorthite; Qtz - quartz; Cc - calcite; Wo - wollastonite.

The highly silicic glasses (melts) may be directly predicted by thermodynamic equilibrium or modeling of partial melting of the calc–silicate xenoliths. The thermodynamic modeling results record silicic melt compositions with the highest SiO_2 = 67–84 wt% and variable CaO = 12–26 wt% contents upon partial melting of the crustal xenoliths due to quartz, garnet, and feldspar consumption. Figure 4 demonstrates that all oxide contents in the modeled highly silicic melts produced at thermodynamic equilibrium during partial melting of calc–silicate xenoliths (at 630°C–1200°C) closely resemble those of the analyzed silicic glasses in the 1994–2010 xenoliths.

Consequently, SiO_2, Al_2O_3, and CaO contents in the generated melts may be controlled by chemical mixing between the silicic melts and generated highly mobile carbonate (Ca-rich) melt. The capacity of carbonate melt rich in CO_3 to be extremely mobile and to migrate from skarns to a

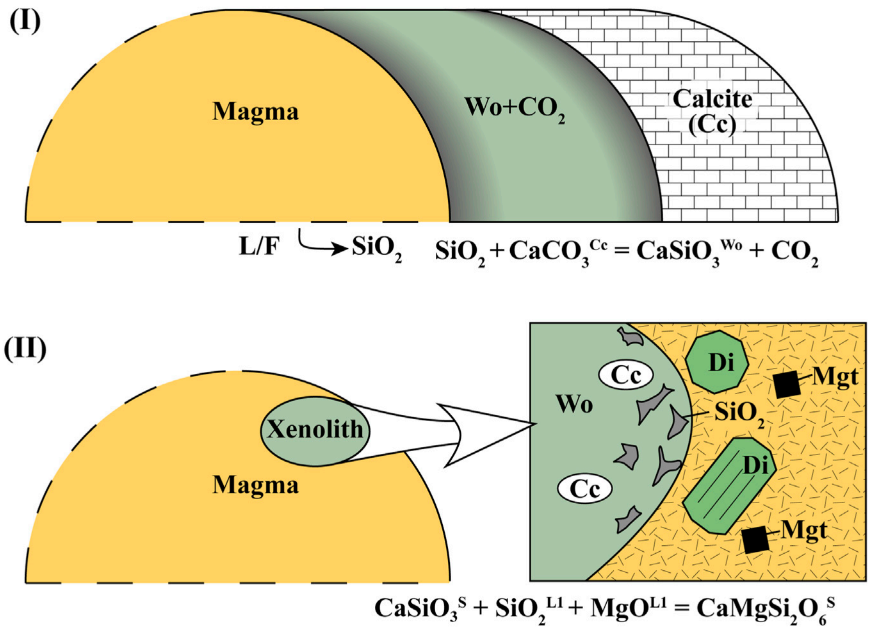

FIGURE 5
Principal schema of (I) the calc–silicate crust production and (II) calc–silicate crust assimilation by the Merapi magma (Merapi volcano, Indonesia). The elevated trace element (Ba, Co, Cr, Cu, V, Zn, and Zr) contents in the calc–silicate crust and the contaminated magma are related to the important flux of these elements from the magmatic source (in form of an aqueous-carbonic fluid) at stage I. Cc, calcite; Wo, wollastonite; Di, diopside; SiO_2, silicic glasses; and Mgt, magnetite. Our hypothesis is that the rate-limiting process is the mixing of the produced crustal melts with andesitic melt (average 65 wt% SiO_2) through chemical diffusion of Si–Al in hybrid aluminosilicate melts.

magma chamber (Gaeta et al., 2009) indicates that CaO-SiO_2-Al_2O_3 contents in the analyzed silicic glasses (Figure 4) can be modeled by mixing between the highly silicic and carbonate melts. In order to explain Al_2O_3 and other major element contents in the assimilating melts (e.g., the 2010 Crustal Assimilant), it is necessary to suggest involvement and chemical mixing with K-Cl-rich andesitic melts (average 65 wt % SiO_2), proposed by Borisova et al. (2013; 2016) as a natural melt component of the resident magma. We hypothesize that the rate limiting process of the crustal assimilation is the mixing of the produced crustal melts with the andesitic to basaltic andesite melts through Si–Al diffusion that explains major and volatile (Cl) element contents in the Merapi glass products.

Physical–chemical disequilibrium *versus* thermodynamic modeling

We predict that because of rapid heat diffusion, the calc–silicate material has to reach the temperature of 900°C rapidly upon the magma–xenolith interaction, suggesting effective partial melting and dissolution of the crustal xenoliths at 900°C. Thermal stability of carbonates is limited to a temperature range of 820°C–870°C (Ar and Doğu, 2001). Calcite starts to decompose at 620°C, and the calcination reaction is completed at 820°C at atmospheric pressure (Stern & Weise, 1966; Ar and Doğu, 2001), suggesting complete consumption of calcite at the pre-eruptive temperatures of 925°C–1100°C. Given the chemical equilibrium during contact metamorphism created by heat flow from basaltic andesite magma, the xenolith (several cm in size) should attain the pre-eruptive temperature of 925°C–1100°C at 200–300 MPa. Nevertheless, the calcite inclusions (Deegan et al., 2010; Borisova et al., 2013) and calcite–larnite–wollastonite assemblage (Figure 2) are observed in the Merapi calc–silicate xenoliths as metastable mineral phases.

These observations suggest that the reaction between the magma and the 1994–2010 calc–silicate xenoliths was out of physical–chemical (or thermodynamic) equilibrium. The disequilibrium may be related to sluggish kinetics of the residual calcite consumption and Si–Al diffusion in the hybrid melt. In any case, it is likely that the crust–magma interaction is controlled by kinetics of reactions such as crustal partial melting, mineral dissolution and recrystallization, and melt mixing. Nevertheless, the mechanism of crustal calc–silicate material assimilation can be well predicted by thermodynamic modeling using rhyolite-MELTS, whereas more experiments are required to constrain the rate of the calc–silicate material-silicate magma interactions. Based on available experimental data (Zhang et al., 1989; Shaw, 2006), we predict that this crustal assimilation rate is controlled by Si–Al diffusion in the hydrous silicic melts produced during the melt–crust interaction. These experimental data suggest that silica activity in the melt defines the maximal dissolution rate, whereas the melt viscosity determines whether this maximum rate may be achieved in the case of diffusion control.

Conclusion

1) *In situ* electron probe microanalyses of the 1994–2010 calc–silicate xenolith minerals and glasses and the observed reactions and thermodynamic modeling using MELTS or MCS suggest that selective assimilation at ~ 650°C–1100°C and 200–300 MPa prior to the 1994–2010 eruptions preserved wollastonite and carbonate melts quenched to natural calcic glasses (32 ± 7 wt% SiO_2, 38 ± 3 wt % CaO) as well as minor calcite mineral as a thermodynamically metastable mineral phases in the calc–silicate xenoliths. The following reaction happened during the 1994–2010 calc–silicate xenolith interaction with the Merapi magma:

$CaSiO_3{}^S + SiO_2{}^{L1/S} + MgO^{L1} = CaMgSi_2O_6{}^S$, where $CaSiO_3{}^S$ is residual metastable wollastonite, $SiO_2{}^{L1/S}$ are SiO_2 and MgO in the initial melt (L_1) or quartz (S), MgO^{L1} is MgO in the initial melt (L_1), and $CaMgSi_2O_6{}^S$ is diopside in the produced highly silicic melt.

2) The mechanism of the 1994–2010 calc–silicate xenolith assimilation is generation of highly silicic (77 ± 4 wt% of SiO_2, 12 ± 3 wt% of Al_2O_3) melts in association with idiomorphic diopside [$Wo_{49}En_{29}$; 57 ± 3 Mg# = Mg/(Mg+Fe^{2+})] or other calcic pyroxenes (Wo_{54-82} En_{2-21}; 16–43 Mg#) due to mineral dissolution and recrystallization reactions. Modeling using rhyolite-MELTS predicts that the major element composition of the generated silicic glasses (up to 67–84 wt % SiO_2) is controlled by the calc–silicate material partial melting.
3) In addition to elevated Sr contents and radiogenic $^{87}Sr/^{86}Sr$ ratio, important geochemical tracers of the calc–silicate assimilation are elevated CO_2, Ba, Co, Cr, Cu, V, Zn, and Zr contents in the minerals and glasses. The re-crystallization/dissolution of wallrock-derived sphene, quartz, garnet, apatite, and ilmenite is predicted by thermodynamic modeling (upon the wallrock partial melting) and, thus, are important mineral tracers of crustal assimilation.
4) Although kinetics of the calc–silicate material–melt interaction likely control the calc–silicate assimilation process, the mechanism of the assimilation process can be well predicted by thermodynamic modeling (MELTS or MCS). Further application of kinetic experiments on the calc–silicate material interaction with aluminosilicate magma is useful to quantify the rates of crustal assimilation. We hypothesize that the rate-limiting process of crustal assimilation is chemical mixing of the produced crustal melts through the chemical diffusion of Si–Al in hybrid melts associated with convection.

Data availability statement

The original contributions presented in the study are included in the article/Supplementary Material; further inquiries can be directed to the corresponding author.

Author contributions

All authors listed have made a substantial, direct, and intellectual contribution to the work and approved it for publication.

Funding

This study was supported by the VELI national site “Volcans Explosifs Laboratoire Indonesien” and the mixed laboratory “Indonesian Subduction and associated risks” or “Subductions Indonésiennes et Risques associés” (SIR) in France and US National Science Foundation projects 1551052 and 2151038.

Acknowledgments

The authors thank the editor Patrizia Fiannacca, S. Erdmann, and another reviewer for the important suggestions on this work, Valentin R. Troll and Frances Deegan for providing the 1998—2006 Merapi xenolith and sediment samples, and Philippe de Parseval for electron probe mapping of the 2010 Merapi sample. The 2015 French expedition provided the 2006–2010 Merapi products for this work.

Conflict of interest

The authors declare that the research was conducted in the absence of any commercial or financial relationships that could be construed as a potential conflict of interest.

Publisher’s note

Supplementary material

The Supplementary Material for this article can be found online at: https://www.frontiersin.org/articles/10.3389/feart.2023.1186207/full#supplementary-material

References

Ar, I., and Doğu, G. (2001). Calcination kinetics of high purity limestones. *Chem. Engeneering J.* 83, 131–137. doi:10.1016/s1385-8947(00)00258-8

Blythe, L. S., Deegan, F. M., Freda, C., Jolis, E. M., Masotta, M., Misiti, V., et al. (2015). CO_2 bubble generation and migration during magma – carbonate interaction. *Contrib. Mineral. Petrol.* 169, 42. doi:10.1007/s00410-015-1137-4

Bohrson, W. A., Spera, F. J., Ghiorso, M. S., Brown, G. A., Creamer, J., and Mayfield, A. (2014). Thermodynamic model for energy-constrained open-system evolution of crustal magma bodies undergoing simultaneous recharge, assimilation and crystallization: the magma chamber simulator. *J. Petrology* 55, 1685–1717. doi:10.1093/petrology/egu036

Bohrson, W. A., Spera, F. J., Heinonen, J. S., Brown, G. A., Scruggs, M. A., Adams, J. V., et al. (2020). Diagnosing open-system magmatic processes using the magma chamber simulator (MCS): part I—major elements and phase equilibria. *Contributions Mineralogy Petrology* 175, 104–129. doi:10.1007/s00410-020-01722-z

Borisova, A. Y., Gurenko, A. A., Martel, C., Kouzmanov, K., Cathala, A., Bohrson, W. A., et al. (2016). Oxygen isotope heterogeneity of arc magma recorded in plagioclase from the 2010 Merapi eruption (Central Java, Indonesia). *Geochimica Cosmochimica Acta* 190, 13–34. doi:10.1016/j.gca.2016.06.020

Borisova, A. Y., Martel, C., Gouy, S., Pratomo, I., Sumarti, S., Toutain, J-P., et al. (2013). Highly explosive 2010 Merapi eruption: evidence for shallow-level crustal assimilation and hybrid fluid. *J. Volcanol. Geotherm. Res.* 261, 193–208. doi:10.1016/j.jvolgeores.2012.11.002

Borisova, A. Y., Martel, C., Pratomo, I., Toutain, J., Sumarti, S., and Surono, S. "Merapidata: new petrologic and geochemical database of the Merapi volcano, central java, Indonesia," in Proceedings of the AGU Fall Meeting Abstracts, San Francisco, California, December 2011, V21E–V2536.

Borisova, A. Y., Pichavant, M., Bény, J.-M., Rouer, O., and Pronost, J. (2005). Constraints on dacite magma degassing and regime of the June 15, 1991, climactic eruption of Mount Pinatubo (Philippines): new data on melt and crystal inclusions in quartz. *J. Volcanol. Geotherm. Res.* 145 (1-2), 35–67. doi:10.1016/j.jvolgeores.2005.01.004

Borisova, A. Y., Pokrovski, G. S., Pichavant, M., Fréydier, R., and Candaudap, F. (2010). Amorphous Materials: properties, Structure, and Durability: arsenic enrichment in hydrous peraluminous melts: insights from femtosecond laser ablation-inductively coupled plasma-quadrupole mass spectrometry, and *in situ* X-ray absorption fine structure spectroscopy. *Am. Mineralogist* 95, 1095–1104. doi:10.2138/am.2010.3424

Borisova, A. Y., Toutain, J-P., Dubessy, J., Pallister, J., Zwick, A., and Salvi, S. (2014). H2O–CO2–S fluid triggering the 1991 Mount Pinatubo climactic eruption (Philippines). *Bull. Volcanol.* 76, 800. doi:10.1007/s00445-014-0800-3

Borisova, A. Y., Toutain, J-P., Stefansson, A., Gouy, S., and de Parseval, Ph. (2012). Processes controlling the 2010 Eyjafjallajökull explosive eruption. *J. Geophys. Res. Solid Earth* 117, B5. doi:10.1029/2012JB009213

Burt, D. M. (1982). Skarn deposits; historical bibliography through 1970. *Econ. Geol.* 77 (4), 755–763. doi:10.2113/gsecongeo.77.4.755

Carignan, J., Hild, P., Mevelle, G., Morel, J., and Yeghicheyan, D. (2001). Routine analyses of trace elements in geological samples using flow injection and low pressure on-line liquid chromatography coupled to icpms: A study of geochemical reference materials br, DR-N, UB-N, AN-G and gh. *Geostand. Geoanal. Res.* 25, 187–198. doi:10.1111/j.1751-908X.2001.tb00595.x

Chadwick, J. P. (2008). "Crustal processes in volcanic systems: case studies from northern Ireland, New Zealand and Indonesia,". Ph.D. Thesis (Dublin, Ireland: University of Dublin), 274.

Chadwick, J. P., Troll, V. R., Ginibre, C., Morgan, D., Gertisser, R., Waight, T. E., et al. (2007). Carbonate assimilation at Merapi volcano, java, Indonesia: insights from crystal isotope stratigraphy. *J. Petrology* 48, 1793–1812. doi:10.1093/petrology/egm038

Cloquet, C., Carignan, J., and Libourel, G. (2006). Atmospheric pollutant dispersion around an urban area using trace metal concentrations and Pb isotopic compositions in epiphytic lichens. *Atmos. Environ.* 40, 574–587. doi:10.1016/j.atmosenv.2005.09.073

Costa, F., Andreastuti, S., Bouvet de Maisonneuve, C., and Pallister, J. (2013). Petrological insights into the storage conditions, and magmatic processes that yielded the centennial 2010 Merapi explosive eruption. *J. Volcanol. Geotherm. Res.* 261, 209–235. doi:10.1016/j.jvolgeores.2012.12.025

Deegan, F. M., Troll, V. R., Freda, C., Misiti, V., Chadwick, J. P., McLeod, C. L., et al. (2010). Magma–carbonate interaction processes and associated CO_2 release atMerapi volcano, Indonesia: insights from experimental petrology. *J. Petrology* 51, 1027–1051. doi:10.1093/petrology/egq010

Deegan, F. M., Troll, V. R., Gertisser, R., and Freda, C. (2023). "Magma-carbonate interaction at Merapi volcano, Indonesia," in *Merapi Volcano. Active volcanoes of the world*. Editors R. Gertisser, V. R. Troll, T. R. Walter, I. G. M. A. Nandaka, and A. Ratdomopurbo (Cham, Germany: Springer). doi:10.1007/978-3-031-15040-1_10

Erdmann, S., Martel, C., Pichavant, M., Bourdier, J. L., Champallier, R., Komorowski, J. C., et al. (2016). Constraints from phase equilibrium experiments on pre-eruptive storage conditions in mixed magma systems: A case study on crystal-rich basaltic andesites from mount Merapi, Indonesia. *J. Petrology* 57 (3), 535–560. doi:10.1093/petrology/egw019

Erdmann, S., Martel, C., Pichavant, M., and Kushnir, A. (2014). Amphibole as an archivist of magmatic crystallization conditions: problems, potential, and implications for inferring magma storage prior to the paroxysmal 2010 eruption of mount Merapi, Indonesia. *Contributions Mineralogy Petrology* 167, 1016–1023. doi:10.1007/s00410-014-1016-4

Freda, C., Gaeta, M., Misiti, V., Mollo, S., Dolfi, D., and Scarlato, P. (2008). Magma–carbonate interaction: an experimental study on ultrapotassic rocks from alban hills (central Italy). *Lithos* 101, 397–415. doi:10.1016/j.lithos.2007.08.008

Gaeta, M., Di Rocco, T., and Freda, C. (2009). Carbonate assimilation in open magmatic systems: the role of melt-bearing skarns and cumulate-forming processes. *J. Petrology* 50, 361–385. doi:10.1093/petrology/egp002

Ghiorso, M. S., and Gualda, G. A. R. (2015). An H2O-CO2 mixed fluid saturation model compatible with rhyolite-MELTS. *Contributions Mineralogy Petrology* 169, 53. doi:10.1007/s00410-015-1141-8

Gualda, G. A., Ghiorso, M. S., Lemons, R. V., and Carley, T. L. (2012). Rhyolite-MELTS: A modified calibration of MELTS optimized for silica-rich, fluid-bearing magmatic systems. *J. Petrology* 53 (5), 875–890. doi:10.1093/petrology/egr080

Heinonen, J. S., Bohrson, W. A., Spera, F. J., Brown, G. A., Scruggs, M. A., and Adams, J. V. (2020). Diagnosing open-system magmatic processes using the magma chamber simulator (MCS): part II—trace elements and isotopes. *Contributions Mineralogy Petrology* 175, 105–121. doi:10.1007/s00410-020-01718-9

Iacono-Marziano, G., Gaillard, F., and Pichavant, M. (2008). Limestone assimilation by basaltic magmas: an experimental re-assessment and application to Italian volcanoes. *Contributions Mineralogy Petrology* 155, 719–738. doi:10.1007/s00410-007-0267-8

Iacono-Marziano, G., Gaillard, F., Scaillet, B., Pichavant, M., and Chiodini, G. (2009). Role of non-mantle CO_2 in the dynamics of volcano degassing: the mount vesuvius example. *Geology* 37, 319–322. doi:10.1130/g25446a.1

Jarosevich, E., Nelen, J. A., and Norberg, J. A. (1980). Reference samples for electron microprobe analysis. *Geostand. Newsletters* 4, 43–47. doi:10.1111/j.1751-908x.1980.tb00273.x

Jolis, E. M., Freda, C., Troll, V. R., Deegan, F. M., Blythe, L. S., McLeod, C. L., et al. (2013). Experimental simulation of magma-carbonate interaction beneath Mt.Vesuvius, Italy. *Contributions Mineralogy Petrology* 166, 1335–1353. doi:10.1007/s00410-013-0931-0

Jousset, P., Pallister, J., and Surono (2013). The 2010 eruption of Merapi volcano. *J. Volcanol. Geotherm. Res.* 261, 1–6. doi:10.1016/j.jvolgeores.2013.05.008

Luais, B., Telouk, P., and Albarède, F. (1997). Precise and accurate neodymium isotopic measurements by plasma-source mass spectrometry. *Geochim. Cosmochim. Acta* 61, 4847–4854. doi:10.1016/S0016-7037(97).00293-7

Manhès, G., Allegre, C. J., Dupré, B., and Hamelin, B. (1980). Lead isotope study of basic-ultrabasic layered complexes–speculations about the age of the Earth and primitive mantle characteristics. *Earth Planet. Sci. Lett.* 47, 370–382. doi:10.1016/0012-821X(80)90024-2

Mollo, S., Gaeta, M., Freda, C., DiRocco, T., Misiti, V., and Scarlato, P. (2010). Carbonate assimilation in magmas: A reappraisal based on experimental petrology. *Lithos* 114, 503–514. doi:10.1016/j.lithos.2009.10.013

Pichavant, M., Martel, C., Bourdier, J.-L., and Scaillet, B. (2002). Physical conditions, structure, and dynamics of a zoned magma chamber: mount Pelée (Martinique, Lesser Antilles Arc). *J. Geophys. Res.* 107 (B5), 2093. doi:10.1029/2001JB000315

Pin, C., Briot, D., Bassin, C., and Poitrasson, F. (1994). Concomitant separation of strontium and samarium-neodymium for isotopic analysis in silicate samples, based on specific extraction chromatography. *Anal. Chim. Acta* 298, 209–217. doi:10.1016/0003-2670(94)00274-6

Pouchou, J. L., and Pichoir, F. (1984). A new model for quantitative X-ray-microanalysis. Application to the analysis of homogenous samples. *La Rech. Aerosp.* 3, 167–192.

Schwarzkopf, L. M., Schmincke, H. U., and Cronin, S. J. (2005). A conceptual model for block-and-ash flow basal avalanche transport and deposition, based on deposit architecture of 1998 and 1994 Merapi flows. *J. Volcanol. Geotherm. Res.* 139 (1-2), 117–134. doi:10.1016/j.jvolgeores.2004.06.012

Shaw, C. S. J. (2006). Effects of melt viscosity and silica activity on the rate and mechanism of quartz dissolution in melts of the CMAS and CAS systems. *Contrib. Mineral. Petrol.* 151, 665–680. doi:10.1007/s00410-006-0086-3

Smyth, H., Hall, R., Hamilton, J., and Kinny, P. "East Java: cenozoic basins, volcanoes and ancient basement," in Proceedings of the Indonesian Petroleum Association, 30th Annual Convention, Jakarta, Indonesia, January 2005, 251–266.

Stern, K. H., and Weise, E. L. (1966). *High temperature properties and decomposition of inorganic salts: Carbonates*. Maryland, USA: US Department of Commerce, National Bureau of Standards.

Thirlwall, M. F. (2002). Multicollector ICP-MS analysis of Pb isotopes using a 207Pb-204Pb double spike demonstrates up to 400 ppm/amu systematic errors in Tl-normalization. *Chem. Geol.* 184, 255–279. doi:10.1016/S0009-2541(01)00365-5

Troll, V. R., Deegan, F. M., Jolis, E. M., Harris, C., Chadwick, J. P., Gertisser, R., et al. (2013). Magmatic differentiation processes at Merapi volcano: inclusion petrology and oxygen isotopes. *J. Volcanol. Geotherm. Res.* 261, 38–49. doi:10.1016/j.jvolgeores.2012.11.001

Voight, B., Constantine, E. K., Siswowidjoyo, S., and Torley, R. (2000). Historical eruptions of Merapi volcano, central Java, Indonesia, 1768–1998. *J. Volcanol. Geotherm. Res.* 100 (1-4), 69–138. doi:10.1016/s0377-0273(00)00134-7

Whitley, S., Halama, R., Gertisser, R., Preece, K., Deegan, F. M., and Troll, V. R. (2020). Magmatic and metasomatic effects of magma–carbonate interaction recorded in calc-silicate xenoliths from Merapi volcano (Indonesia). *J. Petrology* 61, 1–38. doi:10.1093/petrology/egaa048

Zhang, Y., Walker, D., and Lesher, C. E. (1989). Diffusive crystal dissolution. *Contributions Mineralogy Petrology* 102, 492–513. doi:10.1007/bf00371090

Frontiers in Earth Science

TYPE Original Research
PUBLISHED 16 November 2023
DOI 10.3389/feart.2023.1307303

OPEN ACCESS

EDITED BY
Yong Wang,
Southwest Petroleum University, China

REVIEWED BY
Tomoaki Morishita,
Kanazawa University, Japan
Karoly Nemeth,
Institute of Earth Physics and Space Sciences, Hungary
Ian Ernest Masterman Smith,
The University of Auckland, New Zealand

*CORRESPONDENCE
Anastassia Y. Borisova,
✉ anastassia.borisova@get.omp.eu

RECEIVED 04 October 2023
ACCEPTED 23 October 2023
PUBLISHED 16 November 2023

CITATION
Borisova AY, Melnik OE, Gaborit N, Bindeman IN, Traillou T, Raffarin M, Stefánsson A, Laurent O, Leisen M, Llovet X, de Parseval P, Proietti A and Tait S (2023), *In situ* probing of the present-day zircon-bearing magma chamber at Krafla, Northeastern Iceland. *Front. Earth Sci.* 11:1307303. doi: 10.3389/feart.2023.1307303

In situ probing of the present-day zircon-bearing magma chamber at Krafla, Northeastern Iceland

Anastassia Y. Borisova[1]*, Oleg E. Melnik[1,2], Nicolas Gaborit[1], Ilya N. Bindeman[3], Thibault Traillou[1], Marie Raffarin[1], Andri Stefánsson[4], Oscar Laurent[1], Mathieu Leisen[1], Xavier Llovet[5], Philippe de Parseval[1], Arnaud Proietti[6] and Stephen Tait[1]

[1]Géosciences Environnement Toulouse, GET, Centre National de la Recherche Scientifique, Institut de Recherche pour le Développement, Université Toulouse III Paul Sabatier, Université de Toulouse, Toulouse, France, [2]ISTerre, Centre National de la Recherche Scientifique, Université Grenoble Alpes, Grenoble, France, [3]Department of Earth Sciences, University of Oregon, Eugene, OR, United States, [4]Faculty of Earth Sciences, University of Iceland, Reykjavik, Iceland, [5]Scientific and Technological Centers, Universitat de Barcelona, Barcelona, Spain, [6]UAR Raimond Castaing, Centre National de la Recherche Scientifique, Institut National Polytechnique de Toulouse, Université Toulouse III Paul Sabatier, Institut National des Sciences Appliquées de Toulouse, Université de Toulouse, Toulouse, France

Active felsic magmatism has been rarely probed *in situ* by drilling but one recent exception is quenched rhyolite sampled during the 2009 Iceland Deep Drilling Project (IDDP). We report finding of rare zircons of up to ~100 µm in size in rhyolite glasses from the IDDP-1 well products and the host 1724 AD Viti granophyres. The applied SHRIMP U-Th dating for both the IDDP and the Viti granophyre zircons gives zero-age (± 2 kyr), and therefore suggests that the IDDP-1 zircons have crystallized from an active magma intrusion rather than due to the 20–80 ka post-caldera magmatic episodes recorded by nearby domes and ridges. Ti-in-zircon geothermometer for Viti granophyre reveals zircon crystallization temperatures ~800°C–900°C, whereas IDDP-1 rhyolite zircon cores show Ti content higher than 100 ppm, corresponding to temperatures up to ~1,100°C according to the Ti-in-zircon thermometer. According to our thermochemical model at such elevated temperatures as 1,100°C, rhyolitic magma cannot be saturated with zircon and zircon crystallization is not possible. We explain this controversy by either kinetic effects or non-ideal Ti incorporation into growing zircons at low pressures that start to grow from nucleus at temperatures ~930°C. High temperatures recorded by IDDP-1 zircon together with an occurrence of baddeleyite require that the rhyolite magma formed by partial melting of the host granophyre due to basaltic magma intrusion. Zr concentration profiles in glass around zircons are flat, suggesting residence in rhyolitic melt for >4 years. In our thermochemical modeling, three scenarios are considered. The host felsite rocks are intruded by: 1) a basaltic sill, 2) rhyolite magma 3) rhyolite sill connected to a deeper magmatic system. Based on the solution of the heat conduction equation accounting for the release of latent heat and effective thermal conductivity, these data confirm that the rhyolite magma could be produced by felsic crust melting as a result of injection of a basaltic or rhyolite sill during the Krafla Fires eruption (1975 AD).

KEYWORDS

Iceland Deep Drilling Project, IDDP-1 sample, zircon, rhyolite magma genesis, U-Th age, granophyre, melting, thermochemical modeling

Introduction

Icelandic volcanic activity represents an excellent example of a basalt-dominated environment where felsic crust can be produced either due to progressive cooling and interaction with rocks affected by both hydrothermal fluids and basaltic magmatism (e.g., Torsvik et al., 2015; Foulger et al., 2020) or by rejuvenation of the pre-existing continental crust by partial melting (Foulger et al., 2020). The low-δ^{18}O character of Icelandic felsic magmas suggests generation by open-system processes of partial melting of the hydrothermally-altered basaltic crust and melt-fluid-rock interactions (Jónasson, 1994; Gunnarsson et al., 1998; Bindeman et al., 2012; Pope et al., 2013). Other petrogenetic processes involved in the formation of felsic magmas include crustal assimilation coupled with fractional crystallization, and near-solidus differentiation (Nicholson et al., 1991; Jónasson, 2007; Elders et al., 2011; Pope et al., 2013; Hampton et al., 2021). Furthermore, magma mixing and the following hybridization have been documented and acted as a potential trigger for volcanic eruptions (e.g., Borisova et al., 2012 and references therein). Recently, Rooyakkers et al. (2021; 2022) evoked that a plate boundary rifting events and the related mafic recharges trigger hybrid to felsic eruptions of Krafla.

Natural data and experiments on crystallization of Icelandic glassy rhyolite and finely-crystallized (≤1 mm) granophyre partial melting demonstrate efficient partial melting of the felsic crust (e.g., Masotta et al., 2018), and efficient assimilation of hydrothermally altered crust (Hampton et al., 2021). Masotta et al. (2018) suggest that the IDDP-1 (Figure 1) rhyolite magma could originate from a high-degree partial melting of felsic rocks rich in quartz and feldspars by a basaltic intrusive event. Alternatively, the numerical model of Simakin and Bindeman (2022) based on δ^{18}O and δD allows two possible scenarios for IDDP-1 rhyolite production through interaction with *i*) overheated rhyolite or *ii*) basaltic magma. Subsequently, the IDDP-1 rhyolitic magma may have been

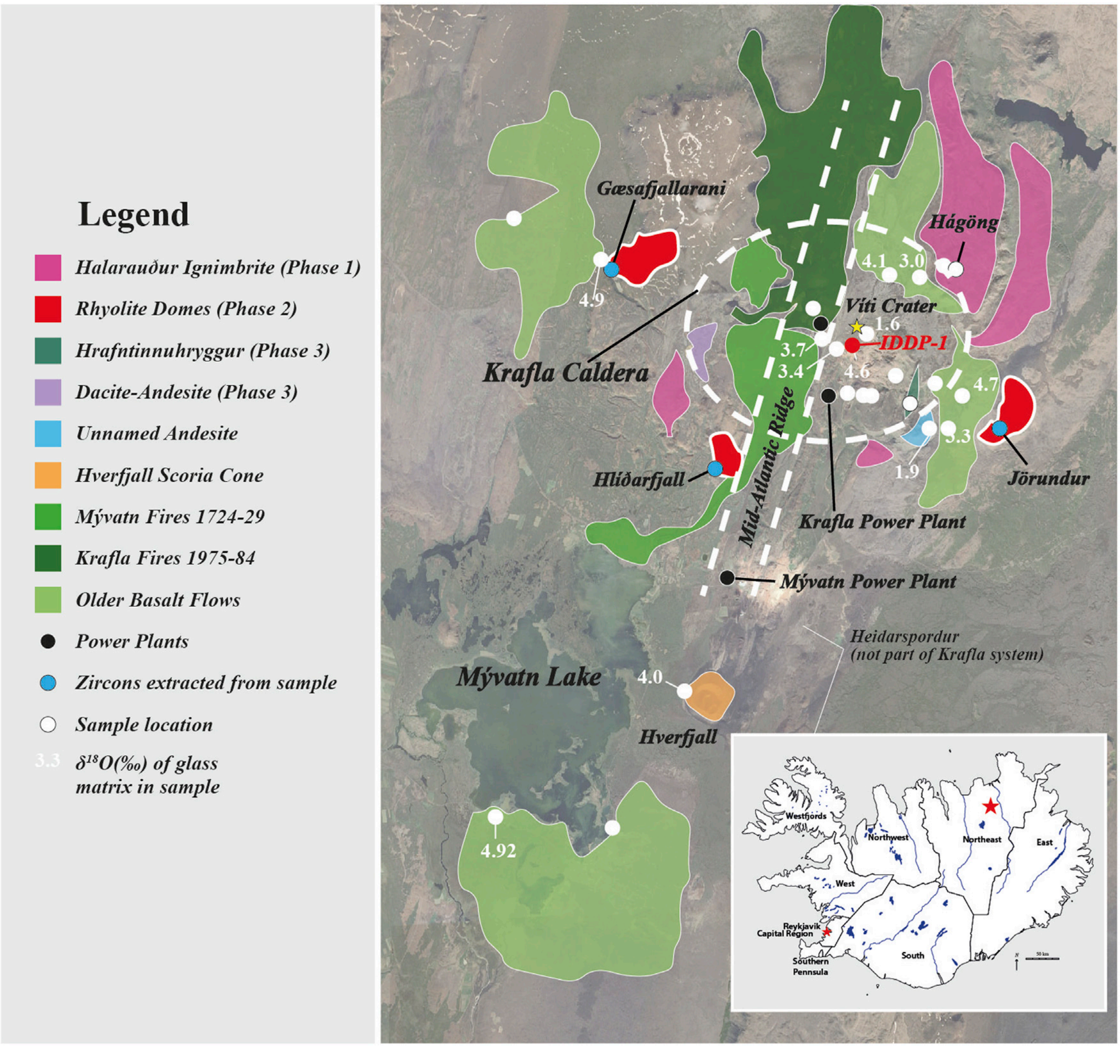

FIGURE 1
Geological map showing the Krafla caldera that is located in the Northeastern Iceland (see insert map) (modified after Hampton et al., 2021). The location of the IDDP-1 well and the Viti Crater are shown (see Supplementary Material).

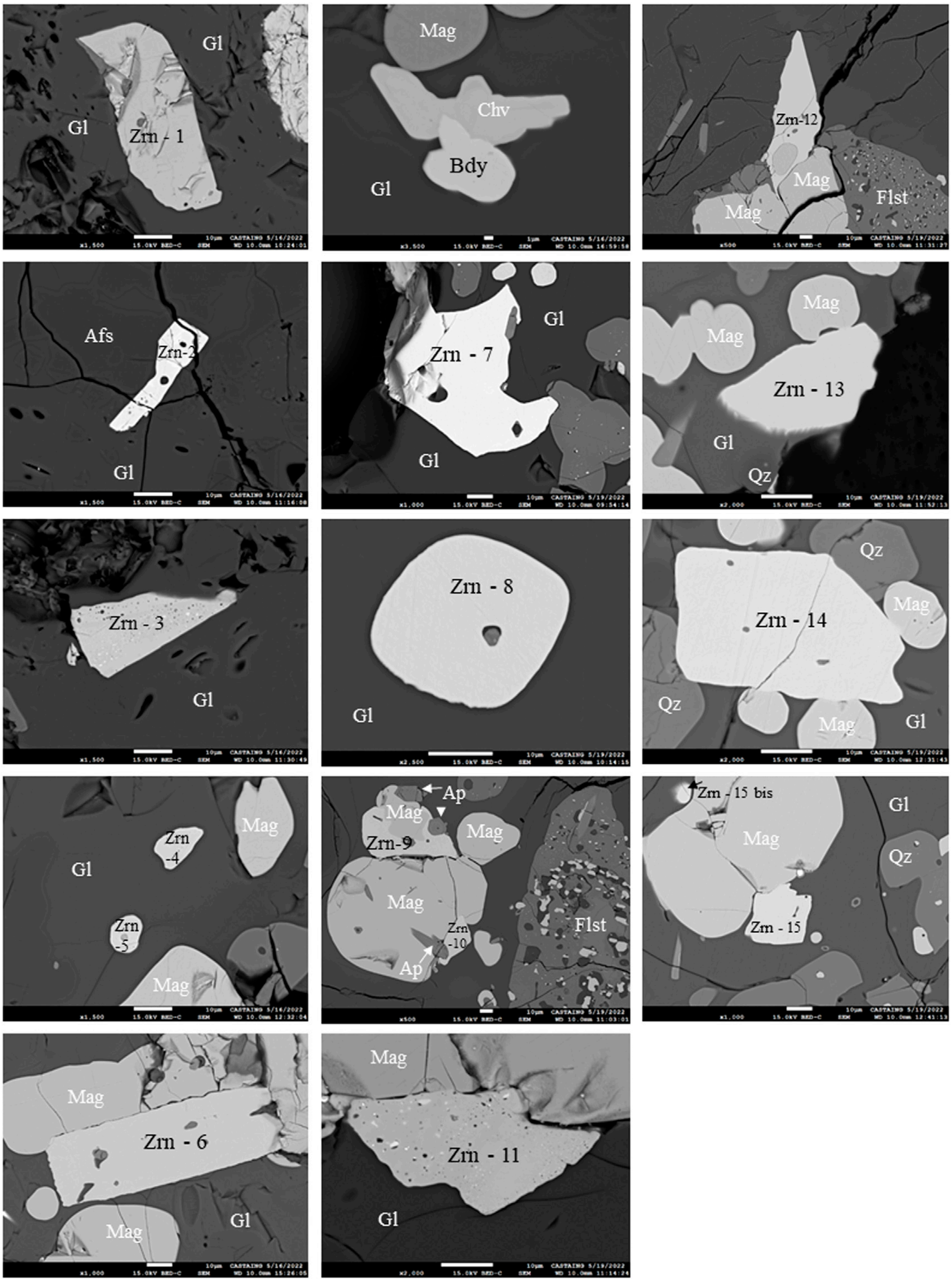

FIGURE 2
Representative backscattered electron (BSE) images of the IDDP-1 zircon (Zrn) and baddeleyite (Bdy) crystals discovered during the SEM sessions (FEG JEOL JSM 7100F TTLS LV SEM at the Center Castaing, Toulouse, France). Zrn, zircon; Bdy, baddeleyite; Chv, chevkinite; Flst, partially melted and residual felsite; Gl, silicate glass of rhyolitic composition; Mag, titanomagnetite; Ap, apatite; Afs, alkali feldspar; Qz, quartz. The scale bars correspond to 10 μm (except for the BSE image with baddeleyite, Bdy, where the scale bar is of 1 μm).

formed at shallow crustal level due to partial melting of the crystalline host rocks. However, no zircon study on the IDDP-1 nor Viti granophyre samples has been performed and the existing data and models do not capture the mechanisms of thermochemical exchange due to the basaltic intrusion(s) nor when the currently molten rhyolite magma was produced.

We report here for the first time the results from an investigation of rare zircon crystals in the IDDP-1 rhyolite sample. We compared these

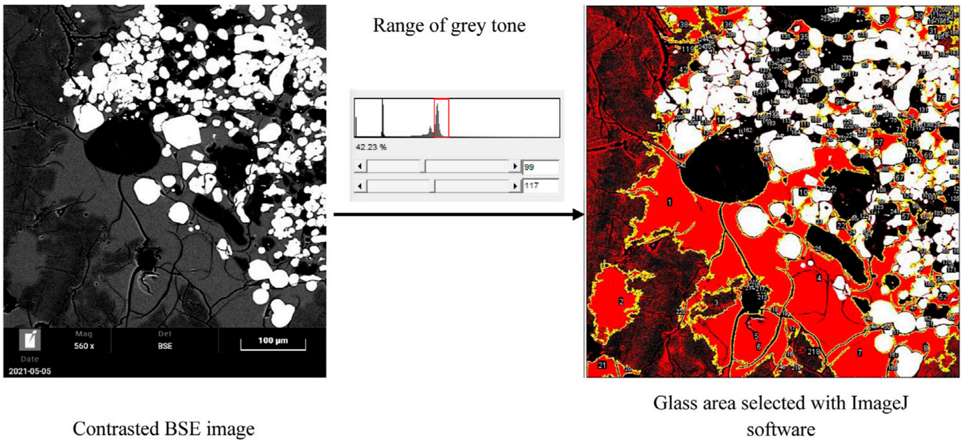

FIGURE 3
Example of glass (quenched silicate melt) fraction calculation. In each zircon-bearing zone, the glass fraction is calculated using BSE images of low magnification.

zircons with those in the host Viti granophyre through micro-analytical and modeling approaches to better constrain the timescales and mechanisms of rhyolite magma production at Krafla volcano. The obtained data point to very recent zircon crystallization, implying that these grains were resident in an active magma reservoir and potentially among the youngest zircons ever studied in the currently active rift volcanic system, likely comparable to those of the mid-ocean ridges (e.g., Bea et al., 2020). Our analytical results coupled to geochemical and thermochemical modelling shed new light on the origin of Icelandic rhyolites and the timescales of zircon formation in silicic melts.

Materials and methods

During the Iceland Deep Drilling Project well 1 (IDDP-1) drilling near the Viti Crater (Figure 1), beyond ~2,100 m depth the dominant fragments were dark brown glass shards interpreted to have quenched by melt interaction with the drilling water. Analysis of these cuttings indicated that the rhyolite melt was emplaced into crystalline felsic intrusive rocks called felsite or granophyre (e.g., Zierenberg et al., 2013). The IDDP-1 rhyolite sample and five host Viti granophyre samples were investigated. The IDDP-1 sample consists of the predominant brown rhyolite glass with plagioclase, two pyroxenes, titanomagnetite, ilmenite and/or apatite forming glomerocrysts and rare zircon grains (Figure 2); quartz and alkali feldspar show textural evidence for resorption, and were previously interpreted by Zierenberg et al. (2013) as xenocrysts. The analytical, imaging and Th-U dating data, and modeling parameters and data are summarized in Supplementary Material and Supplementary Tables S1–S8 and displayed in Figures 3–8. Average compositions of the rhyolite glass and of one representative Viti granophyre sample are given in Table 1.

Zircon and baddeleyite crystals

Most of the studied zircons are small (20–60 µm in size, reaching a maximum of 100 µm) and have euhedral, subhedral to anhedral morphologies (Figures 2, 4A, B). The morphology and the internal oscillatory zoning suggest that the crystals are of magmatic origin. Electron probe microanalysis, EPMA spot analyses and mapping show that the zircon crystals are variably enriched in Fe, Al, P, Hf, Y. Two larger crystals (Z1 and Z3) have inclusions of Si-Al-rich glasses (72–83 wt% SiO_2; 5–11 wt% Al_2O_3), britholite $(Ce, Ca, Th, La, Nd)_5(SiO_4, PO_4)_3(OH,F)$ and chevkinite $((Ce, La, Ca, Th)_4(Fe^{2+}, Mg)_2(Fe^{3+})_3Si_4O_{22})$ phases, which are rich in P, Al, Fe and Y. The analyzed Ti concentrations in the zircon crystals, far from the visible inclusions, range from ~35 ppm (in rims) to 230 ppm (in cores) (n = 35, n being the number of analyses) with an average value of ~125 ppm, which is higher than those previously observed in Icelandic zircons (up to 60 ppm, e.g., Carley et al., 2022) and corresponds to much higher crystallization temperatures (up to 1,000°C–1,100°C) for the rhyolite magma. For example, the application of the Ti-in-zircon geothermometer of Ferry and Watson (2007) assuming activities of $a_{SiO2} = a_{TiO2} = 1$ and 106 ppm gives minimal estimates of ~1,030°C (Figure 4A). Among similar zircon crystals, we filtered those hosted by pure rhyolitic glass and without any trace of Fe-Ti-bearing minerals and glass inclusions (Figure 4A). The IDDP-1 zircons yield "zero" aged ^{238}U-^{230}Th dates for crystallization, with an uncertainty of ±2,000 years (Figure 4B; Supplementary Table S7). Zircon sizes and glass fractions (Figures 3, 5) were investigated to constrain the mechanism of the rhyolite formation based on the thermochemical modelling of zircon behavior presented below. The compositional features of the IDDP-1 zircons were also compared to those of the host Viti granophyre (Ti contents range from ~23 ppm in rims up to 43 ppm in cores), which corresponds to much lower crystallization temperatures (800°C–900°C) for the host granophyre magma. Most of the Viti granophyre zircons yield zero-age isochron dates such as the IDDP-1 sample, but several crystals yield older model dates of ~8–13 ka and up to ~150 ka (Supplementary Table S7; Figure 4B).

The measured Zr contents in the glasses surrounding several analyzed zircon crystals from the glass-zircon interface up to 60–100 µm into the glass show flat concentration profiles and if any, very weak gradients (Figure 6). The data were corrected for secondary fluorescence using the program FANAL (Llovet et al., 2012; Borisova et al., 2018). Zr concentrations in the glass around

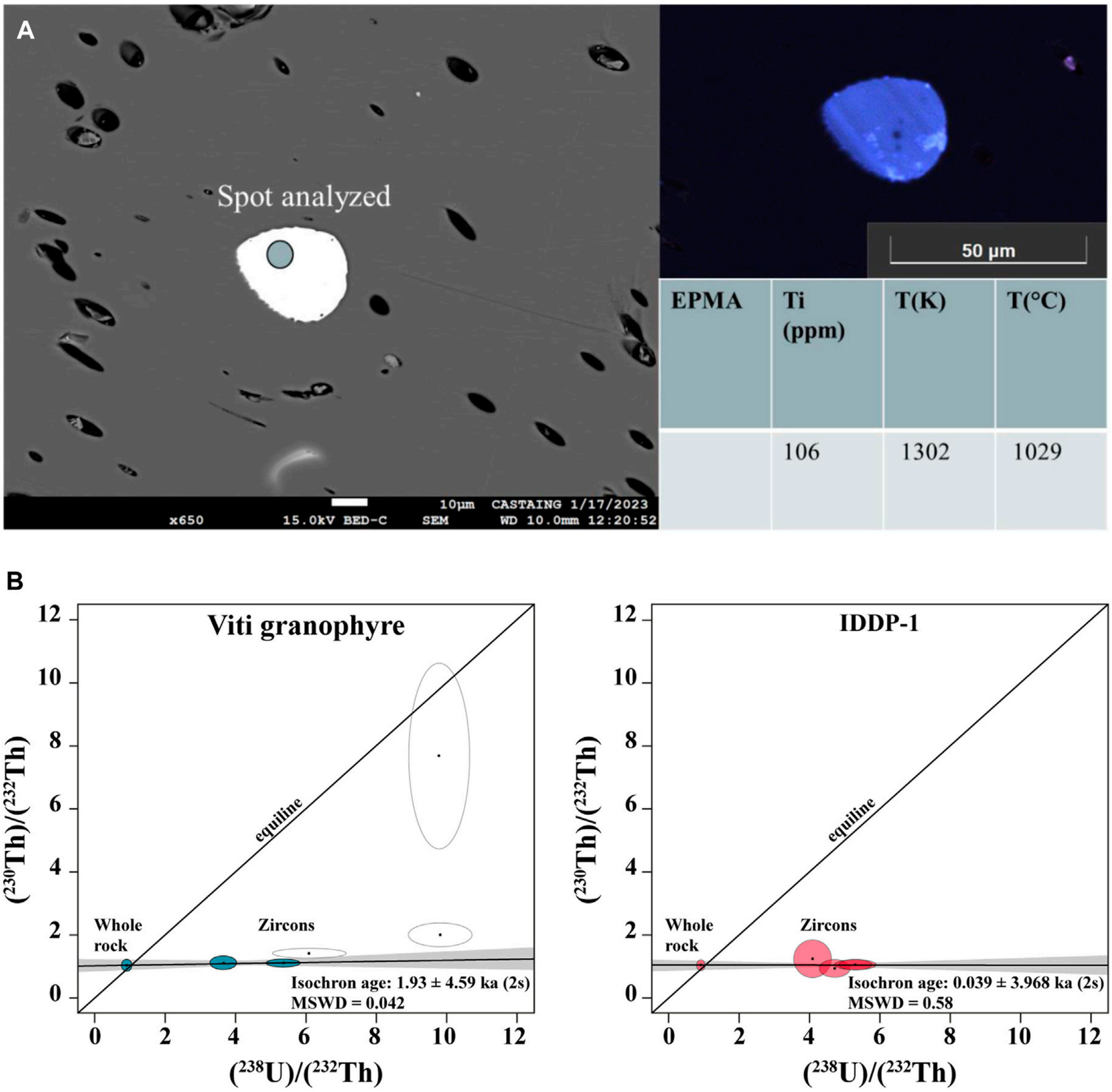

EPMA	Ti (ppm)	T(K)	T(°C)
	106	1302	1029

FIGURE 4
(A) Backscattered electron and cathodoluminescence images of a representative IDDP-1 zircon (Zrn-83 of series 4) surrounded by rhyolite glass. Zrn, zircon. Ti contents in the IDDP-1 zircons and temperature estimates calculated according to the Ti-in-zircon thermometer (Ferry and Watson, 2007) are shown. **(B)** U-Th isochron diagrams for *in-situ* analyses of zircons from Viti granophyre and IDDP-1 rhyolite sample (discovered during the first and the second SEM session). Isochron dates are derived using shaded data for whole rocks and individual zircons with dates calculated using IsoplotR (Vermeesch, 2018). Each datum represents an *in-situ* analysis of a single zircon crystal. Error ellipses are 2σ.

different zircons overlap, suggesting no significant differences in the patterns within this IDDP-1 sample. Overall, the Zr concentration level in the glass is ~420 ppm according to EPMA and 400 ± 50 ppm according to femtosecond laser ablation inductively coupled plasma (fs LA-ICP-MS) (Table 1), which corresponds to zircon saturation temperatures of 830°C–870°C depending on the solubility model used (e.g., Watson and Harrison, 2005) (Supplementary Table S5). This discrepancy between this estimate of crystallization temperatures and the much higher Ti-in-zircon temperatures (>1,000°C, see above) will be discussed below. Observation of several baddeleyite (xeno)crystals in the IDDP-1 glass sample (Figure 2) implies an involvement of mafic (e.g., basaltic) magma rather than hot rhyolite in the magmatic system.

Thermochemical and geochemical modeling of zircon behavior

In order to confirm the plausible scenario of the formation of Krafla rhyolite, a thermochemical model of heat transfer from a convecting magmatic intrusion to felsic (granophyric) host rocks involving melting and production of the hot rhyolite magma was developed. The model is based on the solution of a the 1D heat conduction general equation with account for the release of the latent heat of crystallization and convection in a two layered system of contrasting (in the case of the injection of a basaltic magma) compositions. The lower layer contains initially injected magma that releases heat to the surrounding felsic rocks. The model uses phase

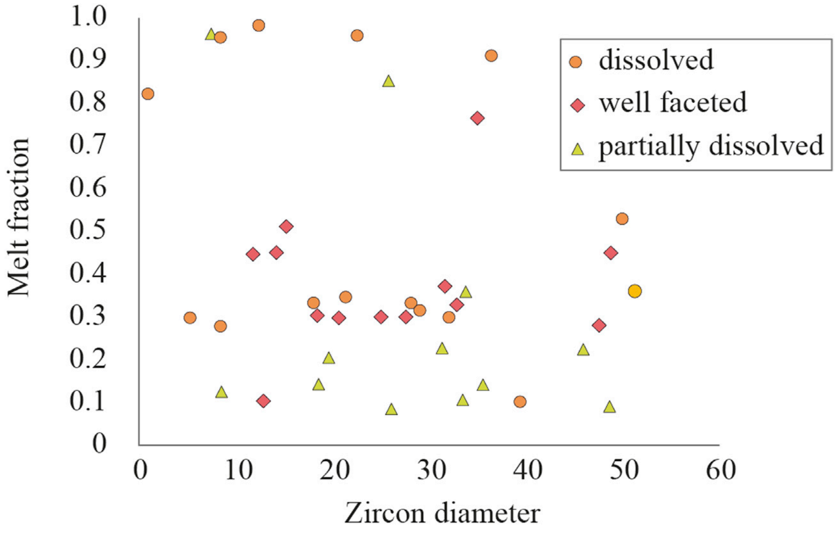

FIGURE 5
Silicate glass (quenched melt) fraction versus zircon diameter (in μm) calculated for the IDDP-1 rhyolite sample. Three types of the zircon were distinguished according to the morphology: 1) dissolved, 2) well faceted and 3) partially dissolved zircon crystals.

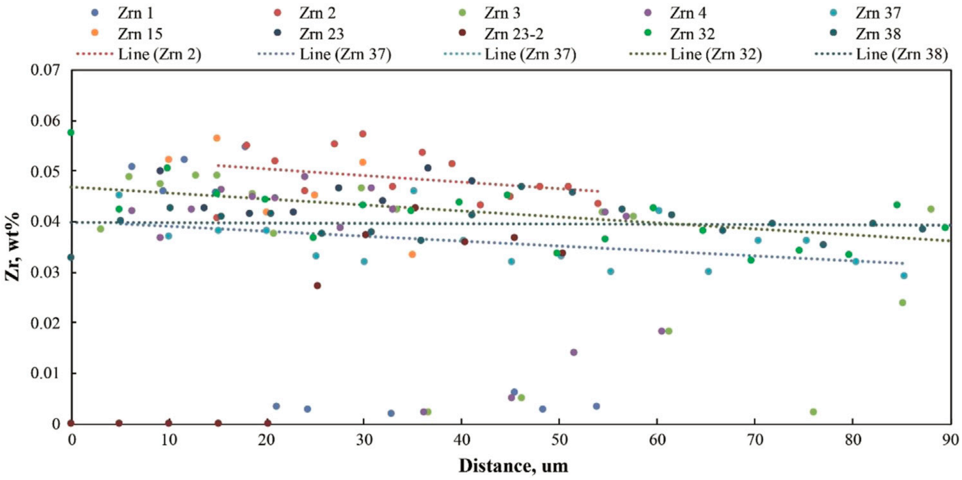

FIGURE 6
Zr concentration profiles (in wt%) along lines across the glass adjacent to the IDDP-1 zircons, corrected for the effect of secondary fluorescence, suggesting at least 4 years of the zircon-bearing rhyolite magma storage. Distance (in μm) corresponds to the distance from the zircon-glass interface.

diagrams for Krafla basalt and the Viti granophyre (melt fraction versus temperature) produced using of the Rhyolite-MELTS software (Gualda et al., 2012, https://melts.ofm-research.org/).

The system of equations has the following form:

$$\rho_i C_i \frac{\partial T}{\partial t} = \frac{\partial}{\partial x} k_i \frac{\partial T}{\partial x};\ C_i = C_i^0 + \frac{\partial X_i}{\partial T} L_*{}^{i};$$

$$k_i = k_i(Nu_i, T);\ Nu_i = \frac{Q_{conv}}{Q_{cond}} = \omega * Ra_i{}^{1/3};$$

$$Ra = \frac{\rho \beta \Delta T h^3}{\kappa \mu (T, X)};\ \kappa = \frac{k_m}{\rho C_i}$$

Here ρ is the density of magma, C is the heat capacity, T is the temperature, X is the crystal content, L^* is the latent heat of crystallization, k is the thermal conductivity, Nu is the Nusselt number, Ra is the Rayleigh number, ω ~0.1–0.3 is a proportionality constant, index i =1,2 corresponds to basaltic and rhyolitic layers, respectively, x is distance and t is time. The Rayleigh number for basalt is calculated based on the thickness h equal to the half width of the injected sill; h for the rhyolitic layer is calculated based on the thickness of the molten felsic crust (melt fraction greater than 95%). The temperature difference between the center of the basaltic sill and the basalt-rhyolite interface is taken as characteristic for ΔT for $i = 1$, we calculate the mean temperature in the rhyolitic layer $<T_r>$ and assume that $\Delta T = <T_r> - T_{rm}$, where T_{rm} is the temperature that corresponds to 5% melting of the felsite. The effective thermal conductivities are parametrized based on Turner's correlation (Turner, 1979). They

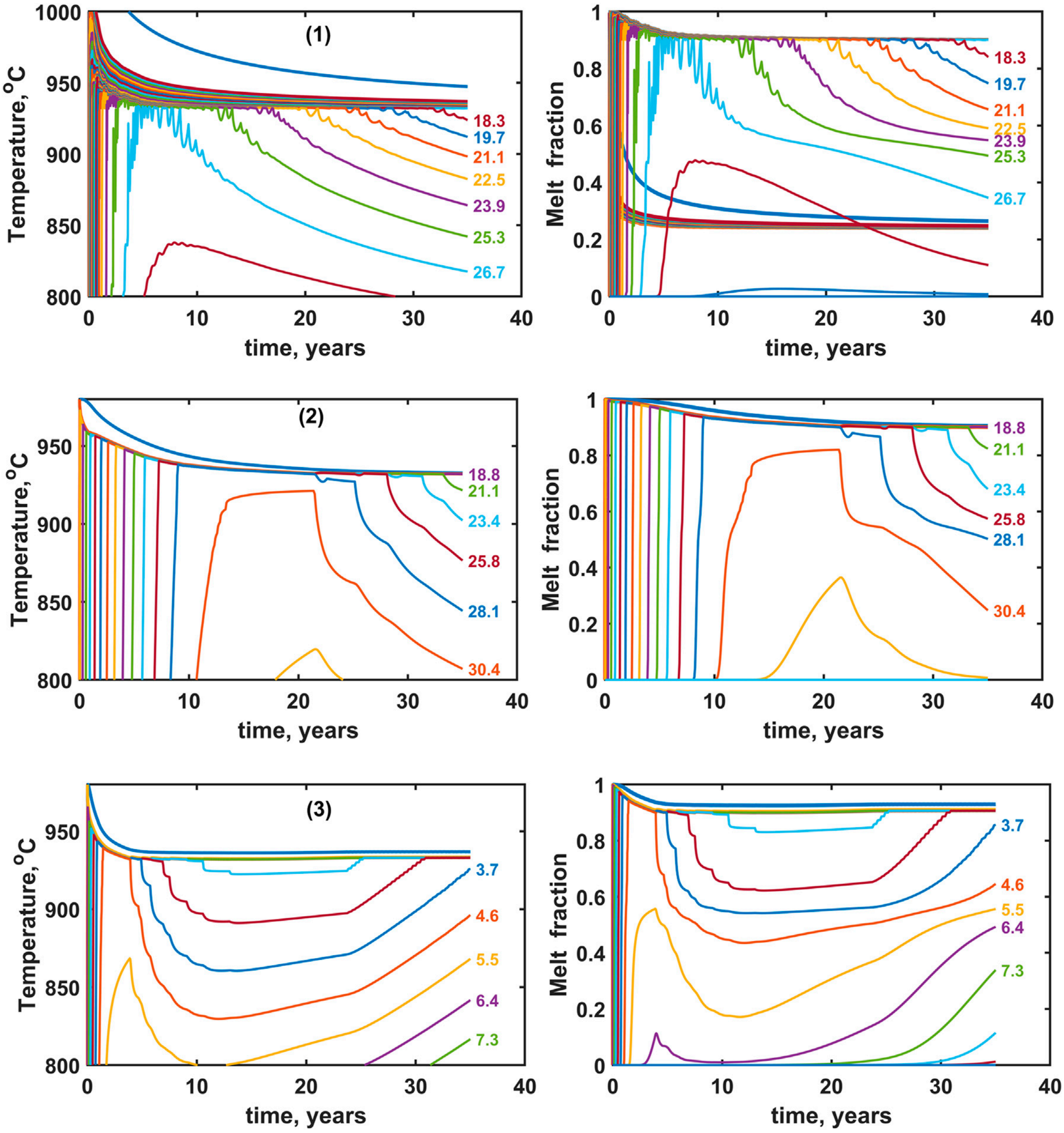

FIGURE 7
Temperature (in °C) and melt fraction versus time (in years) for three scenarios: 1) injection of the basaltic sill of a thickness of a 100 m at initial temperature of 1,150°C. 2) injection of a 900 m rhyolitic sill with the initial temperature of 980°C; 3) the same as (2) but the thickness of the sill is 100 m and the heat flux at the bottom of 12 W/m^2. Thick lines correspond to the basaltic magma for scenario (1), for the center of the sill for scenario (2) and for the bottom of the sill for scenario (3). Thin lines are labeled as a distance (in m) from the contact between the injected magma and host rocks.

are up to 3 orders of magnitude larger than the thermal conductivities resulting in efficient temperature homogenization in the convective layers. In the case of rhyolitic magma injection convection occurs in a single layer. The temperature difference between the center of the sill and T_{rm} is used as a characteristic temperature. Viscosities of basaltic and rhyolitic magmas are calculated using the model from Giordano et al. (2008) with a correction to account for the crystal content by Costa et al. (2009).

Simulation parameters are summarized in Supplementary Table S8. We assume symmetry boundary condition at the center of the injected sill and a constant far field temperature in felsite. The outer boundary was chosen far enough to avoid any influence on the temperature distribution in molten layers. Also, the case of a rhyolitic sill connected to a deep magmatic system is considered. In this case, a constant heat flux at the bottom of the sill is specified.

Based on the temperature histories produced by the thermochemical modeling, zircon dissolution and growth simulations were also carried out following the methods of Bindeman and Melnik (2016; 2022). The model accounts for the experimentally determined equilibrium saturation of silicate melt with zircon and the Zr diffusion coefficient in the silicate melts. The

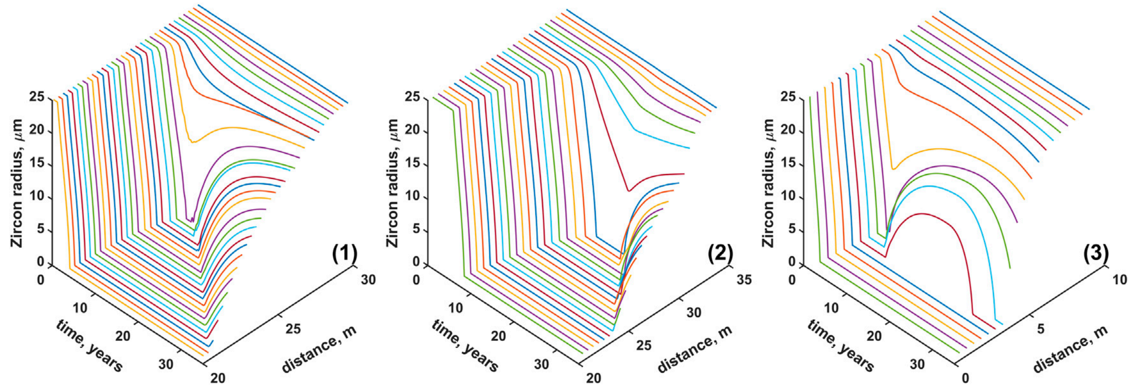

FIGURE 8
Dependence of the zircon radius on both time and distance from the initial contact between the injected magma and host rocks, for the three different scenarios considered (see Figure 7 for full description). At small distances between the contact, zircons dissolve completely, at larger distances they start to regrow, and far away only a limited dissolution of the crystals occurs. For scenario (3) at later stages of the system, evolution growth at intermediate distances switches to dissolution due to progressive heat flux from the deep feeding system.

1D transient diffusion equation is solved inside the melt shell surrounding the growing zircon. The MatLab code is available from https://github.com/crystalworkshop/krafla_sill.

For the geochemical modelling (Supplementary Table S3) of residence times from the Zr profiles surrounding the IDDP-1 zircon crystals, we have applied the diffusion equation $t \sim X^2/D$ (e.g., Crank, 1979), where t is the duration (s), X is the distance (μm) and D is the Zr diffusion coefficient in m^2/s. Residence times calculated with Zr diffusion according to Zhang and Xu (2016) at 900°C gives maximal values of 4 years, suggesting stable conditions of neither growth nor dissolution of zircon prior to sampling by the IDDP-1 borehole in 2009.

Implications for the IDDP-1 rhyolite formation

The maximal duration of rhyolite magma storage may correspond to a period from the beginning of last intrusion of basaltic magma (Krafla Fires, 1975 basaltic intrusions and lavas), which corresponds to 34 years before the IDDP-1 sampling in 2009. The melt batch that was sampled by IDDP-1 glass was likely in thermal contact for up to 34 years with the intruded sill. The uncertainty on the IDDP-1 rhyolite age (±2.0 kyr) does not allow us to distinguish between the Krafla Fires and the phreatomagmatic event during the opening phase of the Mývatn Fires, forming the crater Víti in 1724. In this work, we tested a hypothesis and performed thermochemical modeling of a basaltic or rhyolite intrusion interaction with the host granophyre rock directly related to the 1975 Krafla Fires event. The combined scanning electron microscopy (SEM)-EPMA-LA-ICP-MS-SHRIMP data provide evidence for the formation of the IDDP-1 rhyolite through high-temperature melting of granophyre rock by near-zero-age intrusion of a hot basaltic magma.

The results from thermochemical simulations presented below predict that the heat released from the intruded magma is sufficient for melting of felsite and formation of rhyolitic melt. After a critical melt layer thickness is reached, it begins to convect. Three scenarios are considered. The host felsite rocks are intruded by: 1) a basaltic sill, 2) rhyolitic magma 3) rhyolitic sill connected to a deeper magmatic system. In all scenarios the emplacement occurs during 1975–1983 Krafla Fires eruption and the system evolves for 35 years. The measured temperature distribution (Eichelberger, 2019) in the vicinity of the intrusion is used for model calibration. Sharp temperature gradient near the contact with magma requires intense convection in the magma body for at least 35 years. We use this constraint to estimate the necessary thickness of the intruded sill.

Scenario (1). The density of the rhyolitic melt remains smaller than the density of the basalt and prevents intense mixing between the two magmas by Rayleigh-Taylor instability. An example of the temperature and melt fraction evolution with time is shown in Figure 7, top panels for a system with the starting basaltic layer of 100 m thick at 1,150°C. We assume that the basalt is intruded at liquidus conditions at ~ 1,150°C. We also suggest a thickness of 100 m to fit the temperature profile recorded in the Krafla region (Eichelberger, 2019). Numbers on Figure 7 represent the distance from the initial interface between the magma and the wall rocks. Basaltic magma triggers the melting of ~27 m-thick felsic rocks in a matter of 5 years. The basaltic layer crystallizes significantly (Figure 7, top panel) after ~7 years of cooling and the convection in this layer slows down the rate of heat transfer to the rhyolite convecting above. The melting of the felsite rock slows down, and the upper layer starts to solidify. Basaltic magma cools and crystallizes quickly, while the temperature in the upper felsic layer evolves more slowly. Convection proceeds during the whole simulated period, although the width of the layer and the intensity of the convection decrease. After 35 years, the melt fraction in basaltic magma decreases to less than 0.3, while the crystallinity (inverse function of the melt fraction) of the felsic magma layer remains lower (0.1–0.6, depending on the distance from the contact with basaltic sill). The melt fractions of the rhyolite magma reproduce the real glass fractions estimated in the rhyolite glass of the IDDP-1 sample (Figure 5).

TABLE 1 Composition of the 2009 IDDP-1 glasses and the associated Viti granophyre.

Sample number	IC-82**	IDDP-1***	IDDP-1****	1σ uncertainty
	Viti granophyre	Rhyolite glass (Gl)	Rhyolite glass (Gl)	Rhyolite glass (Gl)
	bulk-rock	EPMA*	fs LA-ICP-MS*	fs LA-ICP-MS
		(265 points)	(145 points)	(145 points)
SiO_2 wt%	74.71	74.65 ± 0.67	68.25 ± 1.55	8.68
TiO_2	0.47	0.33 ± 0.02	0.35 ± 0.01	0.04
Al_2O_3	11.95	11.31 ± 0.15	11.30 ± 0.00****	—
FeO	N.A.	2.91 ± 0.11	3.01 ± 0.09	0.39
Fe_2O_3	3.66	N.A.	N.A.	N.A.
MnO	0.08	0.07 ± 0.03	0.064 ± 0.002	0.01
MgO	0.35	0.21 ± 0.03	0.20 ± 0.01	0.025
CaO	1.84	1.47 ± 0.06	1.43 ± 0.04	0.19
Na_2O	4.06	3.86 ± 0.16	3.54 ± 0.08	0.45
K_2O	2.65	2.88 ± 0.08	3.48 ± 0.36	0.45
P_2O_5	D.L.	0.05 ± 0.03	0.038 ± 0.004	0.006
Total	99.77	97.75 ± 0.78	N.A.	N.A.
Ba ppm	476	N.A.	494.87 ± 8.74	62.10
Ce	80.6	N.A.	80.62 ± 2.12	10.00
La	39.6	N.A.	38.60 ± 0.96	4.67
Nb	29.1	N.A.	34.94 ± 6.43	4.13
Nd	38.5	N.A.	37.57 ± 1.18	4.64
Rb	64.4	N.A.	73.32 ± 2.49	9.55
Sr	72.9	N.A.	58.65 ± 1.59	7.25
Y	61.1	N.A.	62.33 ± 1.28	7.59
Zn	74.3	N.A.	N.A.	N.A.
Zr	425	N.A.	407.52 ± 8.68	50.23
U	1.99	N.A.	2.17 ± 0.11	0.29
Th	6.72	N.A.	7.38 ± 0.20	0.93
H_2O bulk	0.13	1.9[\$]	N.A.	N.A.
CO_2 bulk	0.08	N.A.	N.A.	N.A.
S bulk	<0.01	N.A.	N.A.	N.A.

*Electron probe microanalysis (EPMA) and femtosecond laser ablation inductively coupled plasma (fs LA-ICP-MS) analysis data.
**N.A., not analyzed; D.L., value below detection limit.
***EPMA, data obtained in this work.
****fs LA-ICP-MS, data. Al_2O_3 was used as the internal standard for the major and trace element quantification by SILLS, standard deviation correspond to the sample heterogeneity, which is smaller than the analytical uncertainty.
[\$] Data from Pope et al. (2013).

Scenario (2). In order to keep intensive convection during 35 years of the evolution, the required system has to be composed of the rhyolitic layer with thickness exceeding of 900 m at the temperature of 980°C, which definitely conflicts with geophysical observations (Kim et al., 2020). A thinner layer, which significantly solidifies at the top and the temperature gradient in the host rocks, will become much smoother than that observed during drilling. The thickness of the molten felsic crust in this scenario exceeds 30 m after 21 years and decreases to 18 m at the end of the simulation period (Figure 7, middle panels).

Scenario (3). An alternative to the thick rhyolitic layer, a thin (100 m) layer of rhyolitic magma with a heat supply from a deeper magmatic system can be considered (Figure 7, bottom panels). To retain high convection intensity, the necessary heat flux is estimated to be 12 W/m^2. A magma intrusion rate that supports such heat flux would require an uplift of 9 cm/year over observation period. The rhyolite sill stays close to a steady state with only 4 m of the molten crust produced over 35 years. The temperature of the magma after 20 years of cooling starts to increase slowly due to permanent heat influx. The temperature difference between the bottom and the top of the injected rhyolite magma remains within 5°C due to intense mixing.

Based on the calculated temperatures, we simulate diffusive growth of zircon crystals in molten felsic crust. Because the model does not simulate convection directly, we cannot obtain temperature histories in the individual batch of rhyolite magma, but only at fixed distances from the initial contact between the magma and host rocks. Intensive convection will result in migration of magma batch within the layers and, thus, more complicated thermal evolutions. Although calculated temperatures can be treated only as end-member cases, they shade light on zircon dissolution/growth during felsic crust melting.

Depending on the distance from the contact between the injected magma and the molten felsite, zircons experience different degrees of melting and consequent growth (Figure 8). For scenario (1) at distances less than 23 m, zircon crystals dissolve completely after a few years and do not regrow during 35 years. At larger distances different proportions of zircon cores are preserved. Regrowth of zircons occurs when magma becomes supersaturated with zircon at temperatures of ~900°C–950°C, depending on zirconium bulk content and solubility model. The final size of the crystals depends on the distance from the contact ranging from a few microns to a nearly complete recovery after heat shock, but the zircon age record can be partly removed during dissolution. At distances larger than 27 m, only dissolution of zircons takes place at later stages of the system evolution.

Scenario (2) shows a similar behavior to that of scenario (1) at slightly bigger distances from the initial contact between the magma and the rock. However, in the case of rhyolitic magma injection, convective mixing will occur inside the whole 900 m-thick sill and the zircon crystals will not be preserved. In scenario (3), progressive heating of the system by the influx of hot magma from below results in zircon dissolution in the whole simulated domain.

The timescale required to generate the profiles recorded in the IDDP-1 rhyolite glasses around the idiomorphic crystals of zircon was estimated (Figure 6). Modeling of the residence timescale to flatten Zr profiles generated upon the zircon crystallization/dissolution suggests that any time of >4 years and definitely of <34 years, is sufficient to generate the observed Zr profiles by re-equilibration of the rhyolite melts once the zircon-melt system achieves a stable configuration (Supplementary Table S3). This timescale is in an agreement with the prediction of the thermochemical model.

Zircon crystals that regrow after a complete dissolution in all three scenarios experience extremely fast growth rates at small radii (Figure 8). At later stages, the growth rate decreases significantly and the concentration profiles around zircons become smoother. The drastic increase in Ti contents in the cores of completely resorbed and regrown zircons can be explained either by non-equilibrium Ti partitioning between zircon and melt at highly elevated growth rates or by crystallization of major minerals that enrich the surrounding melt with zirconium and other incompatible elements (Bea et al., 2022). The second option conflicts with the phase diagram for Krafla rhyolite, because these temperatures are well above the liquidus. Basaltic magma should have extremely high Zr contents to become supersaturated with zircon at only 10% reduction of the melt fraction (e.g., Borisova et al., 2020).

The first option requires more theoretical and experimental studies. The dependence of the partition coefficient on the growth rate is well known in different magmatic systems. Phosphorus enrichment in olivine crystals can be explained by this mechanism (Shea et al., 2019). Mollo et al. (2011) experimentally observed non-equilibrium trace element partitioning in plagioclase-melt systems. There are no studies on the non-equilibrium partition of Ti in zircons because large typical felsic magmatic systems do not experience such rapid zircon growth as occurred on Krafla volcano. Additionally, a non-equilibrium or non-Henry's law behavior of Ti-in-zircon together with preferred incorporation of Ti at very low pressures corresponding to the crustal levels (Fu et al., 2008) can explain the elevated Ti contents in zircon cores. Alternatively, nano inclusions of Ti-rich phases such as magnetite or rutile during fast growth can be incorporated into growing crystals. As we examined zircons under the SEM only down to 50 nm resolution, these nano-inclusions could significantly contribute to the apparent Ti concentrations measured by EPMA.

The presence of a baddeleyite (xeno)crystal in the IDDP-1 rhyolite (Figure 2) implies its formation within mafic (low activity of SiO_2, $a_{SiO2} < 1$) rather than felsic (high $a_{SiO2} = 1$) magma. In this case, the baddeleyite crystal can be also interpreted as a proxy of hydrothermal alteration of Zr-bearing phases in the host felsite. However, no baddeleyite crystal was found in the host Viti granophyre and thus this mineral could be a proxy of a mafic source. The 1975 AD eruptions record massive basaltic intrusions, implying that the occurrence of the IDDP-1 baddeleyite crystal is generated by the basalt-granophyre rock interaction. The proposed thermochemical model demonstrated in Figure 7 involves melting of the host granophyre by the hot magma intrusion. The IDDP-1 rhyolite melts produced cool and undergo equilibrium crystallization of silicates and oxides. Our model thus explains how the rhyolite magma can be produced in the hybrid Icelandic crust due to the present-day magmatic activity.

Data availability statement

The original contributions presented in the study are included in the article/Supplementary Material, further inquiries can be directed to the corresponding author.

Author contributions

AYB: Conceptualization, Funding acquisition, Investigation, Methodology, Project administration, Supervision, Validation, Writing–original draft, Writing–review and editing. OEM: Methodology, Software, Writing–review and editing. NG: Investigation, Formal Analysis, Methodology, Writing–review and editing. INB: Funding acquisition, Investigation, Methodology, Writing–review and editing. TT: Investigation, Methodology, Formal Analysis, Writing–review and editing. MR: Investigation, Methodology, Formal Analysis, Writing–review and editing. AS: Funding acquisition, Resources, Writing–review and editing. OL: Investigation, Methodology, Writing–review and editing. ML: Formal Analysis, Investigation, Methodology, Writing–review and editing. XL: Investigation, Methodology, Writing–review and editing. PP: Writing–review and editing. AP: Investigation, Methodology, Writing–review and editing. ST: Methodology, Supervision, Writing–review and editing.

Funding

The author(s) declare financial support was received for the research, authorship, and/or publication of this article. This work was supported by the Institut Carnot ISIFoR (TRACENEO project), and the INSU-CNES project PLAGIOGRAN (2022–2023) to AYB. INB was supported by NSF grant EAR 1822977. XL acknowledges support from grant PID2019-105625RB-C21 funded by MCIN/AEI/10.13039/501100011033. This study has been partially supported through the grant EUR TESS N°ANR-18-EURE-0018 in the framework of the Programme des Investissements d'Avenir. OEM was partially supported by the ERC under the European Union Horizon 2020 Research and Innovation Programme (Grant agreement 787399-SEISMAZE) and College de France PAUSE program (grant #C7H-PUB23A59).

Acknowledgments

Jorge Vazquez (SHRIMP-RG Laboratory, United States) is thanked for U-Th dating. Authors thank A. M. Cousin for the design of all figures.

Conflict of interest

The authors declare that the research was conducted in the absence of any commercial or financial relationships that could be construed as a potential conflict of interest.

Publisher's note

Supplementary material

The Supplementary Material for this article can be found online at: https://www.frontiersin.org/articles/10.3389/feart.2023.1307303/full#supplementary-material

References

Bea, F., Bortnikov, N., Cambeses, A., Chakraborty, S., Molina, J. F., Montero, P., et al. (2022). Zircon crystallization in low-Zr mafic magmas: possible or impossible? *Chem. Geol.* 602, 120898. doi:10.1016/j.chemgeo.2022.120898

Bea, F., Bortnikov, N., Montero, P., Zinger, T., Sharkov, E., Silantyev, S., et al. (2020). Zircon xenocryst evidence for crustal recycling at the Mid-Atlantic Ridge. *Lithos* 354, 105361. doi:10.1016/j.lithos.2019.105361

Bindeman, I. N., Gurenko, A., Carley, T., Miller, C., Martin, E., and Sigmarsson, O. (2012). Silicic magma perogenesis in Iceland by remelting of hydrothermally altered crust based on oxygen isotope diversity and disequilibria between zircon and magma with implications for MORB. *Terra nova.* 24, 227–232. doi:10.1111/j.1365-3121.2012.01058.x

Bindeman, I. N., and Melnik, O. E. (2016). Zircon survival, rebirth and recycling during crustal melting, magma crystallization, and mixing based on numerical modelling. *J. Petrology* 57, 437–460. doi:10.1093/petrology/egw013

Bindeman, I. N., and Melnik, O. E. (2022). The rises and falls of zirconium isotopes during zircon crystallisation. *Geochem. Perspect. Lett.* 24, 17–21. doi:10.7185/geochemlet.2241

Borisova, A. Y., Bindeman, I. N., Toplis, M. J., Zagrtdenov, N. R., Guignard, J., Safonov, O. G., et al. (2020). Zircon survival in shallow asthenosphere and deep lithosphere. *Am. Mineralogist* 105 (11), 1662–1671. doi:10.2138/am-2020-7402

Borisova, A. Y., Freydier, R., Polvé, M., Jochum, K.-P., and Candaudap, F. (2010). Multi-elemental analysis of ATHO-G rhyolitic glass (MPI-DING reference material) by femtosecond and nanosecond LA - ICP - MS: evidence for significant heterogeneity of B, V, Zn, Mo, Sn, Sb, Cs, W, Pt and Pb at mm-scale. *Geostand. Geoanalytical Res.* 34, 245–255. doi:10.1111/j.1751-908X.2010.00077.x

Borisova, A. Y., Toutain, J.-P., Stefansson, A., Gouy, S., and de Parseval, P. (2012). Processes controlling the 2010 Eyjafjallajökull explosive eruption. *J. Geophys. Res.* 117, B05202. doi:10.1029/2012JB009213

Borisova, A. Y., Zagrtdenov, N. R., Toplis, M. J., Donovan, J. J., Llovet, X., Asimov, P. D., et al. (2018). Secondary fluorescence effects in microbeam analysis and their impacts on geospeedometry and geothermometry. *Chem. Geol.* 490, 22–29. doi:10.1016/j.chemgeo.2018.05.010

Burgess, S. D., Coble, M. A., and Vazquez, J. A. (2021). Zircon geochronology and geochemistry of Quaternary rhyolite domes of the Coso volcanic field, Inyo County, California. *J. Volcanol. Geotherm. Res.* 417, 107276. doi:10.1016/j.jvolgeores.2021.107276

Carley, T. L., Bell, E. A., Miller, C. F., Claiborne, L. L., Hunt, A., Kirkpatrick, H. M., et al. (2022). Zircon-modeled melts shed light on the formation of Earth's crust from the Hadean to the Archean. *Geology.* doi:10.1130/G50017.1

Cheng, H., Edwards, R. L., Shen, C. C., Polyak, V. J., Asmerom, Y., Woodhead, J., et al. (2013). Improvements in ^{230}Th dating, ^{230}Th and ^{234}U half-life values, and U–Th isotopic measurements by multi-collector inductively coupled plasma mass spectrometry. *Earth Planet. Sci. Lett.* 371, 82–91. doi:10.1016/j.epsl.2013.04.006

Claiborne, L. L., Miller, C. F., Gualda, G. A. R., Carley, T. L., Covey, A. K., Wooden, J. L., et al. (2018). "Zircon as magma monitor: robust, temperature-dependent partition coefficients from glass and zircon surface and rim measurements from natural systems microstructural geochronology," in *Microstructural geochronology: planetary records down to atom scale: American geophysical union geophysical monograph 232*. Editor D. E. Moser, 3–33. doi:10.1002/9781119227250.ch1

Coble, M. A., Vazquez, J. A., Barth, A. P., Wooden, J., Burns, D., Kylander-Clark, A., et al. (2018). Trace element characterisation of MAD-559 zircon reference material for ion microprobe analysis. *Geostand. Geoanalytical Res.* 42, 481–497. doi:10.1111/ggr.12238

Costa, A., Caricchi, L., and Bagdassarov, N. (2009). A model for the rheology of particle-bearing suspensions and partially molten rocks. *Geochem. Geophys. Geosystems.* doi:10.1029/2008GC002138

Crank, J. (1979). *The mathematics of diffusion*. Oxford University Press.

Eichelberger, J. (2019). Planning an international magma observatory. *Eos* 100, 10–1029. doi:10.1029/2019EO125255

Elders, W. A., Fridleifsson, G. O., Zierenberg, R. A., Pope, E. C., Mortensen, A. K., Gudmudsson, A., et al. (2011). Origin of a rhyolite that intruded a geothermal well while drilling in a basaltic volcano, at Krafla. *Icel. Geol.* 39, 231–234. doi:10.1130/G31393.1

Ferry, J. M., and Watson, E. B. (2007). New thermodynamic models and revised calibrations for the Ti-in-zircon and Zr-in-rutile thermometers. *Contrib. Mineral. Petrol* 154, 429–437. doi:10.1007/s00410-007-0201-0

Foulger, G. R., Doré, T., Emeleus, H., Franke, D., Geoffroy, L., Gernigon, L., et al. (2020). The Iceland microcontinent and a continental Greenland-Iceland-faroe ridge. *Earth-Science Rev.* 206, 102926. doi:10.1016/j.earscirev.2019.102926

Fu, B., Page, F. Z., Cavosie, A. J., Fournelle, J., Kita, N. T., Lackey, J. S., et al. (2008). Ti-in-zircon thermometry: applications and limitations. *Contributions Mineralogy Petrology* 156 (2), 197–215. doi:10.1007/s00410-008-0281-5

Giordano, D., Russell, J. K., and Dingwell, D. B. (2008). Viscosity of magmatic liquids: a model. *Earth Planet. Sci. Lett.* 271, 123–134. doi:10.1016/j.epsl.2008.03.038

Gualda, G. A. R., Ghiorso, M. S., Lemons, R. V., and Carley, T. L. (2012). Rhyolite-MELTS: a modified calibration of MELTS optimized for silica-rich, fluid-bearing magmatic systems. *J. Petrology* 53 (5), 875–890. doi:10.1093/petrology/egr080

Guillong, M., Meier, D. L., Allan, M. M., Heinrich, C. A., and Yardley, B. W. (2008). Appendix A6: SILLS: a MATLAB-based program for the reduction of laser ablation ICP-MS data of homogeneous materials and inclusions. *Mineralogical Assoc. Can. Short Course* 40, 328–333. https://ethz.ch/content/dam/ethz/special-interest/erdw/geopetro/mineralsystems-dam/documents/MAC_SC_40_Sills_description.pdf.

Gunnarsson, B., Marsh, B. D., and Taylor, H. P., Jr. (1998). Generation of Icelandic lavas from the Torfajökull central volcano: J. Volcan. *Geotherm. Res.* 83, 1–45. doi:10.1016/S0377-0273(98)00017-1

Hampton, R. L., Bindeman, I. N., Stern, R. A., Coble, M. A., and Rooyakkers, S. M. (2021). A microanalytical oxygen isotopic and U-Th geochronologic investigation of rhyolite petrogenesis at the Krafla Central volcano, Iceland. *J. Volcanol. Geotherm. Res.* 414, 107229. doi:10.1016/j.jvolgeores.2021.107229

Harrison, T. M., and Watson, E. B. (1983). Kinetics of zircon dissolution and zirconium diffusion in granitic melts of variable water content. *Contributions Mineralogy Petrology* 84, 66–72. doi:10.1007/BF01132331

Jochum, K. P., Stoll, B., Herwig, K., Willbold, M., Hofmann, A. W., Amini, M., et al. (2006). MPI-DING reference glasses for *in situ* microanalysis: new reference values for element concentrations and isotope ratios. *Geochem. Geophys. Geosyst.* 7, 1–44. doi:10.1029/2005GC001060

Jónasson, K. (1994). Rhyolite volcanism in the Krafa central volcano, north-east Iceland. *Bull. Volcanol.* 56, 516–528. doi:10.1007/BF00302832

Jónasson, K. (2007). Silicic volcanism in Iceland: composition and distribution within active volcanic zones. *J. Geodynam. V.* 43, 101–117. doi:10.1016/j.jog.2006.09.004

Kim, D., Brown, L. D., Árnason, K., Gudmundsson, Ó., Ágústsson, K., and Flóvenz, Ó. G. (2020). Magma "bright spots" mapped beneath Krafla, Iceland, using RVSP imaging of reflected waves from microearthquakes. *J. Volcanol. Geotherm. Res.* 391, 106365. doi:10.1016/j.jvolgeores.2018.04.022

Llovet, X., Pinard, P. T., Donovan, J. J., and Salvat, F. (2012). Secondary fluorescence in electron probe microanalysis of material couples. *J. Phys. D. Appl. Phys.* 45, 225301. doi:10.1088/0022-3727/45/22/225301

Masotta, M., Mollo, S., Nazzari, M., Tecchiato, V., Scarlato, P., Papale, P., et al. (2018). Crystallization and partial melting of rhyolite and felsite rocks at Krafla volcano: a comparative approach based on mineral and glass chemistry of natural and experimental products. *Chem. Geol.* 483, 603–618. doi:10.1016/j.chemgeo.2018.03.031

Mollo, S., Putirka, K., Iezzi, G., Del Gaudio, P., and Scarlato, P. (2011). Plagioclase–melt (dis)equilibrium due to cooling dynamics: implications for thermometry, barometry and hygrometry. *Lithos* 125, 221–235. doi:10.1016/j.lithos.2011.02.008

Nicholson, H., Condomines, M., Fitton, J. G., Fallick, A. E., Grönvold, K., and Rogers, G. (1991). Geochemical and isotopic evidence for crustal assimilation beneath Krafla. *Icel. J. Petrol.* 32, 1005–1020. doi:10.1093/petrology/32.5.1005

Paton, C., Hellstrom, J., Paul, B., Woodhead, J., and Hergt, J. (2011). Iolite: freeware for the visualisation and processing of mass spectrometric data. *J. Anal. Atomic Spectrom.* 26 (12), 2508–2518. doi:10.1039/C1JA10172B

Pope, E. C., Bird, D. K., and Arnórsson, S. (2013). Evolution of low-^{18}O Icelandic crust. *Earth Planet Sci. Lett.* 374, 47–59. doi:10.1016/j.epsl.2013.04.043

Rooyakkers, S. M., Stix, J., Berlo, K., Petrelli, M., Hampton, R. L., Barker, S. J., et al. (2022). Rifting and recharge as triggers of the mixed basalt–rhyolite Halarauður ignimbrite eruption (Krafla, Iceland). *Contrib. Mineral. Petrol* 177, 32. doi:10.1007/s00410-021-01881-7

Rooyakkers, S. M., Stix, J., Berlo, K., Petrelli, M., Hampton, R. L., Barker, S. J., et al. (2021). The origin of rhyolitic magmas at Krafla central volcano (Iceland). *J. Petrology* 62, egab064. doi:10.1093/petrology/egab064

Saubin, E., Kennedy, B., Tuffen, H., Nichols, A. R. L., Villeneuve, M., Bindeman, I., et al. (2020). Textural and geochemical window into the IDDP-1 rhyolitic melt, Krafla, Iceland, and its reaction to drilling. *GSA Bull.* 133, 1–16. doi:10.1130/B35598.1

Schmitt, A. K. (2011). Uranium series accessory crystal dating of magmatic processes. *Annu. Rev. Earth Planet. Sci.* 39, 321–349. doi:10.1146/annurev-earth-040610-133330

Shea, T., Hammer, J. E., Hellebrand, E., Mourey, A. J., Costa, F., First, E. C., et al. (2019). Phosphorus and aluminum zoning in olivine: contrasting behavior of two nominally incompatible trace elements. *Contrib. Mineral. Petrol* 174, 85. doi:10.1007/s00410-019-1618-y

Sigmarsson, O., Hémond, C., Condomines, M., Fourcade, S., and Oskarsson, N. (1991). Origin of silicic magma in Iceland revealed by Th isotopes. *Geology* 19, 621–624. doi:10.1130/0091-7613(1991)019<0621:OOSMII>2.3.CO;2

Simakin, A. G., and Bindeman, I. N. (2022). Convective melting and water behavior around magmatic-hydrothermal transition: numerical modeling with application to Krafla Volcano. *Icel. J. Petrology* 63 (8). doi:10.1093/petrology/egac074

Steiger, R. H., and Jäger, E. (1977). Subcommission on geochronology: convention on the use of decay constants in geo-and cosmochronology. *Earth Planet. Sci. Lett.* 36, 359–362. doi:10.1016/0012-821X(77)90060-7

Stern, R. A., and Amelin, Y. (2003). Assessment of errors in SIMS zircon U–Pb geochronology using a natural zircon standard and NIST SRM 610 glass. *Chem. Geol.* 197, 111–142. doi:10.1016/S0009-2541(02)00320-0

Torsvik, T. H., Amundsen, H. E. F., Trønnes, R. G., Doubrovine, P. V., Gaina, C., Kusznir, N. J., et al. (2015). Continental crust beneath southeast Iceland. *PNAS*, E1818–E1827. doi:10.1073/pnas.1423099112

Turner, J. S. (1979). *Buoyancy effects in fluids*. Cambridge University Press.

Vermeesch, P. (2018). IsoplotR: a free and open toolbox for geochronology. *Geosci. Front.* 9, 1479–1493. doi:10.1016/j.gsf.2018.04.001

Watson, E. B., and Harrison, T. M. (2005). Zircon thermometer reveals minimum melting conditions on earliest Earth. *Science* 308 (5723), 841–844. doi:10.1126/science.1110873

Zhang, Y., and Xu, Z. (2016). Zircon saturation and Zr diffusion in rhyolitic melts, and zircon growth geospeedometer. *Am. Mineralogist* 101, 1252–1267. doi:10.2138/am-2016-5462

Zierenberg, R. A., Schiffman, P., Barfod, G. H., Lesher, C. E., Marks, N., Lowenstein, J. B., et al. (2013). Composition and origin of rhyolite melt intersected by drilling in the Krafla geothermal field. *Icel. Contrib. Mineral. Petrol* 165, 327–347. doi:10.1007/s00410-012-0811-z

frontiers | Frontiers in Earth Science

TYPE Original Research
PUBLISHED 19 December 2023
DOI 10.3389/feart.2023.1306460

OPEN ACCESS

EDITED BY
Simona Ferrando,
University of Turin, Italy

REVIEWED BY
Rosario Esposito,
University of Milano-Bicocca, Italy
Tong Hou,
China University of Geosciences, China

*CORRESPONDENCE
Olga A. Andreeva,
✉ oandreeva@igem.ru

RECEIVED 03 October 2023
ACCEPTED 06 December 2023
PUBLISHED 19 December 2023

CITATION
Andreeva OA, Dubinina E, Andreeva IA, Yarmolyuk VV, Bychkov A, Borisova A, Ji J, Zhou X, Kovalchuk EV, Borisovsky SY and Averin AA (2023), Mechanism of carbonate assimilation by intraplate basaltic magma and liquid immiscibility: example of Wangtian'e volcano (Changbaishan volcanic area, NE China). *Front. Earth Sci.* 11:1306460.
doi: 10.3389/feart.2023.1306460

Mechanism of carbonate assimilation by intraplate basaltic magma and liquid immiscibility: example of Wangtian'e volcano (Changbaishan volcanic area, NE China)

Olga A. Andreeva[1]*, Elena Dubinina[1], Irina A. Andreeva[1], Vladimir V. Yarmolyuk[1], Andrey Bychkov[2], Anastassia Borisova[3], Jianqing Ji[4], Xin Zhou[4], Elena V. Kovalchuk[1], Sergey Y. Borisovsky[1] and Alexey A. Averin[5]

[1]Institute of Geology of Ore Deposits, Petrography, Mineralogy and Geochemistry, Russian Academy of Sciences, Moscow, Russia, [2]Department of Geology, Lomonosov Moscow State University, Moscow, Russia, [3]Géosciences Environnement Toulouse, Observatoire Midi-Pyrénées, Université Toulouse III/CNRS/IRD/CNES, Toulouse, France, [4]School of Earth and Space Sciences, Peking University, Beijing, China, [5]Frumkin Institute of Physical Chemistry and Electrochemistry, Russian Academy of Sciences, Moscow, Russia

The balance of CO_2 during abundant basaltic magma production is an important factor of volcanic hazards and climate. In particular, this can be explored based on CO_2-rich mantle-derived magmas or carbonate assimilation by basaltic melts. To reconstruct the origin of Fe-rich carbonates hosted by Cenozoic basalts from Wangtian'e volcano (northeast China), we studied elemental compositions of melt, crystalline and fluid inclusions in magmatic minerals as well as the oxygen and carbon isotope compositions of the plagioclase and carbonates from basalts. The crystallization of basaltic magmas occurred in shallow chamber (~4 km) at temperatures of 1,180°C–1,200°C and a pressure of 0.1 ± 0.01 GPa. Stable Fe-rich carbonates occur in the Wangtian'e tholeiite basalts as groundmass minerals, crystalline inclusions in plagioclase and globules in melt inclusions, which suggests that they crystallized from a ferrocarbonate melt. The values of $\delta^{18}O$ and $\delta^{13}C$ in the minerals analyzed by laser fluorination method are in line with the sedimentary source of Fe-rich carbonates, indicating assimilation and partial decomposition of carbonate phases. The parent ferrocarbonate melt could be produced during interactions between the basaltic magma and the crustal marbles. The phase diagram and thermodynamic calculations show that the ferrocarbonate melt is stable at a temperature of 1,200°C and a pressure of 0.1 GPa. Our thermodynamic calculations show that carbonate melt containing 73 wt% $FeCO_3$, 24 wt% $MgCO_3$ and 3 wt% $CaCO_3$ is in thermodynamic equilibrium with silicate melt in agreement with our natural observations. The proposed mechanism is crustal carbonate sediment assimilation by the intraplate basaltic magma resulting in the melt immiscibility, production of the ferrocarbonate melt and the following Fe-rich carbonate mineral crystallization during magma residence and cooling.

KEYWORDS

intraplate volcanism, melt inclusions, fluid inclusions, silicate liquid immiscibility, silicate-carbonate liquid immiscibility, ferrocarbonates

1 Introduction

Up to date, carbon source and mechanisms of the carbonate formation in basaltic magma remain unclear, whereas the balance of CO_2 during basaltic magmas production is an important factor of volcanic hazards and climate (Martini, 1997; Tobin et al., 2017). For example, origin of ferrocarbonates (or Fe-rich carbonates) genetically associated with basaltic lavas is an unresolved problem (Viladkar and Schidlowski, 2000; Xue and Zhu, 2007; Viladkar, 2018; Randive and Meshram, 2020). Ferrocarbonatite veins and lenses related to flood basalts have been described in the Siberian and Deccan traps (Randive and Meshram, 2020). In addition, siderite of magmatic origin is found in the Jurassic olivine basalts of the Karamay province in northwest China (Xue and Zhu, 2007) and metastable calcite and carbonate melt is reported by Borisova and Bohrson (2023) for Merapi volcano (Indonesia) as well as Na-K-Ca carbonate-chloride melt recorded in melt inclusions at Mount Vesuvius studied by Fulignati et al. (2001) and Klebesz et al. (2015). Nevertheless, such studies are extremely scarce and the mechanism of the carbonate assimilation and the following melt immiscibility in the contest of basaltic magma remains unknown. The present study is of particular interest since it focuses on the origin of Fe-rich carbonates in the Cenozoic intraplate tholeiitic basalts of Wangtian'e volcano in the Changbaishan area of northeast China.

Two hypotheses can be considered. 1) The ferrocarbonates can also be formed during the decarbonation of sedimentary carbonates trapped by the basaltic magma or by interaction between basaltic melts and sedimentary carbonates of the continental crust. 2) The CO_2 excess in basaltic magmas can be produced by partial melting of metasomatized mantle. Numerous experimental works devoted to pure carbonate solubility in mafic melts demonstrate an important role of carbonate material on the magma liquidus phase stability field (Freda et al., 2008; Iacono-Marziano et al., 2008; 2009; Mollo et al., 2010). Additionally, Deegan et al. (2010), Jolis et al. (2013) and Blythe et al. (2015) experimentally studied interaction of carbonate materials with mafic and alkaline melts at conditions corresponding to the deep crust (5 kbar) resulting in chemical reactions between carbonates and silicates with CO_2 exsolving. Nevertheless, the mechanisms of ferrocarbonate melt formation in the shallow mafic magma chambers (up to 5 km) remain unclear. This paper reports results of petrological and geochemical studies on the Wangtian'e basalts, as well as carbon and oxygen isotope compositions, including the analyses of natural melt inclusions trapped by silicate minerals and thermodynamic calculations based on these natural data. Using these results, we propose a quantitative model for the formation of ferrocarbonates in the tholeiitic basalts of Wangtian'e volcano.

2 Geological setting of Wangtian'e volcano and timescale of its formation

The Changbaishan volcanic field (Figure 1) is spatially constrained to the northern margin of the Archean–Proterozoic Sino–Korean craton at the Chinese–North Korean border, at the intersection of the northeast-trending Tanlu rift system and the northwest-trending Paektusan faults (Andreeva et al., 2014; Andreeva et al., 2020). Two large stratovolcanoes are located within this volcanic field: Changbaishan and Wangtian'e. In contrast to the strongly differentiated alkaline series of Changbaishan (Fan et al., 1999; Andreeva et al., 2014; Andreeva et al., 2018; Andreeva et al., 2019), the lavas of Wangtian'e belong to the tholeiite series and show only slight variations in composition from basalts to basaltic andesites (Andreeva et al., 2022). The thick shield platform and cone of Wangtian'e volcano are composed of tholeiitic basalts. Silicic rocks form trachyte necks and a rhyolite extrusive dome (Fan et al., 1999; Andreeva et al., 2020; Andreeva et al., 2022).

The results of K-Ar age dating (Andreeva et al., 2022) indicate that the Wangtian'e volcano was formed within a short geological period of time between 3.8 and 2.7 Ma. The evolution of the volcano comprises three main stages: 1) Changbai period with fissure eruptions of basaltic lavas formed a shield volcano, 2) Wangtian'e period with growth of the basaltic cone, and 3) the Hongtoushan period, marked by the formation of necks and an extrusive dome of trachyte–alkaline rhyolite composition. We examined the northern, southern, and eastern slopes of the cone and the shield volcano and collected samples of all their major rock types. Below, we discuss the results of our geochemical studies of tholeiitic basalts from the southeastern section of the shield volcano (Figure 1).

3 Geochemical characteristics of tholeiitic basalts

The volcanic rocks from the southeastern section of the Wangtian'e shield volcano correspond to basalts with SiO_2 contents of 48.7–50.1 wt%., showing high Fe_2O_{3tot} (9.6–13.5 wt%) but low MgO (2.4–3.7 wt%). The basalts are also enriched in titanium (TiO_2 = 2.4–3.5 wt%) and phosphorus (P_2O_5 up to 1.2 wt%). The total alkali contents of the basalts vary from 4.3 to 5.2 wt% (Table 1). The AFM diagram (Figure 2) shows that the compositions of the shield basalts plot above the Irwin-Baragar line (Irwine and Baragar, 1971) and belong to tholeiitic series.

The basalts were collected from the bottom to the top along the southeastern section of the shield volcano. They all have similar petrographic features and chemical compositions (Table 1). Basalts are represented by massive dark gray porphyritic rocks with large

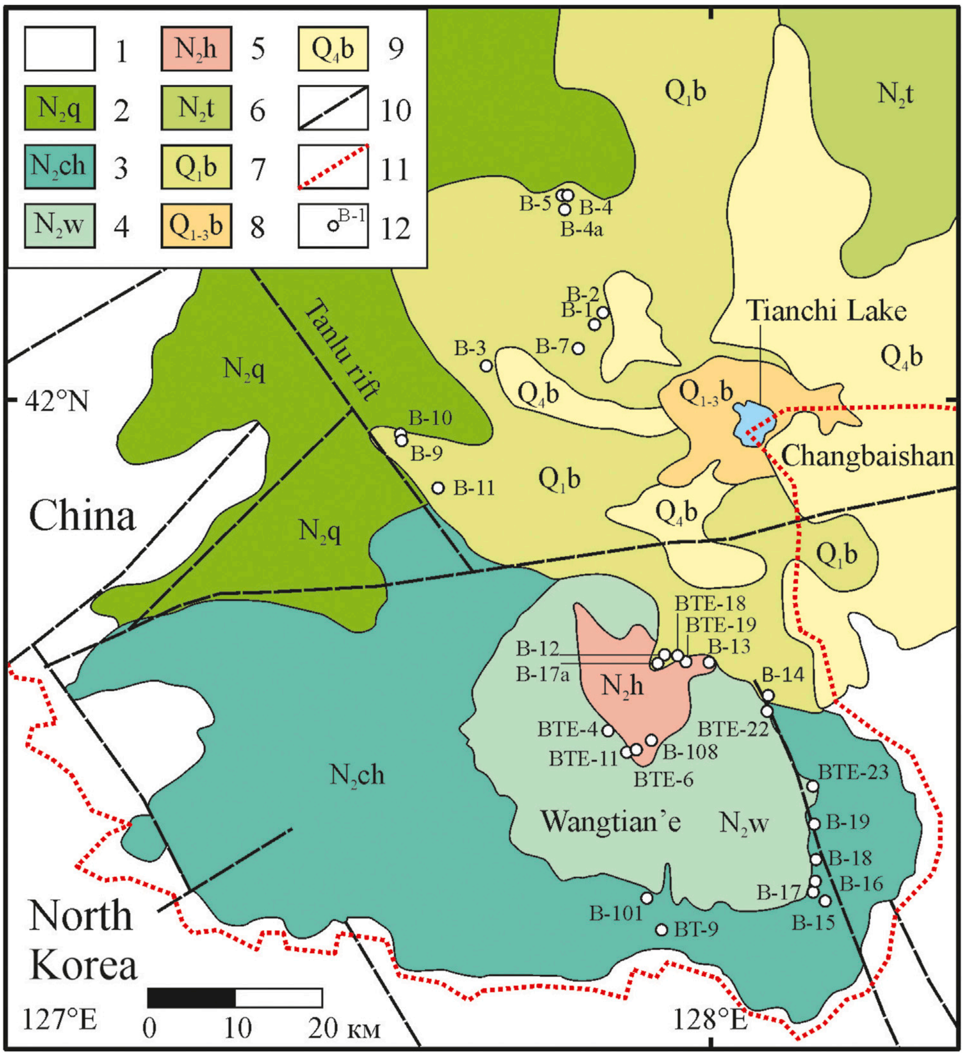

FIGURE 1
Geological sketch map of the Wangtian'e and Changbaishan volcanoes in the Changbaishan Mountains [modified after Andreeva et al. (2022)]. (1) host rocks; (2) flood basalts of the Changbaishan volcanic field, Quanyang period (4.50–4.00 Ma); (3) tholeiitic basalts of the Wangtian'e shield volcano, Changbai period (3.82–2.83 Ma); (4) tholeiitic basalts of the Wangtian'e volcano, Wangtian'e period (2.76–2.67 Ma); (5) dome and necks of Wangtian'e volcano, Hongtoushan period (2.76–2.69 Ma); (6) alkaline basalts of Changbaishan shield volcano, Toudao period (2.77–1.99 Ma); (7) alkaline basalts of Changbaishan shield volcano, Baishan period (1.64–1.11 Ma); (8) trachytes, comendites, and pantellerites of Changbaishan volcanic cone, Baitoushan period (1.12–0.81 Ma); (9) ignimbrites, pumices and ashes of the Changbaishan caldera, Bingchang–Baiyufeng–Baiguamiao periods (7854–825 kyr); (10) faults; (11) sampling sites and sample names.

plagioclase phenocrysts (sometimes megacrysts up to 1 cm). Plagioclase ($An_{74.3-79.1}Ab_{19.8-25.5}Or_{0.1-1.3}$) is the dominant phenocryst phase in these basalts. The basalt (sample B-19) from the upper part of the section of the shield volcano contains some isolated resorbed subphenocrysts of olivine (Fo = 74), which represent xenogenic phases out of equilibrium with the basaltic magma. It has been shown (Andreeva et al., 2020) that plagioclase is the first liquidus phase in the studied basalts. The groundmass minerals are represented by plagioclase, olivine (Fo = 43.2–56.4), titanaugite (#Mg = 0.64–0.70), ilmenite, titanomagnetite, fluorapatite and ferrocarbonate. There are also some "dry" and hydrous Fe-rich and Si-rich glasses present in the groundmass (Figure 3). Si-rich glass is characterized by the following composition: 70–77 wt% SiO_2, up to 9.4 wt% (Na_2O+K_2O) with a predominance of K_2O (ca. 7.5 wt%) over Na_2O (ca. 2.6 wt%), 10.5–14 wt% Al_2O_3, 0.2–2.2 wt% CaO, 0.6–2.2 wt% FeO and 0.9–1.5 wt% TiO_2 (Table 2). Fe-rich "dry" glass is globular and often finely crystallized. It contains 30–40 wt% SiO_2, up to 39 wt% FeO, 12.5–18.7 wt% TiO_2, up to 7.4 wt% P_2O_5 and up to 2.0 wt% SO_3 (Table 2). Hydrous Fe-rich glass is located in an interstitial position and sometimes has a globular morphology. It contains from 48 to 55 wt% SiO_2, 18–25 wt% FeO, 8–15 wt% MgO, 0.7–1.6 wt% Al_2O_3 and 0.9–1.7 wt% CaO, while the total alkalis do not exceed 0.4 wt% (Table 2). Water content is estimated by the difference from a constant sum of 100% of major oxide components in these glasses, leading to values of 10–15 wt% of H_2O, as shown by Andreeva et al. (2020).

The interstitial ferrocarbonate of the groundmass is characterized by distinct or weakly expressed concentric zonation

TABLE 1 Chemical composition (wt%) of basalts from Wangtian'e shield volcano, and the results of isotope analysis of oxygen and carbon (‰) of their groundmass.

Sample	B-15	B-16	B-17	B-18	B-19
SiO_2	48.66	50.10	49.38	48.93	48.66
TiO_2	3.30	3.08	3.22	3.52	2.44
Al_2O_3	15.80	14.00	15.39	15.64	18.51
Fe_2O_{3tot}	13.14	13.53	12.73	12.71	9.62
MnO	0.17	0.20	0.17	0.19	0.13
MgO	2.74	3.66	2.40	2.81	2.98
CaO	8.17	7.65	8.54	8.61	9.62
Na_2O	3.68	3.56	3.20	3.59	3.17
K_2O	1.54	1.75	1.48	1.47	1.09
P_2O_5	0.71	1.19	0.36	0.56	0.36
LOI	1.26	0.45	2.34	1.18	2.66
Total	99.17	99.17	99.21	99.21	99.24
$\delta^{18}O$ (m), ‰	19.38	20.25	19.72	19.56	—
$\delta^{13}C$ (m), ‰	−4.03	−6.84	−5.28	−3.53	—

Note: Fe_2O_{3tot}—total iron oxide content; m—rock groundmass. LOI— loss on ignition. Dashes mean not analysed.

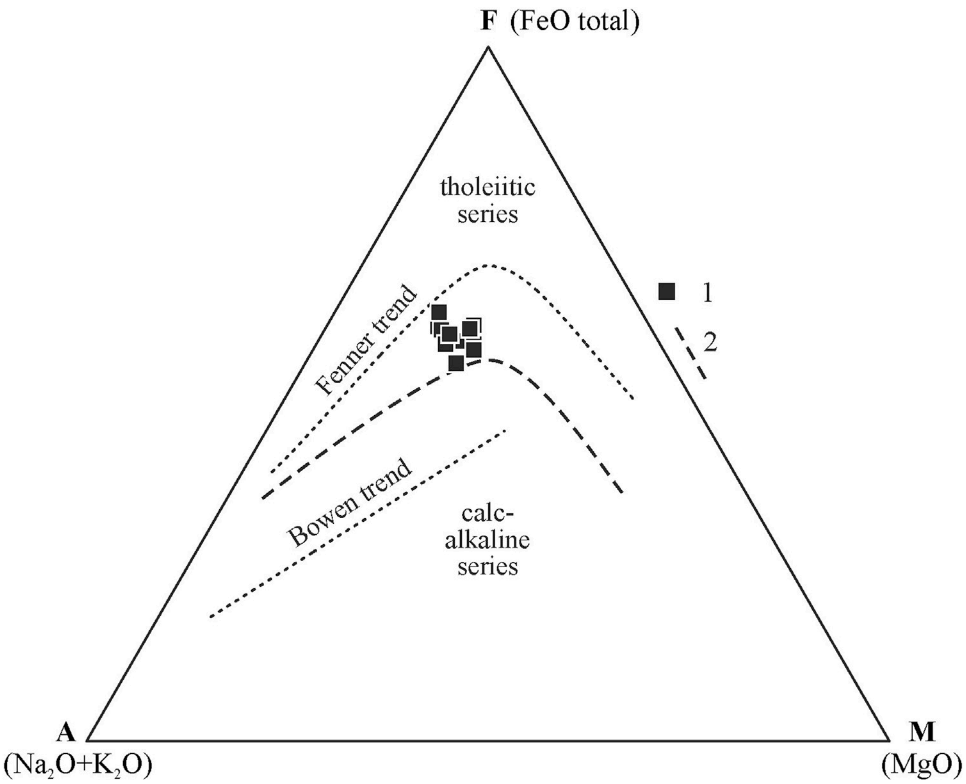

FIGURE 2
AFM diagram [$(Na_2O+K_2O)-FeO_{tot}-MgO$)] for rocks of Wangtian'e volcano. (1) Shield volcano of the Changbai period; (2) line between tholeiitic and calc-alkaline series by (Irvine and Baragar, 1971). Arrows indicate the Fenner and Bowen trends of fractional crystallization.

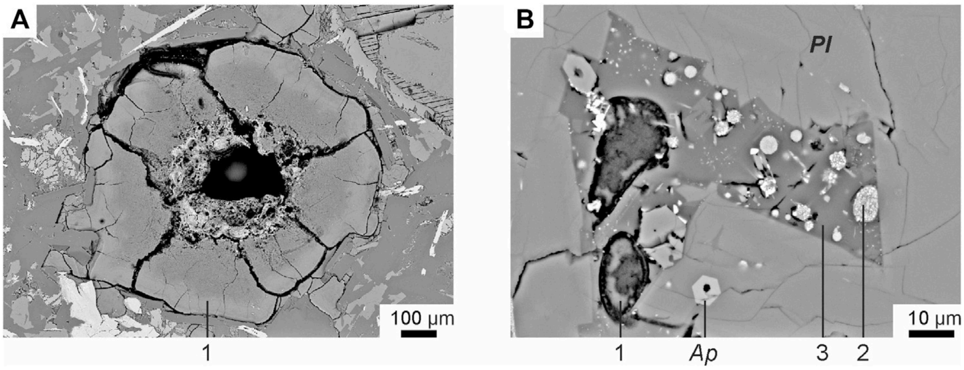

FIGURE 3
Backscattered electron images of groundmass glasses of tholeiitic basalts from Wangtian'e shield volcano (Andreeva et al., 2020): **(A)** groundmass water-bearing Fe-rich glass; **(B)** groundmass Si-rich glass with Fe-rich globules. (1) Water-bearing Fe-rich glass; (2) "dry" Fe-rich glass; (3) "dry" Si-rich glass. Mineral symbols: Ap—apatite, Pl—plagioclase.

TABLE 2 Chemical composition (wt%) of groundmass glasses and glasses in ferrocarbonates from Wangtian'e tholeiitic basalts.

Component	Groundmass "dry" Fe-rich glass		Groundmass "dry" Si-rich glass		Groundmass hydrous Fe-rich glass		Si-rich glass in siderite	
	B-19-2	B-19-5	B-19-8	B-19-11	B-19-15	B-19-16	B-16-4	B-16-5
SiO_2	32.29	30.12	71.81	73.57	48.42	52.41	68.49	68.1
TiO_2	6.31	12.50	0.59	2.70	0.13	0.04	0.63	0.63
Al_2O_3	1.94	1.02	13.68	10.32	1.42	0.90	13.92	14.17
FeO_{tot}	30.71	39.34	2.24	3.29	26.10	18.71	1.41	1.52
MnO	0.68	0.59	0.15	0.07	0.11	0.09	0.03	0.04
MgO	2.16	1.86	0.22	0.12	8.03	15.15	0.07	0.09
CaO	12.26	8.15	2.16	1.30	1.70	0.91	0.37	0.42
Na_2O	1.04	0.30	2.20	1.60	0.12	0.08	2.62	3.03
K_2O	1.06	0.17	5.99	5.23	0.08	0.39	7.41	7.47
P_2O_5	8.03	4.21	0.11	0.53	0.00	0.00	0.14	0.2
SO_3	1.26	2.01	0.05	0.15	0.02	0.02	—	—
ZrO_2	0.15	0.48	0.03	0.09	0.01	0.01	—	—
Cl	0.27	0.12	0.05	0.12	0.03	0.00	0.04	0.04
F	—	—	0.07	0.04	—	—	—	—
Ce_2O_3	0.37	0.31	0.03	0.15	0.07	0.01	—	—
Total	98.99	101.49	99.36	99.23	86.36	88.79	95.15	95.72

Note. FeO_{tot} is total iron oxide content. Dashes mean not analyzed.

(Figures 4A, B; Table 3). It contains inclusions of plagioclase, pyroxene, olivine, apatite and Si-rich glass (Figures 4C, D; Table 2). Ferrocarbonate is also found as crystalline inclusions in plagioclase; like the groundmass ferrocarbonate, it is characterized by 60–75 wt% $FeCO_3$, 14–32 wt% $MgCO_3$, 2–12 wt% $CaCO_3$, and up to 1.5 wt% $MnCO_3$ (Table 3).

4 Materials and methods

4.1 Analytical techniques

All sampled rocks from southeastern section of the Wangtian'e shield volcano (samples B-15, B-16, B-17, B-18,

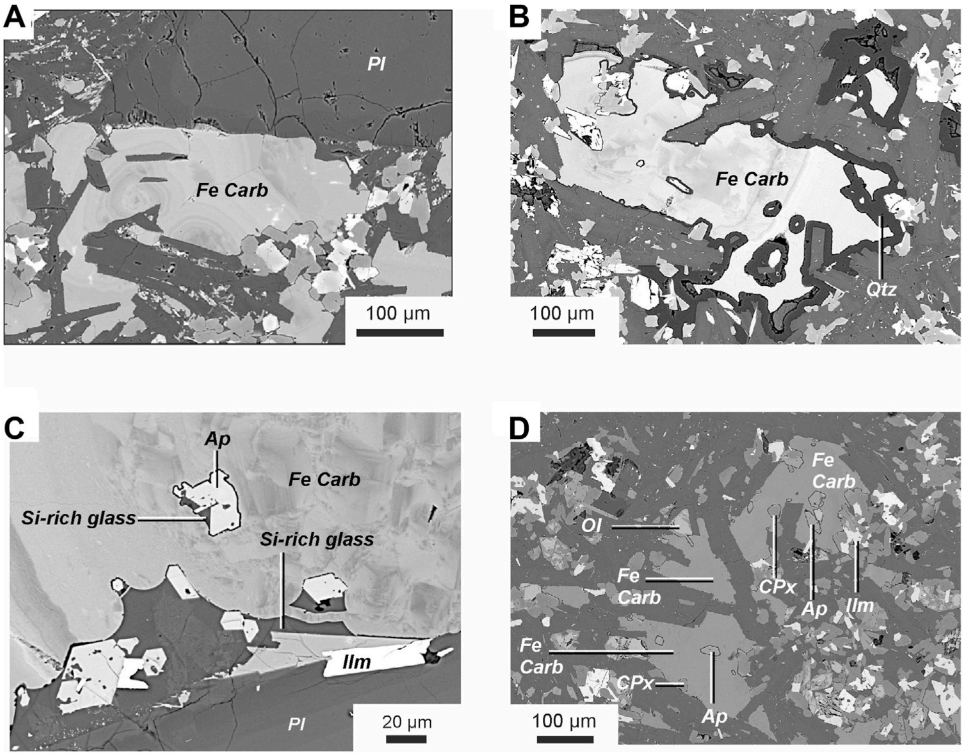

FIGURE 4
Backscattered electron images of ferrocarbonates and the ferrocarbonate-hosted inclusions. Phase symbols: *Pl*—plagioclase, *Fe Carb*—ferrocarbonate, *Ap*—apatite, *Ol*—olivine, *CPx*—clinopyroxene, *Ilm*—ilmenite.

and B-19) were analyzed for their major oxide contents using an X-ray fluorescence spectrometer PW-2400 (IGEM RAS, Moscow, Russia, Andreeva et al., 2018; Andreeva et al., 2020). Glasses in homogenized melt inclusions, daughter mineral phases in inclusions, crystal inclusions and rock-forming minerals were analyzed using EPMA JXA-8200 JEOL microprobe equipped with five WD spectrometrs (IGEM RAS, Moscow, Russia) at an accelerating voltage of 20 kV and beam current on the Faraday cylinder of 20 nA for minerals and 10 nA for glasses. The beam diameter was 1 μm when minerals were analyzed and varied from 2 to 10 μm when glasses were analyzed, depending on the size of the inclusions. The standards were minerals of composition close to that of the analyzed phases. Corrections were calculated by the ZAF routine, using a proprietary JEOL software. Detailed measurement conditions are shown in the (Supplementary Table S1). Trace elements and REE in whole-rocks were analysed on an XII ICP-MS ThermoScientific ICP-MS spectrometer (IGEM RAS, Moscow, Russia) with an accuracy of 1%–3% relative.

Oxygen and carbon isotope compositions of the groundmass ferrocarbonates and plagioclase-hosted ferrocarbonates were analysed using a CF-IRMS DeltaV+ instrument (Thermo, Finnigan) with a GasBenchII configuration and PAL autosampler, after decomposition of hand-picked separates in phosphoric acid at 70°C (Institute of Geology of Ore Deposits, Petrography, Mineralogy and Geochemistry Russian Academy of Sciences, Moscow). The technique is described in detail by Nikiforov et al. (2021). Due to the low content of carbonates in the silicate matrix (1%–3%), the $\delta^{13}C$ and $\delta^{18}O$ values were measured at an estimated accuracy ±0.4% and ±0.8‰ (1 σ), respectively. Measured values of $\delta^{13}C$ and $\delta^{18}O$ are expressed relative to VPDB and VSMOW, respectively (Nikiforov et al., 2021). Calibration of $\delta^{13}C$ and $\delta^{18}O$ values on the VPDB and VSMOW scales was performed by measuring the NBS 19 and NBS 18 international standards in the same analytical series.

The oxygen isotope compositions of plagioclase phenocrysts were determined on carefully picked separates (Institute of Geology of Ore Deposits, Petrography, Mineralogy and Geochemistry Russian Academy of Sciences, Moscow). The analysis was carried out by laser fluorination (Sharp, 1990). The error in $\delta^{18}O$ determination was ±0.1‰ or better. The results given in per mil relative to V–SMOW standard were checked against measurements of NBS 28 (quartz) and UWG 2 (garnet) standards (Valley et al., 1995). The technique is described in detail by Dubinina et al. (2015).

The decarbonation reaction of the initial carbonate is calculated using the fractionation factor “calcite-CO_2” at 1,200°C (Scheele and Hoefs, 1992; Chacko and Deines, 2008).

Thermodynamic calculations were performed using the HCh software package (Shvarov, 2008). Nine component system (Al-C-Ca-Fe-H-Mg-Na-O-Si) was used for the thermodynamic calculations which takes into account 42 mineral phases, a gas solution (H_2O-CO_2-O_2-H_2-CH_4

TABLE 3 Composition (wt%) of groundmass ferrocarbonate, crystalline inclusions represented by ferrocarbonate, and ferrocarbonate globules in melt inclusions in plagioclase from basalts of Wangtian'e shield volcano.

Sample name	$MgCO_3$	$FeCO_3$	$CaCO_3$	$MnCO_3$	Total[a]
B-16-1	14.66	75.21	8.83	1.30	100
B-16-2	27.02	60.11	11.47	1.40	100
B-16-3	22.26	74.01	2.49	1.23	100
B-16-4	28.22	67.39	3.53	0.86	100
B-16-5	31.65	65.50	1.83	1.02	100
B-16-6	22.21	73.08	3.35	1.36	100
B-16-Line 1	17.15	69.24	12.42	1.19	100
B-16-Line 2	17.20	69.37	12.29	1.14	100
B-16-Line 3	20.53	67.21	11.13	1.13	100
B-16-Line 4	22.83	65.99	10.00	1.19	100
B-16-Line 5	22.37	67.14	9.33	1.16	100
B-16-Line 6	20.61	68.46	9.79	1.13	100
B-16-Line 7	19.42	70.50	8.83	1.25	100
B-16-Line 8	17.85	70.33	10.63	1.19	100
B-15-Line-1	21.13	69.28	7.96	1.64	100
B-15-Line-2	19.20	76.01	3.87	0.93	100
B-15-Line-3	18.24	77.42	3.43	0.92	100
B-15-Line-4	14.01	81.62	3.17	1.20	100
B-15-Line-5	13.30	82.44	3.09	1.17	100
B-15-Line-6	29.91	63.62	5.46	1.01	100
B-15-Line-7	19.30	75.70	4.06	0.94	100
B-15-Line-8	14.99	78.67	5.09	1.25	100
B-15-36	18.94	71.32	8.23	1.52	100
B-16-9	17.47	70.83	10.49	1.21	100
B-16-31	16.97	68.15	13.73	1.15	100
B-16-32	14.66	75.21	8.83	1.30	100
B-15-23	14.09	81.07	3.75	1.09	100
B-15-24	14.40	81.30	3.19	1.10	100
B-15-25	17.94	77.19	3.82	1.05	100
B-15-26	18.63	77.12	3.25	1.00	100
B-15-27	16.28	78.76	3.78	1.18	100

Note: B-16-1–B-16-6–composition of ferrocarbonate from rock groundmass; B-16-Line-1–B-16-Line-8–composition by profile of zoned ferrocarbonate from rock groundmass of the sample B-16; B-15-Line-1–B-15-Line-8–composition by profile of zoned ferrocarbonate from rock groundmass of the sample B-15; B-15-36–B-16-32–crystalline inclusions represented by ferrocarbonate in plagioclase of basalts; B-15-23–B-15-27–ferrocarbonate globules in melt inclusions from plagioclase of basalts.

[a]Total normalized to 100 wt%.

mixture) and a carbonate melt. The fugacity of the components of the gas mixture was calculated using the Peng-Robinson equation (e.g., Lopez-Echeverry et al., 2017). The stability of the liquid carbonate melt was defined in the $FeCO_3$-$MgCO_3$-$CaCO_3$ ternary system. Thermodynamic parameters for liquid carbonate end-members were taken from Zhao et al. (2019) and Kang et al. (2016). A silicate melt was not taken into account under the assumption that the association of eutectic minerals was sufficient to describe the liquid-solid phase equilibrium.

TABLE 4 Chemical composition (wt%) of glasses and globules of unheated plagioclase-hosted melt inclusions and their host plagioclase from Wangtian'e tholeiitic basalts.

Compo-nent	Host plagioclase		Melt inclusions										
			a		b		c		d			e	
	2	4	6	9	10	11	12	13	14	16	18	20	22
SiO_2	53.10	52.88	55.59	65.90	42.94	43.15	40.39	43.83	73.80	71.81	72.07	44.73	46.24
TiO_2	0.13	0.12	0.12	0.10	5.68	5.72	7.36	6.47	0.48	0.59	0.94	0.06	0.01
Al_2O_3	29.17	29.20	28.25	21.64	1.94	2.01	2.74	2.91	14.19	13.68	13.57	3.23	3.48
FeO_{tot}	0.59	0.62	0.72	0.64	24.16	23.41	26.10	23.35	1.26	2.24	1.66	21.16	25.02
MnO	dl	0.03	dl	dl	0.33	0.33	0.43	0.35	0.09	0.15	0.04	0.35	0.29
MgO	0.10	0.11	0.18	0.02	10.88	11.75	10.12	10.07	0.07	0.22	0.18	7.69	8.49
CaO	12.52	12.85	10.91	2.48	10.20	10.34	9.70	10.01	0.99	2.16	1.13	1.85	1.43
Na_2O	4.21	4.09	4.94	6.23	0.68	0.72	0.62	0.85	1.03	2.20	2.18	0.11	0.05
K_2O	0.31	0.29	0.51	5.50	0.43	0.37	0.42	0.71	4.69	5.99	5.90	0.48	0.11
P_2O_5	—	—	—	—	0.95	0.88	1.03	1.14	0.05	0.11	0.21	dl	0.02
SO_3	—	—	—	—	0.38	0.34	dl	dl	0.30	0.05	dl	dl	0.09
Cl	—	—	—	—	0.03	0.02	0.05	0.04	0.06	0.05	0.07	0.57	dl
F	—	—	—	—	—	—	—	—	0.02	0.07	0.44	—	—
Total	100.12	100.19	101.23	102.66	98.80	99.29	99.66	100.30	97.20	99.36	98.19	84.17[a]	85.40

Note: (a) zoned rim of melt inclusions; (6) outer zone, (9) inner zone; (b) (10, 11) Fe-rich silicate glass of melt inclusions; (c) (12, 13) fine-grained Fe-rich aggregate of melt inclusions; (d) (14–18) Si-rich globules; (e) (20, 22) hydrous Fe-rich globules. FeO_{tot} is total iron oxide content.

[a] Total is given without H_2O content, that amounts 3.97 wt% (Andreeva et al., 2020). Dl indicates values below detection limit. Dashes mean not analysed.

4.2 Techniques applied to study magmatic inclusions in minerals

The studied more than a hundred melt inclusions are partially or completely crystallized at room temperature, so we carried out experimental re-heating prior to analysis and estimation of the crystallization temperatures of the rock-forming minerals. For this purpose, we used muffle furnaces and a Linkam TS1500 high-temperature stage (Institute of Geology of Ore Deposits, Petrography, Mineralogy and Geochemistry Russian Academy of Sciences, Moscow). The temperature was controlled with a Pt-$Pt_{90}Rh_{10}$ thermocouple calibrated on the melting points of $K_2Cr_2O_7$ (T_m = 398°C), NaCl (T_m = 800°C), and Au (T_m = 1,064°C). The integrated error of the temperature measurements was estimated at ±10°C (Andreeva et al., 2018; Andreeva et al., 2020). The duration of re-heating experiments for melt inclusions in plagioclase in basalts were up to 10–15 min according to (Danyushevsky et al., 2002; Esposito, 2021).

The composition of the fluid phases was analyzed by Raman spectroscopy using a Renishaw spectrometer (Frumkin Institute of Physical Chemistry and Electrochemistry, Russian Academy of Sciences, Moscow, Andreeva et al., 2023). Raman spectra were recorded using the 405-nm line of a Nd:YAG laser at a power of <2 mW and a spectral resolution of ~2 cm^{-1}. The signal acquisition time was ~200 s. The spectra were recorded using a ×100 objective with a scattering cross-section of ~1 µm. The instrument was calibrated using an internal silicon wafer. Experimental spectra were decomposed into several components using Fityk software (Wojdyr M., 2010).

5 Results

5.1 Melt and fluid inclusions

Primary melt and fluid inclusions are recorded in the plagioclase of tholeiitic basalts from Wangtian'e volcano. The primary melt inclusions vary in size from 30 to 100 µm. They are partially or completely crystallized, and consist of anhydrous Fe-rich glass or fine-grained mineral aggregates composed of clinopyroxene, titanomagnetite, ilmenite, apatite and sulfides. Fe-rich glass and fine-grained mineral aggregates were analysed by electron microprobe using an expanded electron beam with a diameter of 10 µm. The compositions of Fe-rich glass and fine-grained mineral aggregates are similar and are characterized by high contents of FeO (up to 24 wt%), CaO (up to 10 wt%), MgO (12 wt%) and TiO_2 (up to 6 wt%) as well as low concentrations of Al_2O_3 (<2 wt%), Na_2O+K_2O (1 wt%), P_2O_5 (1 wt%) and SO_3 (0.3–0.4 wt%), with a SiO_2 content of 40–43 wt% (Table 4). The fine-grained mineral aggregates in the inclusions are interpreted as a crystallized Fe-rich melt. In addition, the inclusions contain wide zonal feldspar rims. The composition of these rims varies from the outer part towards the core of the inclusions from plagioclase ($An_{46\text{-}56}Ab_{39\text{-}47}Or_{4\text{-}7}$) to anorthoclase ($An_{13\text{-}13.5}Ab_{43\text{-}50}Or_{36\text{-}43}$). Globules of various compositions are

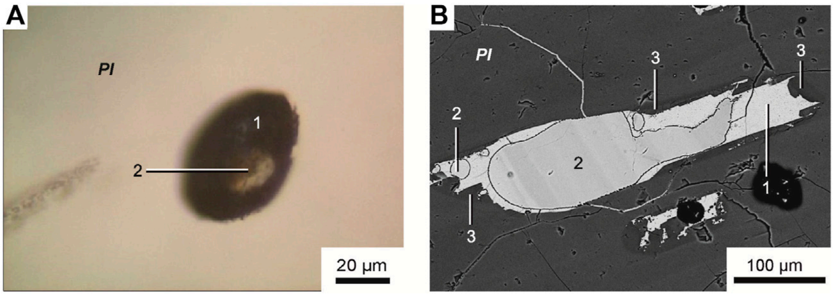

FIGURE 5
(A) Transmitted-light microphotograph and **(B)** backscattered electron image of unheated plagioclase-hosted melt inclusion. (1) Fine-grained Fe-rich aggregate, (2) ferrocarbonate globule, (3) feldspar rim.

TABLE 5 Chemical composition (wt%) of glasses of the homogenized melt inclusions in the host plagioclase from Wangtian'e tholeiitic basalts.

Sample	B-19-1	B-19-2	B-19-3	B-19-4	B-19-5	B-15-1	B-15-2	B-15-3	B-15-4	B-15-5
Homogenization, T°C	1,190	1,190	1,190	1,180	1,170	1,195	1,195	1,200	1,205	1,205
SiO_2	48.78	48.15	48.63	50.33	48.36	49.69	49.47	51.13	51.69	54.28
TiO_2	3.64	3.47	3.60	2.87	3.83	3.00	3.14	2.79	2.49	1.66
Al_2O_3	16.35	16.48	16.42	16.19	14.84	16.43	16.16	17.09	16.90	17.92
FeO_{tot}	11.71	12.09	11.85	11.41	12.34	11.00	10.83	9.47	8.91	8.62
MnO	0.22	0.13	0.16	0.09	0.12	0.19	0.05	0.11	0.10	0.07
MgO	4.33	4.57	4.46	3.95	4.19	4.49	4.44	4.36	3.69	3.58
CaO	8.50	8.51	8.67	8.08	8.81	9.04	9.03	8.79	8.95	8.68
Na_2O	3.14	3.00	2.99	2.98	2.86	3.56	3.52	4.10	3.85	3.12
K_2O	1.32	1.28	1.29	1.59	1.53	1.12	1.10	1.44	1.36	0.95
P_2O_5	0.57	0.61	0.60	0.43	0.65	0.43	0.45	0.34	0.44	0.24
SO_3	0.62	1.65	0.52	0.51	0.57	0.31	0.33	0.28	0.24	0.08
Cl	0.03	0.02	0.02	0.02	0.03	0.02	0.01	0.02	0.01	dl
F	0.17	0.11	0.26	0.07	0.12	0.08	0.11	0.13	dl	0.01
Total	99.34	100.05	99.39	98.53	98.22	99.44	98.71	100.04	98.69	99.30

Note: FeO_{tot}—total iron oxide. Dl indicates values below detection limit.

found in many inclusions. Among them, silicate and carbonate globules are identified. Silicate globules are represented by 1) hydrous Fe-rich glass; 2) hydrous Si-rich glass; 3) anhydrous Si-rich glass (Table 4). The composition of these globules is similar to that of the Si-rich and Fe-rich groundmass glasses. As shown in previous studies (Andreeva et al., 2020), the hydrous Fe-rich glasses contain at least 4 wt% H_2O. The sum of major oxides in these globules and in the groundmass glasses indicate H_2O concentrations of about 10–15 wt%. Carbonate droplets (Figures 5A, B) in the melt inclusions have compositions similar to the ferrocarbonates found in the groundmass (Table 3).

Homogenization experiments performed on the melt inclusions show that most of the inclusions containing carbonate globules are decrepitated on heating. Inclusions that do not contain globules are homogenized in the temperature range of T = 1,180°C–1,200°C. After heating, the inclusions contain glass ± sulfide globule ± gas bubble. The glass composition corresponds to basalt with high contents of FeO (11.5–12.5 wt%) and TiO_2 (up to 4 wt%) (Table 5). The total alkali content reaches 5 wt%. Glass is also characterized by high concentrations of P_2O_5 (up to 0.8 wt%) and SO_3 (up to 0.6 wt%) (Table 5). The H_2O content is low and varies from 0.1 to 0.8 wt% (Andreeva et al., 2020). The formation of sulfide globules during the heating experiments (T = 1,180°C–1,200°C) as well as the presence of sulfide globules in minerals from this rock suggests that the melt exsolved into immiscible silicate and sulfide liquids. Similar results were obtained on melt inclusions in minerals of various rock types from Changbaishan volcano (Andreeva et al., 2019).

Primary fluid inclusions of one phase carbon dioxide coexisting with primary melt inclusions are found in plagioclase phenocrysts (Figures 6A, B). More than 30 fluid inclusions were studied. The positions of the characteristic CO_2 peaks (Fermi dyads) in the

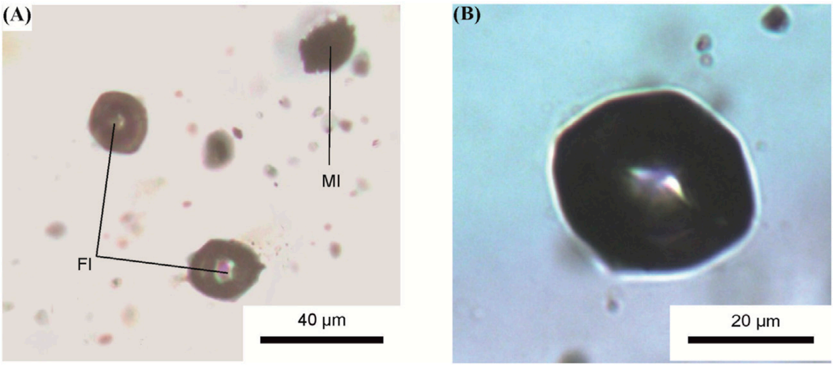

FIGURE 6
Transmitted-light microphotographs **(A,B)** of primary CO_2 fluid inclusions coexisting with primary melt inclusions in plagioclase of tholeiitic basalts from Wangtian'e shield volcano. **(A)** Primary melt and fluid inclusions. FI—fluid inclusions, MI—melt inclusions; **(B)** Primary CO_2 one phase fluid inclusion.

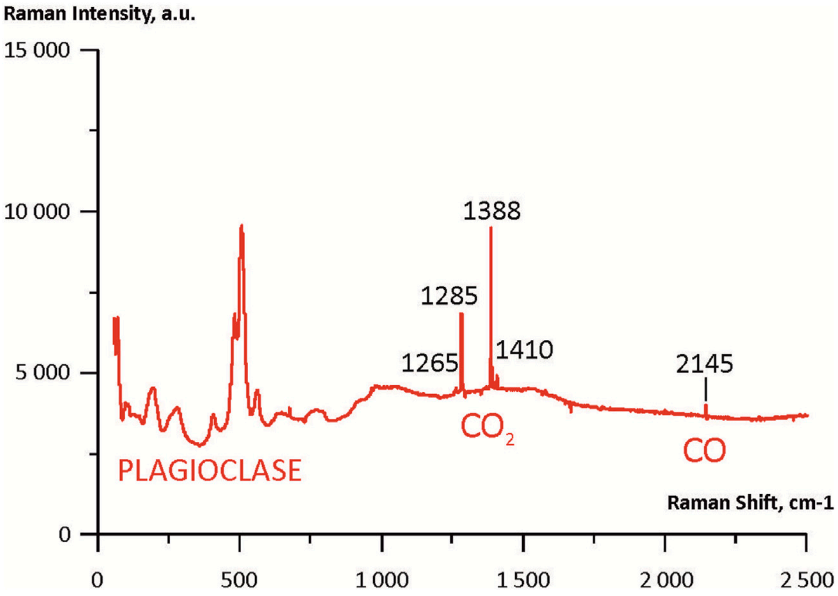

FIGURE 7
Micro-Raman spectra of plagioclase-hosted fluid inclusions.

inclusions were determined by Raman spectroscopy. The peak positions correspond to the range of 1,283.2 and 1,386.6 cm^{-1}–1,285.2 and 1,388.6 cm^{-1} (Figure 7; Supplementary Table S2). The density (ρ) of the CO_2 in the fluid inclusions is calculated according to the following (Equation 1) (Wang et al., 2011):

$$\rho = 47513.64243 - 1374.824414^{*}\Delta + 13.25586152^{*}\Delta^{2} - 0.04258891551^{*}\Delta^{3} \quad (1)$$

where Δ is the distance between the Fermi dyads. The calculated CO_2 density is equal to 0.23–0.33 g/cm^3. The pressures calculated from the pressure-volume-temperature parameters of CO_2 (Bottinga and Richet, 1981) correspond to the range of 0.1 ± 0.01 GPa. As was shown by Remigi et al. (2021), below the critical density gas-like CO_2 (d = 0.34 g/cm^3) narrower bands showed progressively increasing asymmetric profiles, resulting in more challenging to obtain a sufficiently accurate fitting of central positions. However we identified quite symmetric peaks.

5.2 Ferrocarbonate speciation and composition

Ferrocarbonate minerals are found in the groundmass of tholeiitic basalts from the Wangtian'e shield volcano, occurring as crystalline inclusions in plagioclase, and also as globules in melt inclusions in the plagioclase. The ferrocarbonate of the groundmass has an interstitial position and is characterized by distinct or weakly expressed concentric zonation (Figures 4A, B).

TABLE 6 Oxygen and carbon isotopic composition (‰) of ferrocarbonate inclusions in plagioclase and oxygen isotopic composition (‰) of the host plagioclase.

Sample	$\delta^{18}O$ of ferrocarbonate inclusions in plagioclase, ‰	$\delta^{13}C$ of ferrocarbonate inclusions in plagioclase, ‰	$\delta^{18}O$ of plagioclase, ‰
B-15	19.4	−3.78	6.1
B-19	17.2	−9.20	6.1

It contains 60–75 wt% $FeCO_3$, 14–32 wt% $MgCO_3$, 2–12 wt% $CaCO_3$, and up to 1.5 wt% $MnCO_3$ (Table 3). The groundmass ferrocarbonate contains inclusions of plagioclase, pyroxene, olivine, apatite, and Si-rich glass. Crystalline inclusions of apatite in ferrocarbonate are often surrounded by Si-rich glass (Figures 4C, D). Sometimes, quartz rims are observed at the boundary between apatite inclusions and host ferrocarbonate (Figures 4B). In addition, quartz rims are found at the boundaries between ferrocarbonates and various silicate minerals (plagioclase, clinopyroxene) and ore minerals (ilmenite, titanomagnetite). The Si-rich glass in ferrocarbonates (Figures 4C, D), intergrown with apatite has a composition similar to the Si-rich glass of the rock groundmass. It contains 68.0–70.0 wt% SiO_2, up to 0.6 wt% TiO_2, 1.4–1.8 wt% FeO and 12.8–13.9 wt% Al_2O_3. The total alkali content reaches 10.5 wt% with a significant predominance of K_2O (up to 7.5 wt%) over Na_2O (up to 3.0 wt%) (Table 2). Ferrocarbonates are also found as crystalline inclusions in plagioclase. The ferrocarbonate inclusions have a composition similar to the groundmass ferrocarbonates (Table 3; Figures 5A, B).

Globules in the un-reheated melt inclusions (Figures 5A, B) were analysed using Raman spectroscopy method and the electron microprobe. The Raman peak position corresponds to the CO_3^{2-} ion (1,091 cm^{-1}). Compositionally, these globules are characterized by 77.1–81.1 $FeCO_3$, 14.1–18.6 $MgCO_3$, 3.2–3.8 wt% $CaCO_3$ and 1.0–1.2 wt% $MnCO_3$ (Table 3).

5.3 Oxygen and carbon isotope composition

Oxygen and carbon isotope composition in carbonate minerals was determined in samples of tholeiitic basalts from the Wangtian'e shield volcano (samples B-15, B-16, B-17, B-19). The studied basalts contain from 1 to 3 vol% carbonate, which is expressed both among the groundmass minerals and as inclusions in plagioclase. The $\delta^{18}O$ values in the carbonates from bulk rock samples vary in the range +19.4 to +20.3‰ (relative to VSMOW), and $\delta^{13}C$ values vary from −3.5 to −6.8‰ (relative to VPDB) (Table 1). In addition, we studied the oxygen and carbon isotope composition of ferrocarbonate inclusions in plagioclase (Table 6). For two plagioclase-hosted ferrocarbonate inclusions, we obtained closely similar $\delta^{18}O$ and $\delta^{13}C$ values (+17.2, +19.4‰ and −3.78, −9.20‰, respectively). Analyses of the silicate matrix of the same plagioclase samples both yield a $\delta^{18}O$ value of +6.1‰ (Table 6).

6 Discussion

6.1 Origin of ferrocarbonates

The isotope data obtained on basalts from the Wangtian'e volcano are sharply distinguished from the basaltic series of the Changbaishan volcano. Analyses of the bulk isotope composition of Changbaishan basalts yield $\delta^{18}O$ values of +5.6–+5.8‰ (Dubinina et al., 2020). The basalts of Wangtian'e volcano contain up to 3 vol% of carbonates, which clearly affects the isotope compositions of bulk rock samples and ferrocarbonate inclusions contained in the plagioclase of these rocks. The $\delta^{18}O$ isotope characteristics (+17.2–+20.3‰), as well as the $\delta^{13}C$ values (−3.5 to −9.20‰), show that the groundmass ferrocarbonate as well as one sample of an inclusion in plagioclase, are both of sedimentary origin. The carbon isotope composition clearly indicates isotopic disequilibrium and indicates the mechanism of carbonate decomposition. The $\delta^{18}O$ (relative to VSMOW) versus $\delta^{13}C$ (relative to VPDB) diagram (Figure 8) shows that the compositional points of the studied basalts lie on the line representing the decarbonation reaction of the initial sedimentary carbonate at high temperatures. It can be seen from Figure 8 that 4 to 0.4 vol% of the carbonate remains during decarbonation of the initial sedimentary carbonate. Such an effect is regularly observed during the interaction of basaltic melts with carbonates derived from host rocks (e.g., Dubinina et al., 2019; Nikiforov et al., 2021; Nosova et al., 2021).

According to Sheet 1 of the Northeast Asia Geodynamics Map at a scale of 1:5,000,000, (USGS, 2004), the basement of the Changbaishan volcanic field is made up of marbles and limestones belonging to the Archean-Proterozoic granite-gneisses of the Sino-Korean craton. Under the Wangtian'e shield volcano on the southern margin of the Changbaishan volcanic field, the Paleoproterozoic Sangwon sedimentary basin reaches a thickness of several thousand meters. It is composed mainly of detrital rocks, marbles and limestones. Our studies show that basaltic magmas rising to the Earth's surface passed through these marbles and limestones, and assimilated the ancient country rocks. At high temperatures, the marbles and limestones underwent partial decomposition with the release of CO_2. The study of melt inclusions containing ferrocarbonate globules indicates that contamination with sedimentary carbonates occurred simultaneously or even earlier than the crystallization of plagioclase in the basaltic melt. The study of CO_2 fluid inclusions in plagioclase indicates that the contamination of basaltic melts with marbles occurred at a pressure of 0.1 ± 0.01 GPa at a depth of about 4 km.

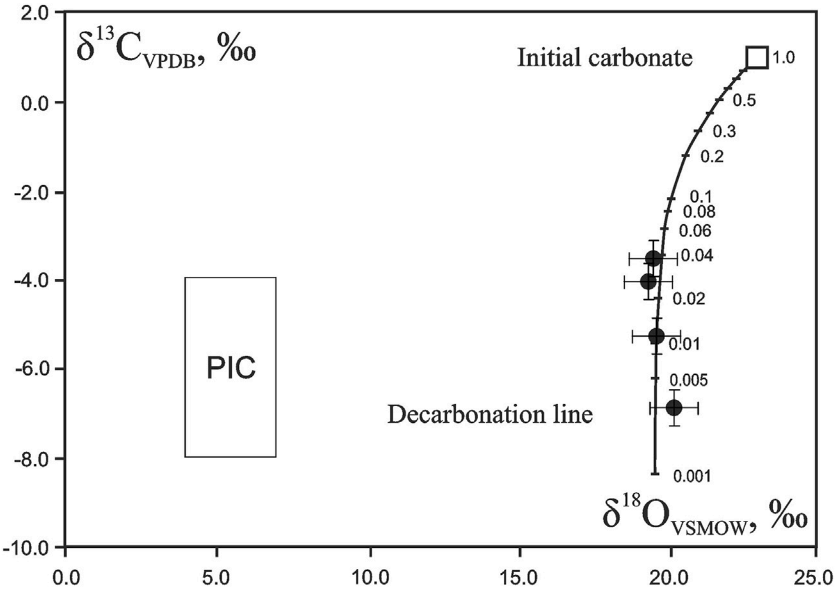

FIGURE 8
$\delta^{13}C$ (‰) versus $\delta^{18}O$ (‰) diagram illustrating evolution of isotopic compositions during decarbonation process associated with basalt formation in Wangtian'e shield volcano. The decarbonation line is calculated using the fractionation factors "calcite-CO_2" for 1,200°C (Scheele and Hoefs, 1992; Chacko and Deines, 2008). PIC represents the compositional field of primary igneous carbonatites according to (Taylor et al., 1967).

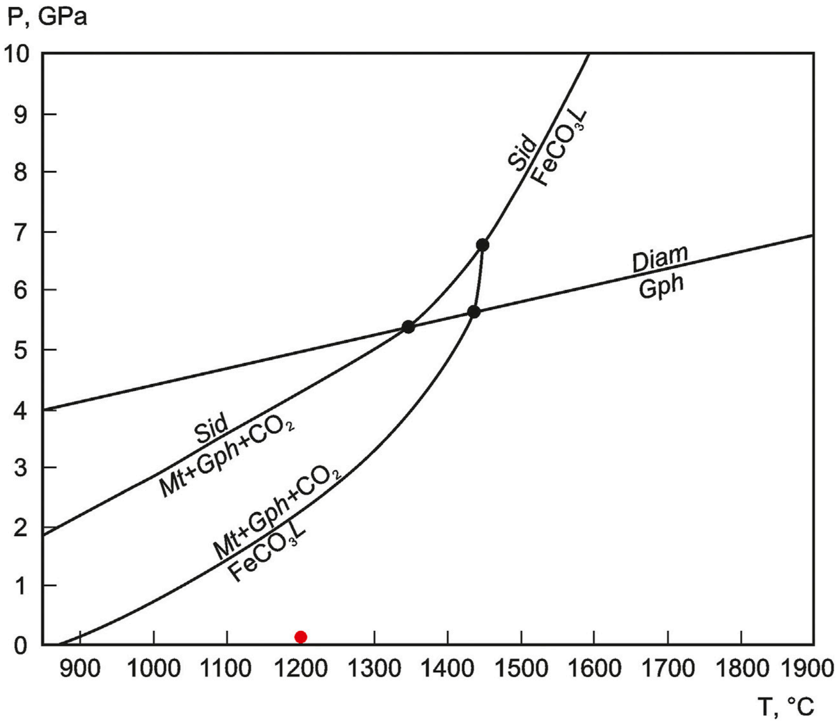

FIGURE 9
P (GPa) versus T (°C) phase diagram illustrating melting reactions of siderite according to the experimental data of Kang et al. (2015). Red point represents T-P parameters of Wangtian'e magmatic chamber. Phase symbols: Sid—siderite, $FeCO_3L$—siderite melt, Mt—magnetite, Gph—graphite, Diam—diamond.

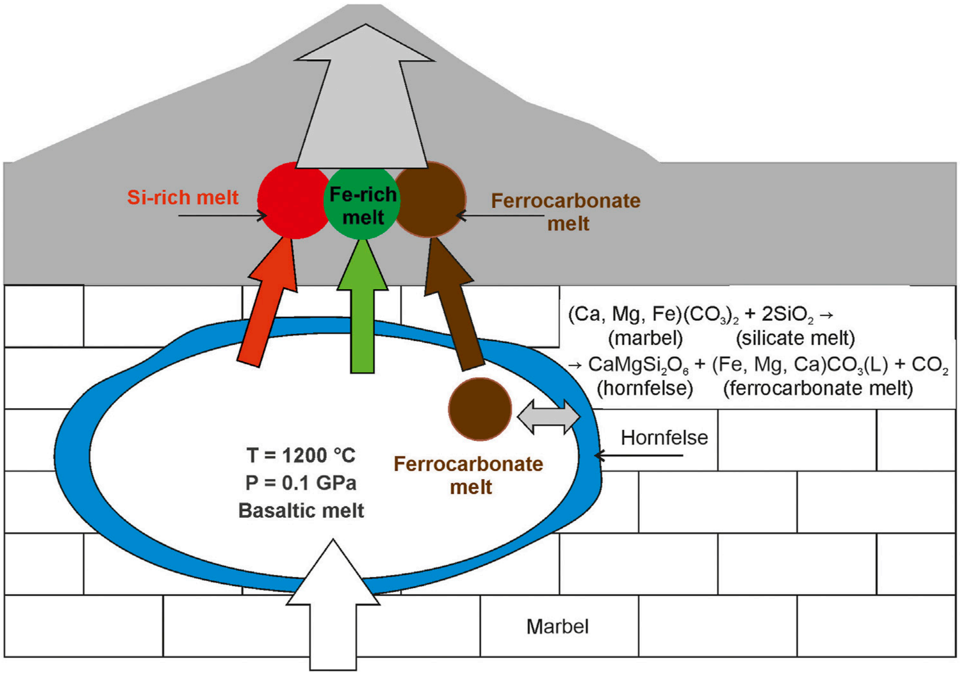

FIGURE 10
Geochemical model of ferrocarbonate formation in Wangtian'e shield basalts showing magma chamber processes: reaction between basaltic melt and host marbel with ferrocarbonate melt production, silicate-ferrocarbonate and silicate-silicate liquid immiscibility.

6.2 Silicate-carbonate immiscibility

The different ferrocarbonate phases in the Wangtian'e tholeiitic basalts occur as groundmass minerals, crystalline inclusions in plagioclase and also as globules in melt inclusions, suggesting that ferrocarbonate minerals crystallized from a ferrocarbonate melt. This is also supported by the occurrence of inclusions of plagioclase, pyroxene, olivine, apatite, and Si-rich glass in ferrocarbonates. According to the experimental phase diagram of Kang et al. (2015), incongruent melting of ferrocarbonate (siderite) occurs with decreasing pressure and temperature, with the formation of a ferrocarbonate liquid (Figure 9). At a temperature of T = 1,200°C and pressure $p = 0.1 \pm 0.01$ GPa, a ferrocarbonate melt exists in the system illustrated on Figure 9. The ferrocarbonate melt can be formed by the interaction of the basaltic melt with host marbles and limestones (Equation 2), according to the following reaction:

$$CaMg(CO_3)_2 + FeCO_3 + 2SiO_2 = CaMgSi_2O_6 + FeCO_3\ (melt) + 2CO_2 \tag{2}$$

where CaMg(CO$_3$)$_2$ is dolomite from limestones, FeCO$_3$ corresponds to iron content in limestone carbonates, SiO$_2$ is a component of silicate melt; and carbon dioxide gas (CO$_2$) is liberated and diopside hornfelses (CaMgSi$_2$O$_6$) with carbonate liquid FeCO$_3$ (melt) which are formed in the magma chamber. At the same time, ferrocarbonate melt coexisted in the magma chamber together with the silicate melt as immiscible liquids. Due to the silicate-carbonate immiscibility and kinetic effect, the ferrocarbonate melt could remained isotopically isolated from the silicate melt.

The stability of the ferrocarbonate melt at temperature and pressure is confirmed by thermodynamic calculations whereby a solidus association of minerals is used instead of a silicate melt. The composition of the initial basaltic melt is taken from the results of the study of melt inclusions in plagioclase (sample B-19). The marble composition is selected from Liu and Jin (2022). Calculations of the interaction between marbles and the solidus association of basalt minerals at T = 1,200°C and pressure $p = 0.1 \pm 0.01$ GPa show that a ferrobasaltic melt is stable in the presence of gaseous carbon dioxide. The calculated composition contains 73.2 wt% FeCO$_3$, 24.0 wt% MgCO$_3$ and 3 wt% CaCO$_3$, which is in good agreement with the observed data. Such a ferrocarbonate melt exists in equilibrium with quartz, wollastonite, diopside and plagioclase. This mineral association corresponds to hornfelses that are formed due to marble assimilation.

The occurrence of quartz rims at the boundary between ferrocarbonate inclusion and the host silicate minerals, apatite, and ilmenite indicates that a certain amount of SiO$_2$ was exsolved from the ferrocarbonate melt upon the inclusion cooling. As the ferrocarbonate cooled and crystallized, the silicic melt initially dissolved in the ferrocarbonate melt was "squeezed" out, forming rims on the inclusion walls.

As shown earlier (Andreeva et al., 2020), the separation of a FeO-enriched (up to 15 wt%) melt into immiscible Fe-rich and Si-rich liquids occurs at the late stages of basalt crystallization upon cooling. Similar processes were described by Lima and Esposito (2023) and Lino et al. (2023). The presence of Si-rich glass in ferrocarbonates suggests that ferrocarbonate mineral crystallization occurred during the final stages of the basalt formation in the Wangtian'e shield volcano upon the magma cooling.

7 Geochemical model

The obtained results lead us to develop a geochemical model for the formation of ferrocarbonates in the basalts of the Wangtian'e shield volcano. As basaltic melts ascended to the surface at a depth of about 4 km, they became to be contaminated with the crustal marbles. The reaction of basaltic melts with marble can be written as follows:

$Ca(Mg, Fe)(CO_3)_2$ (marble) + $2SiO_2$ (silicate melt) → $CaMgSi_2O_6$ (hornfels) + (Fe, Mg, Ca) CO_3 (L) (ferrocarbonate melt) + CO_2 (fluid) (3), where $Ca(Mg, Fe)(CO_3)_2$ is marble component, SiO_2 is silica in the basaltic melt; $CaMgSi_2O_6$ is diopside in hornfels and (Fe, Mg, Ca) CO_3 is ferrocarbonate melt, and CO_2 is fluid component. As a result, diopside hornfelses were formed on the walls of the magma chamber, carbon dioxide exsolved as fluid from the system, and basaltic and ferrocarbonate melts coexisted in the chamber as immiscible (Figure 10). The evolution of the basaltic melt follows the Fenner trend of fractional crystallization, as shown earlier (Figure 2; Andreeva et al., 2020). With decreasing temperature and pressure, the basaltic melt was exsolved to immiscible Fe-rich and Si-rich liquids. At the same time, the ferrocarbonate melt independently crystallized. Thus, three immiscible liquids (Fe-rich, Si-rich, and ferrocarbonate) crystallized during the final stages of tholeiite basalt formation (Figure 10).

8 Conclusion

Ferrocarbonates (or Fe-rich carbonate minerals) are found as minerals in the groundmass of Wangtian'e basalts, and as crystalline inclusions and globules in melt inclusions in the plagioclase. The chemical composition and speciations of ferrocarbonates indicate that they are a product of crystallization of a ferrocarbonate melt. Based on these inclusions we infer that the crystallization of basalts occurred in a near-surface magma chamber at a temperature of 1,180°C–1,200°C and a pressure of 0.1 GPa. Two different silicate-silicate and silicate-carbonate liquid immiscibility processes are distinguished and carbonate immiscibility modeled thermodynamically. The analyzed $\delta^{18}O$ and $\delta^{13}C$ values indicate that ferrocarbonates are of sedimentary origin, undergoing processes of partial decomposition of carbonate and melt-to-carbonate interactions. The isotopically disequilibrium of the ferrocarbonate melt and the host basaltic magma occurred during the interaction of basaltic magma with host crustal marbles. The mineral phase diagram and thermodynamic calculations show that the ferrocarbonate melt is thermodynamically stable at a temperature of 1,200°C and a pressure of 0.1 GPa. Other components of carbonates such as magnesium and calcium are converted to silicates (diopside and wollastonite) in the contact hornfelse rock upon magma cooling.

Data availability statement

The raw data supporting the conclusion of this article will be made available by the authors, without undue reservation.

Author contributions

OA: Conceptualization, Investigation, Methodology, Writing–original draft. ED: Data curation, Investigation, Methodology, Writing–original draft. IA: Investigation, Methodology, Writing–original draft. VVY: Conceptualization, Supervision, Writing–original draft. ABy: Investigation, Methodology, Software, Writing–original draft. ABo: Conceptualization, Supervision, Writing–original draft. J-QJ: Investigation, Writing–original draft. XZ: Investigation, Writing–original draft. EK: Methodology, Writing–original draft. SB: Methodology, Writing–original draft. AA: Methodology, Writing–original draft.

Funding

The author(s) declare financial support was received for the research, authorship, and/or publication of this article. This study was financially supported by the Russian Science Foundation, Project No. 22-17-00033.

Acknowledgments

The manuscript was greatly improved by reviews from Tong Hou, Rosario Esposito and the Editor Simona Ferrando.

Conflict of interest

The authors declare that the research was conducted in the absence of any commercial or financial relationships that could be construed as a potential conflict of interest.

Publisher's note

Supplementary material

The Supplementary Material for this article can be found online at: https://www.frontiersin.org/articles/10.3389/feart.2023.1306460/full#supplementary-material

References

Andreeva, I. A., Yarmolyuk, V. V., and Borisovsky, S. E. (2023). Magma composition and formation conditions of alkali-salic rocks of the Early Mesozoic Adaatsag bimodal association of the Kharkhorin rift zone of Central Asia (data from the study of melt inclusions in minerals). *Dokl. Earth Sci.* 509, 435–442. doi:10.1134/S1028334X22602048

Andreeva, O. A., Andreeva, I. A., and Yarmolyuk, V. V. (2019). Effect of redox conditions on the evolution of magmas of Changbaishan Tianchi volcano, China-North Korea. *Chem. Geol.* 508, 225–233. doi:10.1016/j.chemgeo.2018.09.039

Andreeva, O. A., Andreeva, I. A., Yarmolyuk, V. V., Ji, J.-Q., Zhou, X., and Borisovskii, S. E. (2020). Silicate liquid immiscibility as a result of Fenner-type crystal fractionation of Wangtian'e tholeiitic melts, Northeast China. *Petrology* 28 (4), 357–373. doi:10.1134/s0869591120040025

Andreeva, O. A., Yarmolyuk, V. V., Andreeva, I. A., and Borisovskiy, S. E. (2018). Magmatic evolution of Changbaishan Tianchi volcano, China-North Korea: evidence from mineral-hosted melt and fluid inclusions. *Petrology* 26 (5), 515–545. doi:10.1134/s0869591118050028

Andreeva, O. A., Yarmolyuk, V. V., Andreeva, I. A., Ji, J.-Q., and Li, W. R. (2014). The composition and sources of magmas of Changbaishan Tianchi volcano (China-North Korea). *Dokl. Earth Sci.* 456 (I), 572–578. doi:10.1134/s1028334x14050213

Andreeva, O. A., Yarmolyuk, V. V., Savatenkov, V. M., Andreeva, I. A., Lebedev, V. A., Ji, J.-Q., et al. (2022). Tholeiitic and alkaline basaltic lavas of Wang-Tian'e and Changbaishan volcanoes (northeastern China): timing and genetic relationship. *Dokl. Earth Sci.* 506 (I), 641–649. doi:10.1134/s1028334x22600323

Blythe, L. S., Deegan, F. M., Freda, C., Jolis, E. M., Masotta, M., Misiti, V., et al. (2015). CO_2 bubble generation and migration during magma - carbonate interaction. *Contrib. Mineral. Petrol.* 169, 42. doi:10.1007/s00410-015-1137-4

Borisova, A., and Bohrson, W. A. (2023). How is carbonate crust digested by magma? *Front. Earth Sci.* 11, 1186207. doi:10.3389/feart.2023.1186207

Bottinga, Y., and Richet, P. (1981). High pressure and temperature equation of state and calculation of the thermodynamic properties of gaseous carbon dioxide. *Am. J. Sci.* 281, 615–660. doi:10.2475/ajs.281.5.615

Chacko, T., and Deines, P. (2008). Theoretical calculation of oxygen isotope fractionation factors in carbonate systems. *Geochim. Cosmochim. Acta* 72, 3642–3660. doi:10.1016/j.gca.2008.06.001

Danyushevsky, L. V., McNeill, A. W., and Sobolev, A. V. (2002). Experimental and petrological studies of melt inclusions in phenocrysts from mantle-derived magmas: an overview of techniques, advantages and complications. *Chem. Geol.* 183, 5–24. doi:10.1016/s0009-2541(01)00369-2

Deegan, F. M., Troll, V. R., Freda, C., Misiti, V., Chadwick, J. P., McLeod, C. L., et al. (2010). Magma-carbonate interaction processes and associated CO_2 release at Merapi volcano, Indonesia: insights from experimental petrology. *J. Petrol.* 51, 1027–1051. doi:10.1093/petrology/egq010

Dubinina, E. O., Andreeva, O. A., Avdeenko, A. S., Andreeva, I. A., and Ji, J.-Q. (2020). Oxygen isotope fractionation between phenocrysts and melt: equilibrium estimation for the alkaline lavas of Changbaishan volcano (northeast China). *Petrology* 28 (3), 287–300. doi:10.1134/s0869591120030030

Dubinina, E. O., Aranovich, L. Y., van Reenen, D. D., Avdeenko, A., Varlamov, D., Shaposhnikov, V., et al. (2015). Involvement of fluids in the metamorphic processes within different zones of the Southern Marginal Zone of the Limpopo complex, South Africa: an oxygen isotope perspective. *Precambrian Res.* 256, 48–61. doi:10.1016/j.precamres.2014.10.019

Dubinina, E. O., Filimonova, L. G., and Kossova, S. A. (2019). Isotope ($\delta^{34}S$, $\delta^{13}C$, $\delta^{18}O$) compositions of disseminated sulfide mineralization in igneous rocks of the Dukat ore deposit (Northeastern Russia). *Geol. Ore Depos.* 61 (1), 38–49. doi:10.1134/s1075701519010033

Esposito, R. (2021). "A protocol and review of methods to select, analyze and interpret melt inclusions to determine pre-eruptive volatile contents of magmas," in *Fluid and melt inccusions – applications to geologic processes*. Editor R. Raeside (Canada: MAC) 49, 163–193.

Fan, Q., Liu, R., Li, D., and Li, Q. (1999). Significance of K-Ar age of bimodal volcanic rocks at Wangtian'e volcano, Changbaishan area. *Chin. Sci. Bull.* 44 (7), 660–663. doi:10.1007/bf03182731

Freda, C., Gaeta, M., Misiti, V., Mollo, S., Dolfi, D., and Scarlato, P. (2008). Magma-carbonate interaction: an experimental study on ultrapotassic rocks from Alban Hills (Central Italy). *Lithos* 101, 397–415. doi:10.1016/j.lithos.2007.08.008

Fulignati, P., Kamenetsky, V. S., Marianelli, P., Sbrana, A., and Mernagh, T. P. (2001). Melt inclusion record of immiscibility between silicate, hydrosaline, and carbonate melts: applications to skarn genesis at Mount Vesuvius. *Geology* 29 (11), 1043–1046. doi:10.1130/0091-7613(2001)029<1043:miroib>2.0.co;2

Iacono-Marziano, G., Gaillard, F., and Pichavant, M. (2008). Limestone assimilation by basaltic magmas: an experimental re-assessment and application to Italian volcanoes. *Contributions Mineralogy Petrology* 155, 719–738. doi:10.1007/s00410-007-0267-8

Iacono-Marziano, G., Gaillard, F., Scaillet, B., Pichavant, M., and Chiodini, G. (2009). Role of non-mantle CO_2 in the dynamics of volcano degassing: the Mount Vesuvius example. *Geology* 37, 319–322. doi:10.1130/g25446a.1

Irvine, T. N., and Baragar, W. R. A. (1971). A guide to the chemical classification of the common volcanic rocks. *Can. J. Earth Sci.* 8, 523–548. doi:10.1139/e71-055

Jolis, E. M., Freda, C., Troll, V. R., Deegan, F. M., Blythe, L. S., McLeod, C. L., et al. (2013). Experimental simulation of magma–carbonate interaction beneath Mt. Vesuvius, Italy. *Vesuvius, Italy. Contrib. Mineral. Petrol.* 166, 1335–1353. doi:10.1007/s00410-013-0931-0

Kang, N., Schmidt, M. W., Poli, S., Connolly, J. A. D., and Franzolin, E. (2016). Melting relations in the system $FeCO_3$–$MgCO_3$ and thermodynamic modelling of Fe–Mg carbonate melts. *Contrib. Mineral. Petrol.* 171, 74. doi:10.1007/s00410-016-1283-3

Kang, N., Schmidt, M. W., Poli, S., Franzolin, E., and Connolly, J. A. D. (2015). Melting of siderite to 20GPa and thermodynamic properties of $FeCO_3$-melt. *Chem. Geol.* 400, 34–43. doi:10.1016/j.chemgeo.2015.02.005

Klebesz, R., Esposito, R., De Vivo, B., and Bodnar, R. J. (2015). Constraints on the origin of sub-effusive nodules from the Sarno (Pomici di Base) eruption of Mt. Somma-Vesuvius (Italy) based on compositions of silicate-melt inclusions and clinopyroxene. *Am. Mineral.* 100, 760–773. doi:10.2138/am-2015-4958

Lima, A., and Esposito, R. (2023). New views on Somma Vesuvius subvolcanic system and on mechanism that could increase eruption explosivity by a review and immiscibility in melt inclusions. *J. Geochem. Explor.* 256, 107348. doi:10.1016/j.gexplo.2023.107348

Lino, L. M., Carvalho, P. R., Vlach, S. R. F., and Quiroz-Valle, F. R. (2023). Evidence for silicate liquid immiscibility in recharging, alkali-rich tholeiitic systems: the role of unmixing in the petrogenesis of intermediate, layered plutonic bodies and bimodal volcanic suites. *Lithos* 450-451, 107193. doi:10.1016/j.lithos.2023.107193

Liu, P., and Jin, Z. (2022). Metamorphic evolution of a tremolite marble from the Dabie UHP Terrane, China: a focus on zircon. *J. Earth Sci.* 33, 493–506. doi:10.1007/s12583-020-1363-1

Lopez-Echeverry, J. S., Reif-Acherman, S., and Araujo-Lopez, E. (2017). Peng-Robinson equation of state: 40 years through cubics. *Fluid Phase Equilibria* 447, 39–71. doi:10.1016/j.fluid.2017.05.007

Martini, M. (1997). "CO_2 emission in volcanic areas: case histories and hazards," in *Plant responses to elevated CO_2*. Editors A. Raschi, F. Miglietta, R. Tognetti, and P. van Gardingen (Cambridge University Press), 34–44.

Mollo, S., Gaeta, M., Freda, C., DiRocco, T., Misiti, V., and Scarlato, P. (2010). Carbonate assimilation in magmas: a reappraisal based on experimental petrology. *Lithos* 114, 503–514. doi:10.1016/j.lithos.2009.10.013

Nikiforov, A. V., Dubinina, E. O., Polyakov, N. A., Sugorakova, A. M., and Khertek, A. K. (2021). Influence of host marble rocks on the formation of intrusive alkaline rocks and carbonatites of Sangilen (E. Siberia, Russia). *Minerals* 11, 666. doi:10.3390/min11070666

Nosova, A. A., Sazonova, L. V., Kargin, A. V., Dubinina, E. O., and Minervina, E. A. (2021). Mineralogy and geochemistry of ocelli in the Damtjernite dykes and sills, Chadobets Uplift, Siberian Craton: evidence of the fluid–lamprophyric magma interaction. *Minerals* 11 (7), 724. doi:10.3390/min11070724

Randive, K., and Meshram, T. (2020). An overview of the carbonatites from the Indian subcontinent. *Open Geosci.* 12, 85–116. doi:10.1515/geo-2020-0007

Remigi, S., Mancini, T., Ferrando, S., and Frezzotti, M. L. (2021). Interlaboratory application of Raman CO_2 densimeter equations: experimental procedure and statistical analysis using bootstrapped confidence intervals. *Appl. Spectrosc.* 75 (7), 867–881. doi:10.1177/0003702820987601

Scheele, N., and Hoefs, J. (1992). Carbon isotope fractionation between calcite, graphite and CO_2: an experimental study. *Contrib. Mineral. Petrol.* 112, 35–45. doi:10.1007/bf00310954

Sharp, Z. D. (1990). A laser-based microanalytical method for the *in situ* determination of oxygen isotope ratios of silicates and oxides. *Geochim. Cosmochim. Acta* 54, 1353–1357. doi:10.1016/0016-7037(90)90160-m

Shvarov, Y. V. (2008). HCh: new potentialities for the thermodynamic simulation of geochemical systems offered by Windows. *Geochem. Int.* 46 (8), 834–839. doi:10.1134/s0016702908080089

Taylor, H. P., Frechen, J., and Degens, E. T. (1967). Oxygen and carbon isotope studies of carbonatites from the Laacher See district, West Germany and the Alno district, Sweden. *Geochim. Cosmochim. Acta* 31, 407–430. doi:10.1016/0016-7037(67)90051-8

Tobin, T. S., Bitz, C. M., and Archer, D. (2017). Modeling climatic effects of carbon dioxide emissions fromDeccan Traps Volcanic Eruptions around the Cretaceous–Paleogene boundary. *Palaeogeogr. Palaeoclimatol. Palaeoecol.* 478, 139–148. doi:10.1016/j.palaeo.2016.05.028

USGS (2004). *NE Asia Geodynamics map, 1:5,000,000*. United States: USGS.

Valley, J. W., Kitchen, N., Kohn, M. J., Niendorf, C. R., and Spicuzza, M. J. (1995). UWG-2, a garnet standard for oxygen isotope ratios: strategies for high precision and accuracy with laser heating. *Geochim. Cosmochim. Acta* 59, 5223–5231. doi:10.1016/0016-7037(95)00386-x

Viladkar, S. G. (2018). Ferrocarbonatites in the amba dongar diatreme, Gujarat, India. *J. Geol. Soc. India* 92, 141–144. doi:10.1007/s12594-018-0972-0

Viladkar, S. G., and Schidlowski, M. (2000). Carbon and oxygen isotope geochemistry of the Amba Dongar carbonatite complex, Gujarat, India. *Gondw. Res.* 3 (3), 415–424. doi:10.1016/s1342-937x(05)70299-9

Wang, X., Chou, I.-M., Hua, W., Burruss, R. C., Sun, Q., and Song, Y. (2011). Raman spectroscopic measurements of CO_2 density: experimental calibration with high-pressure optical cell (HPOC) and fused silica capillary capsule (FSCC) with application to fluid inclusion observations. *Geochim. Cosmochim. Acta* 75, 4080–4093. doi:10.1016/j.gca.2011.04.028

Wojdyr, M. (2010). Fityk: a general-purpose peak fitting program. *J. Appl. Cryst.* 43, 1126–1128. doi:10.1107/s0021889810030499

Xue, Y. X., and Zhu, Y. F. (2007). Genesis of the siderite in jurassic olivine basalt, Karamay, xinjiang, NW China. *Acta Petrol. Sin.* 23 (5), 1108–1122. doi:10.0000/5eb7925da4b74345a065c20f6f711d4a

Zhao, S., Schettino, E., Merlini, M., and Poli, S. (2019). The stability and melting of aragonite: an experimental and thermodynamic model for carbonated eclogites in the mantle. *Lithos* 324-325, 105–114. doi:10.1016/j.lithos.2018.11.005

Frontiers in
Earth Science

Investigates the processes operating within the major spheres of our planet

Advances our understanding across the earth sciences, providing a theoretical background for better use of our planet's resources and equipping us to face major environmental challenges.

Discover the latest Research Topics

See more →

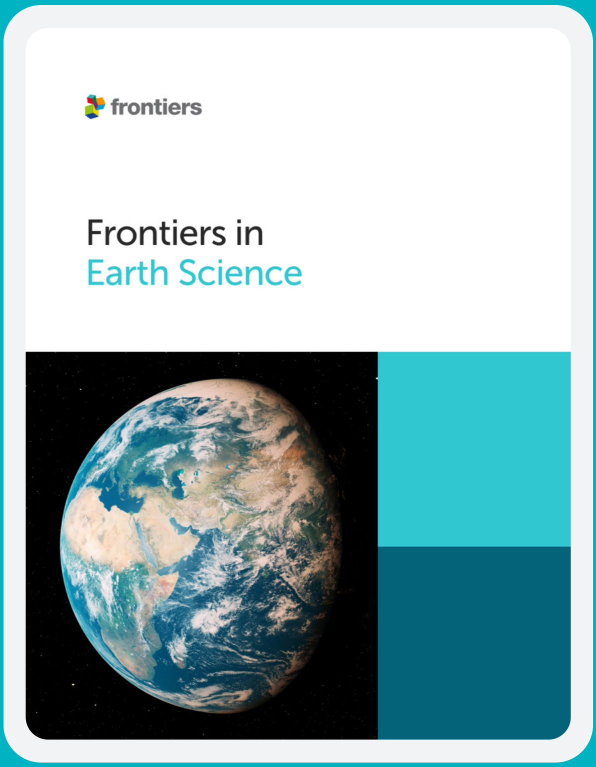

frontiers

Frontiers in
Earth Science

Frontiers

Avenue du Tribunal-Fédéral 34
1005 Lausanne, Switzerland
frontiersin.org

Contact us

+41 (0)21 510 17 00
frontiersin.org/about/contact